Editorial

To see a World in a Grain of Sand
And a Heaven in a Wild Flower,
Hold Infinity in the palm of your ha
An Eternity in an hour.

William Blake

Isotopes which differ from each other by just a few nucleonic masses (10^{-24} gm), are finely ordered in many a natural system as an integrated result of atomic and thermodynamic processes. Relative concentrations of isotopes in an object thus carry incisive information on the rates of natural processes as well as on the chronology of critical events in a system's evolution, right from the time of their formation in the universe. Such information constitutes the key to resolving a host of discriminating questions in

date minerals fro
pioneering work i
amongst the ear
geological process

The scene was
the secrets of eart
isotopic windows.

u
d
r
h
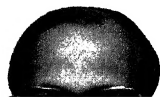
to realize his dream of unravelling the chronology of terrestrial as well as extra-terrestrial processes and objects. This was one of the prime motivations behind the construction of a 4.5″ radius Reynolds' type mass spectrometer which Gopalan and M N Rao built in a record time of a year by drawing upon the excellent glass blowing facilities of TIFR. This ultra-high vacuum mass spectrometer which incidentally drew a compliment from Reynolds himself, was extensively used for over two decades for noble gas measurements in meteorites and soil samples brought by the Russian Luna 16 and 17. A prototype of this instrument built by him later was used to obtain the first K-Ar ages of Deccan basalts and later, the chemical and isotopic make up of their source material in the earth's upper mantle, questions that had held a challenge to Gopalan's psyche.

The second mass spectrometer built to address the by now growing clamour amongst Indian geoscientists for well constrained chronologies of the Indian rocks, was a 9″ radius Thermal Ionization Mass Spectrometer (TIMS) set up by Gopalan at PRL, a mere eight years after his initiation into geochronology at the Indian Institute of Science. This system was literally built from the bits and pieces of a gas source mass spectrometer which had been donated by DTM to TIFR, and fortuitously the yet unused spare flight tube, for the study of Rb-Sr chronologies. This solid source mass spectrometer had a performance comparable to contemporary systems elsewhere, and was immediately used to determine the first most comprehensive and definitive Rb-Sr ages of rocks from the Rajasthan Craton in northwestern India. A serendipitous discovery, in this quest, was the existence of Archean relics of a primitive continental crust in Rajasthan,

These s
landmarks
past, using
and other
important
ion probe
Recent cre
Goswami a
subtle isot
shown tha
responsible
ite parent

Having
later devel
mid-eighti
truly proc
Indian end
by now ha
of purpose
facility at
isotopic c
rocks lodg
actively e
develop n
metry. No
stable isot
sniffer wh
decade to
are diagn
fracture s

Few inc
and uncor
scholarshi
lifelong pa
Gopalan's

painstakingly reviewed by discerning referees. I owe them all a deep debt of gratitude and hope that the scientific quality of papers herein will prove to be an ample reward for their labours, as it might also be an illuminating record of this fast evolving field for students and researchers in this field.

The volume contains four invited papers from Professors D Lal, J D McDougall, R K O'Nions and G J Wasserburg, all of whom deeply empathized with Gopalan's serious endeavours to establish the high culture of geochronology in India. Other papers expose

new significant fin
archives, using iso
Many of these hav
lenting efforts and
individual sensible
and now'. This vo
ever vibrant spirit
lities for many oth

Important crustal growth in the F[
Isotopic evidence of granitoids from e[

BOR-MING JAHN[1], FUYUAN WU[1,2] and DAW[

[1]*Géosciences Rennes, Université de Rennes 1, 35042 Ren[*
email: jahn@univ-rennes1.fr
[2]*Department of Geology, Changchun University of Science and Techno[*
[3]*Lithosphere Research Centre, CAGS, Beijing 100[*

The growth of the continental crust is generally believed to have been [
Precambrian, and the amount of juvenile crust produced in the Phanerozo[
Such idea of negligible growth in the Phanerozoic is now challenged by the r[
of juvenile crust produced in the period of 500 to 100 Ma in several org[
volumes of juvenile terranes in North America (Canadian Cordillera, S[
Range, Appalachians) have been documented based on Nd isotopic data, th[
the East-Central Asian Orogenic Belt (ECAOB), eastern part of the Altaid[
be much greater than the above terranes combined. New and published Nd[
the Phanerozoic granitoids from the southern belt of the ECAOB (X[
Mongolia-NE China) as well as from Mongolia and Transbaikalia were gene[
by a depleted mantle component. These granitoids represent a significant g[
Phanerozoic.

Although most plutons in this huge orogenic belt belong to the calc-alka[
characterized by the emplacement of voluminous A-type granites. The ori[
multiple and is still widely debated. However, the isotopic data (Sr-Nd-O)[
patterns of A-type granites from the ECAOB clearly indicate their mantle[

The evolution of the ECAOB and the entire Altaid Collage is most likely[
of arc complexes. However, the emplacement of a large volume of post-tec[

mass has been added in an episodic or continuous fashion (Moorbath 1978; Stein and Hofmann 1994) is another issue of debate. In all cases, the amounts of new continental material or juvenile crust formed in the Phanerozoic, and especially in the last 250 Ma, have been considered to be very minor or insignificant. However, this scenario has undergone revision in the

last decade
lera (Sams

In east-c
rocks of lat
in the Eas
bounded b
(figure 1).
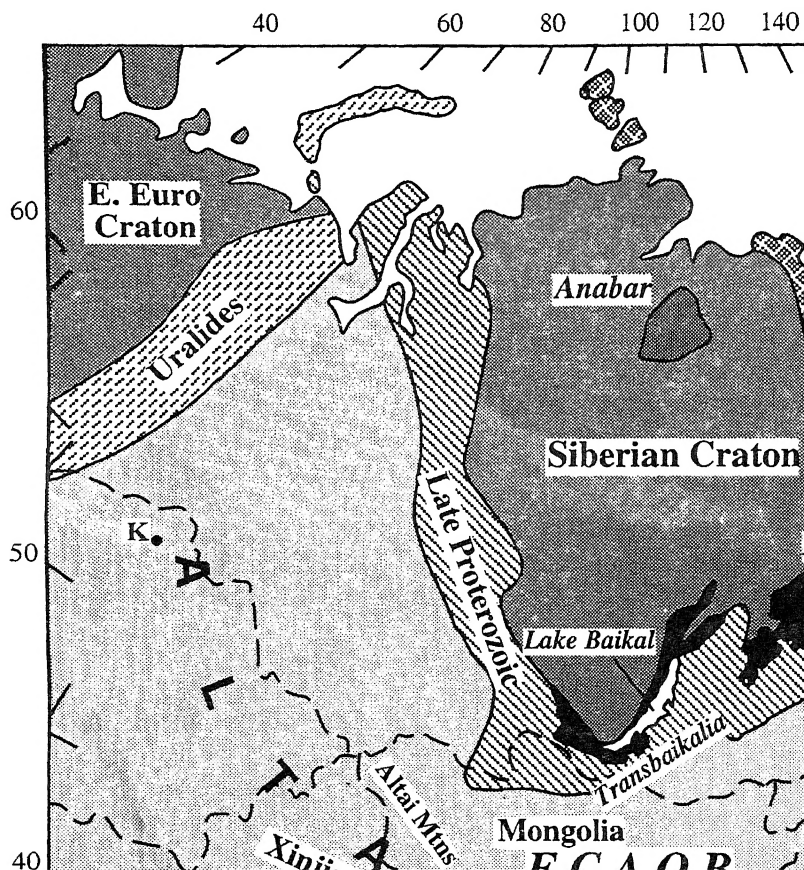
of it and up to the Ural Mountains have been collectively called Altaid Tectonic Collage (Sengör *et al* 1993; Sengör and Natal'in 1996). The Altaid Collage is different from the classical collisional orogens, such as the Alpine, Himalayan, Hercynian and Caledonian belts. According to Sengör and his collaborators (Sengör *et al* 1993; Sengör and Natal'in 1996), it was formed by accretion of arc complexes produced in subduction zones, and is characterized by the emplacement of immense volumes of granitic magmas and the general absence of nappe complexes imbricating older continental crust. However, the statement on the general absence of nappe complexes has been challenged by subsequent works, particularly in Kazakhstan (e.g., Gruschka *et al* 1997).

In the ECAOB, two gigantic belts of alkaline syenites and granites may be recognized: (**1**) a northern belt from northern Mongolia to Transbaikalia, and (**2**) a southern belt from Xinjiang (western China) through southern Mongolia to NE China (Manchuria). According to recent publications, more than 350 distinct granitic plutons are exposed in northern Mongolia and Transbaikalia and occupy a total area $\geq 500,000 \, \mathrm{km}^2$ (Zanvilevich *et al* 1995; Wickham *et al* 1995, 1996). In NE China, several hundred granitic bodies have been identified and constitute an area of $\approx 100,000 \, \mathrm{km}^2$. Numerous granitic bodies also occur in northern Xinjiang and western Mongolia (Altai Mountains). Undoubtedly, this orogenic belt contains the most voluminous young granitic intrusions in the world. However, the precise time of the emplacement and origin of these granitoids, as well as their geodynamic significance in the context of Phanerozoic continental evolution are still poorly known and remain among the most pressing questions of crustal evolution to be answered.

magmas with hig[...]
heritage, the youn[...]
granites, became [...]
their oxygen isoto[...]
series of importan[...]
place in east-centr[...]

The purposes o[...]

- to document th[...]
  granitoids from[...]
  and our unpubl[...]
- to discuss the [...]
  Phanerozoic cru[...]

We advocate th[...]
represent the mos[...]
mantle to the con[...]

2. Brief acco[...]
and empla[...]

According to Kov[...]
in Mongolia and [...]
the entire Phaner[...]
ruption. Most ag[...]
estimated by pal[...]
graphic means, on[...]
mined by radioch[...]

Since the early [...]
have been emplac[...]

- the calc-alkalin[...]
  ite) of Caledon[...]
  Transbaikalia ([...]
  novsky *et al* 19[...]
- the late Caledo[...]

contain abundant miarolitic cavities and igneous layering formed by biotite-rich bands. Mafic enclaves are generally rare; but in Transbaikalia (Zanvilevich *et al* 1995; Wickham *et al* 1995, 1996) significant amounts of mafic rocks occur as enclaves and synplutonic dykes in granitoids of various ages.

The ages of granites roughly decrease from north to south within the ECAOB. In Transbaikalia and northern Mongolia, five main stages of K-rich magmatic activity have been distinguished (Zanvilevich *et al* 1995; Wickham *et al* 1995, 1996): (**1**) Ordovician-Silurian (≈ 450 Ma, U-Pb), (**2**) Devonian (≈ 375 Ma), (**3**) Early Permian (≈ 280 Ma), (**4**) Late Permian (≈ 250 Ma), and (**5**) Triassic (≈ 220 Ma). In northern Xinjiang, granites of high-K to medium-K series appear to dominate; most of these were emplaced intruded in the period of 400-200 Ma (Hu *et al* 2000a, b). However, A-type granites, exposed mainly along the Ulungur River, were intruded at about 300 Ma (Rb-Sr ages, Wang *et al* 1994; Han *et al* 1997). A-type granites in central inner Mongolia were emplaced slightly later at ca. 280 Ma (whole-rock Rb-Sr, Hong *et al* 1995). In both northern Xinjiang and Inner Mongolia, in addition to A-type granites, granitoids of early Paleozoic to Mesozoic ages also occur. Further east to NE China the existing age data indicate three intrusive episodes for K-rich granitoids (Fang, 1992; Wu and Jahn, unpublished results): (**1**) late Permian (270-250 Ma), (**2**) late Triassic-early Jurassic (220-180 Ma), and (**3**) middle Jurassic (170-150 Ma). Thus, there is an apparent younging trend of granitic intrusions from the west to the east along the ECAOB.

In addition to the apparent regional age variation, two trends are also observed:

- a regular decrease in size for younger plutons, and
- an increase in the proportion of syenite and alkaline granite to granite (s.s.), as well as in the ratio of K-feldspar to plagioclase, with the younging of plutons.

That is, the younger plutons tend to be more alkaline in nature. In Transbaikalia, peralkaline granites and syenites containing aegirine and arfvedsonite only occur in the younger Permian and Triassic suites (Kuzmin and Antipin 1993; Wickham *et al* 1995, 1996; Kononova *et al* 1996). However, we note that in the southern belt (Xinjiang-Inner Mongolia-NE China) such an increase of alkalinity of granitoids with the decrease of intrusive ages is not as clearly documented as in Transbaikalia (Hong *et al* 1996).

3. Nd-Sr-O isotopic data for granitoids of the ECAOB

Precise age data are vital to estimate the production rate of juvenile crust. However, within such volumi-

them have been reliably dated. Most of the intrusive ages reported in the literature are based on geological correlations or other non-radiochronometric means (Litvinovsky, personal comm.; see also Kovalenko *et al* 1995).

The age information and Nd-Sr isotopic data used in this paper come from two sources:

- unpublished results obtained in Rennes (on granites of NE China and inner Mongolia), and
- results published in international journals, some of which were obtained in Rennes (Kovalenko *et al* 1992; Zhao 1993; Hong *et al* 1995; Chen *et al* 1995; Zhou *et al* 1995; Arakawa and Shimura 1995; Han *et al* 1997).

We have included here the granitoids of the Hida Belt of Japan, which has been considered as part of the Asian continent prior to the opening of the Japan Sea (Hirooka *et al* 1983; Mizutani and Hattori 1983; Cluzel 1991).

All unpublished data are presented graphically and the analytical values will be reported elsewhere (Wu *et al* 2000). Figure 2 shows a plot of initial Sr isotopic ratios (I_{Sr}) as a function of $^{87}Rb/^{86}Sr$ ratios for some granitoids from the southern belt of the ECAOB. High $^{87}Rb/^{86}Sr$ ratios (up to 100) are indicative of A-type and highly differentiated I-type granitoids. Note that the I_{Sr} values were individually calculated by subtracting the radiogenic components from the measured $^{87}Sr/^{86}Sr$ ratios; they may bear large uncertainties for high Rb/Sr rocks, and not uncommonly yield unreasonably low ratios of less than 0.700 (figure 2). The Rb/Sr induced errors (ξ) for calculated initial $^{87}Sr/^{86}Sr$ ratios are related to three factors: Rb/Sr ratio, assigned uncertainty for the Rb/Sr ratio, and isochron age, all related by the equation:

$$\xi = {}^{87}Rb/^{86}Sr \times \% \text{ error} \times (e^{\lambda t} - 1).$$

Take, for example, three cogenetic 300 Ma granites with $^{87}Rb/^{86}Sr$ ratios of 1, 10, and 100. If a 2% error is assigned for their $^{87}Rb/^{86}Sr$ ratios, then they would have uncertainties for the calculated initial $^{87}Sr/^{86}Sr$ ratios of ± 0.000085, ± 0.00085, and ± 0.0085, respectively. Thus, assuming the initial $^{87}Sr/^{86}Sr$ ratio for them to be 0.705, a calculated I_{Sr} for the third granite as low as 0.6965 is possible, though completely meaningless. We note that a single unreasonably low I_{Sr} of 0.698 was reported for a granite of relatively low Rb/Sr ratio ($^{87}Rb/^{86}Sr \approx 1.2$) from western Mongolia (Kovalenko *et al* 1992). This is likely to be due to postmagmatic Rb/Sr open system behavior or some analytical problem. Nevertheless, most I_{Sr} values for low Rb/Sr rocks seem to show a restricted range of I_{Sr} values from 0.702 to 0.707 (figure 2), which is rather low for most granitic rocks formed in Phanerozoic orogenic belts. The data suggest that contribution of
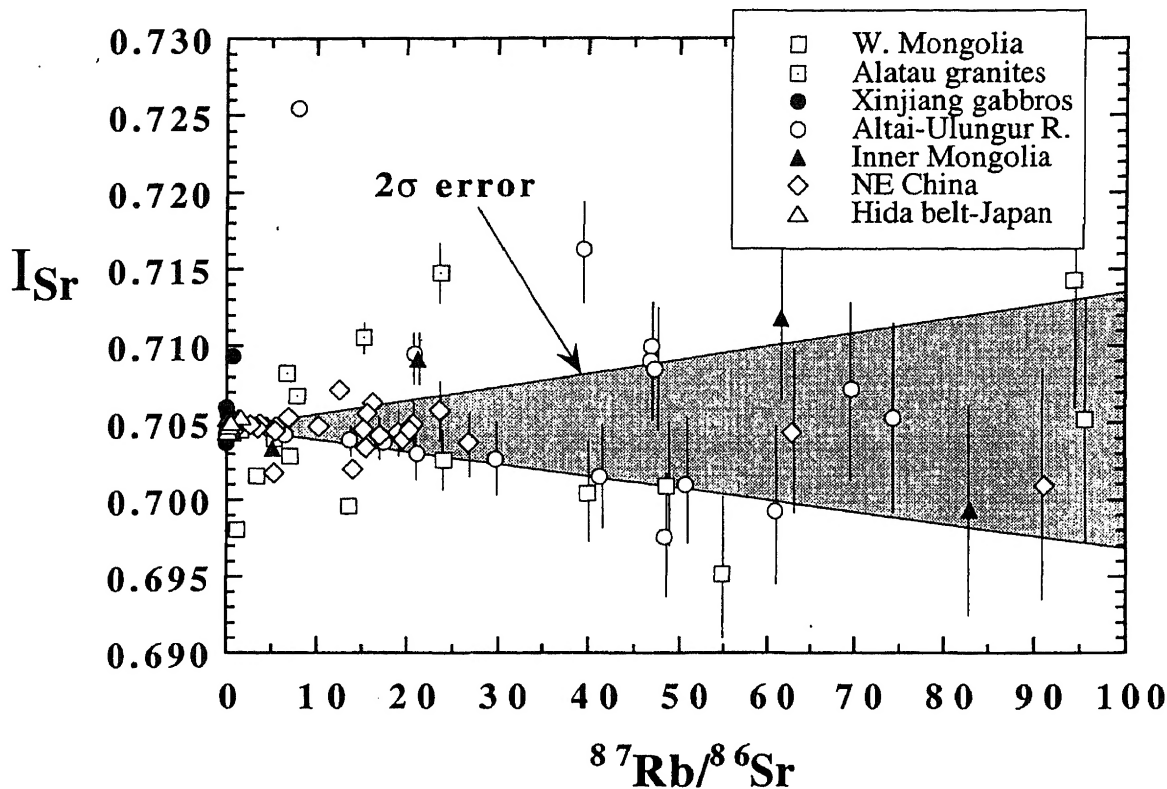
Figure 2. Initial $^{87}Sr/^{86}Sr$ (=I_{Sr}) vs $^{87}Rb/^{86}Sr$ plot for Phanerozoic granitoids from the ECAOB. Data of Xinjiang gabbros (Chen *et al* 1995) are also shown for comparison. The more reliable I_{Sr} values for rocks with Rb/Sr ratios less than 20 are found between 0.702 and 0.707, a range considered as relatively low for Phanerozoic granitic rocks. I_{Sr} values calculated from rocks with high to very high Rb/Sr ratios are too imprecise to have any useful petrogenetic meanings. Grey area indicates the propagation of error size induced by 2% Rb/Sr uncertainty in I_{Sr} values.

ancient crustal material in the petrogenesis of these granitic rocks was limited.

Relative to Sr, Nd isotopic data can provide a much clearer constraint to the origin of granitic rocks. Many Altaid granites are characterized by positive $\varepsilon_{Nd}(T)$ values (figure 3). The ranges for individual terrains are: $+6.7$ to $+5.1$ for 21 A-type granites of Xinjiang (Zhao 1993; Han *et al* 1997), $+5.4$ to $+3.0$ for 4 A-type granites of Inner Mongolia (Jahn, unpublished), and $+2.8$ to $+1.2$ for 25 highly differentiated I-type granites from NE China (Wu *et al* 2000). In addition, a variety of granitic rocks from northern Xinjiang indicate a range of $\varepsilon_{Nd}(T)$ values from as high as $+7$ for alkali granites from the Ulungur River area to as low as -5 for biotite granites from other localities (Zhao 1993). Kovalenko *et al* (1992) obtained a range of $\varepsilon_{Nd}(T)$ values from $+7.7$ to $+3.0$ for 17 granitic rocks (age ≈ 378 Ma) from the Altai Mountains of western Mongolia. Additional data for granites of the Alatau Mountains and for gabbros of west Tianshan in western Xinjiang are shown for comparison in figure 3. Note that many of the granitic rocks have the same $\varepsilon_{Nd}(T)$ values as the mantle-derived gabbroic rocks. These data thus provide strong evidence for depleted material as the major source of magmatism in the southern belt of the ECAOB. The same

conclusion was also reached from Pb isotopic studies on K-feldspars of granitoids from the western Junggar region in Xinjiang (Kwon *et al* 1989; Jin and Zhang 1993).

These isotopic data are in strong contrast to those for most Phanerozoic granites occurring in the classical collisional orogens. The latter were mainly produced by remelting of older continental crust and are characterized by negative $\varepsilon_{Nd}(T)$ and high I_{Sr} values, as exemplified by the Hercynian granites of south Brittany and the Massif Central in France, and the Manaslu leucogranites of the Himalayas (figure 4). So far, we are not aware of any coupled Nd-Sr isotopic data published for granites of Transbaikalia. However, the Triassic Kharitonovo pluton of Transbaikalia (alkaline and peralkaline rocks, $T \approx 240$–220 Ma) is characterized by low initial $^{87}Sr/^{86}Sr$ ratios of about 0.704 (Zanvilevich *et al* 1995). This pluton has a range of "primary" magmatic whole-rock $\delta^{18}O$ values of $+6.5$ to $+4.5‰$, deduced from alteration-resistant titanite $\delta^{18}O$ data (ca. $+3$ to $+0.5‰$), which is consistent with derivation from upper mantle rocks (Wickham *et al* 1995, 1996).

Sm-Nd fractionation during magma genesis may change model ages to some extent, depending on the partition coefficient of Sm/Nd of the fractionated
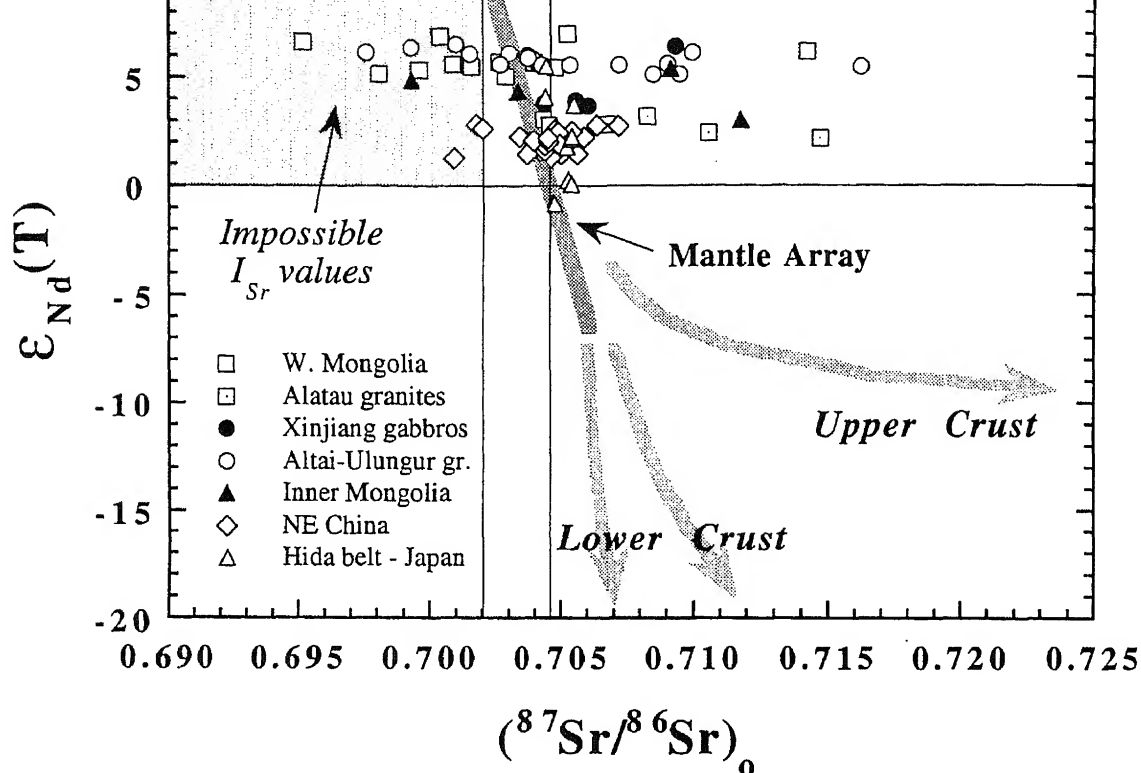
Figure 3. Plot of $\varepsilon_{Nd}(T)$ vs initial $^{87}Sr/^{86}Sr$ isotopic ratios for Phanerozoic granitoids from the ECAOB. Data for Tianshan gabbros of Xinjiang are also shown for comparison. The calculated $(^{87}Sr/^{86}Sr)_o$ or I_{Sr} values have a wide range, which is due partly to the large uncertainty inherent in rocks of high Rb/Sr ratios and partly to open system in low Sr alkaline granites. However, the restricted and positive $\varepsilon_{Nd}(T)$ values are indicative of the juvenile characteristics and formation of new continental crust.

phases. Rocks with high $f_{Sm/Nd}$ ratios (e.g., -0.2 to 0, or positive values) are often observed in A-type granites produced through fractional crystallisation; they often produce aberrant and meaningless T_{DM} ages. Similarly, some of the very low Sm/Nd ratios or highly negative $f_{Sm/Nd}$ values (-0.6 to -0.7) as shown in figure 5 could also reflect a fractionation effect. However, the young and small range of T_{DM} ages, covering a large variation of $f_{Sm/Nd}$ values (figure 5), cannot be only due to REE fractionation. The overall scenario is convincing evidence for a significant mantle contribution in the genesis of these granites.

Abundant Nd isotopic data have been published by Kovalenko *et al* (1992, 1996) for Phanerozoic granitic rocks from the central to northern belts of the ECAOB (Mongolia and Transbaikalia). Using the Nd model age (T_{DM}) approach, Kovalenko *et al* (1996) delineated three isotope provinces (Caledonian, Hercynian, and pre-Riphean) which coincide with three tectonic zones of corresponding ages. In each province the model ages are limited in a narrow range, regardless of the emplacement age of the granites. We re-summarize their Nd isotopic data in figures 6–8. Without exception, Phanerozoic granites emplaced into Caledonian and Hercynian tectonic zones have positive $\varepsilon_{Nd}(T)$ values, suggesting their juvenile characteristics; whereas those intruded into the pre-Riphean basement show variable $\varepsilon_{Nd}(T)$ from positive to negative values, hence indicating variable proportions of old Precambrian crust mixed with the mantle peridotite in their source (figure 6). Note that some late Neoproterozoic to early Paleozoic granites (600–500 Ma) have $\varepsilon_{Nd}(T)$ values as high as $+10$ indicating their derivation from an almost pure depleted mantle component.

Figure 7 illustrates that the majority of the rocks emplaced in the Caledonian and Hercynian belts have Sm-Nd model ages (T_{DM}) younger than 1000 Ma, whereas those intruded in the Precambrian terranes have an older range from ca. 800 to 2500 Ma. If the rocks with high $f_{Sm/Nd}$ values (≥ -0.2, shown in the grey region of figure 8) are excluded, then all granitoids from Mongolia and Transbaikalia would have T_{DM} limited to 1500 Ma (figure 8). Nevertheless, granites intruded in the Pre-Riphean basement generally have lower $\varepsilon_{Nd}(T)$ values and higher T_{DM} than those intruded in the Caledonian and Hercynian belts. This is consistent with the nature of the crustal contaminant (older), but not necessarily a greater proportion of crust/mantle mixing.
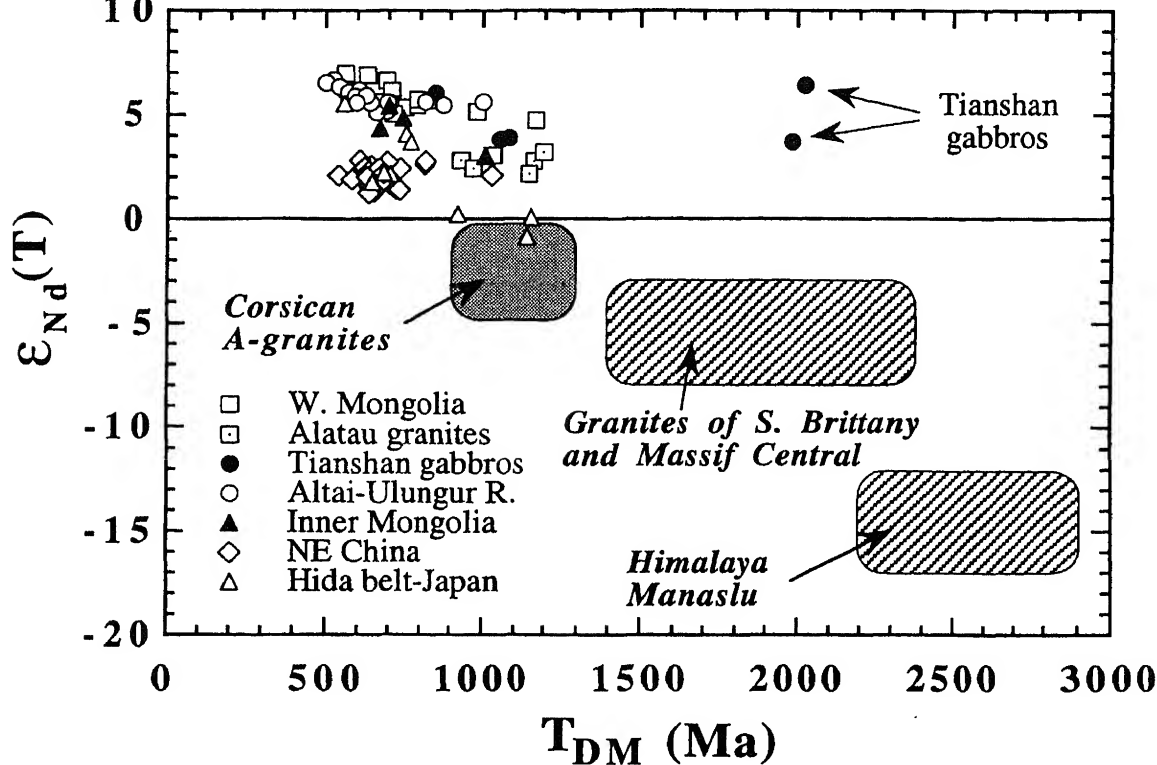
Figure 4. $\varepsilon_{Nd}(T)$ vs T_{DM} plot for Phanerozoic granitoids from the ECAOB. Data for Tianshan gabbros of Xinjiang are shown for comparison. The model ages are young, ranging from 500 to 1200 Ma, and are in strong contrast with those of the majority of Phanerozoic granitic rocks in the world. The young T_{DM} of the Altaid granites suggest their derivation from depleted mantle-dominated source rocks. **Data sources:** Corsican A-type granites (Poitrasson *et al* 1995); granites of S. Brittany (Bernard-Griffiths *et al* 1985); granites of Massif Central (Downes *et al* 1997); leucogranites of Himalaya—Manaslu (Vidal *et al* 1984); Tianshan gabbros (Chen *et al* 1995).
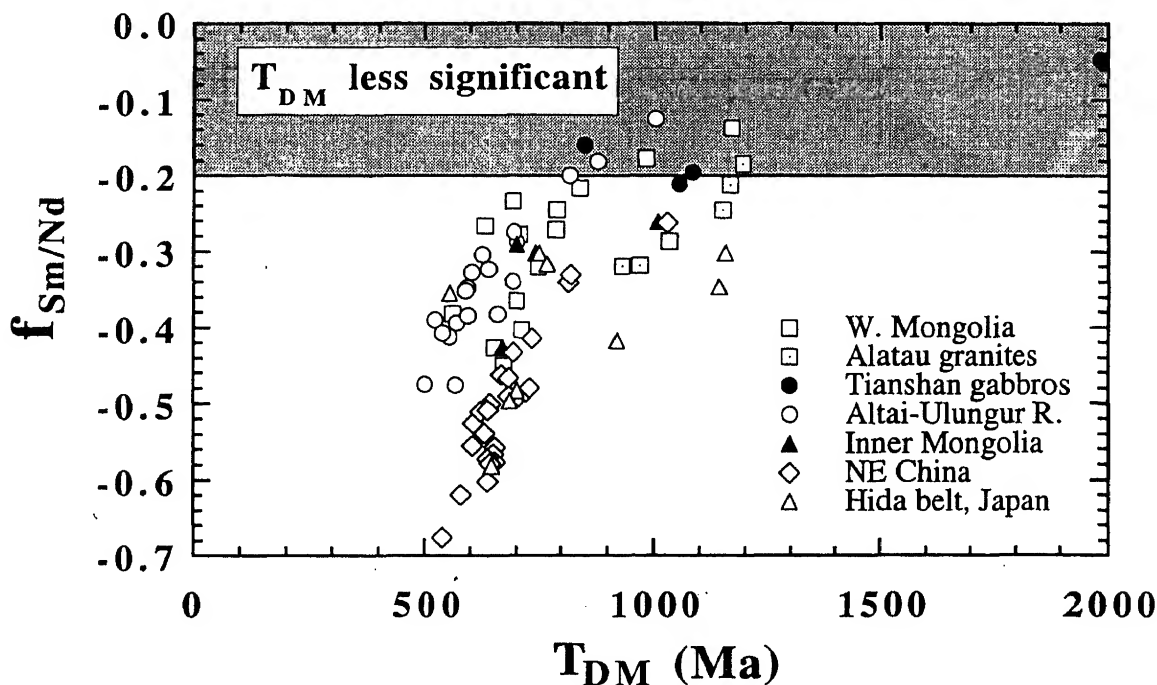
Figure 5. $f_{Sm/Nd}$ vs T_{DM} plot for Phanerozoic granitoids from the ECAOB. Data for Tianshan gabbros are shown for comparison. T_{DM} for rocks with $f_{Sm/Nd}$ values higher than -0.2 (or $^{147}Sm/^{144}Nd$ ratio of 0.157) may produce large uncertainty in model age calculation, hence they are less significant and excluded from discussion. Despite the large range of $f_{Sm/Nd}$ values, the calculated model ages are "young" in comparison with most Phanerozoic granitic rocks (ca. 1.5 to 2.0 Ga).
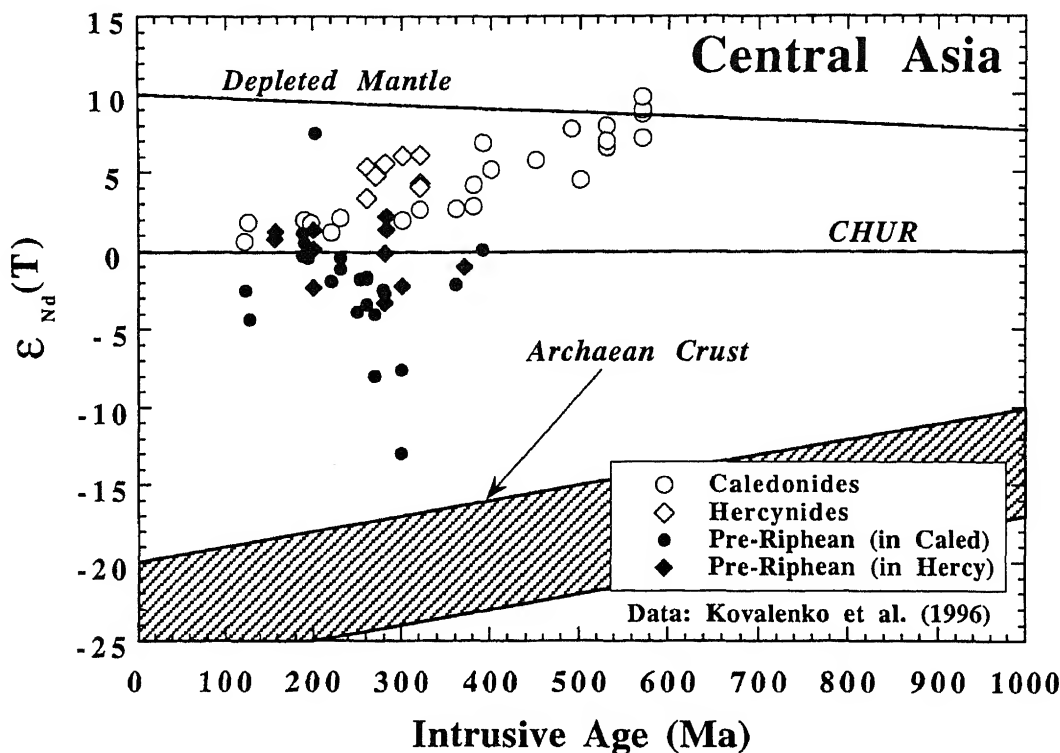
Figure 6. $\varepsilon_{Nd}(T)$ vs intrusive age plot for Phanerozoic granitoids from Mongolia and Transbaikalia (data from Kovalen[ko et al.] 1996). Granites intruded in Caledonian and Hercynian belts (open symbols) are characterized by positive $\varepsilon_{Nd}(T)$ values, [while] those intruded in pre-Riphean basement "enclaves" within Caledonian and Hercynian belts (black symbols) have both [positive] and negative $\varepsilon_{Nd}(T)$ values.
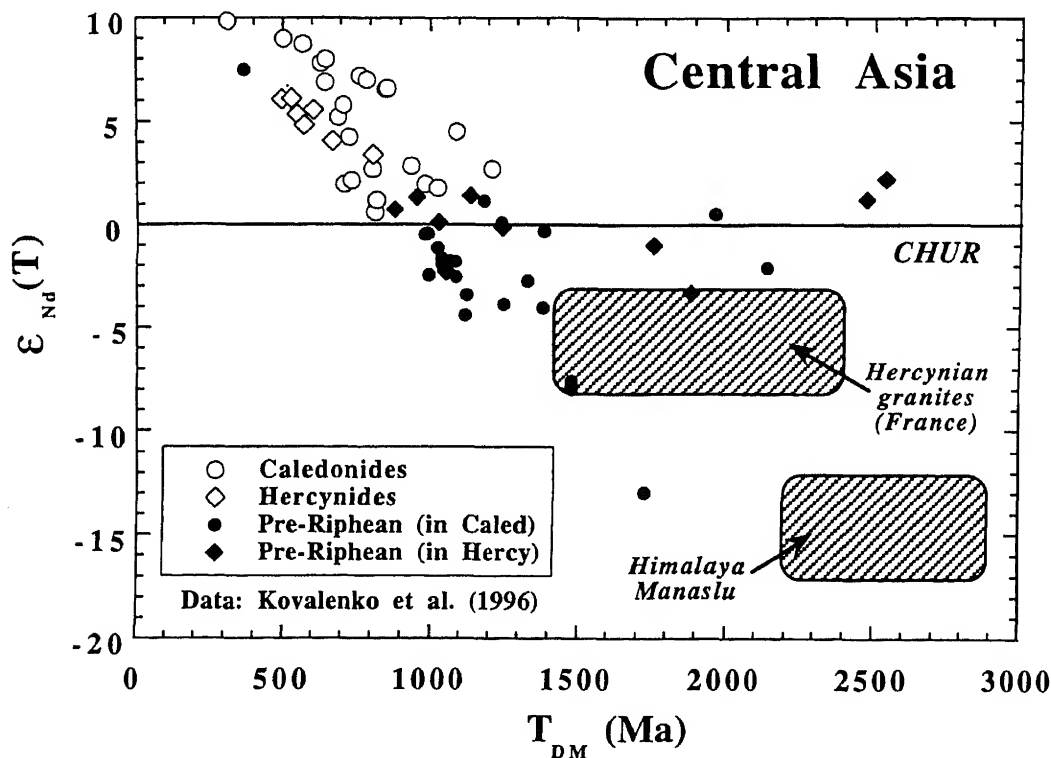
Figure 7. $\varepsilon_{Nd}(T)$ vs T_{DM} plot for Phanerozoic granitoids from Mongolia and Transbaikalia (data from Kovalenko *et al*[.]. Model ages (T_{DM}) are young (300 to 1200 Ma) for those intruded in Caledonian and Hercynian belts, which are sim[ilar to] Phanerozoic granitic rocks from the southern belt of the ECAOB. T_{DM} are generally older (800–2500 Ma) for those intru[ded in] pre-Riphean basement, suggesting more involvement of Precambrian crustal material in their petrogeneses.

Figure 8. $f_{Sm/Nd}$ vs T_{DM} plot for Phanerozoic granitoids from Mongolia and Transbaikalia (data from Kovalenko *et al* 1996). The data in the grey zone are excluded from discussion. The calculated model ages are still "young" in comparison with most Phanerozoic granitic rocks (ca. 1.5 to 2.0 Ga).

4. Discussion

4.A *Genesis of the Phanerozoic crust*
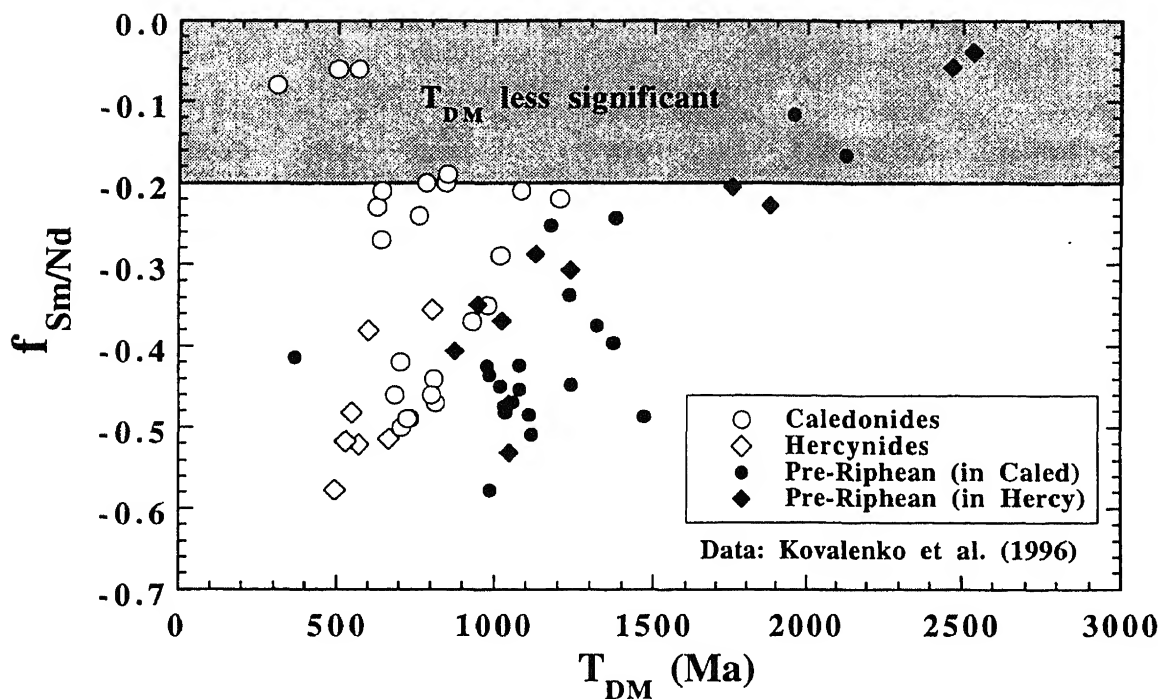
Until now, the best documented examples of Phanerozoic juvenile granitic rocks are those from the Mesozoic Sierra Nevada and Peninsular Range batholiths in the western U.S. (DePaolo 1981), the Canadian Cordillera (Samson *et al* 1989; Samson and Patchett 1991), and the Appalachians (Whalen *et al* 1996; Samson 1998). While a significant mantle contribution to the generation of the Altaid granitoids is indicated by the Nd isotopic evidence, the precise mechanisms for the growth and evolution of the Phanerozoic continental crust remain debatable. Several pertinent questions include:

(1) Could subduction processes (Sengör *et al* 1993) alone be responsible for formation of the juvenile crust?

(2) Could the granites in this region have been formed by partial melting of a "young" mafic lower crust which was underplated during post-thickening extensional collapse, as envisioned for the Hercynides in the Massif Central (Costa and Rey 1995)?

(3) Was intraplate magmatism a significant process of continental growth, particularly during the Phanerozoic?

(4) Did the underplated mantle melts (basaltic liquids) interfinger with pre-existing granulites of various compositions, much like the model given by Wickham *et al* (1996), which together were

then melted to produce granite, with the residue sinking back into the mantle by processes like delamination?

(5) Is the Phanerozoic a major period of continental growth? If so, would that significantly alter the commonly accepted scenario of the growth of continental crust?

Because crustal growth curves were also determined in part from the Sm-Nd model age approach, erroneous conclusions may be reached if the material did not come from the depleted mantle, or important Sm/Nd fractionation occurred during melting and magma differentiation processes (Arndt and Goldstein 1987; Jahn *et al* 1990). Besides, what was the relative role of lithospheric and asthenospheric mantle as the dominant "mantle component" (Whalen *et al* 1996)?

In any case, the striking feature for the granites in the ECAOB is their relatively high $\varepsilon_{Nd}(T)$ values and low T_{DM} model ages (and probably, low I_{Sr} ratios). Windley (1993, 1995) distinguishes two types of orogens:

• collisional orogens, formed by the collision of two or more large continental blocks (e.g., Himalayas, Alps, Grenville, etc.), and

• accretionary orogens, formed by the growth and amalgamation of island arcs, intervening accretionary prisms, etc. (e.g., Altaids, North American Cordillera, Andes, Birimian, Nubian-Arabian, etc.). A depleted isotopic character is unusual for granitic rocks of collisional orogens worldwide, except a few

as exemplified by the Newfoundland Appalachians (Whalen *et al* 1996), but are more commonly observed for those in accretionary orogens. High $\varepsilon_{Nd}(T)$ values could reflect a direct contribution of mantle in subduction zones (DePaolo 1981; Farmer and DePaolo 1983). However, abundant A-type granites are post-orogenic and appear to have no direct connection with subduction processes. Thus, it appears that subduction processes alone could not have been responsible for the formation of all the juvenile crust (Question 1).

4.B *Implication for the origin of alkaline and peralkaline granitoids*

Although many plutons and batholiths of the ECAOB belong to the calc-alkaline series and have differentiated I-type characteristics, the emplacement of

voluminous granites of the alkaline and peralkalin series (A/NK $\leq$ 1 and A/CNK $\leq$ 1, with A,C,N,K molecular proportion of Al_2O_3, CaO, Na_2O and K_2O respectively) is remarkable. Of these rocks, many a post-orogenic A-type granites (A/CNK $\leq$ 1). Th origin of A-type granites is still much debated, an it appears that no single petrogenetic model is appl cable for all cases (Whalen *et al* 1987; Eby 1992 Mechanisms involving melting of crustal sources a favored from trace element geochemistry (Collins *et* 1982; Creaser *et al* 1991; Anderson and Morrison 199 Turner *et al* 1992; Cocherie *et al* 1994; Poitrasson *et* 1995; Landenberger and Collins 1996), whereas mant sources are often advocated from isotopic constrain (Javoy and Weiss 1987; Foland and Allen 199 Turner *et al* 1992; Whalen *et al* 1996; Han *et al* 1997 However, this is not universally true, as many A-typ granites are known to have a crustal isotopic signatu
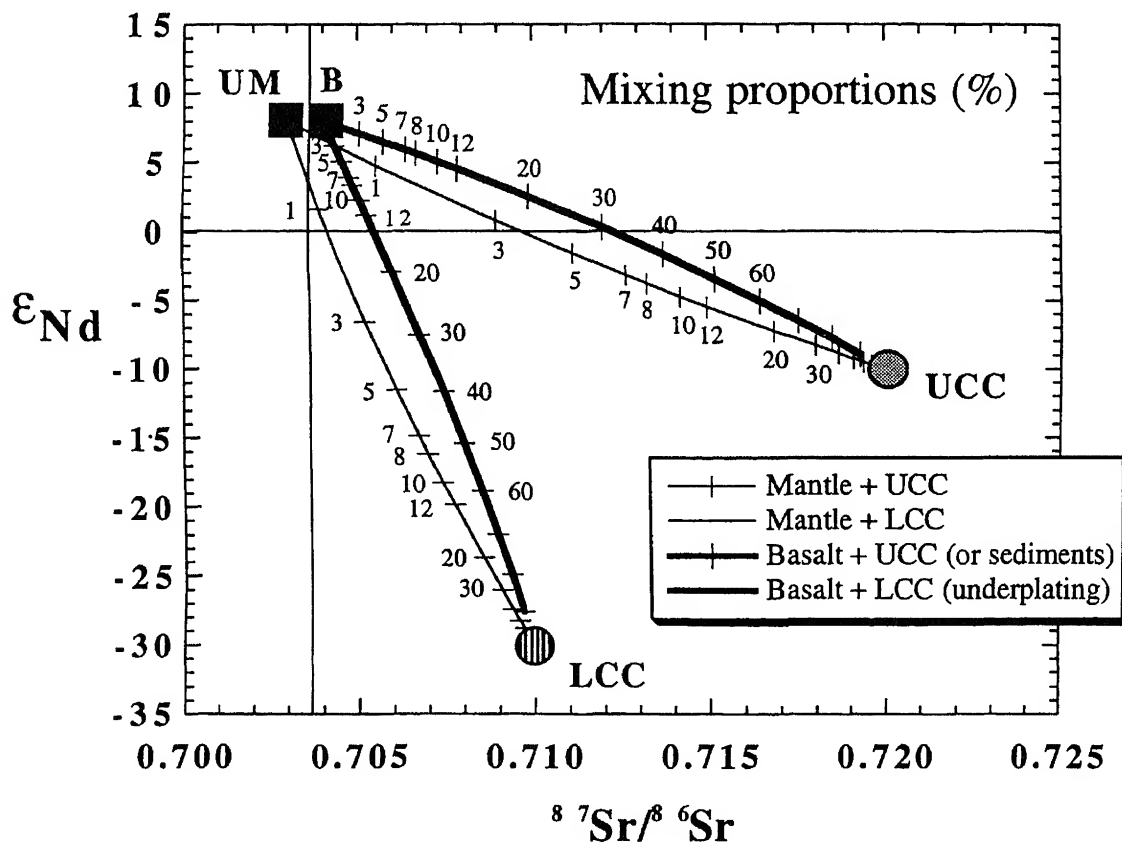
Figure 9. ε_{Nd} vs $^{87}Sr/^{86}Sr$ isotopic ratio plot showing mixing proportions between two end-members: (1) depleted mantle juvenile components (UM = upper mantle peridotite; or B = basalt) and (2) crustal components (LCC = lower continental crus or UCC = upper continental crust). The parameters used are:

	UM	Basalt	UCC	LCC
$^{87}Sr/^{86}Sr$	0.703	0.704	0.720	0.710
[Sr] ppm	20	150	350	300
ε_{Nd}	+8	+8	−10	−30
[Sm] ppm	0.42	3.5	5.2	4.8
[Nd] ppm	1.2	15	26	24
Sr/Nd	16.7	10	13.5	2.5

Sr and Nd concentrations of the UCC from Taylor and McLennan (1985), and those of the LCC from Rudnick and Fountain (1995).

(Charoy and Raimbault 1994; Darbyshire and Sewell 1997). In most cases, rocks of mantle derivation have also been contaminated by crustal material to some extent. Models involving mixing of mantle-derived magmas and crustal components (assimilated crustal rocks or crust-derived magmas), followed by fractional crystallisation are becoming increasingly popular.

A detailed discussion of petrogenetic models for the Altaid granites is beyond the scope of this paper, but it can be found in several related works (Hong *et al* 1995; Han *et al* 1997; Wu *et al* 2000). The available trace element and Nd-Sr isotopic compositions of the A-type (Xinjiang and Inner Mongolia) and differentiated I-type granites (NE China) indicate the mixing model as the most probable process and the dominance of mantle component over crustal material (e.g., Kovalenko *et al* 1996). A simple mixing calculation using different end-members is shown in figure 9. Two depleted juvenile components are used—mantle peridotite (UM) and basaltic rock (B). Because many I_{Sr} values have large uncertainties, we estimate the mixing proportions by using Nd isotopic compositions only. In all cases, granites with positive $\varepsilon_{Nd}(T)$ values would represent at least 70% juvenile component if upper continental crust (UCC) is the crustal end-member, and $\geq 85\%$ if lower continental crust (LCC) is considered. For the granites from the ECAOB, the majority of the southern belt (figures 4, 5) and those emplaced in the Caledonian and Hercynian zones in Mongolia and Transbaikalia (figures 6, 7) would be 100 to 80% juvenile. This implies extensive mantle differentiation and rapid crustal growth during the Phanerozoic. However, those emplaced in the Pre-Riphean zones have variable mixing proportions, from roughly 15 to 50% juvenile component (using Curve B-LCC, figure 9). It appears that the production of a huge amount of alkaline to peralkaline granites was initiated by extensive basalt underplating and accompanied by large-scale crustal extension (Questions 2 and 4, section 4.A). Consequently, intraplate magmatism was probably a significant process of continental growth in the Phanerozoic (Questions 3 and 5).

4.C *Tectonic model of Altaid collage by Sengör et al (1993)*

Sengör *et al* (1993) published an important and stimulating paper on the evolution of the Altaid tectonic collage. It provides an excellent forum for further research. According to this and a subsequent article (Sengör and Natal'in 1996), the Altaids (including the ECAOB and the region westwards to the Urals) provide a spectacular example of continental enlargement in the Phanerozoic, and their tectonic evolution involves accretion of arc complexes. The above authors have estimated that about 5.3 million km^2 of material accreted to Asia, half of which

may be of juvenile origin. Here we point out a few problems with this general model:

(**1**) The idea of using "magmatic front" as a new kind of structural marker in the reconstruction of the tectonic evolution is very creative, but the validity of this approach hinges on reliable age data for all individual granitic plutons. At present, this is far from the reality, and the number of plutons with precise age determination is very small in comparison with the total number of granitic plutons in the ECAOB. We cite here an example of granitoids in NE China. These rocks were assigned Hercynian or late Paleozoic ages (see published geologic maps), but, more recently, they have been found to be Indosinian (≈ 200 Ma) based on some preliminary Rb-Sr and K-Ar dating results. However, our whole-rock and mineral Rb-Sr and Ar-Ar analyses for three of these "Indosinian" plutons show that they were intruded separately during a time interval of 165 to 140 Ma (Wu, Jahn and Lo, unpublished). The above example of incorrect age assignment by geological correlations is not an isolated case in the ECAOB. Until more precise age data are obtained, the tectonic model based on the magmatic front concept must inevitably involve large uncertainties.

(**2**) The model of Sengör *et al* (1993) suggests that the orogenic belts forming the Altaid collage have evolved dominantly along a single subduction zone, in front of a migratory island arc, called the Kipchak arc. In other words, the entire process of arc accretion is achieved by back-stepping of a single subduction zone. Such a process appears to be oversimplistic, particularly with regard to the presence of ancient crustal blocks within the vast ECAOB (see point 3 below). It is questionable, therefore, whether the separately identifiable and seemingly independent arc complexes must be regarded as disrupted and displaced fragments of a single Kipchak arc.

(**3**) The model stresses the paucity of ancient gneiss terrains that represent ancient continental fragments. Although our Nd isotopic data indicate a very significant mantle input for the generation of the Altaid granitoids, the data of Kovalenko *et al* (1996) for Mongolia and Transbaikalia and those for Xinjiang-inner Mongolia-NE China (see also Zhao 1993; Hu *et al* 2000a, b) also suggest the presence of older crustal rocks in the ECAOB. Even the young model ages (T_{DM}) of 500–1000 Ma are still considerably older than the intrusive ages, suggesting the presence of older crust in the granite petrogenesis. The significant negative Nb anomalies in geochemical spidergrams observed in the A-type granites of Xinjiang (Han *et al* 1997) and inner Mongolia (Hong *et al* 1995) and in the I-type granites of NE China (Wu *et al* 2000) are in perfect agreement with the idea that old crustal rocks were involved in the granite petrogenesis. Consequently, the presence of older crustal blocks,

in addition to island arc complexes, is not insignificant in the Altaid collage.

(4) The importance of A-type granites appears to be downplayed in the model of Sengör *et al* (1993), which indicates that high-K granites were only generated widely in the Permian through anatectic magmatism. The high-K granites (A-type) of the Ulungur River, northern Xinjiang, were emplaced in the Carboniferous (≈ 300 Ma) and were generated by melting of sources dominated by mantle components (Han *et al* 1997; figures 3 and 4). The "anatectic" origin of high-K granites (Sengör *et al* 1993) is in contradiction with the isotopic data. By contrast, Coleman (1989) suggested that all A-type granites are generated by underplating of basaltic magmas in the lower crust, followed by partial melting of a mixed lower crustal assemblage. It is speculated that the voluminous post-orogenic A-type granites emplaced (mainly?) during the late Paleozoic could be related to a mantle plume, which supplied the necessary mantle material for the ultimate granite geneses and the necessary thermal energy for lithospheric extension.

4.D *Comparison between the granitoids of the Altaids and Cathaysia*

Cathaysia in the Yangtze Craton (figure 1) is a major Phanerozoic orogenic belt in SE China. Like the ECAOB, it is also characterized by voluminous Phanerozoic granitoids with rich mineralisations. Thus, a brief comparison of their isotopic signatures with those of the ECAOB appears interesting for the understanding of their respective crustal development. Cathaysia has been considered as the easternmost part of the Tethyside orogen (Hsu *et al* 1990;

Sengör *et al* 1993). Cathaysia and the ECAO are situated to the south and north of the Sino-Korea craton, respectively, and they exhibit very contrastin tectonic styles and crustal evolutions. The princip characteristics and differences between the Altaid ar Cathaysia orogens are summarized in table 1. A-typ granites also occur in Cathaysia (Xu *et al* 1992), bi their Nd isotopic signatures are generally "crusta (Martin *et al* 1994; Charoy and Raimbault 199 Darbyshire and Sewell 1997). Most granitic rocks SE China were produced by remelting of Proterozc crustal sources; only very few granitic bodies in coast Fujian and Taiwan have witnessed a greater contrib tion of the depleted mantle component in their magn genesis (Jahn *et al* 1976, 1986, 1990; Huang *et al* 198 Lan *et al* 1995; Gilder *et al* 1996; Chen and Jal 1998).

Figure 10 summarizes the Nd isotopic features Phanerozoic granites from the Cathaysia orogenic be and the Yangtze craton in comparison with tho from the southern belt of the ECAOB. The isotop distinction is very clear, suggesting that the Alta granitoids represent an immense juvenile crustal ad tion, whereas Cathaysian granitoids are main reworked ancient crust, implying little net crust growth.

5. Conclusions

- The vast orogenic belt (ECAOB) that welde together the Siberian and Sino-Korean cratons characterized by voluminous granitic rocks Paleozoic to Mesozoic ages. New Sr-Nd isotopic da and published isotopic and geochemical results sho that abundant granitic rocks from the southern be

Table 1. Comparison of crustal evolution between the ECAOB and SE China.

	East-Central Asia (Altaid)	SE China (Cathaysia)
Type of orogen	**Altaid (accretionary*)**	**Tethyside (collisional*)**
Characteristics	Immense Phanerozoic granitic intrusions	Immense Phanerozoic granitic intrusion
Period of intrusion	550 to 150 (possibly 120) Ma $\Delta T \approx 400$ Ma	400 (?) to 80 Ma $\Delta T \approx 300$ Ma
Total volume	≈ 5.3 M sq. km** ($\approx 11\%$ of total Asia)	not estimated
Granitic type	mainly I- and A-types Alkaline and peralkaline granites dominate	mainly S-type (I, A, M subordinate) CA granites dominate
Crustal type	mainly juvenile	mainly reworked
$e_{Nd}(T)$	+7 to +1	-2 to -17
Tectonics	Assembly of numerous arc complexes; intruded by vast granitic plutons and covered in places by their volcanic equivalent. Plume activities?	Assembly of ancient continental blocks; vast granitic plutons formed by remeltir of old basement rocks
Structure	Nappe complexes absent**; suture zones broad**	Nappe complexes common suture zones narrow and elongate
Basement rocks	Precambrian basement rocks rare**	Proterozoic basement dominates

Note: *Terminology of Windley (1993, 1995).
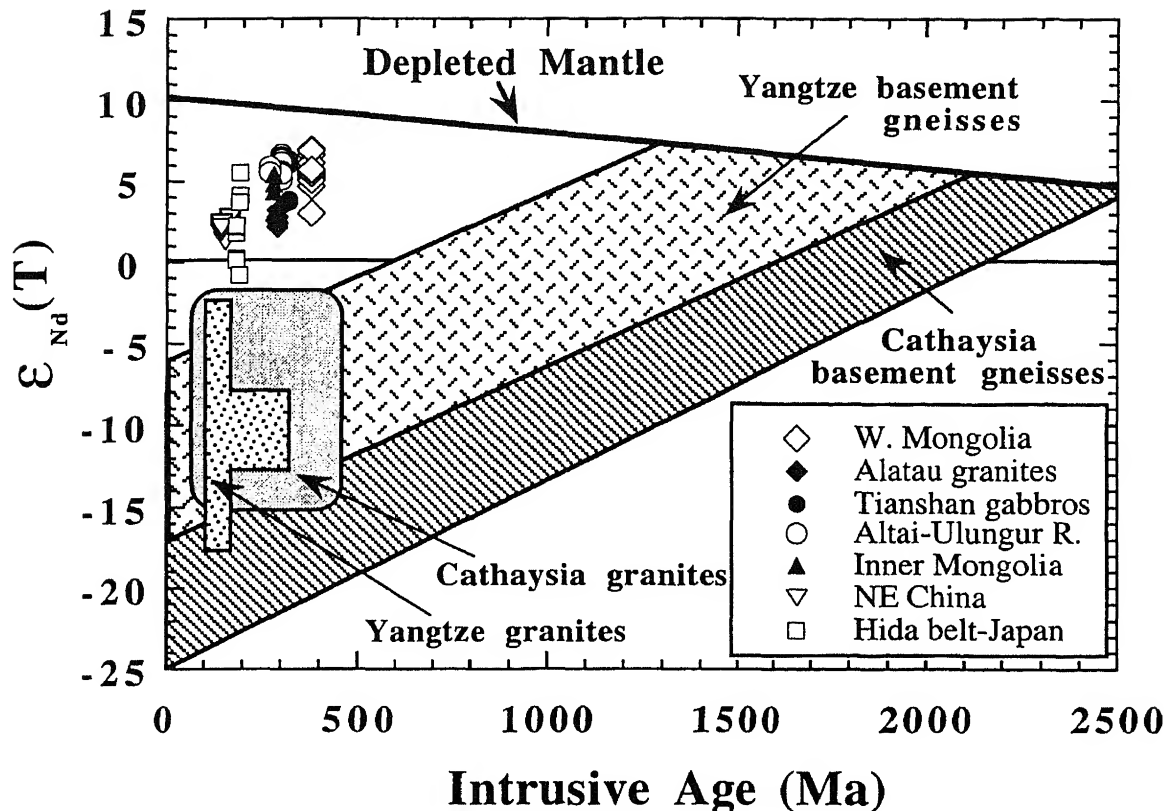**According to Sengör *et al* (1993); controversial.

Figure 10. Comparison of granitic rocks from the Altaids (ECAOB) and Yangtze-Cathaysia in SE China. The granitoids from both orogenic belts were emplaced during approximately the same period (ca. 400 to 100 Ma) but were generated from very different source rocks as shown by the contrasting $\varepsilon_{Nd}(T)$ values. The Yangtze-Cathaysia granites were mainly formed by remelting of Precambrian basement rocks with little contribution from the upper mantle, except for the Cretaceous granitic rocks of coastal Fujian and Taiwan. Data for Cathaysia are from the compilation of Chen and Jahn (1998).

Table 2. Phanerozoic juvenile crustal growth.

Arc magmatism (Reymer and Schubert 1984)	
(Canadian Cordillera and Altaid Collage	
excluded)	$\approx 1.1\,km^3/a$
Canadian Cordillera	
($\Delta T = 350\,Ma; \approx 1$ million km^2)	
(Samson et al 1989)	$\approx 0.15\,km^3/a$
Altaid Collage ($\Delta T = 400\,Ma; \approx 2$ million km^2)	
(Sengör et al 1993)	$\approx 0.30\,km^3/a$
Total Phanerozoic growth rate	$\approx 1.55\,km^3/a$
For comparison:	
Birimian terranes ($\approx 2.1\,Ga; \Delta T = 120\,Ma$)	
Outcrop = W. Africa (0.9 million km^2)	
+ Guyana (0.3 million km^2)	
+ possible extension ≈ 3 million km^2 (total)	
Growth rate (Boher et al 1992)	$\approx 1.6\,km^3/a$
	(overestimated?)
Arabian-Nubian Shield ($\Delta T \approx 300\,Ma; 900\text{-}600\,Ma$)	
Growth rate	$\approx 0.15\,km^3/a$
(similar to that of the Canadian Cordillera)	

of the ECAOB (Xinjiang-western Mongolian-inner Mongolia-NE China) possess un-ambiguous isotopic characteristics for juvenile crust ($I_{Sr} \approx 0.702$ to 0.707; $\varepsilon_{Nd}(T) = +7$ to $+1$). This is also true for Phanerozoic granitoids from Mongolia and Trans-

baikalia. Oxygen isotopic data for granitic rocks from Transbaikalia also support a significant mantle input, particularly for those emplaced during the Permian or later (Wickham et al 1995, 1996). Consequently, the ECAOB represents probably the most important mass transfer from the mantle to the continental crust in Phanerozoic times.

• The origin of A-type granites has long been controversial, and A-type granites seem to have multiple origins. Most of the post-orogenic A-type granites from the ECAOB are demonstratably of predominantly mantle origin based on their Nd-Sr isotopic data. The mantle origin involves a two-stage process, with a basaltic rock or magma as the immediate protolith of the A-type granite through partial melting or fractional crystallisation, respectively.

• The tectonic evolution of the ECAOB (or Altaid Collage) is most probably related to the accretion of arc complexes and the emplacement of juvenile crust as suggested by Sengör et al (1993). This idea is generally compatible with the available Sr-Nd-O isotopic data. However, the emplacement of voluminous post-orogenic A-type granites requires an additional process, probably involving basalt underplating from mantle plume partial melting and followed by extensive fractional crystallisation. If

the volume of the basaltic protoliths is considered, the juvenile material of the Altaid Collage separated from the upper mantle would be much greater than the total mass of the granitoids presently observed. It appears that intraplate magmatism involving plume melting, basalt underplating, differentiation or remelting of a basaltic source, is an important process of continental growth in the Phanerozoic.

- For the entire Altaid Collage, Sengör *et al* (1993) estimated that during the 400 Ma of crustal evolution, a total area of about two million km^2 of juvenile crust was added to Asia. This is translated into a growth rate of about $0.3\,km^3/a$. Combining this with the growth rate of the Canadian Cordillera (about $0.15\,km^3/a$, Samson *et al* 1989; Samson and Patchett 1991), the combined would be at least 50% higher than the global growth rate of ca. $1.1\,km^3/a$ deduced from arc magmatism by Reymer and Schubert (1984, 1986). Consequently, the recent "discovery" of juvenile crust in several Phanerozoic orogenic belts, in particular the ECAOB, may considerably change our views of continental growth.

Acknowledgements

References

Anderson J L and Morrison J 1992 The role of anorogenic granites in the Proteorozic crustal development of North America. In: *Proterozoic Crustal Evolution* (ed) K C Condie, Amsterdam: Elsevier, 263–299

Arakawa Y and Shimura T 1995 Nd-Sr isotopic and geochemical characteristics of two contrasting types of calc-alkaline plutons in the Hida belt; *Japan. Chem. Geol.* **124** 217–232

Armstrong R L 1968 A model for Sr and Pb isotope evolution in a dynamic earth; *Rev. Geophys.* **6** 175–199

Armstrong R L 1981 Radiogenic isotopes: The case for crustal recycling on a near-steady state no-continental-growth earth; *Phil. Trans. Royal Soc. London,* **A 301** 443–472

Armstrong R L 1991 The persistent myth of crustal growth; *Australia J. Earth Sci.* **38** 613–630

Arndt N T and Goldstein S L 1987 Use and abuse of crust-formation ages; *Geology* **15** 893–895

Bernard-Griffiths J, Peucat J J, Sheppard S and Vidal P 1985 Petrogenesis of Hercynian leucogranites from the southern Armorican Massif: contribution of REE and isotopic (Sr, Nd, Pb, and O) geochemical data to the study of source rock characteristics and ages; *Earth Planet. Sci. Lett.* **74** 235–250

Boher M, Abouchami W, Michard A, Albarède F and Arndt NT 1992 Crustal growth in West Africa at 2.1 Ga; *J. Geophys. Res.* **97** 345–369

Charoy B and Raimbault L 1994 Zr-, Th- and REE-rich biotite differentiates in the A-type granites pluton of Suzhou (eastern China): the key role of fluorine; *J. Petrology* 3? 919–962

Chen J F and Jahn B M 1998 Crustal evolution of southeastern China: Nd and Sr isotopic evidence; *Tectonophysics* 28? 101–133

Chen J F, Man F S and Ni S B 1995 Nd and Sr isotopic geochemistry of mafic-ultramafic intrusions from Qinbulak, West Tianshan Mountain, Xinjiang; *Geochimica* **24** 121–127 (in Chinese with English abstract)

Cluzel D 1991 Late Palaeozoic to early Mesozoic geodynamic evolution of the circum-Pacific orogenic belt in South Korea and Southwest Japan; *Earth Planet Sci. Lett.* **108** 289–305

Cocherie A, Rossi Ph, Fouillac A M and Vidal Ph 1994 Crust and mantle contributions to granite genesis: An example from the Variscan batholith of Corsica, France, studied by trace-element and Nd-Sr-O isotope systematics; *Chem. Geol.* **115** 173–211

Coleman R G 1989 Continental growth of northwest China; *Tectonics* **8** 621–635

Collins W J, Beams S D, White A J R and Chappell B W 1982 Nature and origin of A-type granites with particular reference to southeastern Australia; *Contrib. Mineral. Petrol.* **80** 189–200

Costa S and Rey P 1995. Lower crustal rejuvenation and growth during post-thickening collapse: Insights from a crustal cross section through a Variscan metamorphic complex; *Geology* **23** 905–908

Creaser R A, Price R C and Wormald R J 1991 A-type granite revisited: assessment of a residual-source model; *Geology* 1? 163–166

Darbyshire D P F, Sewell R J 1997 Nd and Sr isotope geochemistry of pjutonic rocks from Hong Kong: implications for granite petrogenesis, regional structure and crustal evolution; *Chem. Geol.* **143** 81–93

DePaolo D J 1981 A neodynium and strontium isotopic study of the Mesozoic calc-alkaline granitic batholiths of the Sierra Nevada and Peninsular Ranges, California; *J. Geophys. Res.* **86** 10470–10488

Downes H, Shaw A, Williamson B J and Thirlwall M F 1997 Sr, Nd and Pb isotope geochemistry of the Hercynian granodiorites and monzogranites, Massif Central, France; *Chem. Geol.* **136** 99–122

Eby G N 1992 Chemical subdivision of the A-type granitoids: petrogenetic and tectonic implications; *Geology* **20** 641–644

Foland K A and Allen J C 1991 Magma sources for Mesozoic anorogenic granites of the White Mountain magma series, New England, U.S.A.; *Contrib. Mineral. Petrol.* **109** 195–211

Gilder S A, Gill J, Coe R S, Zhao X, Liu Z, Wang G, Yuan K, Liu W, Kuang G and Wu H 1996 Isotopic and paleomagmatic constraints on the Mesozoic tectonic evolution of south China; *J. Geophys. Res.* **101** 16137–16154

Gruschka S, Kröner A, Avdeev A V, Seitov N S, Oberhänsli R 1997 Early Palaeozoic accretion of arcs and microcontinents in the Central Asian Mobile Belt of southern Kazakhstan as deduced from Pb-Pb zircon and Sm-Nd model ages; *Terra Nova* 9 Abstract Supplement 1, 340

Han B F, Wang S G, Jahn B M, Hong D W, Kagami H and Sun Y L 1997 Depleted-mantle magma source for the Ulungur River A-type granites from north Xinjiang, China: geochemistry and Nd-Sr isotopic evidence, and implication for Phanerozoic crustal growth; *Chem Geol.* 138 135–159

Hirooka K, Nakajima T, Sakai H, Date T, Nittamachi K and Hattori I 1983 Accretion tectonics inferred from paleomagnetic measurements of Paleozoic and Mesozoic rocks in central Japan. In: *Accretion Tectonics in the Circum-Pacific Regions.* M Hashimoto and S Uyeda (eds); Tokyo: Terra Sci. Publ. Co., 179–194

Hong D W, Huang H Z, Xiao Y J, Xu H M and Jin M Y, 1995 Permian alkaline granites in central inner Mongolia and their geodynamic significance; *Acta Geologica Sinica* 8 27–39

Hong D W, Wang S G, Han B F and Jin M Y 1996 Post-orogenic alkaline granites from China and comparisons with anorogenic alkaline granites elsewhere; *J. SE Asian Earth Sci.* 13 13–27

Hsü K J, Li J L, Chen H H, Wang Q C, Sun S and Sengör A M C 1990 Tectonics of South China: key to understanding west Pacific geology; *Tectonophysics* 183 9–39

Hu A Q, Jahn B M, Zhang G, Zhang Q 2000a Crustal evolution and Phanerozoic crustal growth in Northern Xinjiang: Nd-Sr isotopic evidence. Part I: Isotopic characterization of basement rocks. (in preparation).

Hu A Q, Jahn B M, Zhang G, Zhang Q 2000b Crustal evolution and Phanerozoic crustal growth in Northern Xinjiang: Nd-Sr isotopic evidence. Part II: Phanerozoic granite intrusions (in preparation).

Huang X, Sun S H, DePaolo D J and Wu K L 1986 Nd-Sr isotope study of Cretaceous magmatic rocks from Fujian province; *Acta Petrol. Sinica* 2 50–63

Jahn B M, Chen P Y and Yen T P 1976 Rb-Sr ages of granitic rocks in southeastern China and their tectonic significance; *Bull. Geol. Soc. Am.* 86 763–776

Jahn B M, Martineau F, Peucat J J and Cornichet J 1986 Geochronology of the Tananao Schist complex, Taiwan, and its regional tectonic significance; *Tectonophysics* 125 103–124

Jahn B M, Zhou X H and Li J L 1990 Formation and tectonic evolution of southeastern China and Taiwan: Isotopic and geochemical constraints; *Tectonophysics* 183 145–160

Javoy M and Weiss D 1987 Oxygen isotopic composition of alkaline anorogenic granites as a clue to their origin: the problem of crustal oxygen; *Earth Planet. Sci. Lett.* 84 415–422

Jin C W and Zhang X Q 1993 A geochronology and genesis of the western Junggar granitoids, Xinjiang, China; *Scientia Geologica Sinica* 28 28–36 (in Chinese with English abstract).

Kononova V A, Pervov V A, Bogatikov O A, Upton B G J, Suddaby P and Woolley A R 1996 Geochemical constraints on the petrogenesis of the high-K rocks of the southern Sakun Massif, Aldan Shield, Siberia; *J. Conf. Abst.* 1 324

Kovalenko V I, Tsareva G M, Yarmolyuk V V, Troisky V A, Farmer G L and Chernishev I V 1992 Sr-Nd isotopic compositions and the age of rare-metal peralkaline granitoids from western Mongolia; *Dokladi Akad. Nauk* 237 570–574 (in Russian)

Kovalenko V, Yarmolyuk V and Bogatikov O 1995 Magmatism, geodynamics, and metallogeny of Central Asia. Miko Moscow: Commercial Herald Publishers 272 pp.

Kovalenko V I, Yarmolyuk V V, Kovach V P, Kotov A B, Kozakov I K, Sal'nikova E B 1996 Sources of Phanerozoic granitoids in Central Asia: Sm-Nd isotope data; *Geochem. Int'l.* 34 628–640

Kuzmin M I and Antipin V S 1993 Geochemical types of granitoids of the Mongol-Okhotsk belt and their geodynamic settings; *Chinese J. Geochim.* 12 110–117

Kwon S T, Tilton G R, Coleman R G and Feng Y 1989 Isotopic studies bearing on the tectonics of the west Junggar region, Xinjiang, China; *Tectonics* 8 719–727

Lan C Y, Lee T, Jahn B M and Yui T F, 1995 Taiwan as a witness of repeated mantle inputs—Sr-Nd-O isotopic geochemistry of Taiwan granitoids and metapelites; *Chem. Geol.* 124 287–303

Landenberger B and Collins W J 1996 Derivation of A-type granites from a dehydrated charnocktic lower crust: evidence from the Chaelundi Complex, eastern Australia; *J. Petrology* 37 145–170

Litvinovsky B A, Zanvilevich A N, Alakshin A M and Podladchikov Yu 1992 The Angara-Vitin batholith—the largest granitoid pluton. Novosibirsk; *Nauka* 141 pp.

Martin H, Bonin B, Capdevila R, Jahn B M, Lamayre J and Wang Y, 1994 The Kuiqi peralkaline granitic complex (SE China): petrology and geochemistry; *J. Petrology* 35 983–1015

Mizutani S and Hattori I 1983 Hida and Mino: Tectonostratigraphic terranes in central Japan. In: *Accretion Tectonics in the Circum-Pacific Regions.* M Hashimoto and S Uyeda (eds), Tokyo: Terra Sci. Publ. Co. 169–178

Moorbath S 1978 Age and isotopic evidence for the evolution of continental crust; *Phil. Trans. R. Soc. London* 288 401–413

Poitrasson F, Duthou J L and Pin C 1995 The relationship between petrology and Nd isotopes as evidence for contrasting anorogenic granite genesis: example of the Corsican Province (SE France); *J. Petrol.* 36 1251–1274

Reymer A and Schubert G 1984 Phanerozoic addition rates to the continental crust and crustal growth. Tectonics; 3 63–77

Reymer A and Schubert G 1986 Rapid growth of some major segments of continental crust; *Geology* 14 299–302

Rudnick R L and Fountain D M 1995 Nature and composition of the continental crust: a lower crustal perspective; *Reviews Geophys.* 33 267–309

Samson S D 1998 Phanerozoic crustal growth in North America: A Cordilleran and Appalachian perspective. IGCP-420 Workshop, Xinjiang, [abstract] (in press).

Samson S D and Patchett P J 1991 The Canadian Cordillera as a modern analogue of Proterozoic crustal growth; *Aust. Jour. Earth Sci.* 38 595–611

Samson S D, McClelland W C, Patchett P J, Gehrels G E, Anderson R G 1989 Evidence from neodymium isotopes for mantle contributions to Phanerozoic crustal genesis in the Canadian Cordillera; *Nature* 337 705–709

Sengör A M C, Natal'in B A and Burtman V S 1993 Evolution of the Altaid tectonic collage and Paleozoic crustal growth in Eurasia. Nature; 364 299–307, 1993

Sengör A M C and Natal'in B A 1996 Turkin-type orogeny and its role in the making of the continental crust; *Annu. Rev. Earth Planet. Sci.* 24 263–337

Stein M and Hofmann A W 1994 Mantle plumes and episodic crustal growth; *Nature* 372 63–68

Taylor S R and McLennan S M 1985 The continental crust: its composition and evolution. (Blackwell) 312 pp. 1985

Taylor S R and McLennan S M 1995 The geochemical evolution of the continental crust; *Rev. Geophysics* 33 241–265

Turner S P, Foden J D and Morrison R S 1992 Derivation of A-type magmas by fractionation of basaltic magma: an example from the Padthaway Ridge, South Australia; *Lithos* 28 151–179

Vidal P, Bernard-Griffiths J, Cocherie A, Le Fort P, Peucat J J and Sheppard S 1984 Geochemical comparison between Himalayan and Hercynian leucogranites; *Phys. Earth Planet. Interiors* 35 179–190

Wang S G, Han B F, Hong D W, Xu B L and Sun Y L 1994 Geochemistry and tectonic significance of alkali granites along Ulungur River, Xinjiang (in Chinese with English abstract); *Scientia Geologica Sinica* **29** 373–383

Whalen J B, Currie K L and Chappell B W, 1987 A-type granites: geochemical characteristics, discrimination and petrogenesis; *Contrib. Mineral. Petrol.* **95** 407–419

Whalen J B, Jenner G A, Longstaff F J, Robert F and Galiépy C 1996 Geochemical and isotopic (O, Nd, Pb and Sr) constraints on A-type granite petrogenesis based on the Topsails igneous suite, Newfoundland Appalachians; *J. Petrology* **37** 1463–1489

Wickham S M, Litvinovsky B A, Zanvilevich A N and Bindeman I N 1995 Geochemical evolution of Phanerozoic magmatism in Transbaikalia, East Asia: a key constraint on the origin of K-rich silicic magmas and the process of cratonization; *J. Geophys. Res.* **100** 15641–15654

Wickham S M, Alberts A D, Zanvilevich A N, Litvinovsky B A, Bindeman I N and Schuble E A 1996 A stable isotope study of anorogenic magmatism in East Central Asia; *J. Petrology* **37** 1063–1095

Windley B 1993 Proterozoic anorogenic magmatism and its orogenic connections; *J. Geol. Soc. London* **150** 39–50

Windley B 1995, *The Evolving Continent*, 3rd editi (Chichester: John Wiley & Sons) 526 pp.

Wu F Y, Jahn B M, Lin Q, Ge WC and Sun D Y 2000 Hig fractionated I-type granites from NE China: geochemist petrogenesis and implications for continental growth. (to submitted to *J. Petrology*)

Xu K Q, Zhu J C, Liu C S, Shen W Z and Xu S J 1992 Gene series and material sources of granitoids in South China. *Petrogenesis and Mineralisation of Granitoids.* G Z Tu, K Xu and Y Z Qiu (eds), Beijing: Science Press 3–22

Zanvilevich A N, Litvinovsky B A and Wickham S M 19 Genesis of alkaline and peralkaline syenite-granite series: Kharitonovo pluton (Transbaikalia, Russia); *J. Geol.* 1 127–145.

Zhao Z H 1993 REE and O-Pb-Sr-Nd isotopic compositi and petrogenesis of the Altai granitoids. In: *New Devel ment of Solid Earth Science in Northern Xinjiang.* Beiji Science Publishing Co., 239–266

Zhou T X, Chen J F, Chen D G and Li X M 1995 Geochemi characteristics and genesis of granitoids from Alat Mountain, Xinjiang, China; *Geochimica* **24** 32–42 Chinese with English abstract).

Anasagar gneiss: A folded granitoid pluton in the Proterozoic South Delhi Fold Belt, central Rajasthan

DHRUBA MUKHOPADHYAY[1,*], TAPAS BHATTACHARYYA[1], NANDINI CHATTOPADHYAY[1], ROBERT LOPEZ[2], OTHMAR T TOBISCH[2]

[1]*Department of Geology, University of Calcutta, 35 Ballygunge Circular Road, Calcutta 700 019, India.*
[2]*Earth Sciences Department, A232 E. and M.S. Building, University of California, ·Santa Cruz, California, 95064, U.S.A.*
**email: dhruba@cucc.ernet.in*

The Anasagar gneiss was emplaced as a concordant sheet like body along the contact of quartzite and pelitic/semipelitic schist horizons in the northern part of the South Delhi Fold Belt. It is typically a granite gneiss containing megacrysts of K-feldspar set in a recrystallised foliated matrix. The megacrysts are in general converted to granular aggregates, often retaining their crystal outline. Garnet, sillimanite (fibrolite) and rarely staurolite are the metamorphic minerals in the gneiss; these are also present in the enveloping supracrustal rocks. Both the gneiss and the supracrustal rocks are involved in polyphase deformation. F_1 isoclinal folds are present only on minor scale in the supracrustal rocks. F_2 major and minor folding have affected both the gneiss and the supracrustal rocks. These are asymmetrical folds with alternate flat and steep, locally overturned, limbs and have consistent easterly vergence. F_3 folds are upright and coaxial with F_2. F_4 puckers and large scale warps have E-W to ESE-WNW subvertical axial planes. The gneiss is exposed in the core of an F_3 arch on the flat limb of a major F_2 antiform whose axial trace is bent by an F_4 fold. The intrusion was pre-F_2 and late-tectonic with F_1. U-Pb zircon dating suggests a crystallization age of $1849 +/- 8$ Ma. Hence the Anasagar gneiss is older than the late- to post-tectonic "Erinpura-type" granite in the South Delhi Fold Belt.

1. Introduction

The Middle to Late Proterozoic South Delhi Fold Belt (SDFB) in central Rajasthan, India (Sinha Roy *et al* 1995), is subdivided into two segments by a belt of granite gneiss characterised by Heron (1953) as a thrust wedge of Pre-Delhi basement. There are some differences in the lithological associations in the supracrustal sequences on either side of this median belt of gneiss, the principal one being extensive development of felsic and mafic volcanic rocks in the western segment. Late- to post-tectonic "Erinpura-type" granite plutons are typically restricted to the western segment only. It has been suggested that the two segments represent different sub-basins which were telescoped together during the Delhi orogeny (Gupta *et al* 1991).

The Anasagar gneiss is exposed in the central part of the northern extremity of the South Delhi Fold Belt, in the vicinity of Ajmer ($26°27'N : 74°38'E$) and forms an elongate rectangular body enveloped by quartzites (figure 1). Heron (1953) described it as a laccolithic intrusion within the Delhi Supergroup and it is folded into an anticlinal structure. He drew attention to the differences in internal structure between the Anasagar gneiss and the "Erinpura-type" granite exposed further southwest, the former being porphyritic and at many places an augen gneiss. He regarded the Anasagar gneiss to be the earliest phase of the Erinpura magmatism. The quartzites flanking the
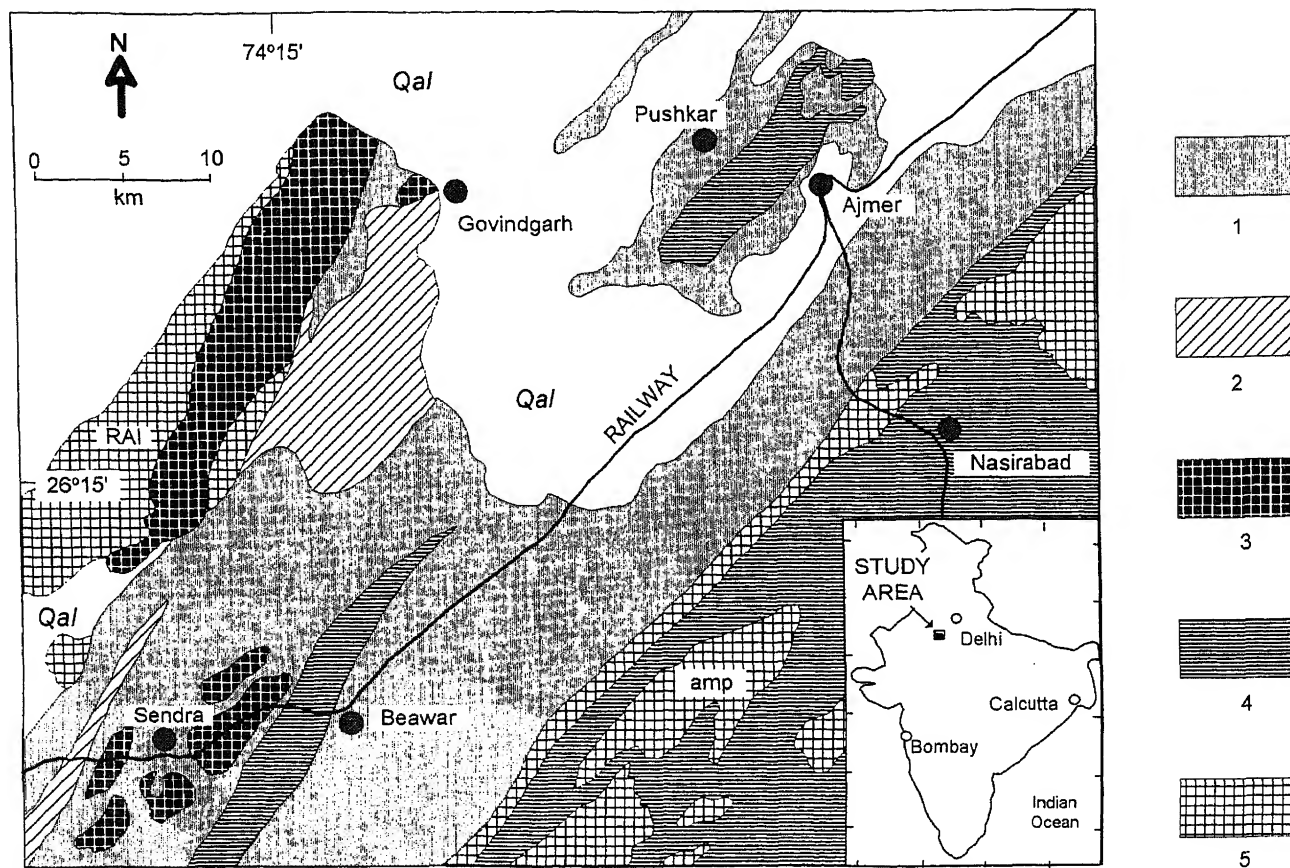
Figure 1.   Generalised geological map of the northern part of the South Delhi Fold Belt, adopted from Tobisch *et al* (1994), w
minor modifications. **(1):** Delhi Supergroup predominantly calc gneiss, mica schist and quartzite; **(2):** Mafic rocks of the Barot
sequence; **(3):** "Erinpura type" granites, **(4):** Anasagar gneiss, Beawar inlier, eastern gneisses; **(5):** gneissic granite a
amphibolite within eastern and western gneisses; **amp:** predominantly amphibolites; **RAI:** includes Raialo beds of Heron (195
Qal: Quarternary and alluvium. Inset shows location of study area.

Anasagar gneiss were assigned by him to the lower unit (Alwar Group) of the Delhi Supergroup.

The Anasagar gneiss lies along the strike continuation of the Pre-Delhi median gneiss exposed near Beawar (26°07'N : 74°19'E) though the two are separated by a sand covered terrain. Fareeduddin *et al* (1995) considered the Beawar gneiss, the Anasagar gneiss and its enveloping supracrustal rocks to be older than the tectonostratigraphic units of the SDFB and tentatively correlated them with the Aravalli Supergroup.

Geochronological data from the SDFB are meagre. The Rb-Sr dates for the "Erinpura-type" plutons range from 0.73 to 0.83 Ga, while the Anasagar gneiss yielded Rb-Sr date of 1.6–1.7 Ga (Choudhary *et al* 1984). Thus the Anasagar gneiss is older than the "Erinpura-type" granites and is comparable in age to some granite bodies in the North Delhi Fold Belt (Choudhary *et al* 1984); however, the stratigraphic status of the latter, whether intrusive granite or partially remobilised basement, is controversial (Gangopadhyay and Das 1974). Tobisch *et al* (1994) report Rb-Sr dates of 0.96 Ga with a large uncertainty for the "Erinpura-type" granites from Sendra. The Sm-Nd model ages (T_{DM}) of the Anasagar gneiss are 2.86 and 2.66 Ga and the Rb-Sr data suggest a thermal

resetting at 1.7 Ga. The Ranakpur diorite intrus into the western supracrustal sequence of the SD yielded an Sm-Nd date of $1.01 +/- 0.08$ Ga with later thermal event at 0.8 Ga (Volpe and Mcdoug 1990). Recently Deb (1996) has reported a Pb-model age of 0.99 Ga from sulphide ore bodies in t western segment of SDFB.

The present study focusses on the structural a stratigraphical relations of the Anasagar gneiss a presents some new geochronological data. The ma structure of the Anasagar gneiss has been worked and it contradicts both the simple laccolith mo of Heron (1953) and the interpretation of Tobis *et al* (1994) as a simple domal structure. The over structure essentially controlled by large scale fe interference related to Delhi orogeny precludes t possibility that the plutonic body belongs to the l Delhi Erinpura suit. This is substantiated by new Pb dates of the gneiss.

2. Petrography of the Anasagar gneiss

Fareeduddin *et al* (1995) described the Anasag gneiss as a migmatite unit in which biotite

Figure 2. Sharp contact between megacryst rich and megacryst free bands in Anasagar gneiss. Note the elliptical xenolith of quartz mica schist, unoriented megacrysts and no pronounced gneissosity.

paragneiss forms a major part. These are extensively migmatised by polyphase potash feldspathic neosomes. They reported that within this migmatite there is a late phase granite pluton exposed near Ajesar (26°25′N : 74°34′E) south of Ajmer. Though several petrographic types are present within the Anasagar gneiss we see no ground to differentiate it into a migmatitic gneiss and a late phase pluton.

The Anasagar gneiss is typically a porphyritic granite gneiss. In the commonest variety megacrysts of microcline are embedded in a gneissose crystalline matrix containing quartz, microcline, plagioclase and biotite. Megacrysts may constitute up to 30% by volume of the rocks. Some of the varieties are even grained and relatively free of megacrysts. In some outcrops the two varieties occur in bands about a meter in width with a sharp contact between the two (figure 2). Some bands are made up of only closely clustered megacrysts. The modal compositions (table 1) suggest that the rocks are dominantly granite (*sensu stricto*) with varieties ranging to granodiorite and tonalite.

At many places the microcline megacrysts are euhedral to subhedral, but almost invariably they are recrystallised to granular aggregates with occasional relicts of the original crystals. They often show two or more concentric zones separated by biotitic septa (figure 3) parallel to the outer margin of the grain. This resulted from punctuated crystallisation of the individual megacrysts from the melt. The euhedral megacrysts may be parallel or athwart to the foliation (figures 4, 5). The parallel arrangement of the euhedral crystals suggests magmatic flowage. This would imply that the foliation is partly magmatic in origin though it is accentuated by later deformation. The gneissosity swerves round the athwart megacrysts (figure 5). At places the megacrysts have a circular or elliptical outline (figures 6, 7 and 8); this resulted from magmatic corrosion and/or later deformation. Some megacrysts are deformed and recrystallised into elliptical granular aggregates within which the internal biotitic septa are also deformed retaining the parallelism with the outer boundary (figure 6). In such septa, however, the individual biotite grains are parallel to the external rock foliation. As a result where the megacryst boundary is not parallel to the gneissosity the biotitic rims are also oblique to the gneissosity but individual grains are parallel to it. Tectonic movements along certain zones within the body and particularly at many places close to the contact with the overlying supracrustal rocks have deformed the megacrysts into thin elongate granular aggregates and the rock becomes a thinly banded gneiss (figures 9 and 10). The microcline megacrysts have inclusions of small altered plagioclase grains and flakes of biotite. Myrmekitic intergrowth is seen where plagioclase is in contact with microcline.

The megacrysts represent late stage magmatic cystallisation products (Hyndman 1985; Vernon 1986; Pitcher 1997). Experimental support for near solidus

Modal composition of Anasagar Gneiss.

Quartz	K-feldspar	Plagioclase	Muscovite	Biotite	Apatite	Zircon	Sphene	Sillimanite	Garnet	Staurolite	Tourmaline	Opaque	Myrmekite
35.5	27.8	6.5	2.4	25.2	1.9	0.7							
34.9	34.2	9.7	1.4	17.4	1.8	0.4				0.2			
42.4	30.6	6.4	5.0	11.2	1.6	0.8							
21.6	47.7	2.8	8.6	17.2		0.6							
39.9	24.6	2.0	11.0	19.3	1.3	0.6							
42.9	15.5	16.0		21.9	1.7	1.1	0.9		1.6				
36.0	16.1	22.9		22.5	1.8	0.7			1.1				
41.9	12.8	21.3	11.3	15.8	2.2	1.3			1.1				
30.2	13.5	24.7	4.9	19.9	0.38	0.02			4.3				
38.5	7.2	25.7	1.9	20.4	2.4	0.9							
40.1	7.0	22.1		27.8	0.2	0.9							
25.0	6.5	34.6		30.8	1.5	0.4		0.2	0.3		0.2	0.5	
38.7	5.4	31.8	2.9	15.4	2.9	1.2			1.4				
23.5	3.5	11.2	25.7	27.2	0.7				0.7			0.6	6.9
32.9	2.8	23.3	16.7	23.1	0.7	0.5							
40.5	2.8	26.9	3.0	23.1	1.3	0.4		0.6					
35.1	2.4	29.6	6.4	21.9	1.7	0.6							
38.2	1.5	26.0	2.3	29.5	1.3	0.8		0.4					0.9
35.8	1.0	32.2	7.3	21.1	1.5	0.7							1.9
35.2		15.2	28.2	17.3	1.9	0.9			0.9				

Figure 3. Rectangular nearly euhedral K-feldspar megacrysts with zones separated by biotitic septa. Crude parallelism of megacrysts.

Figure 4. Subparallel orientation of euhedral to subhedral K-feldspar megacrysts (magmatic foliation), weak gneissosity.

ormation of large K-feldspar megacrysts from a ranitic melt has been provided by Swanson (1977). e showed that granites crystallised rapidly through significant undercooling are equigranular, whereas those crystallised slowly with a small degree of undercooling develop large K-feldspar megacrysts.

Figure 5. Euhedral K-feldspar megacrysts athwart to the gneissosity which swerves round the megacryst.
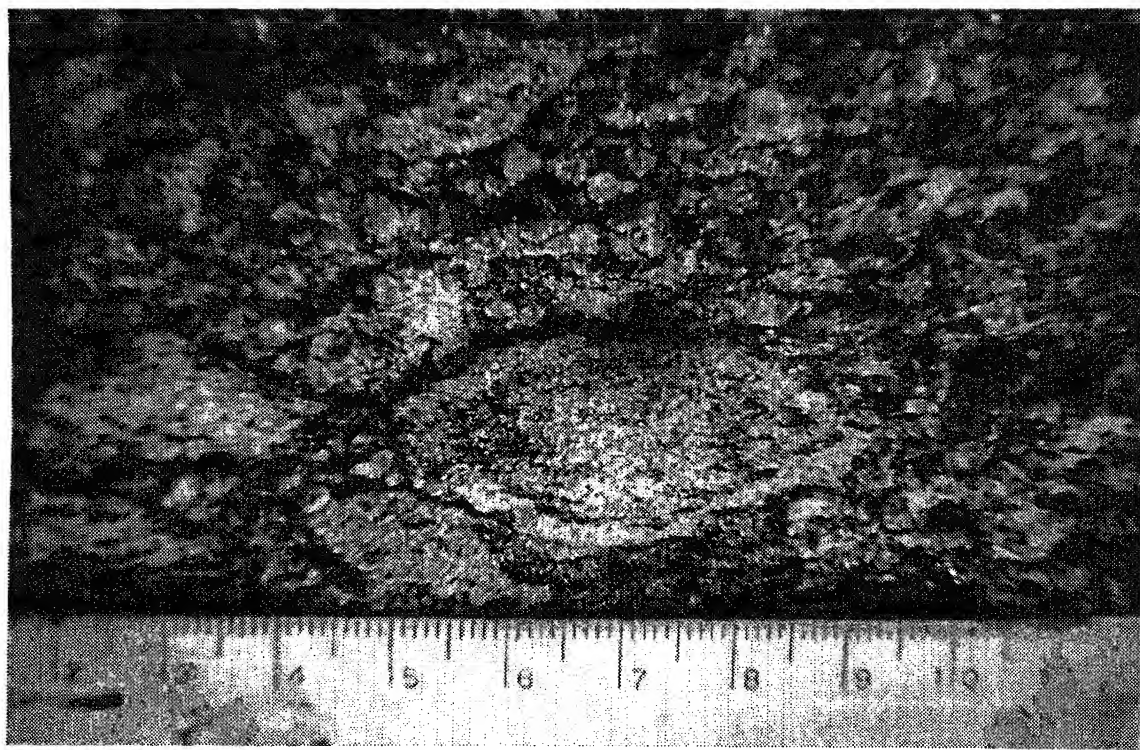
Figure 6. K-feldspar megacryst deformed into elliptical shape elongated parallel to the gneissosity. The megacr recrystallized into granular aggregate. The internal biotitic septum is deformed into elliptical form. Individual biotite flakes septum are parallel to the gneissosity.

Megacrysts have also grown in some xenoliths (figure 8), which may be due to growth in a near solid state (cf. Pitcher 1997).

At some places there are centimetre sized of coarse grained quartz which are produc late magmatic or hydrothermal crystallisation.

Figure 7. K-feldspar megacrysts whose shapes are modified by magmatic corrosion and/or deformation. Matrix shows well-developed gneissosity.

Figure 8. Unoriented xenoliths of quartz-muscovite schist. K-feldspar megacrysts are euhedral, elliptical, and circular. Note development of megacrysts within the xenolith.

larger grains of quartz show strong intracrystalline deformation features, e.g., deformation bands, sub-grain formation, deformation induced recrystallisa-tion. The matrix of the rocks shows a well developed gneissosity defined by thin biotitic laminae. The quartz-feldspar grains form a recrystallised granoblas-

Figure 9. Well-developed foliation in Anasagar gneiss. Megacrysts are deformed into thin lenticles. Elongated xenolith is [p]
to the gneissosity. Aplite vein cuts across the gneissosity. Note that the vein does not cut across the xenolith.

Figure 10. Well-foliated Anasagar gneiss. Megacrysts are deformed into thin lenticles parallel to the gneissosity. A few
megacrysts are still recognisable. F_2 crenulations on gneissosity on the steep limb of a mappable F_2 fold.

tic mosaic. Large athwart flakes of muscovite are seen in some rocks. They show vermicular intergrowth with quartz (figure 11). The growth of such muscovite is due to reactions in the late magmatic or metamo[rphic] stage. Ashworth (1972) and Phillips et al ( ) suggested that this may be tied up with rea[ctions]
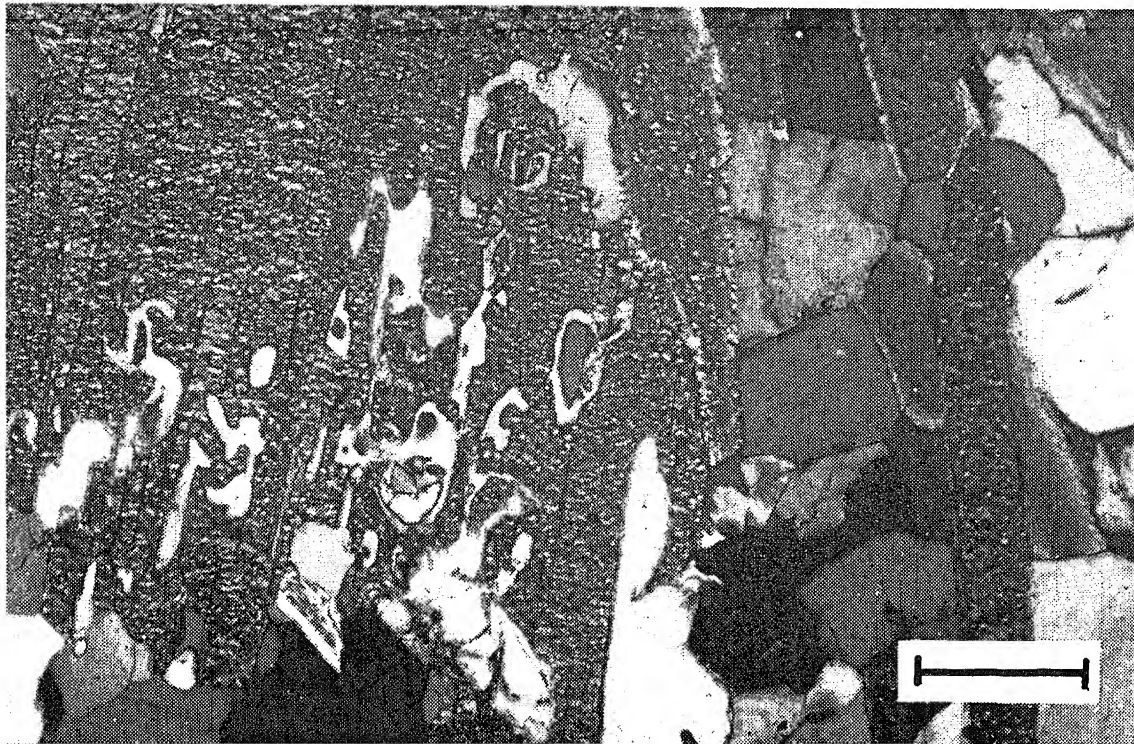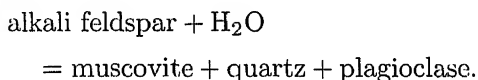
Figure 11. Quartz muscovite intergrowth in Anasagar gneiss. Scale bar – 0.5 mm.

involving K-feldspar. One possible reaction is:

alkali feldspar + H_2O

= muscovite + quartz + plagioclase.

However, Phillips *et al* (1972) have suggested other reactions also. Accessory minerals in the gneiss are apatite, zircon, tourmaline, epidote, sphene. Some varieties contain rare amphibole crystals.

Metamorphic impress in the rocks is indicated by the presence of garnet porphyroblasts, elliptical fibrolite aggregates and rare staurolite. The same metamorphic index minerals are present in the enveloping rocks.

Xenoliths of semipelitic schist are quite common (figures 8 and 9). Amphibolite enclaves are also present, some of which are extensively altered to a biotitic rock. At one locality close to the western boundary near the road connecting Ajmer with Pushkar (26°29′N : 74°33′E) a mappable enclave of calc gneiss is observed. Close to the upper contact of the Anasagar gneiss along the Ajmer-Pushkar road large patches of migmatised mica schist are present within the gneiss.

3. Structural and stratigraphical relations

In only one small area north of Ajmer, both the upper and the lower contacts of the Anasagar gneiss are exposed. Here quartzite lies above and pelitic/semi-pelitic schist lies below the gneiss. In this part the concordant sheet like nature is clearly evident with strong parallelism of bedding and schistosity in the metasediments with the gneissosity and the boundary of the Anasagar gneiss. The thickness of the gneissic body is of the order of 50 metres. Elsewhere only the upper contact of the Anasagar gneiss is seen and mature quartz arenites with shallow water deposi-tional features such as ripple marks and cross laminations (figure 12) occur above it, the bedding and formational contact being parallel to the gneiss-osity. The younging direction is everywhere away from the gneiss. Interbedded with the quartzites are schists and amphibolites. The quartzites are locally separated from the gneisses by several metres thick band of migmatised micaceous gneiss. Amphibolite bodies are also common along the contact.

The intensity of deformation within the Anasagar gneiss is variable. A foliation is regionally well deve-loped but as already discussed this is partly magmatic in origin and it has been accentuated by subsequent solid state deformation. In the central parts of the gneiss many megacrysts are euhedral maintaining a discordant relation to a weak foliation, whereas in areas close to the contact the megacrysts are strongly deformed into long linear aggregates forming an intense lineation (figures 9, 10 and 13). Discrete shear zones, a few centimetres wide, some with sinistral and others with dextral sense of movement, are present within the gneiss (figure 14). Inside the shear zones the megacrysts disappear and the rock acquires a protomylonitic to mylonitic fabric. The relation of the shear zones with the folding episodes could not be unequivocally established.
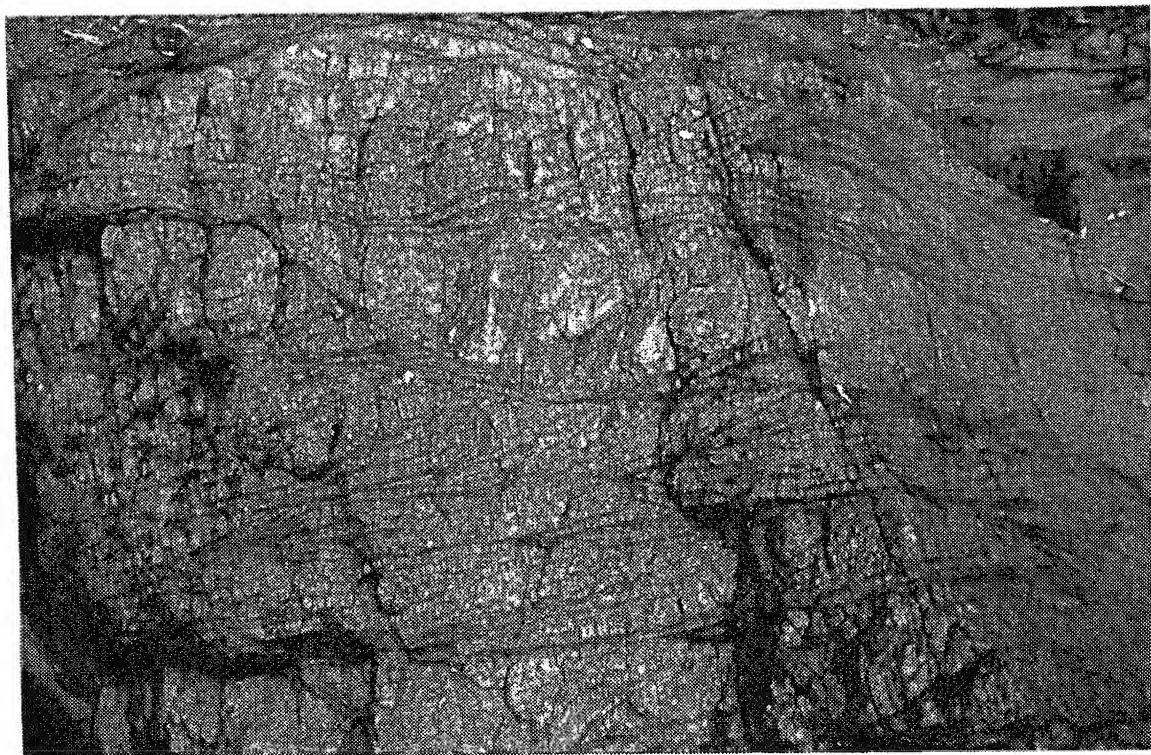
Figure 12.   Cross lamination in quartzite on gentle limb of F$_2$ fold.

Figure 13.   Well developed striping and feldspathic rodding on the gneissosity in Anasagar gneiss close to the conta
quartzite.

Polyphase deformation has affected both the Anasagar gneiss and the enveloping supracrustal rocks. The most commonly observed structures in the

alternate subhorizontal and steep, at places turned, limbs (figure 15). The axial planes are w dipping, the dips varying from subhorizontal to
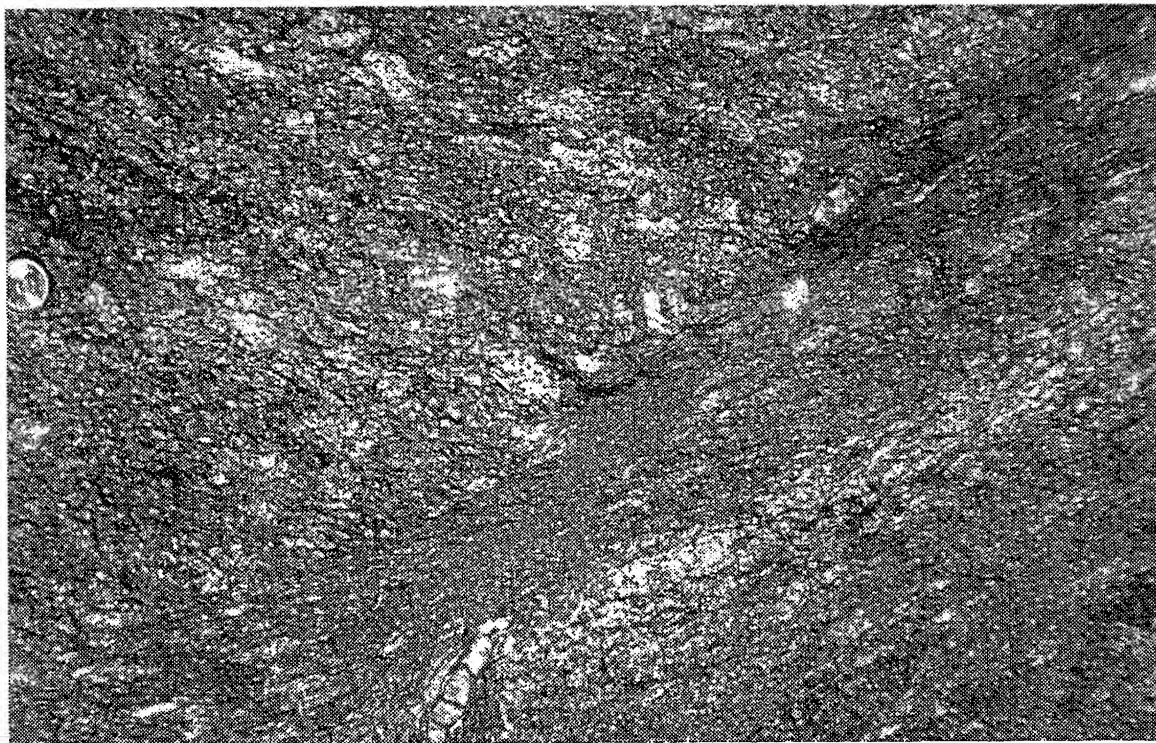
Figure 14.   Shear zone in Anasagar gneiss. Note the deformation of the megacrysts within the shear zone.

Figure 15.   F$_2$ fold with subhorizontal axial plane, long flat limb and subvertical short limb. Note development of higher order folds on the short limb. Subvertical face, east to the left.

bedding within the quartzite and the schistosity in the pelitic/semipelitic schists are folded by these asymmetrical folds which have a consistent sense of easterly vergence (figure 15). The axial planar structure is generally a crenulation cleavage (figures 10 and 17) but in the micaceous quartzite it is a disjunctive spaced cleavage. The fold axes are gently plunging with culminations and depressions. In the vicinity of

Figure 16. F_1 isoclinal fold refolded by F_2 folds with steep westerly dipping axial plane. Long edge of the photograph – 15 cm.
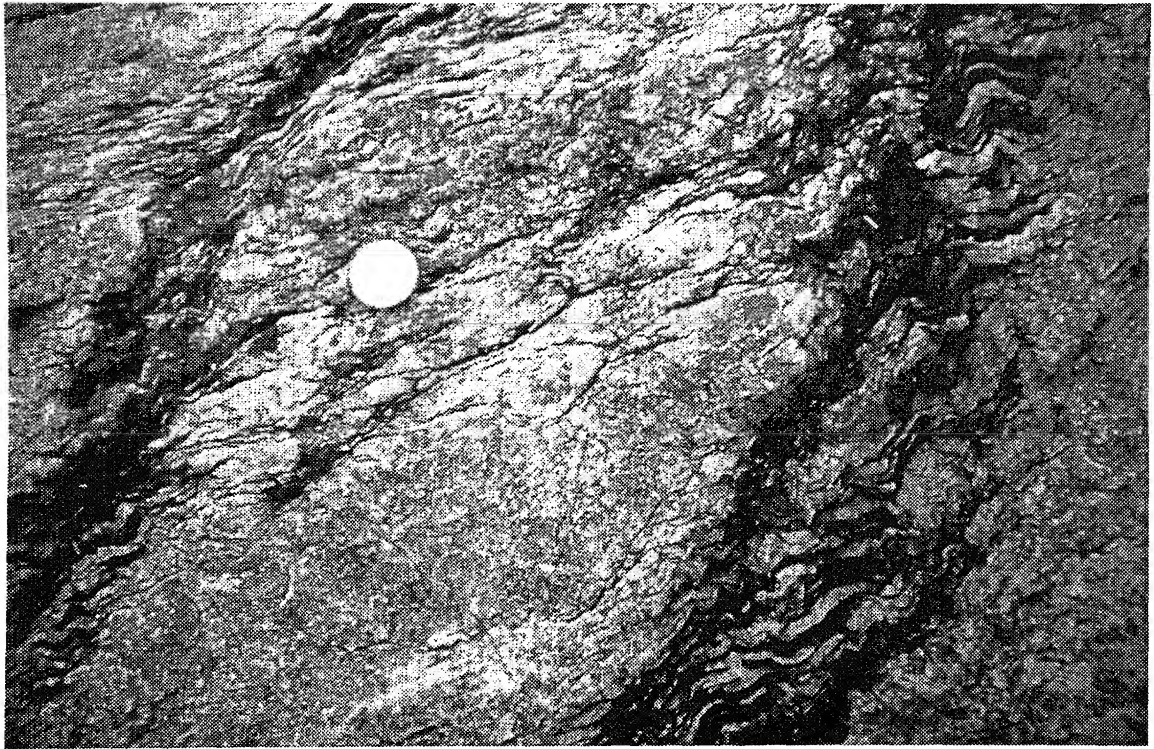
Figure 17. Eastward dipping bed on the steep limb of F_2 fold in quartzite. Gentler dipping first generation schistosity which is crenulated by F_2 having steep westerly dipping axial planes. Note that the S_0-S_1 relation and S_0/S_1-S_2 relation indicate opposite sense of vergence. Subvertical face, east to the left.

Ajmer the plunge is gentle to the south, but further north near Makarwali the folds are plunging to the north. This suggests a large scale F_2 culmination.

The consistent sense of vergence of the folds indicates their development in a simple shear regime with the top to the east sense of movement.

Folds with these characteristics are assigned to the second generation (F_2) as they refold isoclinal folds (F_1) with axial plane schistosity (figure 16). The F_1 folds are observed only within the supracrustal rocks. Because of the long limbed nature of the F_1 folds their sense of vergence is not clearly discernible everywhere. In some outcrops the bedding (S_0)-first schistosity (S_1) relation indicates a sense of vergence opposite to that shown by F_2 folds and cleavage (figure 17). Although this relation may be from one limb of a larger F_1 fold, no major F_1 fold has been mapped in the area. The two sets of folds are nearly coaxial, but at places there is a small angle between the two axes. The gneissosity within the Anasagar gneiss is definitely pre-F_2. F_1 folds are absent within the Anasagar gneiss; however, the overall attitude of the gneissosity is parallel to the axial planes of the F_1 isoclinal folds within the supracrustals.

The gentler limbs of the F_2 folds are folded by nearly upright coaxial folds (F_3) on both major and minor scales. It is possible that the F_2 and F_3 folds were formed during the earlier and later stages of the same deformation episode; in several outcrops the dip of the axial planes of F_3 folds varies from subhorizontal to steep (figures 15, 16 and 17). Nowhere are the F_3 folds observed to refold the F_2 asymmetrical folds.

The contact between the gneiss and the supracrustal rocks is invariably parallel to the gneissosity and at most places also parallel to the bedding of the overlying rocks. In the vicinity of Ajmer the eastern contact of the gneiss is folded by major F_2 and F_3 folds. Locally the contact acted as a plane of detachment during the folding of the quartzites and there is a discordance between the bedding in the overlying rocks and the contact surface which is parallel to the gneissosity of the underlying gneiss. In a spectacular outcrop near Makarwali (26°33'N : 74°38'E) subvertical bedding (steep limb of F_2 fold) is truncated by a subhorizontal contact with the underlying gneiss exhibiting horizontal foliation (figure 18). Such marked discordance is seen only at a few localities. Movement along some stretches of the contact is responsible for the finely banded nature of the gneiss described earlier.

The last episode of deformation (F_4) has given rise to puckers on the schistosity and large scale swings in the strike of bedding of quartzite on the eastern flank. These folds have E-W to ESE-WNW subvertical axial planes.

The field data collected during this study indicate that the gneiss is exposed in the core of an F_3 antiformal arch on the upper limb of an F_2 antiform (figure 19). The eastern contact of the gneiss is folded by F_2 with alternate flat and steep limbs. The western contact is the western limb of the large F_3 arch and is westerly dipping at gentle to steep angles. The southern closure of the gneiss is caused by the refolding of the steep westerly dipping (overturned) limb of the F_2 antiform on transverse axial plane (F_4), so that on the southern closure the sequence is overturned with the quartzite dipping northerly below the gneiss.
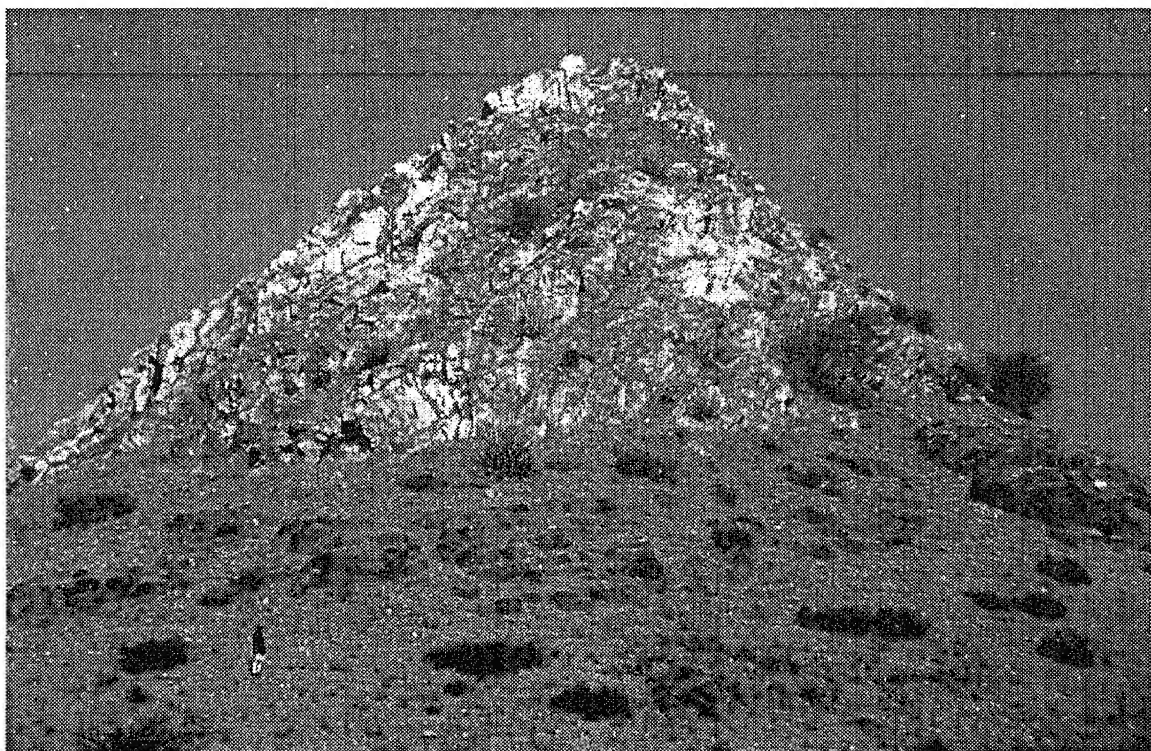

Figure 18. Quartzite with subvertical bedding resting on granite gneiss with subhorizontal gneissosity. Small F_2 folds with subhorizontal axial planes are present on the vertical bedding in quartzite near the left edge of the photograph. The subhorizontal contact is parallel to gneissosity but truncates the bedding in quartzite.
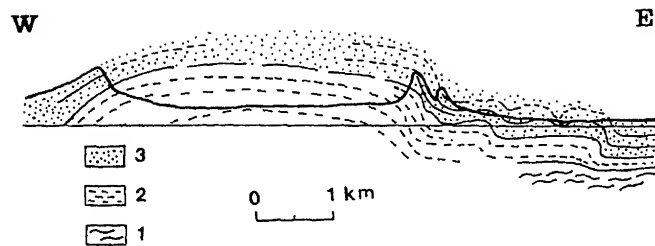
Figure 19. Interpretative E–W cross section across the Anasagar gneiss and its envelope. (1): underlying semipelitic schist; (2): Anasagar gneiss; (3): overlying quartzite.

The axial trace of the major F_2 antiform is bent by this F_4 fold and the hinge of the former is located in the southwestern corner of the gneiss outcrop. This structural pattern is schematically shown in figure 20. This interpretation contradicts the earlier model of a gneiss dome structure suggested by Tobisch et al (1994). As is also shown in Heron's (1953) map, the outcrop of the gneiss only closes at its southern end without any corresponding closure in the north. However, as mentioned earlier, there is a major culmination of F_2/F_3 axes near Makarwali, 8 km north of Ajmer. The westerly closing V on the contact between the Anasagar gneiss and the overlying quartzite 4 km to the north of Ajmer is an outcrop V only and not a fold closure. This V is formed where the contact is exposed on the subhorizontal western limb of a large F_2 fold. Being nearly horizontal the contact has traced the contour of a valley flowing to east. However, the Vs on the contact to the WSW and SW of Ajmer are

due to F_4 folds developed on the steep eastern limb of the large F_2.

The field relations, the nature of the xenoliths and the petrographic characters point to magmatic intrusion of the protolith of the Anasagar gneiss into a supracrustal psammo-pelitic sequence during the F_1 deformation. The magmatic foliation was enhanced into a gneissosity during the F_1 that has also engendered the S_1 schistosity in the country rocks. The other deformations are equally well recorded by the gneiss and the metasediments. Hence the onset of tectonism in the present sector coincided with the intrusion of the granite pluton now described as the Anasagar gneiss.

4. U-Pb geochronology

The zircon geochronology data presented below are part of a larger data set from several Precambrian gneiss units in northern Rajasthan. This work is nearly completed and will be published elsewhere (Lopez et al, in preparation). Some of these gneisses are considered part of the Banded Gneissic Complex from which ages ranging from Proterozoic to Archean have been reported (Choudhary et al 1984; Gopalan et al 1990; Tobisch et al 1994). The Anasagar sample dated herein is located within a 100 meter radius of sample #4 of Tobisch et al (1994, figure 1), who interpreted their data as defining a 2.8 Ga Sm–Nd reference isochron based on four samples (Tobisch et al 1994, figures 2 and 3). Subsequent work (Lopez et al 1996), however, indicates that the 2.8 Ga isochron reference age is significantly overestimated.

The sample of Anasagar gneiss used for the U-Pb dating contained abundant turbid gray zircon displaying euhedral, bipyramidal prismatic forms with 3:1 to 4:1 aspect ratios. Crystals ranged from 100 to 300 μm [microns] in length and contained large distinct cores. The zircon rims showed closely spaced growth rings typical of igneous zircon, while the cores were generally rounded, clear forms that displayed minor cracks and darkened areas. Cathodoluminescence and HF acid etching of polished grain mounts also revealed growth rings within some cores, which were concordant with the growth rings observed in the zircon rims.

Seven zircon fractions were analyzed for U-Pb isotopes using either a $^{208}Pb/^{235}U$ or a $^{205}Pb/^{235}U$ mixed isotope tracer. All fractions were mechanically air-abraded at 3 p.s.i. for approximately twenty four hours. Zircon geochronology analytical methods are briefly described in table 1 and follow conventional chromatography methods (Krogh 1973). The Anasagar zircon analyses consisted of one ~80 grain fraction, three 9 grain or less fractions, and three single grain fractions (table 2). The single grain analyses are of mechanically separated and abraded cores. All analyses are discordant between 3.8% and 31%.
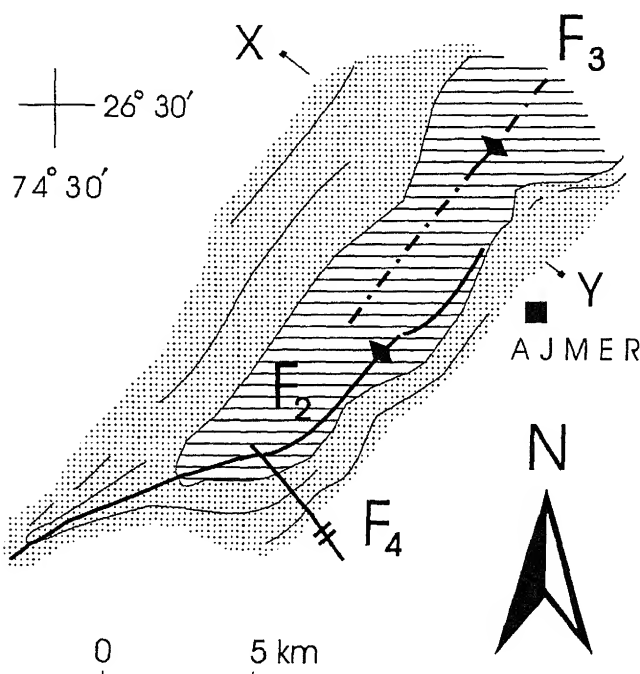

Figure 20. Generalized geological map of Anasagar gneiss and its envelope. Axial traces of some major folds shown. X–Y line of section in figure 19. Horizontal ruling – Anasagar gneiss,

Table 2. *U-Pb geochronologic data from the Anasagar Gneiss, central Rajasthan, India.*

Fraction[†]	Weight mg	Pb ppm	U ppm	Pb* (pg)	Common Pb (pg)	Observed Ratios[††]			Atomic ratios[††]			Ages Ma[†††]		
						$^{206}Pb/^{204}Pb$	$^{207}Pb/^{206}Pb$	$^{208}Pb/^{206}Pb$	$^{206}Pb^*/^{238}U$	$^{207}Pb^*/^{235}U$	$^{207}Pb^*/^{206}Pb^*$	$^{206}Pb^*/^{238}U$	$^{207}Pb^*/^{235}U$	$^{207}Pb^*/^{206}Pb^*$
nm,abr,4 grains	6	44	127	262	2.3	1,088	7.955	7.519	0.31892	4.9905	0.11349	1785	1817	1856 ± 3
nm,abr,9 grains	35	98	308	3430	0.3	35,299	8.855	10.311	0.30539	4.7439	0.11266	1718	1775	1842 ± 1
nm,abr,6 grains	20	57	192	1139	0.9	10,011	8.801	9.154	0.28147	4.3621	0.11240	1599	1705	1839 ± 1
nm,abr,single grain	7	118	426	808	18	1,991	8.433	10.174	0.26421	4.0855	0.11215	1511	1651	1835 ± 2
nm,abr,single grain	7	124	454	864	0.9	4,186	8.872	10.967	0.26307	4.0664	0.11211	1506	1648	1834 ± 1
nm,abr,single grain	4	148	612	587	3.1	4,322	8.708	10.387	0.23254	3.5954	0.11214	1348	1549	1834 ± 2
mag,abr,~80 grains	152	145	645	22013	73	10,908	8.991	9.125	0.21397	3.2819	0.11124	1250	1477	1820 ± 4

[†] * denotes radiogenic Pb. Fractions 1 through 6 are nonmagnetic at 2 amperes on the Frantz[TM] isodynamic magnetic separator, nm = non-magnetic; mag = magnetic; abr = abraded. Zircon dissolutions and chemistry were made following the methods of Krogh (1973) using Parrish (1987)-type microcapsules.

[††] Two sigma uncertainties on the $^{207}Pb/^{206}Pb$ and $^{208}Pb/^{206}Pb$ ratios are <0.4% and generally better than 0.08%; uncertainties in the $^{206}Pb/^{204}Pb$ ratios vary from 0.4% to 1.8%.

[†††] Decay constants used: $^{238}U = 1.55125 \times 10^{-10}$, $^{235}U = 9.8485 \times 10^{-10}$, $^{238}U/^{235}U = 137.88$. Estimated uncertainties of the $^{206}Pb^*/^{238}U$ and $^{207}Pb^*/^{235}U$ ratios are ±0.4% based on replicate analysis of a single zircon fraction. $^{207}Pb^*/^{206}Pb^*$ age uncertainties are 2 sigma and from the data reduction program PBDAT of K Ludwig (1991). Observed ratios are not corrected. In calculating ages, the measured ratios are adjusted for mass fractionation of 1‰ per a.m.u. for Pb and <10pg of Pb blank. Initial Pb corrections are from Stacy and Kramers (1975) two stage Pb evolution model. Isotopic data were measured on the UC Santa Cruz VG 54-30 sector multicollector mass spectrometer equipped with a pulse counting Daly detector.
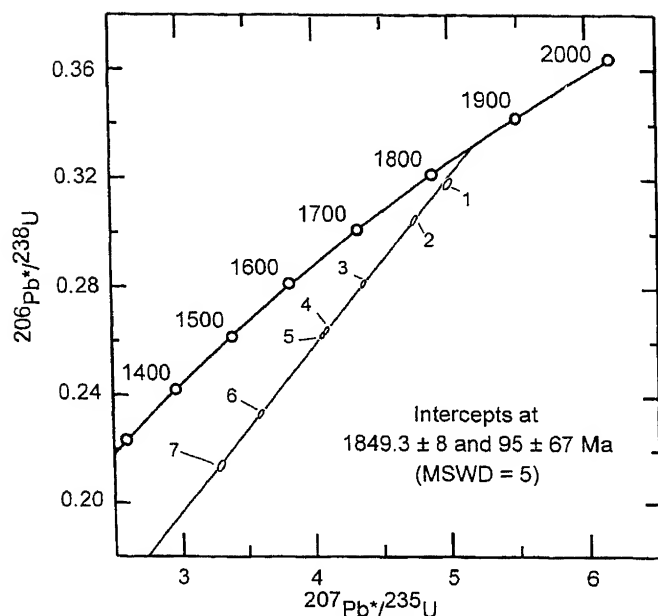
Figure 21. U-Pb concordia diagram for the Anasagar gneiss. Numbered ellipses correspond to numbered fractions in table 2.

(MSWD = 5) with an upper intercept age of 1849 Ma +/− 8 m.y. and a lower intercept age of 95 Ma +/− 67 m.y. (figure 21). The upper intercept of 1849 Ma is interpreted as the crystallization age of the Anasagar granite gneiss. The lower intercept is interpreted as present day Pb loss. Abrasion of the zircons enhanced the core material, and the single grain analyses also increased the likelihood of constraining the age of the core component. However, no Archean component was observed.

Based on the zircon geochronology described above, the crystallization age of Anasagar gneiss is interpreted to be Paleoproterozoic (1.85 Ga). The previously reported Sm/Nd isochron age of 2.8 Ga (Tobisch et al 1994) can be explained by open system behaviour of the Sm/Nd isotopic ratios for one or more samples used in the regression or by a selection of samples with heterogeneous ages for the isochron regression. It is further noted that we are not excluding the possibility of an Archean component in northern BGC of Rajasthan. Our conclusion is that there is no evidence of an Archean component in the zircon cores of the Anasagar gneiss, and that further U/Pb zircon geochronology is required to corroborate the Archean component inferred from other isotopic systems. This interpretation is evaluated in some detail in Lopez et al (in preparation).

5. Conclusions

From the relationships described above we conclude that the Anasagar gneiss was emplaced as a concordant granitic body at the late stage of F_1 deformation and prior to F_2. It intruded along the boundary between an overlying psammitic and an underlying pelitic/semipelitic unit probably because this provided an easy pathway for the magma. It was suggested earlier that the magma may have been derived by melting of the Pre-Delhi basement and intruded as a sill like body (Tobisch et al 1994).

The consistent sense of vergence of the major F_2 folds in the area suggests their development in a simple shear regime with the top to the east sense of movement. Within the Delhi supracrustal rocks in the south of the area the major F_1 folds also show an identical sense of vergence (Mukhopadhyay and Matin 1991; Sengupta 1996). This easterly vergence fits with the model of westward subduction in the Delhi orogeny (Sinha Roy et al 1995; Sharma 1995).

Our field observations do not provide unambiguous evidence concerning the stratigraphic status of the supracrustal envelope. Such thick quartz arenites are not typically present in the South Delhi Fold Belt, with the exception of the locally developed Rajgarh Formation which is supposed to be older than the typical carbonate association in SDFB (Gupta et al 1991). It is possible that the Anasagar gneiss with its supracrustal envelope is part of a Pre-Delhi sequence. A point in favour is the similarity in structural styles of the F_2 and F_3 folds at Anasagar with those of the F_1 and F_2 folds respectively in the eastern flank of SDFB (Mukhopadhyay and Matin 1991). The crystallization age of the Anasagar gneiss is ca. 1850 Ma; no granitic intrusives as old as the Anasagar gneiss are presently documented in the SDFB. U-Pb zircon geochronology on wall rock and granitic samples currently in progress may clear some of these uncertainties.

Acknowledgements

References

Ashworth J R 1972 Myrmekites of exsolution and replacement origins; Geol. Mag. 109 45–62

Choudhary A K, Gopalan K and Sastry C A 1984 Present status of the geochronology of the Precambrian rocks of Rajasthan; Tectonophysics 105 131–140

Deb M 1996 VMS deposits: A contemporary genetic model and a review of the data base of these deposits in the southern Aravalli range. Abstract Vol. Seminar on Mineralisation in western Indian craton, Delhi University, 26–30

Fareeduddin Reddy M S and Bose U 1995 Reappraisal of the Delhi stratigraphy in the Ajmer-Sambhar sector, north-central Rajasthan; J. Geol. Soc. India 45 667–679

Gangopadhyay P K and Das D 1974 Dadikar granite: a study on a Precambrian intrusive body in relation to structural

environment in north-eastern Rajasthan; *J. Geol. Soc. India* **15** 189–199

Gopalan K, Macdougall J D, Roy A B and Murali A V 1990 Sm-Nd evidence for 3.3 Ga old rocks in Rajasthan, north-western India; *Precamb. Res* **48** 287–297

Gupta P, Mukhopadhyay K, Fareeduddin and Reddy M S 1991 Tectono-stratigraphic framework and volcanic geology of the South Delhi Fold Belt in central Rajasthan; *J. Geol. Soc. India* **37** 431–441

Heron A M 1953 The geology of central Rajputana; *Geol. Surv. India Mem.* **79** 389p

Hyndman D W 1985 Petrology of igneous and metamorphic rocks; 2nd ed. (McGraw Hill), 786p

Krogh T E 1973 A low contamination method for hydrothermal decomposition of zircon and extraction of U and Pb for isotopic age determination; *Geochim. et Cosmochim. Acta* **46** 560–567

Lopez R, Mukhopadhyay D, Bhattacharyya T and Tobisch O T 1996 Proterozoic rim and core zircon ages from the Anasagar gneiss, central Rajasthan, India; *Geol. Soc. Am. Abs. Programs* **28(7)** A492

Ludwig K R 1991 PBDAT: a computer program for processing Pb-U-Th isotope data, version 1.20; U.S. Geological Survey, Open-File Report 88–542

Mukhopadhyay D and Matin A 1991 Early major folds in the Delhi Supergroup around Hatankhera, Ajmer District, Rajasthan; *Indian J. Geol.* **63** 67–74

Parrish R R 1987 An improved micro-capsule for zircon dissolution in U-Pb geochronology; *Chemical Geol.* (Isotope Geoscience Section) **66** 99–102

Phillips E R, Ransom D M and Vernon R H 1972 Myrmekite and muscovite developed by retrograde metamorphism at Broken Hill, New South Wales; *Mineral. Mag.* **38** 570–578

Pitcher W S 1997 The nature and origin of granite (Chapman and Hall), 387p.

Sengupta P 1996 Structures in the Delhi Supergroup in the area around Baila, East of Beawar, Ajmer District, Rajasthan. (Unpublished M.Sc. dissertation, University of Calcutta.)

Sharma R S 1995 An evolutionary model for the Precambrian crust of Rajasthan: some petrological and geochronological considerations; *Mem. Geol. Soc. India* **31** 91–115

Sinha Roy S, Malhotra G and Guha D B 1995 A transect across Rajasthan Precambrian terrain in relation to geology, tectonics, and crustal evolution of south-central Rajasthan; *Mem. Geol. Soc. India* **31** 63–89

Stacey J S and Kramers J D 1975 Approximation of terrestrial lead isotope evolution by a two-stage model; *Earth Planet. Sci. Lett.* **26** 207–221

Swanson S E 1977 Relation of nucleation and crystal growth to the development of granitic structures; *Am. Mineral.* **62** 966–978

Tobisch O T, Collerson K D, Bhattacharya T and Mukhopadhyay D 1994 Structural relationships and Sm-Nd isotope systematics of polymetamorphic granitic gneisses and granitic rocks from central Rajasthan, India: implications for the evolution of the Aravalli craton; *Precamb. Res.* **65** 319–339

Vernon R H 1986 K-feldspar megacrysts in granites-phenocrysts, not porphyroblasts; *Earth. Sci. Rev.* **23** 1–63

Volpe A M and Macdougall J D 1990 Geochemistry and isotope characteristics of mafic (Phulad ophiolite) and related rocks in the Delhi Supergroup, Rajasthan, India: implications for rifting in the Proterozoic; *Precamb. Res.* **48** 167–191

Emplacement of Amba Dongar carbonatite-alkaline complex at Cretaceous/Tertiary boundary: Evidence from ^{40}Ar-^{39}Ar chronology

JYOTIRANJAN S RAY, KANCHAN PANDE* and T R VENKATESAN

Physical Research Laboratory, Ahmedabad 380 009, India.
*email: kanchan@prl.ernet.in

^{40}Ar-^{39}Ar analyses of three fresh alkaline rock samples and a phlogopite separate from a carbonatite from Amba Dongar carbonatite-alkaline complex of the Deccan Flood Basalt Province, India, yield indistinguishable precise plateau ages of 64.8 ± 0.6, 64.7 ± 0.5, 65.5 ± 0.8 and 65.3 ± 0.6 Ma, giving a mean plateau age of 65.0 ± 0.3 Ma, which is the age of emplacement of this complex. This age implies contemporaneity of Amba Dongar with several other carbonatite-alkaline activities of Chhota Udaipur subprovince and is consistent with their Reunion-Deccan plume origin hypothesis. The emplacement of these complexes at 65 Ma makes them very significant in the ongoing debate on the K/T extinctions owing to their capacity to rapidly inject a substantial amount of CO_2 and SO_2 into the atmosphere.

1. Introduction

The Amba Dongar carbonatite-alkaline complex, the first carbonatite complex to be identified in Asia (Sukheswala and Udas 1963), is located 2 km north of the Narmada river in Baroda district of Gujarat state and is a part of a large alkaline district of Chhota Udaipur (Sukheswala and Viladkar 1978). The rocks of this complex intrude into the Precambrian basement gneisses (Aravallis), Cretaceous Bagh sediments (sandstones and limestones) and some earlier flows of Deccan tholeiites. The general belief is that the Amba Dongar alkaline complex, like Phenai Mata of the same alkaline province (Chhota Udaipur), represents one of the late magmatic pulses of the Deccan flood basalts (Basu *et al* 1993). However there is no unambiguous age data in support of this hypothesis. Very early attempts by Deans and Powell (1968) and Deans *et al* (1973) to date the pyroxenes from nephelinites and two feldspars from potash fenites, using K-Ar method of dating, yielded varying ages of 37.5 ± 2.5 Ma, 61 ± 2 Ma and 76 ± 2 Ma, respectively. Basu *et al* (1993) reported an ^{40}Ar-^{39}Ar age of 65 Ma (by dating the

olivine gabbro) for the Phenai Mata alkaline complex, which is geographically close to Amba Dongar and is a part of the Chhota Udaipur alkaline district. However, it has so far not been clearly established whether Phenai Mata and Amba Dongar are temporally related. To establish the temporal relationship between the Amba Dongar alkaline complex and the Deccan Traps, precise ^{40}Ar-^{39}Ar dating of samples from Amba Dongar was undertaken. This would also allow one to assess the postulated relationship of these carbonatite complex with the Reunion-Deccan plume activity.

2. Geology and earlier work

The Amba Dongar complex is characterized by concentric ring dykes of carbonatites and carbonatite breccia with tholeiitic basalt at the central depression. The alkaline silicate rocks are present as plugs and dykes in the low surrounding area of the main ring dyke (figure 1). Fenitization, both potash and sodic, of the country rocks is an easily noticeable feature in this

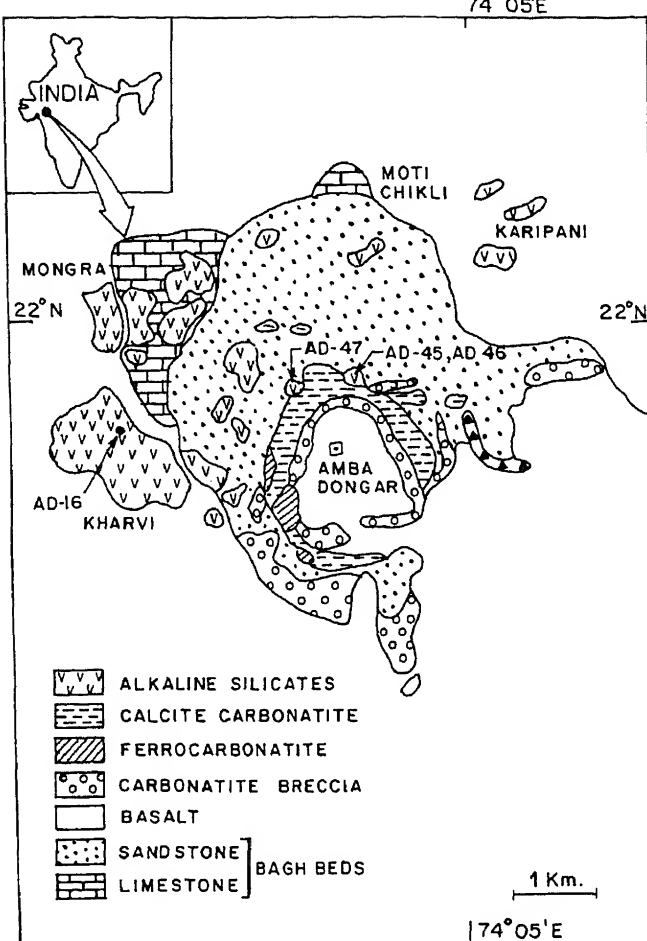**Keywords.** Amba Dongar carbonatites; Deccan Flood Basalts; ^{40}Ar-^{39}Ar chronology; K/T boundary.

Figure 1. Geological map of Amba Dongar carbonatite-alkaline complex (after Viladkar 1996) showing various lithologies and sample locations.

~ 76 Ma; Deans *et al* (1973)]. We believe that the lower age (~ 37 Ma) reflects the loss of argon from the system, whereas the higher age (~ 76 Ma) possibly resulted from the selection of the wrong feldspar samples that might have been from a fenitized gneissic xenolith. However, it is very difficult to give a critical comment on such ages as the authors neither provide the details of the samples nor the experimental procedure that was followed for the analyses. In a recent study, Basu *et al* (1993) have dated the Phenai Mata alkaline complex to 64.9 ± 0.11 Ma. Owing to its occurrence within the same alkaline district (Chhota Udaipur) of Deccan, Amba Dongar was also believed to have been emplaced close to Phenai Mata in time (Sen 1995; Simonetti *et al* 1998).

Earlier geochemical studies have not clearly established the genetic link between Amba Dongar with the surrounding Deccan tholeiites. Nevertheless, based on Wyllie (1988)'s model and the chronology of alkaline activities Basu *et al* (1993) have proposed that such alkaline activities either represent early or late igneous pulses of the Deccan flood basalt province. Based on combined Sr-Nd-Pb isotopic study on Amba Dongar carbonatites Simonetti *et al* (1995) suggested that these rocks bear signatures of a mantle plume and the similarity of various isotopic ratios with those of the least altered Deccan tholeiites has been interpreted by the authors as the evidence for the Reunion-Deccan plume derivation for Amba Dongar. According to Sen (1995), in a plume model the alkaline and carbonatite magmas are generated from the volatile rich rim of the plume, which is consistent with the observation that most of such complexes of Deccan occur in the periphery of the main tholeiitic eruptive center.

The relationship between the carbonatites and associated silicate rocks of Amba Dongar has not yet been established firmly. Some workers believe that these rocks were derived by means of silicate-carbonate melt immiscibility (Srivastava 1997; Ray 1997) and some believe that they have crystallized from two different parent magmas with the alkaline silicate being the older (Viladkar 1996). However, in a recent work of Sr isotope systematics in Amba Dongar and adjacent complexes (Ray 1998), it has been proposed that the silicate-carbonate melt immiscibility was responsible for their generation.

3. Experimental technique

Whole rock samples of alkaline silicates and phlogopite mineral separates from carbonatites were analyzed. For whole rocks, fresh samples were powdered in a stainless steel mortar and pestle to 100–150 μm size. About 600–700 mg aliquot of homogenized powders were used. For mineral separates (phlogopite), minerals were hand picked from whole rock powders and about 100–200 mg of pure mineral

complex. In addition, the carbonatites of this complex host a massive fluorite deposit. Carbonatites of this complex are of two types, calcite carbonatite and ferrocarbonatite. Calcite carbonatite forms the ring dyke with ferrocarbonatite as plugs within it. These also occur as numerous veins within earlier formed varieties. The alkaline silicate rocks have been identified as tinguaite, nephelinite and phonolite. Petrographic studies revealed that the calcite carbonatites vary from very coarse grained to fine grained with calcite as the major mineral (>70%) and magnetite, apatite and phlogopite as common accessories. Ferrocarbonatites are fine grained dark red coloured rocks in which ankerite is the major carbonate mineral. These rocks are invariably altered and contain lots of secondary products and are heavily affected by the fluorite mineralization. Alkaline silicate rocks contain nepheline, aegerine-aguite and melanite as phenocrysts, and analcite and calcite in the ground mass.

As mentioned above, earlier attempts to date the time of emplacement of Amba Dongar (by K-Ar method) have not been successful as the results showed a large variation in the age [from ~ 37 Ma to

separates were taken for analysis. Whole rock powders and mineral separates were ultrasonicated with 0.05 N HCl (to remove unwanted carbonates) and water several times and dried before being packed for irradiation. The 520.4±1.7 Ma old Minnesota Hornblende (MMhb-1) (Samson and Alexander 1987) was used as a monitor. Samples along with the monitor were irradiated in the central core of the light water moderated APSARA reactor at the Bhabha Atomic Research Center, Mumbai, for about 100 hours. The reactor was not operative continuously, therefore, appropriate correction for ^{37}Ar decay was used (Venkatesan $et\ al$ 1993). Maximum neutron fluence variation was estimated to be ~5%. Interference corrections were based on analysis of pure CaF_2 and K_2SO_4 salts irradiated with the samples. The values for $^{36}Ar/^{37}Ar$, $^{39}Ar/^{37}Ar$ and $^{40}Ar/^{39}Ar$ salt ratios are: 0.0003112, 0.0006827 and 0.079, respectively.

For each irradiated sample, argon gas was extracted in a series of fifteen or more steps of increasing temperatures up to 1400°C in an electrically heated ultra-high vacuum furnace. The isotopic ratios of the argon gas released in each step, after a two-step purification, was measured using an AEI MS10 mass spectrometer in static mode. We define a plateau as comprising four or more contiguous steps in an apparent age spectrum with apparent ages that overlap the mean at 2σ level of error excluding the error contribution from the J-value. The plateau ages are weighted means of the apparent ages of steps forming the plateaus. Weighted means of apparent ages are calculated using the method of Bevington (1969). Isochron ages have been computed using the two error regression method outlined by York (1969) of data points corresponding to the plateau steps.

4. Results and discussion

Three fresh alkaline rock samples (AD-16, AD-45 and AD-47) and a phlogopite separate from a carbonatite (AD-46) were dated (see figure 1 for sample locations). The plateau ages along with per cent ^{39}Ar included for the plateaus; isochron ages and inverse isochron ages of plateau steps along with ratios of

trapped argon and MSWD values; and integrated (total) ages are summarized in table 1. The age spectra along with isotope correlation plots for all four samples are shown in figures 2–5. Errors quoted in all the values are at 2σ level. Two alkaline rocks (AD-16 and AD-45) and the phlogopite separate from a carbonatite (AD-46) yielded good plateaus in the age spectra (figures 2(a), 3(a) and 4(a)) giving ages of 64.8 ± 0.6 Ma, 64.7 ± 0.5 Ma, and 65.5 ± 0.8 Ma, respectively. The third alkaline rock (AD-47) yielded a 10 step high temperatures plateau (from 600°C to 1050°C) with an age of 65.3 ± 0.6 Ma (figure 5(a)). The three low temperature steps of AD-47 (figure 5(a)) showed higher apparent ages, perhaps due to recoil effect (Venkatesan $et\ al$ 1993). The one or more initial and final temperature steps (figures 2(a), 3(a), 4(a) and 5(a)), which are not included in the plateaus, showed large errors in their apparent ages due to the very small amount of ^{39}Ar-release in these steps. For all the four samples, there is an excellent agreement between plateau and isochron ages indicating that these samples have not lost any significant amount of radiogenic argon since their crystallization. The undisturbed nature of these samples is also reflected in the total ages, which are indistinguishable from the plateau ages within the 2σ level of error. In the isotope correlation plots of the plateau steps of all these samples showed atmospheric trapped argon composition [i.e. $(^{40}Ar/^{36}Ar)_i = 295.5$] within the limits of uncertainties (2σ errors) implying that the plateau ages are the true ages of the samples. Indistinguishable ages of alkaline silicate rocks and carbonatites suggest that these two rock types of Amba Dongar complex are contemporaneous. Therefore, the weighted mean (determined following Bevington (1969)'s procedures) of all plateau ages, 65.0 ± 0.3 Ma, is the age of emplacement of the Amba Dongar complex.

The contemporaneity of alkaline silicate rocks and carbonatites of Amba Dongar complex is consistent with the idea of their formation as a result of carbonate-silicate liquid immiscibilty. The 65.0 ± 0.3 Ma age of this complex also suggests that the complex got emplaced towards the end phase of Deccan Trap magmatism and it is ~2.0 Ma younger than the main pulse of Deccan (67.0 Ma; Venkatesan $et\ al$ 1993). As

Table 1. *Summary of results of ^{40}Ar-^{39}Ar dating of Amba Dongar samples.*

Sample	Plateau			Isochron			Inverse isochron			Integrated age
	steps	%^{39}Ar	Age (Ma)	Age (Ma)	Trap	MSWD	Age (Ma)	Trap	MSWD	
AD-16	13	97.88	64.8±0.6	64.5±1.7	297.4±13.2	0.064	65.0±4.3	292.7±11.5	0.047	64.5±1.5
AD-45	14	98.27	64.7±0.5	65.0±1.4	297.7±12.8	0.282	64.5±4.2	306.7±13.2	0.069	65.5±1.4
AD-46	10	98.27	65.5±0.8	65.4±1.9	295.9±6.5	0.115	65.4±3.3	295.9±6.5	0.115	65.4±1.6
AD-47	9	61.05	65.3±0.6	65.4±1.4	296.9±23.4	0.116	65.0±9.3	310.6±29.9	0.059	67.2±1.4

Note: Trap: Initial $^{40}Ar/^{36}Ar$ (trapped argon); MSWD: Mean Square Weighted Deviate.
Errors are 2σ.
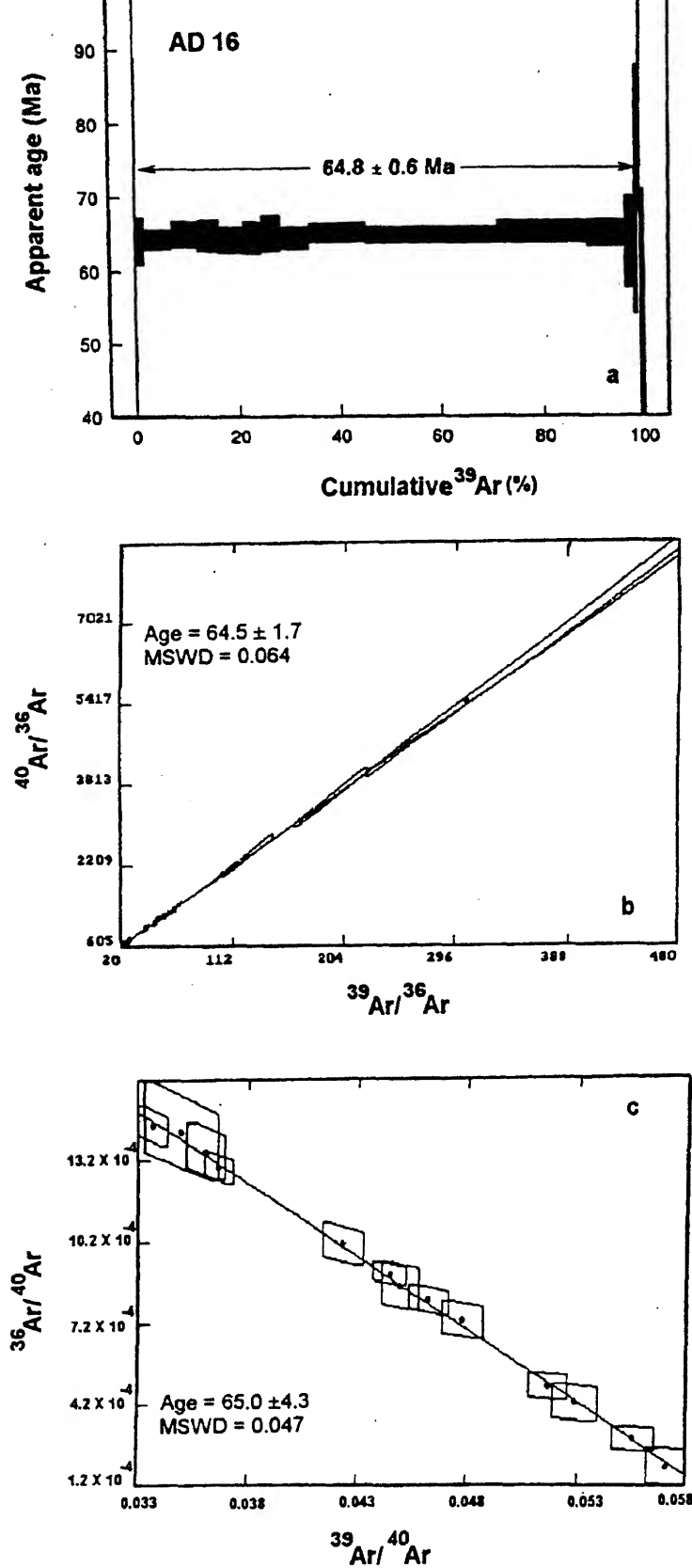
Figure 2. (a) Step heating ^{40}Ar-^{39}Ar apparent age spectrum for AD-16 (nephelinite). The age shown is the plateau age, which includes 2σ error on J but the vertical width of individual plateau boxes indicate 2σ errors calculated without error on J. (b) and (c) are isotope correlation diagrams (^{40}Ar/^{36}Ar vs. ^{39}Ar/^{36}Ar and ^{36}Ar/^{40}Ar vs. ^{39}Ar/^{40}Ar isochron diagrams, respectively) for AD-16 showing 2σ error envelopes and regression lines.
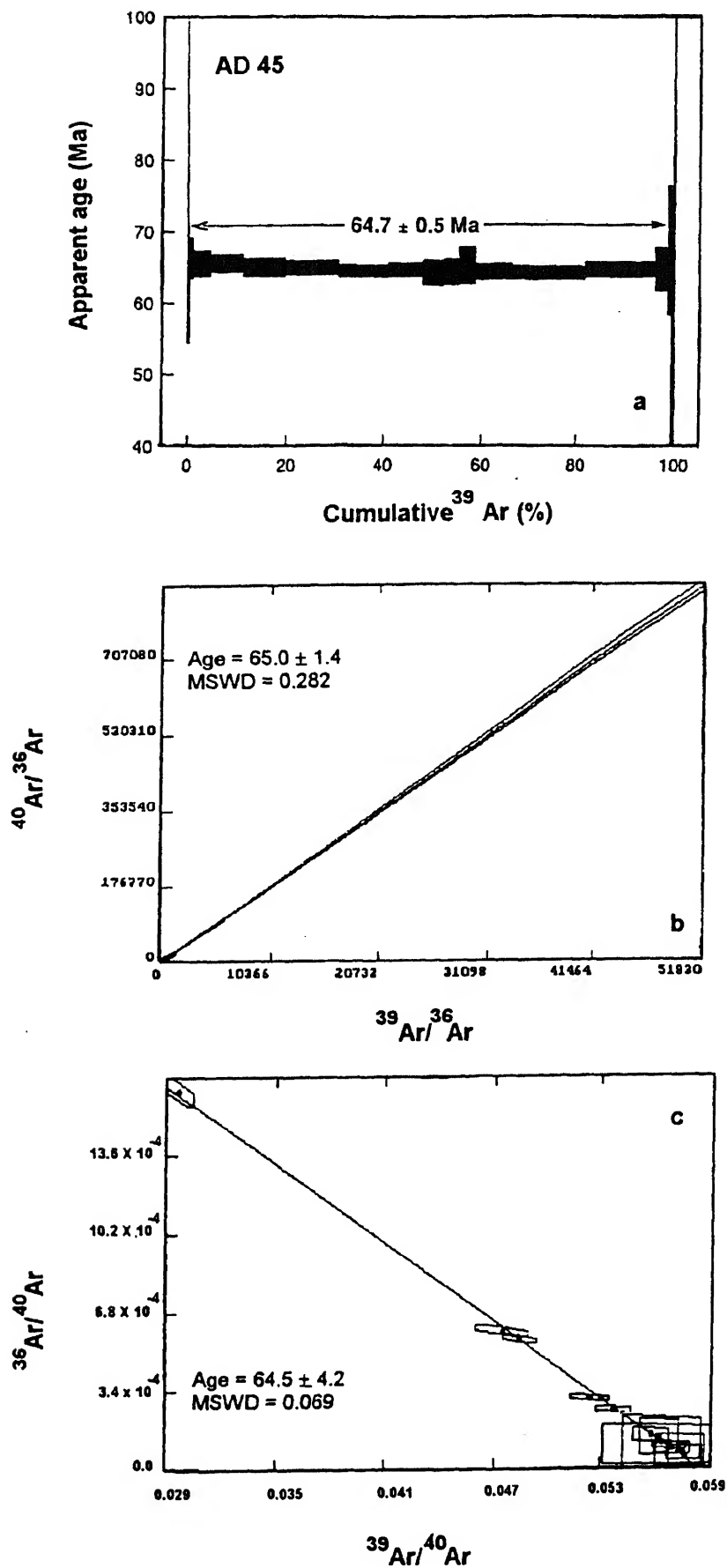
Figure 3. Step heating ^{40}Ar-^{39}Ar apparent age spectrum for AD-45 (tinguaite) (a) and isotope correlation diagrams (b and c). Please also see the caption of figure 2.
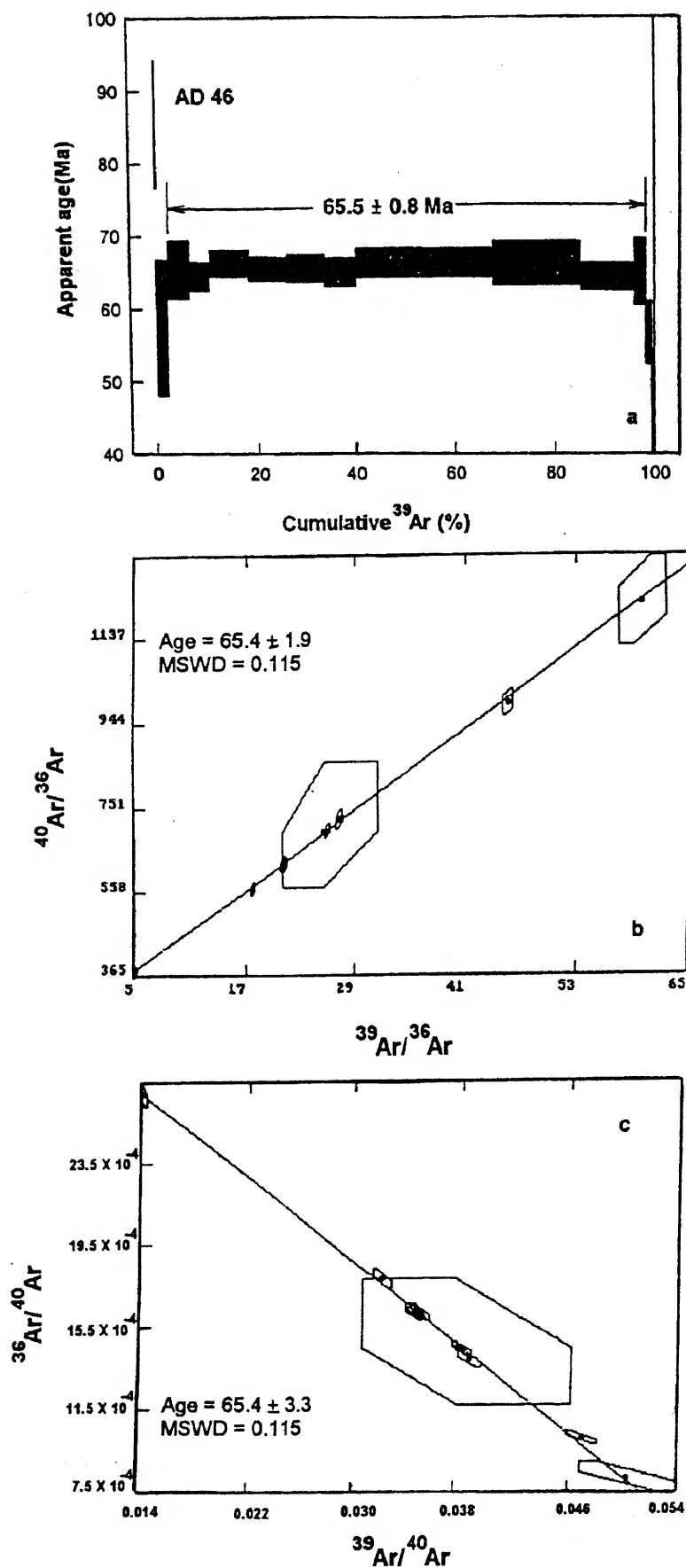
Figure 4. Step heating ^{40}Ar-^{39}Ar apparent age spectrum for AD-46 (phlogopite separate from a carbonatite) (a) and isotope correlation diagrams (b and c). Please also see the caption of figure 2.
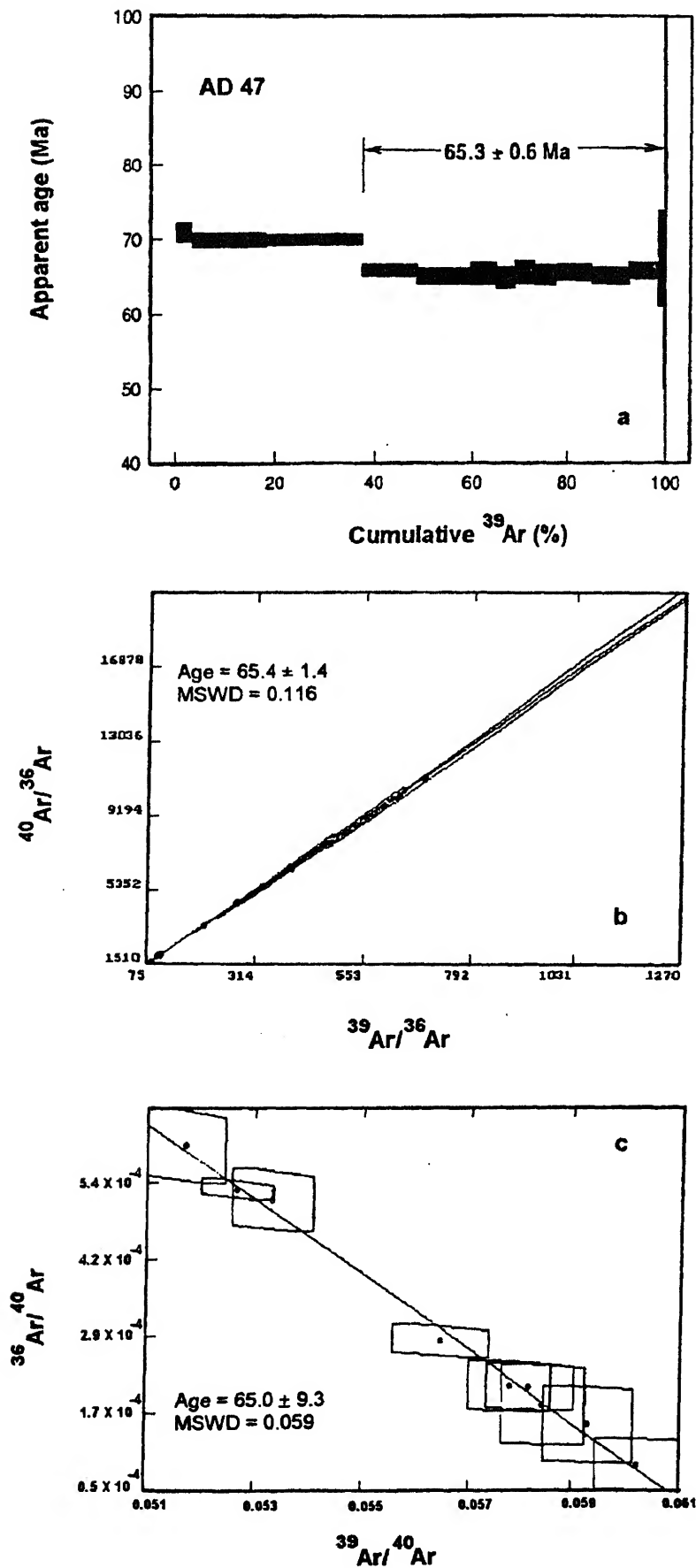
Figure 5. Step heating ^{40}Ar-^{39}Ar apparent age spectrum for AD-47 (tinguaite) (a) and isotope correlation diagrams (b and c). Please also see the caption of figure 2.

mentioned earlier, the Amba Dongar complex intrudes into the Deccan tholeiites of this region. Therefore, the Traps of this region are older than 65.0 Ma. This age of Amba Dongar complex along with the two northern most 68.5 Ma old alkaline complexes at Sarnu-Dandali and Mundwara fits well in the plume theory for the generation of Deccan flood basalts and is consistent with the idea of 10–15 cm/year northward motion of the Indian plate over nascent Reunion hotspot (Basu *et al* 1993). In this plume model, Amba Dongar complex would represent a late stage alkaline magmatism on the northern end of the rim of the plume head at 65 Ma.

Amba Dongar is a part of the Chhota Udaipur carbonatite-alkaline district of Gujarat, which covers an area of $\sim 200\,km^2$ (Viladkar 1996) and consists of several alkaline complexes. Phenai Mata alkaline complex (present to the northwest of Amba Dongar), which is also a part of this district, has been dated to 64.96 ± 0.11 Ma by Basu *et al* (1993). This probably indicates that the carbonatite-alkaline magmatism of this district occurred at 65.0 Ma, which happens to be just at the K/T boundary (Izett *et al* 1991). This coincidence makes these carbonatite alkaline magmatisms very important in the ongoing debate on the K/T mass-extinctions. Alkaline and carbonatite magmatism are associated with the release of very high amount of $CO_2 + SO_2$ gases (Bailey and Hampton 1990). Owing to their very low viscosity and density (Treiman 1989) these melts get emplaced/erupted very fast (in a few years); (Williams *et al* 1986), which obviously results in a lot of volatile input into the atmosphere in a very short interval of time. A conservative estimation, using the procedures described by Leavitt (1982), shows that the total CO_2 flux from just the carbonatites of Chhota Udaipur district was 2.67×10^{14} moles, which came out in a very short period of time (in a few years). Workers who believe in the internal cause (i.e. Deccan Volcanism) to be responsible for the mass-extinctions at K/T boundary suggest that the high amount of CO_2 released due to the Deccan volcanism ($\sim 5 \times 10^{17}$ moles in ~ 1 Ma; McLean *et al* 1985) is one of the major reasons for the catastrophism. In this context the carbonatite-alkaline magmatism of Chhota Udaipur district would have enhanced the catastrophic effects due to addition of a very significant amount of CO_2 in a very short time into the already disturbed atmosphere. A similar estimation for SO_2 released during these activities is in progress.

5. Conclusion

The age of Amba Dongar carbonatite-alkaline complex is 65 Ma. This age implies that the complex got emplaced late in the Deccan flood basalt volcanism and is consistent with the Reunion-Deccan plume

hypothesis proposed for the origin of this complex. This complex appears to be coeval with many other alkaline complexes of Chhota Udaipur subprovince of the Narmada region. Being emplaced just at the K/T boundary these could have enhanced the catastrophic effects leading to mass extinctions, by rapidly injecting a substantial amount of CO_2 and probably SO_2 as well into the atmosphere.

References

Bailey D K and Hampton C M 1990 Volatiles in alkaline magmatism; *Lithos* **26** 156–165

Basu A R, Renne P R, Das Gupta D K, Teichman F and Poreda R J 1993 Early and late alkali igneous pulses and a high ³He plume origin for the Deccan flood basalts; *Science* **261** 902–906

Bevington P R 1969 *Data reduction and error analysis for the physical sciences* (New York: McGraw Hill Co.)

Deans T and Powell J L 1968 Trace elements and strontium isotopes in carbonatites, fluorites and limestone from India and Pakistan; *Nature* **218** 750–752

Deans T, Sukheswala R N and Viladkar S G 1973 Discussions and contributions; *Trans. Inst. Min. and Metall.* **82** B33–B40

Izett G A, Dalrymple G B and Snee L W 1991 ⁴⁰Ar-³⁹Ar age of Cretaceous-Tertiary boundary tektites from Haiti; *Science* **252** 1539–1542

Leavitt S W 1982 Annual volcanic carbon dioxide emission: an estimate from eruption chronology; *Env. Geol.* **4** 15–21

McLean D M 1985 Deccan Traps mantle degassing in the terminal Cretaceous marine extinction; *Cretaceous Research* **6** 235–259

Ray J S 1997 *Stable and radioisotopic constraints on the evolution of Mesozoic carbonatite-alkaline complexes of India.* Ph.D. thesis, MS Univ., Bododara

Ray J S 1998 Trace element and isotope evolution during concurrent assimilation, fractional crystallization and liquid immiscibility of a carbonated silicate magma; *Geochim. Cosmochim. Acta* (in press)

Samson S D and Alexander Jr E C 1987 Calibration of the interlaboratory ⁴⁰Ar-³⁹Ar dating standard MMhb-1; *Chem. Geol. (Isot. Geosci.)* **66** 27–34

Sen G 1995 A simple petrological model for the generation of Deccan Trap Magmas. *Int. Geol. Rev.* **37** 825–850

Simonetti A, Bell K and Viladkar S G 1995 Isotopic data from the Amba Dongar Carbonatite complex west-central India: Evidence for an enriched mantle source; *Chem. Geol. (Isot. Geosci.)* **122** 185–198

Simonetti A, Goldstein S L, Schmidbrger S S and Viladkar S G 1998 Geochemical and Nd, Pb, and Sr Isotope Data from Deccan Alkaline Complexes – Inferences for Mantle Sources

and Plume – Lithosphere Interaction; _J. Petrol._ **39** 11/12 1847–1864

Srivastava R K 1997 Petrology, Petrochemistry and Genesis of rift-related carbonatites of Ambdungar, India; _Miner. Petrol._ **61** 47–66

Sukheswala R N and Udas G R 1963 Note on the carbonatite of Amba Dongar and its economic potentialities; _Sci. and Cult._ **29** 563–568

Sukheswala R N and Viladkar S G 1978 The carbonatites of India; _Proc. 1st Intl. Symp. on Carbonatites, Brazil_ pp 277–293

Treiman A H 1989 Carbonatite magma: properties and processes; _Carbonatites: Genesis and Evolution_ (ed.) K Bell (London: Unwin Hyman), pp 89–102

Venkatesan T R, Pande K and Gopalan K 1993 Did Deccan volcanism pre-date the Cretaceous/Tertiary transition?; _Earth Planet. Sci. Lett._ **122** 263–265

Viladkar S G 1996 _Geology of the carbonatite-alkalic diatreme of Amba Dongar, Gujarat._ A monograph published by GMDC, Ahmedabad

Williams R W, Gill J B V and Bruland K W 1986 Ra-Th disequilibria systematics: Timescale of carbonatite magma formation at Oldoinyo Lengai volcano, Tanzania; _Geochim. Cosmochim. Acta_ **50** 1249–1259

Wyllie P J 1988 Solidus curves, mantle plumes, and magma generation beneath Hawaii; _J. Geophys. Res._ **93** 4171–4181

York D 1969 Least square fitting of a straight line with correlated errors; _Earth Planet. Sci. Lett._ **5** 320–324

Sr isotopic evidence on the spilitic degradation of the Deccan basalt

K V Subbarao

Department of Earth Sciences, Indian Institute of Technology, Mumbai (Bombay) 400 076, India.
email: subbu@geos.iitb.ernet.in

Similar Sr isotopic ratios ($\sim$ 0.7055) for the tholeiite-spilite flow unit and the associated mineral phases, of Bombay (Deccan Traps) provide a direct evidence for the spilitic degradation of tholeiite. In contrast, a dramatic increase in the rare earth elements (REE) from basalt to spilite is rather puzzling as rare earths are considered to be relatively immobile. The geochemistry thus suggests that the process of spilitization is due to the reaction with a complex fluid having identical Sr-isotopic composition as that of the basaltic magma—thereby masking the details of the mixing process.

1. Introduction

An unusual occurrence of tholeities grading into spilites in the Bhoiwada section of Bombay Island (Deccan basalt) was first described by Sukheswala (1953, 1960) who invoked a hydromagmatic model to explain such an association (Sukheswala 1974). Concurrently, Vallence (1974) proposed a secondary low-grade alteration model based on the presence of chemically similar relict clinopyroxenes in both basalt and spilite. While studying the Bhoiwada sequence, Hellman and Henderson (1977) showed for the first time that rare earth elements (REE) are mobile during spilitization, which is indeed a very significant observation. Hence the method of Sr isotopic finger-printing of the whole rock and mineral components has been used, for the first time, for a better understanding of the process of spilite formation in the Bombay Island.

2. Bhoiwada section of Bombay

The 30 m-thick Bhoiwada section (figure 1(a)) is divided into three zones: tholeiite, transitional (spilite-tholeiite) and pillowed and non-pillowed spilite (figure 1(b)). The dark compact tholeiitic basalt (at the top) is usually aphyric with intergranular clinopy-

roxenes (Ca 36) and anhedral magnetite, occasionally with plagioclase micro-phenocrysts (An 63). The lower green albitized pillowed basalt (spilite) contains clino-pyroxene (Ca 32), dusty albite (An 10), K-feldspar, prehenite and laumontite as groundmass minerals, with relatively unaltered magnetite and amygdales with chlorite and zeolite. This rock also shows distinct relict quench textures. The green rock grades upward into a transitional zone of spilite-tholeiite which is fine grained, intergranular with clouded plagioclase (An 83), clinopyroxene (Ca 30), and subordinate secondary minerals (table 1, figures 2 and 3).

3. Geochemistry

The spilite is enriched in Na, K, La, Ce, Sm and Eu relative to basalt, and the transitional type lies between the two. While the spilite is ol-hy normative, the basalt is distinctly qtz-normative. A decrease in normative diopside in spilite is observed due to lower concentrations of CaO (table 1). These changes are quite consistent and follow the geochemical principles of spilitization, i.e., as a secondary process (Vallence 1969).

As pointed out by earlier workers (Hellman and Henderson 1974; Subbarao *et al* 1979), the marked increase of RE elements in the Bhoiwada suite of

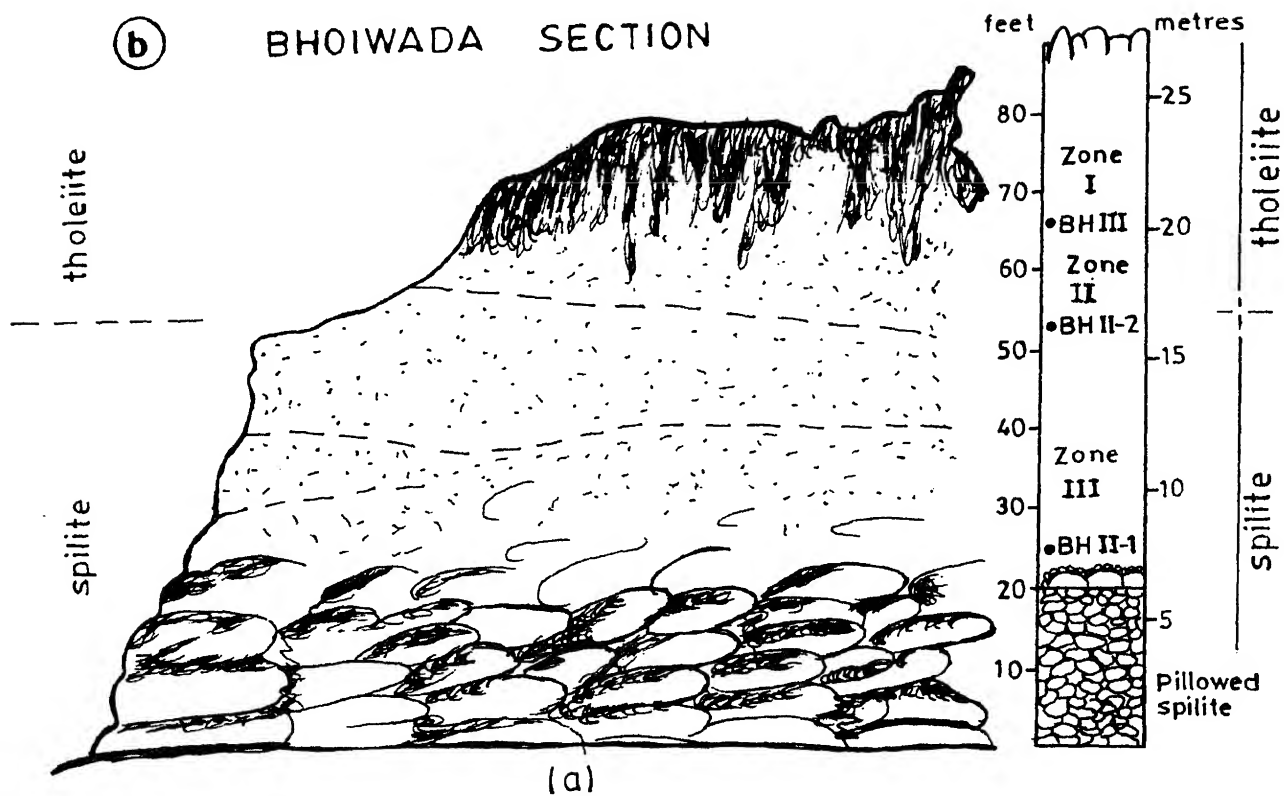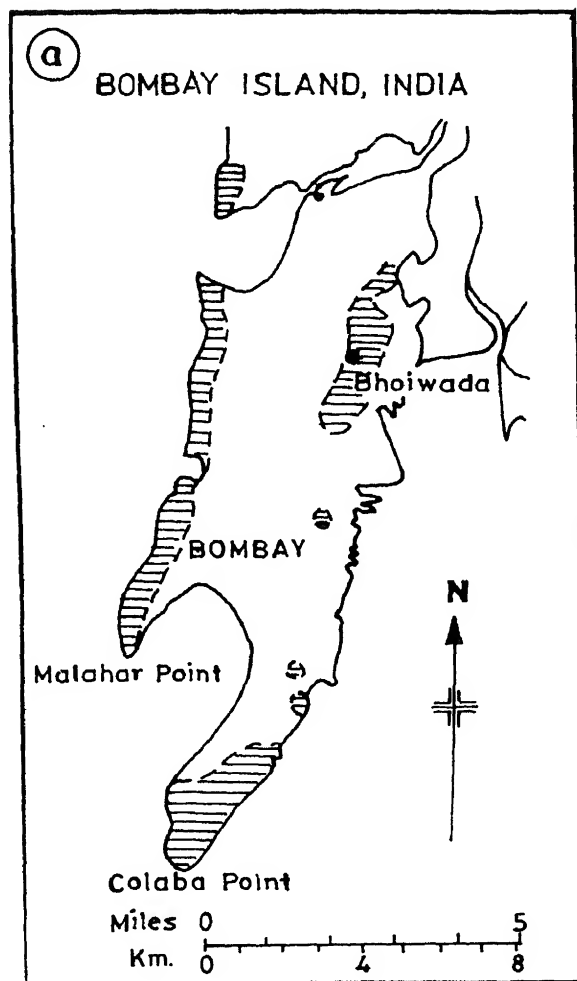**Keywords.** Spilites; Deccan basalt; Sr isotopes.

49

Figure 1(a). Location of Bhoiwada spilite-basalt section, Bombay island (Deccan Traps). Shaded areas represent basalt

Table 1. *Representative rock and mineral analyses from the Bhoiwada basalt-spilite sequence.*

Oxides	Zone I: Basalt			Zone II: Basalt-Spilite Transition			Zone III: Spilite		
	BH III-2	BH III-1F	BH III-1Px	BH II-2	BH II-2F	BH II-2Px	BH II-1	BH II-1F	BH II-1Px
SiO_2	50.73	53.33	51.62	50.14	47.39	50.09	50.53	67.68	49.64
Al_2O_3	13.85	29.33	1.94	13.18	32.79	1.69	13.18	21.20	2.34
TiO_2	1.11		0.42	1.11		0.60	1.04		0.65
FeO	8.21	1.22[+]	11.32[+]	7.54	0.64[+]	18.45[+]	7.98	0.35[+]	17.2[+]
Fe_2O_3	3.64			4.38			3.31		
MgO	6.99	0.10	15.93	6.60	0.17	13.50	7.19		13.85
CaO	11.36	12.87	17.54	11.36	17.12	14.81	8.66	1.71	15.25
Na_2O	2.73	3.99	0.19	2.64	1.90	0.24	3.58	10.44	0.22
K_2O	0.64	0.16		0.64	0.06		1.50	0.05	
MnO	0.19		0.32	0.15		0.42	0.19		0.38
P_2O_5	0.14			0.16			0.14		
Moisture	0.81			0.99			0.86		
L.O.I	0.39			1.21			2.60		
Mg*	57.89		76.63	56.34		63.03	59.74		65.23
Rb(ppm)	12.70			12.70			44		
Sr	192			195			634		
Ba	140			183			676		
Zr	69			69			58		
Y	25			25			21		
La	10.30			13.53			31.50		
Ce	18			26.17			74.70		
Sm	3.04			2.81			7.06		
Eu	0.93			1.02			2.38		
Yb	3.81			2.77			3.06		
CIPW Norm									
Q	4.88			5.73					
Or	3.79			3.79			9.11		
Ab	23.1			22.34			31.13		
An	23.65			22.23			15.9		
Di	22.38			23.26			22.23		
Hy	7.04			5.65			3.43		
Ol							10.91		
Mt							4.93		
Hm	12.76			12.76					
Il	0.4			0.32			2.03		
Tn	2.2			2.31					
Ap	0.33			0.38			0.34		
Cc									
Plagioclase									
Ca		63.50			83			8.30	
Na		35.60			16.70			91.50	
K		0.90			0.30			0.30	
Pyroxene									
Ca			36.10			30.80			31.80
Mg			45.70			39.10			40.20
Fe			18.20			30			28

- **BH III-2** = Basalt; **BH II-2** = Spilite-basalt transitional type; **BH II-1** = Spilite; **F** = Felspar; **Px** = Pyroxene (this study).
- Major elements **Ba, Zr and Y**: Inductively Coupled Plasma Atomic Emission Spectrometry (ICPAES) at the Royal Holloway, University of London (Thompson & Walsh 1981).
- **REE**: INAA at BARC Mumbai.
- **Rb & Sr**: Isotope dilution at the University of British Columbia, Vancouver.
- **Mineral Analyses**: Electron microprobe (Macquaria University, North Ryde, Australia).
- **Mg***: $100*MgO/(MgO + (0.85*FeO)$. The Mg-number is calculated assuming 15% of the Fe is Fe_2O_3 following Cox (1980).
- [+] All the Fe is expressed as FeO.

basalt-spilite undermines the utility as a petrogenetic indicator (figure 4; this study). On the contrary, however, the basalts and zeolite facies metabasalts from the Troodos massif and Carlsberg Ridge (basalt-spilite) display similar REE patterns (Smewing and Potts 1976; Subbarao *et al* 1979), unlike the basalt-spilite suite of the Deccan province. The reasons for this diverse chemical behaviour of REEs are not clear
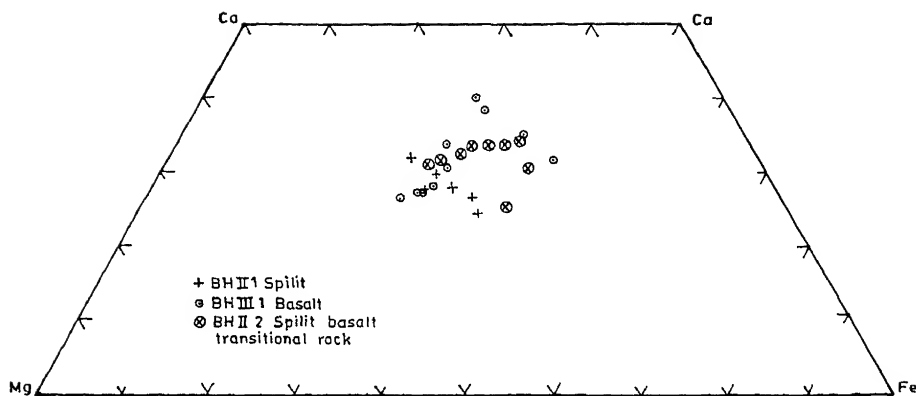
Figure 2.   Pyroxene compositional plots (Ca-Mg-Fe diagram) for spilite-basalt sequence.

4. Sr isotopic composition

In this paper Sr isotopic composition and concentrations of Sr and Rb for the basalt, transitional rock and spilite, and the associated minerals (Pl, Cpx) are reported to trace the ancestry of the spilite (table 2).

The age corrected $(^{87}Sr/^{86}Sr)_i$ and Rb/Sr ratios of the basalt, transitional rock and spilite are nearly identical (0.7055, 0.7056, 0.7056; 0.066, 0.065, 0.069; table 2). Interestingly, the minerals (Pl and Cpx) from all the three rock types have similar 87/86 ratios as their respective host rocks (see table 2 for details). These results suggest that

(a) both minerals and the respective host rocks are in equilibrium despite low-degrees of alteration metamorphism, and

(b) the isotopically similar basalt-spilite association represents a single isochronous flow unit.

5. Discussion

The observed variations in the mineralogy (albite in spilite and An rich plagioclase in basalt; chlorite, zeolites, prehenite) and major element geochemistry in the Bombay basalt-spilite association are largely due
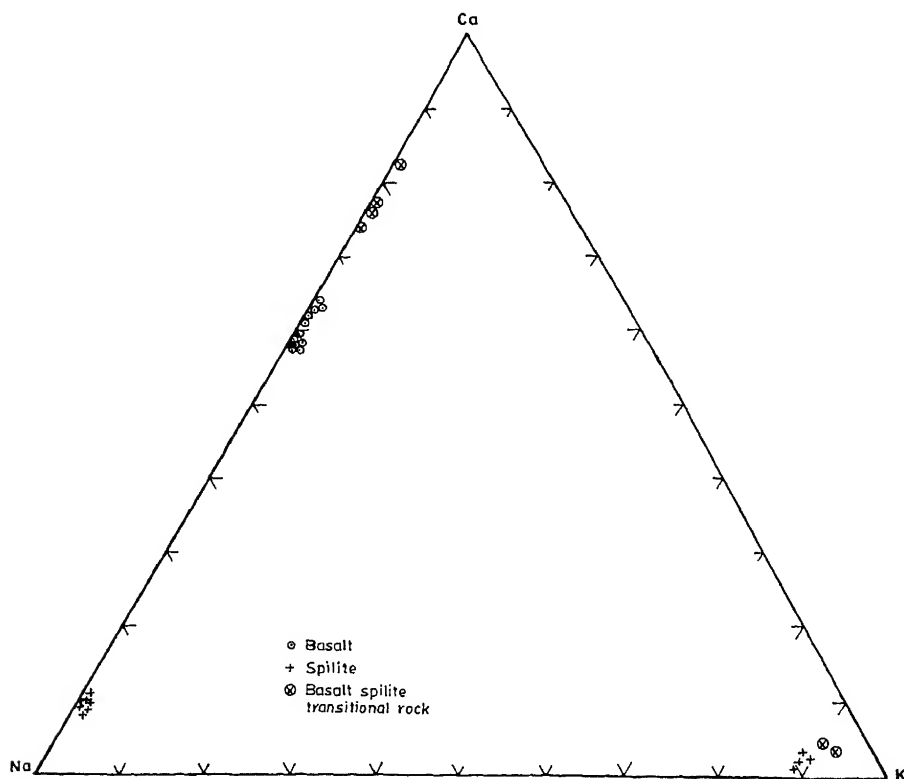
Figure 3.   Variation in feldspar compositional data (Ca-Na-K diagram) from spilite-basalt sequence. Note the

Figure 4. Chondrite normalized REE patterns (see table 1 for data).

presence of K-feldspars. Marked increase in Sr with rising A.I., is perhaps reflected in the presence of laumontite (Sr can proxy for Ca). As expected, the immobile elements (Ti, Zr, Y) remained unaffected by the alteration process. However, the presence of similar Sr isotopic composition for the basalt and spilite is rather unusual and uncommon, and strongly contrasts with Sloman's observations on the Triassic spilites of Italy (basalt: $\sim$ 0.7040, spilite: 0.7060).

5.2 *Sr isotopes*

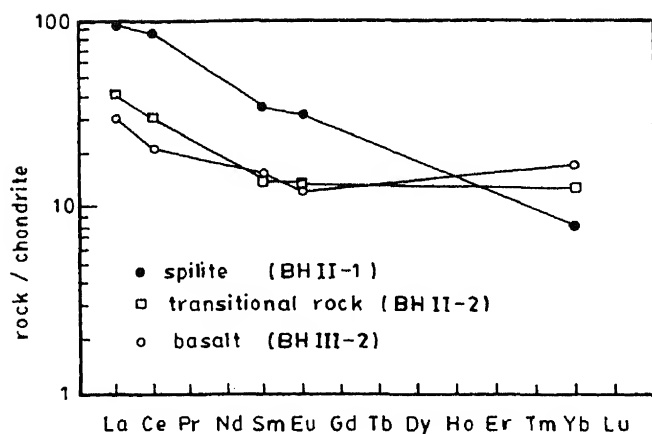Sr isotopic similarity between spilite and basalt and associated mineral phases-pl and cpx confirms the ancestry of the spilites (i.e., tholeiite) through secondary degradation scheme. If this were to be due to hydromagmatic process, the isotopic ratios ought to have been different. Despite compositional adjustments in spilitization, the Bombay suite permits a still unique opportunity to examine such adjustments (in particular, the mobility of REE) and also establishes the usefulness of isotopic finger printing to get an insight into the magmatic systems as well as the pathways of secondary processes.

to secondary reaction process. Interestingly the pyroxene display limited variation and rather remained unchanged in the basalt-spilite sequence (figure 2). This indeed is a very valuable signature to trace the ancestry of spilites (Vallence 1974).

5.1 *Alteration*

It is clearly evident from the petrography (sericitization) and mineralogy (chlorite, prehenite, calcite) that the spilite and spilite-basalt transitional rock suffered different degrees of alteration, while the basalt remained nearly fresh or least altered. In terms of the "Alteration-Index (A.I)" of Sloman (1987; see figure 5), the Bhoiwada rocks fall approximately into three groups, i.e., A.I.: 1–2 (basalts), 3–4 (basalt-spilite transitional rocks, spilites), 5–6 (spilites) (1 = least altered, 6 = highly altered associated with high degree of sericitization). Figure 5 shows that SiO_2 and CaO decrease from basalt (A.I = 1–2) to spilite (A.I = 5–6) indicating an increase in secondary minerals; where as increase of Na_2O, K_2O, Ba and Rb reflects the change from the An-rich to Ab-rich plagioclase and also the

5.3 *Nature of the fluids*

Field and fossil evidences indicate shallow marine or brackish water environment for the Bombay eruptions (Sukheswala 1974). Thus the process of low-temperature spilitization involves ionic exchange between solid rock and alkaline rich marine fluids with adjustments in chemistry in both phases. It is likely that the alkaline saline conditions could have been achieved in the early part of the secondary adjustments due to an increase in pH with base leaching. The hydrolysis of basalt results in residues impoverished in Ca, alkalies and Si as seen in the interstitial chloritic material of the Bhoiwada spilites. In places, chlorite is also associated with other secondary hydrous minerals

Table 2. *Sr isotopic and Sr and Rb isotope dilution data.*

Sample no.		Name	Sr (ppm)	Rb (ppm)	Rb/Sr	$^{87}Rb/^{86}Sr$	$^{87}Sr/^{86}Sr$
Zone I	BH III-1	Basalt	192	12.7	0.066	0.192	0.7055
	BH III-1F	Feldspar	337	3.1	0.009	0.026	0.7053
	BH III-1Px	Pyroxene	36.8	11.1	0.302	0.873	0.7058
Zone II	BH II-2	Spilite-Basalt Transition	195	12.7	0.065	0.189	0.7056
	BH II-2F	Feldspar	192	1.3	0.007	0.021	0.7055
	BH II-2Px	Pyroxene	33.7	6.6	0.195	0.565	0.7057
Zone III	BH II-1	Spilite	634	43.7	0.069	0.199	0.7056
	BH II-1F	Feldspar	935	50.3	0.054	0.156	0.7054
	BH I- 2Px	Pyroxene	100	8	0.08	0.23	0.7056

• Isotopic data are reported relative to standard values measured at the University of British Columbia: $(^{87}Sr/^{86}Sr) = 0.70800$ for E & A Sr and 0.71022 for NBS 987 Sr.
• Isotopic fractionation correction $^{87}Sr/^{86}Sr = 0.1194$.
• Total procedural blanks are < 100 picograms for Sr and < 20 picograms for Rb.
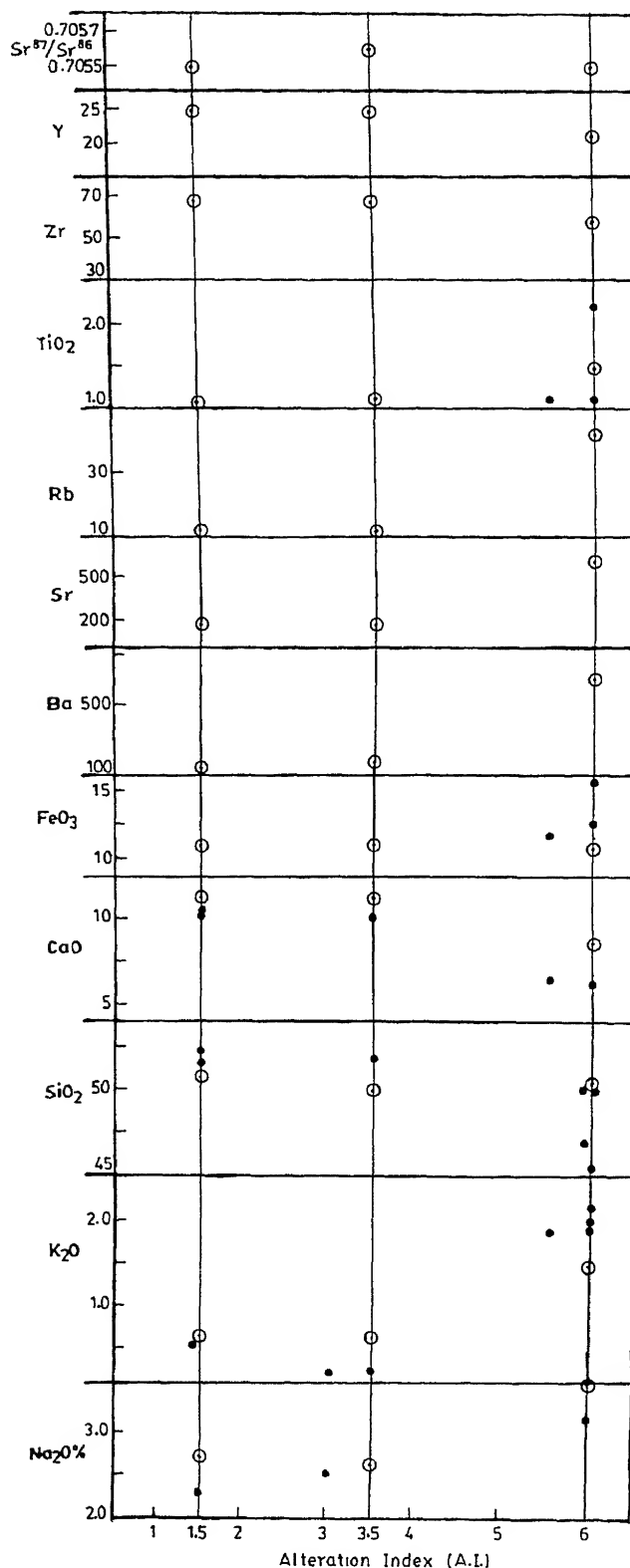• Uncertainties on Sr and Rb abundances: < 0.5% and < 1%.

Figure 5. Variation of selected elements with "Alteration Index (I.D)". Open circle with dot represents analyses from this study (see table 1 for data). Solid dot represents analyses from the literature (Sukheswala 1974; Vallence 1974).

The important point to be considered at this stage is the absence of any change in Sr-isotopic composition between the basalt and spilite as well as the mineral phases—Pl and Cpx. Based on the field and chemical evidences, we are justified in assuming sea water as the principal fluid that is responsible for spilitization. If so, the Sr-isotopic composition of Tertiary sea water (~0.708, Burke et al 1982) should have been reflected in the spilitized basalt. From the available data, it thus appears that the fluid and magma have nearly identical Sr-isotopic composition and therefore not picking up a mixing or equivalent process. This might suggest that the fluid is of a more complex or unexpected origin unlike originally assumed.

The second puzzling problem relates to the dramatic increase of REE in the spilite, while the Sr isotopic composition in the entire basalt-spilite sequence remained nearly constant. Earlier, Menzies et al (1993) demonstrated that "extremely high water/rock ratio ($> 10^4$) are required to promote the exchange of REE between basaltic rocks and sea water...". However, the mineralogical data and Sr isotopic composition negate the role of high-temperatures in the case of the Bhoiwada spilite association. It is also unlikely that the secondary hydrothermal fluids (zeolitization) would have had any effect, as the zeolites are formed around 200°C (Jeffrey et al 1988) with extremely poor REE concentrations (James and Walsh, in press; and personal discussions).

6. Summary

New Sr isotopic and elemental data for the unique sequence of basalt grading into albite-chlorite spilite from the Bombay island (Deccan Traps) provide new clues to the problems of spilitization.

- Nearly identical $^{87}Sr/^{86}Sr$ (~0.7055) for the basalt spilite and associated pyroxene and plagioclase indicates perfect equilibrium condition; and points out either the inert nature of the minerals (in particular pyroxene) or the presence of a complex fluid
- REE are preferentially mobilized during spilitization. This is rather unexpected in such a low temperature hydrothermal system.
- Reaction between interstitial residues (i.e. chlorite) and fluid could easily result in the formation of secondary minerals such as laumontite, prehnite, calcite and quartz.

Acknowledgements

such as laumontite, prehnite, calcite and quartz, which perhaps represent the products of subsequent reaction between chlorite and fluid (Vallence 1974).

References

Burke W H, Denison R E, Hetherington E A, Koepnick R B, Nelson H F and Otto J B 1982 Variation of seawater $^{87}Sr/^{86}Sr$ throughout Phanerozoic time; *Geology* **10** 516–519

Cox K G 1980 A model for flood basalt volcanism; *J. Petrol.* **21** 629–650

Hellman P L and Henderson P 1977 Are rare earth elements mobile during spilitization?; *Nature* **267** 38–40

James S and Walsh J N Zeolites from the Deccan Basalts; *Mem. Geol. Soc. India (West volume)* **43** (in press)

Jeffrey K L, Henderson P, Subbarao K V and Walsh J N 1988; The zeolites of the Deccan basalt—a study of their distribution; *Mem. Geol. Soc. India* **10** 151–162

Menzies M A, Long A, Ingram G, Tatnell M and Janecky D 1993 MORB peridotite sea water interaction experimental constraints on the behaviour of trace elements, $^{87}Sr/^{86}Sr$ and $^{143}Nd/^{144}Nd$ ratios; In *Magmatic processes and Plate Tectonics.* (eds) H M Prichard *et al;* *Geol. Soc. Special Publication* **76** pp. 309–322

Sloman L E 1987 *Middle Triassic magmatism in the Dolomites, Nothern Italy;* Unpublished D. Phil Thesis University of Oxford

Smewing J D and Potts P J 1976 Rare-earth Contrib Mineral Petrol abundances in basalts and metabasalts from the Troodos Massif, Cyprus; *Contrib. Mineral. Petrol.* **57** 245–258

Subbarao K V, Reddy V V, Reddy G R and Sukheswala R N 1979 Rare earth element geochemistry of basalt-spilite association of Bombay and Carlsberg Ridge—a preliminary study; *J. Geol. Soc. India* **20** 517–519

Sukheswala R N 1953 Notes on the field occurrence and petrography of the rocks of the Bombay Island, Bombay; *Trans. Mining Geol. Met. Inst. India* **50** 101–126

Sukheswala R N 1960 Albitized basalts of Bombay and the associated intertrappeans: A preliminary survey; *Indian Science Congress Association, Bombay* (abstract)

Sukheswala R N 1974 Gradation of tholeiitic Deccan basalt into spilite, Bombay, India. In *Spilites and Spilitic Rock.* (eds) G C Amstutz (Heidelberg: Springer-Verlag) pp. 229–250

Thompson M and Walsh J N 1989 *Handbook of inductively coupled plasma spectrometry;* (London: Chapman and Hall)

Vallence T G 1969 Spilites again: Some consequences of the degradation of basalts; *Proc. Linn. Soc. N.S.W.* **85** 8–51

Vallence T G 1974 Spilitic degradation of a tholeiitic basalt; *J. Petrol.* **15** 79–9

Sm-Nd ages of two meta-anorthosite complexes around Holenarsipur: Constraints on the antiquity of Archean supracrustal rocks of the Dharwar craton

Y J Bhaskar Rao[1], Anil Kumar[1], A B Vrevsky[2], R Srinivasan[1] and G V Anantha Iyer[3]

[1]National Geophysical Research Institute, Hyderabad 500 007, India; email: postmast@csngri.ren.nic.in
[2]Institute of Precambrian Geology and Geochronology, St. Petersburg, Russia.
[3]Department of Inorganic and Physical Chemistry, Indian Institute of Sciences, Bangalore 560 012, India

Whole-rock Sm-Nd isochron ages are reported for two stratiform meta-anorthosite complexes emplaced into the Archean supracrustal-gneiss association in the amphibolite facies terrain around Holenarsipur, in the Dharwar craton, South India. While these metaperidotite-pyroxenite-gabbro-anorthosite complexes are petrologically and geochemically similar, they differ in the intensity of tectonic fabric developed during the late Archean (c. 2.5 Ga) deformation. They also differ in their whole-rock Sm-Nd isochron ages and initial Nd isotopic compositions: 3.285 ± 0.17 Ga, $\varepsilon_{Nd} = 0.82 \pm 0.78$ for the Honnavalli meta-anorthosite complex from a supracrustal enclave in the low-strain zone, and 2.495 ± 0.033 Ga, $\varepsilon_{Nd} = -2.2 \pm 0.3$ for the Dodkadnur meta-anorthosites from the high-strain southern arm of the Holenarsipur Supracrustal Belt (HSB). We interpret these results as indicating that the magmatic protoliths of both meta-anorthosite complexes were derived from a marginally depleted mantle at c. 3.29 Ga but only the Dodkadnur rocks were isotopically reequilibrated on a cm-scale about 800 Ma later presumably due to the development of strong penetrative fabrics in them during Late Archean thermotectonic event around 2.5 Ga. Our results set a younger age limit at c. 3.29 Ga for the supracrustal rocks of the HSB in the Dharwar craton.

1. Introduction

A general consensus is that the Archean gneiss-supracrustal associations of the Dharwar craton, southern India constitute a polyphase assemblage that developed between ~3.4 and 2.5 Ga ago (reviewed by Naqvi and Rogers 1987). However, aspects of spatial and temporal relationships between gneisses and supracrustals, and the antiquity of the supracrustal rocks remain ambiguous. The region encompassing the Holenarsipur Supracrustal Belt (HSB, figure 1) has long been recognised as one of the oldest crustal nuclei in the Dharwar craton based on the evidence for preservation of the ≤ 3.3 Ga tonalitic orthogneisses (Beckinsale et al 1980, 1982; Bhaskar Rao et al 1991; Meen et al 1992; Naha et al 1993; Peucat et al 1993). Geological and geochronological studies have

been inconclusive on the temporal relationship between the spatially associated gneissic and supracrustal rocks. While some authors (e.g. Naqvi 1981; Hussain and Naqvi 1983) proposed that supracrustal rocks pre-date the gneisses, several others (e.g. Ramakrishnan and Viswanatha 1981; Monrad 1983; Meen et al 1992) suggested that the gneisses were older. U/Pb ages of detrital zircons from a quartzite-metapelite unit from the HSB indicate granitoid rocks as old as ~3.6 Ga in its provenance (Nutman et al 1992). Peucat et al (1995) reported a precise U/Pb age of 3.298 ± 0.007 Ga for zircons in a metarhyolite in the upper part of the stratigraphic sequence in the HSB implying that the entire supracrustal succession in this belt could be at least as old as the oldest dated (~3.3 Ga) Gorur gneiss nearby. In a different and complementary approach to the age of the supracrustal

Keywords. Archean; anorthosite; Dharwar craton; Sm-Nd; Geochronology.
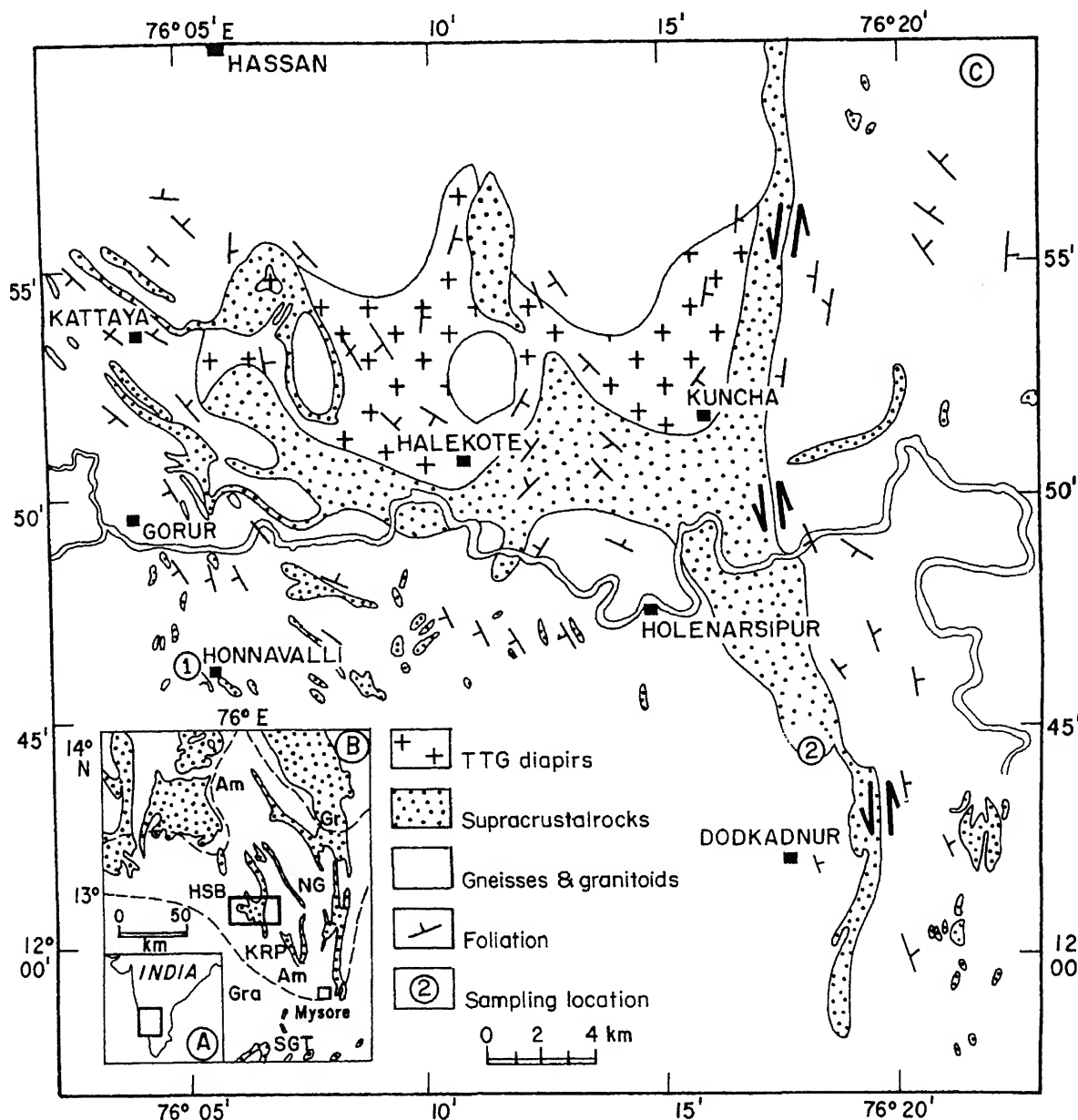
Figure 1. Generalised geological map of the Archean Holenarsipur Supracrustal Belt (HSB) and surrounding gneissic co[...] showing location of the Honnavalli and Dodkadnur meta-anorthosite complexes (based on Hussain and Naqvi 1983). Inset [...] shows the location of the HSB in the amphibolite (Am) – facies terrain of the western part of the Dharwar craton, south [...] which is bounded by greenschist facies (Gr) and Granulite (Gra) facies domains. Other supracrustal belts containing si[...] stratiform complexes include: Sargur (SG), Nuggihalli (NG) and Krishnarajpet (KRP).

sequence of the HSB, we have dated two isolated bodies of multiply deformed and metamorphosed stratiform periodite-gabbro-anorthosite suite from around Holenarsipur.

Many deformed stratiform dunite/periodite-pyroxe-nite-gabbro-anorthosite complexes are known from the lower sections of supracrustal belts such as the Holenarsipur, Nuggihalli, Sargur and Krishnarajpet in the western part of the Dharwar craton (WDC). Geology, petrology and geochemistry of these bodies have been described by Ramiengar et al (1978); Ramakrishnan et al (1978); Drury et al (1978); Naqvi and Hussain (1979);

Ahmad (1982); Kutty et al (1984) and have [...] reviewed recently by Nijagunappa (1994). Structu[...] these bodies are identical to their host supracru[...] and/or gneiss rocks suggesting their emplacem[...] before the regional deformation and metamo[...] events. Relative to the metarhyolite dated [...] Peucat et al (1995), the stratiform suites consid[...] here occupy a much lower stratigraphic positio[...] the supracrustal succession around Holenarsi[...] Therefore, the primary (crystallisation) age of t[...] stratiform suites would set a strict younger (m[...] mum) limit to the age of the supracrustal rocks o[...]

A potential problem in using Sm-Nd whole-rock isochron method to date deformed and metamorphosed mafic-ultramafic rock systems is the mobility of rare earth elements during secondary geological processes, particularly those involving exchange reactions between rocks and hydrothermal fluids. However, adoption of a proper sampling strategy considering the scale of tectonic fabrics developed in the rocks could help retrieve primary age information irrespective of their metamorphic grade (Black 1988). Many examples where whole rock Sm-Nd isochrons yielded reliable primary ages for stratiform anorthosite complexes in Archean greenstone belts elsewhere have been reviewed by Ashwal (1993).

2. Geological setting

In a tilted cratonic block exposing an oblique cross-section of Archean rocks ranging in metamorphic grade from greenschist facies in the north to granulite facies in the south, the Holenarsipur region forms a central medium-grade (amphibolite facies) domain. The trident shaped HSB has narrow northern, southern and western arms. The southern part of the western arm and the entire southern arm are believed by some workers to comprise the lower part of the supracrustal succession described variedly as the > 3.0 Ga Sargur Group (Swami Nath *et al* 1976; Ramakrishnan and Viswanatha 1981), the oldest supracrustals (Naqvi 1981), and the Holenarsipur Group (Naqvi and Rogers 1987). This sequence is dominated by ultramafic schists of komatiite-tholeiite affinites, metapelites and minor quartzite, banded iron formation and numerous lensoid and/or sheet like bodies of stratiform dunite-periodite-pyroxenite gabbro-anorthosite. The northern part of the western arm and the northern arm contain a mafic metavolcanic-dominated sequence with rare spinifex textured komatiites. Minor felsic volcanic rocks occur in the upper stratigraphic level. The mafic volcanic rocks are interlayered with thin quartzite, argillite and a banded iron formation. This latter sequence was correlated with the < 3.0 Ga Dharwar Supergroup, the younger Archean supracrustal cycle of the Dharwar craton (Swami Nath *et al* 1976; Ramakrishnan and Viswanatha 1981). This two-fold subdivision of the supracrustal sequence in the HSB has been refuted by other workers (Hussain and Naqvi 1983; Naha *et al* 1986, 1993; Srinivasan 1988; Srinivasan and Naha 1996).

Tonalitic orthogneisses west and northwest of the HSB have yielded whole rock Rb-Sr, Pb-Pb and zircon U/Pb ages between 3.350 and 3.305 Ga (Beckinsale *et al* 1980, 1982; Monrad 1983; Taylor *et al* 1984; Bhaskar Rao *et al* 1991; Meen *et al* 1992; Naha *et al* 1993;

minor episodes of deformation with metamorphism reaching up to amphibolite facies (Chadwick *et al* 1978, 1981; Naha *et al* 1986, 1993; Naqvi and Rogers 1987; Bhaskar Rao *et al* 1991). During the first episode (D_1 and D_{1a}) the rocks were isoclinally folded and co-axially refolded. An axial planar schistosity (S_1) was developed, and metamorphic conditions varied from greenschist facies in the north to amphibolite facies in the southern part of the HSB. Synkinematic tonalite-trondhjemite-granodiorite (TTG) diapirs invaded both the gneisses and supracrustal rocks. The distribution of L, L-S and S fabric dominated domains in the region is suggested to have been controlled by deformation associated with the rising TTG-diapirs (Bouhallier *et al* 1993, 1995). Several of these TTG suites have been dated at ∼3.0 Ga (Beckinsale *et al* 1982; Monrad 1983; Stroh *et al* 1983; Taylor *et al* 1984). The c. 3.0 Ga event was also associated with migmatisation, remobilization of large ion lithophile elements and re-equilibration of Rb-Sr and Pb-Pb isotopic systematics in the gneisses (Bhaskar Rao *et al* 1983; Naqvi and Rogers 1987; Meen *et al* 1992). The D_1-episode of deformation culminating at c. 3.0 Ga is generally believed to mark a strict younger age limit to the deposition and early deformation and metamorphism of the Holenarsipur supracrustal rocks. During a second major episode of deformation (D_2), the earlier isoclinal folds and axial planar schistosity were refolded into N-S upright folds with N-S striking axial planes. The D_2-folding is associated with development of a zonal crenulation cleavage, marked by micas in the northern part and amphibole in the southern arm of the HSB. The D_2-phase is also associated with strong transcurrent-shearing along N-S belts, such as the one along the eastern margin of the HSB that affected much of the southern arm (e.g. Drury *et al* 1984; Chadwick *et al* 1992; Bouhallier *et al* 1993, 1995). The N-S fabrics related to D_2 are weak along much of the western arm of the HSB, where the pre-D_2 structures and compositions are expected to be better preserved. Garnet-bearing amphibolites developed syntectonically with D_2 give consistent whole rock-garnet Sm-Nd isochron ages at ∼2.5 Ga (Bouhallier 1995). In a regional context, the D_2-episode coincides with a craton-wide late Archean tectonometamorphic event that culminated at c. 2.5 Ga with charnockite formation at deeper levels and widespread emplacement of K-rich granites at the shallow crustal levels (reviewed by Naqvi and Rogers 1987; Friend and Nutman 1991; Peucat *et al* 1993). Locally around the HSB, late warps (D_3) with E-W axial planes accentuated the plunges of the D_2-folds.

3. The stratiform meta-anorthosite complexes

- the *Honnavalli meta-anorthosite*, at the Honnavalli village approximately 20 km west of Holenarsipur and 3 km south of Gorur and
- the *Dodkadnur meta-anorthosite*, located ~5 km south of Holenarsipur, ~3.5 km north of Dodkadnur (figure 1).

The Honnavalli meta-anorthosite, first described by Hussain and Ahmad (1982), is a (~ 50 × 20 m) oval shaped body included in banded tonalitic gneisses and associated with actinolite-tremolite-talc-antigorite schists. The meta-anorthosite with > 90% modal plagioclase grades into gabbroic anorthosite with 80–90% modal plagioclase. The rock is coarse to medium-grained with a feeble foliation defined by a crude alignment of clots rich in hornblende. The foliation strikes NNW and dips ~60–65° easterly which is parallel to foliation in the enclosing gneisses (also see Hussain and Ahmed 1982; Hussain and Naqvi 1983). Plagioclase (An$_{92}$) in the anorthositic rock is variably sassuritised. The anorthosites are conformably associated with a thin (20 × 2 m) band of schistose amphibolite containing largely hornblende and subordinate plagioclase (An$_{70-85}$). These can be interpreted as metagabbro (<30%, modal plagioclase) and anorthositic gabbro (70–80% plagioclase), zoisite, calcite, scapolite, titanomagnetite and chlorite are accessory minerals.

The Dodkadnur meta-anorthosite is exposed over a strike length of ~300 m. About a dozen other smaller, isolated bodies of meta-anorthosite are known approximately along its strike extension over a N-S zone of ~12 km. Detailed descriptions of the petrology and geochemistry of several of these bodies have been given by Drury *et al* (1978), Ramakrishnan *et al* (1978) Naqvi and Hussain (1979), Ramakrishnan and Viswanatha (1981) Kutty *et al* (1984). In the Dodkadnur complex, meta-anorthosite grades to metagabbro across strike. Locally, metagabbro grades to magnetite gabbro and a small band of titaniferous magnetite. Elsewhere, ~8 km north of this body, gradations between meta-gabbro, metapyroxenite and metaperidotite/dunite were noted (Kutty *et al* 1984). Unlike the Honnavalli rocks, the Dodkadnur outcrops show a strong N-S gneissic foliation marked by alternate plagioclase and hornblende-rich laminae and a distinct lineation due to parallelism of hornblende. This foliation, parallel to the axial planes of large isoclinal folds (D$_1$), is refolded by open folds associated with well-developed NNW to N striking axial planes. Granulation and recrystallisa-tion of the coarse polysynthetically twinned plagio-clase into aggregates of fine untwined plagioclase is ubiquitous. The recrystallised domains show grano-blastic polygonal equilibrium texture. Garnet has developed in some metagabbroic anorthosites and metagabbros. Typically the garnets are euhedral, up to 1 cm across, and show faces truncating foliation. Some contain abundant inclusions of fine aggregates

of plagioclase and hornblende. The textures suggest that garnet growth outlasted D$_2$-deformation. Acces-sories include sphene and traces of apatite besides others noted for the Honnavalli rocks.

The available major and trace element compositions (data from Drury *et al* 1978; Naqvi and Hussain 1979; Hussain and Ahmad 1982; Kutty *et al* 1984 and our unpublished results) indicate that the Dodkadnur and Honnavalli meta-anorthosite suites are geochemically similar among themselves and to many other anortho-site complexes of the Archean greenstone belts (e.g., Henderson *et al* 1976; Phinney *et al* 1988; Ashwal 1993). The most significant feature of the present set of rocks is their extremely low abundance of K, Rb, Sr, Y and REE, even in the garnet-bearing samples. This is consistent with their mineral composition which is devoid of light rare earth element (LREE)-rich accessory phases like zircon, allanite, and monazite. The meta-anorthosites and gabbroic anorthosites show a marginal enrichment of LREE in their chondrite-normalised REE pattterns (Ce$_N$/Yb$_N$ = 1–2.6), low REE (4–9 × chondrite) and variable positive Eu-anomalies (Eu/Eu* between 1.8 and 7.2). Kutty *et al* (1984) described that the compositional variations within the Dodkadnur complex resulted from low-pressure fractionation of a tholeiitic magma. They suggested distinct fractionation trends controlled by separation of olivine, clinopyroxene, plagioclase and magnetite. Hussain and Ahmad (1982) also suggested a similar magmatic evolution for the Honnavalli suite. The samples analysed here are limited mostly to a narrow compositional window where fractionation of clinopyroxene and plagioclase is important.

4. Sm-Nd geochronology

4.1 *Experimental techniques*

3–5 kg samples were collected from fresh outcrops within an area of ~ 30 × 20 m (Honnavalli) and ~ 200 × 70 m (Dodkadnur). Fresh interior fragments or slabs ~ 1.5–2.5 cm thick, 6 × 5 cm on a face, were prepared along foliation. In the case of samples, YBL-19, 20B and 21A, blocks of ~5 kg each was processed. All samples were powdered to ~200 mesh using a steel jaw crusher and a ring mill.

Sm-Nd isotopic analysis of the Dodkadnur samples was carried out at the NGRI, Hyderabad while that of the Honnavalli samples at the IPGG, St. Petersburg. Analytical procedures were broadly similar and involved dissolution of ~100 mg powders in HF + HNO$_3$ in screw capped teflon (Savilex) vials. Clear solutions were split for isotope dilution (ID) and isotopic composition (IC) measurements. Chromato-graphic separations of Nd and Sm followed procedures described by Richard *et al* (1976) with minor modi-fications. Isotopic compositions were measured on

Table 1. *Sm-Nd isotopic data for Holenarsipur meta-anorthosite complexes.*

Sample (rock type)	Sm (ppm)	Nd (ppm)	$^{147}Sm/^{144}Nd^a$ (atomic)	$^{143}Nd/^{144}Nd^b$ (atomic)	T_{CHUR}^c (Ga)	T_{DM}^d (Ga)
Honnavalli						
O8-19 (LA)	0.64	2.30	0.1381	0.51143 ± 5	3.12	3.32
YBL-20B (LA)	0.61	2.27	0.1449	0.51155 ± 5	3.18	3.42
O8-19-4 (MA)	1.06	4.22	0.1518	0.51171 ± 5	3.13	3.38
O8-19-3 (S)	0.90	3.28	0.1651	0.51202 ± 5	2.95	3.31
YBL-21A (H)	2.10	7.46	0.1707	0.51204 ± 5	3.40	3.69
O8-19-2 (H)	1.60	5.27	0.1839	0.51239 ± 5	–	–
YBL-19 (H)	1.63	5.44	0.1880	0.51254 ± 5	–	–
Dodkadnur						
M-11 (MA)	0.535	2.432	0.1318	0.511447 ± 15	2.78	3.11
M-3-2 (Gt.A)	0.418	1.708	0.1478	0.511729 ± 15	2.82	3.26
M-18 (LA)	0.420	1.706	0.1486	0.511716 ± 15	2.90	3.33
M-13 (S)	0.250	0.785	0.1922	0.512431 ± 15	–	–
M-4 (H)	3.231	8.907	0.2187	0.512886 ± 15	–	–

LA = leucocratic meta-anorthosite, **MA** = mesocratic meta-anorthosite (gabbroic anorthosite), **S** = Serpentinite (metaperdotite/pyroxene), **H** = Hornblendite (pyroxenite-gabbro), **Gt. A** = garnet bearing leucocratic meta-anorthosite. Errors are 2 sigma of mean. [a] Error in $^{147}Sm/^{144}Nd$ ratios is 0.15% for Dodkadnur samples and 0.5% for Honnavalli samples. [b] normalised to $^{146}Nd/^{144}Nd = 0.7219$. [c] CHUR model ages calculated using: $(^{143}Nd/^{144}Nd)_{CHUR}$ 0.512638; $(^{147}Sm/^{144}Nd)_{CHUR}$ = 0.1967; [d] T_{DM} calculated using the equation of DePaolo (1981) for samples with $^{147}Sm/^{144}Nd < 0.17$.

metal-ion species using the automated, multicollector thermal ionization mass spectrometers, VG 354 at the NGRI and Finnigan MAT 261 at the IPGG, as described in detail elsewhere (Anil Kumar *et al* 1996 and Kotov *et al* 1995). $^{143}Nd/^{144}Nd$ ratios were normalized to $^{146}Nd/^{144}Nd = 0.7219$ and weighted mean of $^{143}Nd/^{144}Nd$ for a La Jolla Nd standard were 0.511861 ± 14 (2σ) at the NGRI (13 measurements) and 0.511845 ± 4 (2σ) at the IPGG (31 measurements). Ages were calculated using the two-error regression method of Williamson (1968) in a computer program after Provost (1990). ε_{ND} were calculated by the method of Fletcher and Rossman (1982). All errors on age and initial Nd isotopic compositions (Nd_i) reported in this article are quoted at 2σ.

4.2 Results

Sm-Nd data for the two meta-anorthosite complexes are given in table 1 and plotted in figures 2(a) and 2(b). The samples from both the Honnavalli and Dodkadnur suites show a good mutual spread in their $^{147}Sm/^{144}Nd$ ratios–from 0.1381 to 0.1880 in the former and from 0.1318 to 0.2187 in the latter. Both sets define very good linear arrays as evident from MSWDs of 0.53 and 0.78, respectively. If these straight lines are interpreted as isochrons (see next section), they give distinct ages and initial Nd ratios for the two suites: 3.285 ± 0.170 Ga, $\varepsilon_{Nd} = 0.82 \pm 0.78$ for the Honnavalli rocks and 2.493 ± 0.033 Ga, $\varepsilon_{Nd} = -2.2 \pm 0.03$ for the Dodkadnur rocks. However, T_{DM} model ages (DePaolo 1981) for rocks with $^{147}Sm/^{144}Nd < 0.15$ from either suite are quite consistent (3.11 to 3.42 Ga) with their mean being indistinguishable from the older isochron age of ∼3.3 Ga.

5. Discussion

Three important lines of evidence show that the linear arrays (figures 2(a) and 2(b)) are indeed isochrons and not mere mixing lines without time significance. Firstly, the data in either case do not show a linear correlation between $^{143}Nd/^{144}Nd$ and 1/Nd that would be expected for a mixture of just two arbitrary components (Faure 1986). Secondly, as argued by previous workers, e.g., Kutty *et al* (1984), petrological and geochemical data indicate that the meta-anorthosite suites formed by crystal-melt fractionation processes from a homogeneous parent magma of tholeiitic composition. The observed differentiation trends are consistent with early segregation of olivine + pyroxene, closely followed by plagioclase and a middle stage precipitation of magnetite. Finally, the T_{DM} model ages of the rock samples are concordant not only among themselves but also with the older isochron age of 3.3 Ga. This would not be the case if these samples were mixtures of two genetically unrelated components.

So, the two isochrons indicate that the Honnavalli samples evolved as closed systems for ∼3.3 Ga from a common initial Nd ratio of $\varepsilon_{Nd} = 0.82 \pm 0.78$, whereas the Dodkadnur rocks evolved for ∼2.5 Ga from a common initial ratio of -2.2 ± 0.03. But the good agreement of the T_{DM} model ages between the two compositionally similar suites together with the older Sm-Nd isochron age of ∼3.3 Ga argues that both crystallized from a homogeneous parental magma close to 3.3 Ga ago. The two complexes may be either isolated intrusions of compositionally very similar parental melts or segments of a large tectonically dismembered stratiform complex.
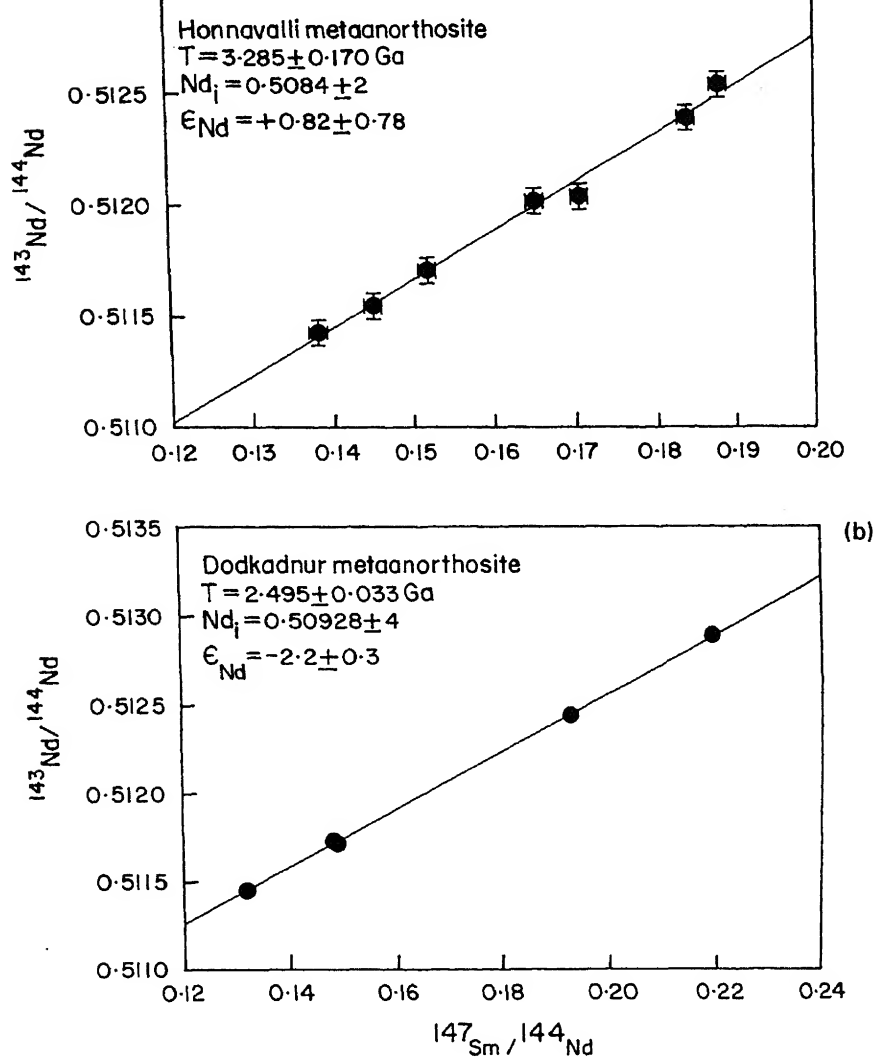
Figure 2. Sm-Nd whole rock isochron diagrams for the Honnavalli and Dodkadnur meta-anorthosite complexes around Holenarsipur.

If the Dodkadnur complex was originally coeval with the Honnavalli complex, its whole rock Sm-Nd isochron age of ~2.5 Ga implies that the rocks of this complex were re-equilibrated in their Nd isotopes to a common value of $\varepsilon_{Nd} = -2.2 \pm 0.03$ in a secondary event about 2.5 Ga ago. Assuming that the mean $^{147}Sm/^{144}Nd$ ratio of the five Dodkadnur rocks itself represent that of their parental magma, the Nd ratio of the latter 3.3 Ga ago can be calculated from the present day mean $^{147}Sm/^{144}Nd$ ratio of 0.1678 and its $^{143}Nd/^{144}Nd$ ratio of 0.50928 ± 4 ($\varepsilon_{Nd} = -2.2 \pm 0.3$) 2.5 Ga ago. As the calculated ratio of 0.50838 ± 4 ($\varepsilon_{Nd} = 0.65 \pm 0.3$) is well within the errors of the initial ratio of the Honnavalli rocks, the Nd isotopic compositions of the sources of both suites of rocks are quite similar, if not identical. In fact a regional event leading to generation of magmatic rocks and metamorphic resetting of pre-existing rocks at 2.5 Ga has been extensively documented (see reviews Naqvi and Rogers 1987; Friend and Nutman 1991; Peucat *et al*

1993). More specifically, a mica schist and an amphobolite from the southern arm of the HSB both containing garnets that developed syntectonically during the D_2-event gave whole rock-garnet isochrons of essentially the same age as the Dodkadnur rocks—2.473 ± 0.010 Ga, $\varepsilon_{Nd} = -6.1 \pm 0.5$ and 2.527 ± 0.034 Ga, $\varepsilon_{Nd} = -8.7 \pm 0.4$ (Bouhallier 1995). What is then surprising about the Dodkadnur rocks is that they were isotopically re-equilibrated not on a mineral scale (as in the case of the metapelite and amphibolite) but on a scale of a few tens of centimeters, whereas the Honnavalli rocks were not. Since the only major difference between these two complexes is in the intensity of tectonic fabric developed in them, we believe that this may be responsible for the differential response of the two complexes to the secondary or metamorphic event at 2.5 Ga. The Dodkadnur complex is located within the southern arm of the HSB, which is more intensely deformed than the western part of the region hosting the Honnavalli complex—resulting in

the development of strong D_2-penetrative planar and linear mineral fabrics (Bouhallier *et al* 1993, 1995). The Dodkadnur rocks also show significant syntectonic recrystallisation accompanied by growth of garnets in some rock types. Evidence of sensitivity of Sm-Nd and Rb-Sr systematics to the intensity of deformation and the scale of penetrative fabric development in rocks rather than the intensity of the causative metamorphic event has indeed been found from studies elsewhere on multiply deformed and metamorphosed terrains (Black 1988).

Based on Rb-Sr data of 10 whole rock samples from the Dodkadnur complex, Kutty *et al* (1984) proposed that this complex was emplaced 3095 ± 58 Ma ago. Our Sm-Nd results indicate not only a much earlier time of emplacement but also the imprint of a strong secondary thermotectonic event much later. We believe the large scatter in their Rb-Sr data could be due to open system behavior of the whole rock Rb and Sr during the 2.5 Ga event.

The general agreement of T_{DM} ages with the Sm-Nd isochron age precludes significant crustal contamination of the magma parental to the meta-anorthosite complexes. This is further supported by the absence of LREE enriched refractory accessory minerals, extremely low abundances of K, Rb, Zr, Y, and LREE, and the restricted range of contamination-sensitive Rb/Sr and La_N/Sm_N in different members of the anorthosite-gabbro complexes. The ε_{Nd} of 0.82 ± 0.78 therefore reflects that of the magma parental to the rocks. So their mantle source is either chondritic or marginally depleted with a maximum ε_{Nd} of $+1.5$. This is in general agreement with the finding that other Archean stratiform complexes in greenstone-gneiss and granulite-gneiss terrains were derived from mantle sources with a long term depletion in LREEs (summarised by Ashwal 1993). What is perhaps of more significance is the similarity of the mantle source ($\varepsilon_{Nd} = 1.86 \pm 0.16$) for the 2.94 Ga old Sittampundi anorthosite complex at the southern margin of the craton (Bhaskar Rao *et al* 1996).

The age of deposition of the supracrustal rocks in the HSB, especially its basal section, is crucial to the understanding of its relationship with the spatially associated ~ 3.33–3.0 Ga old orthogneisses, and to the resolution of the debate on its two-fold subdivision into an older Sargur Group and a younger Dharwar Supergroup. In the HSB, both the Sargur (> 3 Ga) and Dharwar (< 2.9 Ga) rocks are believed to be in juxtaposition over a fairly large area with the former exposed only in the southern and western arms and the latter mainly in the northern arm (Ramakrishnan and Viswanatha 1981). But for the differing views on the nature of the contact (intrusive or tectonic) between the ~ 3.0 Ga old TTG plutons and the supracrustals in the northern part, the HSB sequence would have long been accepted as a single unbroken sequence older than 3.1 Ga. The first direct indication that the

sequence could be as old as 3.3 Ga came from magmatic zircons in metarhyolites, which gave a precise age of 3298 ± 7 Ma. Since these zircons are interpreted as magmatic and not detrital, and the metarhyolite occurs in the upper part of the sequence close to the trondhjemite-supracrustal contact in the northern sector of the HSB, Peucat *et al* (1995) concluded that the entire sequence is as old, arguing that the younger Sm-Nd isochron age of ~ 2.6 Ga for basaltic rocks (Drury *et al* 1987) in the same location is ambiguous.

Although the Sm-Nd data from ultrabasic-basic rocks from the southern part of the HSB are far less coherent than for the metabasalts of the northern part, Drury *et al* (1987) concluded that the so-called southern 'Sargur' rocks are also not older than 3.0 Ga. The meta-anorthosite rocks we have dated now occur in the southern and western parts and at lower stratigraphic levels than the ~ 3.3 Ga metarhyolite in the northern part dated by Peucat *et al* (1995). Since the stratiform complexes are believed to be intrusives, their age of 3.285 ± 0.170 Ga shows that the southern part of the sequence was also deposited before 3.30 Ga ago. Considered together with the age of 3298 ± 7 Ma for zircons in metarhyolite in the upper levels of the northern part, our results would further imply that the entire supracrustal succession in the HSB is a single unbroken sequence deposited not later than 3.0 Ga ago. Peucat *et al* (1995) have further proposed that the surrounding gneisses differ only marginally in their age relative to the supracrustal rocks and so were accreted at the same time as the accumulation of sediments in adjacent basins. But, from the presence of detrital zircons as old as 3.6 Ga in the supracrustal rocks (Nutman *et al* 1992) it is equally conceivable that the protoliths of the existing or otherwise gniesses could be as old as 3.6 Ga and their erosion provided the sediments before all of them were deformed in a region wide event.

References

Anil Kumar, Bhaskar Rao Y J, Sivaraman T V and Gopalan K 1996 Sm-Nd ages of Archaean metavolcanics of the Dharwar craton, South India; *Precambrian Res.* **80** 205–216

Ashwal L D 1993 *Anorthosites*, (Berlin: Springer) 422 p.

Beckinsale R D, Drury S A and Holt R W 1980 3,360 Myr old gneisses from the South Indian craton; *Nature* **283** 469–470

Bekinsale R D, Reeves-Smith G, Gale N A, Holt R L W and Thompson B 1982 Rb-Sr ages and Pb-Pb whole rock isochron ages and REE data for the Archean gneisses and granites, Karnataka State, South India; In: Indo-US workshop on the Precambrian of south India [abs.]: National Geophysical Research Institute, Hyderabad, India 35–36

Bhaskar Rao Y J, Beck W, Rama Murthy V, Nirmal Charan S and Naqvi S M 1983 Geology, geochemistry and age of metamorphism of Archean grey gneisses around Chennarayapatna, Hassan district, Karnataka, South India; In: *Precambrians of South India* (eds) S M Naqvi and J J W Rogers *Geol. Soc. India Mem.* **4** 309–328

Bhaskar Rao Y J, Naha K, Srinivasan R and Gopalan K 1991 Geology, geochemistry and geochronology of the Archaean Peninsular Gneiss around Gorur, Hassan district, Karnataka, India; *Proc. Indian Acad. Sci. (Earth Planet. Sci.)* **100** 399–412

Bhaskar Rao Y J, Chetty T R K and Janardhan A S 1996 Sm-Nd and Rb-Sr ages and P-T history of the Archean Sittampundi and Bhavani layered meta-anorthosite complexes in Cauvery shear zone, south India: evidence for Neoproterozoic reworking of Archean crust; *Contrib. Mineral Petrol.* **125** 237–250

Black L P 1988 Isotopic resetting of U-Pb zircon and Rb-Sr and Sm-Nd whole rock systems in Enderbyland, Antarctica: implications to the interpretation of isotopic data from polymetamorphic and multiply deformed terranes; *Precambrian Res.* **38** 355–385

Bouhallier H, Choukroune P and Ballevre M 1993 Diaprirism, bulk homogeneous shortening, and transcurrent shearing in the Archean Dharwar craton: the Holenarsipur area, southern India; *Precamb. Res.* **63** 43–58

Bouhallier H 1995 Evolution structurale et metamorpique de la croute continentale Archeanne (Cratone de Dharwar, Indie du sud); unpubl. Phd dissertation, Geosciences-Rennes, University of Rennes, France

Bouhallier H, Chardon D and Choukroune P 1995 Strain patterns in Archaean dome-and-basin structures: The Dharwar craton (Karnataka, South India); *Earth. Planet. Sci. Lett.* **135** 57–75

Chadwick B, Ramakrishnan M, Viswanatha M N and Srinivasa Murthy V 1978 Structural studies in the Archean Sargur and Dharwar supracrustal rocks of the Karnataka craton; *J. Geol. Soc. India* **19** 531–549

Chadwick B, Ramakrishnan M, Viswanatha M N and Srinivasa Murthy V 1981 Structural and metamorphic relations between Sargur and Dharwar supracrustal rocks and Peninsular gneisses in central Karnataka; *J. Geol. Soc. India* **22** 557–569

Chadwick B, Vasudev V N, Krishna Rao B and Hedge G V 1992 The Dharwar Supergroup: basin development and implications for Late Archaean tectonic setting in western Karnataka, Southern India; In: *The Archaean: Terrains, Processes and Metallogeny*; (eds) J E Glover and S E Ho, *Univ. W. Aust. Publ.* **22** 3–15

DePaolo D J 1981 Neodymium isotopes in the Colorado Front Range and the crust-mantle evolution in the Proterozoic; *Nature* **291** 193–196

Drury S A, Naqvi S M and Hussain S M 1978 REE distribution in basaltic anorthosites from the Holenarsipur greenstone belt, Karnataka, South India; In: *Archean Geochemistry* I (eds) B F Windley and S M Naqvi, Elsevier, Amsterdam, 363–374

Drury S A, Harris N B W, Holt R N, Reeves Smith and Whitman T 1984 Precambrian tectonics and crustal evolution in South India; *J. Geology* **92** 3–20

Drury S A, Van Calsteren P L C and Reeves-Smith G J 1987 Sm-Nd isotopic data from Archean metavolcanic rocks at Holenarsipur, South India; *J. Geology* **95** 837–843

Faure G 1986 *Principles of Isotope geology* (New York: John Wiley) 589 p

Fletcher I R and Rossman K J R 1982 Precise determination of initial ϵ_{Nd} from Sm-Nd isochron data; *Geochim. Cosmochim. Acta.* **46** 1983–1987

Friend C R L and Nutman A P 1991 SHRIMP U-Pb geochronology of the Closepet granite and Peninsular gniess, Karnataka, S. India; *J. Geol. Soc. India* **38** 357–368

Henderson P, Fishlock S J, Laul J C, Cooper T D, Conard R L, Boynton W V and Schmitt R A 1976 Rare earth element abundances in rocks and minerals from the Fiskenaesset complex, West Greenland; *Earth Planet. Sci. Lett.* **30** 37–49

Hussain S M and Ahmad S M 1982 Anorthosite enclaves in the gneisses around Holenarsipur schist belt, Hassan district, Karnataka; *J. Geol. Soc. India* **26** 387–391

Hussain S M and Naqvi S M 1983 Geological, geophysical and geochemical studies over the Holenarsipur schist belt, Dharwar craton, India; In: *Precambrian of South India*; (eds) S M Naqvi and J J W Rogers, *Geol. Soc. India Mem.* **4** 73–95

Jackson M and Barton Jr 1996 The Messina layered intrusion, Limpopo belt, South Africa: an example of *in situ* contamination of an Archaean anorthosite complex by continental crust; *Precambrian Res.* **78** 139–150

Kotov A B, Kovach V P, Sal'nikova E B, Glebovitskii V A, Yakovleva S Z, Berezhmaya N G and Myskova T A 1995 Continental crust age and formation stages in the central Aldan granulite-gneiss terrain: U-Pb and Sm-Nd isotopic data for granitoids; *Petrology* **3** 87–97

Kutty T R N, Anantha Iyer G V, Ramakrishnan M and Verma S P 1984 Geochemistry of meta-anorthosites from Holenarsipur, Karnataka, south India; *Lithos* **17** 317–328

Meen J K, Rogers J J W and Fullegar P D 1992 Lead isotopic compositions of the western Dharwar craton, southern India: Evidence for distinct Middle Archaean terranes in a Late Archean craton; *Geochim. Cosmochim. Acta* **56** 2455–2470

Monrad J R 1983 Evolution of sialic terranes in the vicinity of the Holenarsipur belt, Hassan district, Karnataka, India; In: *Precambrian of South India* (eds) S M Naqvi and J J W Rogers, *Geol. Soc. India Mem.* **4** 343–364

Naha K, Srinivasan R and Naqvi S M 1986 Structural unity in the Early Precambrian Dharwar tectonic province, Peninsular India; *Quart. J. Geol. Min. Metal Soc. India* **58** 218–243

Naha K, Srinivasan R, Gopalan K, Pantulu G V C, Subba Rao M V, Vrevksy A B and Bogomolov Ye S 1993 The nature of the old basement in the Archean Dharwar craton of southern India and the age of the Precambrian gneiss; *Proc. Indian Acad. Sci. (Earth Planet. Sci.)* **102** 547–565

Naqvi S M 1981 The oldest supracrustals of the Dharwar craton, India; *J. Geol. Soc. India* **23** 458–469

Naqvi S M and Hussain S M 1979 Geochemistry of meta-anorthosites from a greenstone belt in Karnataka, India; *Can. J. Earth Sci.* **16** 1254–1264

Naqvi S M and Rogers J J W 1987 *Precambrian Geology of India*; (New York: Oxford University Press) 223 pp.

Nutman A P, Chadwick B, Ramakrishnan M and Viswanatha M N 1992 SHRIMP U-Pb ages of detrital zircon in Sargur supracrustal rocks in western Karnataka, southern India; *J. Geol. Soc. India* **39** 367–374

Nijagunappa R 1994 Chromite mineralisation in Karnataka: a review; In: *Geokarnataka – Mysore geological department centenary volume.* (eds) B M Raveendra and N Renganathan, *Karnataka Asst. Geologists Association, Bangalore,* 148–167

Peucat J J, Mahabaleswar B C and Jayananda M 1993 Age of younger tonalitic magmatism and granulitic metamorphism in the south Indian transition zone (Krishnagiri area;

comparison with older Peninsular gneisses from the Gorur-Hassan area; *J. Metamorphic Geol.* **11** 879–888

Peucat J J, Bouhallier C, Fanning C M and Jayananda M 1995 Age of the Holenarsipur greenstone belt, relationships with the surrounding gneisses (Karnataka, South India); *J. Geology* **103** 701–710

Phinney W C, Morrison D A and Maczuga D E 1988 Anorthosites and related megacrystic units in the evolution of Archaean crust; *J. Petrology* **29** 1283–1323

Provost A 1990 An improved diagram for isotope data; *Chem. Geol. (Isotope Geosci. Section)* **80** 85–89

Ramakrishnan M, Viswanatha M N, Chayapathi N and Narayanan Kutty T R 1978 Geology and geochemistry of anorthosites of Karnataka Craton and their tectonic significance; *J. Geol. Soc. India* **19** 115–134

Ramakrishnan M, Viswanatha M N 1981 Holenarsipur belt; In: *Early Precambrian supracrustals of Southern Karnataka*, (eds) J Swami Nath and M Ramakrishnan, *Geol. Survey India Mem.* **112** 115–141

Ramiengar A S, Chayapathi N, Raghunandan K R, Rao M S and Rama Rao P L 1978 Mineralogy and geochemistry of vandiferous titano-magnetite deposit and associated copper mineralisation in gabbro-anorthosites near Masanikere, Shimoga District, Karnataka, India; In: *Archean Geochemistry* (eds) B F Windley and S M Naqvi, (Amsterdam: Elsevier) 395–406

Richard P, Shimizu N, Allegre C J 1976 ^{143}Nd/^{146}Nd, a natural tracer, an application to oceanic basalts; *Earth Planet. Sci. Lett.* **31** 269–278

Srinivasan R 1988 Present role of the Sargur group of the Archaean Dharwar craton, south India; *Indian J. Geol.* **60** 57–72

Srinivasan R and Naha K 1996 Apropos of the Sargur Group in the Early Precambrian Dhawar tectonic province, southern India. In: *Recent Researches in Geology* (ed) A K Saha (New Delhi: Hindustan Publishers) **16** 43–46

Stroh P T, Monrad J R, Fullagar P O, Naqvi S M, Hussain S M and Rogers J J W 1983 3000-m.y.-old Halekote trondjhemite, a record of stabilisation of the Dharwar craton, In: *Precambrian of South India*; (eds) S M Naqvi and J J W Rogers *Geol. Soc. India Mem.* **4** 365–376

Swami Nath J, Ramakrishnan M and Viswanatha M N 1976 Dharwar stratigraphic model and Karnataka craton evolution; *Geol. Surv. India Records* **107** 149–175

Taylor P N, Chadwick B, Moorbath S, Ramakrishnan M and Viswanatha M N 1984 Petrography, chemistry and isotopic ages of Peninsular gneiss, Dharwar acid volcanic rocks and the Chitradurga granite with special reference to the late Archean volution of the Karnataka craton, Southern India; *Precambrian Res.* **23** 349–375

Williamson J H 1968 Least-squares fitting of a straight line; *Can. J. Phys.* **46** 1845–1849

Compilation of radiogenic isotope data in Mexico and their petrogenetic implications

IGNACIO S TORRES-ALVARADO[1], SURENDRA P VERMA[1] and GERARDO CARRASCO-NÚÑEZ[2]

[1]Centro de Investigación en Energía, UNAM, Priv. Xochicalco s/n, Col. Centro, Apdo. Postal 34, 62580 Temixco, Morelos, Mexico.
email: ita@mazatl.cie.unam.mx
[2]Instituto de Geología, UNAM, Circuito Exterior, Cd. Universitaria, 04510 Mexico, D.F., Mexico.

Seven hundred and twenty-five Sr, two hundred and forty-three Nd and one hundred and fifty-one Pb isotopic ratios from seven different Mexican magmatic provinces were compiled in an extensive geochemical database. Data were arranged according to the Mexican geological provinces, indicating for each province total number of analyses, range and mean of values and two times standard deviation (2σ). Data from seven provinces were included in the database: Mexican Volcanic Belt (MVB), Sierra Madre Occidental (SMO), Baja California (BC), Pacific Ocean (PacOc), Altiplano (AP), Sierra Madre del Sur (SMS), and Sierra Madre Oriental (SMOr). Isotopic values from upper mantle and lower crustal xenoliths, basement outcrops and sediments from the Cocos Plate were also compiled. In the MVB the isotopic ratios range as follows: $^{87}Sr/^{86}Sr$ 0.703003–0.70841; $^{143}Nd/^{144}Nd$ 0.512496–0.513098; $^{206}Pb/^{204}Pb$ 18.567–19.580; $^{207}Pb/^{204}Pb$ 15.466–15.647; $^{208}Pb/^{204}Pb$ 38.065–38.632. The SMO shows a large variation in $^{87}Sr/^{86}Sr$ ranging from ~0.7033 to 0.71387. $^{143}Nd/^{144}Nd$ ratios are relatively less variable with values from 0.51191 to 0.51286. Pb isotope ratios in the SMO are as follows: $^{206}Pb/^{204}Pb$ 18.060–18.860; $^{207}Pb/^{204}Pb$ 15.558–15.636; $^{208}Pb/^{204}Pb$ 37.945–38.625. PacOc rocks show the most depleted Sr and Nd isotopic ratios (0.70232–0.70567 for Sr and 0.512631–0.513261 for Nd). Pb isotopes for PacOc show the following range: $^{206}Pb/^{204}Pb$ 18.049–19.910; $^{207}Pb/^{204}Pb$ 15.425–15.734; $^{208}Pb/^{204}Pb$ 37.449–39.404. The isotopic ratios of the AP rocks seem to be within the range of those from the PacOc.

Most samples with reported Sr and Nd isotopic data are spread within and around the "mantle array". The SMO seems to have been formed by a mixing process between mantle derived magmas and continental crust. The MVB appears to have a larger mantle component, with AFC as the dominant petrogenetic process for the evolved rocks. There is still a need for Pb isotopic data in all Mexican magmatic provinces and of Nd isotopes in BC, AP, SMS, and SMOr.

1. Introduction

During the past three decades radiogenic isotopes have been developed into a powerful tool helping to identify geological processes and geochemical sources. Isotope ratios in a magma are characteristic of the source region and remain constant during later simple fractional crystallisation processes. Furthermore, contamination processes and mixing between isotopically distinct sources can be recognised (Faure 1986; Rollinson 1993). Due to the availability of modern analytical techniques and facilities, the number of radiogenic isotope analyses has increased rapidly in Mexico. However, little work has been done to compile and interpret these data in a unifying form since Verma and Verma (1986). This paper presents the preliminary results of an extensive compilation of published and some unpublished Sr, Nd and Pb isotopic data from Mexican magmatic provinces and points out their petrogenetic implications. For other isotopes no observations were compiled in this database because only a few data are available (Th
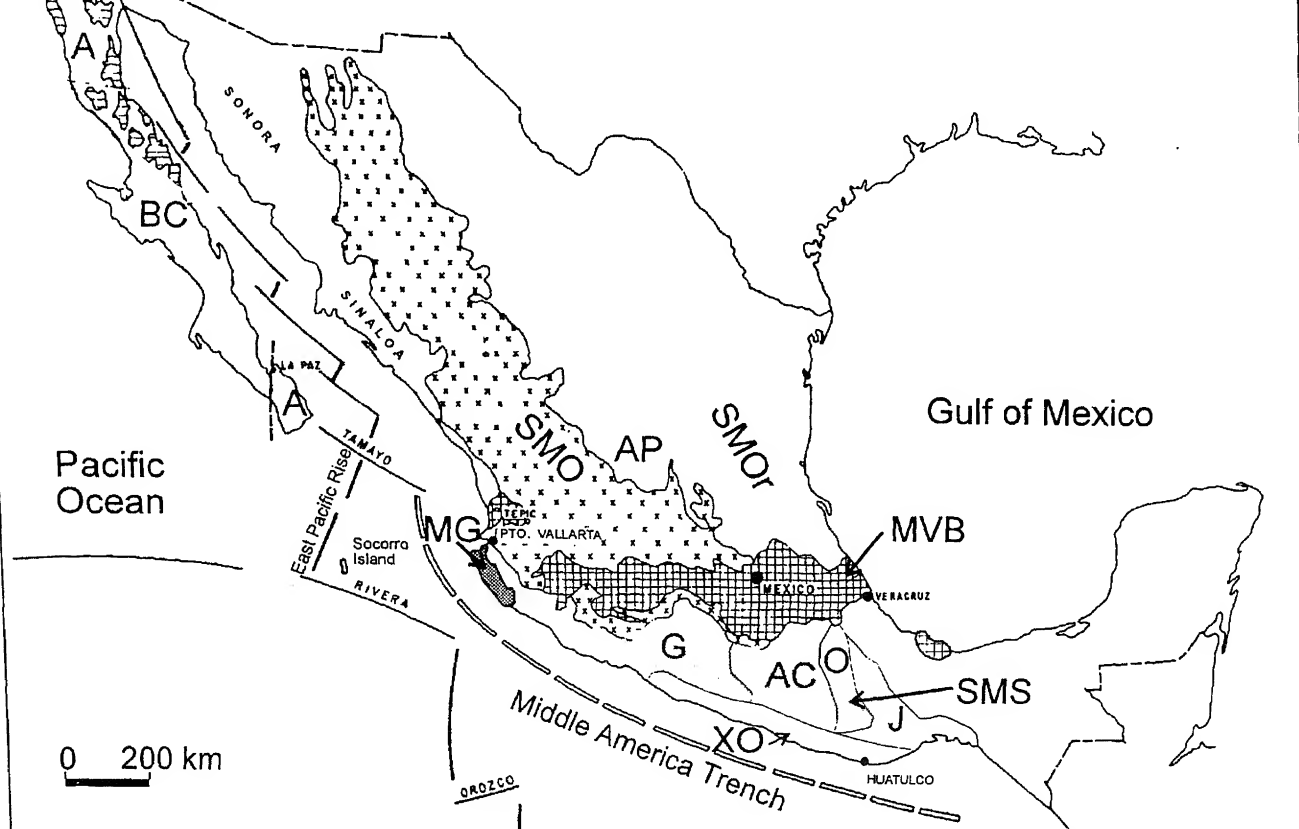
Figure 1. Principal magmatic provinces and tectono-stratigraphic terranes of Mexico. Abbreviations are **MVB** = Mexican Volcanic Belt; **SMO** = Sierra Madre Occidental; **BC** = Baja California; **AP** = Altiplano; **SMS** = Sierra Madre del Sur; **SMOr** = Sierra Madre Oriental. The SMS overlays the Guerrero terrane (**G**), the Xolapa complex (**XO**), the Acatlan complex (**AC**), the Oaxaca complex (**O**), and the Juarez terrane (**J**; Campa and Coney 1983). **A** = Alisitos arc; **MG** = Mesozoic granites.

and U: Chen *et al* 1986; Hf: Salters 1996; Be: Tera *et al* 1986; He, Graham *et al* 1988; and O: Ferriz and Mahood 1987; Verma and Dobson 1987; Mahood and Halliday 1988).

2. Geological setting

Figure 1 shows the main magmatic provinces in Mexico. De Cserna (1989) has presented a summary of the geology of Mexico. Magmatic activity occurred relatively continuously since Jurassic times. The distribution, nature and structure of this magmatism are a response of important changes in the plate tectonic dynamics involving complex interactions among several plates: North American, Pacific, Cocos, Rivera, Caribbean and the extinct Farallon plate.

The Jurassic-Cretaceous volcanism occurred mainly among the Baja California Peninsula as part of a large island arc (Demant and Robin 1975) known as the Alisitos arc (Gastil *et al* 1971), when the ancient Farallon plate subducted under the North American plate, approximately parallel to the present coast line.

An extensive plutonism developed since the Cretaceous time from the northern states of Mexico (Baja California, Sonora and Sinaloa) to the Pacific coast in central Mexico, forming a large batholithic belt showing a relative migration towards the east. This resulted from changes in dip and velocity of the NNW-SSE trending Cretaceous-Tertiary subduction zone (Demant and Robin 1975; Molnar and Stock 1987; Atwater 1989; Lyle and Ness 1991; Delgado 1994).

The plutonic activity has been identified along the Pacific coast from Puerto Vallarta to Huatulco showing a systematic decrease in age eastward. This change in age has been attributed to a geometric artifact of oblique continental margin truncation (Schaaf *et al* 1995). The tectonic erosion associated with the subduction was the most important mechanism in the northwestern segment, and the lateral removal of material associated with the displacement of the Chortis block in the southeastern segment.

According to Herrman *et al* (1994) a plate reorganisation, originated from changes in rate, direction and dip of convergence between the Farallon and North

Caribbean, seems to have induced a shift of the magmatic arc from its Cretaceous and early Tertiary location (Sierra Madre Occidental, SMO) to its present mid-Mexican position of Mexican Volcanic Belt (MVB).

During the Oligocene and early Miocene, an intense episode of ignimbritic volcanism occurred in Northwest Mexico forming the SMO, which is oriented parallel to the coast. This is the largest felsic province in the world (Lanphere *et al* 1980). In contrast, the E-W trending MVB crosses the central part of Mexico, includes active volcanism and is dominantly andesitic in composition (Aguilar-Y-Vargas and Verma 1987; Verma and Aguilar-Y-Vargas 1988). The limits and relationship between these provinces, including the definition of the MVB has been a matter of discussion for many years. The onset of volcanism in the MVB is still under debate because of a lack of systematic geochronologic studies and a unified plate tectonic model for its origin. This initiation has been proposed in late Oligocene (Gunn and Mooser 1971; Mooser 1972), Miocene (Venegas S. *et al* 1985; Verma 1987), early Pliocene (Nixon *et al* 1987), Pliocene (Cantagrel and Robin 1979; Robin 1981), or Quaternary (Demant 1978, 1981). Ferrari *et al* (1994) proposed that the volcanism migration from the SMO to MVB occurred gradually in response to the development of the Middle American Trench (MAT) in early to middle Miocene times. They also pointed out that the overall orientation of the arc did not change since 16 Ma to the Present, although a general trenchward migration of the volcanic front is observed, suggesting that the MVB proper began about that age.

Although many different models have been proposed to explain the origin of the MVB, such as those related to a week crustal zone associated with long strike-slip faults (Gastil and Jensky 1973), of a continental extension of the Clarion transform fault (Mooser and Maldonado 1961), or a gigantic "geosuture" between continental blocks (Mooser 1972), most authors believe that the MVB is a continental margin province that resulted from a subduction mechanism along the MAT (i.e. Molnar and Sykes 1969; Moorbath *et al* 1978; Demant 1981; Nixon 1982; Urrutia and Böhnel 1987). The lack of parallelism of the volcanic belt with the trench is explained by the variation in the subduction dip along the MAT (Pardo and Suárez 1995) and during different times. Alternative or more complex models are still not totally outdated (Shurbet and Cebull 1984; Cebull and Shurbet 1987; Verma 1994, 1999, 2000; Márquez *et al* 1999).

The MVB is a complex province composed of different zones (Demant 1978; Venegas S *et al* 1985; Pasquaré *et al* 1987; Aguilar-Y-Vargas and Verma 1987; Luhr 1997), whose characteristics have been attributed in part to different tectonic response of the

include:

- Paleozoic and Mesozoic tectonostratigraphic terranes to the south (Ortega-Gutiérrez 1981; Campa and Coney 1983), which are affected by granitoid rocks and are covered by an important Tertiary volcanism that forms the Sierra Madre del Sur (SMS) province (Morán-Zenteno *et al* 1998).
- To the NW is the ignimbritic sequence of SMO.
- To the central and eastern parts there are thick sedimentary sequences of highly deformed Mesozoic rocks that build the Sierra Madre Oriental (SMOr).

The southern terranes of Mexico (Ortega-Gutiérrez 1981, 1983; Campa and Coney 1983; Carfantan 1986) that form the basement of the MVB and the SMS Tertiary provinces are (figure 1): the Guerrero terrane (G; Jurassic-Cretaceous), the Acatlán complex (AC; late Paleozoic and younger), the Oaxaca terrane (O; Grenvillian age), the Xolapa terrane (XO; Paleozoic-Tertiary) and the Juárez terrane (J; Mesozoic). It is not at present possible to clearly define the relationships between these terranes to unravel the structure of the basement rocks. However, Ortega-Gutiérrez (1983) proposed that different blocks of continental crust accreted around the Oaxaca complex during Paleozoic and Mesozoic times.

There are other regions in Mexico with minor but not less important volcanism. The high plains of Central Mexico, called as the Altiplano (AP) region, show a scattered alkaline volcanism that has been associated with the southern extension of the Basin and Range province. This Pliocene-Quaternary volcanism comprises several maar volcanoes, which produced abundant xenoliths from the mantle and the lower crust (Luhr *et al* 1995). Also, within the Mesozoic sedimentary province of the SMOr, numerous plutonic bodies were responsible for various ore deposits produced during the Tertiary. Finally, volcanic islands in the Pacific Ocean represent an isolated volcanism producing Ocean Island Basalts (Bohrson and Reid 1995), associated with a still active magmatic system.

3. Methodology

$^{87}Sr/^{86}Sr$, $^{143}Nd/^{144}Nd$, $^{206}Pb/^{204}Pb$, $^{207}Pb/^{204}Pb$, and $^{208}Pb/^{204}Pb$ ratios were compiled in one thousand one hundred and nineteen analyses of rock samples. Depending on the geological region, samples may include volcanic rocks of different composition, plutonic units, as well as some mineral separates. These data were extracted from forty-seven literature sources (some of them still unpublished or in press), which include most of the isotopic analyses performed to date in the major magmatic regions in Mexico. In order to save space, the complete compilation is not
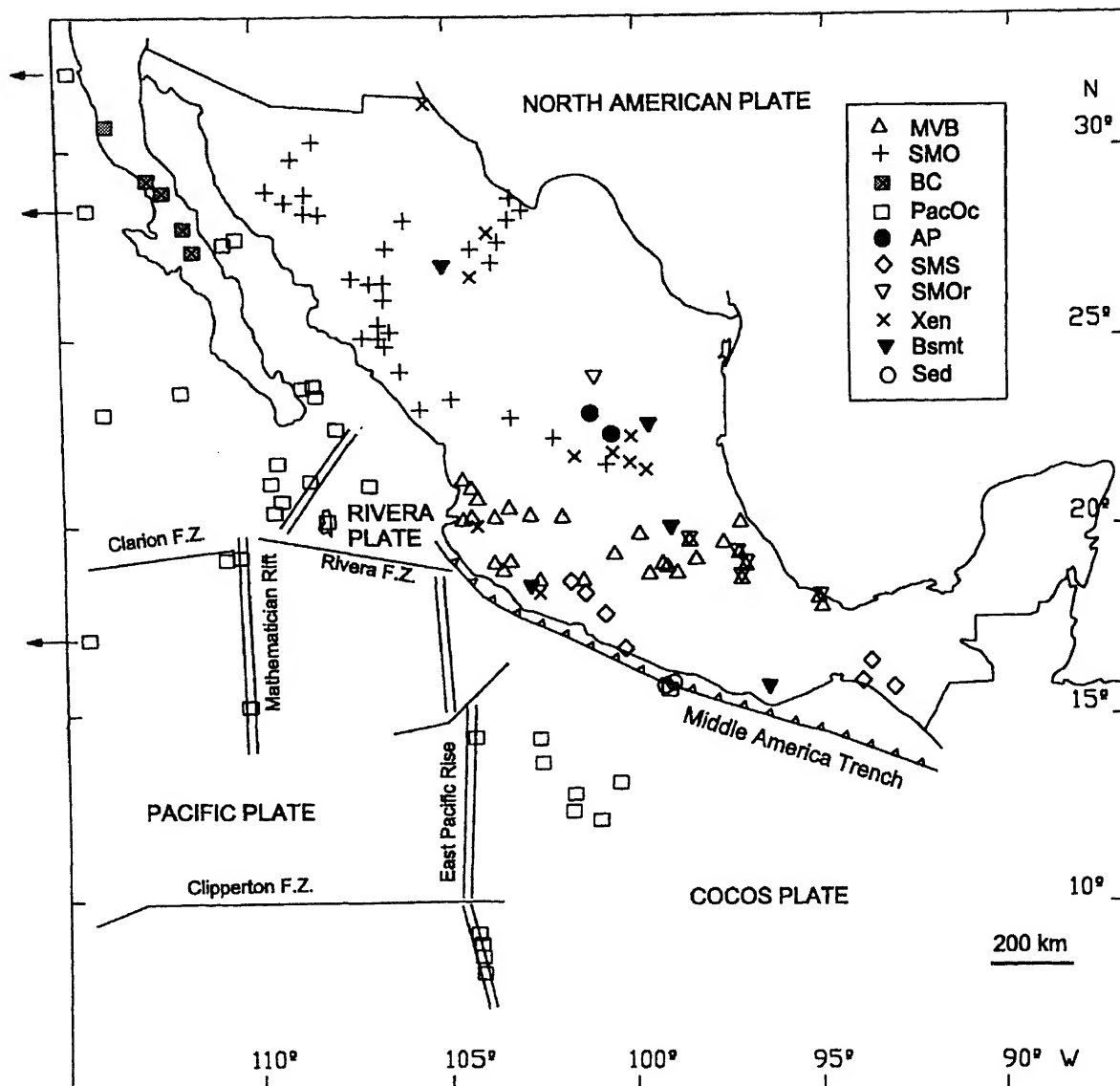
Figure 2. Sample locations from where Sr, Nd and/or Pb data were compiled for this work. **PacOc** = Pacific Oc
Xen = Xenolith; **Bsmt** = Basement outcrops; **Sed** = sediments; **F.Z.** = Fracture Zone. Other abbreviations are the same a
figure 1.

included in this paper, but a summary of the isotopic
data organised in terms of geological provinces is
presented here. Sample locations are shown schema-
tically in figure 2. Only initial $^{87}Sr/^{86}Sr$ and
$^{143}Nd/^{144}Nd$ values were included in the database,
excepting those for xenoliths, basement outcrops and
sediments, for which present isotopic values were
compiled. Measured $^{87}Sr/^{86}Sr$ and $^{143}Nd/^{144}Nd$ were
recalculated to their initial ratios in those cases when
the $^{87}Rb/^{86}Sr$ and $^{147}Sm/^{144}Nd$ values, as well as the
sample age, were available. Values of $1.42 \times 10^{-11} y^{-1}$
(Steiger and Jäger 1977) and $6.54 \times 10^{-12} y^{-1}$ (Lug-
mair and Marti 1978) were used as decay constants for
Rb-Sr and Sm-Nd respectively. Finally, $^{143}Nd/^{144}Nd$
ratios were expressed in the epsilon notation (ε_{Nd})
for comparison between samples of different ages as
suggested by DePaolo and Wasserburg (1976).

4. Data analysis and discussion

Table 1 presents the summary of the compiled d
for $^{87}Sr/^{86}Sr$, $^{143}Nd/^{144}Nd$, $^{206}Pb/^{204}$
and $^{208}Pb/^{204}Pb$ values and organised into differ
magmatic provinces according to figure 1. Maxim
and minimum values are shown for each provi
Arithmetic mean and two standard deviation val
(2σ) were also calculated. Important differences e
in the total number of available data for each isoto
ratio. For Sr isotopic values a total of seven hund
and twenty-five analyses was compiled, two hund
and forty-three values were reported for Nd and
hundred and fifty-one for Pb isotopes. Unfortunat
all the five isotopic ratios were measured in only
samples. This fact presents serious limitations in
possible interpretation of geochemical data

4.1 *Mexican Volcanic Belt (MVB)*

Approximately 45% of the published Sr isotopic data have been reported for rocks sampled from the MVB. The $^{87}Sr/^{86}Sr$ values of these rocks range from 0.703003 to 0.70841 (arithmetic mean 0.70403). Volcanic rocks from this province show an increment in their Sr isotopic ratios with increasing SiO_2 content. The histogram in figure 3(a) illustrates this trend, where basaltic rocks present the highest

Table 1. *Sr, Nd and Pb isotope data of the main magmatic provinces in Mexico. Initial isotopic ratios are shown for all provinces, except for xenolith samples (Xen), basement outcrops (Bsmt) and sediments (Sed), for which the present values were compiled.*

			$^{87}Sr/^{86}Sr$			
Province	n (725)	Min	Max	Mean	2σ	References
MVB	329	0.703003	0.70841	0.70403	0.00099	7, 10, 11, 12, 13, 14, 17, 18, 19, 20, 23, 26, 27, 31, 34, 37, 41, 42, 43, 47
SMO	105	0.7033	0.71387	0.7058	0.0034	1, 2, 3, 5, 6, 9, 21, 36
BC	18	0.70311	0.70629	0.70404	0.00164	1, 15, 24
PacOc	123	0.70232	0.70567	0.703007	0.001249	16, 22, 32, 33, 38, 47
AP	28	0.70286	0.70395	0.70318	0.00058	25, 28
SMS	22	0.70220	0.70670	0.70411	0.00256	4, 5, 30
SMOr	5	0.704	0.710	0.707	0.005	8
Xen	57	0.702570	0.731853	0.706675	0.012118	31, 34, 44, 45, 46
Bsmt	21	0.703855	0.749957	0.712846	0.021334	31, 34, 44, 45, 46
Sed	17	0.707986	0.710340	0.708597	0.001157	47
			$^{143}Nd/^{144}Nd$			
Province	n (243)	Min	Max	Mean	2σ	References
MVB	167	0.512396	0.513098	0.512819	0.000189	11, 12, 17, 18, 19, 20, 23, 27, 31, 37, 41, 42, 47
SMO	25	0.51191	0.51286	0.51256	0.00038	1, 3, 21, 36
BC	2	0.51263	0.51287	0.51275	0.00034	1
PacOc	100	0.512631	0.513261	0.513044	0.000253	16, 22, 32, 33, 38, 47
AP	28	0.51278	0.51301	0.51292	0.00011	25, 28
Xen	52	0.511920	0.513122	0.512615	0.000593	31, 35, 41, 44, 45, 46
Bsmt	19	0.511833	0.512613	0.512145	0.000345	45, 46
Sed	17	0.512437	0.512556	0.512485	0.000075	47
			ε_{Nd}			
MVB	167	−2.77	8.97	3.40	3.67	11, 12, 17, 18, 19, 20, 23, 27, 31, 37, 41, 42, 47
SMO	25	−13.45	5.08	−0.77	7.42	1, 3, 21, 36
BC	2	−0.16	4.53	2.18	6.62	1
PacOc	100	0.40	12.20	7.95	4.87	16, 22, 32, 33, 38, 47
AP	28	3.10	7.60	5.70	2.04	25, 28
Xen	52	−13.90	9.60	−0.45	11.55	31, 35, 41, 44, 45, 46
Bsmt	19	−15.70	−0.49	−9.30	6.96	45, 46
Sed	17	−3.90	−1.60	−2.99	1.46	47
			$^{206}Pb/^{204}Pb$			
Province	n (151)	Min	Max	Mean	2σ	References
MVB	53	18.567	19.580	18.737	0.289	16, 18, 19, 31, 37, 41, 47
SMO	10	18.060	18.860	18.390	0.540	29, 36
PacOc	71	18.049	19.910	18.736	0.707	16, 33, 38, 39, 47
AP	10	18.740	18.980	18.872	0.166	28
Xen	2	18.804	19.368	19.086	0.798	31, 41
Bsmt	1	18.862	18.862	18.862	0.000	31
Sed	4	18.592	18.935	18.805	0.303	47
			$^{207}Pb/^{204}Pb$			
MVB	53	15.466	15.647	15.587	0.071	16, 18, 19, 31, 37, 41, 47
SMO	10	15.558	15.636	15.583	0.055	29, 36
PacOc	71	15.425	15.734	15.545	0.130	16, 33, 38, 39, 47
AP	10	15.540	15.650	15.602	0.066	28
Xen	2	15.618	15.649	15.634	0.044	31, 41
Bsmt	1	15.599	15.599	15.599	0.000	31
Sed	4	15.577	15.671	15.632	0.079	47

Table 1. (*Continued*)

		$^{208}Pb/^{204}Pb$				
MVB	53	38.065	38.632	38.433	0.248	16, 18, 19, 31, 37, 41, 47
SMO	10	37.945	38.625	38.295	0.497	29, 36
PacOc	71	37.449	39.404	38.293	0.917	16, 33, 38, 39, 47
AP	10	38.340	38.870	38.590	0.358	28
Xen	2	38.662	38.711	38.687	0.069	31, 41
Bsmt	1	38.699	38.699	38.699	0.000	31
Sed	4	38.312	38.729	38.517	0.397	47

Abbreviations are **MVB** = Mexican Volcanic Belt; **SMO** = Sierra Madre Occidental; **BC** = Baja California; **PacOc** = Pac
Ocean; **AP** = Altiplano; **SMS** = Sierra Madre del Sur; **SMOr** = Sierra Madre Oriental. Total amount of analyses in parenthe

References: (**1**) Cameron and Cameron 1985; (**2**) Lanphere *et al*, 1980; (**3**) Verma 1984; (**4**) Damon *et al* 1981; (**5**) Damon *
1983a; (**6**) Damon *et al* 1983b; (**7**) Moorbath *et al* 1978; (**8**) Ohmoto *et al* 1966; (**9**) McDowell *et al* 1978; (**10**) Cantagrel
Robin 1978; (**11**) Verma 1983a; (**12**) Verma and Armienta-H 1985; (**13**) Verma *et al* 1985; (**14**) Whitford and Bloomfield 19
(**15**) Basu 1979; (**16**) Bohrson and Reid 1995; (**17**) Verma *et al* 1991; (**18**) Verma and Luhr 1993; (**19**) Verma and Dobson 19
(**20**) Verma and Nelson 1989; (**21**) Gunderson *et al* 1986; (**22**) Macdougall and Lugmair 1986; (**23**) Besch *et al* 19
(**24**) Saunders *et al* 1987; (**25**) Pier *et al* 1989; (**26**) Martín del Pozzo *et al* 1989; (**27**) Mahood and Halliday 1988; (**28**) Luhr
1995; (**29**) James and Henry 1993; (**30**) González-Partida *et al* 1989; (**31**) Heatherington 1988; (**32**) Verma 1983b; (**33**) Ve
1992; (**34**) McBirney *et al* 1987; (**35**) Nimz *et al* 1986; (**36**) Cameron *et al* 1986; (**37**) Nelson *et al* 1995; (**38**) Graham *et al* 19
(**39**) Chen *et al* 1986; (**40**) Ferriz and Mahood 1987; (**41**) Verma 2000; (**42**) Wallace and Carmichael 1994; (**43**) Nixon 19
(**44**) Schaaf *et al* 1994; (**45**) Ruiz *et al* 1988b; (**46**) Ruiz *et al* 1988a; (**47**) Verma 1999.
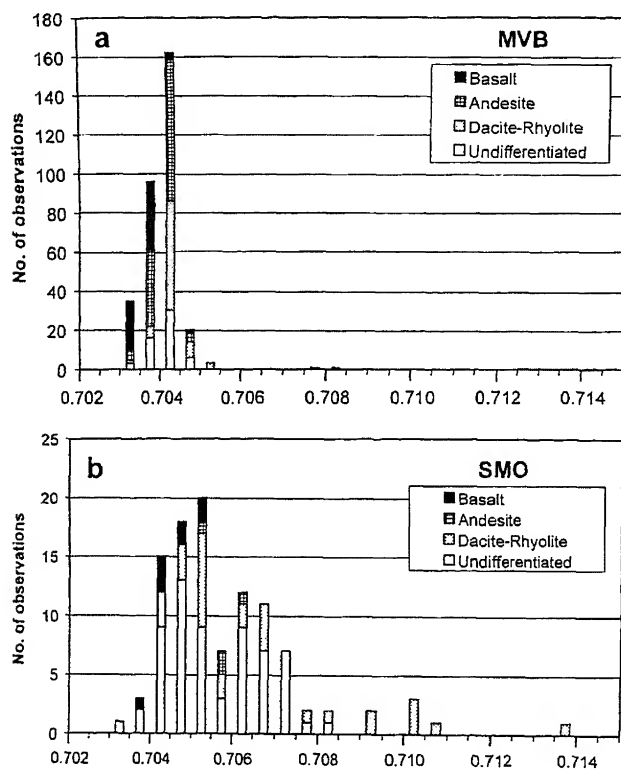

Figure 3. Sr isotopic composition of magmatic rocks from the
Mexican magmatic provinces. (a) Mexican Volcanic Belt
(MVB) and (b) Sierra Madre Occidental (SMO). To facilitate
comparison of provinces same scale is used for $^{87}Sr/^{86}Sr$ (x-
axis) in all histogram plots (this figure and figures 4 and 5).
Under the "undifferentiated" composition are included all
rocks with unspecified chemical character; it may include
plutonic rocks, mineral separates and generic volcanic rocks.

number of observations between 0.7030 and 0.7040;
andesites show the highest number of observations at
between 0.7035 and 0.7045 and dacites and rhyolites
between 0.7040 and 0.7050. Nd isotopic ratios rang

from 0.512496 to 0.513098 (arithmetic me
0.512819). Lead isotopes have been analysed in fi
three volcanic rocks from this province showing
following range: $^{206}Pb/^{204}Pb$ 18.567–19.5
$^{207}Pb/^{204}Pb$ 15.466–15.647; $^{208}Pb/^{204}Pb$ 38.0
38.632.

4.2 *Sierra Madre Occidental (SMO)*

The SMO depicts one of the largest isotopic variati
according to this compilation. Sr isotopic composit
varies from 0.7033 to 0.71387, with arithmetic me
at 0.7058 (table 1). Figure 3(b) shows the distribut
of these ratios. Andesites from this province ha
relatively uniform $^{87}Sr/^{86}Sr$ but slightly higher val
than basalts. Dacites and rhyolites, on the other ha
show a very wide distribution from between 0.70
and ~0.7140. $^{143}Nd/^{144}Nd$ values range from 0.511
to 0.51286 (arithmetic mean: 0.51256). Ten samp
have been analysed for their lead isotopic charact
istics, yielding relatively homogeneous values.
isotope ratios are as follows: $^{206}Pb/^{204}Pb$ 18.0
18.860; $^{207}Pb/^{204}Pb$ 15.558–15.636; and $^{208}Pb/^{204}$
37.945–38.625.

4.3 *Baja California (BC)*

Only eighteen samples from the BC magma
province have been analysed for Sr isotopic compo
tion, two for Nd and none for Pb (table 1). $^{87}Sr/^{86}$
varies from 0.70311 to 0.70629 (mean 0.7040
The distribution of these values is shown in figu
4(a). Baja Californian andesites are geochemica
unusual and have been interpreted by Saunders *et*
(1987) as the product of the subduction of you
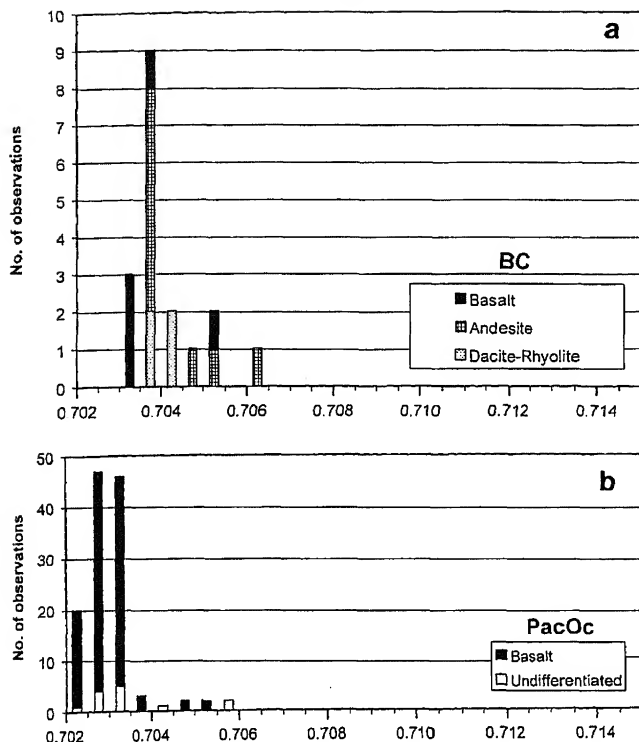oceanic lithosphere or subduction of a spreadi

Figure 4. Sr isotopic composition of magmatic rocks from the Mexican magmatic provinces (a) Baja California (BC) and (b) Pacific Ocean (PacOc). Under the "undifferentiated" composition are all those rocks, whose chemical character was not specifically reported.

4.4 *Pacific Ocean (PacOc)*

Basalts from the East Pacific Rise, Socorro Island, seamounts and subducting Cocos Plate are included in the present compilation in the PacOc magmatic province. This kind of grouping has a geographical rather than a petrogenetic character. A total of one hundred and twenty-three samples for Sr isotopes, one hundred for Nd isotopes and seventy-one for Pb isotopes have been reported (table 1). These rocks show the most depleted Sr and Nd isotopic ratios (0.70232–0.70567 for Sr and 0.512631–0.513261 for Nd). Pb isotopes for Pacific Ocean show the following range: $^{206}Pb/^{204}Pb$ 18.049–19.910; $^{207}Pb/^{204}Pb$ 15.425–15.734; $^{208}Pb/^{204}Pb$ 37.449–39.404, with arithmetic mean values of 18.736, 15.545, and 38.293 respectively. Figure 4(b) shows the distribution of Sr isotopic ratios. Most isotopic values are between 0.7020 and 0.7035. Altered basalts have higher $^{87}Sr/^{86}Sr$ as expected from interaction with seawater. In addition, two fresh rocks from Shimada seamount have high $^{87}Sr/^{86}Sr$ (figure 4(b)) and low ε_{Nd} (Graham *et al* 1988). The isotopic signature of PacOc samples indicates a mantle origin for these magmas. However, the data from East Pacific Rise and Socorro Island indicate some regional mantle heterogeneities. Macdougall and Lugmair (1986) include a "plume" component to explain the relatively high Sr and Nd

isotopic ratios and high incompatible element concentrations in the East Pacific Rise. On the other hand, Bohrson and Reid (1995) in their study of basaltic rocks from Socorro Island conclude that ocean crustal contamination may be introduced into magmatism of Ocean Island Basalt.

4.5 *Altiplano (AP)*

In the AP magmatic region interesting rocks (hawaiite, basanite, olivine nephelinite and some alkali basalt) have been studied for their Sr, Nd and Pb isotopic compositions by Pier *et al* (1989) and Luhr *et al* (1995). These authors reported twenty-eight Sr and Nd isotopic analyses, as well as ten Pb isotopic measurements. Sr isotopic ratios range from 0.70286 to 0.70395. $^{143}Nd/^{144}Nd$ values vary between 0.51278 and 0.51301. Lead isotopic ratios present a very narrow range, with calculated mean values of 18.872, 15.602, and 38.590 for $^{206}Pb/^{204}Pb$, $^{207}Pb/^{204}Pb$, and $^{208}Pb/^{204}Pb$ respectively. The isotopic ratios of the AP rocks are within the range of those from the Pacific Ocean.

Although most of the samples from AP region show a mantle origin, crustal contamination and mixing processes have also been interpreted. Pier *et al* (1989) concluded from the analyses of eighteen basanite samples from San Luis Potosi, that a mixing model of three different mantle reservoirs best explains the isotopic signatures of those rocks: a depleted source, a St. Helena type component, and a third source rich in radiogenic Sr. Miocene hawaiites which crop out in the eastern margin of the Mexican Basin and Range Province present crustal contamination; up to 45% of the Pb in these rocks has been crustally derived (Luhr *et al* 1995).

4.6 *Sierra Madre del Sur (SMS) and Sierra Madre Oriental (SMOr)*

The SMS and SMOr have been sparsely studied for their isotopic characteristics. For these provinces only twenty-seven analyses for $^{87}Sr/^{86}Sr$ and none for Nd or Pb isotopes have been reported in the literature. Sr isotopic values for SMS range between 0.70220 and 0.70670 (arithmetic mean 0.70411). For the SMOr $^{87}Sr/^{86}Sr$ varies between 0.704 and 0.710. The heterogeneous nature of the basement under SMS and its wide range of ages (between 32 Ma and 246 Ma) suggest that the magmas in this region could not have been derived from a homogeneous source. For the SMOr scarcity of data and their low quality (considering modern standards) make it difficult to give any petrogenetic significance to these Sr isotopic values.

4.7 *Xenoliths, basement rocks and Cocos Plate sediments*

Present values for $^{87}Sr/^{86}Sr$, $^{143}Nd/^{144}Nd$, $^{206}Pb/^{204}Pb$, $^{207}Pb/^{204}Pb$, and $^{208}Pb/^{204}Pb$ in upper
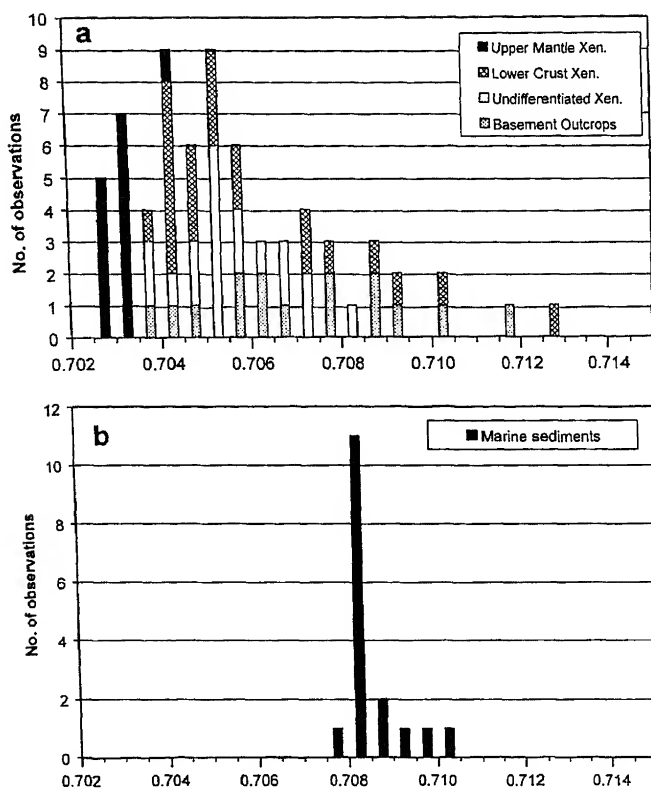
Figure 5. Sr isotopic composition of other rocks compiled in this database. (a) Xenoliths and basement outcrops, (b) Cocos Plate sediments. Four highest Sr isotopic ratios of xenolith samples (metasediments: 0.715183 and 0.727928; undifferentiated: 0.730435 and 0.731853) were not included in the histogram. Under the "undifferentiated xenoliths" are all those rocks, whose chemical character was not specifically reported.

mantle and lower crustal xenoliths as well as basement outcrops have been compiled in this database. The main reason for compiling measured values rather than initial ratios estimated from "model ages" is that the present isotopic compositions are more useful in petrogenetic interpretations of Mexican provinces. Statistical parameters and literature sources of these data are presented in table 1. Figure 5(a) shows the distribution of Sr isotopic compositions of these samples, arranged according to their provenance. Unfortunately many of the xenoliths were not properly classified and therefore are grouped as "undifferentiated" in this diagram. Upper mantle xenoliths show the lowest Sr isotopic ratios ranging from about 0.7025 to 0.7045 (figure 5(a)). Lower crustal xenoliths as well as basement rocks present a wide variation of $^{87}Sr/^{86}Sr$ (from about 0.7035 to 0.7130). $^{143}Nd/^{144}Nd$ also shows a similar variation for these xenoliths and basement rocks. For Pb isotopes only two measurements are available for xenoliths and one for basement rocks (table 1).

The wide variation in Sr and Nd isotopic data observed in xenoliths and basement rocks is a strong evidence of a heterogeneous lower crust in Mexico.

in crustal xenoliths and basement outcrops are sim to those observed in many andesitic to rhyolitic r from the MVB and basaltic rocks from the S (figure 3). This similarity in Sr isotopic composi makes it difficult to model the petrogenesis of volc rocks in subduction environment such as for the M and SMO.

Figure 5(b) shows the distribution of $^{87}Sr/$ analysed in sediments from the Cocos Plate in vicinity of the Middle American Trench (figure For these sediments the isotopic ratios rang follows: $^{87}Sr/^{86}Sr$ 0.707986–0.710340; $^{143}Nd/^{1}$ 0.512437–0.512556; $^{206}Pb/^{204}Pb$ 18.592–18. $^{207}Pb/^{204}Pb$ 15.577–15.671; $^{208}Pb/^{204}Pb$ 38. 38.729 (table 1).

4.8 *Some implications of Sr-Nd isotopic dat*

Figure 6 presents a conventional $^{87}Sr/^{86}Sr$-ε_{Nd} gram for basaltic rocks compiled in our database the MVB, SMO, PacOc, and AP provinces. Mc the samples plot on or close to the "mantle a (White 1985; Faure 1986). Altered rocks from ocean floor are shifted to the right of the "m array" as a result of seawater interaction. Diff contributions from the underlying crust may b reason for the spread in isotopic compositior basaltic rocks from these provinces. This may b case of the MVB, with a large spread in this diag indicating a higher addition of crustal material an other magmatic processes (such as AFC).

As an attempt to examine regional variation $^{87}Sr/^{86}Sr$ and ε_{Nd} data for all samples from compilation are plotted in figure 7, in contras figure 6 where only basaltic rocks were plotted. simplicity, the data for the MVB, SMO, PacOc,
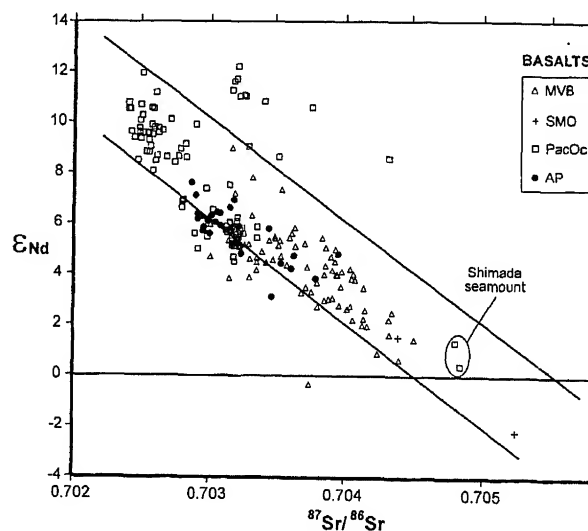

Figure 6. ε_{Nd} vs. $^{87}Sr/^{86}Sr$ diagram for basaltic rocks three better-studied magmatic provinces of Mexico. Slo lines approximate the "mantle array" (White 1985). Abbr

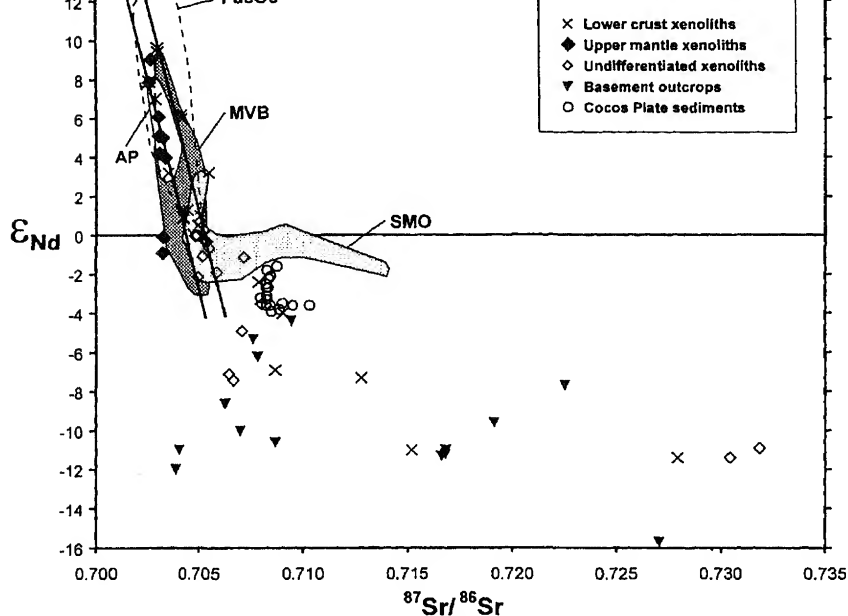Figure 7. ε_{Nd} vs. $^{87}Sr/^{86}Sr$ diagram for the magmatic provinces of Mexico. Sloping lines approximate the "mantle array" (White 1985). Abbreviations are the same as in figure 1. One basement sample with high Sr and low ε_{Nd} value (0.749957 and -13.2 respectively) is not included in this diagram. See text for explanation.

AP are shown as closed fields. Fields for the BC, SMS, and SMOr provinces are not included because of scarcity of data. Most samples from the studied magmatic provinces fall on the "mantle array" (White 1985). The SMO shows a special subhorizontal trend extending from the "mantle array" to Sr isotopic values up to $\sim$0.714. At first sight, the PacOc field seems to encompass most of the AP and MVB isotopic data. This is due to two samples from Shimada seamount, which fall near the "bulk Earth" value (see figure 6) and apparently enlarge the PacOc field. Xenolith analyses show a large spread of Sr and Nd isotopic values. Many of them fall on the "mantle array" but extend up to very high $^{87}Sr/^{86}Sr$ and low ε_{Nd} values. On the other hand, Cocos Plate sediments are relatively uniform in Sr and Nd isotopes, occupying a small area just below the SMO field.

The special trend presented by the SMO (figure 7), with relatively constant ε_{Nd} values has been explained by Verma (1984) and Cameron and Cameron (1985) as the product of a two-component mixing model. According to them, mantle derived magmas (composition similar to the basalts represented by crosses in figure 6) mix with different proportions of continental crust. This mixing process is supposed to be accompanied by extensive fractional crystallisation at shallow levels before eruption, thus producing large volumes of differentiated magmas in this province.

$^{87}Sr/^{86}Sr$ and $^{206}Pb/^{204}Pb$ for all samples are presented in figure 8. The MVB samples fall on the right side of the Prevalent Mantle reservoir (PREMA, Zindler and Hart 1986). Low $^{87}Sr/^{86}Sr$ and high
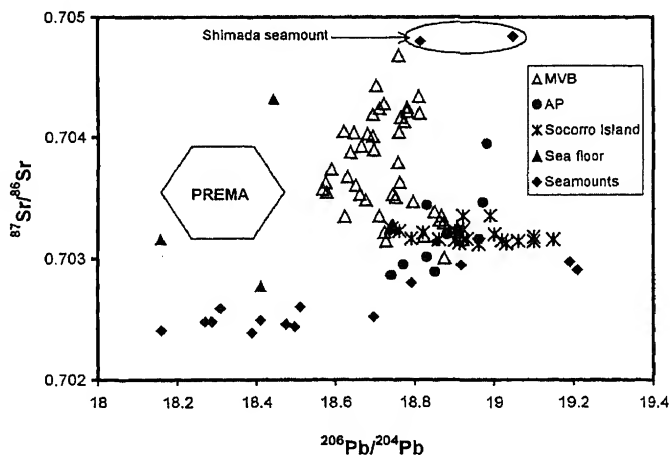
Figure 8. $^{87}Sr/^{86}Sr$ vs. $^{206}Pb/^{204}Pb$ diagram for magmatic rocks from Mexican provinces. PREMA: Prevalent Mantle reservoir (Zindler and Hart 1986).

$^{206}Pb/^{204}Pb$ samples from the MVB overlap with the field occupied by the AP and Socorro Island rocks. Sr isotopic values from Socorro Island are much more homogeneous than those of AP samples. Bohrson and Reid (1995) suggested oceanic crust as a contamination source of Socorro Island basalt. Large variation in Pb isotopic data from Socorro Island indicates a component with a high $^{206}Pb/^{204}Pb$. Seamounts from the Pacific Ocean show the largest spread in Pb isotopic ratios, as compared to $^{87}Sr/^{86}Sr$. Two samples from Shimada seamount plot on the top of the diagram. Their origin has been related to a young intraplate hotspot (Graham et al 1988).

There is no doubt that more data are needed, especially for Pb and Nd isotopes (see table 1), in order to have a better understanding of the origin of Mexican magmatic provinces and for the construction of more reliable petrologic models. Other major and petrogenetically important trace elements should also be compiled to better understand the origin and evolution of Mexican magmatic provinces.

5. Conclusions

Most magmatic rocks lay on the "mantle array" in $^{87}Sr/^{86}Sr$–$^{143}Nd/^{144}Nd$ diagram, suggesting the mantle as an important magma source for all Mexican magmatic provinces. The source is however not uniform. Different magmatic processes, such as crustal contamination, magma mixing and AFC, also contribute to the diversity of magmas in these provinces. This may be the case of the MVB, with a large spread in Sr and Nd isotopic ratios. The presence of lower crustal xenoliths with similar isotopic compositions to the "mantle array" makes it difficult to adopt the upper mantle as a unique source. The SMO seems to have been formed by a mixing process between mantle derived magmas and continental crust. More isotopic data, particularly Nd and Pb isotopes, are required for a better understanding of the origin and evolution of Mexican magmatic provinces.

Acknowledgements

References

Aguilar-Y-Vargas V H and Verma S P 1987 Composición química (elementos mayores) de los magmas en el Cinturón Volcánico Mexicano; *Geofís. Int.* **26** 273–290.

Atwater T 1989 Plate tectonic history of the northeast Pacific and western North America. Chapter 4, In: *The Eastern Pacific Ocean and Hawaii. The Geology of North America, Boulder, Colorado,* (eds) E L Winterer, D M Hussong and R W Decker, The Geological Society of America 21–72.

Basu A R 1979 Geochemistry of ultramafic xenolith from San Quintin, Baja California, (eds) F R Boyd and H O A Meyer, In: *The mantle sample: Inclusions in kimberlites and other volcanics.* (Washington, DC: AGU) 2: 391–423

Besch T, Verma S P, Kramm U, Negendank J F W, Tobschall H J, and Emmermann R 1995 Assimilation of sialic crustal material by volcanics of the easternmost extension of the Trans-Mexican Volcanic Belt Evidence from Sr and Nd isotopes; *Geofis. Int.* **34** 263–281

Bohrson W A and Reid M R 1995 Petrogenesis of alkaline basalts from Socorro Island, Mexico: trace element evidence for contamination of ocean island basalt in the shallow acean crust; *J. Geophys. Res.* **100** 24555–24576

Cameron K L and Cameron M 1985 Rare earth element, $^{87}Sr/^{86}Sr$ and $^{143}Nd/^{144}Nd$ compositions of Cenozoic ore

genic dacites from Baja California, northwestern Me and adjacent west Texas: evidence for the predominance subcrustal component; *Contrib. Mineral. Petrol.* **91** 1–

Cameron K L, Cameron M and Barreiro B 1986 Orig voluminous mid-tertiary ignimbrites of the batopilas re Chihuahua: implications for the formation of contin crust beneath the Sierra Madre Occidental; *Geofís. Ir* 39–59

Campa M F and Coney P J 1983 Tectono-stratigr terranes and mineral resource distributions of Mexico; *J. Earth Sci.* **20** 1040–1051

Cantagrel J-M and Robin C 1978 Géochemie isotopiqu strontium dans quelques séries types du volcanisme de mexicain; *Bull. Soc. Geol. France* **20** 935–939

Cantagrel J M and Robin C 1979 K-Ar dating on Ea Mexican volcanic rocks-relations between the andesiti the alkaline provinces; *J. Volcanol. Geotherm. Res.* **5** 9

Carfantan J C 1986 Du systeme cordilletain Nor-Americ domaine Caraibe. Thèse Doctorat d'Etat, Universi Savoie, 558 pp.

Cebull S E and Shurbet D H 1987 Mexican Volcanic Be intraplate transform?; *Geofís. Int.* **26** 1–13

Chen J H, Wasserburg G J, von Damm K L and Edmon 1986 The U-Th-Pb systematics in hot springs on th Pacific Rise at 21°N and Guaymas Basin; *Ge Cosmochim. Acta* **50** 2467–2479

De Cserna Z 1989 An outline of the geology of Mexico. (W Bally and A R Palmer, In: *The Geology of North Ar An overview, The Geology of North America, Bc Colorado* (Geological Society of America), 233–264

Demant A 1978 Características del eje neovolcánico tran icano y sus problemas de interpretación; *Rev. Inst. UNAM* **2** 172–187

Demant A 1981 L'Axe Néovolcanique Mexicain, étude vo logique et pétrographique-signification géodynamique. Doctorat d'Etat, Aix-Marseille University, 259 pp

Demant A and Robin C 1975 Las fases del vulcanism México: una síntesis en relación con la evolución geodin desde el Cretácico; *Rev. Inst. Geol. UNAM,* **1** 70–82

Damon P E, Shafiqullah M and Clark K F 1981 Age tre igneous activity in relation to metallogenesis in the Sou Cordillera. (eds) W R Dickinson and W D Payn *Relations of Tectonics to Ore deposits in the Sou Cordillera, XIV,* (Tucson, Arizona: Arizona Geol Society Digest) 137–154

Damon P E, Shafiqullah M and Clark K F 1983a Geochron of the porphyry copper deposits and related mineralizat Mexico; *Can. J. Earth Sci.* **20** 1052–1071

Damon P E, Shafiqullah M, Roldán Q J and Jauqes, C J El batolito Laramide (90–40 m.a.) de Sonora. Mem Convención Nac. Asoc. Ing. Minas, Metalurg. Geol. M Guadalajara, Jal. 63–95

Delgado G H 1994 Comparative studies on the Tectonic Volcanism of Circum-Pacific Arcs; *Geofís. Int.* **33** 5–1

DePaolo D J and Wasserburg G J 1976 Nd isotopic varia and petrogenetic models; *Geophys. Res. Lett.* **3** 249–2

Faure G 1986 Principles of isotope geology. (New York: V 653 pp.

Ferrari L, Garduño V H, Pascuaré G and Tibaldi A Volcanic and tectonic evolution of central Mexico: Olig to present; *Geofís. Int.* **33-1** 91–105

Ferriz H and Mahood G A 1987 Strong compositional zon in a silicic magmatic system: Los Humeros, Me Neovolcanic Belt; *J. Petrol.* **28** 171–209

Gastil R G and Jensky W 1973 Evidence for strik displacement beneath the Trans-Mexican Volcanic (eds) R I Kovach and A Nur, In: *Proc. Conf. Te Problems of the San Andreas Fault System* (Stanford

Gastil G, Allison E C and Phillips R P 1971 Reconocimiento geológico del Edo. de Baja California; *Mapa* 1:250,000.

González-Partida E, Casar-Aldrete I, Morales-Puente P and Nieto-Obregón J 1989 Fechas de Rb-Sr (Maastrichtiano y Oligoceno) de rocas volcánicas e intrusivas de la región de Zihuatanejo, Sierra Madre del Sur de México; *Rev. Inst. Geol. UNAM*, 8 248–249.

Graham D W, Zindler A, Kurz M D, Jenkins W J, Batiza R and Staudigel H 1988 He, Pb, Sr and Nd isotope constraints on magma genesis and mantle heterogeneity beneath young Pacific seamounts; *Contrib. Mineral. Petrol.* 99 446–463

Gunderson R, Cameron K and Cameron M 1986 Mid-Cenozoic high-K calc-alkalic and alkalic volcanism in eastern Chihuahua, Mexico: geology and geochemistry of the Benavides-Pozos area; *Geol. Soc. Am. Bull.* 97 737–753

Gunn B M and Mooser F 1971 Geochemistry of the volcanics of Central Mexico; *Bull. Volcanol.* 34 577–616

Heatherington A L 1988 Isotopic systematics of volcanics from south-central Rio Grande Rift and the western Mexican Volcanic Belt: Implications for magmatic and tectonic evolution of Cenozoic extensional regimes in Western North America. (Ph.D. Thesis, Washington University, St. Louis. MO), 207 pp.

Herrmann U R, Nelson B K and Ratschbacher L 1994 The origin of a terrane: U/Pb zircon geochronology and tectonic evolution of the Xolapa complex (southern Mexico); *Tectonics* 13 455–474

James E W and Henry C D 1993 Southeastern extent of the North American craton in Texas and northern Chihuahua as revealed by Pb isotopes; *Geol. Soc. Am. Bull.* 105 116–126

Lanphere M A, Cameron K L and Cameron M 1980 Sr isotopic geochemistry of voluminous rhyolitic ignimbrites and related rocks, Batopilas area, western Mexico; *Nature* 286 594–596

Lugmair G W and Marti K 1978 Lunar initial $^{143}Nd/^{144}Nd$: differential evolution of the lunar crust and mantle; *Earth Planet. Sci. Lett.* 39 349–357

Luhr F J, Pier G J, Aranda-G and Podosek F 1995 Crustal contamination in early Basin-and-Range hawaiites of the Los Encinos Volcanic Field, central Mexico; *Contrib. Mineral. Petrol.* 118 321–339

Luhr J F 1997 Extensional tectonics and the diverse primitive volcanic rocks in the western mexican volcanic belt; *Can. Mineral.* 35 473–500

Lyle M and Ness G E 1991 The opening of the southern Gulf of California. (eds) J P Dauphin and B R T Simoneit In: The Gulf and Peninsular Province of the Californias. (AAPG Memoir 47, Tulsa, Oklahoma) 403–423

Macdougall J D and Lugmair G W 1986 Sr and Nd isotopes in basalts from the East Pacific Rise: significance for mantle heterogeneity; *Earth Planet. Sci. Lett.* 77 273–284

Mahood G A and Halliday A N 1988 Generation of high-silica rhyolite: a Nd, Sr, and O isotopic study of Sierra La Primavera, Mexican Neovolcanic Belt; *Contrib. Mineral. Petrol.* 100 183–191

Márquez A, Verma S P, Anguita F, Brandle J L and Oyarzun R 1999 Tectonics and volcanism of Sierra Chichinautzin: Extension at the front of the central Trans-Mexican Volcanic Belt; *J. Volcanol. Geotherm. Res.* 93 125–150

Martín del Pozzo A L, Morales Puente P, Casar Aldrete I and Urrutia Fucugauchi J 1989 Strontium isotopic and geochemical data from the Chichinautzin monogenetic volcanic field, basin of Mexico crustal structure, and composition of the magmatic arc; *Comunicaciones Técnicas Instituto de Geofísica UNAM, Serie Investigación* 105 1–11

McBirney A R, Taylor H P and Armstrong R L 1987 Paricutin re-examined: a classical example of crustal assimilation in calc-alkaline magma; *Contrib. Mineral. Petrol.* 95 4–20

McDowell F W, Duex T W, Henry C D and Long L E 1978 Age and strontium isotope chemistry of the Sierra Mader

Occidental volcanic province, western Mexico; *U.S.G.S. Open-file Report* 78–701 289–291

Molnar P and Sykes L R 1969 Tectonics of the Caribbean and Middle American region from focal mechanism and seismicity; *Geol. Soc. Am. Bull.* 80 1639–1684

Molnar P and Stock J 1987 Relative motions of hotspots in the Pacific, Atlantic and Indian oceans since late Cretaceous time; *Nature* 327 587–591

Moorbath S, Thorpe R S and Gibson I L 1978 Strontium isotope evidence for petrogenesis of Mexican andesites; *Nature* 271 437–438.

Mooser F 1972 The Mexican Volcanic Belt-structure and tectonics; *Geofís. Int.* 12 55–70

Mooser F and Maldonado K M 1961 Penecontemporaneous tectonics along the Mexican Pacific coast; *Geofís. Int.* 1 1–20

Morán Zenteno D J, Alba-Aldave L A, Martínez-Serrano R, Reyes-Salas M, Corona-Esquivel R and Angeles-García S 1998 Stratigraphy, geochemistry and tectonic significance of the Tertiary volcanic sequences of the Taxco-Quetzalapa region; *Rev. Mex. Cienc. Geol.* (in press)

Nelson S A, Gonzalez-Caver E and Kyser T K 1995 Constraints on the origin of alkaline and calc-alkaline magmas from the Tuxtla volcanic field, Veracruz, Mexico. *Contrib. Mineral. Petrol.* 122 191–211

Nimz G J, Cameron K L, Cameron M and Morris S L 1986 The petrology of the lower crust and upper mantle beneath southeastern Chihuahua, Mexico: A progress report; *Geofís. Int.* 25 85–116

Nixon G T 1982 The relationship between Quaternary volcanism in central Mexico and the seismicity and structure of subducted ocean lithosphere; *Geol. Soc. Am. Bull.* 93 514–523

Nixon G T 1988 Petrology of the younger andesites and dacites of Iztaccíhuatl Volcano, Mexico: II. Chemical stratigraphy, magma mixing, and the composition of basaltic magma influx; *J. Petrol.* 29 265–303

Nixon G T, Demant A, Amstrong R L and Harakal E 1987 K-Ar and geologic data bearing on the age and evolution of the Trans-Mexican Volcanic Belt; *Geofís. Int.* 26 109–158

Ohmoto H, Hart S R and Holland H D 1966 Studies in the provincia area, Mexico, II K-Ar and Rb-Sr ages of intrusive rocks and hydrothermal minerals; *Econ. Geol.* 61 1205–1213

Ortega-Gutiérrez F 1981 Metamorphic belts of southern Mexico and their tectonic significance; *Geofís. Int.* 20 177–202

Ortega-Gutiérrez F 1983 Tectonostratigraphic analysis and significance of the Paleozoic Acatlán Complex of Southern Mexico: First Circum-Pacific and Circum-Atlantic Conference Terrane Geology of Southern Mexico; *Guidebook of field trip B, Instituto de Geologia, UNAM* 54–60.

Pardo M and Suárez G 1995 Shape of the subducted Rivera and Cocos plates in southern Mexico: seismic and tectonic implications; *J. Geophys. Res.* 100 12357–12373

Pasquaré G, Vessoli L and Zanchi A 1987 Morphological and structural model of Mexican Volcanic Belt; *Geofís. Int.* 26 159–176

Pier J G, Podosek F A, Luhr J F, Brannon J C and Aranda-Gomez J J 1989 Spinel-lherzolite-bearing Quaternary volcanic centers in San Luis Potosí, Mexico. 2. Sr and Nd isotopic systematics; *J. Geophys. Res.* 94 7941–7951

Robin C 1981 Relations volcanologie-magmatologie-géodynamique: application au passage entre volcanismes alcalin et andésitique dans le sud Mexicain. Thése Doctorat d'Etat, Clermont-Ferrand University, 503 pp.

Rollinson H R 1993 Using Geochemical Data: Evaluation, Presentation, Interpretation. (Longman Scientific Technical, Esex, England), 344 pp.

Ruiz J, Patchett P J and Arculus R J 1988a Nd–Sr isotope composition of lower crustal xenoliths – evidence for the origin of mid-Tertiary felsic volcanics in Mexico; *Contrib. Mineral. Petrol.* 99 36–43

Ruiz J, Patchett P J and Ortega-Gutierrez F 1988b Proterozoic and Phanerozoic basement terranes of Mexico from Nd isotopic studies; *Geol. Soc. Am. Bull.* **100** 274–281

Salters V J M 1996 The generation of mid-ocean ridge basalts from the Hf and Nd isotope perspective; *Earth Planet. Sci. Lett.* **141** 109–123

Saunders A D, Rogers G, Marriner G F, Terrell D J and Verma S P 1987 Geochemistry of Cenozoic volcanic rocks, Baja California, Mexico: implications for the petrogenesis of post-subduction magmas; *J. Volcanol. Geotherm. Res.* **32** 223–245

Schaaf P, Heinrich W and Besch T 1994 Composition and Sm-Nd isotopic data of the lower crust beneath San Luis Potosí, central Mexico: evidence from a granulite-facies xenolith suite; *Chem. Geol.* **118** 63–84

Schaaf P, Morán Zenteno D, Hernández-Bernal M S, Solís-Pichardo G, Tolson G and Köhler H 1995 Paleogene continental margin truncation in southwestern Mexico: Geochronological evidence; *Tectonics* **14–5** 1339–1350

Shurbet D H and Cebull S E 1984 Tectonic interpretation of the Trans-Mexicano Volcanic Belt; *Tectonophysics* **101** 159–165

Steiger R H and Jäger E 1977 Subcommission on geochronology: convention on the use of decay constants in geo- and cosmochronology; *Earth Planet. Sci. Lett.* **36** 359–362

Tera F, Brown L, Morris J, Sacks I S, Klein J and Middleton R 1986 Sediment incorporation in island-arc magmas: inferences from [10]Be; *Geochim. Cosmochim. Acta* **50** 535–550

Urrutia J and Böhnel H 1987 Tectonic interpretation of the Trans-Mexican Volcanic Belt- discussion; *Tectonophysics* **138** 319–323

Venegas S S, Herrera J and Macial F 1985 Algunas caracteristicas de la Faja Volcanica Mexicana y sus recursos geotermivos; *Geofís. Int.* **24–1** 47–83

Verma S P 1983a Magma genesis and chamber processes at Los Humeros caldera, Mexico-Nd and Sr isotope data; *Nature* **301** 52–55

Verma S P 1983b Strontium and neodymium isotope geochemistry of igneous rocks from the North East Pacific and Gulf of California; *Isot. Geosci.* **1** 339–356

Verma S P 1984 Sr and Nd isotopic evidence for petrogenesis of mid-tertiary felsic volcanism in the mineral district of Zacatecas, Zac. (Sierra Madre Occidental), Mexico; *Isot. Geosci.* **2** 37–53

Verma S P 1987 Mexican Volcanic Belt: present state of knowledge and unsolved problems; *Geofís. Int.* **26** 309–340

Verma S P 1992 Seawater alteration effects on REE, K, Rb, Cs, Sr, U, Th, Pb, and Sr-Nd-Pb isotope systematics of Mid-Ocean Ridge Basalt; *Geochem. J.* **26** 159–177

Verma S P 1994 Geochemical and isotopic constraints o origin of mafic volcanism in central Mexico; *Mineral.* **58A** 938–939

Verma S P 1999 Geochemistry of subducting Cocos plat the origin of subduction-unrelated mafic volcanism a volcanic front of the central Mexican Volcanic Belt; Soc. Am. Spec. Paper on Cenozoic Tectonics and Volc of Mexico 334, chapter 13 (in press)

Verma S P 2000 Geochemical evidence for a lithospheric s for magmas from Los Humeros Caldera, Puebla, M *Chem. Geol.* **164** 35–60

Verma S P and Aguilar-Y-Vargas V H 1988 Bulk che composition of magmas in the Mexican Volcanic (Mexico) and inapplicability of generalized arc-m *Chem. Erde* **48** 203–221

Verma S P and Armienta-H M A 1985 [87]Sr/[86]Sr, alka alkaline earth element geochemistry of Chichinautzin S Mexico; *Geofís. Int.* **24** 665–678

Verma S P and Dobson P F 1987 Sr, Nd, O and Pb iso evidence for complex petrogenetic evolution of silicic la the Los Azufres volcanic field, Michoacán, Mexico: *Trans. Am. Geophys. Un.* **68** 1520 (abstract)

Verma S P and Luhr J F 1993 Sr-Nd-Pb isotope and element geochemistry of calc-alkaline andesites from V Colima, Mexico; *Geofís. Int.* **32** 617–631

Verma S P and Nelson S A 1989 Isotopic and trace ele constraints on the origin and evolution of alkaline and alkaline magmas in the northwestern Mexican Volcanic *J. Geophys. Res.* **94** 4531–4544

Verma S P and Verma M P 1986 A compilation of Sr ar isotope data on Mexico; *J. Geol. Soc. India* **27** 130–14

Verma S P, Lopez-Martinez M and Terrell D J 1985 chemistry of tertiary igneous rocks from Arandas-Atot area, northeast Jalisco, Mexico; *Geofís. Int.* **24–1** 31–

Verma S P, Carrasco-Núñez G and Milán M 1991 Geolog geochemistry of Amealco caldera, Qro., Mexico; *J. Vol Geotherm. Res.* **47** 105–127

Wallace P J and Carmichael I S E 1994 Petrology of V Tequila, Jalisco, Mexico: Disequilibrium phenocryst a blages and evolution of the subvolcanic magma sy *Contrib. Mineral. Petrol.* **117** 345–361

White W M 1985 Sources of oceanic basalts: radiogenic iso evidence; *Geology* **13** 115–118

Whitford D J and Bloomfield K 1976 Geochemistry of Cenozoic volcanic rocks from the Nevado de Toluca Mexico; *Carnegie Inst. Wash. Yearb.* **75** 207–213

Zindler A and Hart S 1986 Chemical geodynamics; *Annu.* *Earth Planet. Sci.* **14** 493–571

Error propagation in equations for geochemical modeling of radiogenic isotopes in two-component mixing

SURENDRA P VERMA

*Centro de Investigación en Energía, UNAM, Priv. Xochicalco S/N, Col. Centro,
Apartado Postal 34, Temixco, Mor. 62580, Mexico.
email: spv@mazatl.cie.unam.mx*

This paper presents error propagation equations for modeling of radiogenic isotopes during mixing of two components or end-members. These equations can be used to estimate errors on an isotopic ratio in the mixture of two components, as a function of the analytical errors or the total errors of geological field sampling and analytical errors. Two typical cases ("Small errors" and "Large errors") are illustrated for mixing of Sr isotopes. Similar examples can be formulated for the other radiogenic isotopic ratios. Actual isotopic data for sediment and basalt samples from the Cocos plate are also included to further illustrate the use of these equations. The isotopic compositions of the predicted mixtures can be used to constrain the origin of magmas in the central part of the Mexican Volcanic Belt. These examples show the need of high quality experimental data for them to be useful in geochemical modeling of magmatic processes.

1. Introduction

Data reduction and error analysis have become fundamental in physical and chemical sciences (e.g., Bevington 1969; Taylor 1990; Guedens *et al* 1993a, b). Error evaluation and propagation are a routine matter in geochronology and isotope geology (Dalrymple and Lanphere 1969; Faure 1986; Rollinson 1993; Dickin 1995), but have not attracted adequate attention in other branches of earth sciences, such as trace element determination and modeling of magmatic processes using these elements (Wilson 1989; López Ruiz and Cebriá Gómez 1990; Albarède 1995, Verma 1996a). For major element mass-balance modeling, least-squares regression techniques are routinely applied in geochemistry (e.g. Bryan *et al* 1969; Wright and Doherty 1970; Albarède and Provost 1977; Verma *et al* 1992).

In petrological and thermodynamic problems, error analysis has gained importance as evidenced in several books (Le Maitre 1982; Taylor 1982; McBirney 1984; Ragland 1989; Rollinson 1993). Error propagation theory has been applied recently to geothermal research for evaluating three geothermometers and proposing new geothermometric equations from outlier detection and elimination (Santoyo and Verma 1991, 1993; Verma and Santoyo 1995, 1997).

Accuracy and precision provide two parameters to assess analytical errors. For isotopic ratios, precision is generally estimated in each sample run (expressed as $2\sigma_E$; two times the standard error of the mean), but can also be determined by replicate analyses. Accuracy is also controlled by running an "accepted" standard several times during the course of a study and adjusting the isotopic ratios of unknown samples for a probable instrumental bias in isotopic determinations. For trace elements, on the other hand, the precision and accuracy are generally estimated by analyzing an international geochemical reference material (RM). Unfortunately, most RM still show a large spread of elemental data (e.g., Gladney and Roelandts, 1988; Govindaraju *et al* 1994; Imai *et al* 1995; Velasco and Verma 1998), although better-characterized mean concentration values can be obtained by a procedure

Keywords. Isotopic ratios; geochemistry; error propagation; mixing; Mexico; Cocos plate.

involving a large number of statistical tests for outlier detection and rejection (Verma 1996b, 1997, 1998; Verma *et al* 1998). Quality-value parameter based on the relative standard deviation of the final data population can be used to decide the usefulness of these RM to specific analytical problems (Potts and Kane 1992; Verma 1997). It is not customary to adjust the trace element data for possible bias, although statistical tests are sometimes applied for establishing new methods or for testing the quality of data from existing analytical procedures (Sutarno and Steger 1985; Velasco and Verma 1995).

The errors of trace element determination in individual geological samples are therefore not precisely known. It is however not difficult to estimate the precision of individual analysis, using error propagation theory (Bevington 1969; Guedens *et al* 1993a, b; Verma 1995). In fact, this has been done for mass spectrometric isotope dilution measurements (Verma 1981; Verma and Schilling 1982).

The consequences of the experimental errors inherent in the determination of trace elements and isotopic ratios have not been evaluated for modeling of igneous processes, such as partial melting (Schilling and Winchester 1967; Gast 1968; Shaw 1970, Hertogen and Gijbels 1976; Hanson 1978; Albarède 1983; Maaløe 1994), fractional crystallization (Neumann *et al* 1954; Greenland 1970; Albarède 1976; Allègre and Minster 1978; Langmuir 1989; O'Hara and Fry 1996a, b), magma mixing or source mixing (Anderson 1976; Langmuir *et al* 1978; DePaolo and Wasserburg 1979; Myres *et al* 1987; López Ruiz and Cebriá Gómez 1990), and combined assimilation and fractional crystallization (Taylor 1980; DePaolo 1981, 1985; Powell 1984; Taylor and Sheppard 1986; Hagen and Neumann 1990). Recently, although Albarède (1995) has presented some worked examples, systematic work, reporting explicit error propagation equations and illustrative examples, is in fact required for a more extensive application of these concepts in geochemistry.

A series of papers will be devoted to analyze the consequences of experimental errors inherent in the determination of trace elements and isotopic ratios for modeling of igneous processes. This first part deals with error propagation for isotopic ratios in two-component mixtures. The case of inverse modeling in which the composition of one or both components or end-members is predicted from the composition of several mixture samples will be presented elsewhere.

2. New error equations for two-component mixing

Error propagation theory provides the rules for combining errors of two variables related to each other by a mathematical operation, such as summa-tion, subtraction, multiplication, and division, or for a variable involved in a mathematical function, such as exponent or logarithm (Bevington 1969; Taylor 1982; Guedens *et al* 1993a, b). New equations are derived from this theory by propagating errors of different parameters involved in geochemical modeling of mixing of two components. The resulting equations express explicitly the error of the predicted variable (isotopic ratio in the mixture) in terms of the errors in the initial variables (e.g., original concentration of the corresponding trace element and isotopic ratio of the two components). These equations predict the uncertainty in the composition of the mixture of two components, prior to its possible modification from other processes that might take place after the mixing has been completed.

2.1 *Equations for an isotopic ratio*

As many other igneous processes, the mixing process is controlled by mass-balance. For radiogenic isotopes, such as $^{87}Sr/^{86}Sr$, $^{143}Nd/^{144}Nd$, $^{206}Pb/^{204}Pb$, etc., the mixing of two components is given by equations similar to the ones developed here for $^{87}Sr/^{86}Sr$.

For mixing of Sr concentration, the mixing equations (Faure 1986) of element concentration will not be strictly applicable in their present form, as the atomic weight depends on the actual value of the isotopic ratio of radiogenic Sr (i.e., $^{87}Sr/^{86}Sr$). However, the differences in atomic weights are generally very small as shown below.

The element Sr consists of four stable isotopes (Faure 1986): ^{88}Sr, ^{87}Sr, ^{86}Sr, and ^{84}Sr. One of them (^{87}Sr) is radiogenic and therefore has a variable abundance. The absolute abundance of these isotopes can be obtained from the measured isotopic ratios of different isotopes of Sr. As an example, let us assume for a sample that $^{87}Sr/^{86}Sr = 0.710$ (crust-type Sr), $^{86}Sr/^{88}Sr = 0.1194$ (by definition, this value is used in corrections of isotopic fractionation effects), and $^{84}Sr/^{88}Sr = 0.006756$. Using the atomic masses of the isotopes $^{88}Sr = 87.905625$ amu, $^{87}Sr = 86.908890$ amu, $^{86}Sr = 85.909273$ amu, and $^{84}Sr = 83.913428$ amu (Walker *et al* 1977), it is a simple matter to show that the atomic weight of such a Sr is 87.6167 amu. If the $^{87}Sr/^{86}Sr$ in the sample were 0.703 (mantle-type Sr), then the atomic weight of such a Sr will be 87.6172 amu, not very different from crust-type Sr. The differences are thus too small to be of much significance in modeling of magmatic processes described in this paper.

The equations are simpler if one assumes very similar, almost identical atomic weights of Sr and absolute abundance of ^{86}Sr in components A and B. This assumption is generally justified as shown above for all cases where the isotopic ratios of the two end-members are not drastically different. The mixing equation for the isotopic ratio is as follows (e.g., Faure

1986, Albarède 1995):

$$\left(\frac{^{87}Sr}{^{86}Sr}\right)_M = \frac{f Sr_A \left(\frac{^{87}Sr}{^{86}Sr}\right)_A + (1-f) Sr_B \left(\frac{^{87}Sr}{^{86}Sr}\right)_B}{f Sr_A + (1-f) Sr_B}$$

$$(1)$$

where Sr_A and Sr_B are the concentrations of Sr in components A and B respectively; f is the fraction of the component A in the mixture. The concentration of Sr in the mixture Sr_M is estimated as follows:

$$Sr_M = f Sr_A + (1-f) Sr_B . \quad (2)$$

For convenience, I define two new variables α and β as follows:

$$\alpha = f Sr_A \left(\frac{^{87}Sr}{^{86}Sr}\right)_A , \quad (3)$$

$$\beta = (1-f) Sr_B \left(\frac{^{87}Sr}{^{86}Sr}\right)_B . \quad (4)$$

Using equations (2) to (4), the equation (1) can be written simply as:

$$\left(\frac{^{87}Sr}{^{86}Sr}\right)_M = \frac{\alpha + \beta}{Sr_M} . \quad (5)$$

Both the concentration and isotopic ratio are characterized by experimental errors, although the former error (for concentration) is generally much greater than the latter one (for isotopic ratio). Let σ_A^{Sr} and $\sigma_A^{87/86}$ be the respective errors for component A; σ_B^{Sr} and $\sigma_B^{87/86}$ for component B; σ_M^{Sr} and $\sigma_M^{87/86}$ for the mixture M. In many practical cases, these errors could be total sampling and experimental errors. In other words, they could represent the actual variability of heterogeneous end-members, provided their distribution is not too different from a "normal" statistical sample.

The general error propagation equation for Sr_M is:

$$\sigma_M^{Sr^2} = f^2 \sigma_A^{Sr^2} + (1-f)^2 \sigma_B^{Sr^2} + 2f(1-f)\sigma_{AB}^{Sr} \quad (6)$$

where σ_{AB}^{Sr} is the covariance of Sr concentration in the components A and B.

The covariance term should tend to zero because, in practically all cases, the measurements of Sr concentration in the two components A and B are independent and therefore $\sigma_{AB}^{Sr} \to 0$. In that case, the equation (6) reduces to:

$$\sigma_M^{Sr^2} = f^2 \sigma_A^{Sr^2} + (1-f)^2 \sigma_B^{Sr^2} . \quad (7)$$

The general error propagation equation for $Sr_M^{87/86}$ is:

$$(\sigma_M^{86/86})^2 = \left(\frac{^{87}Sr}{^{86}sr}\right)_M^2 \left[\frac{\sigma_u^2}{u^2} + \frac{\sigma_v^2}{v^2} - 2\frac{\sigma_{uv}}{uv}\right] \quad (8)$$

where

$$u = \alpha + \beta . \quad (9)$$

Neglecting the covariance term (as the determinations of Sr concentration and $^{87}Sr/^{86}Sr$ in the components A and B are independent),

$$\sigma_u^2 = \alpha^2 \left[\left\{\frac{\sigma_A^{Sr}}{Sr_A}\right\}^2 + \left\{\frac{\sigma_A^{87/86}}{\left(\frac{^{87}Sr}{^{86}Sr}\right)_A}\right\}^2\right]$$

$$+ \beta^2 \left[\left\{\frac{\sigma_B^{Sr}}{Sr_B}\right\}^2 + \left\{\frac{\sigma_B^{87/86}}{\left(\frac{^{87}Sr}{^{86}Sr}\right)_B}\right\}^2\right] \quad (10)$$

$$v = Sr_M \quad (11)$$

$$\sigma_v^2 = f^2 \sigma_A^{Sr^2} + (1-f)^2 \sigma_B^{Sr^2} . \quad (12)$$

Although Bevington (1969) used σ_{uv}^2 to denote covariance of the variables u and v, Taylor (1982) encouraged the use of the term σ_{uv}, simply because the covariance can be negative and that σ_{uv} has the dimensions of uv. The latter notation is therefore used in this paper. The covariance σ_{uv} is given by,

$$\sigma_{uv} = \langle (u - \bar{u})(v - \bar{v}) \rangle . \quad (13)$$

The variables u and v are respectively the numerator and denominator of the right hand side of equation (5). The covariance can be expressed as Schwarz inequality (Taylor 1982):

$$|\sigma_{uv}| \le \sigma_u \sigma_v . \quad (14)$$

If it is assumed that these two variables u and v are "perfectly" correlated, then the inequality (14) can be written as equality equation (15):

$$|\sigma_{uv}| = \sigma_u \sigma_v \quad (15)$$

and therefore equation (8) can be modified as,

$$(\sigma_M^{87/86})_{\min}^2 = \left(\frac{^{87}Sr}{^{86}Sr}\right)_M^2 \left[\frac{\sigma_u^2}{u^2} + \frac{\sigma_v^2}{v^2} - 2\frac{\sigma_u \sigma_v}{uv}\right] \quad (16)$$

or, simplifying one can obtain

$$(\sigma_M^{87/86})_{\min} = \left(\frac{^{87}Sr}{^{86}Sr}\right)_M \left[\frac{\sigma_u}{u} - \frac{\sigma_v}{v}\right] . \quad (17)$$

Equation (17) gives the minimum error of $^{87}Sr/^{86}Sr$ in the mixture of A and B, in the case when the variables u and v are perfectly correlated.

The general case is when the variables u (numerator) and v (denominator) of the right hand side of equation (1) are not perfectly correlated. Although the concentration terms Sr_A and Sr_B are present in both numerator and denominator, the isotopic terms $(^{87}Sr/^{86}Sr)_A$ and $(^{87}Sr/^{86}Sr)_B$ occur only in the numerator. Therefore, the variations of the concentration variables will contribute to the covariance term σ_{uv}, leaving the effects of the isotopic variables almost negligible in this term. A reasonable estimate

(18) below:

$$|\sigma_{uv}| \approx (\sigma_u)_{\text{cov}}(\sigma_v)_{\text{cov}} \qquad (18)$$

where $(\sigma_u)_{\text{cov}}$ and $(\sigma_v)_{\text{cov}}$ are approximated as follows for this covariance term only:

$$(\sigma_u)^2 = \sqrt{\alpha^2 \left[\left\{\frac{\sigma_A^{\text{Sr}}}{\text{Sr}_A}\right\}^2\right] + \beta^2 \left[\left\{\frac{\sigma_B^{\text{Sr}}}{\text{Sr}_B}\right\}^2\right]}, \qquad (19)$$

$$(\sigma_v)_{\text{cov}} = \sqrt{f^2 \sigma_A^{\text{Sr}^2} + (1-f)^2 \sigma_B^{\text{Sr}^2}}. \qquad (20)$$

Therefore, the final error can be estimated from equation (21), using equations (10) and (12) as well as (18) to (20).

$$\left(\sigma_M^{87/86}\right)^2 \approx \left(\frac{{}^{87}\text{Sr}}{{}^{86}\text{Sr}}\right)_M^2 \left[\frac{\sigma_u^2}{u^2} + \frac{\sigma_v^2}{v^2} - 2\frac{(\sigma_u)_{\text{cov}}(\sigma_v)_{\text{cov}}}{uv}\right]. \qquad (21)$$

3. Results and discussion

Equation (21) is for propagated error, whereas equation (17) gives a minimum estimate of this error. Equation (21) should therefore provide a more realistic estimate of the propagated error. It will be used to characterize the mixtures with propagated errors in predicted variables of radiogenic isotopic ratios for two-component mixing. As stated above, sample variability reflecting its heterogeneity can be used in place of experimental errors, unless there is strong evidence that the parameter distribution is not symmetrical. Myers *et al* (1987) presented a mathematical-graphical procedure to take into account such end-member variability. Instead of this approach, the equations derived here are used to understand and predict the effects of such variability.

3.1 *Illustrative examples of application to radiogenic isotopes*

In order to keep the paper short I will use the Sr isotopes for illustrative purposes. Similar examples can be put forth for other radiogenic isotopes ($^{143}\text{Nd}/^{144}\text{Nd}$, $^{206}\text{Pb}/^{204}\text{Pb}$, $^{207}\text{Pb}/^{204}\text{Pb}$, and $^{208}\text{Pb}/^{204}\text{Pb}$). In fact, it will be done so in the next section for the actual data from the Cocos plate.

As an example, $\text{Sr}_A = 10$ ppm, $\text{Sr}_B = 100$ ppm, $\left(^{87}\text{Sr}/^{86}\text{Sr}\right)_A = 0.703$, and $\left(^{87}\text{Sr}/^{86}\text{Sr}\right)_B = 0.720$ are assumed. The predicted Sr isotopic ratio $\left(^{87}\text{Sr}/^{86}\text{Sr}\right)_M$ of a mixture of these two components or end-members A and B as a function of f (f is the proportion of the component A in the mixture) is plotted in figure 1. This is a general mixing curve for isotopes. Its curvature depends on the relative value of the ratio of the end-member concentrations. Only in the special
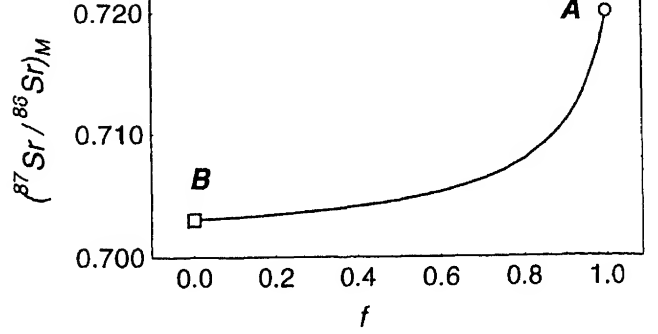

Figure 1. Predicted Sr isotopic ratio $\left(^{87}\text{Sr}/^{86}\text{Sr}\right)_M$ of a mixture of two components or end-members A and B as a function of f (f is the proportion of the component A in the mixture). $\text{Sr}_A = 10$ ppm, $\text{Sr}_B = 100$ ppm, $\left(^{87}\text{Sr}/^{86}\text{Sr}\right)_A = 0.703$ and $\left(^{87}\text{Sr}/^{86}\text{Sr}\right)_B = 0.720$ are assumed for this example. The component A is represented by a circle and the component B by a square in this and later diagrams. Note the mixing curve is, in general, not a straight line on this diagram.

circumstance when $\text{Sr}_A = \text{Sr}_B$ that this mixing curve becomes a straight line. No error bars are shown in this diagram. It therefore represents only the mixing of two totally homogenous and error-free end-members. However, this is a highly improbable situation, as the end-member compositions will generally be variable and also characterized by experimental error, or both sampling and experimental errors, reflecting end-member heterogeneity. The propagated error $\sigma_A^{87/86}$ on the $^{87}\text{Sr}/^{86}\text{Sr}$ of the mixture as a function of f for the example of figure 1 is given in figure 2. The experimental errors of Sr concentrations are totally correlated, as explained above, and therefore seem to cancel out from the mixture $^{87}\text{Sr}/^{86}\text{Sr}$. The errors on the isotopic ratios are therefore reflected in the final propagated error on the $^{87}\text{Sr}/^{86}\text{Sr}$ in the mixture. Two extreme cases can be considered.

3.1.1 *Small errors*

This case is computed for $\sigma_A^{87/86} = 0.01\%$ and $\sigma_B^{87/86} = 0.01\%$. Figure 2(a) gives the mixing curve with error bars and figure 2(b) shows $(\%\text{Rsd})_M$ vs. f curve for the same data as in figure 2(a). It is of interest to see how the equal errors of the end-members are propagated to lower errors in the mixture isotopic ratio (figure 2(b)). This behavior depends on the difference between the actual isotopic ratios of the two end-members. In this case of small errors, the size of the symbols generally used in such diagrams is sufficient to represent the propagated errors.

3.1.2 *Large errors*

$\left(^{87}\text{Sr}/^{86}\text{Sr}\right)_M$ vs. f curve with resulting $\sigma_M^{87/86}$ vertical error bars for $\sigma_A^{87/86} = 0.16\%$ and $\sigma_B^{87/86} = 0.08\%$ is
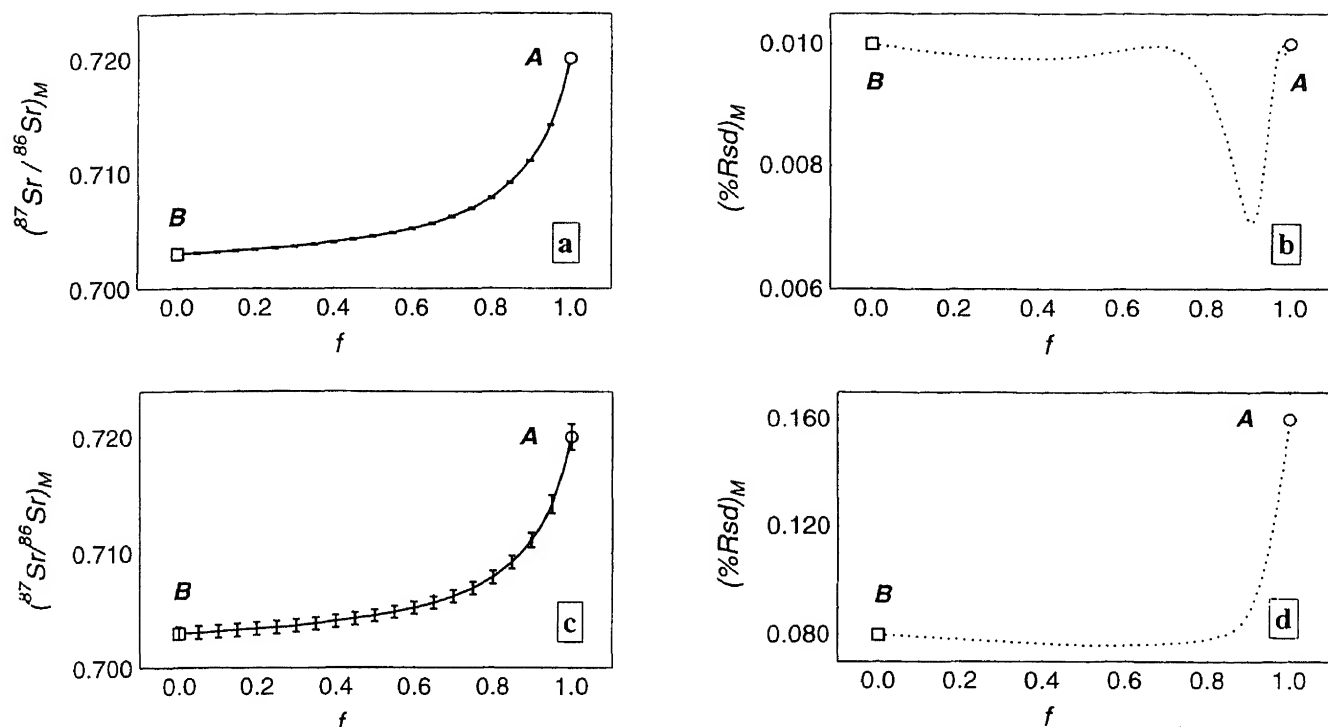
Figure 2. Propagated error $\sigma_M^{87/86}$ on the $^{87}\mathrm{Sr}/^{86}\mathrm{Sr}$ of the mixture as a function of f for the example of figure 1. "Small errors" example: (a) $(^{87}\mathrm{Sr}/^{86}\mathrm{Sr})_M$ vs. f curve with resulting $\sigma_M^{87/86}$ vertical error bars for both $\sigma_A^{87/86} = 0.01\%$ and $\sigma_B^{87/86} = 0.01\%$ (the experimental errors of Sr are totally correlated and seem to cancel out from the mixture $^{87}\mathrm{Sr}/^{86}\mathrm{Sr}$; see text for more explanation); (b) $(\%\mathrm{Rsd})_M$ vs. f curve for the same data as in figure 2(a). "Large errors" example: (c) $(^{87}\mathrm{Sr}/^{86}\mathrm{Sr})_M$ vs. f curve with resulting $\sigma_M^{87/86}$ vertical error bars for $\sigma_A^{87/86} = 0.16\%$ and $\sigma_B^{87/86} = 0.08\%$; (d) $(\%\mathrm{Rsd})_M$ vs. f curve for the same data as in figure 2(c).

shown in figure 2(c). The corresponding $(\%\mathrm{Rsd})_M$ vs. f curve for the data of figure 2(c) is presented in figure 2(d). The propagated error in this case is somewhat larger than the size of the symbols used. For this case of unequal large errors, the propagated error lies between the two values for the end-members.

3.2 *Application to isotopic ratios from the Cocos plate*

Radiogenic isotopes and related trace element data are summarized in table 1, taken from Verma (1992, 1999) and Leggett (1981). The more important statistical parameters are also included for their use

Table 1. *Isotopic and relevant trace element data (with total geological field sampling and analytical errors, reflecting heterogeneity of the compositions) in sediment and altered basalt samples from DSDP Site 487 located at the Cocos plate, Mexico (summarized from Verma 1998b)*

Isotopic ratio/ element	Sediment				Basalt			
	n	$(\chi)_A$	$\pm\,\mathrm{S}_A$	$(\%\mathrm{Rsd})_A$	n	$(\chi)_B$	$\pm\,\mathrm{S}_B$	$(\%\mathrm{Rsd})_B$
$^{87}\mathrm{Sr}/^{86}\mathrm{Sr}$	9	0.70851	$\pm\,0.00041$	0.06	6	0.70324	$\pm\,0.00008$	0.011
$^{143}\mathrm{Nd}/^{144}\mathrm{Nd}$	9	0.51251	$\pm\,0.00003$	0.006	6	0.51322	$\pm\,0.00003$	0.006
$^{206}\mathrm{Pb}/^{204}\mathrm{Pb}$	2	18.74	$\pm\,0.21$	1.1	2	18.22	$\pm\,0.25$	1.4
$^{207}\mathrm{Pb}/^{204}\mathrm{Pb}$	2	15.61	$\pm\,0.05$	0.32	2	15.50	$\pm\,0.07$	0.45
$^{208}\mathrm{Pb}/^{204}\mathrm{Pb}$	2	38.50	$\pm\,0.27$	0.7	2	37.75	$\pm\,0.42$	1.1
Sr	*	204	$\pm\,2$	1.0	*	65	$\pm\,1$	1.5
Rb	*	92	$\pm\,2$	2.2	*	3.0	$\pm\,0.2$	6.7
Nd	7	26	±15	58	5	4.2	$\pm\,0.6$	13
Sm	7	5.6	$\pm\,3.3$	59	5	1.47	$\pm\,0.13$	8.8
Pb	42	105	±25	24	2	0.18	$\pm\,0.05$	28

S_A and S_B are one standard deviation values of isotopic ratio or element concentration data $(\chi)_A$ and $(\chi)_B$ respectively; $(\%\mathrm{Rsd})_A$ and $(\%\mathrm{Rsd})_B$ are the relative standard deviations in % of the components A and B respectively; n is the number of data on which the average and standard deviations are based. Sr and Rb concentration data $(n =^*)$ were obtained in sediment and altered basalt composite samples. Each of them was a physical mixture of equal weights of six samples from Site 487 (Verma 1999). Pb concentration data for sediments are summarized from Leggett (1981) and for basalt from Verma (1992).

Table 2. *Predicted isotopic ratios (with their errors or variability estimated from the error propagation theory) in mixtures of sediment and altered basalt samples from the Cocos plate, Mexico*

Ratio	M1S			M5S			M20S		
	$(\chi)_M$	$(S)_M$	$(\%\mathrm{Rsd})_M$	$(\chi)_M$	$(S)_M$	$(\%\mathrm{Rsd})_M$	$(\chi)_M$	$(S)_M$	$(\%\mathrm{Rsd})_M$
$^{87}\mathrm{Sr}/^{86}\mathrm{Sr}$	0.703402	0.000079	0.011	0.703987	0.000090	0.013	0.705557	0.000186	0.02?
$^{143}\mathrm{Nd}/^{144}\mathrm{Nd}$	0.513178	0.000028	0.006	0.513046	0.000055	0.011	0.512789	0.000095	0.01?
$^{206}\mathrm{Pb}/^{204}\mathrm{Pb}$	18.66	0.18	1.0	18.72	0.20	1.1	18.74	0.21	1.1
$^{207}\mathrm{Pb}/^{204}\mathrm{Pb}$	15.59	0.04	0.28	15.61	0.05	0.31	15.61	0.05	0.32
$^{208}\mathrm{Pb}/^{204}\mathrm{Pb}$	38.39	0.24	0.62	38.48	0.26	0.68	38.49	0.27	0.70

M1S, M5S, and M20S are mixtures of sediment and altered basalt, with respectively 1%, 5%, and 20% sediment components. $(\chi)_M$, $(S)_M$, and $(\%\mathrm{Rsd})_M$ are respectively the mean isotopic ratio, its propagated error, and relative % error.
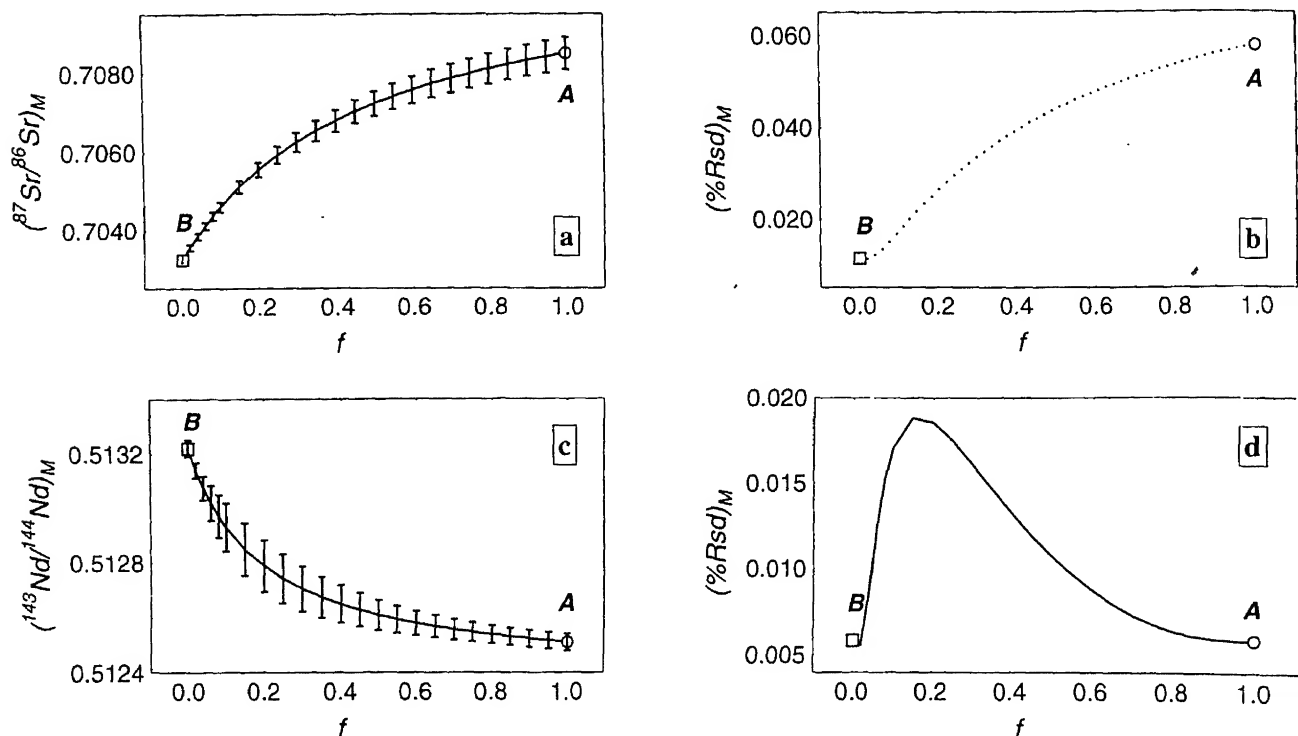

Figure 3. Isotopic compositions of Sr and Nd with propagated errors (shown as vertical error bars) as a function of f on predicted mixtures of sediment (component A) and basalt (component B), estimated on the basis of the actual data (Verma 1999) from the Cocos plate. (a) $(^{87}\mathrm{Sr}/^{86}\mathrm{Sr})_M$ vs. f (error bars are $\sigma_M^{87/86}$ for the predicted mixture); (b) $(\%\mathrm{Rsd})_M$ vs. f curve for the same data as in figure 3(a); (c) $(^{143}\mathrm{Nd}/^{144}\mathrm{Nd})_M$ vs. f (error bars are $\sigma_M^{143/144}$ for the predicted mixture); (d) $(\%\mathrm{Rsd})_M$ vs. f curve for the same data as in figure 3(c).

in error propagation equations to compute the five radiogenic isotopic compositions of the mixtures with respective propagated errors. The more important results are included in table 2.

Figure 3 (a–d) gives the isotopic compositions of Sr (figure 3a) and Nd (figure 3c) with propagated errors (figures 3b and 3d) as a function of f on predicted mixtures of sediment (component A) and basalt (component B) from the Cocos plate. The propagated error on $^{87}\mathrm{Sr}/^{86}\mathrm{Sr}$ varies almost regularly from basalt to sediment (figure 3b), whereas that for $^{143}\mathrm{Nd}/^{144}\mathrm{Nd}$ reaches a maximum for $f \sim 0.15$ (figure 3(d)).

The isotopic compositions of Pb, with propagated errors ($\sigma^{206/204}$ shown as vertical error bars) as a func-

tion of f on predicted mixtures of sediment (component A) and basalt (component B) from the Cocos plate are shown in figure 4 (a–d). Figures 4(a) and 4(b) give the $(^{206}\mathrm{Pb}/^{204}\mathrm{Pb})_M$ vs. f and $(\%\mathrm{Rsd})_M$ vs. f curves, whereas figures 4(c) and 4(d) are for $(^{207}\mathrm{Pb}/^{204}\mathrm{Pb})_M$ vs. f and $(^{208}\mathrm{Pb}/^{204}\mathrm{Pb})_M$ vs. f curves respectively. Here both end-members are highly variable, resulting in very large error bars also for the predicted mixtures.

Figure 5 presents the conventional $(^{87}\mathrm{Sr}/^{86}\mathrm{Sr})_M$–$(^{143}\mathrm{Nd}/^{144}\mathrm{Nd})_M$ diagram for predicted mixtures of sediment (component A) and basalt (component B) from the Cocos plate, but includes the respective error bars representing end-member variability. The error bars ($\sigma^{87/86}$ and $^{143/144}$)
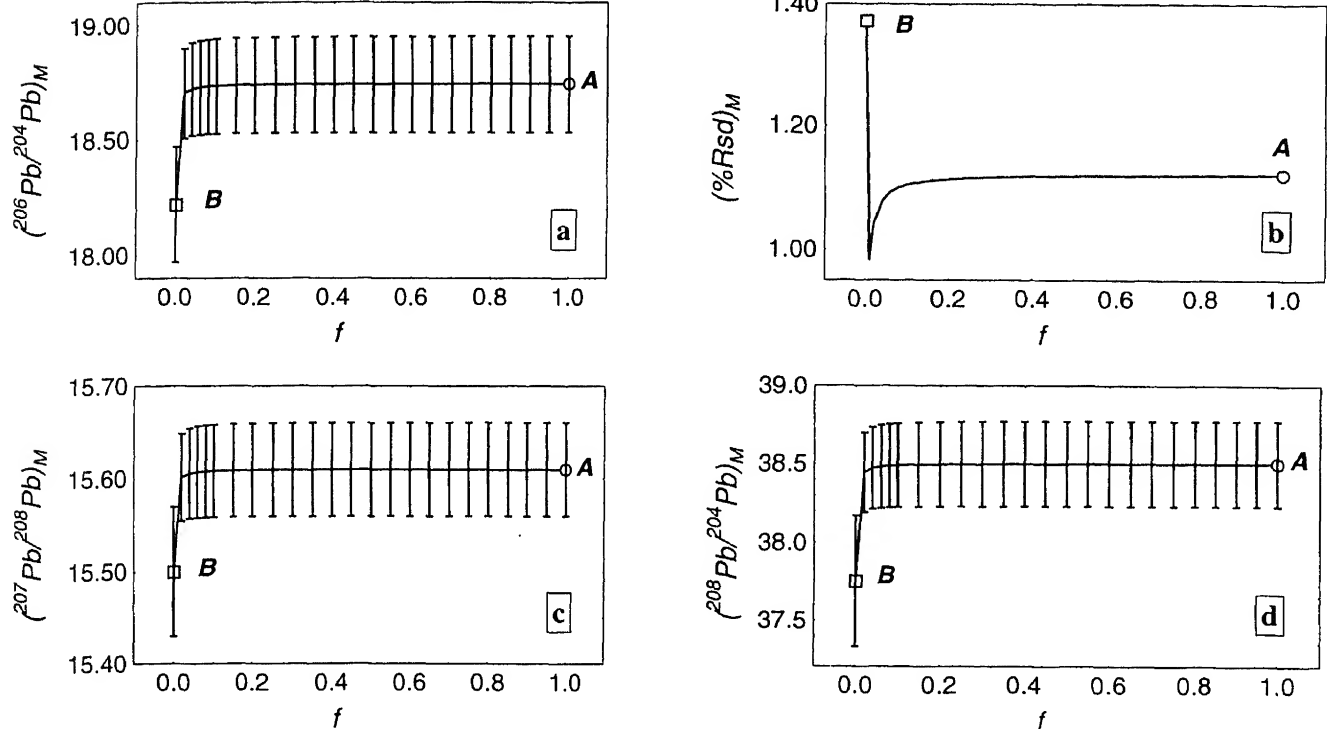
Figure 4. Isotopic compositions of Pb with propagated errors (shown as vertical error bars) as a function of f on predicted mixtures of sediment (component A) and basalt (component B) from the Cocos plate. **(a)** $(^{206}Pb/^{204}Pb)_M$ vs. f (error bars are $\sigma_M^{206/204}$ for the predicted mixture); **(b)** $(\%Rsd)_M$ vs. f curve for the same data as in figure 4(a); **(c)** $(^{207}Pb/^{204}Pb)_M$ vs. f (error bars are $\sigma_M^{207/204}$ for the predicted mixture); **(d)** $(^{208}Pb/^{204}Pb)_M$ vs. f (error bars are $\sigma_M^{208/204}$ for the predicted mixture).
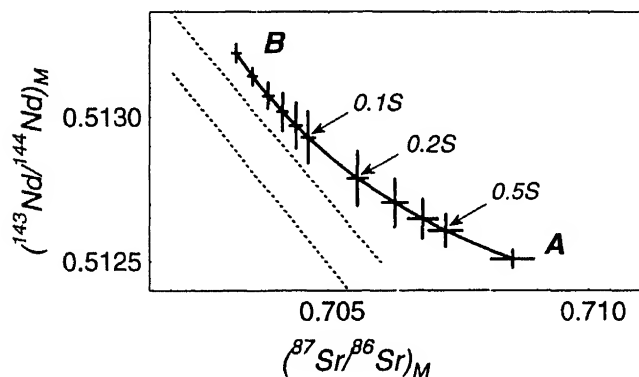

Figure 5. $(^{87}Sr/^{86}Sr)_M$ - $(^{143}Nd/^{144}Nd)_M$ diagram for predicted mixtures of sediment (component A) and basalt (component B) from the Cocos plate. The error bars are $\sigma_M^{87/86}$ and $\sigma_M^{143/144}$ for sediment fractions of 0.00 (pure basalt component), 0.02, 0.04, 0.06, 0.08, 0.10, 0.20, 0.30, 0.40, 0.50, and 1.00 (pure sediment component). An approximate trace of the "mantle array" is also included for reference (from Rollinson 1993).

sediment fractions of 0.00 (pure basalt component), 0.02, 0.04, 0.06, 0.08, 0.10 (designated 0.1S), 0.20 (designated 0.2S), 0.30, 0.40, 0.50 (designated 0.5S), and 1.00 (pure sediment component). An approximate trace of the "mantle array", included for reference (from Rollinson 1993), shows that the mixing curve for the upper part of the subducting Cocos plate lies far to the right of the most probable mantle compositions. This result has important bearing on the origin

of magmas in the central part of the Mexican Volcanic Belt, as most mafic and evolved magmas lie well within the "mantle array" (Verma *et al* 1991; Verma 1999 and unpublished data). An inescapable conclusion would be that partial melting of the subducting Cocos plate can not generate magmas of the central part of this complex volcanic province.

Some other conventional isotopic diagrams, but with error bars, for predicted mixtures of sediment (component A) and basalt (component B) from the Cocos plate are presented in figure 6 (a–d). The error bars correspond to the sediment fraction of 0.00 (pure basalt component), 0.01 (designated 0.01S), 0.02, 0.05 (designated 0.05S), 0.10, 0.50, and 1.00 (pure sediment component). Figures 6(a) to 6(d) are respectively for $(^{87}Sr/^{86}Sr)_M$-$(^{206}Pb/^{204}Pb)_M$, $(^{143}Nd/^{144}Nd)_M$-$(^{206}Pb/^{204}Pb)_M$, $(^{207}Pb/^{204}Pb)_M$-$(^{206}Pb/^{204}Pb)_M$, and $(^{208}Pb/^{204}Pb)_M$-$(^{206}Pb/^{204}Pb)_M$ mixing curves. The large error bars indicate high variability of the end-members for the Pb isotopes.

4. Conclusions

Error propagation theory is successfully applied to isotopic modeling during mixing of two components in order to predict the effects of analytical errors, or of both sampling and analytical errors. Two probable (extreme) cases identified by "Small errors" and
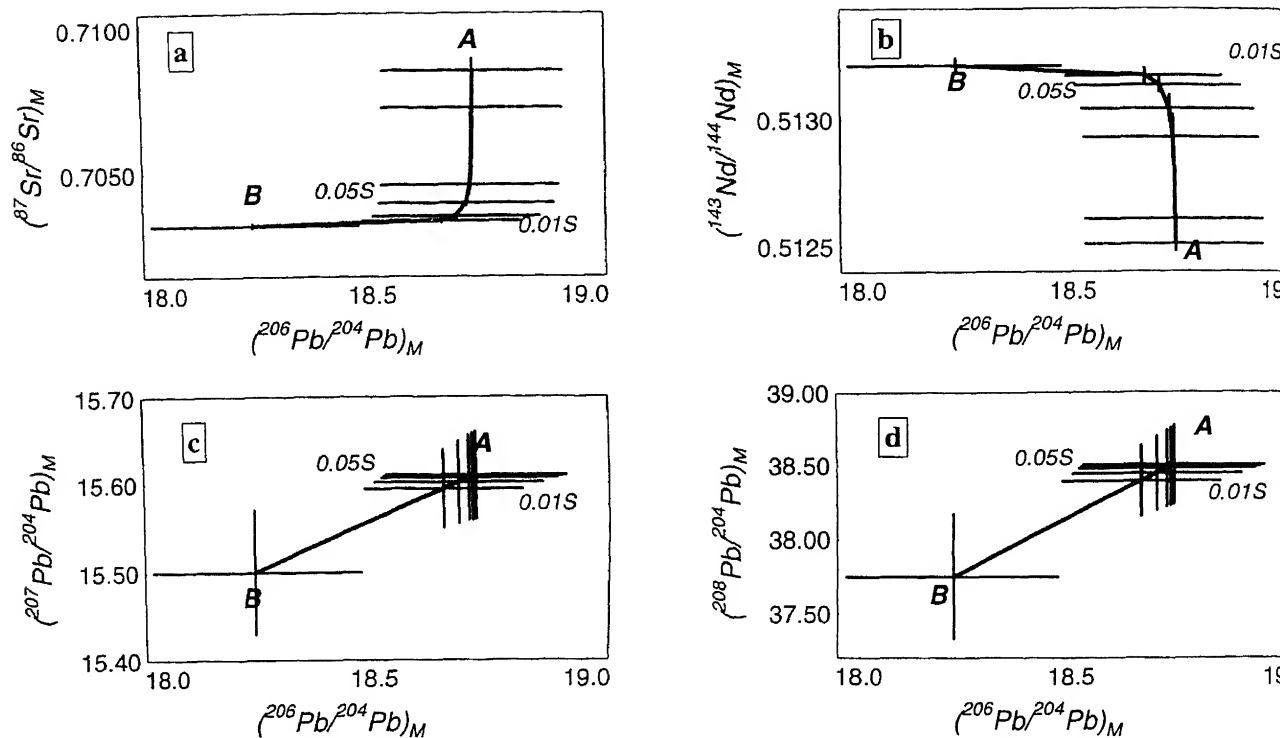
Figure 6. Isotopic diagrams with error bars for predicted mixtures of sediment (component A) and basalt (component B) from Cocos plate. The error bars correspond to the sediment fraction of 0.00 (pure basalt component), 0.01, 0.02, 0.05, 0.10, 0.50, 1.00 (pure sediment component). **(a)** $(^{87}Sr/^{86}Sr)_M$ - $(^{206}Pb/^{204}Pb)_M$ mixing curve; **(b)** $(^{143}Nd/^{144}Nd)_M$ - $(^{206}Pb/^{204}Pb)_M$ mixing curve; **(c)** $(^{207}Pb/^{204}Pb)_M$ - $(^{206}Pb/^{204}Pb)_M$ mixing curve (straight line); **(d)** $(^{208}Pb/^{204}Pb)_M$ - $(^{206}Pb/^{204}Pb)_M$ mixing curve (straight line).

"Large errors" are presented to illustrate the use of the newly derived error propagation equations for two-component mixing. The results are presented graphically to show the effect of error propagation in isotopic modeling. Actual examples of radiogenic isotope data from the Cocos plate are presented to demonstrate the usefulness of this approach in isotopic modeling of two component mixing.

Acknowledgements

References

Albarède F 1976 Some trace element relationships amongst liquid and solid phases in the course of the fractional crystallization of magmas; *Geochim. Cosmochim. Acta* 667–673.

Albarède F 1983 Inversion of batch melting equations and trace element pattern of the mantle; *J. Geophys. Res.* 10573–10583.

Albarède F 1995 *Introduction to geochemical model* (Cambridge, Cambridge University Press) 543 p.

Albarède F and Provost A 1977 Petrological and geochem mass balance: an algorithm for least-squares fitting general error analysis; *Comput. Geosci.* 3 309–326.

Allègre C J and Minster J F 1978. Quantitative models of tr element behavior in magmatic processes; *Earth Planet.* Lett. 38 1–25.

Anderson A T 1976 Magma mixing: petrological and volca logical tool; *J. Volcanol. Geotherm. Res.* 1 3–33.

Bevington P R 1969 *Data reduction and error analysis for physical sciences* (New York: McGraw Hill) 336 p.

Bryan W B, Finger L W and Chayes F 1969 Estima proportions in petrographic mixing equations by least-squ approximations; *Science* 163 926–927

Dalrymple G B and Lanphere M A 1969 *Potassium-Ar Dating* (San Francisco: Freeman) 258 p.

DePaolo D J 1981 Trace element and isotopic effects combined wallrock assimilation and fractional crystall tion; *Earth Planet. Sci. Lett.* 53 189–202

DePaolo D J 1985 Isotopic studies of processes in mafic mag chambers; *J. Petrol.* 4 925–951.

DePaolo D J and Wasserburg G J 1979 Nd isotopic variati and petrogenetic models; *Geophys. Res. Lett.* 3 249–252

Dickin A P 1995 *Radiogenic isotope geology* (Cambri Cambridge University Press) 490 p.

Faure G 1986 *Principles of isotope geology* (New York: J Wiley) 589 p.

Gast P W 1968 Trace element fractionation and the origin of tholeiitic and alkaline magma types; *Geochim. Cosmochim. Acta* **32**, 1057–1086

Gladney E S and Roelandts I 1988 1987 compilation of elemental concentration data for USGS BIR-1, DNC-1 and W-2; *Geostand. Newslett.* **12** 63–118

Govindaraju K, Potts P J, Webb P C and Watson J S 1994 1994 report on Whin Sill dolerite WS-E and Pittscurrie microgabbro PM-S from Scotland: assessment by one hundred and four international laboratories; *Geostand. Newslett.* **18** 211–300

Greenland L P 1970 An equation for trace element distribution during magmatic crystallization; *Am. Mineral.* **55** 455–465

Guedens W J, Yperman J, Mullens J, Van Poucke L C and Pauwels E J 1993a Statistical analysis of errors: a practical approach for an undergraduate Chemistry lab. Part 1. The concepts; *J. Chem. Educ.* **70** 776–779

Guedens W J, Yperman J, Mullens J, Van Poucke L C and Pauwels E J 1993b Statistical analysis of errors: a practical approach for an undergraduate Chemistry lab. Part 2. Some worked examples; *J. Chem. Educ.* **70** 776–779

Hagen H and Neumann E-R 1990 Modeling of trace element distribution in magma chambers using open-system models; *Comput. Geosci.* **16** 549–556

Hanson G N 1978 The application of trace elements to the petrogenesis of igneous rocks for granitic composition; *Earth. Planet Sci. Lett.* **38** 26–43

Hertogen J and Gijbels R 1976 Calculation of trace element fractionation during partial melting; *Geochim. Cosmochim. Acta* **40** 313–322

Imai N, Terashima S, Itoh S and Ando A 1995 1994 compilation of analytical data for minor and trace elements in seventeen GSJ geochemical reference samples, "igneous rock series"; *Geostand. Newslett.* **19** 135–213

Langmuir C H 1989 Geochemical consequences of *in situ* crystallization; *Nature* **340** 199–205

Langmuir C H, Vocke R D, Hanson G N and Hart S R 1978 A general mixing equation with applications to Icelandic basalts; *Earth Planet. Sci. Lett.* **37** 380–392

Leggett J K 1981 Geochemistry of Cocos plate pelagic-hemipelagic sediments in Hole 487, Deep Sea Drilling Project Leg 66. In: *Init. Repts. Deep Sea Drilling Project*, (eds) J S Watkins, J C Moore *et al* (Washington, D.C.: U.S. Government Printing Office) 683–686.

Le Maitre R W 1982 *Numerical petrology* (Amsterdam: Elsevier)

López Ruiz J and Cebriá Gómez J M 1990 *Geoquimica de los Procesos Magm*áticos. Madrid: Editorial Rueda 168 p.

Maaløe S 1994 Estimation of the degree of partial melting using concentration ratios; *Geochim. Cosmochim. Acta* **58** 2519–2525

McBirney A R 1984 Igneous petrology (San Francisco: Freeman)

Myers J D, Angevine C L and Frost C D 1987 Mass balance calculations with end member compositional variability: applications to petrologic problems; *Earth Planet. Sci. Lett.* **81** 212–220

Neumann H, Mead J and Vitaliano C J 1954 Trace element variations during fractional crystallization as calculated from the distribution law; *Geochim. Cosmochim. Acta* **6** 90–99

O'Hara M J and Fry N 1996a The highly compatible trace element paradox-fractional crystallization revisited; *J. Petrol.* **37** 859–890

O'Hara M J and Fry N 1996b Geochemical effects of small packet crystallization in large magma chambers – further resolution of the highly compatible element paradox; *J. Petrol.* **37** 891–925

Potts P J and Kane J S 1992 Terminology for geological reference material values: a proposal to the International Organization of Standardisation (ISO), producers and users; *Geostand. Newslett.* **16** 133–341

Powell R 1984 Inversion of the assimilation and fractional crystallisation (AFC) equations: characterization of contaminants from isotope and trace element relationships in volcanic suites; *J. Geol. Soc. London* **141** 447–452

Ragland P C 1989 *Basic analytical petrology* (New York: Oxford University Press)

Rollinson H R 1993 *Using geochemical data: evaluation, presentation, interpretation* (New York: Wiley) 352 p.

Santoyo E and Verma S P 1991 Evaluación de errores en el uso de los geotermómetros químicos para la prospección de recursos geotérmicos; *Actas Fac. Ciencias Tierra UANL Linares* **6** 5–10

Santoyo E and Verma S P 1993 Evaluación de errores en el uso de los geotermómetros de SiO_2 y Na/K para la determinación de temperaturas en sistemas geotérmicos; *Geofis. Int.* **32** 287–298.

Schilling J-G and Winchester J W 1967 Rare-earth fractionation and magmatic processes. In: *Mantles of earth and terrestrial planets*, (ed) S K Runcorn, 267–283

Shaw D M 1970 Trace element fractionation during anatexis; *Geochim. Cosmochim. Acta* **34** 237–243

Sutarno R and Steger H F 1985 Validation of accuracy by interlaboratory programme; *Talanta* **32** 1088–1091

Taylor H P Jr 1980 The effects of assimilation of country rocks by magmas on $^{18}O/^{16}O$ and $^{87}Sr/^{86}Sr$ systematics; *Earth Planet. Sci. Lett.* **47** 243–254

Taylor H P, Jr and Sheppard S M F 1986 Igneous Rocks: I. Processes of isotopic fractionation and isotope systematics. In: *Stable Isotopes in High Temperature Geological Processes Rev. Mineral*, (eds) J M Valley, H P Taylor, Jr. and J R O'Niel, **16**: 227–271

Taylor J R 1982 *An introduction to error analysis* (New York: University Science Books) 270 p.

Taylor J K 1990 *Statistical techniques for data analysis.* Chelsea, Michigan; Lewis Publishers 200 p.

Velasco F and Verma S P 1995 Aplicación de materiales de referencia en los programas de control de calidad/aseguramiento de calidad en geoquímica; *Actas INAGEQ* **1** 187–192

Velasco F and Verma S P 1998 Importance of skewness and kurtosis statistical tests for outlier detection and elimination in evaluation of geochemical reference materials; *Math. Geol.* **30** 109–128

Verma S P 1981 Mass spectrometric isotope dilution determination of K, Rb, Cs, Ba and Sr in five geochemical reference samples; *Geostand. Newslett.* **5** 129–131

Verma S P 1992 Seawater alteration effects on REE, K, Rb, Cs, Sr, U, Th, Pb and Sr-Nd-Pb isotope systematics of Mid-Ocean Ridge Basalt; *Geochem. J.*, **26** 159–177.

Verma S P 1995 Nueva metodología para la evaluación de errores en técnicas analíticas en geoquímica; *Actas INAGEQ* **1** 215–220

Verma S P 1996 Error propagation in trace element modelling of some igneous processes; *J. Conf. Abstr.* **1** 649

Verma S P 1996b Evaluation of accuracy in analytical geochemistry; *J. Conf. Abstr.* **1** 650

Verma S P 1997 Sixteen statistical tests for outlier detection and rejection in evaluation of international geochemical reference materials: example of microgabbro PM-S; *Geostand. Newslett.: J. Geostand. Geoanal.* **21** 59–75

Verma S P 1998 Improved concentration data in two international geochemical reference materials (USGS basalt BIR-1 and GSJ peridotite JP-1) by outlier rejection; *Geofis Int.* **37** 215–250

Verma S P 1999 Geochemistry of subducting Cocos plate and the origin of subduction-unrelated mafic volcanism at the volcanic front of central Mexican Volcanic Belt; *Geol. Soc.*

Am. Spec. Paper on Cenozoic Tectonics and Volcanism of Mexico **334**, Chapter 13 (in press)

Verma S P and Santoyo E 1995 New improved equations for Na/K and SiO₂ geothermometers by error propagation; *Proc. World Geotherm. Congr.* **2** 963–968

Verma S P and Santoyo E 1997 New improved equations for Na/K, Na/Li and SiO2 geothermometers by outlier detection and rejection; *J. Volcanol. Geotherm. Res.* **79** 9–23

Verma S P and Schilling J-G 1982 Galapagos Hotspot-Spreading Center system. 2. ^{87}Sr/^{86}Sr and large ion lithophile element variations (85°W-101°W); *J. Geophys. Res.* **87**, 10838–10856

Verma S P, Carrasco-Núñez G and Milán M 1991 Geology and geochemistry of Amealco caldera, Qro., Mexico; *J. Volcanol. Geotherm. Res.* **47** 105–127

Verma S P, Navarro-L I and Garcia Cacho L 1992 Major-element geochemistry and mineralogy of the Huichapan caldera, Hidalgo, Mexico; *J. South Am. Earth Sc...* 327–336

Verma S P, Orduña-Galván J L and Guevara M 1... SIPVADE: A new computer program with seven... statistical tests for outlier detection in evaluation... international geochemical reference materials and its ap... cation to Whin Sill dolerite WS-E from England and S... from Peru; *Geostand. Newslett.: J. Geostand. Geoanal...* 209–234

Walker F W, Kiroac G J and Rourke F M 1977 *Chart o... Nuclides*. Twelfth edition, General Electric, 52 p.

Wilson M 1989 *Igneous petrogenesis. A global tect... approach*, London: Harper Collins

Wright T L and P C Doherty 1970 A linear programming... least squares computer method for solving petrologic mi... problems; *Geol. Soc. Am. Bull.* **81** 1995–2008

Isotopic composition of xenon in petroleum from the Shell Bullwinkle Field

J Nuzzo*, M Hyman and M W Rowe**

Department of Chemistry, Texas A&M University, College Station, TX 77843.
* Present address: Barrens Consulting Co., 273 Pepe's Farm Road, Milford, CT 06470.
**email: MWRowe@tamu.edu

M N Rao‡ and R L Palma

Department of Physics, Sam Houston State University, Huntsville, TX 77341.
‡Present address: SN4, NASA-JSC, Houston, TX 77858.

J Westrich

Shell Development Corporation, P.O. Box 481, Houston, Texas 77001.

We have measured the abundance and isotopic composition of xenon in petroleum samples from the Shell Bullwinkle Field off the coast of Louisiana. We used an oxidation and purification procedure designed to insure complete extraction and clean up of xenon from the petroleum.

The xenon isotopic composition was found to be similar to the atmospheric value for one petroleum sample. While the results of the second sample suggest possible enrichment of the heavier isotopes, the errors associated with these excesses preclude a definitive statement to that effect. No monoisotopic enrichment in ^{129}Xe was detected in either sample, the presence of which might have allowed us to deduce the petroleum age. Our results represent only the second xenon measurement from petroleum, and the concentrations are within the range of values published in the earlier report.

1. Introduction

Noble gas isotopes as conservative tracers are increasingly applied to a variety of terrestrial systems. Elemental abundances and isotopic compositions of noble gases have been determined in natural gas (Zartman *et al* 1961; Hennecke and Manuel 1975; Murthy 1992; Hiyagon and Kennedy 1992; Xu *et al* 1995), and in ground water and geothermal systems (Mazor *et al* 1983; Andrews *et al* 1985; Torgerson and Clark 1985; Tolstikhin *et al* 1996). Rare gases have been used to characterize the degree of interaction between natural gas, hydrocarbon assemblages and associated ground water and to quantify the contribu-

tion of mantle- and crustal-derived rare gases to hydrocarbon accumulation (Ballentine *et al* 1991, 1996; Elliot *et al* 1993).

Bosch and Mazor (1988) used noble gas measurements in natural gas samples to test a proposed model for equilibrium distribution of atmospheric noble gases between natural gas associated with water and oil and between natural gas associated with water alone. They found that for both cases (association with and without oil), relative abundances of the heavier noble gases, Kr, and especially Xe, were enriched compared to atmosphere by factors ranging from two to ten. Enrichment was greatest for natural gas samples associated with petroleum. The enrichment of the

Keywords. Xenon; petroleum; isotopic composition; mass spectrometry.

heavier noble gases is believed to be due to the initial enrichment of these gases in the aqueous phase and (or) petroleum, followed by desorption to natural gas. By fitting their results and other published data to their model, they concluded that atmospheric noble gases found in natural gases were initially contained in an air-saturated water phase and subsequently distributed between this water phase and the natural gas phase. Kharaka and Specht (1988) showed that under reservoir conditions, solubilities of noble gases in petroleum are higher than in subsurface waters by factors ranging from 2 to 300, with the solubility enrichment factor being greatest for the heavier noble gases.

While the utility of noble gas measurements in ground waters and natural gas samples has been well established, it is only recently that detailed noble gas measurements were reported from petroleum (Pinti and Marty 1995; Ballentine *et al* 1996). Ballentine *et al* (1996) in their comprehensive study of noble gas isotope systematics in a liquid hydrocarbon reservoir (using He, Ne and Ar) showed that noble gas partitioning between gas, water and oil phases is a function of solubility, phase volume and temperature in this system and for calculating the noble gas inventory of an oil reservoir, carefully determined values for these parameters need to be used. Pinti and Marty (1995) carried out similar studies of oil reservoirs using He, Ne, Ar, Kr and Xe isotopes. In their method the petroleum sample is drained into an evacuated ($\sim 10^{-10}$ torr) extraction vessel where it is magnetically stirred, and a small gas fraction isolated, cleaned and subsequently analyzed in a noble gas mass spectrometer. In contrast, we designed and built an off-line system to extract xenon by complete oxidation of petroleum. This was to ensure purification of the evolved gases, eliminating possible contamination of the noble gas mass spectrometer. The purpose of our study is to explore the feasibility of detecting ^{129}Xe excesses in petroleum due to decay of cosmogenic ^{129}I produced in the atmosphere, thereby providing under favorable conditions a potential geochronological technique for estimating ages of petroleum reservoirs.

2. Analytical procedures

Two petroleum samples from their offshore Bullwinkle Field, Louisiana, were provided by the Shell Exploration and Production Technology Corporation, Houston, Texas: NG-G-548A from well A-2, and NG-G-550A from well A-32. The location of A-2 is 27.88311°N, 90.90153°W, with production depth interval 13,657–13,704 feet; and A-32 is at 27.88293°N, 90.90155°W, with production depth interval 12,858–12,970 feet. This field consists of approximately 40–50% bacterial gas with the remainder of the gas and

oil derived from a Middle Cretaceous rock dated at about 100×10^6 years. Samples were taken directly from the head of a gas-liquid separator into high pressure stainless steel containers by Shell Exploration and Production Technology personnel. The filled cylinders contained a mixture of petroleum, natural gas, and a small amount of water.

To minimize exposure of the petroleum samples to the atmosphere, several precautions were taken during retrieval of petroleum from the high pressure stainless steel cylinder. A stainless steel collection finger was connected directly to the closed cylinder valve, the collection finger was evacuated and then filled with natural gas from the cylinder. This process was repeated several times to further purge the collection finger of any atmospheric component initially present in the finger. Petroleum was then allowed to drain under gravity into the collection finger.

With the collection finger closed to the cylinder, excess pressure within the collection finger was vented under a nitrogen atmosphere. While still under nitrogen atmosphere, the collection finger was removed from the cylinder and the petroleum was quickly transferred to 1 ml glass vials. The vials were filled completely so there were no gas pockets present when sealed with a gas-tight Teflon-lined screw cap. The samples were wrapped with parafilm and stored in a freezer until their analysis. Storage time was kept below 48 hours.

Xenon was extracted by completely oxidizing the petroleum sample in an off-line ultra-high-vacuum system shown schematically in figure 1. This allowed xenon to be extracted and purified before introduction into the mass spectrometer for analysis. A stainless steel reaction chamber (45 cm long with an inner diameter of 3.8 cm and tapered at both ends) was constructed for oxidizing petroleum. It was loosely packed with quartz wool to enhance oxidation by providing more surface area and/or by impeding the escape of volatile organic fractions from the reaction tube before they were completely oxidized.

Petroleum was deposited at the end of the reaction chamber with a glass insertion tube (8 cm long with an inner diameter of 3 mm) fitted with a gas-tight Teflon plunger. To minimize exposure to the atmosphere, petroleum was transferred from the storage vial to the insertion tube under a nitrogen atmosphere. The filled insertion tube was quickly weighed under nitrogen atmosphere, then reweighed after the petroleum was transferred, yielding the weight of the petroleum transferred into the extraction system.

While the petroleum was being introduced, the reaction chamber was isolated from the remainder of the system. Ultra-high-purity (99.999%) oxygen was flowed into the chamber, producing a pressure slightly greater than one atmosphere. With this positive oxygen pressure maintained, a blank flange at the end of the reaction chamber was removed and the
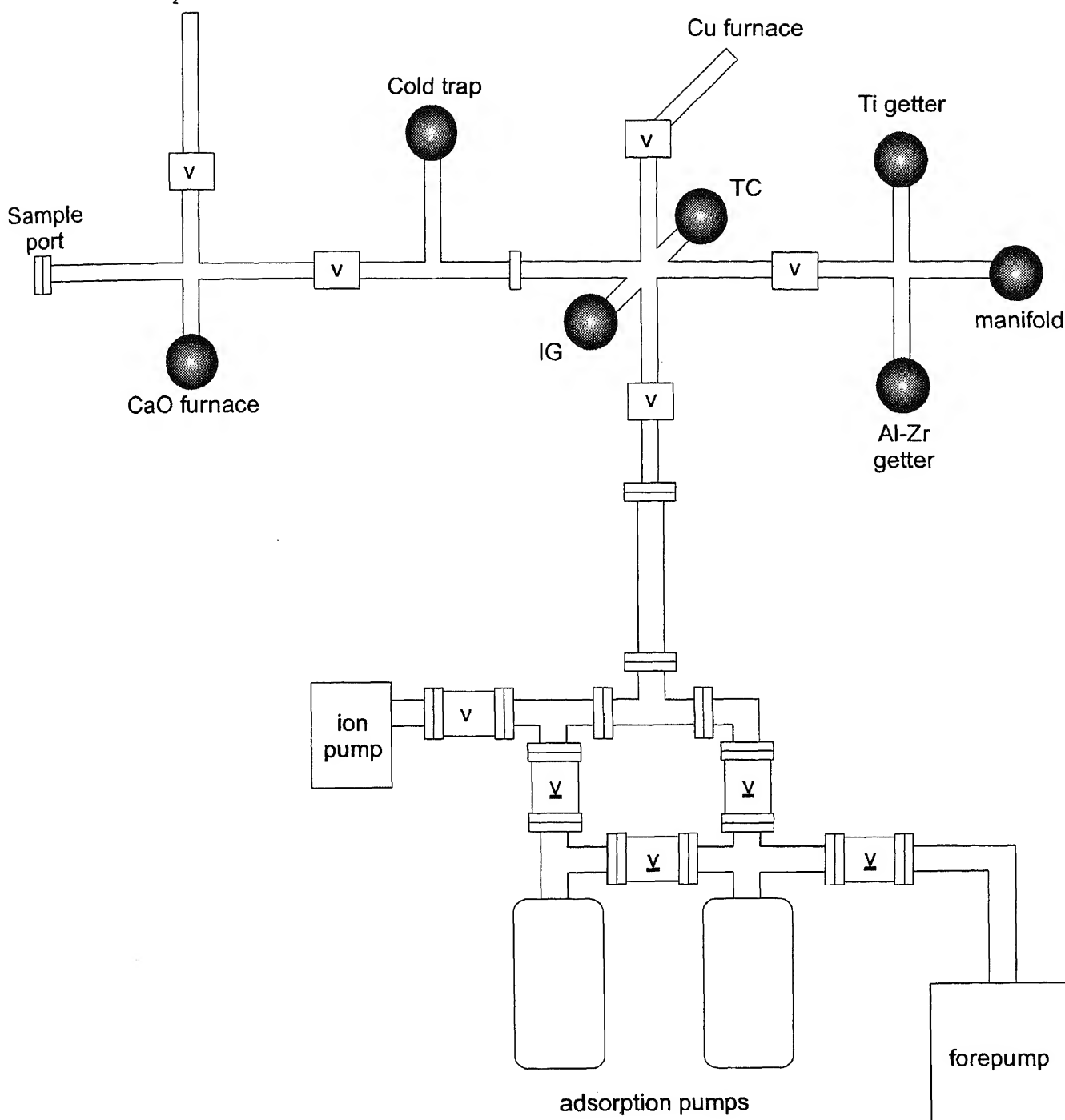
Figure 1. Schematic diagram of the noble gas extraction system. The abbreviations TC and IG represent the thermocouple and ion gauge, respectively. All-metal bakeable valves are designated with v. Non-bakeable valves are abbreviated with v̲. Other components are labeled on the diagram.

tube containing the petroleum sample inserted. Once the sample was deposited and the tube removed, the blank flange was replaced. The entire insertion and transfer took approximately 25 seconds.

With the sample deposited at the end of the reaction chamber, and an oxygen pressure of ~1000 torr, the entire reaction column was heated in stages using two independent resistance heaters. In stage one, the half of the reaction tube opposite the sample introduction end was heated to 800°C. Once this section of the reaction tube reached temperature, the other half of the reaction tube was heated to 800°C. We earlier determined that oxidizing the petroleum in just one heating stage caused the petroleum components

to volatilize during heating, only to deposit on cooler surfaces of the system, leaving behind an oily film. In the two-stage heating procedure, volatile components released during heating of the petroleum are oxidized upon entering the hotter zone of the second heater. Xenon extraction was found to be nearly complete as the third step yielded only small amounts of xenon.

Three clean-up stages were employed to separate xenon from copious amounts of unwanted gases, primarily CO_2 and H_2O, as well as possible hydrocarbons. In the first stage of the clean-up, the bulk CO_2 and H_2O formed from the oxidation of the petroleum was removed with a CaO getter, and unreacted O_2 was removed using a Cu getter. In the second stage of the clean-up, both a bulk Ti/Zr getter and a Zr/Al (SORBAC) getter were used to remove any reactive gases remaining from the first stage of the clean-up. The third stage of the clean-up involved preferential adsorption of xenon onto activated charcoal cooled by $CHCl_3$ and liquid nitrogen slurry ($-66°C$) while pumping off unadsorbed gases. The second and third stages of the clean-up were repeated alternately for several cycles to further clean the xenon.

The purified xenon samples were removed from the extraction system by collection onto an activated charcoal finger cooled to $-66°C$; at this temperature only xenon was completely adsorbed. The collection finger was sealed and subsequently attached to the mass spectrometer system. When the sample gas was released from the cold finger for analysis, the evolved gas was further cleaned in the mass spectrometer sample line by bulk Ti/Zr and Zr/Al getters. A Nuclide, 15 cm radius, 60° magnetic sector, noble gas mass spectrometer operated in the static mode was employed for elemental and isotopic analysis (Reynolds 1956).

3. Results

Procedural blanks were measured to determine the background level of xenon. All conditions were the same as for the later petroleum processing with the exception that no petroleum was added to the system. Signal intensities of ^{132}Xe for a procedural blank and the two petroleum samples, NG-G-548A (and its duplicate, NG-G-548A-1) and NG-G-550A, are given

Table 1. ^{132}Xe and total xenon concentrations. Uncertainties in all values are < 10%.

Sample	^{132}Xe $(10^{-10}\,cm^3\,STP)$	Xenon $(10^{-8}\,cm^3$ STP/g petroleum)
NG-G-548A	4.05	3.35
NG-G-548A-1	5.90	2.93
NG-G-550A	5.38	2.67
Procedural blank	0.052	

in table 1. The procedural blank xenon intensity was approximately two orders of magnitude lower than the petroleum samples. While the xenon concentrations listed in table 1 do not take into consideration possible xenon losses and additions prior to sampling, the values fall within the range of xenon from petroleum measured by Pinty and Marty (1995) of 1.7 to $18.5 \times 10^{-8}\,cm^3$ STP/g. As petroleum is a heterogeneous liquid comprised of oil, brine and gas, it is necessary to know the gas/water and oil/water ratios for a given sample. Unfortunately, these data were not available to us from the supplier of the petroleum samples.

The blank and mass discrimination corrected xenon isotopic compositions for the petroleum samples are given in table 2. For comparison, average values of an air xenon spike, measured on four separate occasions, are also given in this table. The only other isotopic compositions measured for xenon from petroleum are reported by Pinti and Marty (1995), as being "identical to those of air."

4. Discussion

The measured ^{129}Xe contents here are essentially mixtures of atmospheric plus fissiogenic and cosmogenic components and under favorable conditions, atmospheric (^{130}Xe or ^{132}Xe based) and fissiogenic (^{136}Xe based) contributions can be subtracted to yield, the content of the cosmogenic component. However large errors associated with the resultant values are unavoidable because of cumulative subtraction procedure. Several points can be made from the isotopic compositions listed in table 2. The isotopic compositions of sample NG-G-548A and its duplicate, NG-G-548A-1, are indistinguishable from one another and the air xenon spikes within experimental uncertainty. However, for sample NG-G-550A, light isotopic ratios $^{124-130}$Xe/^{132}Xe fall distinctly below those measured for air xenon, suggesting a heavy isotope-rich component in this sample. The two lightest, low abundance isotopes, ^{124}Xe and ^{126}Xe, are found in lower concentrations than those determined in the blank. Although caution must be employed because of somewhat larger uncertainties in isotopic ratios for sample NG-G-550A, we examined the possibility of heavy xenon isotopic excesses by renormalizing all data for this sample to ^{130}Xe, which is a fission shielded isotope and thus useful for this purpose. These ^{130}Xe normalized isotopic ratios were subtracted from air xenon values, and the resulting excesses compared to the compositions resulting from ^{238}U spontaneous fission and ^{238}U and ^{235}U neutron-induced fission (Ragettli $et\ al$ 1994) by plotting $\Delta_i\Delta_{136}$, where $\Delta_i = (^iXe/^{130}Xe)_{sample} - (^iXe/^{130}Xe)_{air}$ and i is a mass number of xenon (figure 2). Error propagation introduces large uncertainties when subtracting data of similar values,

Table 2. *Xenon isotopic compositions.*

Sample NG-G-	$\frac{^{124}Xe}{^{132}Xe}$	$\frac{^{126}Xe}{^{132}Xe}$	$\frac{^{128}Xe}{^{132}Xe}$	$\frac{^{129}Xe}{^{132}Xe}$	$\frac{^{130}Xe}{^{132}Xe}$	$\frac{^{131}Xe}{^{132}Xe}$	$\frac{^{134}Xe}{^{132}Xe}$	$\frac{^{136}Xe}{^{132}Xe}$
548A	0.0031 ±0.0008	0.0029 ±0.0008	0.0721 ±0.0009	0.9905 ±0.0079	0.1512 ±0.0012	0.7916 ±0.0054	0.3908 ±0.0018	0.3273 ±0.0021
548A-1	0.0035 ±0.0002	0.0033 ±0.0002	0.0712 ±0.0006	0.9806 ±0.0059	0.1510 ±0.0011	0.7891 ±0.0049	0.3930 ±0.0024	0.3342 ±0.0019
550A	*	*	0.0676 ±0.0059	0.974 ±0.014	0.1471 ±0.0054	0.7886 ±0.0078	0.3907 ±0.0048	0.3329 ±0.0060
Air spike	0.0035 ±0.0003	0.0033 ±0.0003	0.0713 ±0.0017	0.9842 ±0.0064	0.1523 ±0.0008	0.7884 ±0.0059	0.3899 ±0.0024	0.3318 ±0.0026

*Below blank levels.

which is commonly encountered in xenon data analyses.

In figure 2, if $\Delta_{134}/\Delta_{136}$ for sample NG-G-550A is considered to represent fission xenon extracted from this sample, there is a suggestion of a ^{235}U and ^{238}U neutron-induced fission component, although the uncertainties associated with these data do not rule out a ^{238}U spontaneous fission contribution. However, measured excesses at ^{131}Xe and ^{132}Xe are greater than expected from any fission component, indicating possible contributions from $^{130}Te(n,\gamma)^{131}Xe$, ^{130}Ba $(n,\gamma)^{131}Xe$ and $^{133}Cs(n,2n)^{132}Xe$ reactions in the subsurface rock environment through which th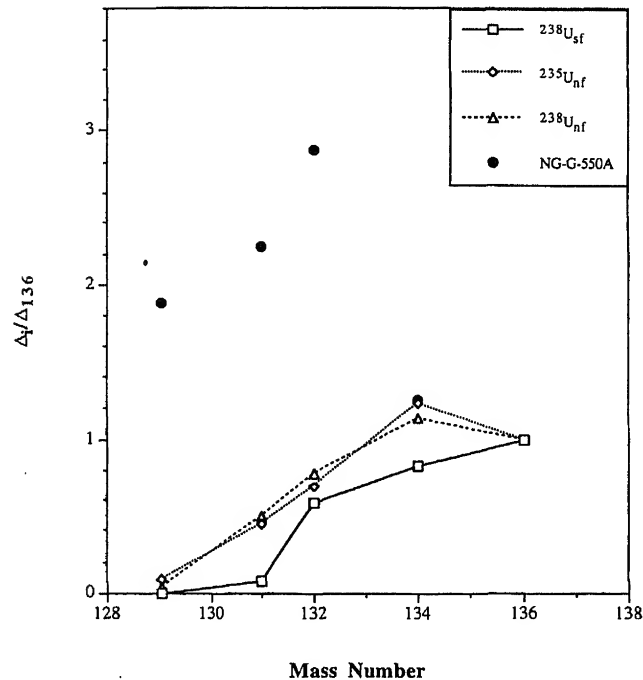e petroleum migrated over the last several million years. In particular, the large $\Delta_{129}/\Delta_{136}$ suggests the possibility of neutron induced reactions, since a ^{129}Xe excess could be produced from $^{128}Te(n,\gamma)^{129}Xe$ and ^{130}Te $(n,2n)^{129}Xe$. Even though tellurium is not a common element in the earth's crust, its role in ^{129}Xe subsurface production is found to be important (Bennett and Manuel 1970; Murthy 1992). Thermal and epithermal/fast neutrons are produced in nature from ^{238}U fission. The n,γ reactions on ^{128}Te and ^{130}Te result in $^{129}Xe/^{131}Xe$ production ratios of 0.7 for thermal neutrons and 4.0 for epithermal neutrons (Brown and Berman 1973; Murthy 1992). The observed $^{129}Xe/^{131}Xe$ excess of 0.8 for petroleum sample NG-G-550A is consistent within our experimental uncertainties with the value of 0.7 for thermal neutrons. If this explanation is correct, it may be difficult to resolve any excess ^{129}Xe from decay of radioactive ^{129}I from neutron-produced ^{129}Xe. When xenon isotopic data with smaller uncertainties are obtained, it will be possible to estimate the neutron-induced contributions to $^{129-132}Xe$ from average abundances of Te, Ba and Cs in subsurface rocks associated with petroleum.

Differences in xenon concentrations observed between the two petroleum samples may be indicative of a varying degree of interaction with either the atmosphere and/or atmospheric sources of xenon, such as air-saturated ground waters. The smaller deviation from atmospheric isotopic ratios for samples NG-G-548A and 548A-1, compared to NG-G-550A, would suggest a greater interaction with one of these sources, and would be consistent with the concentrations of xenon found in these samples (table 1).

Figure 2. Petroleum sample NG-G-550A shows an enrichment in ^{129}Xe, ^{131}Xe and ^{132}Xe relative to the ^{238}U spontaneous fission composition ($^{238}U_{sf}$), the ^{235}U neutron-induced fission composition ($^{235}U_{nf}$) and the ^{238}U neutron-induced fission composition ($^{238}U_{nf}$). Error bars are omitted for figure clarity, and $\Delta_i = (^iXe/^{130}Xe)_{sample} - (^iXe/^{130}Xe)_{air}$. [$\Delta_{129} = 0.15$ (±0.26); $\Delta_{131} = 0.18$ (±0.20); $\Delta_{132} = 0.23$ (±0.25); $\Delta_{134} = 0.10$ (±0.10); $\Delta_{136} = 0.08$ (±0.09)].

5. Conclusions

A xenon gas extraction and purification system was constructed and utilized to isolate the xenon from two petroleum samples. Xenon compositions were subsequently determined by high sensitivity noble gas mass spectrometry. For sample NG-G-548A and its duplicate NG-G-548A-1, the isotopic composition is indistinguishable from that of the atmosphere, as was found

for the only other measurements of xenon extracted from petroleum (Pinti and Marty 1995). However, in sample NG-G-550A, the isotopic composition of the heavy xenon isotopes, $^{129-134}$Xe, showed tentative evidence of enrichment compared to atmospheric ratios. Nuclear processes which might have contributed to this putative heavy isotope enriched component cannot be firmly established given the uncertainties in the data. In neither sample was there evidence of a monoisotopic enrichment of ^{129}Xe, relative to the atmospheric value, from the decay of ^{129}I. However, the subtle suggestion of a heavy xenon isotope enrichment in sample NG-G-550A leaves the possibility open that future work on additional samples may yield definitive isotopic anomalies which may allow a geochronological dating technique for petroleum to be established.

Acknowledgements

List of Symbols

1. $\Delta_i = (^{i}\mathrm{Xe}/^{130}\mathrm{Xe})_{\mathrm{sample}} - (^{i}\mathrm{Xe}/^{130}\mathrm{Xe})_{\mathrm{air}}$ and i is a mass number of xenon.
2. n is the symbol for neutron.
3. γ is the symbol for gamma ray emission.
4. $^{130}\mathrm{Te}(n, \gamma)^{131}\mathrm{Xe}$ represents the nuclear reaction in which ^{130}Te captures a neutron and emits a gamma ray, producing ^{131}Xe.
5. $^{130}\mathrm{Ba}(n, \gamma)^{131}\mathrm{Xe}$ represents the nuclear reaction in which ^{130}Ba captures a neutron and emits a gamma ray, producing ^{131}Xe.
6. $^{133}\mathrm{Cs}(n, 2n)^{132}\mathrm{Xe}$ represents the nuclear reaction in which ^{133}Cs captures one neutron and emits two neutrons, producing ^{132}Xe.
7. $^{128}\mathrm{Te}(n, \gamma)^{129}\mathrm{Xe}$ represents the nuclear reaction in which ^{128}Te captures a neutron and emits a gamma ray, producing ^{129}Xe.
8. $^{130}\mathrm{Te}(n, 2n)^{129}\mathrm{Xe}$ represents the nuclear reaction in which ^{130}Te captures one neutron and emits two neutrons, producing ^{129}Xe.

References

Andrews J N, Goldbrunner J E, Darling W G, Hooker P J, Wilson G B, Youngman M J, Eichinger L, Rauert W and Stichler W 1985 A radiochemical, hydrochemical and dissolved gas study of groundwaters in the Molasse basin of Upper Austria; Earth Planet. Sci. Lett. 73 317–332

Ballentine C J, O'Nions R K, Oxburgh E R, Horvath F and Deak J 1991 Rare gas constraints on hydrocarbon accumulation, crustal degassing and groundwater flow in the Pannonian Basin; Earth Planet. Sci. Lett. 105 229–246

Ballentine C J, O'Nions R K and Coleman M L 1996 A magnus opus: helium, neon and argon isotopes in a North Sea oilfield; Geochim Cosmochim Acta 60 831–849

Bennett G A and Manuel O K 1970 Xenon in natural gases; Geochim. Cosmochim. Acta. 34 593–610

Bosch A and Mazor E 1988 Natural gas association with water and oil as depicted by atmospheric noble gases: case studies from the southeastern Mediterranean Coastal Plain; Earth Planet. Sci. Lett. 87 338–346

Browne J C and Berman B L 1973 Neutron capture cross-sections for ^{128}Te and ^{130}Te and the xenon anomaly in old tellurium ores; Phys. Rev. C 8 2405–2411

Elliot T, Ballentine C J, O'Nions R K and Ricchiuto T 1993 Carbon, helium, neon and argon isotopes in a Po Basin natural gas field; Chem. Geol. 106 429–440

Hennecke E W and Manuel O K 1975 Noble gases in CO$_2$ well gas, Harding County, New Mexico; Earth Planet. Sci. Lett. 27 346–355

Hiyagon H and Kennedy B M 1992 Noble gases in CH$_4$-rich gas fields, Alberta, Canada; Geochim. Cosmochim. Acta 56 1569–1589

Kharaka Y K and Specht D J 1988 The solubility of noble gases in crude oil at 25–100°C; Appl. Geochem. 3 137–144

Mazor E, Van Everdingen R D and Krouse H R 1983 Noble-gas evidence for geothermal activity in a karstic terrain: Rocky Mountains, Canada; Geochim. Cosmochim. Acta 36 1111–1115

Murthy S V S 1992 Noble gases and nitrogen in natural gases from Gujarat, India; Chem. Geol. 94 229–240

Pinti D L and Marty B 1995 Noble gases in crude oils from the Paris Basis, France: Implications for the origin of fluids and constraints on oil-water-gas interactions; Geochim. Cosmochim. Acta 59 3389–3404

Ragettli R A, Hebeda E H, Signer P and Wieler R 1994 Uranium-xenon chronology: Precise determination of λ_{sf}, $^{136}y_{\mathrm{sf}}$ for spontaneous fission of ^{238}U; Earth Planet. Sci. Lett. 128 653–670

Reynolds J H 1956 High sensitivity mass spectrometer for noble gas analysis; Rev. Sci. Instrum. 69 928–934

Tolstikhin I, Lehmann B E, Loosli H H and Gautschi A 1996 Helium and argon isotopes in rocks, minerals and related groundwaters: A case study in northern Switzerland; Geochim. Cosmochim. Acta 60 1497–1514

Torgersen T and Clarke W B 1985 Helium accumulations in groundwater, I: An evaluation of sources and the continental flux of crustal ^{4}He in the Great Artesian Basin, Australia; Geochim. Cosmochim. Acta 49 1211–1218

Xu S, Nakai S, Wakita H and Wang X 1995 Mantle-derived noble gases in natural gases from Songliao Basin, China; Geochim. Cosmochim. Acta 59 4675–4683

Zartman R E, Wasserburg G J and Reynolds J H 1961 Helium, argon and carbon in some natural gases; J. Geophys. Res. 66, 277–306

Factors controlling the groundwater transport of U, Th, Ra, and Rn

A Tricca, D Porcelli and G J Wasserburg

The Lunatic Asylum of the Charles Arms Laboratory, Division of Geological and Planetary Sciences, California Institute of Technology, Pasadena, CA 91125 USA
email: tricca@gps.caltech.edu

A model for the groundwater transport of naturally occurring U, Th, Ra, and Rn nuclides in the ^{238}U and ^{232}Th decay series is discussed. The model developed here takes into account transport by advection and the physico-chemical processes of weathering, decay, α-recoil, and sorption at the water-rock interface. It describes the evolution along a flowline of the activities of the ^{238}U and ^{232}Th decay series nuclides in groundwater. Simple sets of relationships governing the activities of the various species in solution are derived, and these can be used both to calculate effective retardation factors and to interpret groundwater data. For the activities of each nuclide, a general solution to the transport equation has been obtained, which shows that the activities reach a constant value after a distance $\bar{x}_i$, characteristic of each nuclide. Where $\bar{x}_i$ is much longer than the aquifer length, (for ^{238}U, ^{234}U, and ^{232}Th), the activities grow linearly with distance. Where $\bar{x}_i$ is short compared to the aquifer length, (for ^{234}Th, ^{230}Th, ^{228}Th, ^{228}Ra, and ^{224}Ra), the activities rapidly reach a constant or quasi-constant activity value. For ^{226}Ra and ^{222}Rn, the limiting activity is reached after 1 km.

High δ^{234}U values (proportional to the ratio $\varepsilon_{234\mathrm{Th}}/w_{238\mathrm{U}}$) can be obtained through high recoil fraction and/or low weathering rates. The activity ratios ^{230}Th/^{232}Th, ^{228}Ra/^{226}Ra and ^{224}Ra/^{226}Ra have been considered in the cases where either weathering or recoil is the predominant process of input from the mineral grain. Typical values for weathering rates and recoil fractions for a sandy aquifer indicate that recoil is the dominant process for Th isotopic ratios in the water. Measured data for Ra isotope activity ratios indicate that recoil is the process generally controlling the Ra isotopic composition in water. Higher isotopic ratios can be explained by different desorption kinetics of Ra. However, the model does not provide an explanation for ^{228}Ra/^{226}Ra and ^{224}Ra/^{226}Ra activity ratios less than unity.

From the model, the highest ^{222}Rn emanation equals 2ε. This is in agreement with the hypothesis that ^{222}Rn activity can be used as a first approximation for input by recoil (Krishnaswami *et al* 1982). However, high ^{222}Rn emanation cannot be explained by production from the surface layer as formulated in the model. Other possibilities involve models including surface precipitation, where the surface layer is not in steady-state.

1. Introduction

Numerous studies have been conducted on the groundwater transport of trace elements in order to predict the impact of anthropogenic contaminants (e.g. Allen *et al* 1993; Zheng and Bennett 1995). Naturally occurring U, Th, and Ra isotopes can serve as analogues for radioactive pollutants (e.g. Ivanovich *et al* 1992; Dozol *et al* 1993). These isotopes have a wide range of half-lives, and their inter-relationships in the ^{238}U and ^{232}Th decay series can be used to constrain groundwater supply and removal rates over different time-scales. Examples of pronounced U series disequilibrium have been found in groundwaters, clearly showing that in open systems such as natural aquifers, water-rock interactions can induce

significant elemental and isotopic fractionations (see e.g. Hubbard *et al* 1984; Andrews *et al* 1989, Banner *et al* 1990; Osmond and Cowart 1992; Bonotto and Andrews 1993). Although the thermodynamic properties of actinides and their daughter products are reasonably well known (see Langmuir 1997), data acquired under simple and well-constrained laboratory conditions are difficult to apply to more complex natural systems (e.g. Coles and Ramspott 1982), and interpretations of field data using theoretical models of U/Th series nuclide groundwater transport are limited (see review by Ku *et al* 1992). Andrews *et al* (1982, 1989) considered physico-chemical mechanisms for radionuclide supply and removal, but not advective transport, and calculated the time-scale of water-rock interaction. In an important contribution, Krishnaswami *et al* (1982) calculated sorption reaction rate constants and residence times of daughter nuclides by deducing recoil inputs from ^{222}Rn activities, although without considering the effects of dissolution, precipitation or advective transport. Davidson and Dickson (1986) included dispersive flow in a model of the transport of U and Ra isotopes, but did not consider dissolution and precipitation.

A model for the combined groundwater transport of naturally occurring U, Th, Ra, and Rn nuclides in the ^{238}U and ^{232}Th decay series is discussed here that takes into account transport by advection as well as the physico-chemical processes of weathering, decay, α-recoil, and sorption at the water-rock interface. General transport equations for the nuclides are used to obtain analytical solutions for groundwater concentrations along a flowline. Simple sets of relationships governing the activities of the various species in solution are derived, and these can be used both to calculate effective retardation factors and to interpret groundwater data. Comparison of the model and aquifer data provide quantitative values for geochemical parameters in a natural aquifer such as weathering rates, distribution constants between the solid and the aqueous phases, and sorption kinetics. The model can also be used as a benchmark for determining whether the distributions of naturally occurring nuclides are consistent with the simple retardation models for point-source anthropogenic nuclides that are typically employed. A complete discussion of the model will be provided elsewhere as well as application of the model to interpreting data from an confined sandy aquifer (Tricca, Porcelli, Baskaran, Wasserburg, submitted).

2. Radionuclide groundwater transport model

2.1 *Model development*

The one-dimensional groundwater model discussed considers three phases: groundwater with a constant linear velocity v; the rock comprised of large grains typical of the aquifer mineralogy and of small minor phases enriched in radioactive elements; and a surface layer that coats some fraction of the grains and where physico-chemical reactions take place (figure 1). The rock has a porosity n. The surface layer is characterized by a specific surface area S (area per unit volume of rock) and has a thickness ξ. All parameters used in the model are listed in table 1. The model aquifer is in steady state; i.e., the concentrations of species in solution, in the rock, and in the surface layer do not vary with time at any given location. Flow through an aquifer that has changes in physical parameters can be simply solved for the steady state case by using the values from one segment as the initial boundary conditions for the next segment.

The model considers transport of radionuclides by advection along a flowline; diffusive transport and hydrodynamic dispersion are not considered. The distance along the flowline is x, where $x = 0$ at the water table. The supply of each radionuclide to the groundwater occurs by weathering from primary phases with a nuclide-specific weathering rate w_i, desorption from the surface layer, and recoil from decay of parent nuclides within both aquifer mineral grains and the surface coating. Removal from solution occurs by adsorption onto the active surface layer and decay in the dissolved phase.

In the present discussion, it is assumed that U in the groundwater does not react with the surface layer. This is consistent with various field studies that have concluded that U in oxic groundwaters can exhibit generally conservative behavior (e.g. Hodge *et al* 1996). In contrast, Th and Ra are assumed to be highly surface-reactive. Rn, a noble gas, is not surface-reactive. Given the typically low activities of the radionuclides in natural ground waters relative to those in the solids, the production by parent decay in solution of any long-lived radionuclide is negligible compared to that supplied to the water by parent decay in the rock or in the surface layer. The steady state general transport equation for any nuclide i in the dissolved phase is:

$$\frac{\mathrm{d}^i c_w}{\mathrm{d}x} = \frac{\rho_r \cdot (1-n)}{\rho_w \cdot n \cdot v} \cdot \left(w_i \cdot {}^i c_r + \varepsilon_i \cdot \lambda_p \cdot {}^p c_r + {}^i \hat{k}_{-1} \right.$$
$$\left. \cdot \frac{\rho_{sc} \cdot S}{\rho_r} \cdot {}^i c_{sc} + f_i \cdot \frac{\rho_{sc} \cdot S \cdot \xi}{\rho_r} \cdot \lambda_p \cdot {}^p c_{sc} \right)$$
$$+ \frac{\lambda_p}{v} \cdot {}^p c_w - \left(\frac{\lambda_i}{v} + {}^i \hat{k}_i \cdot \frac{S \cdot (1-n)}{v \cdot n} \right) \cdot {}^i c_w \quad (1)$$

where ρ_r, ρ_w and ρ_{sc} are the densities of the rock, water, and surface layer, respectively, and ${}^i c_w, {}^i c_r$, and ${}^i c_{sc}$ are the concentrations of i in these respective phases. The parameter ε_i is the fraction of nuclide i produced by α-decay in the rock and released into the water by recoil. For simple geometries, ε_i is directly
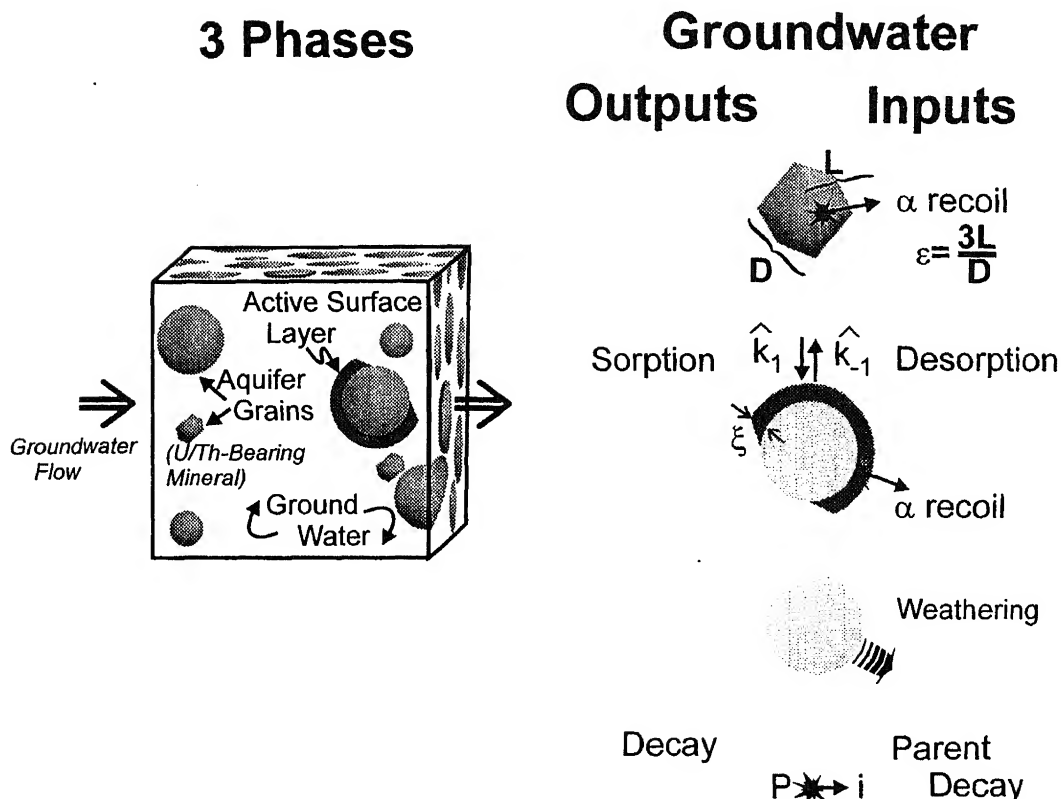
Figure 1. Model of an aquifer with the three phases and fluxes considered.

Table 1. *Model parameters.*

Symbol	Parameter	Units	Value[1]
n	porosity	–	0.3
ρ_r	rock density	g/cm^3	2.7
ρ_w	water density	g/cm^3	1
ρ_{sc}	surface coating density	g/cm^3	2.7
v	average linear water flow velocity	cm/sec	$(2-7) \times 10^{-4}$
$^{i}c_w$	concentration of the nuclide i in solution	mol/kg of water	
$^{i}c_{sc}$	concentration of i in the surface layer	mol/kg of surface layer	
$^{i}c_r$	concentration of i in the rock	mol/kg of rock	
r	average grain radius	m	$(10-100) \times 10^{-6}$
L_i	α-recoil length of the nuclide i	m	2×10^{-8}
ξ	surface coating thickness	m	10^{-6}
S	specific surface area per volume of rock	cm^{-1}	
w_i	weathering rate	sec^{-1}	
ε_i	recoil fraction of the nuclide i		$(0.6-6) \times 10^{-5}$
R_{eman}	emanation fraction of Rn		
λ_i	decay rate of nuclide i	sec^{-1}	
$^{i}\hat{k}_{-1}$	velocity of the nuclide i desorbing from the surface layer into the liquid phase	cm.sec^{-1}	
$^{i}\hat{k}_{1}$	velocity of nuclide i adsorbing onto the surface layer	cm.sec^{-1}	
f_p	fraction of nuclide i released in the water by decay of its sorbed parent p		0.5
F_p	fraction of nuclide i released in the water by desorption of i and decay of its sorbed parent		0.5
^{i}D	Distribution coefficient of nuclide i between the surface coating and the groundwater		
χ_i	Ratio of the number of atoms i in the surface coating to the number of atoms of i in solution		See table 2
$\bar{x}_i$	Characteristic length scale of i		See table 2

[1] Typical values for the Upper Glacial aquifer in Long Island, New York.

Table 2. $\bar{x}_i$ *values for the different radionuclides in the Long Island aquifer.*

Radionuclide	Half life	λ_i sec^{-1}	χ_i	$\bar{x}_{i\,max}(\chi_{i=0})$ meters	$\bar{x}_i$ meters
^{238}U	4.47×10^9 y	4.29×10^{-18}	0	4.07×10^{11}	4.07×10^{11}
^{234}Th	24.1 d	3.33×10^{-7}	700	6.01	1×10^{-2}
^{234}U	2.46×10^5 y	8.93×10^{-14}	0	2.24×10^7	2×10^7
^{230}Th	7.54×10^4 y	2.92×10^{-13}	2×10^6	6.86×10^6	3
^{226}Ra	1599y	1.37×10^{-11}	700	1.46×10^5	3×10^2
^{222}Rn	3.82d	2.10×10^{-6}	0	9.54×10^{-1}	9×10^{-1}
^{232}Th	1.4×10^{10} y	1.57×10^{-18}	2×10^6	1.27×10^{12}	6×10^5
^{228}Ra	5.76 y	3.82×10^{-9}	100	5.24×10^2	5
^{228}Th	1.913 y	2×10^4	1000	1.74×10^2	9×10^{-3}
^{224}Ra	3.6 d	2.23×10^{-6}	0.2	8.97×10^{-1}	0.9
^{220}Rn	55 sec	1.26×10^{-2}	0	1.59×10^{-4}	1.59×10^{-4}

related to the radius r of the emitting mineral and to the specific recoil length L of the nuclide by $\varepsilon_i \cong 3L/2r$ when $L \ll r$ (Kigoshi 1971). For the nuclides of interest here, L $\sim$ 200 Å (Fleischer 1982). Note that U-Th bearing accessory mineral grains are often much smaller than the major aquifer mineral grains. For U-Th bearing grains in the size range of 10–100 μm, the range of ε is 6×10^{-3} to 6×10^{-4}. The fraction of daughter atoms i produced by decay of the parent nuclides that are adsorbed at the surface layer and released into solution is f_i. For α-decay, f_i is dependent on the thickness ξ of the surface layer, with a maximum value of 0.5 when $\xi \ll L$. For low-energy β-decay, f_i is either 1 if the daughter i is not adsorbed and so completely released into solution, or 0 if it is strongly adsorbed. Sorption is characterized by the parameter $\hat{k}_1$, the average velocity with which atoms i in solution impact and sorb onto the surface layer. $\hat{k}_{-1}$ is the velocity of atoms i in the surface layer that cross the surface-water boundary to go into solution. Sorption kinetics are assumed to follow a first-order rate law.

Assuming that the surface layer is in steady state (i.e. $d^i c_{sc}/dt = 0$), then:

$$^i c_{sc} = {}^i D \cdot \left(\frac{\rho_w}{\rho_{sc}}\right) \cdot {}^i c_w + (1 - \theta \cdot f_i)$$
$$\cdot \left(\frac{\xi}{{}^i\hat{k}_{-1} + \lambda_i \cdot \xi}\right) \cdot \lambda_p \cdot {}^p c_{sc} \qquad (2)$$

where

$$^i D = \frac{{}^i\hat{k}_1}{({}^i\hat{k}_{-1} + \lambda_i \cdot \xi)}. \qquad (3)$$

In the case of α-decay, $\theta = 2$, while for β-decay, $\theta = 1$. Note that combining equations (1) and (2) gives a linear differential equation for $^i c_w$ with a characteristic exponential solution of the form $\exp(-x/\bar{x}_i)$, where

$$\bar{x}_i \equiv \frac{v}{\lambda_i \cdot (1 + \chi_i)} \qquad (4)$$

and

$$\chi_i \equiv {}^i D \cdot S \cdot \xi \cdot \frac{(1 - n)}{n}. \qquad (5)$$

The parameter $\bar{x}_i$ is the length scale for transport and determines the distance required so that $d^i c_w/dx \approx 0$. Values of $\bar{x}_i$, calculated for a typical sandy aquifer, are listed in table 2 and will be used in the discussion. Radionuclide groundwater concentrations as a function of distance are obtained by sequentially solving equations (1) and (2) for each nuclide along the ^{238}U and ^{232}Th decay series. Note that if the solution is saturated in a species, the above treatment is not appropriate. In the case that the solution is saturated (or supersaturated), the "surface" layer concentration grows and is not in steady state. The steady state treatment presented here does not include the complexities involved with a growing adsorptive layer.

3. Discussion

The exact solutions to equations (1) and (2) are given for all nuclides in Appendix I. The equations for the asymptotic values for $x \to \infty$ are in Appendix II. Note that the concentrations are expressed in activities, where $^i A = {}^i c\lambda_i$. For the purposes of discussion, typical values for the characteristics of a sandy aquifer will be used below for parameters of the model (see table 1). In the following sections, we consider the evolution along a flowline of the activity of some relevant nuclides from the ^{238}U and ^{232}Th decay series in groundwater. We then discuss the different general evolutions with distance of the activities in the groundwater, and the relevance of the initial input for the activities along the flowline. This is followed by consideration of the Th and Ra isotopic ratios in the water in case of predominant weathering or recoil. The last point focuses on the model predictions for ^{222}Rn activities in the water and their compatibility with measured high values in natural aquifers.
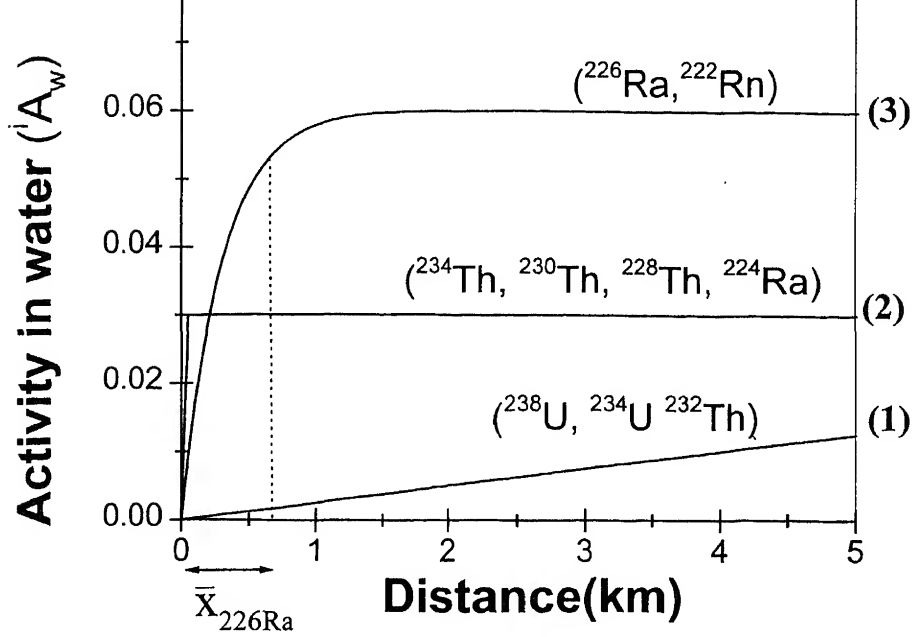
Figure 2. Nuclide activities in solution as a function of distance for different $\bar{x}_i$ values and arbitrary values for ^iA_w. Curve (**1**): the value of $\bar{x}_i$ is long compared to the length of the aquifer and ^iA_w grows linearly with distance; curve (**2**): $\bar{x}_i$ is short compared to the aquifer length: ^iA_w reaches rapidly a constant value; curve (**3**): $\bar{x}_i$ is intermediate ^iA_w reaches a constant value after a characteristic distance. Values of $\bar{x}_i$ have been calculated using data from a typical sandy aquifer.

3.1 *The Behavior of long-lived ^{238}U and ^{232}Th*

For the very long-lived nuclides ^{232}Th and ^{238}U, the $\bar{x}_i$ values $\bar{x}_{238\text{U}} = v/\lambda_{238\text{U}}$ and $\bar{x}_{232\text{Th}} = v/\lambda_{232\text{Th}}(1 + \chi_{232\text{Th}})$ are much larger than aquifer length scales; for instance, even assuming a high $\chi_{232\text{Th}}$ value of 10^6, $\bar{x}_{232\text{Th}}$ remains of the order of 1000 km (see equation (4) and table 2). Consequently, for distances typically encountered in natural aquifers, the characteristic exponential of the general solutions given in Appendix I can be approximated by $\exp(-x/\bar{x}_i) \approx 1 - x/\bar{x}_i$, so that ^{232}Th and the ^{238}U activities are

$$^iA_w = {}^iA_{w\infty}\left(\frac{x}{\bar{x}_i}\right) + {}^iA_{w0}$$

$$= \frac{\rho_r(1-n)}{\rho_w n}\left(\frac{w_i x}{v}\right){}^iA_r + {}^iA_{w0} \tag{6}$$

where $^iA_{w\infty}$ is defined in Appendix II and $^iA_{w0}$ represents the activity of nuclide i in the recharging water that meets the aquifer at the water table. Note that ^iA_w increases linearly with distance along a flowline (figure 2) and is independent of χ_i, the parameter that reflects the distribution of i between the surface layer and the water. This is a direct result of the steady state treatment, so that the equation for the activity in the water is not dependent on the surface reactivity of nuclide i. For weathering rates of $3 \times 10^{-14}\,\text{sec}^{-1}$ (corresponding to a rapid aquifer weathering time scale of 1 My) to 3×10^{-16} sec^{-1} (corresponding to a long weathering time scale

of 100 My), ^{238}U activities of $(0.002\text{–}0.2)$ dpm/kg $((3\text{–}300)\times10^{-9}\,\text{g U/kg})$ are generated over 5 km, respectively. Note that in general, the activities of U and Th are proportional to $w_i x/v$ so that, for a given distance, the determining parameter is w_i/v. Hence increasing the weathering rate or decreasing the groundwater velocity have equivalent effects upon ^iA_w. The ^{232}Th/^{238}U ratios in the groundwater are controlled by the relative supply rates of these nuclides by weathering; if $^{232\text{Th}}A_{w0} = {}^{238\text{U}}A_{w0} = 0$, then $^{232\text{Th}}A_w/^{238\text{U}}A_w = w_{232\text{Th}}/w_{238\text{U}}(^{232\text{Th}}A_r/^{238\text{U}}A_r)$. Typical values of both Th and U activities found in ground waters $(^{238\text{U}}c_w \approx 4\text{–}20\,\text{ng/kg}$ and $^{232\text{Th}}c_w \approx 30\text{–}200\,\text{pg/kg})$ and a Th/U activity ratio in the rock ~ 1, generally found in aquifers, therefore implies: $w_{232\text{Th}}/w_{238\text{U}} \approx 10^{-2}$. Generalizing these results, it is seen that the weathering rate for Th is about 100 times smaller than that of U.

3.2 ^{234}Th

The nuclide ^{234}Th is distinctive in being a short-lived daughter nuclide produced by a non-reactive parent (^{238}U). Therefore, there are no inputs due to production within the surface layer. The activity of ^{234}Th in the water is given by

$$^{234\text{Th}}A_w = {}^{234\text{Th}}A_{w\infty}(1 - e^{-x/\bar{x}_{234\text{Th}}}) + {}^{234\text{Th}}A_{w0}e^{-x/\bar{x}_{234\text{Th}}} \tag{7}$$

where

$$^{234}\mathrm{Th}A_{w\infty} = \frac{\rho_r(1-n)}{\rho_w n} \frac{(w_{234\mathrm{Th}} + \varepsilon_{234\mathrm{Th}}\lambda_{234\mathrm{Th}})}{\lambda_{234\mathrm{Th}}(1+\chi_{234\mathrm{Th}})}^{238\mathrm{U}}A_r.$$

(8)

The very short half-life of $^{234}\mathrm{Th}$ results in a value of $\bar{x}_{234\mathrm{Th}}$ that is small, and so the evolution along a flowline of $^{234}\mathrm{Th}$ activity in groundwater is distinctive from that of the parent $^{238}\mathrm{U}$. For a sandy aquifer, where $\chi_{234\mathrm{Th}}$ equals 10^3 (table 2), $\bar{x}_{234\mathrm{Th}} = 1\,\mathrm{cm}$ and the $^{234}\mathrm{Th}$ activity reaches the asymptotic value $^{234}\mathrm{Th}A_{w\infty}$ after a distance of only a few cm (figure 2). It follows that $^{234}\mathrm{Th}$ is locally governed and the input from the vadose zone does not govern its behavior over significant distances. Note that, because $^{238}\mathrm{U}A_{sc} = 0$, $^{234}\mathrm{Th}A_{sc} = {}^{234}\mathrm{Th}D(\rho_w/\rho_{sc})^{234}\mathrm{Th}A_w$ (equation (2)). It can be seen that $\chi_{234\mathrm{Th}}$ is equal to the ratio of number of $^{234}\mathrm{Th}$ atoms in the surface layer to that in the water (see equation (5)). The input process that dominantly controls the concentration of $^{234}\mathrm{Th}$ in groundwater is determined by the relative magnitudes of $w_{234\mathrm{Th}}$ and $\varepsilon_{234\mathrm{Th}}\lambda_{234\mathrm{Th}}$ (equation (8)). Even for a rapid weathering rate of $^{234}\mathrm{Th}$ of $w_{234\mathrm{Th}} \leq 10^{-14}\,\mathrm{sec}^{-1}$, $w_{234\mathrm{Th}}$ is very small compared to the expected $\lambda_{234\mathrm{Th}}\varepsilon_{234\mathrm{Th}}$ values of 10^{-10} to $10^{-9}\,\mathrm{sec}^{-1}$. As we expect $w_{234\mathrm{Th}} \approx w_{232\mathrm{Th}} \ll w_{238\mathrm{U}}$ (see section 3.1), it follows that, compared to recoil, weathering is a minor source for $^{234}\mathrm{Th}$ in solution. The weathering term therefore can be neglected in equation (8), so that the $^{234}\mathrm{Th}$ activity in the water is directly proportional to the ratio $\varepsilon_{234\mathrm{Th}}/(1+\chi_{234\mathrm{Th}})$.

3.3 ^{234}U and U isotope compositions

The equation for the activity of dissolved $^{234}\mathrm{U}$ is given in equation (9), and using $w_{234\mathrm{Th}}/\lambda_{234\mathrm{Th}} \ll \varepsilon_{234\mathrm{Th}}$ (see section 3.2), becomes

$$^{234}\mathrm{U}A_w = \left(\frac{\rho_r \cdot (1-n)}{\rho_w \cdot n}\right)\frac{(w_{234\mathrm{U}} + \varepsilon_{234\mathrm{Th}}\lambda_{234\mathrm{Th}})^{238\mathrm{U}}A_r}{v}x$$
$$+ {}^{234}\mathrm{U}A_{w0}$$

(9)

The activity $^{234}\mathrm{U}A_w$ increases linearly with distance, like $^{238}\mathrm{U}A_w$ (figure 2 curve 1). However, unlike $^{238}\mathrm{U}$, the $^{234}\mathrm{U}$ activity depends not only upon the weathering rate but also upon the amount of $^{234}\mathrm{Th}$ produced in the solid by α-decay and ejected into solution by recoil. Note that the $^{234}\mathrm{U}$ concentration does not depend on the extent to which $^{234}\mathrm{Th}$ is associated with the surface layer; since in the present discussion U is assumed not to be surface reactive, the $^{238}\mathrm{U}$ in the groundwater represents the total U produced by decay of $^{234}\mathrm{Th}$ both in the surface layer and in the solution. Therefore, the amount of $^{234}\mathrm{U}$ produced by decay only depends on the abundance of total $^{234}\mathrm{Th}$ ejected out of the aquifer solid.

The $^{234}\mathrm{U}/^{238}\mathrm{U}$ isotopic ratio, expressed as $\delta^{234}U$ (the permil deviation from secular equilibrium), is:

$$\delta^{234}\mathrm{U}$$
$$= \left[\frac{\frac{\rho_r(1-n)}{\rho_w n}\left(\lambda_{234\mathrm{U}}\varepsilon_{234\mathrm{Th}}\right)\frac{^{238\mathrm{U}}A_r}{^{238\mathrm{U}}A_{w0}}\cdot\frac{x}{v} + \delta^{234}\mathrm{U}_0\cdot 10^{-3}}{\left(\frac{\rho_r(1-n)w_{238\mathrm{U}}}{\rho_w\cdot n}\cdot\frac{^{238\mathrm{U}}A_r}{^{238\mathrm{U}}A_{w0}}\right)\frac{x}{v}+1}\right]\cdot 10^3$$

(10)

Here, the value of $\delta^{234}\mathrm{U}$ at the water table equals $\delta^{234}\mathrm{U}_{w0}$ and we have assumed $w_{234\mathrm{U}} = w_{238\mathrm{U}}$. The variation in $^{234}\mathrm{U}/^{238}\mathrm{U}$ ratio with distance can be viewed as a mixing relationship between the component added at the water table and a component from weathering and recoil that is progressively added. Therefore, $\delta^{234}\mathrm{U}_w$ increases with distance and reaches an asymptotic value ($\delta^{234}\mathrm{U}_{w\infty}$) at large values of x (figure 3). The distance necessary to reach the asymptotic value depends on the relative importance of $\delta^{234}\mathrm{U}_{w0}$, $^{238}\mathrm{U}A_{w0}$, $\varepsilon_{234\mathrm{Th}}$, and $w_{234\mathrm{U}}$. For example, starting with $\delta^{234}\mathrm{U}_{w0} = 40‰$, $^{238}\mathrm{U}A_{w0} = 2\times 10^{-3}\,\mathrm{dpm/kg}$ (3 ng/kg), $\varepsilon_{234\mathrm{Th}} = 1\times 10^{-3}$, and $w_{234\mathrm{U}} = 1\times 10^{-15}\,\mathrm{sec}^{-1}$, the $\delta^{234}\mathrm{U}_{w\infty}$ value of 90‰ would be reached at a distance of 10 km. Therefore, it is clear that the input at the water table can be important for long distances in the aquifer. The asymptotic value is $\delta^{234}\mathrm{U}_{w\infty} = (\lambda_{234\mathrm{U}}\varepsilon_{234\mathrm{Th}}/w_{238\mathrm{U}})10^3$ and is directly proportional to $\varepsilon_{234\mathrm{Th}}/w_{238\mathrm{U}}$. To generate larger isotopic shifts, either the fraction of $^{234}\mathrm{Th}$ ejected by α-recoil must be increased or the weathering rate of $^{238}\mathrm{U}$ must be decreased. For a recoiled fraction $\varepsilon_{234\mathrm{Th}} = 1\times 10^{-2}$ (corresponding to a U-bearing mineral grain size of $10\,\mu\mathrm{m}$), and $w_{234\mathrm{U}} \approx 10^{-15}\,\mathrm{sec}^{-1}$, a $\delta^{234}\mathrm{U}_w$ value of
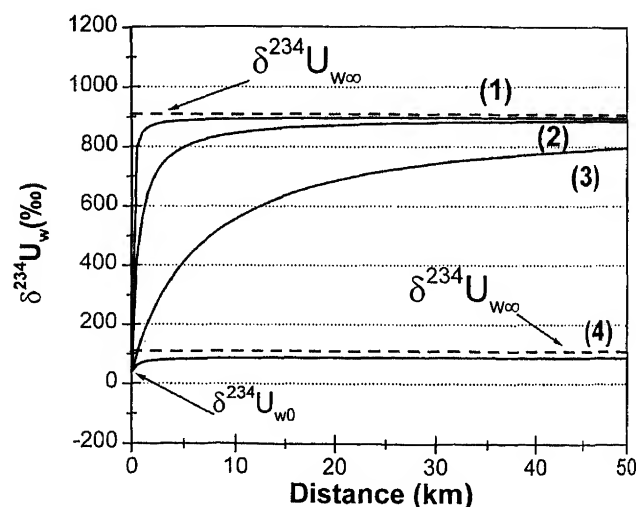

Figure 3. Isotopic evolutions of $\delta^{234}\mathrm{U}$ (in permil deviation from secular equilibrium) in the water versus distance. Evolution for a $\delta^{234}\mathrm{U}_{w\infty}$ value of 1000‰ (1) low water velocity and typical recoil and weathering values; (2) typical flow velocity, recoil and weathering values; (3) typical flow velocity, low weathering rate and low recoiled fraction. Evolution for $\delta^{234}\mathrm{U}_{w\infty}$ of 90‰; (4) typical flow velocity, recoil and weathering values.

1000‰ would be generated, while for $\varepsilon_{234\text{Th}} \approx 10^{-3}$, $\delta^{234}\text{U}_w \approx 100‰$. Very large values of $\delta^{234}\text{U}$ associated with high U activities (see Osmond and Cowart 1992) either reflect a combination of both high U activities and high isotopic shifts in waters from the vadose zone, or require very low weathering rates with very long transit distances within the saturated zone. Note that water with low water velocities will more rapidly reach the limiting value of $\delta^{234}\text{U}_w$ (see figure 3, curve 1).

3.4 *Other Radionuclides*

Unlike all the nuclides described above, ^{228}Ra is the first nuclide in the ^{238}U and ^{232}Th decay series that is surface reactive and has a surface-reactive parent. This can be used as an example for most of the remaining nuclides in the chain. The activity of ^{228}Ra in groundwater along a flowline (see Appendix I and figure 4) is

$$
\begin{aligned}
^{228\text{Ra}}A_w = {} & ^{228\text{Ra}}A_{w0} \cdot e^{-x/\bar{x}_{228\text{Ra}}} \\
& + \frac{F_{228\text{Ra}}\chi_{232\text{Th}}(^{232\text{Th}}A_{w0})}{(1 + \chi_{228\text{Ra}})}(1 - e^{-x/\bar{x}_{228\text{Ra}}}) \\
& + \left(^{228\text{Ra}}A_{w\infty} - \frac{F_{228\text{Ra}}\chi_{232\text{Th}}(^{232\text{Th}}A_{w\infty})}{(1 + \chi_{228\text{Ra}})} \right) \\
& \times (1 - e^{-x/\bar{x}_{228\text{Ra}}}) \\
& + \frac{F_{228\text{Ra}}\chi_{232\text{Th}}(^{232\text{Th}}A_w - {}^{232\text{Th}}A_{w0})}{(1 + \chi_{228\text{Ra}})}. \quad (11a)
\end{aligned}
$$

The first term in equation (11a) represents the removal from solution of ^{228}Ra supplied at the water table from the interaction with the vadose zone. The second term represents the approach to a balance between ^{228}Ra removal by decay and input from the ^{232}Th supplied at the water table. The third term describes the approach to the balance between ^{228}Ra removal by decay and inputs by weathering and recoil of ^{228}Ra from the aquifer grains. The last term is the production of ^{228}Ra in groundwater by decay of the ^{232}Th adsorbed on the surface layer that have been added along the flowline by weathering. For the activity of ^{228}Ra beyond the scale of a few kilometers (where $x \gg \bar{x}_{228\text{Ra}}$, see table 2), equation (11a) becomes (with $1 + \chi_{228\text{Ra}} \approx \chi_{228\text{Ra}}$):

$$
\begin{aligned}
^{228\text{Ra}}A_w = {} & \left(^{228\text{Ra}}A_{w\infty} - \frac{F_{228\text{Ra}}\chi_{232\text{Th}}}{\chi_{228\text{Ra}}}{}^{232\text{Th}}A_{w\infty} \right) \\
& + \frac{F_{228\text{Ra}}\chi_{232\text{Th}}}{\chi_{228\text{Ra}}}{}^{232\text{Th}}A_w \\
= {} & ^{228\text{Ra}}A_{wI} + \frac{F_{228\text{Ra}}\chi_{232\text{Th}}}{\chi_{228\text{Ra}}}{}^{232\text{Th}}A_w. \quad (11b)
\end{aligned}
$$

Substituting for $^{228\text{Ra}}A_{w\infty}$ and $^{232\text{Th}}A_{w\infty}$, then

$$
^{228\text{Ra}}A_{wI} = \frac{\rho_r(1-n)}{\rho_w n}\frac{(w_{228\text{Ra}} + \varepsilon_{228\text{Ra}}\lambda_{228\text{Ra}})}{\lambda_{228\text{Ra}}(1 + \chi_{228\text{Ra}})}{}^{232\text{Th}}A_r. \quad (12)
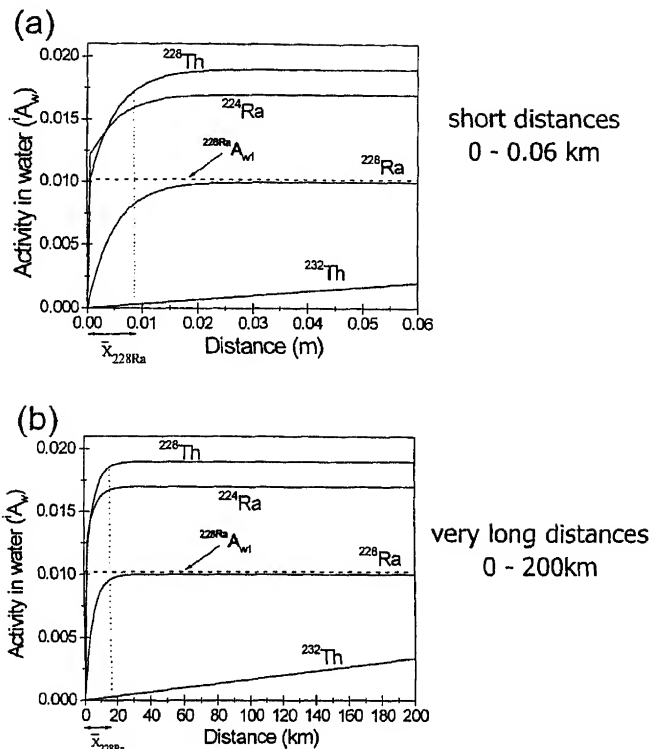$$

Figure 4. Activities in solution ^{232}Th decay series nuclides as a function of distance. The three graphs represent the evolutions at several scales. $^{228\text{Th}}A_w$ and $^{224\text{Ra}}A_w$ reach very rapidly a constant activity for $x \gg \bar{x}_{228\text{Ra}}$ (**graph a**); $^{232\text{Th}}A_w$ evolves linearly with distance (**graph b**); $^{228\text{Ra}}A_w$ reaches rapidly an intermediate activity $^{228\text{Ra}}A_{wI}$ and then grows linearly (**graph b**) over long distances.

$^{228\text{Ra}}A_{wI}$ represents the balance between input from the aquifer mineral grains and removal of ^{228}Ra in solution. After $^{228\text{Ra}}A_{wI}$ is reached, the ^{228}Ra activity follows a very slowly changing value and its increase with distance is proportional to the slow increase of adsorbed ^{232}Th represented by the term ($\chi_{232\text{Th}}$ $^{232\text{Th}}A_w$). As discussed previously, however, ^{232}Th never reaches its asymptotic value $^{232\text{Th}}A_{w\infty}$ on the scale of an aquifer (section 3.1). Consequently, the ^{228}Ra activity also will not reach its limiting activity $^{228\text{Ra}}A_{w\infty}$ (figure 4). Note in equation (11b), where $x \gg \bar{x}_{228\text{Ra}}$, the linear relationship between ^{228}Ra and ^{232}Th activities can be used to obtain a value for the ratio $\chi_{232\text{Th}}/\chi_{228\text{Ra}}$.

The solutions to the differential equations for the other radionuclide concentrations are presented in Appendixes I and II. As described for ^{228}Ra, the activity of each nuclide along the flowline generally is dependent upon the distribution of all precursor nuclides within the decay series, so that the governing equations become progressively more complicated. However, the equations exhibit a common form of

$$
^iA_w = {}^iA_{w0}e^{-x/\bar{x}_i} + {}^iA_{w\infty}(1 - e^{-x/\bar{x}_i}) + {}^iJ(x) \quad (13)
$$

where the first term describes the evolution of the activity of i supplied at the water table. The function

$^iJ(x)$ represents the component of the activity (the "transitional activity") of nuclide i that evolves with distance, produced by the "transitional" decay of the precursors. The constant value of $^iA_{w\infty}$ is reached when $\lim(^iJ)_{x\to\infty} = 0$ and $x \gg \bar{x}_i$; then the decay rate of nuclide i in both the solution and the surface layer equals the net inputs into solution and the surface layer. The evolution to this constant value is described by $^iJ(x)$:

$$^iJ(x) = \sum_k^i \Omega_k \lambda_i (^kA_{w\infty} - {}^kA_{w0})(e^{-x/\bar{x}_k} - e^{-x/\bar{x}_i}).$$

$$(14)$$

The distance required to reach the condition when $^iJ(x)$ is negligible, depends upon the relative importance of these terms, which is controlled by the values of $^i\Omega_k$, the groundwater activities at infinite distance $^kA_{w\infty}$, and the length scales $\bar{x}_k$ (see Appendices I and II). Note that for the daughters of ^{238}U, the term $^i\Omega_{^{238}\text{U}} = 0$, since U is assumed not to adsorb onto the surface layer, so that U does not contribute to their activities. Numerical values of $\bar{x}_i$, calculated with χ_i values typical for a sandy aquifer, are listed in table 2 and will be used for discussion.

3.4.1 Evolution types

The evolution of each radionuclide activity along a flowline fall into three general patterns: (**1**) long-lived nuclides that evolve linearly with distance over the length of the aquifer (see curve 1, figure 2); (**2**) short-lived nuclides that reach a constant value $^iA_{w\infty}$ within a short distance (see curve 2); and (**3**) nuclides that have more complex evolutionary patterns evolving toward a constant value that is achieved only over considerable distances (curve 3).

The first case applies to ^{238}U, ^{234}U and ^{232}Th, since $\bar{x}_{^{238}\text{U}}$, $\bar{x}_{^{234}\text{U}}$, and $\bar{x}_{^{232}\text{Th}}$ are very large (see table 2), and where the transport equation solutions are of the form $^iA_w = {}^iA_{w\infty} \cdot x/\bar{x}_i + {}^iA_{w0}$ (see section 3.1 above). Note that $^iA_{w\infty}/\bar{x}_i$ (the slope of the evolution curve) is independent of the sorption characteristics (χ_i) of the nuclide. The second case, where the activity reaches its limiting value very rapidly along the flow line, is illustrated by short-lived ^{234}Th (see section 3.1). The third case is applicable to the remaining nuclides of both decay series and is illustrated in section 3.4 by the example of ^{228}Ra. For the ^{232}Th daughter nuclides ^{228}Ra, ^{228}Th and ^{224}Ra, the $\bar{x}_i$ values are less than 3 m (figure 4 and table 2). Consequently, the activities of ^{228}Ra, ^{228}Th and ^{224}Ra first grow rapidly, and then follow a linear evolution following that of the ^{232}Th activity in the surface layer as the contribution from the decay of ^{232}Th in the surface layer increases. However, the activity of ^{232}Th within the surface layer is typically small over aquifers of moderate size, and so is a minor effect upon the activities of ^{228}Ra, ^{228}Th

and ^{224}Ra. Therefore, the activities of the ^{232}Th series daughters reach a quasi-constant value after a few meters (figure 4).

Regarding the nuclides in the ^{238}U decay series, ^{234}U is not surface reactive and so is not present in the surface layer. Also, the contribution to the daughter nuclide ^{230}Th from its parent ^{234}U in solution is minor compared to the contributions from weathering or recoil from the rock and the surface layer. Therefore, the only input of daughter ^{230}Th occurs from decay of ^{234}U in the rock and the concentration of ^{230}Th is not affected by the evolution of the parent nuclides in the decay series. Consequently, the ^{230}Th activity reaches $^{230\text{Th}}A_{w\infty}$ after a distance controlled by $\bar{x}_{^{230}\text{Th}}$, while the ^{226}Ra activity reaches its limiting value after a distance controlled by $\bar{x}_{^{226}\text{Ra}}$ (since $\bar{x}_{^{226}\text{Ra}} > \bar{x}_{^{230}\text{Th}}$) (see table 2). The very short-lived nuclide ^{222}Rn is produced mainly by decay of ^{226}Ra in the rock and the surface layer; consequently, the value of $^{222\text{Rn}}A_w$ approaches $^{222\text{Rn}}A_{w\infty}$ (at a distance controlled by a characteristic of parent ^{226}Ra, $\bar{x}_{^{226}\text{Ra}}$ (and not $\bar{x}_{^{222}\text{Rn}}$).

3.5 Initial inputs from the vadose zone and at aquifer discontinuities

The composition of groundwater at the water table ($x = 0$) generally is the result of interactions between meteoric water and the vadose zone. The solute concentrations of these waters can be low, e.g. where the volume of the unsaturated zone is minimal, or significant, e.g. where weathering rates are high over a significant soil thickness. Note that transport through the vadose zone can be modeled with a mathematical treatment similar to that developed here by incorporating the appropriate unsaturated water flow parameters. The distances over which the radionuclides in recharging groundwater are important is determined by the values of $\bar{x}_i$ (see table 2). The effect of the recharging groundwater activities on groundwater evolution is represented by the first term of the equation for $^iA_w(x)$ of $^iA_{w0} \exp(-x/\bar{x}_i)$ (see equation (14)), where $^iA_{w0}$ is the initial input at $x = 0$. The influence of water table activities disappears for $x \gg \bar{x}_i$. For nuclides such as ^{234}Th, ^{230}Th, ^{222}Rn, ^{224}Ra, and ^{228}Th, the vadose zone input is negligible after distances of 10 m. Consequently, the activities of these nuclides in solution reflect the water-rock interactions taking place only within the aquifer.

For the long-lived nuclides ^{238}U, ^{234}U and ^{232}Th, $\bar{x}_i$ is very large so that the term $^iA_{w0}$ can contribute significantly or dominates the groundwater activity over substantial distances. The importance of this term for radionuclide activities downgradient of groundwater flow depends upon the relative magnitudes of the subsequent inputs into solution from weathering and recoil (for ^{234}U). In the case where the integrated input throughout the aquifer is substantially lower than the initial activity, the value of ^iA_w remains
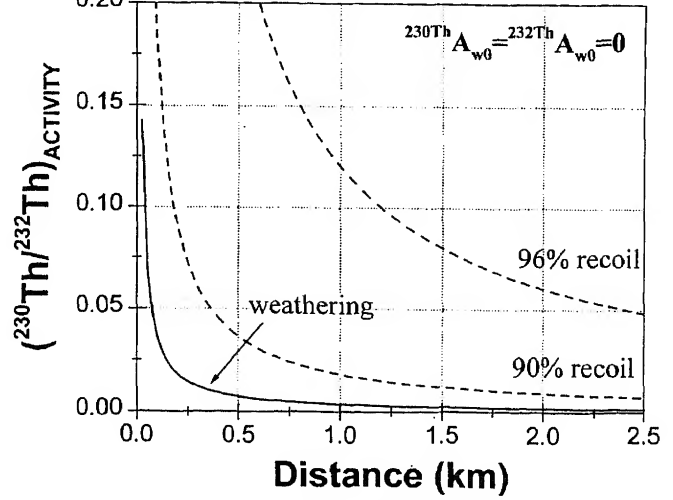
Figure 5. Evolution of ^{230}Th/^{232}Th activity ratios versus distance in the water for the case where weathering is the dominant input of ^{230}Th (solid line) and for the cases where input by recoil represents 90 and 96% of the ^{230}Th in water (dashed lines). Input from the water table is zero.

relatively constant and equal to A_{w0}. In this case, the activities of these nuclides in solution within the aquifer reflect the interactions in the vadose zone. If the inputs into groundwater are greater than $^{i}A_{w0}$, the initial activity will be a progressively lower fraction of the total activity $^{i}A_w$, depending upon the magnitude of the weathering rate and/or recoil rate. Therefore, it is clear that in any aquifer study, the determination of input from the vadose zone is of great importance.

Where discontinuities in the characteristics of an aquifer occur, the continuing evolution of radionuclide groundwater concentrations can be calculated by considering each homogenous segment of the aquifer as sub-units, using the activities at the discontinuity as initial values for subsequent evolution. The groundwater flowing through each aquifer segment is subject to the same controls as discussed above for a homogenous aquifer.

3.6 Th and Ra isotope compositions

In this section both extreme cases of dominant weathering and dominant recoil and their consequences for Th and Ra isotopic ratios will be considered. For Th, only the ^{230}Th activity is affected by recoil as well as weathering, since ^{232}Th is solely produced by weathering of the rock. In addition, we have seen in section 3.1 that ^{232}Th cannot reach the limiting activity $^{232\text{Th}}A_{w\infty}$ at the scale of an aquifer, while $^{230\text{Th}}A_w$ reaches the limiting value $^{230\text{Th}}A_{w\infty}$ after a few meters. Therefore, for distances much longer than a few meters, $^{230\text{Th}}A_w/^{232\text{Th}}A_w = \left(^{230\text{Th}}A_{w\infty}/^{232\text{Th}}A_{w\infty}\right)\bar{x}_{232\text{Th}}/x$. For Th, $(\chi_{232\text{Th}}/\chi_{230\text{Th}}) \approx 1$ because the desorption kinetics are much faster than the decay rate of ^{232}Th and ^{230}Th (see equations (3) and (5)). Moreover, $\left(^{232\text{Th}}A_r/^{238\text{U}}A_r\right) \approx 1$ for a typical $(\text{Th/U})_{wt}$ ratio of 3.8 in a crustal rock. In the case where weathering is the dominant input process for ^{230}Th, the ^{230}Th/^{232}Th activity ratio then is equal to

$$\frac{^{230\text{Th}}A_{w\infty}]_{\text{WEATH}}}{^{232\text{Th}}A_w} = 6 \times 10^{-6} \left(\frac{w_{230\text{Th}}}{w_{232\text{Th}}}\right)\frac{\bar{x}_{232\text{Th}}}{x}. \quad (15)$$

In the case of comparable Th weathering rates, this yields $\left(^{230\text{Th}}A\right)_{\text{WEATH}}/^{232\text{Th}}A_w \approx 6 \times 10^{-6}\bar{x}_{232\text{Th}}/x$. When recoil is the dominant input process for ^{230}Th $(w_{230\text{Th}}/\lambda_{230\text{Th}} \ll \varepsilon_{230\text{Th}})$, the Th isotopic ratio is

$$\frac{^{230\text{Th}}A_{w\infty}]_{\text{RECOIL}}}{^{232\text{Th}}A_{w\infty}} = \left(\frac{\varepsilon_{230\text{Th}}\lambda_{232\text{Th}}}{w_{232\text{Th}}}\right)\frac{\bar{x}_{232\text{Th}}}{x}. \quad (16)$$

In this case, $^{230\text{Th}}A_w/^{232\text{Th}}A_w$ depends on $\varepsilon_{230\text{Th}}/w_{232\text{Th}}$. For values of $w_{232\text{Th}} = 1 \times 10^{-17}\text{ sec}^{-1}$ and $\varepsilon_{230\text{Th}} = 1 \times 10^{-3}$, then $\left(^{230\text{Th}}A\right)_{\text{RECOIL}}/^{232\text{Th}}A \approx 2 \times 10^{-4}\bar{x}_{232\text{Th}}/x$. Lower $\varepsilon_{230\text{Th}}/w_{232\text{Th}}$ values yield lower values of $\left(^{230\text{Th}}A_w\right)_{\text{RECOIL}}/^{232\text{Th}}A_w$. The condition that recoil predominates is $w_{230\text{Th}}/\lambda_{230\text{Th}} \ll \varepsilon_{230\text{Th}}$. It follows that if $w_{230\text{Th}} = w_{232\text{Th}}$, then $\varepsilon_{230\text{Th}}\lambda_{232\text{Th}}/w_{232\text{Th}} \gg \lambda_{232\text{Th}}/\lambda_{230\text{Th}} = 6 \times 10^{-6}$. Figure 5 shows the evolution with distance of the ^{230}Th/^{232}Th activity ratio for different

values of $\varepsilon_{230\text{Th}}\lambda_{232\text{Th}}/w_{232\text{Th}}$. Since ^{230}Th reaches its limiting activity after a few meters and ^{232}Th grows linearly with distance, the ^{230}Th/^{232}Th activity ratio decreases with distance from an initial value determined by the input at the water table. The $\left(^{230\text{Th}}A_w/^{232\text{Th}}A_w\right)$ values for dominant recoil (greater than 90% of the ^{230}Th produced) are at least an order of magnitude higher than in the case of dominant weathering. Knowing the concentration of ^{232}Th, a value for $w_{232\text{Th}}$ can be obtained and the ratio $\left(^{230\text{Th}}A_w/^{232\text{Th}}A_w\right)$ measured along a flowline (for different values of x) gives the fraction of recoiled ^{230}Th $(\varepsilon_{230\text{Th}})$.

The ratio of ^{230}Th from recoil to that from weathering is equal to $\varepsilon_{230\text{Th}}\lambda_{230\text{Th}}/w_{230\text{Th}}$ (Appendix II). In a sandy aquifer with $\varepsilon_{230\text{Th}} = 10^{-3}$ and $w_{230\text{Th}} = w_{232\text{Th}} = 10^{-17}\text{ sec}^{-1}$, then this ratio is equal to 30, and the recoil process accounts for more than 96% of the ^{230}Th in solution. With $\bar{x}_{232\text{Th}} \approx 600$ km, values of $\sim 2 \times 10^{-2}$ for $\left(^{230\text{Th}}A_w/^{232\text{Th}}A_w\right)$ are expected after 6 km. However, there is no data available for ^{230}Th and ^{232}Th in aquifers with low total dissolved charge, where recoil is likely to be the most important. The only examples are in the study for an aquifer dominated by carbonates by Banner et al (1990), who found activity ratios of around 8, which is far above those calculated here for Th/U ~ 4. Further measurement of ^{230}Th/^{232}Th in aquifers with low carbonate ratio will provide key test of the model.

For the Ra isotopic ratios, the case of predominance of weathering, as input process from the aquifer rock, requires that $w_{230\text{Th}}/\lambda_{230\text{Th}} \gg \varepsilon_{230\text{Th}}$ (see equations in Appendices I and II) and the activity ratios become

$$\frac{^{228\text{Ra}}A_{w\infty}]}{^{226\text{Ra}}A_{w\infty}]_{\text{WEATH}}} = 3 \times 10^4 \left(\frac{\chi_{226\text{Ra}}}{\chi_{228\text{Ra}}}\frac{w_{232\text{Th}}}{w_{230\text{Th}}}\right) \quad (17)$$

and

$$\left.\frac{^{224}\text{Ra} A_{w\infty}}{^{226}\text{Ra} A_{w\infty}}\right]_{\text{WEATH}} = 5 \times 10^4 \left(\frac{\chi_{^{226}\text{Ra}}}{\chi_{^{224}\text{Ra}}} \frac{w_{^{232}\text{Th}}}{w_{^{230}\text{Th}}}\right). \qquad (18)$$

If $w_{^{230}\text{Th}}/w_{^{232}\text{Th}} = 1$, then the terms in the parentheses in equations (17) and (18), which depend on the decay constants, must be greater than unity, in which case $(^{228}\text{Ra} A/^{226}\text{Ra} A)_{\text{WEATH}} \approx 3 \times 10^4$ and $(^{224}\text{Ra} A/^{226}\text{Ra} A)_{\text{WEATH}} \geq 5 \times 10^4$. If recoil is more significant than weathering, then

$$\left.\frac{^{228}\text{Ra} A_{w\infty}}{^{226}\text{Ra} A_{w\infty}}\right]_{\text{RECOIL}} = \frac{\varepsilon_{^{228}\text{Ra}}}{\varepsilon_{^{226}\text{Ra}} + F_{^{226}\text{Ra}}\varepsilon_{^{230}\text{Th}}} \left(\frac{\chi_{^{226}\text{Ra}}}{\chi_{^{228}\text{Ra}}}\right) \quad (19)$$

and

$$\left.\frac{^{224}\text{Ra} A_{w\infty}}{^{226}\text{Ra} A_{w\infty}}\right]_{\text{RECOIL}} = \frac{\varepsilon_{^{224}\text{Ra}} + F_{^{224}\text{Ra}}(1 - f_{^{228}\text{Th}})\varepsilon_{^{228}\text{Ra}}}{\varepsilon_{^{226}\text{Ra}} + F_{^{226}\text{Ra}}\varepsilon_{^{230}\text{Th}}}$$
$$\times \left(\frac{\chi_{^{226}\text{Ra}}}{\chi_{^{224}\text{Ra}}}\right). \qquad (20)$$

With $F_{^{226}\text{Ra}}$, $F_{^{224}\text{Ra}}$, and $f_{^{228}\text{Th}} \approx 0.5$, and if the recoil fractions of all nuclides are comparable, then $(^{228}\text{Ra} A/^{226}\text{Ra} A)_{\text{RECOIL}} \approx 2\chi_{^{226}\text{Ra}}/3\chi_{^{228}\text{Ra}} \approx 0.7$, and $(^{224}\text{Ra} A/^{226}\text{Ra} A)_{\text{RECOIL}} \approx \chi_{^{226}\text{Ra}}/\chi_{^{224}\text{Ra}} \geq 1$. The Ra isotopic ratios then reflect the ratios of the χ_{Ra} values (figure 6). Assuming that the desorption kinetics are faster than the decay rate of ^{226}Ra, the mean time $\xi/^{\text{Ra}}\hat{k}_{-1}$ of the desorption reaction from the surface layer is much shorter than the mean life of ^{226}Ra ($\xi/^{\text{Ra}}\hat{k}_{-1} \ll 1/\lambda_{^{226}\text{Ra}}$) and $\chi_{^{226}\text{Ra}}/\chi_i = 1 + \lambda_i\xi/^{\text{Ra}}\hat{k}_{-1}$ with $i = {}^{228}$Ra or ^{224}Ra (see equations 3 and 5). Note that $\lambda_{^{228}\text{Ra}} < \lambda_{^{224}\text{Ra}}$ gives $\chi_{^{226}\text{Ra}}/\chi_{^{224}\text{Ra}} \geq \chi_{^{226}\text{Ra}}/\chi_{^{228}\text{Ra}}$; and $1.5 (^{228}\text{Ra} A/^{226}\text{Ra} A)_{\text{RECOIL}} \leq (^{224}\text{Ra} A/^{226}\text{Ra} A)_{\text{RECOIL}}$ (equations (19) and (20)). The following points can be deduced: (**1**) the Ra activity ratios in the case when recoil is the dominant input are lower than those obtained in the case of dominant weathering. (**2**) Knowing λ_i and ξ places bounds on $^{\text{Ra}}\hat{k}_{-1}$ values which can be deduced from measurements of ^{228}Ra/^{226}Ra and ^{224}Ra/^{226}Ra activity ratios. As an example, assuming a thickness ξ of the surface layer of 1 μm, and with the data for a sandy aquifer (table 2), a ratio $\chi_{^{226}\text{Ra}}/\chi_{^{224}\text{Ra}} = 3 \times 10^3$ gives $^{\text{Ra}}\hat{k}_{-1} \approx 5 \times 10^{-14}$ cm/sec and a mean time for the desorption reaction of ~ 1 year. With $\chi_{^{226}\text{Ra}} = 10^3 \approx {}^{\text{Ra}}\hat{k}_1/{}^{\text{Ra}}\hat{k}_{-1}$, then $^{\text{Ra}}\hat{k}_1 \approx 2 \times 10^{-11}$ cm/sec and a mean time for the adsorption reaction of ~ 10 hours.

Typical ^{228}Ra/^{226}Ra and ^{224}Ra/^{226}Ra activity ratios measured in groundwater vary between 0.07 and 10 (Cherdyntsev 1971; King *et al* 1982). The most common values are ≈ 1 and indicate that recoil is the relevant process for Ra input to groundwater. However, the models developed have provided no explanation for the rather uncommon cases where observed ratios are less than unity. Note that the condition for predominance of recoil or weathering for Th and Ra is controlled by the same ratio $w_{^{230}\text{Th}}/$

$(\lambda_{^{230}\text{Th}}\varepsilon_{^{230}\text{Th}})$ and so the same process must be the dominant input for both Th and Ra.

3.7 *Recoil and ^{222}Rn activities*

The ^{222}Rn activity in water is typically orders of magnitudes higher than that of its parent, ^{226}Ra (see, for example, King *et al* 1982; Andrews *et al* 1989; Copenhaver *et al* 1993). Therefore, the ^{226}Ra activity in water is too low to produce the ^{222}Rn in the water. Input of ^{222}Rn by weathering from the rock is also not significant because it would require extremely high weathering rates of 10^{-8} sec^{-1}. Consequently, the dominant ^{222}Rn input into the water must be attributed to recoil from the rock and the surface layer. Due to its very short half-life (3.8 days), the ^{222}Rn activity mostly reflects local processes. The model equation for ^{222}Rn activity along the flowline depends on distance (see Appendix I). It rapidly reaches the value $^{222}\text{Rn} A_{w\infty} - f_{^{222}\text{Rn}}\chi_{^{226}\text{Ra}}{}^{226}\text{Ra} A_{w\infty}$ (for $x \gg \bar{x}_{^{230}\text{Th}}$) and then grows to the limiting activity $^{222}\text{Rn} A_{w\infty}$ according to the evolution with distance of ^{226}Ra in the surface layer (figure 2). Thus, the distance required to reach a constant ^{222}Rn activity depends mainly on the value of $\bar{x}_{^{226}\text{Ra}}$. For a typical sandy aquifer, the input from ^{226}Ra in the surface layer increases along the flowline and reaches a constant value after about 1 km.

The value of $^{222}\text{Rn} A_{w\infty}$ is

$$^{222}\text{Rn} A_{w\infty} = \frac{\rho_r(1-n)}{\rho_w \cdot n} \cdot \left(\varepsilon_{^{222}\text{Rn}} + f_{^{222}\text{Rn}}\right.$$
$$\cdot \left(\frac{w_{^{226}\text{Ra}}}{\lambda_{^{226}\text{Ra}}} + \varepsilon_{^{226}\text{Ra}} + (1 - f_{^{226}\text{Ra}})\right.$$
$$\left.\left.\cdot \left(\frac{w_{^{230}\text{Th}}}{\lambda_{^{230}\text{Th}}} + \varepsilon_{^{230}\text{Th}}\right)\right)\right) \cdot {}^{238}\text{U} A_r \qquad (21)$$

and depends on the recoiled fraction of ^{222}Rn ($\varepsilon_{^{222}\text{Rn}}$), as well as the weathering rates and recoiled fractions of both ^{226}Ra and ^{230}Th (w_i and ε_i) (Appendix II). The presence of $w_{^{230}\text{Th}}$ and $\varepsilon_{^{230}\text{Th}}$ represent the ^{226}Ra that contributes to ^{222}Rn in water, and was produced by ^{230}Th decay in the surface layer.

The emanation fraction is the amount of ^{222}Rn in the water of a volume of the aquifer divided by the amount of ^{222}Rn produced in the rock within the same volume. It is therefore equal to $R_{\text{eman}} = \rho_w n {}^{222}\text{Rn} A_w / \rho_r(1-n){}^{222}\text{Rn} A_r$. Note that R_{eman} depends on the porosity of the aquifer rock. For a given R_{eman} value, the lower the porosity, the higher the ^{222}Rn activity in the water $(^{222}\text{Rn} A_w)$. Therefore, for low porosity aquifers, a high $^{222}\text{Rn} A_w$ value can be reached and still correspond to relatively low emanation fractions. The key issue is the measurement of high ^{222}Rn *emanation fractions* in groundwater. The model equation for $^{222}\text{Rn} A_{w\infty}$, with $w_{^{226}\text{Ra}} = 10^{-15}$ sec^{-1}, $w_{^{230}\text{Th}} \approx 10^{-17}$ sec^{-1} and $f_{^{222}\text{Rn}} = f_{^{226}\text{Ra}} \approx 0.5$ and $\varepsilon_{^{222}\text{Rn}} \approx \varepsilon_{^{226}\text{Ra}} \approx \varepsilon_{^{230}\text{Th}}$, shows that $R_{\text{eman}} \approx 2\varepsilon_{^{226}\text{Ra}}$. The model shows the

following: (**1**) it is justified to use measured ^{222}Rn activities in water as a first order approximation of the ε_i values for the decay series nuclides. This confirms the approach used earlier by Krishnaswami et al (1982). (**2**) By this model, high ^{222}Rn levels in solution could be explained by very small grain sizes. Yet ε_i values up to 10^{-1} imply grain sizes smaller than $1\,\mu m$, and this is difficult to understand in terms of typical grain sizes of the radioactive minerals. It has been argued that efficient release of ^{222}Rn can occur within the mineral grain from a distance greater than the recoil length due to diffusion through nanopores (Rama and Moore 1984; 1990). However, laboratory experiments failed to find evidence for such mechanisms (Krishnaswami and Seidemann 1988) and further work is required to determine whether there are conditions under which such a process occurs.

Therefore, we conclude that the model of ^{222}Rn production from a surface layer in steady state does not provide an explanation for measured high ^{222}Rn emanations in pore fluids (equal to 10–20% of the rock activity). This has been a long-standing problem and recognized by many authors (e.g. Fleischer 1982; Krishnaswami and Seideman 1988; Rama and Moore 1990). One possible mechanism for explaining such high values is by attaining higher recoil fluxes from ^{226}Ra in the surface layer. In the present treatment the abundance of ^{226}Ra in the surface layer is limited by the assumption that it is in steady state and in equilibrium with the ^{226}Ra in groundwater. However, higher ^{226}Ra abundances in the surface layer, and so higher fluxes of ^{222}Rn from the layer, would result from processes that allow continuous deposition of ^{226}Ra; e.g., if Ra is trapped in precipitated phases and does not remain in equilibrium with the water, or if barite saturation is reached. The nonsteady state will be treated elsewhere. Note also that localized zones of high weathering rates (e.g. carbonates) may be an additional source of ^{222}Rn; such a mechanism may be discernible through correlations with other elements. However, at present the Rn problem remains unresolved.

4. Conclusions

The model developed here describes the evolution along a flowline of the activities of the ^{238}U and ^{232}Th decay series nuclides in groundwater. The processes considered here are weathering, decay, recoil by decay, and sorption. The results show that the activities reach a constant value after a distance $\bar{x}_i = v/\lambda_i(1+\chi_i)$, characteristic of each nuclide. When $\bar{x}_i$ is much longer than the aquifer length (for ^{238}U, ^{234}U, and ^{232}Th), the activities grow linearly with distance. In this case the vadose zone input may predominate throughout the aquifer. When $\bar{x}_i$ is short compared to the aquifer length (for ^{234}Th, ^{230}Th, ^{228}Th, ^{228}Ra, and

^{224}Ra), the activities rapidly reach a constant or quasi-constant activity value. For ^{226}Ra and ^{222}Rn, a limiting activity is reached after 1 km. The vadose contributions for these nuclei are then overwhelmed by the aquifer contribution. At long distances, all activity values depend mainly on four groups of parameters: the decay constants (λ_i) and the weathering rates (w_i), the recoil fractions (ε_i), and the distribution of the nuclides between the surface layer and the water (χ_i).

The isotopic ratios have been found to obey the following rules. The asymptotic value of $\delta^{234}U_{w\infty}$ is $(\lambda_{234U}\varepsilon_{234Th}/w_{238U})10^3$. High values of $\delta^{234}U$ will thus be provided by low weathering rates or high ε_{234Th}. The activity ratios ^{230}Th/^{232}Th, ^{228}Ra/^{226}Ra and ^{224}Ra/^{226}Ra have different behavior dependent on whether weathering or recoil is the predominant input mechanism. Typical values of weathering rate and recoiled fraction for a sandy aquifer indicate that recoil is the dominant input process for Th isotopes in the water. Measured data for the Ra isotopes activity ratios indicate that recoil is the process generally controlling the Ra isotopic composition in water. Higher isotopic ratios can be explained by different desorption kinetics of Ra.

From the model, the highest ^{222}Rn emanation equals 2ε. This is in agreement with the hypothesis that ^{222}Rn activity can be used as a first approximation for input by recoil (Krishnaswami et al 1982). However, high ^{222}Rn emanation implies unlikely small grain sizes of less than $1\,\mu m$, and cannot be explained by production from the surface layer as formulated in the model. The condition of equilibrium between a surface layer and the water (steady state hypothesis) fails to provide an effective means of enhancing ^{222}Rn activities. Clarification of this matter may involve study of models in which the surface layer is not in steady-state but has a continuous enhancement in precipitated material and radionuclide abundances, or models that include local rapid weathering in parts of the aquifer with very soluble phases.

The activities of the radionuclides at the water table, originating from interaction in the vadose zone, are significant. The continuing influence of these activities along the flowline depends on the nuclide half-life and on its sorption properties. For long-lived ^{238}U, ^{234}U and ^{232}Th, the term $^iA_{w0}$ can represent a significant fraction of the activity in solution over large distances. For ^{234}Th, ^{230}Th, ^{222}Rn, ^{224}Ra, and ^{228}Th, the vadose zone input has a negligible effect after distances of 10 m.

The model can be applied to natural aquifers to obtain $\bar{x}_i$ and χ_i values from measured radionuclide activities, and to obtain information on retardation factors and on the kinetics of sorption processes. Inversely, nuclide activities in groundwater can be predicted from the model, using distribution coefficients determined in laboratory experiments. Future

cases where the water and the surface layer are not in steady state, in particular the case where precipitation onto the surface layer occurs.

Appendix I

Radionuclide groundwater concentrations as a function of distance are obtained by sequentially solving equations 1 and 2 for nuclides along the ^{238}U and ^{232}Th decay series. (See Appendix II for the expressions of $^iA_{w\infty}$).

^{238}U-Series

- $^{238}\text{U}A_w = {}^{238}\text{U}A_{w0}\,e^{-x/\bar{x}_{238}\text{U}} + {}^{238}\text{U}A_{w\infty}(1 - e^{-x/\bar{x}_{238}\text{U}}),$

- $^{234}\text{Th}A_w = {}^{234}\text{Th}A_{w0}\,e^{-x/\bar{x}_{234}\text{Th}} + {}^{234}\text{Th}A_{w\infty}(1 - e^{-x/\bar{x}_{234}\text{Th}}),$

- $^{234}\text{U}A_w = {}^{234}\text{U}A_{w0}\,e^{-x/\bar{x}_{234}\text{U}} + {}^{234}\text{U}A_{w\infty}(1 - e^{-x/\bar{x}_{234}\text{U}}),$

- $^{230}\text{Th}A_w = {}^{230}\text{Th}A_{w0}\,e^{-x/\bar{x}_{230}\text{Th}} + {}^{230}\text{Th}A_{w\infty}(1 - e^{-x/\bar{x}_{230}\text{Th}}),$

- $^{226}\text{Ra}A_w = {}^{226}\text{Ra}A_{w0}\,e^{-x/\bar{x}_{226}\text{Ra}} + {}^{226}\text{Ra}A_{w\infty}(1 - e^{-x/\bar{x}_{230}\text{Th}})$
$+ \dfrac{F_{226\text{Ra}}\lambda_{226\text{Ra}}\chi_{230\text{Th}}\cdot({}^{230}\text{Th}A_{w\infty} - {}^{230}\text{Th}A_{w0})}{\lambda_{226\text{Ra}}(1 + \chi_{226\text{Ra}}) - \lambda_{230\text{Th}}(1 + \chi_{230\text{Th}})}$
$\cdot(e^{-x/\bar{x}_{230}\text{Th}} - e^{-x/\bar{x}_{226}\text{Ra}}),$

- $^{222}\text{Rn}A_w = {}^{226}\text{Ra}A_{w\infty} + f_{222\text{Rn}}\lambda_{222\text{Rn}}\lambda_{226\text{Ra}}\chi_{226\text{Ra}}$
$\cdot\left[\dfrac{F_{226\text{Ra}}\chi_{226\text{Th}}({}^{230}\text{Th}A_{w\infty} - {}^{230}\text{Th}A_{w0})}{(\lambda_{226\text{Ra}}(1 + \chi_{226\text{Ra}}) - \lambda_{230\text{Th}}(1 + \chi_{230\text{Th}}))}\right]$
$\cdot\left(\dfrac{e^{-x/\bar{x}_{226}\text{Ra}}}{(\lambda_{222\text{Rn}}(1 + \chi_{222\text{Rn}}) - \lambda_{226\text{Ra}}(1 + \chi_{226\text{Ra}}))}\right)$
$- f_{222\text{Rn}}\lambda_{222\text{Rn}}\lambda_{226\text{Ra}}\chi_{226\text{Ra}}$
$\cdot\left[\dfrac{F_{226\text{Ra}}\chi_{230\text{Th}}({}^{230}\text{Th}A_{w\infty} - {}^{230}\text{Th}A_{w0})}{(\lambda_{226\text{Ra}}(1 + \chi_{226\text{Ra}}) - \lambda_{230\text{Th}}(1 + \chi_{230\text{Th}}))}\right]$
$\cdot\left(\dfrac{e^{-x/\bar{x}_{230}\text{Th}}}{(\lambda_{222\text{Rn}}(1 + \chi_{222\text{Rn}}) - \lambda_{230\text{Th}}(1 + \chi_{230\text{Th}}))}\right)$
$- f_{222\text{Rn}}\left[\dfrac{\lambda_{222\text{Rn}}\chi_{230\text{Th}}({}^{230}\text{Th}A_{w\infty} - {}^{230}\text{Th}A_{w0})}{(\lambda_{226\text{Ra}}(1 + \chi_{226\text{Ra}}) - \lambda_{230\text{Th}}(1 + \chi_{230\text{Th}}))}\right.$
$\left.\cdot(1 - 2f_{226\text{Ra}})\cdot\left(\dfrac{\lambda_{226\text{Ra}}\xi}{Ra\,\hat{k}_{-1} + \lambda_{226\text{Ra}}\xi}\right)\right]\cdot e^{-x/\bar{x}_{230}\text{Th}}$
$- f_{222\text{Rn}}\left(\dfrac{\lambda_{222\text{Rn}}\chi_{226\text{Ra}}}{\lambda_{222\text{Rn}} - \lambda_{226\text{Ra}}(1 + \chi_{226\text{Ra}})}\right)$
$\cdot({}^{226}\text{Ra}A_{w\infty} - {}^{226}\text{Ra}A_{w0})\,e^{-x/\bar{x}_{226}\text{Ra}}.$

- $^{222}\text{Rn}A_w = \left[{}^{222}\text{Rn}A_{w\infty} - f_{222\text{Rn}}\chi_{226\text{Rn}}\,{}^{226}\text{Ra}A_{w\infty}\right.$
$\left. - f_{222\text{Rn}}\chi_{226\text{Ra}}F_{226\text{Ra}}\dfrac{\lambda_{226\text{Ra}}}{\lambda_{222\text{Rn}}}\chi_{230\text{Th}}\,{}^{230}\text{Th}A_{w\infty}\right]$
$+ f_{222\text{Rn}}\chi_{226\text{Ra}}\,{}^{226}\text{Ra}A_w$
$- f_{222\text{Rn}}\chi_{226\text{Ra}}F_{226\text{Ra}}\dfrac{\lambda_{226\text{Ra}}}{\lambda_{222\text{Rn}}}\chi_{230\text{Th}}\,{}^{230}\text{Th}A_w.$

^{232}Th-Series:

- $^{232}\text{Th}A_w = {}^{232}\text{Th}A_{w0}\,e^{-x/\bar{x}_{232}\text{Th}} + {}^{232}\text{Th}A_{w\infty}(1 - e^{-x/\bar{x}_{232}\text{Th}}),$

- $^{228}\text{Ra}A_w = {}^{228}\text{Ra}A_{w0}\,e^{-x/\bar{x}_{228}\text{Ra}} + {}^{228}\text{Ra}A_{w\infty}(1 - e^{-x/\bar{x}_{228}\text{Ra}})$
$- \dfrac{F_{228\text{Ra}}\chi_{232\text{Th}}\lambda_{228\text{Ra}}({}^{232}\text{Th}A_{w\infty} - {}^{232}\text{Th}A_{w0})}{(\lambda_{228\text{Ra}}(1 + \chi_{228\text{Ra}}) - \lambda_{232\text{Th}}(1 + \chi_{232\text{Th}}))}$
$\times(e^{-x/\bar{x}_{232}\text{Th}} - e^{-x/\bar{x}_{228}\text{Ra}}),$

- $^{228}\text{Th}A_w = {}^{228}\text{Th}A_{w0}\,e^{\frac{-x}{\bar{x}_{228}\text{Th}}} + {}^{228}\text{Th}A_{w\infty}(1 - e^{\frac{-x}{\bar{x}_{228}\text{Th}}})$
$- \dfrac{F_{228\text{Th}}\chi_{232\text{Th}}({}^{232}\text{Th}A_{w\infty} - {}^{232}\text{Th}A_{w0})(e^{\frac{-x}{\bar{x}_{232}\text{Th}}} - e^{\frac{-x}{\bar{x}_{228}\text{Th}}})}{(1 + \chi_{228\text{Th}})}$
$\times\left(\dfrac{(1 - 2f_{228\text{Ra}})\lambda_{228\text{Ra}}\xi}{Ra\,\hat{k}_{-1} + \lambda_{228\text{Ra}}\xi} + \dfrac{F_{228\text{Ra}}\lambda_{232\text{Th}}}{\lambda_{228\text{Ra}}}\right)$
$- \dfrac{F_{228\text{Ra}}\lambda_{228\text{Th}}\chi_{228\text{Th}}({}^{228}\text{Ra}A_{w\infty} - {}^{228}\text{Ra}A_{w0})(e^{\frac{-x}{\bar{x}_{228}\text{Ra}}} - e^{\frac{-x}{\bar{x}_{228}\text{Th}}})}{\lambda_{228\text{Th}}(1 + \chi_{228\text{Th}}) - \lambda_{228\text{Ra}}(1 + \chi_{228\text{Ra}})}$
$\times\left[\dfrac{F_{228\text{Ra}}\chi_{232\text{Th}}\lambda_{232\text{Th}}}{\lambda_{228\text{Ra}}(1 + \chi_{228\text{Th}})} - 1\right],$

- $^{224}\text{Ra}A_w = {}^{224}\text{Ra}A_{w\infty}$
$- \dfrac{F_{224\text{Ra}}\chi_{228\text{Th}}\lambda_{224\text{Ra}}({}^{228}\text{Th}A_{w\infty} - {}^{228}\text{Th}A_{w0})}{(\lambda_{224\text{Ra}}(1 + \chi_{224\text{Ra}}) - \lambda_{228\text{Th}}(1 + \chi_{228\text{Th}}))}(e^{-x/\bar{x}_{228}\text{Th}})$
$- \dfrac{\chi_{228\text{Th}}F_{228\text{Ra}}\lambda_{228\text{Th}}(e^{-x/\bar{x}_{228}\text{Ra}})}{\lambda_{228\text{Th}}(1 + \chi_{228\text{Th}}) - \lambda_{228\text{Ra}}(1 + \chi_{228\text{Ra}})}$
$\times\dfrac{\chi_{228\text{Ra}}({}^{228}\text{Ra}A_{w\infty} - {}^{228}\text{Ra}A_{w0})}{(1 + \chi_{224\text{Ra}})}\left(\dfrac{F_{228\text{Ra}}\chi_{232\text{Th}}\lambda_{232\text{Th}}}{\lambda_{228\text{Ra}}(1 + \chi_{228\text{Ra}})} - 1\right)$
$- (1 - f_{228\text{Th}})\left(\dfrac{\lambda_{228\text{Th}}\xi}{Th\,\hat{k}_{-1} + \lambda_{228\text{Th}}\xi}\right)\dfrac{F_{224\text{Ra}}\chi_{228\text{Ra}}(e^{-x/\bar{x}_{228}\text{Ra}})}{(1 + \chi_{224\text{Ra}})}$
$\times\left[\dfrac{({}^{228}\text{Ra}A_{w\infty} - {}^{228}\text{Ra}A_{w0}) + F_{228\text{Ra}}\chi_{232\text{Th}}({}^{232}\text{Th}A_{w\infty} - {}^{232}\text{Th}A_{w0})}{(1 + \chi_{228\text{Ra}})}\right]$
$- \dfrac{F_{224\text{Ra}}\chi_{232\text{Th}}({}^{232}\text{Th}A_{w\infty} - {}^{232}\text{Th}A_{w0})(e^{-x/\bar{x}_{232}\text{Th}})}{(1 + \chi_{224\text{Ra}})}$

$$\times (1 - f_{228Ra})$$
$$\times \left[F_{228Th} + \left(\frac{(1 - f_{228Th})\lambda_{228Th}\xi}{{}^{Th}\hat{k}_{-1} + \lambda_{228Th}\xi} \right) \left(\frac{\lambda_{228Ra}\xi}{{}^{Ra}\hat{k}_{-1} + \lambda_{228Ra}\xi} \right) \right].$$

$$\times \frac{\left(\dfrac{w_{228Th}}{\lambda_{228Th}} + F_{228Th} \left(\dfrac{w_{228Ra}}{\lambda_{228Ra}} + \varepsilon_{228Ra} + (1 - f_{228Ra}) \dfrac{w_{232Th}}{\lambda_{232Th}} \right) \right)}{1 + \chi_{228Th}}$$
$$\times {}^{232Th}A_r,$$

Appendix II

Equations for the activities of the ^{238}U and ^{232}Th decay series nuclides when $x \to \infty$.

^{238}U-Series

- $$^{238U}A_{w\infty} = \left(\frac{\rho_r \cdot (1 - n)}{\rho_w \cdot n} \right) \frac{w_{238U}}{\lambda_{238U}} {}^{238U}A_r,$$

- $$^{234Th}A_{w\infty} = \left(\frac{\rho_r \cdot (1 - n)}{\rho_w \cdot n} \right) \cdot \frac{(w_{234Th} + \varepsilon_{234Th} \cdot \lambda_{234Th})}{\lambda_{234Th}(1 + \chi_{234Th})} {}^{238U}A_r,$$

- $$^{234U}A_{w\infty} = \left(\frac{\rho_r (1 - n)}{\rho_w \cdot n} \right)$$
$$\times \frac{\left(w_{234U} + w_{234Th} \frac{\lambda_{234U}}{\lambda_{234Th}} + \varepsilon_{234Th}\lambda_{234U} \right)}{\lambda_{234U}} {}^{238U}A_r,$$

- $$^{230Th}A_{w\infty} = \left(\frac{\rho_r (1 - n)}{\rho_w \cdot n} \right) \frac{(w_{230Th} + \varepsilon_{230Th}\lambda_{230Th})}{\lambda_{230Th}(1 + \chi_{230Th})} {}^{238U}A_r,$$

- $$^{226Ra}A_{w\infty} = \frac{1}{1 + \chi_{226Ra}}$$
$$\times \left(\frac{\rho_r \cdot (1 - n)}{\rho_w \cdot n} \left(\frac{w_{226Ra}}{\lambda_{226Ra}} + \varepsilon_{226Ra} \right) {}^{230Th}A_r \right.$$
$$\left. + F_{226Ra}\chi_{230Th} {}^{230Th}A_{w\infty} \right),$$

- $$^{222Rn}A_{w\infty} = \frac{\rho_r(1 - n)}{\rho_w n} \left(\varepsilon_{222Rn} + f_{222Rn} \left(\frac{w_{226Ra}}{\lambda_{226Ra}} \right. \right.$$
$$\left. \left. + \varepsilon_{226Rn} + (1 - f_{226Rn}) \left(\frac{w_{230Th}}{\lambda_{230Th}} + \varepsilon_{230Th} \right) \right) \right) {}^{238U}A_r.$$

^{232}Th-Series:

- $$^{232Th}A_{w\infty} = \frac{\rho_r(1 - n)}{\rho_w n} \left(\frac{w_{232Th}}{\lambda_{232Th}(1 + \chi_{232Th})} \right) {}^{232Th}A_r,$$

- $$^{228Ra}A_{w\infty} = \frac{\rho_r(1 - n)}{\rho_w n}$$
$$\times \frac{\left(\frac{w_{228Ra}}{\lambda_{228Ra}} + \varepsilon_{228Ra} + F_{228Ra} \frac{w_{232Th}}{\lambda_{232Th}} \right)}{1 + \chi_{228Ra}} \cdot {}^{232Th}A_r,$$

- $$^{228Th}A_{w\infty} = \frac{\rho_r(1 - n)}{\rho_w n}$$

- $$^{224Ra}A_{w\infty} = \frac{\rho_r(1 - n)}{\rho_w n} \frac{\left(\frac{w_{224Ra}}{\lambda_{224Ra}} + \varepsilon_{224Ra} \right)}{1 + \chi_{224Ra}} {}^{228Th}A_r$$
$$+ \frac{F_{224Ra}\chi_{228Th}}{1 + \chi_{224Ra}} {}^{228Th}A_{w\infty}$$
$$+ \frac{F_{224Ra}(1 - f_{228Th}) \left(\frac{\lambda_{228Th}\xi}{{}^{Th}\hat{k}_{-1} + \lambda_{228Th}\xi} \right) \chi_{228Ra}}{1 + \chi_{224Ra}} {}^{228Ra}A_{w\infty}$$
$$+ \frac{F_{224Ra}(1 - f_{228Th}) \left(\frac{\lambda_{228Th}\xi}{{}^{Th}\hat{k}_{-1} + \lambda_{228Th}\xi} \right)}{1 + \chi_{224Ra}}$$
$$\frac{(1 - f_{228Ra}) \left(\frac{\lambda_{228Ra}\xi}{{}^{Ra}\hat{k}_{-1} + \lambda_{228Ra}\xi} \right) \chi_{232Th}}{1 + \chi_{224Ra}} {}^{232Th}A_{w\infty}.$$

References

Allen H E, Perdue E M and Brown D S 1993 *Metals in Groundwater* (Lewis Publishers)

Andrews J N and Kay R L F 1982 ^{234}U/^{238}U activity ratio of dissolved uranium in groundwaters from a Jurassic limestone aquifer in England; *Earth Planet. Sci. Lett.* **57** 139–151

Andrews J N, Ford D J, Hussain N, Trivedi D and Youngman M J 1989 Natural radioelement solution by circulating groundwaters in the Stripa granite; *Geochim. Cosmochim. Acta* **53** 1791–1802

Banner J, Wasserburg G J, Chen J H and Moore C H 1990 ^{234}U-^{238}U-^{230}Th-^{232}Th systematics in saline groundwaters from central Missouri; *Earth Planet. Sci. Lett.* **101** 296–312

Bonotto D M and Andrews J N 1993 The mechanism of ^{234}U/^{238}U activity ratio enhancement in karstic limestone groundwater; *Chemical Geology (Isotope Geoscience Section)* **103** 193–206

Cherdyntsev V V 1971 Uranium-234. 234p. Israel Program for Scientific Translations, Jerusalem pp. 62–68

Coles D G and Ramspott L 1982 Migration of Ru-106 in a Nevada test-site aquifer – Discrepancy between field and laboratory results; *Science* **215** 1235–1237

Copenhaver S A, Krishnaswami S, Turekian K, Epler N and Cochran J K 1993 Retardation of ^{238}U and ^{232}Th decay chain radionuclides in Long Island and Connecticut aquifers; *Geochim. Cosmochim. Acta* **57** 597–603

Davidson M R and Dickson B L 1986 A porous flow model for steady state transport of radium in groundwater; *Wat. Resour. Res.* **22** 34–44

Dozol M *et al* 1993 Radionuclide migration in groundwaters: review of the behaviour of actinides (Technical report); *Pure and Applied Chemistry* 1082–1101

Fleischer R L 1982 Alpha-recoil damage and solution effects in minerals: uranium isotopic disequilibrium and radon release; *Geochim. Cosmochim. Acta* **46** 2191–2201

Hodge V F, Johannesson K H and Stetzenbach K 1996 Rhenium, Molybdenum, and Uranium in groundwater from the Southern Great-Basin, USA-Evidence for conservative behavior; *Geochim. Cosmochim. Acta* **60** 3197–3214

Hubbard N, Laul J C and Perkins R W 1984 The use of natural radionuclides to predict the behavior of radwaste radionuclides in far-field aquifers; *Scientific basis for nuclear waste management V*

Ivanovich M, Latham A G, Longworth G and Gascoyne M 1992 Uranium-series disequilibrium: application to radioactive waste disposal studies; In *Uranium-series Disequilibrium* (ed) Ivanovich and Harmon (Oxford Science Publications) pp. 583–630

Kigoshi K 1971 Alpha-Recoil Thorium-234: Dissolution into water and the Uranium-234/Uranium-238 disequilibrium in nature; *Science* **173** 47–48

King P T, Michel J and Moore W S 1982 Ground water geochemistry of ^{224}Ra, ^{226}Ra and ^{222}Rn. *Geochim. Cosmochim. Acta* **46** 1173–1182

Krishnaswami S, Graustein W S and Turekian K K and Dowd J F 1982 Radium, thorium and radioactive lead isotopes in groundwaters: application to the *in situ* determination of adsorption-desorption rate constants and retardation factors; *Water Resour. Res.* **18(6)** 1663–1675

Krishnaswami S and Seidemann D E 1988 Comparative study of ^{222}Rn, ^{40}Ar, ^{39}Ar and ^{37}Ar leakage from rocks and minerals. Implication for the role of nanopores in gas transport through natural silicates; *Geochim. Cosmochim. Acta* **52** 655–658

Ku T L, Luo S, Leslie B W and Hammond D E 1992 Decay-series disequilibria applied to the study of rock-water interaction and geothermal systems. In *Uranium-series Disequilibrium: application to Earth, Marine, and Environmental Sciences* (ed) M Ivanovich and R S Harmon (Oxford Science Publications)

Langmuir D 1997 *Aqueous environmental geochemistry* 600p. (Prentice Hall)

Osmond J K and Cowart J B 1992 Ground water. In *Uranium-series Disequilibrium: application to Environmental Problems* (ed) M Ivanovich and R S Harmon (Oxford Science Publications) pp. 204–245

Osmond J K and Ivanovich M 1992 Uranium-series mobilization and surface hydrology; In *Uranium-series Disequilibrium: application to Earth, Marine, and Environmental Sciences* (ed) M Ivanovich and R S Harmon (Oxford Science Publications) pp. 290–333

Rama and Moore W S 1984 Mechanism of transport of U-Th series of radioisotopes from solids into groundwater; *Geochim. Cosmochim. Acta* **48** 395–399

Rama and Moore W S 1990 Submicronic porosity in common minerals and emanation of radon; *Nuc. Geophy.* **4** 467–473

Tricca A, Porcelli D, Baskaran M and Wasserburg G J (2000) The transport of U- and Th-Series nuclides in a sandy unconfined aquifer, *Geochim. Cosmochim. Acta* (submitted)

Zheng C and Bennett G D 1995 *Applied contaminant transport modeling* (Van Nostrand Reinhold) 440 p

Stable isotope systematics of surface water bodies in the Himalayan and Trans-Himalayan (Kashmir) region

KANCHAN PANDE[†], J T PADIA, R RAMESH and K K SHARMA[*]

Physical Research Laboratory, Ahmedabad 380 009, India.
* Wadia Institute of Himalayan Geology, Dehradun 248 002, India.
[†]*email: kanchan@prl.ernet.in*

Stable hydrogen (δD) and oxygen (δ^{18}O) isotope ratios of the headwaters of the Indus and its tributaries, surface ice in glaciers, saline and fresh water lakes and thermal springs in the Himalayan and Trans-Himalayan (Kashmir) region are reported. The δD-δ^{18}O relationship for the river samples shows a slope of 9.12 ± 0.29 which agrees well with the estimate of 8.99 ± 0.33 based on a simple Rayleigh fractionation model. The unique signature of a higher deuterium excess (d) of the 'Western Disturbance' is preserved in these samples. An altitude effect of -0.9 per mil/km is observed in the δ^{18}O of Indus waters. At a lower altitude (Beas) the altitude effect is almost double, indicating that the altitude effect decreases with elevation in this region.

1. Introduction

Stable isotope studies on the water bodies of the Himalayan region can be useful to model the hydrological cycle and delineate sources of water to various reservoirs in this region. Such studies have been limited (Giggenbach *et al* 1983; Ramesh and Sarin 1992; Bartarya *et al* 1995). To fill this gap we have undertaken a stable isotope study of the headwaters of the Indus and its tributaries, surface ice in glaciers, fresh and saline lakes and thermal springs in the Himalaya and Trans-Himalaya (Kashmir), a hydrometeorologically significant but difficult and inaccessible region. In addition stable isotope measurements of surface water bodies help to interpret stable isotope data on other geological reservoirs (carbonates, organic matter, etc.) in terms of palaeoclimatic changes.

The area sampled (figure 1) comprises two distinct physiographic regions. The Trans Himalayan (Ladakh) region is bounded in the N-E by Tibet and is one of the most elevated regions in the world with no place being less than 3000 m in elevation. The joint effect of elevation and insolation on snowy mountains produces a unique and extreme climate (Raina 1977). Rainfall is very low (only 116 mm/yr) and the minimum temperature is $-8.5°$C (January) and the maximum $17.4°$C (July) (World Weather Records 1967). From November to March precipitation is in the form of snow (38% of the annual). There is practically no vegetation in this arid region. The Indus source water, glaciers, lakes and spring water samples belong mainly to this region. The other samples are from the lower, Himalayan region. This region is highly vegetated, experiences summer monsoon rain (in contrast to the Trans-Himalaya) and has a range of elevation from 600 m to 3000 m.

2. Sampling

Water samples were collected during August 1991 in clean 30 ml tightly capped polyethylene bottles. Fresh surface ice from the snouts of glaciers was collected, melted and stored in sample bottles. The lids were secured tightly to prevent evaporation

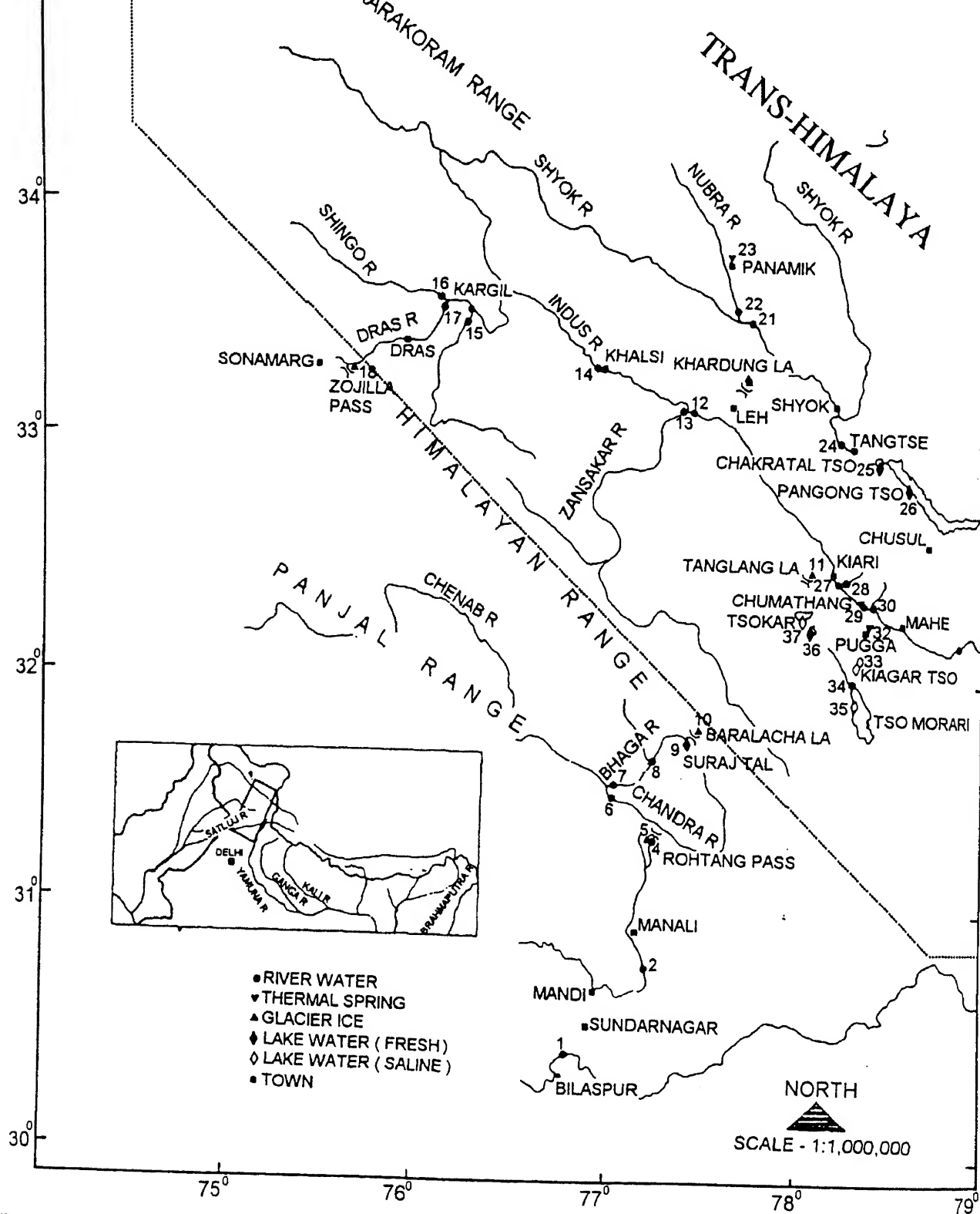**Keywords.** Himalaya; springs; stable isotopes; altitude effect.

Figure 1. Map of the area sampled; numbers denote sample locations.

and exchange with the atmospheric water vapour. All samples were analysed within a month of collection. Sample numbers and locations are shown in figure 1.

3. Analytical methods

About 2 ml of each sample was equilibrated with tank CO_2 at 25°C for 48 h and the CO_2 then extracted,

purified and let into a VG Micromass 602D mass spectrometer (VG Analytical, Wythenshawe Manchester, UK). δ^{18}O was determined with an overall precision of ± 0.2‰ (Epstein and Mayeda 1953). About $10\,\mu l$ of each sample was passed through uranium filings kept at 800°C and reduced to hydrogen gas, which was then transferred to 602D VG Micromass mass spectrometer for δD measurement; δD was measured with an overall precision of ± 1‰ (Friedman 1953). All values are reported relative to V-SMOW (Vienna Standard Mean Ocean Water; Gonfiantini 1981).

4. Results and discussion

The results are presented in table 1. The Indus river and its tributaries have δ^{18}O values in the range -11 to -17‰ and δD from -70 to -124‰, typical of high altitude precipitation. A plot of δD$-\delta^{18}$O is shown in figure 2. The 19 river water samples define a best fit line given by

$$\delta D = (9.12 \pm 0.29)\delta^{18}O + (31.1 \pm 4.2)$$

with a correlation coefficient (r) 0.98, significant at 0.01 level (P) (dashed line). This regression was

Table 1. δD, $\delta^{18}O$ and deuterium excess (d) values in (‰) relative to SMOW in rivers, lakes, glaciers and hot springs in the Kashmir Himalaya. Analytical uncertainty ± 0.2‰ for $\delta^{18}O$ and ± 1‰ for δD.

| Sample No. (see map)	Description	Altitude (m)	δ^{18}O	δD	d
	Rivers				
1	Sutlej	600	−13.7	−95	14.6
2	Beas	985	−11.1	−71	17.8
6	Chandra	2950	−14.1	−95	17.8
7	Bhaga	2935	−14.7	−102	15.6
8	Darcha	3400	−15.3	−107	15.4
12	Indus	3230	−14.6	−109	7.8
13	Zanskar	3230	−16.1	−114	14.8
14	Indus	3030	−15.2	−108	13.6
15	Suru	2750	−14.8	−104	14.4
16	Shingo	2770	−13.4	−91	16.2
17	Dras	2770	−12.8	−84	18.4
21	Shyok	3260	−16.2	−121	8.6
22	Nubra	3230	−15.5	−113	12.0
24	Tangtse	4945	−15.2	−104	17.6
27	Indus	3560	−15.3	−108	14.4
28	Indus	3630	−14.3	−96	18.4
30	Indus	4060	−15.9	−111	16.2
31	Indus	4130	−15.7	−115	10.6
34	Samdoh	4640	−17.3	−124	14.4
	Lakes				
4	Beas Kund (fresh)	3740	−10.3	−65	17.4
9	Suraj Tal (fresh)	4650	−15.7	−110	15.6
25	Chakratal Tso (fresh)	4250	−15.1	−111	9.8
26	Pengong Tso (salt)	4250	−1.4	−42	−30.8
33	Kiagar Tso (salt)	4610	−2.3	−54	−35.6
35	Tso Morari (salt)	4480	−6.3	−62	−11.6
36	Sputtsong Tso (fresh)	3510	−7.9	−75	−11.8
37	Tso Kar (salt)	3510	−6.6	−79	−26.2
	Glaciers				
5	Rohtang	3748	−18.1	−128	16.8
10	Balacha La	4650	−15.9	−119	8.2
11	Tanglang La	5210	−24.7	−180	17.6
18	Zozilla	3540	−12.2	−90	7.6
19	Khardung La	5629	−17.2	−127	10.6
20	Khardung La	5649	−15.3	−107	15.4
	Hot springs				
23	Ponamik	3320	−17.1	−126	10.8
29	Chumathan	4060	−15.9	−128	−0.8
32	Pugga	4640	−15.0	−126	−6.0
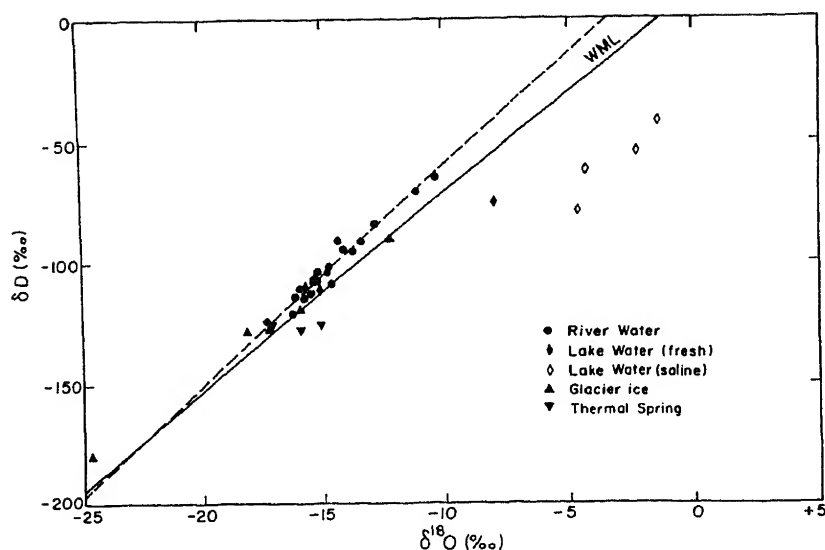
Figure 2. δD - δ^{18}O plot of samples shown in figure 1. Solid line denotes the World Meteoric Water Line (WML). Dashed line is the best fit line for the river water data only.

carried out by weighting the data points with their analytical uncertainties, following the procedure of Williamson (1968). This can be compared with the world meteoric water line (Yurtsever and Gat 1981) (WML, solid line):

$$\delta D = (8.17 \pm 0.28)\delta^{18}O \pm (10.55 \pm 0.64)$$

and that for the Ganges (Ganga) headwaters (Ramesh and Sarin 1992).

$$\delta D = (7.45 \pm 0.23)\delta^{18}O + (8 \pm 2).$$

In the case of Trans-Himalayan rivers sampled, it is clearly seen that both the slope and the intercept are significantly higher than those of WML and Ganges (Ganga). The main reason for the slope being greater than 8 is that part of the annual precipitation falls as snow in this region and the mean annual temperature is low (5.5°C). Table 2 shows the monthly precipitation and temperature data for the Trans-Himalayan Ladakh region. It is seen that for five months (November to March) the air temperature is less than or close to 0°C. Precipitation during these months is in the form of snow (about 38% of the total annual precipitation). If we use a simple Rayleigh Fractionation model (Gat 1981) to calculate the slope of the δD-δ^{18}O relationship, in which the rate of change of δ value with respect to logarithm of the fraction of vapour left in the cloud is equal to $(\alpha - 1) \times 10^3$‰, where α is the fractionation factor between liquid water and vapour [this applies for both the isotopes D

Table 2. *Model calculation of slope of the δD-δ^{18}O relationship based on meteorological (World Weather Records 1967) and equilibrium fractionation factors (Majoube 1971) between liquid-vapour except for winter months (marked with *) where ice-vapour fractionation is considered.*

| Month | Precipitation (mm) | Temperature (°C) | Fractionation factors | | Slope |
			Deuterium	Oxygen-18	
January*	12	−8.5	1.148	1.0164	9.02
February*	9	−5.5	1.142	1.0160	8.88
March*	12	0.1	1.132	1.0152	8.68
April	7	5.6	1.113	1.0113	10.00
May	7	10.0	1.098	1.0107	9.16
June	4	13.9	1.090	1.0101	8.91
July	16	17.4	1.085	1.0098	8.67
August	19	16.9	1.083	1.0100	8.30
September	12	13.1	1.094	1.0103	9.13
October	7	6.7	1.111	1.0111	10.00
November*	3	0.6	1.129	1.0130	9.92
December*	8	−4.8	1.140	1.0150	9.33
Mean (or total)	116	5.5	–	–	8.99 ±0.33

and ^{18}O], the slope of the δD-δ^{18}O relationship for precipitation is given by $(\alpha_D-1)/(\alpha^{18}O-1)$. The fractionation factors for the corresponding monthly temperatures are also shown in table 2. The slope is calculated for each month and an average of all the slopes, weighted with precipitation, is found to be 8.99 ± 0.33, in good agreement with the observed value of 9.12 ± 0.29. For the period November to March we have used ice-vapour equilibrium fractionation factors while for other months we have used those of liquid water-vapour (Majoube 1971). Thus to a first order approximation, the higher than 8 slope appears to be mainly caused by the low air temperatures and snow precipitation. Rozanski *et al* (1993) note that for stations with substantial contribution of snow precipitation, higher deuterium excess values (discussed below) during winter may result from additional kinetic fractionation during snow formation (Jouzel and Merlivat 1984). This could also lead to a slope greater than 8.

However, stable isotope studies of cold springs and rivers in Tapoban and Badrinath in UP Himalaya (elevation ~ 3000 m) showed a relationship

$$\delta D = 7.7\delta^{18}O + 13.0\,(r^2 = 0.94, n = 7)$$

(Navada *et al* 1985). In similar high altitude stations elsewhere in the world (e.g. Ecuador 3058 m, Columbia 2547 m and Adis Ababa 2360 m) the slopes are either 8 or slightly less. Therefore our results could be specific to the Ladakh region only.

We examine the deuterium excesses parameter (d) defined as δD-$8\delta^{18}O$, shown in table 1. As about 38% of the annual precipitation is derived from westerlies ('Western Disturbance') whose source is the Mediterranean Sea (Raina 1977) with a characteristically higher deuterium excess (Gat and Carmi 1970) the river water samples also exhibit higher deuterium excess. The average d value is 14.7 ± 3.1‰. All along the path of the Western Disturbance (Iran, Afghanistan, Pakistan and Kashmir) the precipitation is characterised by high deuterium excess (Yurtsever and Gat 1981). In a compilation of deuterium excess data from precipitation samples collected world wide, Rozanski *et al* (1993) found that between 30° and 40°N, most samples show high deuterium excess (in the range 15 to 25 per mil). Thus the high values of deuterium excess in our samples confirm the findings of Rozanski *et al* (1993), who also showed that the increase of the deuterium excess was correlated with the seasonal bias of precipitation towards winter. High deuterium excess values ($\sim 13.00 \pm 3.29$‰) have also been reported from Parbati Valley ground and cold spring waters (Giggenbach *et al* 1993).

The enhanced d values could also be due partly to a contribution of moisture from evaporation from local water bodies to the cloud formation. Such local
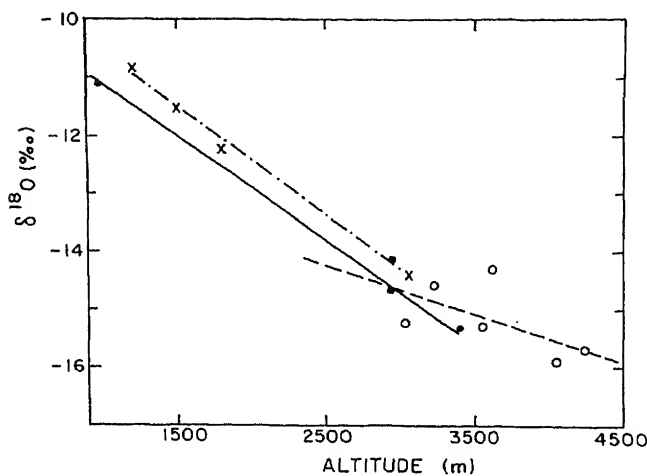

Figure 3. δ^{18}O as a function of altitude; solid line – Beas (filled circles); dashed line – Indus (open circles); dashed dotted line – Ganges main channel (crosses) (data from Ramesh and Sarin 1992).

the four saline lakes and one fresh water lake (Sputtsong Tso) plot well below the local meteoric line and WML indicating that these have undergone significant evaporation. The point of intersection of the best fit line for these points with the best fit line for the river water samples gives an approximate estimate of their original isotopic composition. It can therefore be estimated that annual evaporation could be as high as 70% of the annual precipitation in these lakes (estimate based on Rayleigh isotopic fractionation model taking into account the δ^{18}O atmospheric water vapour). Further, the six glacier snout ice samples also show a reduced slope (line not shown in figure 2): $\delta D = (7.29 \pm 0.19)\,\delta^{18}O + (0.4 \pm 3.4)$ with $r = 0.99$, $P = 0.01$ suggestive of sublimation of ice and local contribution of moisture to the clouds.

Figure 3 shows a plot of δ^{18}O of some of the samples as a function of altitude. As different rivers in this region (Beas, Sutlej and Indus) receive their water from different source regions, it is possible to detect the altitude effect only along the main channel of a single river. For the Indus river (open circles) in the Trans-Himalaya, the equation is

$$\delta^{18}O = -(0.086 \pm 0.011)\text{alt} - (12.07 \pm 0.41)$$

with $r = -0.58\,P = 0.01$
where alt is altitude in units of 100 m.
For Beas,

$$\delta^{18}O = -(0.17 \pm 0.01)\text{alt} - (9.39 \pm 0.16)$$

with $r = -0.99\,P = 0.01$.
Thus the altitude effect for Indus (Trans Himalaya) is about -0.09‰ for 100 m whereas for Beas (Himalaya) it is -0.17‰ per 100 m, comparable to that for Ganges (Ramesh and Sarin 1992). Giggenbach

altitude effect of −1‰ per km for cold springs. This is similar in magnitude to the value observed by us for the Indus river data.

It has been shown that the "altitude effect" in Ganges river water samples is about half that in precipitation in the source region of Ganges (Ramesh and Sarin 1992) due to the averaging of the $\delta^{18}O$ values as the river picks up water at different altitudes during its descent. A similar conclusion is valid for the Beas samples. However, for the Indus samples (higher altitude compared to Beas) the altitude effect is about half that seen for Beas. The reason could be that the altitude effect rapidly decreases with elevation in this region. It has been shown that $\delta^{18}O$ in fresh snow from Garhwal does not show any altitude effect in the range 4400 to 6050 m (Niewodniczanski et al 1981). Our results are consistent with their finding. Another possible explanation would be as follows : Most of the air masses come south and as they are rising on the southern slope of Himalaya, the vapour condenses and produces precipitation. When the top elevation is reached there is not much vapour left (and therefore the northern slope is arid) and the influence of altitude on the condensation process and isotopic composition of precipitation becomes negligible. This phenomenon has also been observed in Gran Canaria, Canary Islands (Gonfiantini et al 1976). Therefore the small altitude effect could be mainly due to evaporation during rainfall. According to another view (Navada, personal communication) the Indus during its descent may not be picking up much water and this could be a cause of the reduced altitude effect.

Mayewski and Lyons (1983) reported δD data for 8 snow samples from Zanskar between 5100 and 5500 m elevations. Our glacier samples show similar values (table 1). Giggenbach et al (1983) reported δD, $\delta^{18}O$ values for 3 snow samples from an altitude range 3400 ∼ 3800 m in Himachal Pradesh. Their values are enriched by an average of 10‰ in $\delta^{18}O$ and 80‰ in δD compared to the glacier samples reported in table 1 (from the altitude range 3500 to 5600 m) indicating substantial amount of high altitude snow precipitation in our samples. Likewise, the isotopic composition of thermal springs are also lower (by the same magnitude) than those of the hot springs from Parbati Valley (Giggenbach et al 1983) and Nepal (Grabczak and Kotarba 1985). This indicates that the former are being recharged by precipitation from higher altitudes.

5. Conclusion

We have reported δD, $\delta^{18}O$ data for the Himalayan and Trans-Himalayan water bodies including Indus river and its tributaries. The Indus waters have a higher than normal slope in the δD-$\delta^{18}O$ plot as the precipitation in this region is partly in the form of snow and the mean annual temperature is in general low. The theoretically calculated slope is in good agreement with the observed value. Also, these samples have in general higher deuterium excess values indicating that they preserve the signature of 'Western Disturbance'. The altitude effect in this region decreases with elevation.

References

Bartarya S K, Bhattacharya S K, Ramesh R and Somayajulu B L K 1995 $\delta^{18}O$ and δD systematics in the surficial waters of the Gaula river catchment area, Kumaun Himalaya, India; *J. Hydrology* **167** 369–379

Epstein S and Mayeda T 1953 Variation of $\delta^{18}O$ content in waters from natural sources; *Geochim. Cosmochim. Acta* **4** 213–224

Friedman I 1953 Deuterium content of natural waters and other substances; *Geochim. Cosmochim. Acta* **4** 89–103

Gat J R and Carmi I 1970 Evolution of the isotopic composition of atmospheric waters in the Mediterranean sea area; *J. Geophys Res*, **75** 3039–3048

Gat J R 1981 In *Stable Isotope Hydrology* (eds.) J R Gat and R Gonfiantini, IAEA Tech. Rep. Ser. **210** 7–19

Giggenbach W F, Gonfiantini R, Jangi B L and Truesdell A H 1983 Isotopic and chemical composition of Partabi Valley geothermal discharges, north-west Himalaya, India; *Geothermics* **12**(2/3) 199–222

Gonfiantini R, Gallo G, Payne B R and Taylor C B 1976 Environmental isotopes and hydrochemistry in ground water of Gran Canaria. In: *Interpretation of environmental isotope and hydrochemical data in ground water hydrology* pp 159–170 Vienna: IAEA

Gonfiantini R 1981 In: *Stable Isotope Hydrology* (eds) J R Gat and R Gonfiantini, IAEA Tech Rep Ser **210** 35–85

Grabczak J and Kotarba M 1985 Isotopic composition of the thermal waters in the central part of the Nepal Himalayas; *Geothermics* **14**(4) 567–575

Jouzel J and Merlivat L 1984 Deuterium and oxygen 18 in precipitation: Modelling of the isotopic effect during snow formation; *J. Geophys. Res.* **89** 11749–11757

Majoube M 1971 Fractionnement en oxygene 18 et en deuterium entre l'eau et sa vapeur; *J. Chim. Phys.* **10** 1423–1436

Mayewski P A and Lyons W B 1983 Chemical composition of a high altitude fresh snow fall in the Ladakh Himalayas; *Geophys. Res. Lett.* **10**(1) 105–108

Navada S V, Nair A R, Sharma S and Kulkarni U P 1985 Geochemical and Isotope studies of the geothermal areas of central and northern India; *Isotope and geochemical techniques applied to geothermal investigations.* (IAEA-TECDOC-) **788** 63–82

Niewodniczanski J, Grabczak J, Baranski L and Rzepka J 1981 The altitude effect on the isotopic composition of snow in higher mountains; *J Glaciol* **27** 99–112

Raina A N 1977 *Geography of Jammu and Kashmir* (New Delhi: National Book Trust) 271 p

Ramesh R and Sarin M M 1992 Stable isotope study of the Ganges (Ganga) river system; *J. Hydrol.* **139** 49–62

Rozanski K, Arguas L A and Gonfiantini R 1993 Isotopic patterns in modern global precipitation; In: *Climate change in continental isotopic indicators geophys mon* **78** *Am. Geophys. Union* 1–36

Williamson J H 1968 Least square fitting of a straight line; *Can. J. Phys.* **46** 1845–1847

World Weather Records 1967 Washington DC: U.S. Dept. of Commerce 4 372

Yurtsever Y and Gat J R 1981 In: *Stable isotope hydrology* (eds) J R Gat and R Gonfiantini (IAEA Tech Rep Ser) **210** 103–142

Climatic significance of D/H and ^{13}C/^{12}C ratios in Irish oak cellulose

M G L BAILLIE[1], J R PILCHER[1], A M POLLARD[2] and R RAMESH[3]

[1]*Palaeoecology Centre, Queen's University, Belfast, BT7 1NN, UK*
[2]*Department of Archaeological Sciences, University of Bradford, Bradford, BD7 1DP,UK*
[3]*Physical Research Laboratory, Ahmedabad 380 009, India.*
[3]*email: ramesh@prl.ernet.in*

δD and δ^{13}C analyses of cellulose nitrate from two modern Irish oak trees that form part of the 7400 year long chronology were carried out, covering a period of 123 years (1861–1983 A.D.) with a 5 year resolution so as to assess the potential of this long chronology for retrieval of palaeoenvironmental data. One of the trees (Q5293) showed significant correlations of δD, δ^{13}C and ring width with mean annual temperatures as recorded at the Armagh weather station nearby and the mean fall temperatures of Central England. The other tree (Q5296) did not exhibit any significant climatic correlations either because it grew utilizing a nearby permanent source of ground water or because the intra-ring isotopic variations in Irish oak are significant enough to mask the climatic signal. Whilst our results have given a positive indication of the usefulness of these trees for palaeoenvironmental information, more trees need to be analysed to confirm our findings.

Even though one of the trees did not exhibit climatic correlations, both trees show a significant positive correlation of δ^{13}C and a negative correlation of δD with ring width variations. Furthermore, two tree samples that grew during the 1620s B.C., when a volcano is thought to have erupted on the Aegean island of Santorini, show increased δD and decreased δ^{13}C for one to two decades following the eruption, though the magnitudes of change seem to vary with site and trees. We have proposed a possible mechanism based on tree phenology to explain both the above effects.

1. Introduction

Information on the variations of marine climate over the past several hundred thousand years has been obtained by numerous studies of the oxygen and carbon isotope ratios in marine invertebrate shells preserved in ocean sediments, with a typical resolution of a few thousand years (Shackleton and Opdyke 1973; Duplessy 1978). Similar studies on long tree ring chronologies can yield information on climatic changes on land, potentially with a resolution of one year. This is because trees that lay down annual growth rings preserve a chronological record of regional environmental changes. A large number of studies on the relationship between instrumentally measured climatic parameters (e.g., temperature, rainfall and relative humidity) on the one hand and ring width, ring density and stable isotope ratios of hydrogen, carbon and oxygen (δD, δ^{13}C and δ^{18}O respectively) on the other hand have shown that in many instances the spatial and temporal climatic variations are indeed recorded by trees (Fritts 1976; Hughes *et al* 1982; Yapp and Epstein 1982a, 1982b; Ramesh *et al* 1985, 1986a, 1986b; Pant *et al* 1988). Furthermore, specific events such as volcanic eruptions may leave their imprint on trees, thereby giving us a means to study the accompanying climatic changes (Baillie and Munro 1988).

Three long ring chronologies have so far been developed. Firstly, the bristlecone pine (*Pinus aristata* and *Pinus longaeva*) chronology from the White Mountains, California, USA, covering a period of

Keywords. Tree-rings; Irish oak; hydrogen isotopes; carbon isotopes; palaeoclimate.

8681 years (Ferguson and Graybill 1983). Secondly, the oak (*Quercus robur* and *Quercus petraea*) chronology for Germany, now going back approximately 9200 years (Becker and Schmidt 1989). Thirdly, the oak chronology for Northern Ireland, U.K., which now extends back approximately 7400 years before present. In addition, several shorter tree long chronologies exist. Some of them are: 1089 year chronology of Huon pine from Tasmania (Cook *et al* 1992), 800 year chronology of *Chamaecyparis obtusa* from central Japan (Sweda 1994; Sweda and Takeda 1994) and >300 year chronologies of *Cedrus deodara* from Himalaya, India (Bhattacharyya and Yadav 1990; Borgaonkar *et al* 1996; Yadav *et al* 1997).

1.1 *Previous work*

So far, stable isotopic investigations of these long chronologies are limited. Epstein and Yapp (1976) measured δD values for a 1000 year period in the bristlecone pine chronology. They demonstrated a qualitative positive correlation between the long term trends (40 year means) in the δD values and Central England winter temperatures (long temperature records are not available in the USA). $\delta^{13}C$ values were measured on the same specimens by Grinstead *et al* (1979), for the same 1000 years period. They showed a negative correlation between long term (50 year means) trends in $\delta^{13}C$ values and Central England temperatures (in both the cases, the comparison of δ values with temperature trends was for a span of 900 to 1000 years). However, the δD and $\delta^{13}C$ variations in tree cellulose were not significantly related to each other. Grinstead and Wilson (1979) also measured $\delta^{13}C$ values in a single Kauri tree (*Agathis australis*) that grew in New Zealand during the same 1000 year period. Again, they compared the long term (50 year means) trends in $\delta^{13}C$ values and Central England temperatures. In this case, they found a positive correlation. More recently, Stuiver and Braziunas (1987) reported the mean $\delta^{13}C$ values of 19 North American trees of different species collected from different latitudes, for a period of 2000 years. They compared the long term (40 to 50 years) means of $\delta^{13}C$ values with those of general Northern Hemisphere temperature indices, derived from Central England temperatures, California (White Mountains) tree ring width indices and Greenland ice sheet $\delta^{18}O$ values. They observed a positive correlation between the two variables, but only after introducing a 70 to 90 year lag in the $\delta^{13}C$ values. With a similar lag, they also found a negative correlation between $\delta^{13}C$ values and acidity peaks in Greenland ice sheets (Hammer *et al* 1980). They argued that higher acidity in the ice sheets corresponded to higher volcanic activity, which throws dust into the stratosphere and consequently cools the

atmosphere, thereby reducing $\delta^{13}C$ values in tree cellulose.

Epstein and Krishnamurthy (1990) analyzed 23 trees of different species from widely differing locations for δD and $\delta^{13}C$. One sample of bristlecone pine covered the last 1000 years, but the majority of samples spanned less than 200 years. They concluded from the δD values that the earth's temperature has risen over the last 100 years, and probably over the last 1000 years, with the rate being higher in the cooler regions. More recently, Feng and Epstein (1994) reported a 8000 year δD record from North American bristlecone pines. They found evidence for a post-glacial climatic optimum 6800 years ago and a continuous cooling since then.

There are number of shortcomings associated with some of the above studies. Firstly, whilst trees can yield information with a very high resolution of one year, all the above studies deal with long term average trends. Second, since long temperature records are not available near the tree sites, tree ring data are compared with British temperature records. Obviously, British climate is very different from the arid climate of South West USA, where the bristle cone pines grow, or the climate of New Zealand, where the Kauri trees thrive. Thirdly, there are specific problems with each of the above studies. The methodology used by Epstein and Yapp (1976) for preparation of cellulose nitrate from wood for δD measurements is known to yield inconsistent results (DeNiro 1981). In Grinstead *et al*'s (1979) study the $\delta^{13}C$ of two bristlecone pine trees did not match either in their magnitude or in the general trend for the 90 year period overlap. Additionally, the bristle cone pines grow at high altitudes (~3000m above mean sea level) where relative humidities are generally low. This will result in a higher evapotranspiration rate and affect the $\delta^{13}C$ values of the tree apart from temperature (Ramesh *et al* 1986b). Grinstead and Wilson's (1979) study is not based on a well developed tree ring chronology, but a single specimen of Kauri tree. This might give rise to dating errors of a few years (this is perhaps one of the reasons why $\delta^{13}C$ values were averaged for 50 years before comparing them with temperature records). Furthermore, a single tree growing for about 1000 years will have age related physiological changes which might obliterate to some extent the climate dependence of $\delta^{13}C$ values. Also, unlike the bristle cone pine trees, the kauri tree shows a positive correlation with temperature trends. The opposite behavior of two trees (analysed by the same authors) from two hemispheres is puzzling (Ramesh 1984). The trees analysed by Stuiver and Braziunas (1987) are also not part of a standardized tree ring chronology. Additionally, $\delta^{13}C$ values of six different species growing in different periods of time were used to derive the mean $\delta^{13}C$ curve. It is known that different species have slightly different responses to changing

climate (Ramesh *et al* 1986b). Two bristlecone pines (BrPn2 and BrPn3) analyzed by Feng and Epstein (1994), had an overlapping period of ~1000 years, but they do not show similar variations, casting serious doubt on the validity of climatic reconstruction based on stable isotope measurements in a few trees.

Thus, although the existing work on relatively long (1000 to 2000 years) tree ring sequences has demonstrated a gross correlation between isotope ratios and temperature, there is still much scope for careful detailed investigations on long tree ring chronologies to obtain high resolution information on post-glacial climatic changes on land.

1.2 *Objectives of the present work*

The aim of the present work is two-fold. Firstly, to investigate the climatic significance of δD and $\delta^{13}C$ variations in modern Irish oak trees, which form part of the 7400 year long chronology developed by Baillie and co-workers (Pilcher *et al* 1984; Baillie and Brown 1988). Secondly, to determine the effect (if any) of the proposed major volcanic eruption of the Aegean island of Santorini in 1628 B.C. on the isotope variations in the oak trees of the Irish chronology.

The Irish oaks grow at low altitudes (<200m above mean sea level), where the relative humidities are more than 80% throughout the year. The trees have a life span of about 150 to 250 years, thus reducing the chances of major age-related physiological effects on isotope ratios in cellulose. Also, being ring-porous,

their rings are clear and unambiguous. They do not suffer from missing or double rings (Baillie 1973). Finally, they grow relatively much closer to Central England, where long temperature records are available. However, since oaks are known to store their photosynthates of a particular year in the parenchyma cells for use in the next year's growth, it was decided to measure the isotope ratios in groups of 5 rings rather than individual rings. This, we believe, would, to some extent, reduce the autocorrelation between the isotope ratios of successive sample intervals.

2. Sample selection

We chose two healthy-looking tree samples (Q5293 and Q5296) from the collection at the Palaeoecology Centre, Queen's University, Belfast. These trees grew in Castle Coole, Co. Fermanagh, Northern Ireland, U.K. (54°20′N, 7°36′W). Q5293 was 123 years old (1861 to 1983 A.D.) and Q5296 was 273 years old (1711 to 1983 A.D.). A period of 123 years (1861 to 1983 A.D.) was chosen for stable isotopic analysis, because rainfall and temperature records for this period are available from the Armagh Weather Observatory, situated about 60 km away from the sample location (figure 1).

For determining the effect of the Santorini eruption on the isotope ratios in oaks, we selected two trees that grew during the period 1641 to 1590 B.C. One was Q5392 from Sentry Hill, Co. Antrim and the
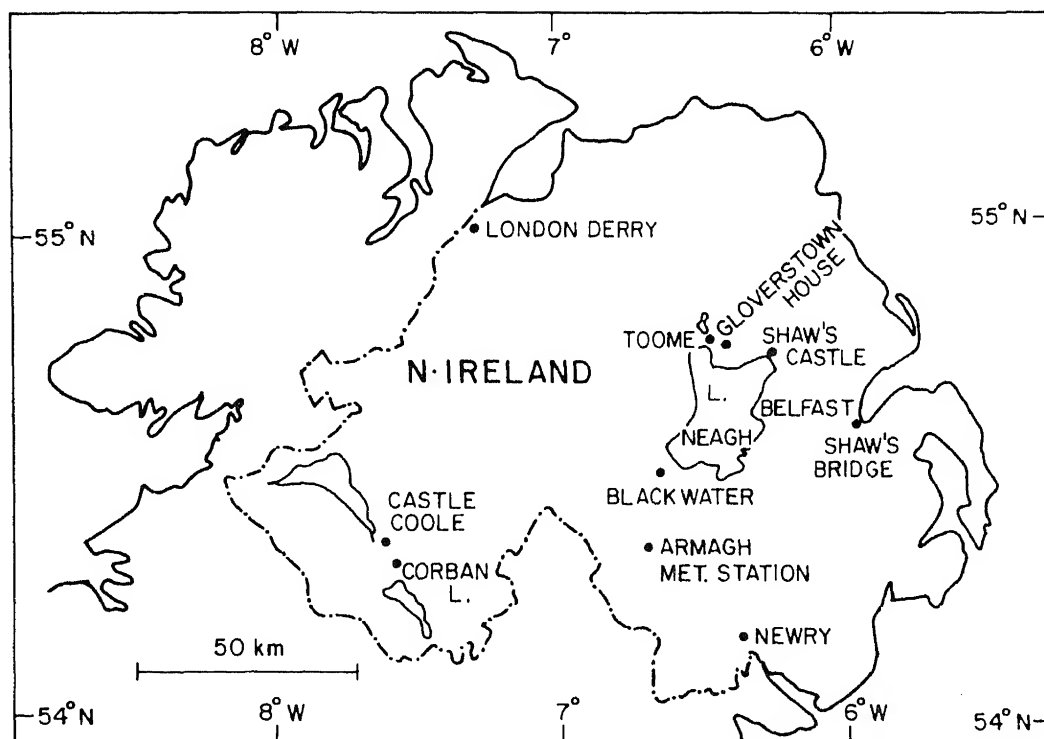

Figure 1. Map of northern Ireland showing sample locations and Armagh weather station.

other, Q1276 from Derryland, Co. Armagh. Both these trees showed very narrow rings in the 1620s B.C. Also, Q1276 showed a color change beginning 1628 B.C. and Q1276 showed anomalously small early wood vessels in the growth ring for 1625 B.C. These two trees, however, grew rooted in the peat of raised bogs (Baillie and Munro 1988), unlike the modern trees Q5293 and Q5296 which grew in normal soils; isotopic responses may therefore be different between the two periods.

3. Experimental methodology

Twenty four samples, each covering 5 year intervals from 1861–5 A.D. to 1976–80 A.D., and one sample covering 3 years, 1981–83 A.D. were cut from each of the modern trees Q5293 and Q5296.

Six samples of 10 year intervals from 1651–40 B.C. to 1600–1591 B.C. were cut from each of the prehistoric samples Q5492 and Q1276. Furthermore, the 1630–21 B.C. block of Q1276 was cut into five sub-samples, each covering a two year period from 1630–29 B.C. to 1622–21 B.C. so as to detect the effect of the proposed Santorini eruption in 1628 B.C.

All four tree samples were in the form of radial strips approximately 30mm × 30mm across. Each of the samples was powdered in a Wiley mill and the 40 to 60 mesh size fraction was recovered. Cellulose was extracted and nitrated using a mixture of nitric and phosphoric acids to remove the 30% hydrogen atoms in cellulose which might have undergone isotopic exchange with modern waters. The cellulose nitrate, which contains only the non-exchangeable carbon-bound hydrogen, was then combusted with copper oxide at 800°C and carbon dioxide was quantitatively collected for $\delta^{13}C$ measurement. The water of combustion was passed through metallic uranium at 800°C to convert it into hydrogen gas, which was then quantitatively recovered for δD measurement. Standard procedures were followed throughout and details are reported elsewhere (Ramesh *et al* 1988). The δD and $\delta^{13}C$ values were measured using two mass spectrometers (both VG Micromass 602D) with an overall precision of ±2‰ and ±0.1‰ respectively. The values are reported relative to international standards SMOW (Standard Mean Ocean Water) and PDB (Belemnitic calcium carbonate from the Pee Dee formation, South Carolina, USA) respectively.

Ring width values were measured with an optical microscope to a precision of 0.02 mm. Total ring growth (denoted here as ring width) for the 5 year (or 3 year) blocks were calculated from these data.

4. Results

The δD, $\delta^{13}C$ and ring width values for the two trees Q5293 and Q5296 are presented in table 1. δD and

Table 1. δD_{SMOW} (‰), $\delta^{13}C_{PDB}$(‰) *and ring width (mm) values for the two trees Q and Q5296. Analytical uncertainties (1σ) are* ± 2‰, ± 0.1‰ *and 0.02 mm respectively.*

Years (A.D.)	Q5293			Q5296		
	δD	$\delta^{13}C$	R.W.	δD	$\delta^{13}C$	R.W.
1861–65	−60	−25.3	17.70	−43	−24.4	9.40
66–70	−58	−24.1	24.74	−38	−24.2	7.04
71–75	−63	−23.9	26.60	−42	−24.8	8.28
76–80	−63	−24.3	20.40	−39	−24.2	10.02
81–85	−62	−24.3	17.92	−38	−23.8	7.12
86–90	−62	−23.8	16.36	−43	−24.2	7.28
91–95	−58	−24.1	16.16	−40	−24.5	8.88
1896–1900	−61	−24.1	14.96	−40	−24.8	8.62
1901–5	−62	−25.0	6.46	−43	−24.4	7.32
06–10	−57	−24.6	7.00	−37	−24.8	6.30
11–15	−63	−24.0	11.44	−37	−24.6	6.14
16–20	−58	−24.9	11.48	−39	−25.1	6.06
21–25	−51	−25.0	8.76	−33	−25.4	4.18
26–30	−50	−25.5	5.40	−38	−24.8	4.16
31–35	−50	−25.4	6.68	−37	−24.6	5.58
36–40	−53	−25.4	6.42	−28	−24.6	4.08
41–45	−46	−25.6	6.64	−38	−24.6	7.90
46–50	−58	−25.3	8.30	−45	−24.2	13.72
51–55	−52	−26.0	7.46	−46	−24.4	10.32
56–60	−54	−25.5	6.28	−50	−24.4	9.06
61–65	−52	−25.6	7.06	−46	−25.5	4.10
66–70	−54	−25.8	6.68	−35	−25.0	5.00
71–75	−54	−26.2	6.96	−35	−24.5	4.94
76–80	−52	−26.9	6.88	−38	−24.7	5.44
81–83	−38	−26.1	3.52	−43	−24.0	6.04

Table 2. δD_{SMOW} (‰) and $\delta^{13}C_{PDB}$ (‰) values for two trees, Q5392 and Q1276. Analytical uncertainties are ±2‰ and ±0.1‰, respectively.

Q5392			Q1276		
Years (B.C.)	δD	$\delta^{13}C$	Years (B.C.)	δD	$\delta^{13}C$
1591–1600	−48	−27.5	1591–1600	−40	−25.5
1601–1610	−47	−28.0	1601–1610	−43	−26.1
1611–1620	−47	−28.3	1611–1620	−51	−26.7
1621–1630	−35	−28.3	1621–1622	−47	−26.7
			1623–1624	−55	−26.2
			1625–1626	−45	−25.7
			1627–1628	−47	−24.9
			1629–1630	−41	−25.5
1631–1640	−51	−28.2	1631–1640	−48	−25.2
1641–1650	−54	−27.8	1641–1650	−58	−26.1

$\delta^{13}C$ data for Q5392 and Q1276 are given in table 2. The δD values for the two trees Q5293 and Q5296 are shown in figure 2, $\delta^{13}C$ values in figure 3 and ring width values in figure 4. δD and $\delta^{13}C$ values of Q5392 and Q1276 are shown in figure 5.

5. Discussion

5.1 *Modern Trees*

The range of variation in the δD values is 25‰ for Q5293 and 22‰ for Q5296, more than ten times the experimental uncertainty of ±2‰ (1σ). For $\delta^{13}C$, the ranges are 3.1‰ and 1.4‰ respectively, again more than ten times the uncertainty of +0.1‰ (1σ). Ranges in the ring width variations are 23.08mm and 9.64mm (5 year total ring widths) respectively. The common variance between the two trees in the δD, $\delta^{13}C$ and ring width signals are 12.3%, 12.1% and 36.4% respectively. These values were calculated using a procedure for analysis of variance outlined by Fritts (1976). The δD, $\delta^{13}C$ and ring width variations of the two trees are not similar, as is evident from figures 2, 3, and 4. The actual geographical distance between the two trees is not known. There are two conceivable reasons for the discrepancy between the signals from these two trees. First, the intra-ring isotopic variation might be so large a mask the similarity between the isotopic variations in the two trees, especially considering the measurements were carried out only along a single radial strip from each tree. Second, one of the trees could have grown near a permanent source of ground water and therefore does not reflect the variations in the δD of rainfall and consequently the climatic variations.

Straaten (1981) has measured the intra-ring isotopic variation for δD in a Dutch red oak tree (*Quercus rubra*) ring which formed in 1970 A.D. He found the magnitude to be about 16‰. Tans and Mook (1980) measured $\delta^{13}C$ values in 4 Dutch red oak trees, observing a maximum difference of 4.4‰ in the $\delta^{13}C$ values along the circumference of a single growth ring. However, while Straaten (1981) found that the
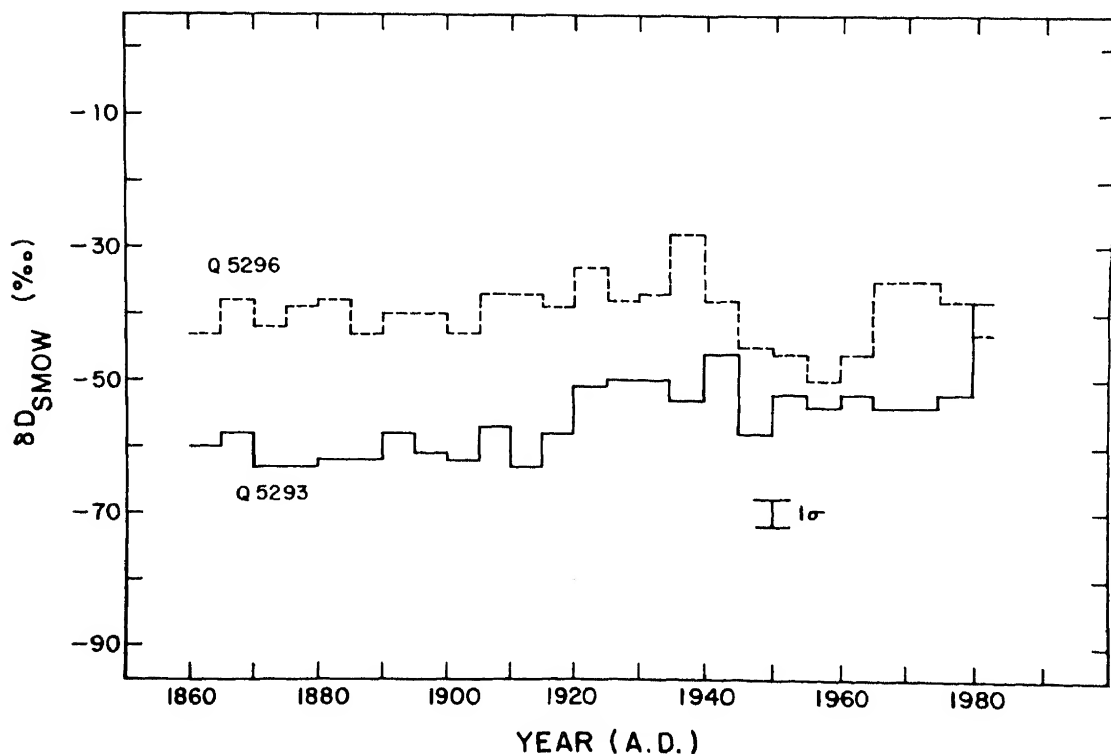

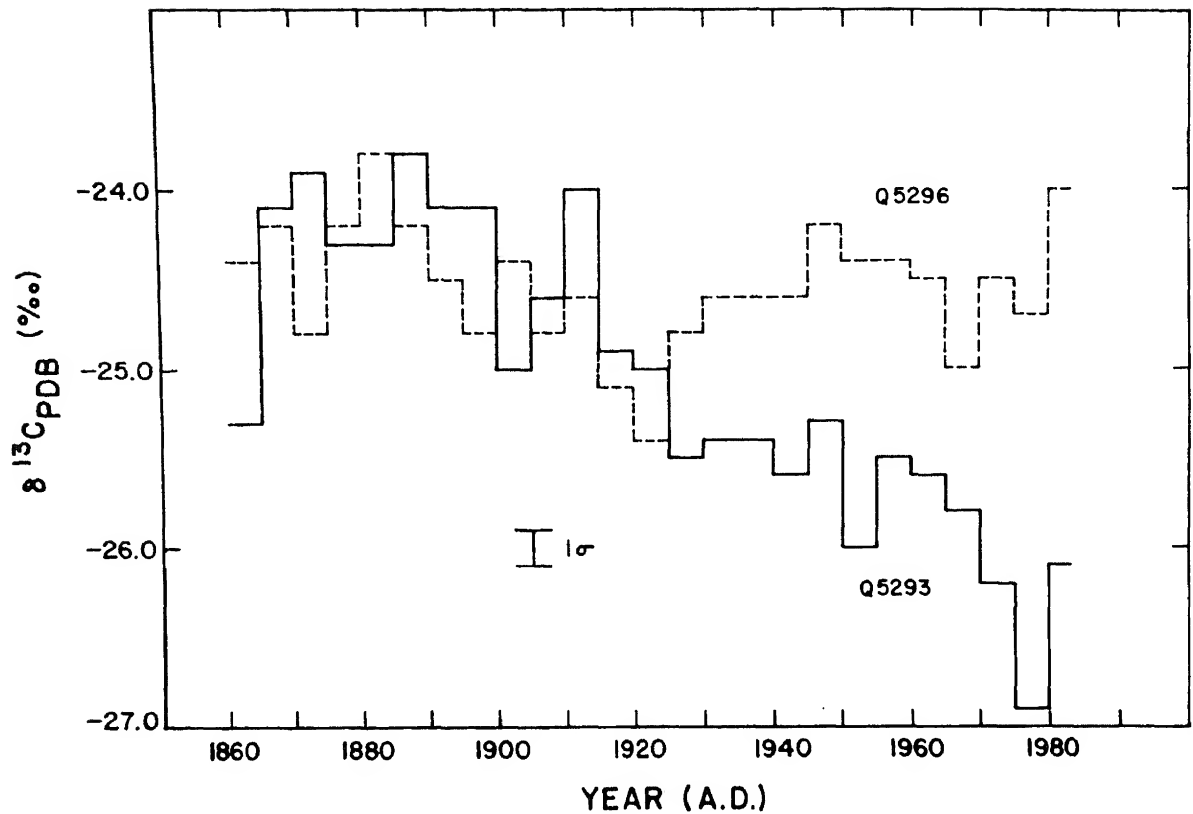Figure 2. δD variations of two Irish oak trees (Q5293 and Q5296) from 1861 to 1983A.D.

Figure 3. $\delta^{13}C$ variations of two Irish oak trees (Q5293 and Q5296) from 1861 to 1983 A.D.
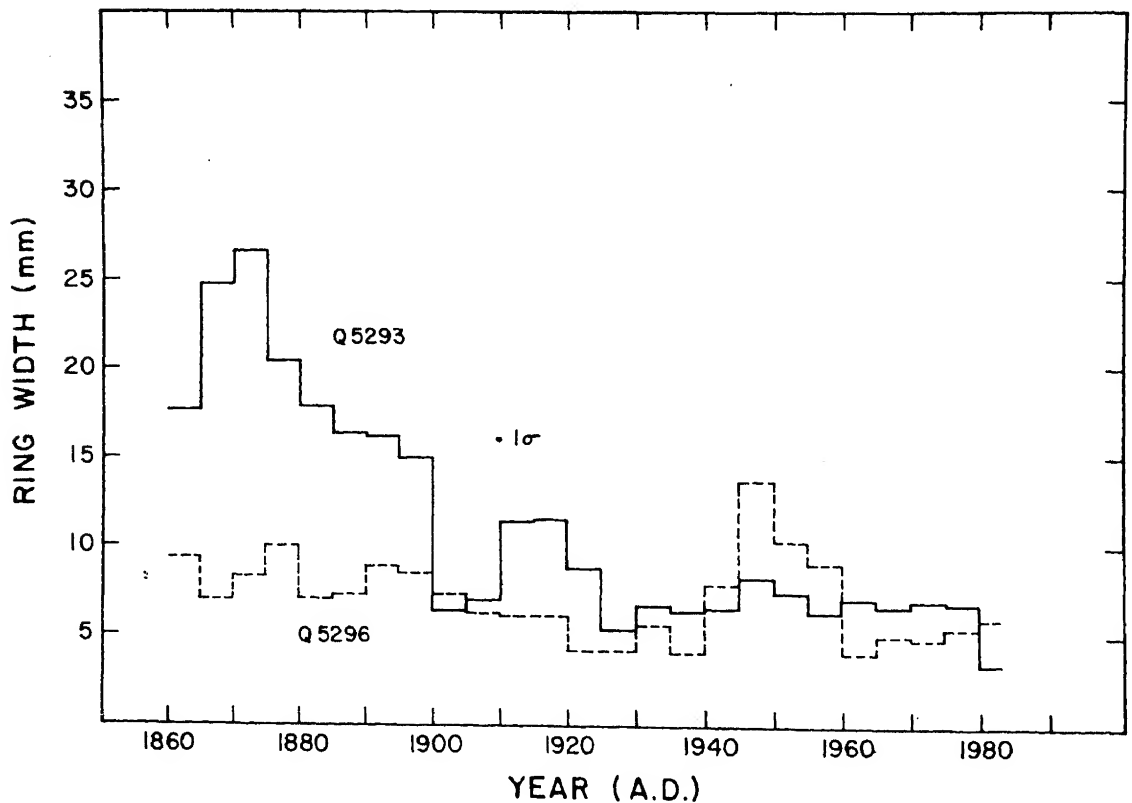

Figure 4. Ring width variations of two Irish oak trees (Q5293 and Q5296) from 1861 to 1983 A.D. (here ring width denotes five year total ring growth).
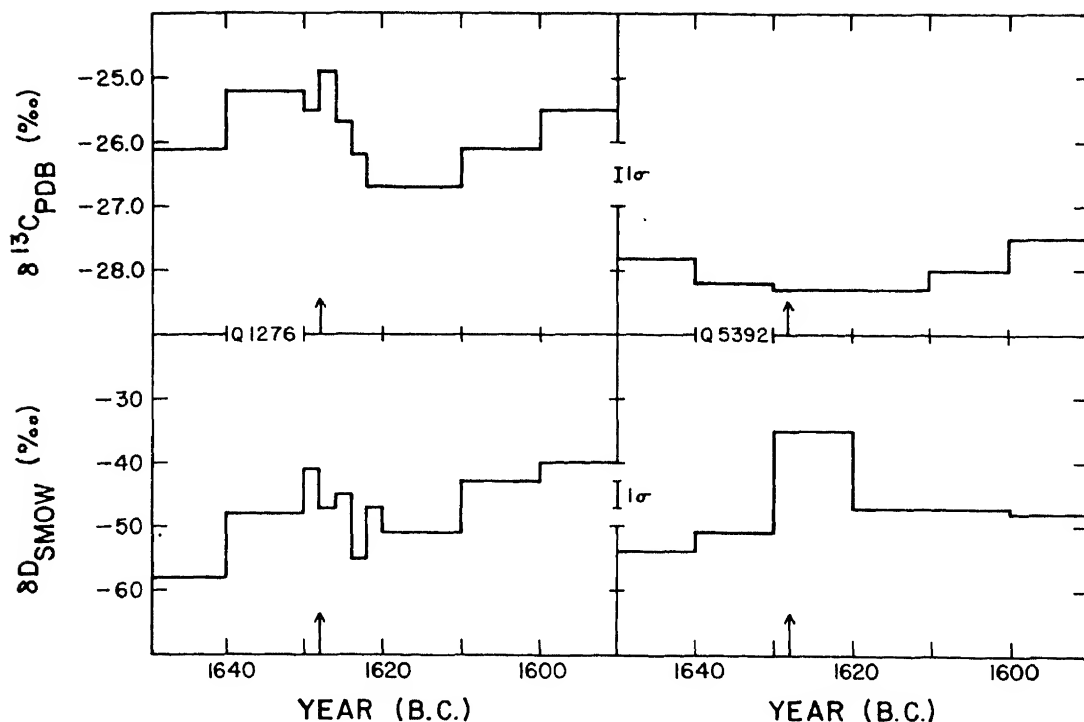
Figure 5. δD and $\delta^{13}C$ values of two Irish bog oaks (Q1276 and Q5392) for the period 1650 to 1591 B.C. Arrows denote the likely year of volcanic eruption in the Aegean island of Santorini, 1628 B.C. (Baillie & Munro 1988).

intra-ring δD variation was unsystematic for an 11 year period (1962 to 1972 A.D.), Tans and Mook observed that the year to year variations of $\delta^{13}C$ among different radial directions were more or less similar. They also state that similar results have been obtained for *Quercus robur*. If the limited data on the intra-ring isotopic variability in oak trees is indeed true, then a large number of trees in a site must be analysed and mean δD, $\delta^{13}C$ curves derived before attempting correlations with climatic parameters. Nevertheless, we computed the linear correlation coefficients between δD, $\delta^{13}C$ and ring width values of the two trees and the mean annual temperature (t), the mean annual maximum temperature (t_{max}) and the total annual rainfall (r) between March and

October (taken to be the growing season for Irish oaks). The climatic parameters were available from the Armagh weather observatory. These results are presented in table 3.

The tree Q5293 shows significant (at the 0.05 confidence level) positive correlations between δD and $t(0.66)$, and δD and t_{max} (0.63); predictably, t and t_{max} are themselves highly correlated (0.89). The tree also shows significant negative correlations between $\delta^{13}C$ and t (-0.66), $\delta^{13}C$ and t_{max} (-0.59), $\delta^{13}C$ and r (-0.46), ring width and t (-0.68) and, finally, ring width and $t_{max}(-0.83)$.

The above significant correlations with climatic parameters seem to indicate that Q5293 was a tree which grew utilizing mainly rain water for its growth

Table 3. *Linear correlation matrix between δD, $\delta^{13}C$, ring widths of the two trees Q5293 and Q5296 (δD_1, $\delta^{13}C_1$, R.W.1 and δD_2, $\delta^{13}C_2$ and R.W.2 respectively) and Armagh mean annual temperature (t), mean annual maximum temperature (t_{max}) and March-October rainfall (r). No. of data points = 22.*

	δD_1	$\delta^{13}C_1$	R.W.1	δD_2	$\delta^{13}C_2$	R.W.2	t	t_{max}	r
δD_1	1.0	−0.77	−0.67	0.17	−0.37	−0.36	0.66	0.63	0.24
$\delta^{13}C_1$		1.0	0.76	0.09	0.20	0.11	−0.66	−0.59	−0.46
R.W.1			1.0	−0.06	0.32	0.29	−0.68	−0.83	−0.35
δD_2				1.0	−0.40	−0.59	−0.04	+0.02	−0.44
$\delta^{13}C_2$					1.0	0.50	−0.29	−0.36	−0.05
R.W.2						1.0	0.02	−0.06	0.12
t							1.0	0.89	0.38
t_{max}								1.0	0.30

and did not have a permanent source of ground water nearby. This is also evident from the fact that the ring width of this tree shows a steady decreasing trend (figure 3) from 1860 to 1983 A.D. (figure 4), and the $\delta^{13}C$ values show a steady declining trend, probably because of fossil fuel injections into the atmosphere subsequent to the world-wide development of large scale industries after 1850 A.D., known as the Suess effect. Most normal trees analysed so far have shown these trends (Epstein and Krishnamurthy 1990).

The other tree, Q5296, appears to be an exception in that it does not show these trends. Furthermore, as evident from table 3, the δD, $\delta^{13}C$ and ring width values of this tree do not show significant correlation with climatic parameters, except for δD, which shows a barely significant negative correlation with r (-0.44). It seems likely that this tree utilized a permanent source of ground water nearby and consequently the ambient climate is not the main governing factor for its isotope or ring width variations. As suggested earlier in this section, this could perhaps be one possible reason for the absence of any similarity between the two trees in their δD, $\delta^{13}C$ and ring width time series.

It is also evident from table 3 that both trees show significant (at the 0.05 level) correlations between isotope ratios and ring width; positive in the case of $\delta^{13}C$ (0.76 for Q5293, 0.50 for Q5296) and negative in the case of δD (-0.67 and -0.59 respectively for Q5293 and Q5296). Such correlations have been reported earlier by a few workers (Ramesh *et al* 1988). This observation has led to a few speculative explanations. Of these, the most likely is that the climatic parameters have an opposing effect on the isotope ratios (δD for example) and the ring width. It has been argued that lower rainfall results generally in smaller ring width; at the same time the δD of rainfall is higher because of the 'amount effect' present in the rainfall (Dansgaard 1964). If the source water for a tree is mainly rainfall, the δD of tree cellulose would also be higher in such a condition. One would then expect a negative correlation between δD values and ring width. This explanation is not tenable in the present case because the ring width variations of neither tree show a significant correlation with rainfall. Furthermore, the $\delta^{13}C$ values are positively correlated with ring width, unlike the few earlier studies reported so far (Ramesh *et al* 1988). Temperature variations are also not responsible for this effect, because the second tree (Q5296) does not show any correlation with temperature, in δD, $\delta^{13}C$ or ring width variations.

We propose the following explanation as a likely possibility. In cases where ring width variations are not controlled by ambient climatic parameters, then a narrow ring, for example, can be produced by a relative shortfall of nutrients to a tree or because of competition among trees for nutrients. Consequently

the mean assimilation rate (A) of carbon during this period of narrow ring growth will be less. This could imply that the growing season for the tree is limited to a short time, presumably to the summer months, when the ambient humidity is lower and temperature higher than the rest of the normal growing season, especially in the case of the Irish oaks under consideration. Such a condition would mean that the photosynthates produced in the shorter than normal growing season would be enriched in δD values because of the relatively higher evapotranspiration and the consequent enrichment of δD of leaf water, which is the source for synthesis of tree cellulose. Thus one would find a negative correlation between δD and ring width regardless of whether the tree used only rain water for its growth or it tapped water from a nearby permanent source of ground water. Also an "amount effect" is not necessary to be present in the regional rainfall to explain the observed negative correlation between δD ring width.

Similarly, decreased assimilation rate A (narrow ring) would result in a higher $\delta^{13}C$ value for tree cellulose, from the model of Francey and Farquhar (1982). According to this model, the $\delta^{13}C$ value of the cellulose ($\delta^{13}C_p$) is related to the $\delta^{13}C$ of the atmospheric carbon dioxide ($\delta^{13}C_a$), partial pressures of carbon dioxide inside and outside the leaves (C_i and C_a, respectively) through two parameters: a (the difference in the diffusivities of $^{12}CO_2$ and $^{13}CO_2$ in air, about 4.4‰), and b (the biochemical fractionation factor for carbon isotopes during cellulose synthesis, about 30‰).

$$\delta^{13}C_p = \delta^{13}C_a - a - (b-a)C_i/C_a \qquad (1)$$

C_i and C_a are related by the assimilation rate (A) and stomatal conductance (g):

$$C_i = C_a - A/g. \qquad (2)$$

Reduced A will increase C_i and hence decrease $\delta^{13}C_p$. This would lead to a positive correlation between $\delta^{13}C$ and ring width, as has been observed by us. The stomatal conductance of carbon dioxide (g) would not perhaps change, because the trees are not water stressed.

We also performed a stepwise multiple regression analysis (Ramesh *et al* 1986b) of δD, $\delta^{13}C$ and ring width values of each of these trees with the Armagh mean annual temperature (t), mean annual minimum and maximum temperatures (t_{min}, t_{max}) and total rainfall during the growing season (r). Again, we found that in the case of the first tree, Q5293, δD and $\delta^{13}C$ were related only to t whilst ring widths were related to t_{max}. Rainfall did not explain any significant additional variance in the δD, $\delta^{13}C$ and ring width values. In the case of the second tree, Q5296, no correlations were found, except that the δD values showed a barely significant correlation with r. The regression equations are:

For tree Q5293:

$$\delta D = -(145 \pm 3) + (9.78 \pm 2.51)t$$

$$\text{Correlation coefficient } R = 0.66 \qquad (3)$$

$$\delta^{13}C = -(12.77 \pm 0.34) - (1.34 \pm 0.34)t$$

$$R = -0.66 \qquad (4)$$

$$\text{Ring width (mm)} = (134.5 \pm 3.2) - (9.81 \pm 1.49)t_{max}$$

$$R = -0.82 \qquad (5)$$

For tree Q5296:

$$\delta D = -(3.65 \pm 4.44) - (0.013 \pm 0.006)r$$

$$R = -0.44 \qquad (6)$$

The autocorrelations of residuals (observed-calculated values) were not significant except in the case of equation (6). After adjusting the degrees of freedom for the autocorrelation of 0.40, the correlation R of equation (4) is not significant at the 0.05 level.

Gray and Song (1984) have reported temperature coefficients of δD in cellulose nitrate from three white spruce trees that grew in Edmonton, Canada, to be 7.3 ± 2, 13 ± 1 and 15 ± 2. Yapp and Epstein (1985) have reported a value of 14.1 ± 2 for an aspen tree that grew in Fairbanks, Alaska. Ramesh *et al* (1986b) have reported a value of 6.6 ± 2.3 for silver fir trees that grew in Kashmir, India. Within the quoted errors, our value of 9.78 ± 2.51 for the Irish oak (Q5293, equation (3)) agrees well with the above values.

Finally, we calculated the linear correlation coefficients of our tree ring data with Central England temperature and rainfall (Lamb 1977). The climate data were in the form of 3 month averages: December of the previous calendar year to February of the current year (winter); March to May (spring); June to August (summer); September to November (fall); and annual mean values for the current calendar year (January to December). The correlation coefficients are shown in table 4.

Again, the tree Q5293 shows significant correlations of δD, $\delta^{13}C$ and ring width with mean fall tempera-

tures whilst Q5296 does not show any correlation. Q5293 also shows a significant correlation of $\delta^{13}C$ values with mean annual temperature. This confirms our earlier suggestion that the tree Q5296 must have had a local source of ground water, whilst Q5293 had used mainly rainfall for its growth. However, the tree reflects more closely the nearby Armagh temperatures rather than Central England temperatures (A season-wise correlation with Armagh climatic parameters was not attempted because monthly mean data were not available). Neither tree shows any significant relationship with Central England rainfall values. High resolution stable isotope studies such as those of Ogle and McCormac (1994) and Loader *et al* (1995) may help to resolve this problem.

5.2 *Prehistoric samples*

Figure 5 shows that the range in the variations of $\delta^{13}C$ and δD during the period of analysis (1650–1591 B.C.) were 1.9‰ and 18‰ respectively for Q1276 and 0.8‰ and 19‰ respectively for Q5392.

In the case of $\delta^{13}C$, compared to the decade previous to the purported Santorini eruption in 1628 B.C. (1640–1631 B.C.), both trees show a decline during the subsequent two decades (1630 to 1611 B.C.), although Q5392 shows this to a lesser degree (1.5‰ for Q1276 and 0.1‰ for Q5392). Although the decrease of 0.1‰ in Q5392 is not significant, considering the experimental error of ±0.1‰ in $\delta^{13}C$, it is noteworthy that the 1630–1611 B.C. decades are in general lower in $\delta^{13}C$ than other decades prior and after, at least in this tree.

In the case of δD, Q5392 shows an increase of 16‰ (compared to the previous decade, 1640–31 B.C.) during 1630–1621 B.C.; Q1276 also shows a similar increase (1 to 7‰) in all the sub-samples of the 1630–1621 B.C. decade except 1624–23 B.C., where it shows a decrease of 7‰.

The lack of agreement in the magnitudes of isotopic shifts in both the above trees after the Santorini eruption is perhaps partly because of the intra-ring

Table 4. *Linear correlation matrix between δD, $\delta^{13}C$, ring widths of the two trees Q5293 and Q5296 (notations same as in table 3) with Central England climatic parameters. No. of data points = 23.*

	δD_1	$\delta^{13}C_1$	R.W.1	δD_2	$\delta^{13}C_2$	R.W.2
Mean winter temperature	0.00	−0.07	−0.06	0.36	−0.19	−0.18
Mean spring temperature	0.32	−0.31	−0.21	−0.16	−0.02	0.19
Mean summer temperature	−0.25	0.12	0.18	0.00	0.08	0.10
Mean fall temperature	<u>0.54</u>	<u>−0.62</u>	<u>−0.62</u>	−0.15	−0.06	0.10
Mean annual temperature	0.38	<u>−0.41</u>	−0.32	0.12	−0.14	0.08
Mean winter rainfall	−0.02	0.09	0.00	0.40	−0.22	−0.15
Mean spring rainfall	−0.08	−0.15	−0.20	−0.06	−0.15	−0.13
Mean summer rainfall	−0.21	0.00	−0.02	−0.26	0.10	0.22
Mean fall rainfall	−0.01	0.01	0.32	−0.01	0.09	0.11
Mean annual rainfall	−0.07	0.03	0.03	0.16	−0.14	−0.02

study. However, it seems reasonable to believe that, following the volcanic eruption, the δD values tend to increase whilst the $\delta^{13}C$ values tend to decrease, the magnitude of change varying depending on the nature of the site and trees.

Stuiver and Braziunas (1987) have reported a negative correlation of tree cellulose $\delta^{13}C$ trends with Greenland ice sheet acidity peaks. Our results confirm this observation, but such an effect cannot be explained by the decreasing atmospheric temperature that generally accompanies an explosive eruption, caused by dust thrown into the stratosphere. This is because the trees in question grew on peat bogs, which provided a more or less permanent source of water. The trees, therefore, may not have utilized the rainwater directly for their growth to a significant amount. Consequently, even if the δD of precipitation decreased following the general cooling trend, the trees might not record the shifts in rainwater δD.

However, the mechanism proposed by us in the earlier section to explain the correlations between isotope ratios and ring width seems to offer an explanation for this effect as well. Baillie and Munro (1988) argue that pressure changes in the northern hemisphere months after the northern eruptions can produce a negative pressure anomaly over the British Isles. Such anomalies, associated with increased precipitation in the middle latitudes, could have resulted in flooding of the peat bogs and thereby reducing soil aeration. This will lead to a drastic reduction in the ring widths of oaks that grew on marginal bog environments. Consequently the assimilation rate of carbon (A) decreases, which will lead to a reduction of $\delta^{13}C$ in tree cellulose and an increase in δD, as explained previously. However, this result needs to be confirmed by analyzing more tree samples from this region.

explanation for this observation. A reduction in the assimilation rate (A) during the formation of a narrow ring implies decreased $\delta^{13}C$ values for the tree cellulose according to the Francey and Farquhar (1982) model. Furthermore, the growing season is shortened, perhaps to one or two summer months, when the δD of leaf water (and hence that of cellulose) is higher due to increased evapotranspiration.

Our results on the climatic correlations of the two modern oaks indicate that the intra-ring variability in oak trees could be significant enough to prevent the derivation of a climate signal by isotopic analysis of a single radial strip from one tree. Hence, sufficiently large number of trees must be analysed to obtain a mean isotopic curve.

Our results on trees that grew during the 1620s B.C., when the Santorini volcanic eruption is thought to have taken place, show that in general δD values increased and $\delta^{13}C$ values decreased in tree cellulose following the eruption. We have explained this effect with a similar argument presented above for the isotope ratio-ring width correlations.

Acknowledgements

6. Conclusions

We have investigated the potential of the 7400 year long Irish oak chronology for palaeoenvironmental records, by analyzing the δD and $\delta^{13}C$ of two modern trees for a period of 123 years with a 5 year resolution. We find that one tree (Q5293) shows significant correlations of δD, $\delta^{13}C$ and ring width with mean annual temperatures recorded at a nearby weather station, as well as the mean fall temperatures of Central England. The other tree (Q5296), which grew in the same general area, did not show such significant correlations. The reason could be that the latter tree had a permanent source of water nearby and did not record changes in the precipitation δD values and hence climatic temperature. However, both trees

References

Baillie M G L 1973 A recently published Irish tree ring chronology; *Tree Ring Bulletin* **33** 15–28

Baillie M G L and Brown D M 1988 An overview of oak chronologies; In: *Science and Archaeology Glasgow 1987* (ed) E A Slater and J O Tate (Oxford) BAR British Series **196** 543–548

Baillie M G L and Munro M A R 1988 Irish tree rings, Santorini and Volcanic dust veils; *Nature* **332** 344–346

Becker B and Schmidt B 1989 Extension of the European oak chronology to the past 9224 years; *PACT* **29** 1–10

Bhattacharyya A and Yadav R R 1990 Growth and climate relationship in *Cedrus deodara* from Joshimath Uttar Pradesh; In: *Proceedings of the Symposium Vistas in Indian Palaeobotany, Paleobotanist* **38** 411–414

Borgaonkar H P, Pant G B and Rupakumar K R 1996 Ring-width variations in *Cedrus deodara* and its climatic response over the western Himalaya; *Int. J. Clim.* **16** 1409–1422

Cook E R, Bird T, Peterson M, Barbetti M, Buckley B, D'Arrigo R and Francey R 1992 Climate change over the last millennium in Tasmania reconstructed from tree rings; *The Holocene* **2** 205–217

Dansgaard W 1964 Stable isotopes in precipitation; *Tellus* **16** 436–468

DeNiro M J 1981 The effects of different methods of preparing cellulose nitrate on the determination of the D/H ratios of non-exchangeable hydrogen of cellulose; *Earth and Planet. Sci. Lett.* **54** 177–185

Duplessy J C 1978 Isotope studies; In: *Climate Change* (ed) J Gribbin (Cambridge: Cambridge University Press) pp. 46–67

Epstein S and Krishnamurthy R V 1990 Environmental information in the isotopic record in trees; *Philos. Trans. R. Soc. London* **330A** 427–439

Epstein S and Yapp C J 1976 Climatic implications of the D/H ratio of hydrogen in C-H groups in tree cellulose; *Earth Planet. Sci. Lett.* **30** 252–261

Feng X and Epstein S 1994 Climatic implications of an 8000-year hydrogen isotope time series from bristlecone pine trees; *Science* **265** 1079–1081

Ferguson C W and Graybill D A 1983 Dendrochronology of bristlecone pine: a progress report; *Radiocarbon* **25** 287–288

Francey R J and Farquhar G D 1982 An explanation of $^{13}C/^{12}C$ variations in tree rings; *Nature* **297** 28–31

Fritts H C 1976 *Tree Rings and Climate* (New York: Academic Press)

Gray J and Song S J 1984 Climatic implications of the natural variations of D/H ratios in tree ring cellulose; *Earth Planet. Sci. Lett.* **70** 129–138

Grinstead M J, Wilson A T and Ferguson C W 1979 $^{13}C/^{12}C$ variations in *Pinus longaeva* (Bristlecone pine) cellulose during the last millennium; *Earth Planet. Sci. Lett.* **42** 251–253

Grinstead M J and Wilson A T 1979 Variations of $^{13}C/^{12}C$ ratio in cellulose of *Agathis australis* (Kauri) and climatic change in New Zealand during the last millennium; *New Zealand J. Sci.* **22** 230–235

Hammer C U, Clausen H B and Dansgaard W 1980 Greenland ice sheet evidence of post glacial volcanism and its climatic impact; *Nature* **288** 230–235

Hughes M K, Kelly P M, Pilcher J R and LaMarche V C (Jr) 1982 *Climate from Tree Rings* (Cambridge University Press, Cambridge)

Lamb H H 1977 *Climate: Present, Past and Future* Vol. 2 (Methuen, London)

Loader N J, Switsur V R and Field E M 1995 High resolution stable isotope analysis of tree rings: implications of micro-dendroclimatology for palaeoenvironmental research; *Holocene* **5**(4) 457–460

Ogle N and McCormac 1994 High resolution $\delta^{13}C$ measurements of oak show a previously unobserved spring depletion; *Geophys. Res. Lett.* **21**(22) 2373–2375

Pant G B, Rupakumar K and Borgaonkar H P 1988 Statistical models of climate reconstruction using tree ring data; *Proc. Indian Natl. Sci. Acad.* **54**(A3) 354–364

Pilcher J R, Baillie M G L, Schmidt B and Becker B 1984 A 7272 year tree-ring chronology for western Europe; *Nature* **312** 150–152

Ramesh R 1984 *Stable Isotope Systematics in Plant Cellulose: Implications to Past Climate* PhD Thesis, University of Gujarat, India

Ramesh R, Bhattacharya S K and Gopalan K 1985 Dendroclimatological implications of isotope coherence in trees from Kashmir Valley India; *Nature* **317** 802–804

Ramesh R, Bhattacharya S K and Gopalan K 1986a Stable isotope systematics in tree cellulose as palaeoenvironmental indicators – a review; *J. Geol. Soc. India* **27** 154–167

Ramesh R, Bhattacharya S K and Gopalan K 1986b Climatic correlations in the stable isotope records of silver fir (*Abies pindrow*) trees from Kashmir India; *Earth Planet. Sci. Lett.* **79** 66–74

Ramesh R, Bhattacharya S K and Gopalan K 1988 Climatic significance of variations in the width and stable isotope ratios of tree rings; In: *Science and Archaeology Glasgow 1987* (eds) E A Slater and J O Tate (BAR Oxford) BAR British Series **196** 591–609

Shackleton N J and Opdyke N D 1973 Oxygen isotope and palaeomagnetic stratigraphy of equatorial Pacific core V 28–V 38: Oxygen isotope temperatures and ice volumes on a 105 and 106 year scale; *Quat. Res.* **3** 39–55

Straaten C M V 1981 *Deuterium in Organic Matter* PhD Thesis, University of Groningen, Netherlands

Stuiver M and Braziunas T F 1987 Tree cellulose $^{13}C/^{12}C$ isotope ratios and climatic change; *Nature* **328** 58–60

Sweda T 1994 Dendroclimatological reconstruction for the last submillenium in Central Japan; *Terrestrial Atmospheric and Ocean Sciences* **5**(3) 431–442

Sweda T and Takeda S 1994 Construction of an 800 year long *Chamaecyparis* dendrochronology for central Japan; *Dendrochronologia* **11** 79–86

Tans P P and Mook W G 1980 Past atmospheric CO_2 levels and the $^{13}C/^{12}C$ ratios in tree rings; *Tellus* **32** 268–283

Yadav R R, Park W K and Bhattacharyya A 1997 Dendroclimatic reconstruction of April May temperature fluctuations in the western Himalaya of India since AD 1698; *Quat. Res.* **48** 187–191

Yapp C J and Epstein S 1982a A re-examination of cellulose carbon bound hydrogen δD measurements and some factors affecting plant-water D/H relationships; *Geochim. Cosmochim. Acta* **46** 955–965

Yapp C J and Epstein S 1982b Climatic significance of hydrogen isotope ratios in tree cellulose; *Nature* **297** 636–639

Yapp C J and Epstein S 1985 Seasonal contributions to the climatic variations recorded in tree ring deuterium/hydrogen data; *J. Geophys. Res.* **90** 3747–3752

Late Glacial and Holocene Paleolimnology of two temperate lakes inferred from sediment organic δ^{13}C chronology

N A LOVAN and R V KRISHNAMURTHY

Department of Geology, Western Michigan University, Kalamazoo, Michigan, USA.
email: lovan1NA@mail.cmich.edu

The stable carbon isotope (δ^{13}C) and elemental C/N ratios in Total Organic Carbon (TOC) extracted from radiometrically dated cores from two Midwestern USA lakes were determined to investigate the factors that control these values in temperate lakes. The range of δ^{13}C values (-26 to -32‰) and C/N ratios (mean value ~10.8) are typical of values reported for other temperate lake organic matter in this region. In the core from Lake Winnebago, Wisconsin, a negative correlation was seen between the TOC and δ^{13}C, which can be interpreted in terms of a re-mixing and consumption of sedimented organic carbon along with rapid equilibration throughout the water column. No correlation was seen between the TOC and δ^{13}C in the record from Ladd Lake, Ohio, implying that in this latter lake productivity alone was not a singular process controlling the isotope ratio. Here, it is suggested that equilibrium conditions are maintained such that the DIC of the water is never depleted of aqueous CO_2 during high organic production and the resulting δ^{13}C of the organic carbon lacks correlation with the TOC. Further, in this lake a fine resolution analysis was carried out which indicated a possible anthropogenic influence on the isotope ratio around times when human settlement (~300 yrs ago) and enhanced agricultural practices (~80 yrs ago) were significant. The study shows that carbon isotope studies are useful in paleolimnologic investigations.

1. Introduction

The stable carbon isotope ratios (δ^{13}C) of sediment bulk organic matter have been used in discussions of lacustrine carbon cycling to explain variations in lacustrine productivity and atmospheric CO_2 levels (Arthur *et al* 1985; Jasper and Hayes 1990; Hollander and McKenzie 1991; Schelske and Hodell 1991 and 1995). The use of C/N ratio was suggested by Nakai (1972) and coworkers to constrain and assist the interpretation of the source of organic carbon in lake sediments (C/N of lower aquatic organisms <10, while terrestrial plants yield values from 70 to 200). This technique has been successfully applied by numerous others (Krishnamurthy *et al* 1986; Talbot and Johannessen 1992; Meyers and Horie 1993; Meyers 1994). The dissolved inorganic carbon (DIC) in lacustrine environments provides the carbon source for lake organic carbon. Lacustrine DIC is controlled by the DIC of waters that recharge the lake, CO_2 exchange with the atmosphere, and photosynthesis and respiration of the organic matter in the lake. Thus, the δ^{13}C of lacustrine organic carbon can be dictated by water temperature, atmospheric CO_2 concentration, lake productivity and contribution from terrestrial sources. Jasper and Hayes (1990) and Rau *et al* (1991) have argued that atmospheric CO_2 is a determinant of the ultimate isotopic carbon ratio of sedimentary organic matter. This study examines the isotopic carbon signal from sediment organic carbon in two Midwestern USA lakes.

2. Study Area

Samples used in this study came from radiometrically dated cores raised from Ladd Lake (44° 09′ N; 88° 10′ W) in northwestern Ohio and Lake Winnebago

(44° 09′ N; 88° 10′ W) in east central Wisconsin (figure 1). Many, if not most, of the Midwestern USA lakes were formed in glacial drift as kettle or pro-glacial lakes related to the last glacial advance of the specific area. The oldest dates, 14,680 radiocarbon years before the present (^{14}C yr BP) for the Ladd Lake core and 12,050 ^{14}C yr BP for the Lake Winnebago core, are consistent with geological observations in both areas that these lakes formed at the termination of the last glacial period in response to a melting and retreating ice mass (uncalibrated radiocarbon dates are used throughout this paper).

Ladd Lake is located on the outer edge of the Fort Wayne moraine. The predominant local landform is the lake plain formed by a series of pro-glacial lakes ancestral to Lake Erie that filled the Lake Erie basin. The ice free date for Ladd Lake corresponds to ~14,500 to 14,000 ^{14}C yr BP (Shane, personal communication). Lewis and Anderson (1992) reported that the ice was out of Ohio and the Lake Erie Basin by 14,100 radio-

carbon years BP. The various glacial levels of Lake Erie do not affect Ladd Lake directly as it is outside the maximum Erie basin of Lake Maumee. Shane (1987, 1991) suggested that modern south to north climatic gradients were not established until about 11,000 years ago, being several thousand years after the area was free of glacial ice.

Lake Winnebago is a 747 km^2 lake (45 km × 16.6 km), having an average and very uniform depth of 5.3 meters (Smith 1997). The contemporary lake is a remnant of the larger glacial Lake Oshkosh that occupied the lake basin during the Two Rivers-Younger Dryas advance 11 to 8 k ^{14}C yr BP (Thwaites 1943; McKee and Laudon 1972; Smith 1997). During the Two Rivers oscillation the Green Bay lobe of the Laurentide ice sheet re-advanced over Two Creeks-age forests (12.5–11 k yr BP) to a position along the northern end of contemporary Lake Winnebago. Here, it deposited a low moraine that now forms the retaining dam of the lake and marks the terminal
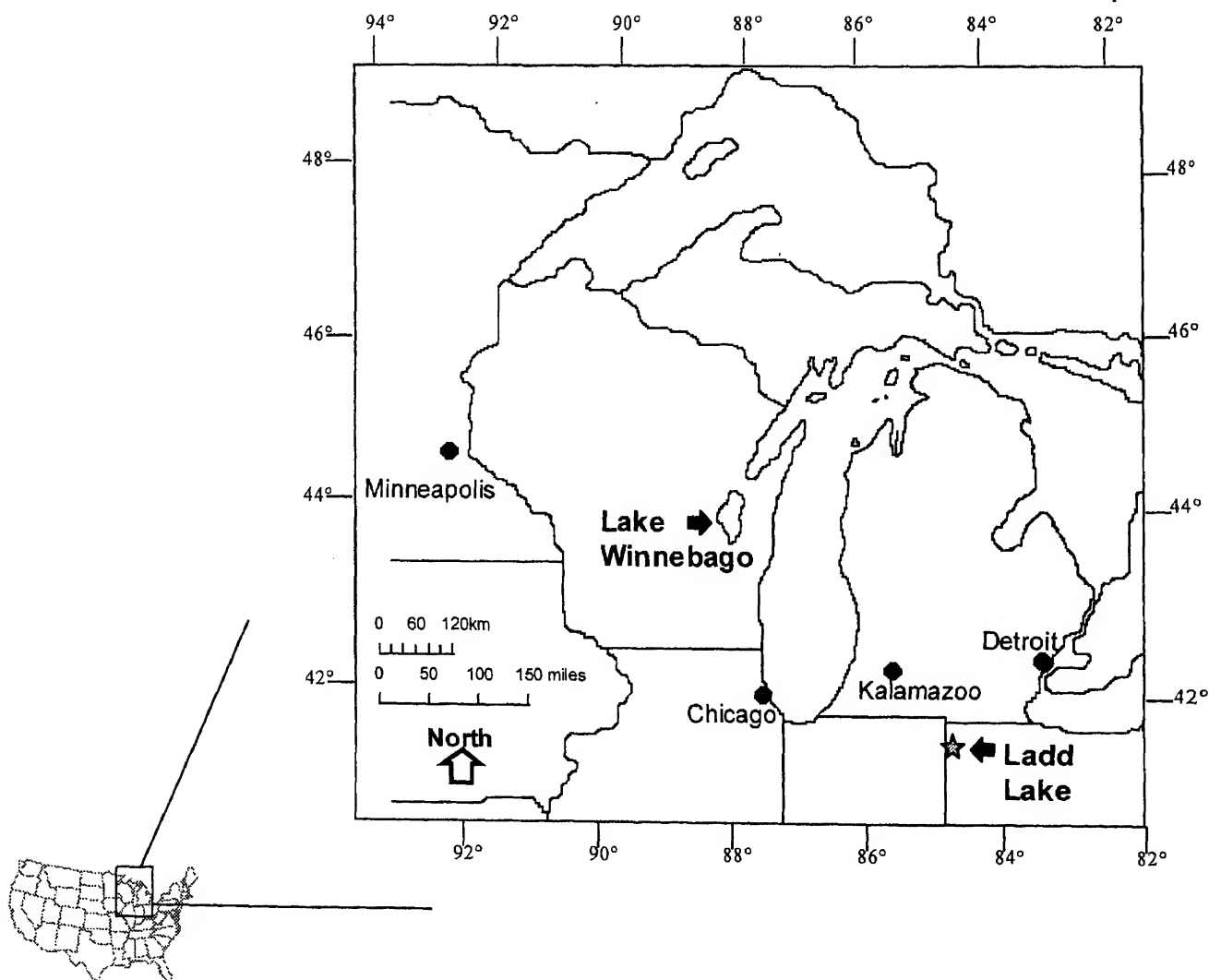

Figure 1. Map showing the Midwestern United States and the location of Ladd Lake in northwestern Ohio and Lake Winnebago in east-central Wisconsin (exploded view).

position of the last glacial re-advance in the area (Smith 1997). A 23-meter drop in lake-level, to near modern levels, has been documented by mapping the elevations of raised paleo-shorelines and outlets (Weidman 1911; Thwaites 1943). Groundwater provides a major source of recharge to the lake (Smith, personal communication). The lake is seasonally ice covered at which time the groundwater charges the lake with dissolved solids (420 ppm in late winter) emanating from the carbonate bedrock (Olcott 1966) and carbonate-rich glacial drift aquifers. Olcott (1966) reports a seasonal variation in the pH of the lake water with winter pH values of 7.4 compared to summer pH values of 8.4 indicating that the lake is a HCO_3-dominated system.

3. Sample collection and radiocarbon chronology

The 12-meter Ladd Lake core was raised in November, 1986, by the University of Minnesota Limnologic Research Center using a 5 cm diameter Wright-Livingston piston sampler. Samples were extracted in 1995 for isotopic analysis using washed and modified (blunt cut) plastic 3, 6 and/or 10 cc syringes then extruded using the syringe plunger. Approximately 3 to 5 grams of sediment was collected for each sample. Individual samples were collected at 4 to 5 cm intervals over the length of the core. Approximately 300 samples were removed and 137 were processed for use in this study. Workers from Lawrence University in Appleton, Wisconsin, raised several vibracores from the north-central portion of Lake Winnebago during the summer of 1995. Sixty sediment samples from core LW7, a single 3-meter core, were extracted and provided for stable isotope study. Sediment samples were extracted using an acid-washed plastic utensil then individually placed into separate new, acid-washed and pre-labeled 20 ml vials.

Six radiocarbon dates were obtained from each core. Radiocarbon dates for the Ladd Lake core were obtained from bulk sediment organic matter in samples collected from select intervals over the length of the core. Dates were generated by the Illinois State Geological Survey for the University of Minnesota Limnologic Research Center (UMLRC). Sample pretreatment included use of acid to remove carbonates and KOH to remove humics. Radiocarbon dates obtained for the Lake Winnebago samples are from the CO_2 gas evolved from sediment organic matter by combustion of the carbonate free organic fraction. AMS dating analysis was performed for Western Michigan University at Purdue University's Prime Laboratory for Rare Isotope Measurement.

Plotted as core depth versus ^{14}C yr BP, the sedimentation rate for the Ladd Lake and Lake Winne-

a) Ladd Lake, Ohio
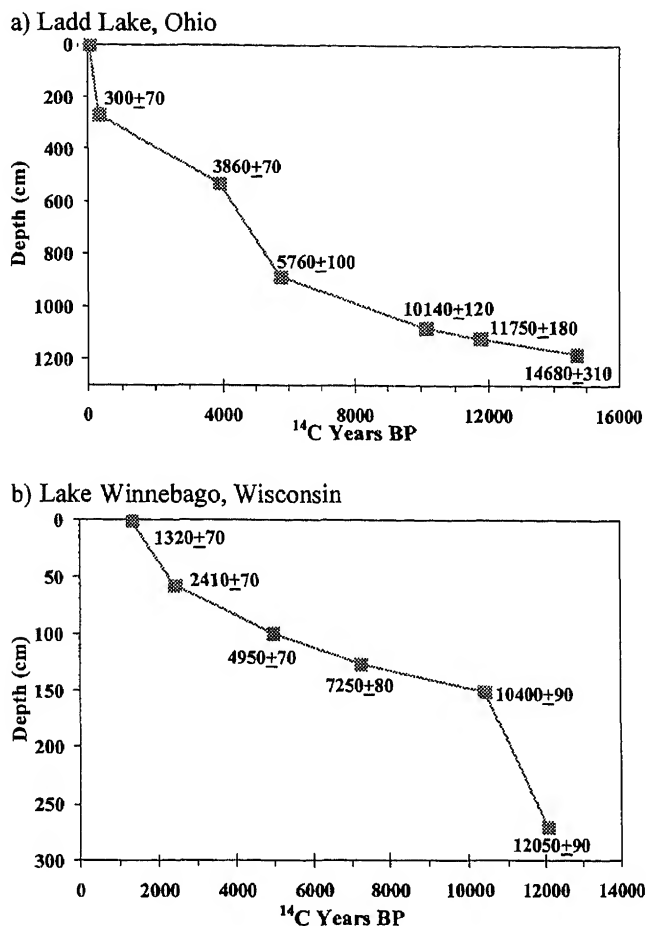
b) Lake Winnebago, Wisconsin

Figure 2. Sedimentation rates for Ladd Lake (a) and Lake Winnebago (b) plotted as a function of core depth versus radiocarbon age.

bago cores are shown in figure 2(a) and 2(b), respectively. Depths shown on the Ladd Lake core were zeroed by subtracting the water column depth from the core depth (the water surface was considered 0 cm; the top of core starts at 930 cm and the base of core at 2132 cm). The radiocarbon date at 264–270 cm in the Ladd Lake core is taken just below the so-called European settlement horizon and dates to ~300 ^{14}C yr BP (Shane 1991). The dates from the 521–529 cm interval (3860 ^{14}C yr BP) and the 877–885 cm interval (5760 ^{14}C yr BP) are generally correct. However, it should be noted that the basal three dates from the Ladd Lake core are considered generally correct but are thought potentially off by a few hundred years. The error arises due to hard water effects, slow sedimentation rates through these intervals, and the several centimeter span of bulk sample used for the radiocarbon analysis. Dates assigned to intervals below the oldest radiocarbon interval were based on use of the previous up core sedimentation rate and should be used with a modest degree of caution. Dates younger than 300 years in the Ladd Lake core were based on extrapolation to the surface (designated as zero).

Similar problems in the Lake Winnebago core were avoided by analysis of CO_2 gas from organic matter extracted at a discrete depth interval. Dates for individual samples were estimated by using a linear sedimentation rate between radiocarbon dated intervals. The age of the topmost Lake Winnebago sample is 1320 yr BP based on the radiocarbon chronology determined. This result is most likely due to the loss of the first few centimeters during core recovery. A living clam sample, collected from the lake's surface sediment, gave a "modern" radiocarbon age suggesting very little hard water effect. Dates for samples separated by less than 140 years (i.e. twice the standard deviation reported for the radiocarbon dates) were averaged.

4. Experimental methods

Sediment samples were first digested in concentrated HCl (38%) to remove carbonates. Three sequential digestions at 80°C for 3–5 hours each were performed. Samples were then rinsed to pH neutral and freeze dried. Sediment organic matter was further concentrated using a newly developed microwave digestion procedure (Lovan 1998). Aliquots of carbonate free residues were digested in HF:HCl [mixed as a 1:1 (v:v) solution from concentrated HF (48%) and HCl (38%)] within sealed containers under microwave conditions (120°C and ~35 PSI) to remove silicates. The prime purpose for this later digestion was the removal of hydrogen bearing silicates in preparation for isotopic analysis of hydrogen in the residual organic matter. Analysis of the carbon from these HF:HCl residues was undertaken as a secondary study and is noted here.

Carbon isotope ratios ($\delta^{13}C$) of the organic matter were obtained from the Ladd Lake and Lake Winnebago samples. Isotopic analysis of organic carbon ($\delta^{13}C$) was accomplished by combustion of insoluble HCl and HF:HCl residues in the presence of CuO at 900°C for 3 hours. Their gaseous CO_2, H_2O and N_2 combustion by-products were cryogenically separated and measured. Percent organic carbon and the atomic carbon to nitrogen (C/N) ratios were determined for both the carbonate free residue (HCl-residue) and the HF:HCl residues. The C/N ratios of the carbonate free fraction were used to constrain the interpretation of the organic carbon data. The $\delta^{13}C$ of the CO_2 gas were determined for both residual materials only in a pilot series of 42 samples from Ladd Lake. Isotopic analysis was accomplished using a Micromass-Optima isotope ratio mass spectrometer. All isotopic ratio data are expressed in the delta notation per mil where:

$$\delta\text{‰} = [(R_{\text{sample}}/R_{\text{standard}}) - 1]10^3$$

where R is $^{18}O/^{16}O$, D/H, $^{13}C/^{12}C$ etc. Carbon isotope ratios are reported relative to the PDB Standard (calibrated using NBS-19) with a precision of ±0.1‰.

5. Results and Discussion

5.1 *Background and preliminary findings*

In general, lakes respond quickly to environmental pressures. Because of the limited size of their reservoir, the isotopic signals resulting from environmental perturbations are amplified (McKenzie 1985). The main sources of organic carbon in a lake are the submerged plants (i.e. macrophytes and plankton) living in the lake that take their isotopic signal from the lake DIC. Thus, the $\delta^{13}C$ of lake organic matter can be related to climatically induced changes in the trophic state of the lake.

Francey and Farquhar (1982) and Farquhar et al (1989) modeled the physical and enzymatic basis of carbon isotope discrimination during photosynthesis. This model equation, in its simplest form, is given by $\delta^{13}C_p = \delta^{13}C_{\text{air}} - a - (b - a)(C_i/C_a)$ where $\delta^{13}C_p$ is the isotope ratio of the fixed carbon (photosynthate); $\delta^{13}C_{\text{air}}$ is the isotope ratio of the source carbon (i.e. atmospheric carbon); a is the fractionation due to diffusion of CO_2 in the leaf (4.4‰); b is the fractionation due to fixation of CO_2 via enzyme action (~27‰ for C_3 plants); C_i is the concentration of CO_2 in the leaf intercellular space; C_a is the concentration of CO_2 in the atmosphere. Smith and Epstein (1971) subdivided photosynthetic plants into two large categories based on their $\delta^{13}C$ values. Most terrestrial plants range from −24 to −34‰, while the $\delta^{13}C$ of aquatic plants, tropical grasses, corn, and desert and salt marsh plants vary from −6 to −19‰. An intermediate group is formed by algae and lichen with $\delta^{13}C$ values from −12 to −23‰. Organic matter in Holocene sediment has $\delta^{13}C$ values ranging from −10 to −30‰ (Eckelman et al 1962; Shultz and Calder 1976; Meyers et al 1984; Krishnamurthy et al 1986; Meyers and Eadie 1993). Most aquatic plants fix CO_2 by the normal C_3 pathways with diffusion taking place in the aqueous phase (Farquhar et al 1989). When disequilibrium conditions exist (i.e. during high productivity) a depletion of the CO_2 available for plant photosynthesis can result and bicarbonate is used as the carbon source. This leads to more enriched $\delta^{13}C$ values. Measured $\delta^{13}C$ values for aquatic plants range between −11 and −39‰.

The percent organic content and the C/N ratios of the Ladd Lake and Lake Winnebago cores are shown in figures 3(a–d). Figure 3(a) shows the Ladd Lake percent organic carbon content from both the HCl and HF:HCl residues. Historically, literary reference to percent organic carbon data has been presented with respect to the HCl (carbonate free) residue. Here, these data show a mid-core increase to roughly 25% organic carbon with the basal and surface portions of the core having as low as 2% organic carbon. The general scatter of the HCl-percent organic carbon data over the length of the core and the similarity in

the surface and basal percent organic content suggests that no diagenetic effects have altered the sediment mass in the Ladd Lake core. An apparent concentration of the sediment organic matter during the HF : HCl digestion is graphically evidenced by the higher percent organic content of the HF : HCl residues. These values mirror the temporal change seen in the HCl residues.

Although generally lower in % organic content, the Lake Winnebago HCl and HF : HCl residues (figure 3c) again show mirrored temporal variation. Percent organic carbon in the HCl residues show a generally increasing trend from the base of the core upwards ranging from ~1% to ~9%. Basal marsh peat samples exhibited individual % organic carbon contents > 60%. These samples (at ~12,000 ^{14}C yr BP) sit stratigraphically above a basal clay-till. Subsequent regression analysis omits these lower units from analysis using only the lacustrine samples above the marsh peat.

Atomic carbon to nitrogen (C/N) ratios from both the HCl and the HF:HCl residues for the Ladd Lake

and Lake Winnebago samples are shown in figure 3(b) and 3(d), respectively. The C/N ratios of the organic carbon in the HCl-residues reflect mean values of ~10.7 at Ladd Lake and 10.9 for Lake Winnebago. Values near and below 10 are indicative of lacustrine origins for the residual organic matter (Meyers and Ishiwatari 1993). The general positive shift in the HF : HCl values from both cores compared to their corresponding C/N ratios in the HCl-residues is due to loss of nitrogen. One potential source for nitrogen in the residual organic matter is protein (Meyers and Ishiwatari 1993). These data may suggest that N_2 may have been lost from the protein portion of the organic matter during the successive acid digestions.

Figure 4(a) shows the δ^{13}C from both the HCl and the HF : HCl residues in the pilot series of 42 samples from Ladd Lake. The δ^{13}C in the HCl-residues range from $-26.2‰$ to $-32.8‰$. The δ^{13}C of the HF : HCl-residues closely mimic those of the HCl-residues. Interestingly, the δ^{13}C of organic matter reported
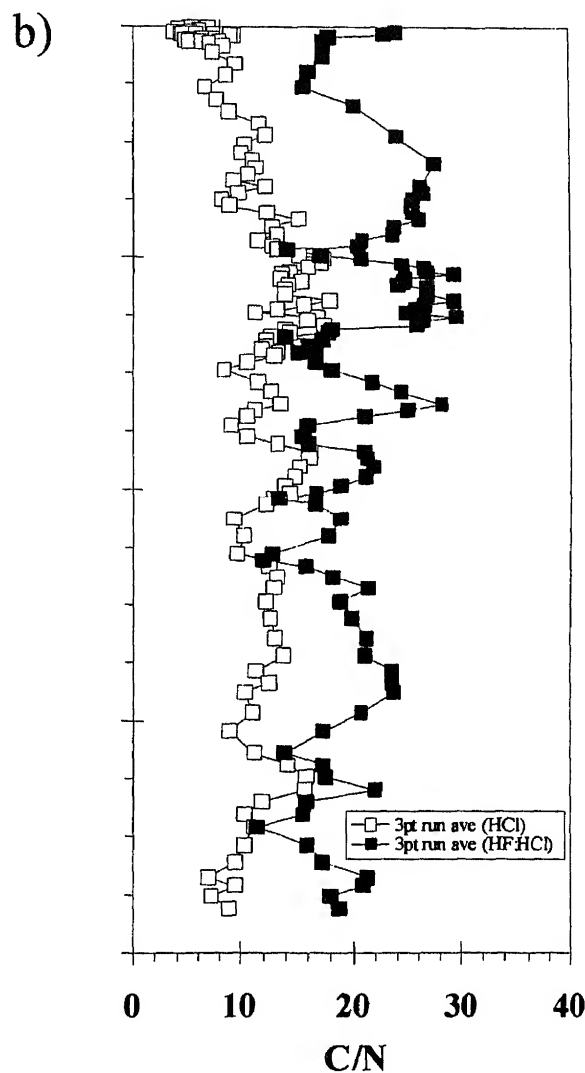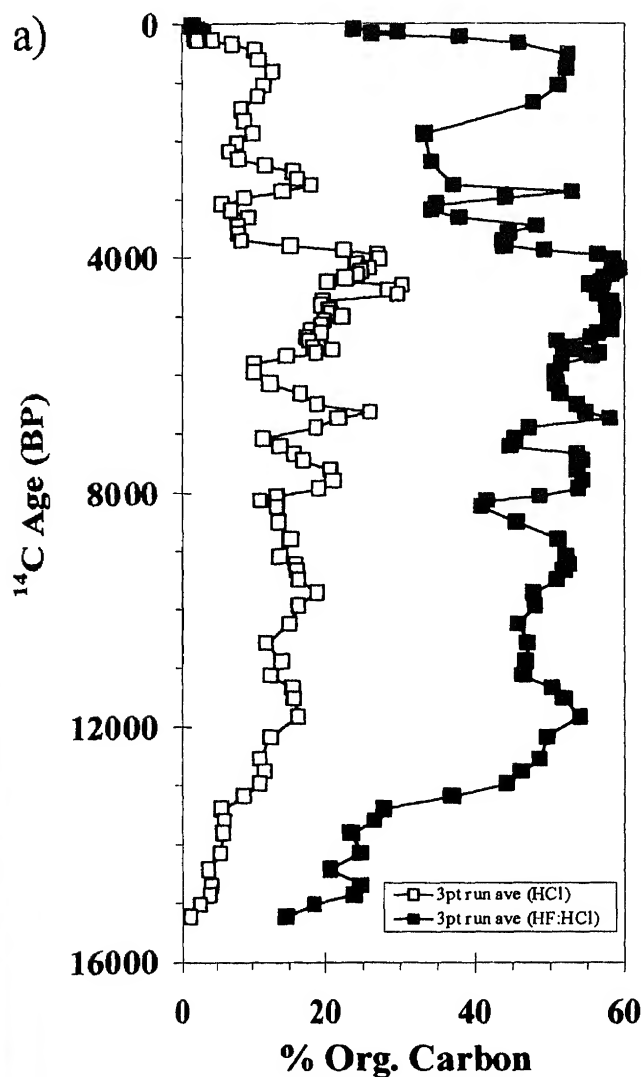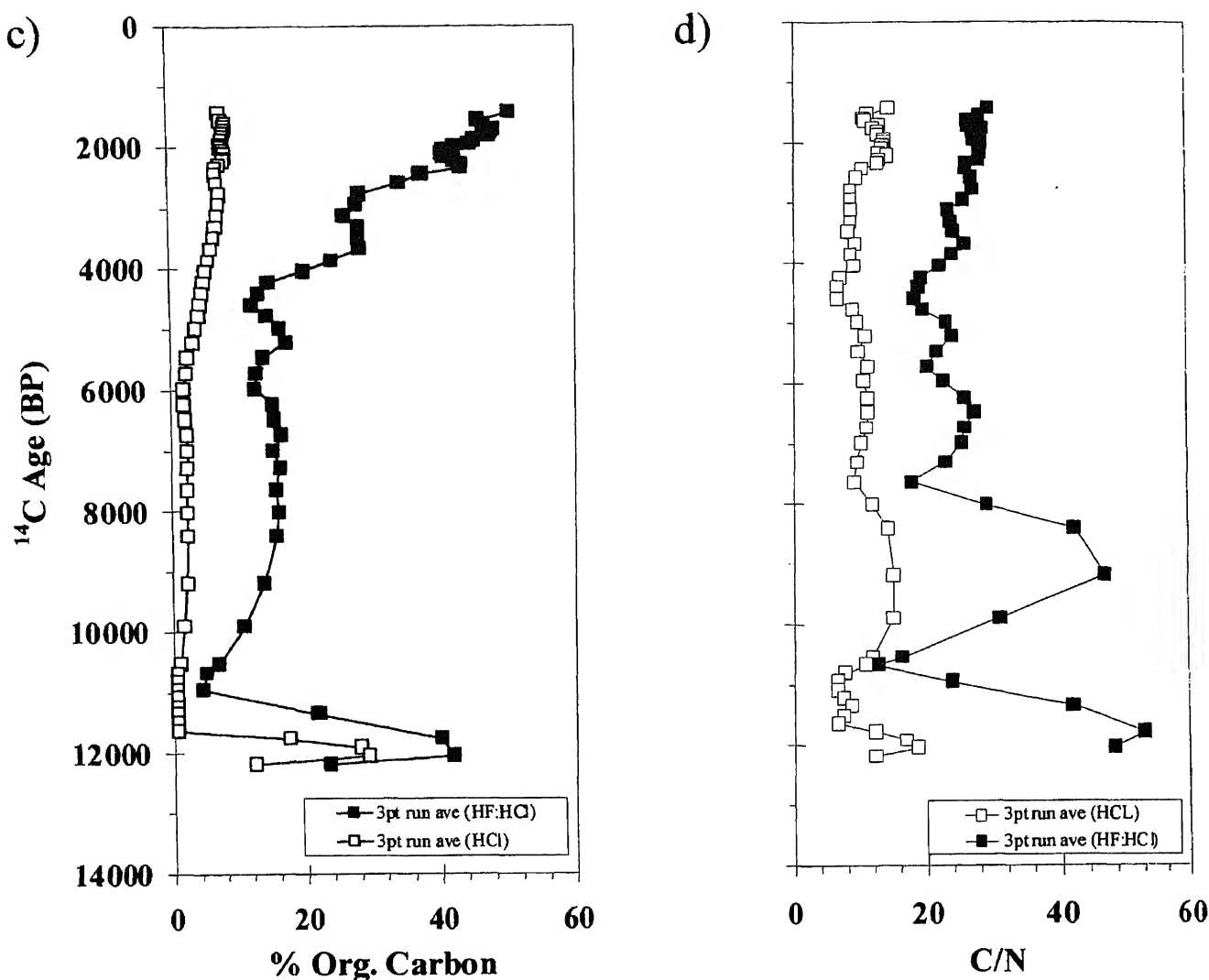

Figure 3(a–b). (*Continued*)

Figure 3. Ladd Lake percent organic carbon (a) and (b) atomic carbon to nitrogen ratios, C/N, plus Lake Winnebago percent organic carbon (c) and C/N ratios (d) for insoluble sediment organic matter in both the HCl and HF:HCl residues plotted vs. ^{14}C Age as years Before Present (BP).

from both the HCl residues and the HF:HCl residues are consistent with values reported in organic matter from Holocene sediment in other studies (Eckelman *et al* 1962; Shultz and Calder 1976; Meyers *et al* 1984; Krishnamurthy *et al* 1986; Meyers and Eadie 1993). This similarity in δ^{13}C values from the respective insoluble residues with a lack of correlation on regression of the δ^{13}C vs. the % organic carbon within their respective residual materials (figures 4(b) and 4(c)) may indicate very little destruction of the organic carbon during the successive acid digestions. If this is true, future work using the HF:HCl residues for isotopic hydrogen studies in bulk organic matter may be able to rely on cryogenically separated CO_2 from the combustion by-products in corresponding carbon studies. That aside, regression of the difference in the δ^{13}C ($\delta^{13}C_{HCl} - \delta^{13}C_{HF:HCl}$) with respect to the % organic carbon content showed no correlation for either the HF:HCl residues ($R^2 = 0.028$, $n = 42$) or the HCl residues ($R^2 = 0.012$, $n = 42$). Because the

δ^{13}C of the HCl and HF:HCl residues were similar, the remainder of the discussion will focus only on the $\delta^{13}C_{HCl}$.

5.2 $\delta^{13}C_{HCl}$ from sediment organic carbon

The $\delta^{13}C_{HCl}$ from the whole core analysis of the Ladd Lake organic carbon is shown in figure 5. Isotopic values range from -25.4‰ to -32.8‰. The $\delta^{13}C_{HCl}$ from organic carbon in the Lake Winnebago core range from -31.0 to -28.5‰ (figure 6). Carbon isotopic values from both cores are consistent with values reported from δ^{13}C of lacustrine organic carbon in other Midwestern USA studies. Regression of the Ladd Lake $\delta^{13}C_{HCl}$ with respect to % organic carbon (TOC) content (figure 5) shows a lack of correlation ($R^2 = 0.054$, $n = 137$). This lack of correlation may suggest that the δ^{13}C of the organic matter from Ladd Lake is not singularly controlled by productivity in the lake. Conversely, regression of the $\delta^{13}C_{HCl}$ vs.

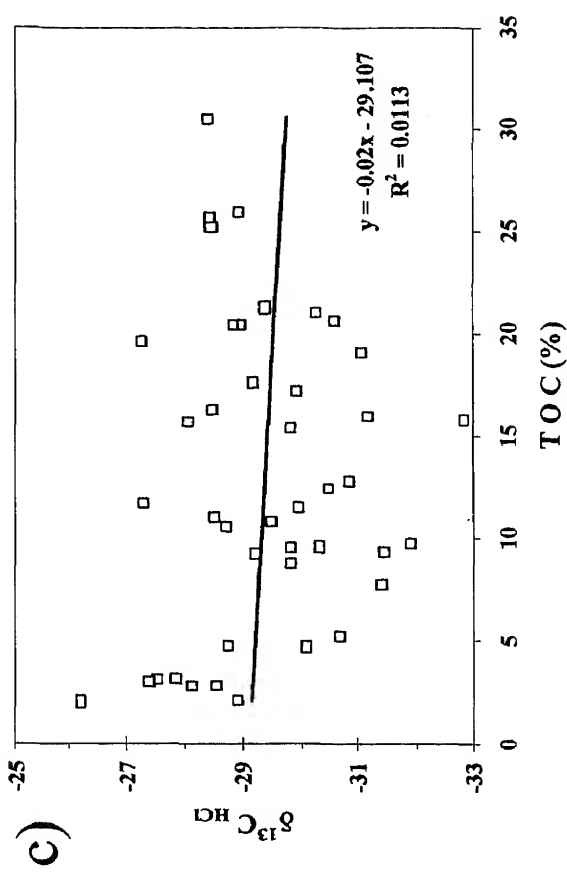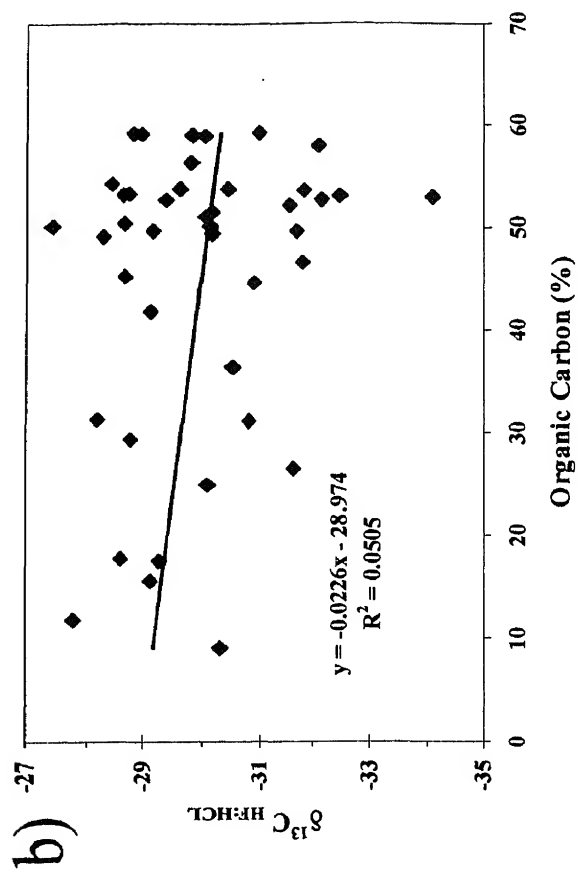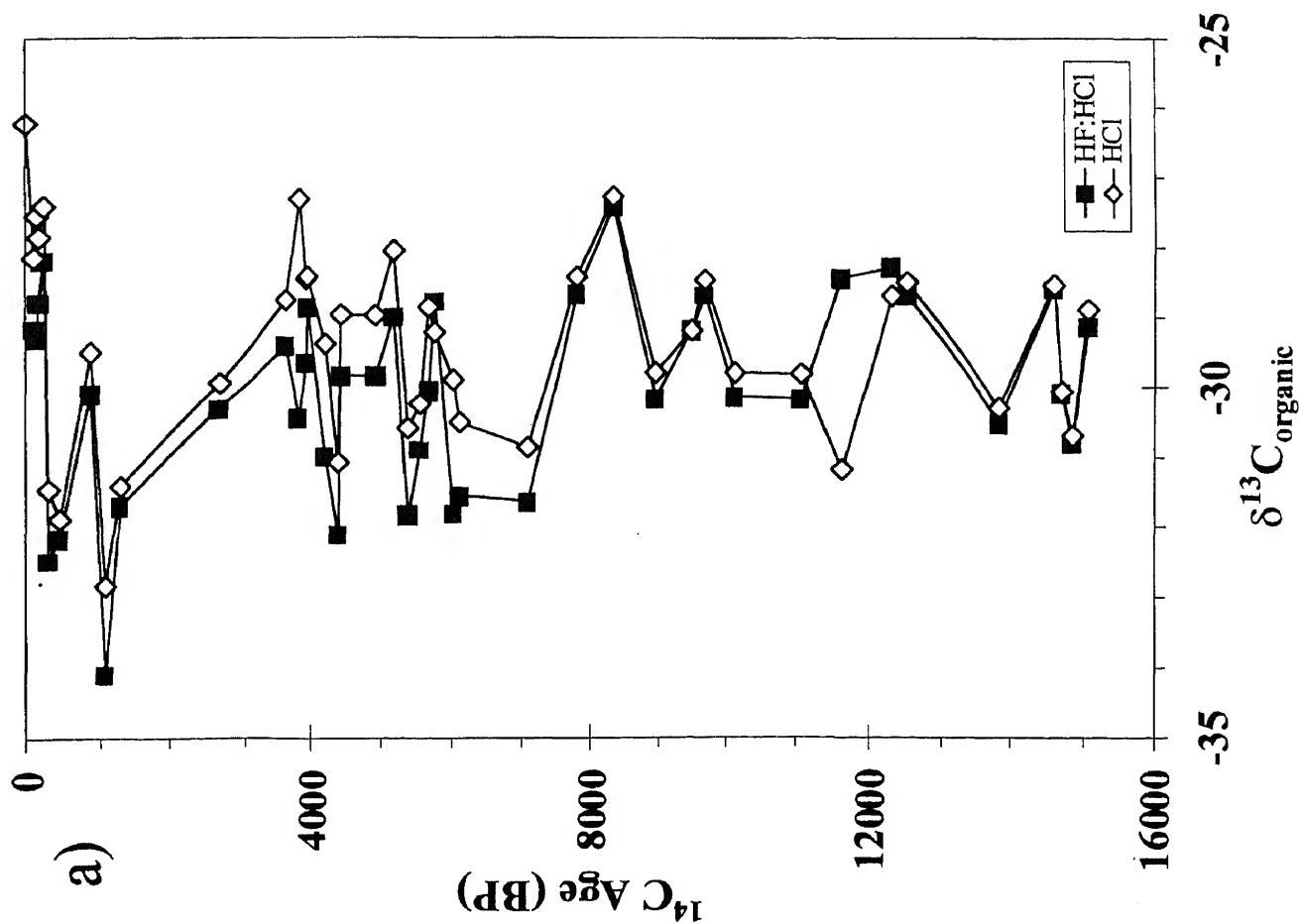Figure 4.   Ladd Lake Pilot Group δ^{13}C vs. ^{14}C years BP (a) and regression of δ^{13}C vs. per cent organic carbon for both the HCl and HF:HCl residual organic material (b and c).

TOC of the Lake Winnebago core indicates a negative correlation with $R^2 = 0.6$.

When CO_2 dissolves in water to form carbonic acid and its ions, isotopic exchange reactions enrich HCO_3^- in ^{13}C relative to the CO_2. If isotopic equilibrium is maintained between the atmospheric CO_2 and the lake, the $\delta^{13}C$ of the lake organic matter reflects this equilibrium value via the aqueous CO_2. However, when a lake goes into a state of enhanced photosynthesis, disequilibrium conditions exist and the production zone is depleted in dissolved CO_2 resulting in uptake of the isotopically heavier bicarbonate. Therefore, an increase of productivity in a stratified lake should be reflected by an increase in the $\delta^{13}C$ of the organic carbon that is produced in the surface water and subsequently sedimented. While the Ladd Lake core shows a low correlation coefficient for TOC vs. $\delta^{13}C$, its % organic content (TOC) is generally higher than that of the Lake Winnebago core. If high organic content were controlled by periods of high productivity, a positive covariance would be expected between the % organic carbon and the $\delta^{13}C$. Where negative covariance is evidenced with a high correlation coefficient, such as that seen in the Lake Winnebago core, a longer period of lake stratification may be implied wherein relatively little of the production is sedimented (Lean *et al* 1987; Schelske and Hodell 1991). If, however, equilibrium conditions are maintained such that the DIC of the water is never depleted of aqueous CO_2 during high organic production, the resulting $\delta^{13}C$ of the organic carbon should lack correlation with the % organic matter. This latter seems evident in the Ladd Lake core. However, unpublished water temperature data taken from 1 and 4-meter depths in Lake Winnebago suggest that thermal stratification in this large and uniformly shallow lake is evidenced only during the winter months of January, February and March. Lack of stratification during the warmer, ice-free months may be effected by persistent westerly winds that create wind driven lake-circulation, preventing thermal stratification and allowing rapid equilibrium throughout the shallow water column. Re-mixing and consumption of sedimented organic carbon and rapid equilibration may account for the negative correlation while very little of the net production is sedimented at Lake Winnebago.

5.3 *Anthropogenic influence?*

Figure 7 shows a plot of the $\delta^{13}C_{HCl}$ over the most recent 500 years where a fine resolution analysis was carried out for the Ladd Lake samples. Interestingly, regression of the $\delta^{13}C_{HCl}$ vs. % organic carbon for the 300 year period since European settlement shows a negative correlation with $R^2 = 0.58$ ($n = 33$) while the whole core regression shows an $R^2 = 0.054$. Within this 300 year interval, two phases are indicated where

the $\delta^{13}C_{Organic}$ show rapid positive shifts in value. The shift beginning at ~300 years ago corresponds to the time of settlement and land clearing while the positive shift from ~80 years ago to the present corresponds to more modern and intensified agricultural practices. During these periods, increased nutrient supply to the lake may have afforded greater productivity. The positive shifts in $\delta^{13}C$ would represent periods of increased productivity wherein the available CO_2 becomes depleted and photosynthesis continues while consuming the isotopically heavier bicarbonate. If high organic content were controlled by periods of high productivity, a positive covariance would be expected between the % organic carbon and the $\delta^{13}C$ signature. The negative correlation may indicate longer periods of thermal stratification of the lake wherein primary production is restricted mainly to the mixed layer (Lean *et al* 1987) and during which time relatively little of the production is sedimented (Schelske and Hodell 1991). Thus the higher % organic content mid core in Ladd Lake may reflect primary production early in the seasonal cycle when fixed carbon goes unused in the water column and is sedimented (Gardner *et al* 1985) whereas the trend in the most recent 300 years from the Ladd Lake core may reflect greater productivity during a period of longer seasonal stratification when relatively little of the production is sedimented.

6. Conclusions

In this study, the organic matter extracted from lake sediment was analyzed for $\delta^{13}C$ in two Midwestern United States lake cores. Total organic carbon (% organic carbon) was calculated and the atomic C/N ratios were used to constrain the interpretation of the isotopic carbon data. The range of $\delta^{13}C$ values and C/N ratios from both lakes are typical of values reported for other temperate lake organic matter in this region. Regression of the TOC vs. $\delta^{13}C$ for both cores shows that sedimented organic carbon from Lake Winnebago in Wisconsin reflects more negative $\delta^{13}C$ with higher % organic carbon. No correlation was seen in the record from Ladd Lake core implying that productivity alone was not controlling the isotope ratio. Where negative covariance is evidenced a longer period of lake stratification may be implied wherein relatively little of the production is sedimented (Schelske and Hodell 1991). Alternatively, a re-mixing and consumption of sedimented organic carbon and rapid equilibration throughout the water column may account for the negative correlation while very little of the net production is sedimented at Lake Winnebago. In the Ladd Lake core, a fine resolution analysis was carried out which indicated a possible anthropogenic influence on the isotope ratio around time periods when human settlement
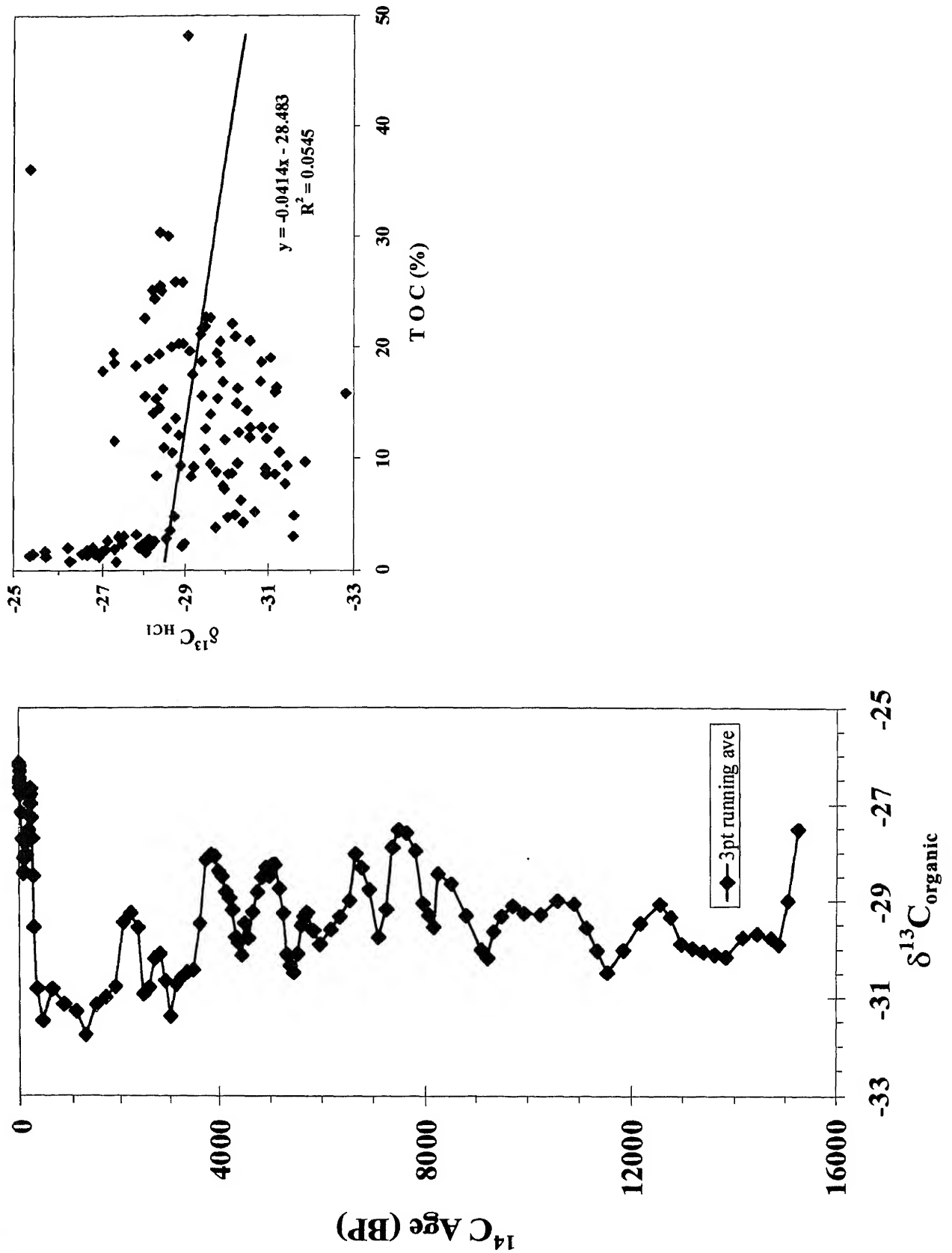
Figure 5. Ladd Lake $\delta^{13}C_{Organic}$ vs. ^{14}C Age and regression of $\delta^{13}C$ vs. total organic carbon for the HCl residual organic material.
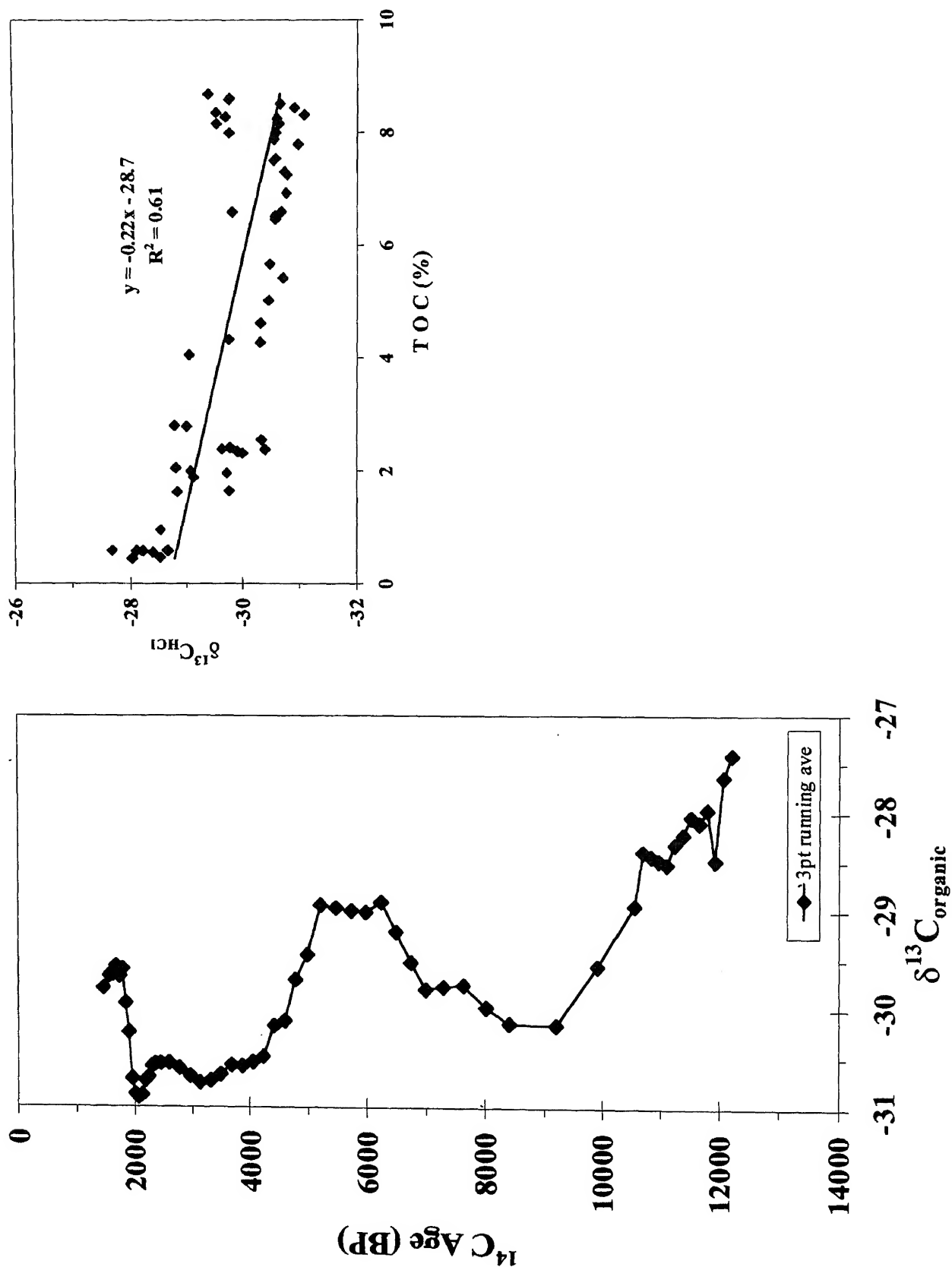
Figure 6.   Lake Winnebago $\delta^{13}C_{Organic}$ vs. ^{14}C Age and regression of $\delta^{13}C$ vs. total organic carbon for the HCl residual organic material.
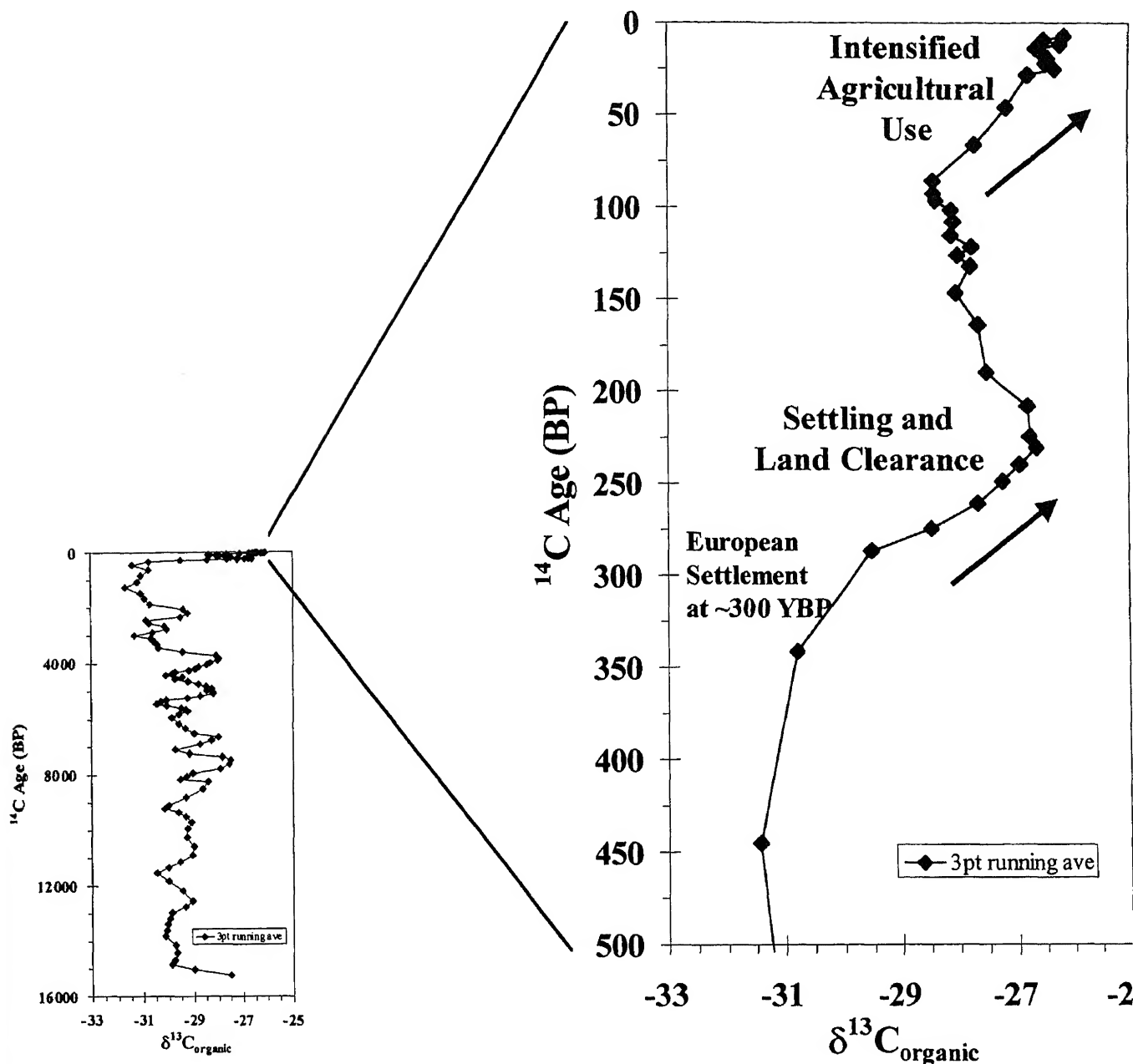
Figure 7. Plot of the $\delta^{13}C_{HCl}$ over the most recent 500 years (exploded view) from the Ladd Lake samples.

($\sim$300 yrs ago) and enhanced agricultural practices ($\sim$80 yrs ago) were significant. The study shows that carbon isotope studies are useful in paleolimnologic investigations.

References

Arthur M A, Dean W E and Claypool G E 1985 Anomalous C-13 enrichment in modern marine organic carbon; *Nature* **315** 216–218

Eckelman W R, Broecker W S, Whitlock D W and Allsup JR 1962 Implications of carbon isotopic composition of total organic carbon of some recent sediments and ancient oils, *Bull. Am. Assoc. Petrol. Geol.* **46** 699–704

Farquhar G D, Ehleringer J R, and Hubick KT 1989 Carbon isotope discrimination and photosynthesis, *Ann. Rev. Plant Physiol. Plant Mol. Biol.* **40** 503–537

Acknowledgements

Francey R J and Farquhar G D 1982 An explanation of $^{13}C/^{12}C$ variations in tree rings *Nature* **297** 28–31

Gardner W S, Nalepa T F, Frez E A, Cichochi E A and Landrum P F 1985 Seasonal pattern in lipid content of Lake Michigan macro-invertebrates *Canadian Journal Fish. Aquat. Sci.* **42** 1827–1832

Hollander D J and McKenzie J A 1991 CO_2 control on carbon-isotope fractionation during aqueous photosynthesis: A paleo-$pCO2$ barometer; *Geology* **19** 929–932

Jasper J P and Hayes J M 1990 A carbon isotope record of CO_2 levels during the late Quaternary; *Nature* **347** 462–446

Krishnamurthy R V, Bhattacharya S K and Kusumgar S 1986 Palaeoclimatic changes deduced from $^{13}C/^{12}C$ and C/N Ratios of Karewa Lake Sediments, India; *Nature* **323** 150–152

Lean D R S, Fricker H J, Charlton M N, Cuhel R L, and Pick F R 1987 The Lake Ontario life support system; *Can. J. Fish. Aquat. Sci.* **44** 2230–2240

Lewis C F M and Anderson T W 1992 Stable isotope (O and C) and pollen trends in eastern Lake Erie, evidence for a locally induced climatic reversal of Younger Dryas age in the Great Lakes basin; *Climate Dynamics* **6** 241–250

Lovan N A 1998 *A Paleoclimatic Study of the Midwestern United States from the Stable Isotope Records in Lake Sediments*; Ph.D. Dissertation, Department of Geology, Western Michigan University, 263p

McKee J W and Laudon T S 1972 University of Wisconsin–Oshkosh Limnology Laboratory Report of Investigations Number 3, University of Wisconsin–Oshkosh: 66p

McKenzie J A 1985 Carbon isotopes and productivity in the lacustrine and marine environment; In W. Stumm (Ed.) Chemical Processes in Lakes (Wiley, New York) p. 99–118

Meyers P A 1994 Preservation of elemental and isotopic source identification of sedimentary organic matter; *Chemical Geol.* **114** 289–302

Meyers P A and Eadie B J 1993 Sources, degradation, and recycling of organic matter associated with sinking particles in Lake Michigan; *Org. Geochem.* **20** 47–56

Meyers P A and Horie S 1993 An organic carbon isotopic record of glacial–postglacial change in atmospheric pCO_2 in the sediments of Lake Biwa; *Japan Paleogeog. Paleoclim. Paleoecol.* **105** 171–178

Meyers P A and Ishiwatari R 1993 Lacustrine organic geochemistry – an overview of indicators of organic matter sources and diagenesis in lake sediments; *Org. Geochem.* **20** 867–900

Meyers P A, Leenheer M J, Eadie B J and Maule S J 1984 Organic geochemistry of suspended and settling particulate matter in Lake Michigan; *Geochim. Cosmochim. Acta* **48** 443–452

Nakai N 1972 Carbon isotopic variation and the palaeoclimate of sediments from lake Biwa; *Proc. Jpn. Acad.* **48** 516–521

Olcott P E 1966 Geology and water resources of Winnebago County, Wisconsin, USGS Water-Supply Paper 1814, Dept. of the Interior, Washington, D.C., 263 p

Rau G H, Froelich P N, Takahashi T and Des Marais D J 1991 Does sedimentary organic $\delta^{13}C$ record variations in quaternary ocean $CO_2(aq)$?; *Paleoceanography* **6** 335–347

Schelske C L and Hodell D A 1991 Recent changes in productivity and climate of Lake Ontario detected by isotopic analysis of sediments; *Limnol. Oceanogr.* **36** 961–975

Schelske C L and Hodell D A 1995 Using carbon isotopes of bulk sedimentary organic matter to reconstruct history of nutrient loading and eutrophication in Lake Erie; *Limnol. Oceanogr.* **40** 918–929

Shane L C K 1987 Late-Glacial vegetational and climatic history of the Allegheny Plateau and the Till Plains of Ohio and Indiana; *Boreas* **16** 1–20

Shane L C K 1991 *Vegetation History of Western Ohio*, Final Report on 1990 Grant from The Ohio Department of Natural Resources, University of Minnesota, Limnological Research Center, pp 24

Shultz D J and Calder J A 1976 Organic carbon $^{13}C/^{12}C$ variations in estuarine sediments; *Geochim. Cosmochim. Acta* **40** 381–386

Smith B N and Epstein S 1971 Two categories of $^{13}C/^{12}C$ ratios for higher plants; *Plant Physiol.* **47** 380–384

Smith G L 1997 Late Quaternary climates and limnology of the Lake Winnebago basin, Wisconsin, based on ostracodes; *J. Paleolimnol.* **18** 249–261

Talbot M R and Johannessen T 1992 A high resolution paleoclimatic record for the last 27,500 years in tropical West Africa from the carbon and nitrogen isotopic composition of lacustrine organic matter; *Earth. Planet. Sci. Lett.* **110** 23–37

Thwaites F T 1943 Pleistocene of part of northeastern Wisconsin; *Geological Society of America Bulletin* **54** 87–144

Weidman S 1911 The Glacial Lake of the Fox River Valley and Green Bay and its outlet; *Science* **33** 467

Is there a stable isotope evidence for the CO_2 fertilization effect?

R V KRISHNAMURTHY and M MACHAVARAM

Department of Geology, Western Michigan University, Kalamazoo, MI 49008, USA
email: r.v.krishnamurthy@wmich.edu

It has been suggested that part of the so-called "missing sink" of carbon dioxide introduced into the atmosphere by anthropogenic activities, that is the imbalance between estimated anthropogenic carbon dioxide emissions and oceanic uptake, may be stored in the vegetation in midlatitudes. Precise mechanisms of abstraction of additional carbon dioxide by vegetation, also known as the "fertilization effect", are poorly understood. Stable carbon and hydrogen isotope ratios of cellulose extracted from annual growth rings (covering the time period 1980–1993) in an oak tree from Kalamazoo, SW Michigan provide a basis to investigate at a physiological level how the fertilization effect may operate. The carbon isotope ratios show that the intercellular concentration of carbon dioxide increased due to an increase in stomatal opening. Although increased intercellular concentration of carbon dioxide translated to increased Water Use Efficiency and assimilation rates, it also resulted in increased transpiration rate as shown by higher D/H of the fixed carbon. The two-fold significance of the isotope data are: first, they provide the first field evidence based on isotope studies for excess CO_2 induced biomass production and second, they suggest that this mechanism is likely to operate only in limited environments. Vegetation in regions where moisture availability is not restricted so that there can be a gain in water use efficiency despite increased leaf evaporation are best suited to sequester excess carbon from the atmosphere.

1. Introduction

Recent estimates show that between 1980–1989, the total emission of CO_2 was equivalent to about 6.3×10^{16} g of C (Dixon *et al* 1994). Of these, 2.88×10^{16} g of carbon remains in the atmosphere and the oceans are estimated to have absorbed about 1.8×10^{16} g of C. The amount of carbon that is unaccounted for is thus estimated to be 1.62×10^{16} g. It has been suggested that low and mid-latitude terrestrial ecosystems may be significant repositories of this missing carbon, the so-called "missing sink" of atmospheric CO_2. The process in which more dry matter is produced by plants via increased photosynthetic activity is also sometimes called the "fertilization effect". Consequently, fertilization effect can in principle abstract large amounts of CO_2 and sequester as vegetation. Fertilization effect in vegetation in these ecosystems should be accompanied by physiological responses a knowledge of which will enable us to identify regions of the world where this might be taking place. At present growth chamber experiments are the main focus in studies related to this important process. Here recent trends in the carbon and hydrogen isotope ratio (expressed as δ values) of annual growth rings from an oak tree in Kalamazoo (42.10 N, 85.30 W), southwestern Michigan has been used to demonstrate how the fertilization effect might operate in the natural environment.

2. Results and discussion

Samples representing individual years from an oak tree cut in 1993 were analyzed for $\delta^{13}C$ and δD after extracting cellulose from the whole wood. A total number of 47 individual rings (1947–1993) were analyzed. For all the samples both the $\delta^{13}C$ and δD

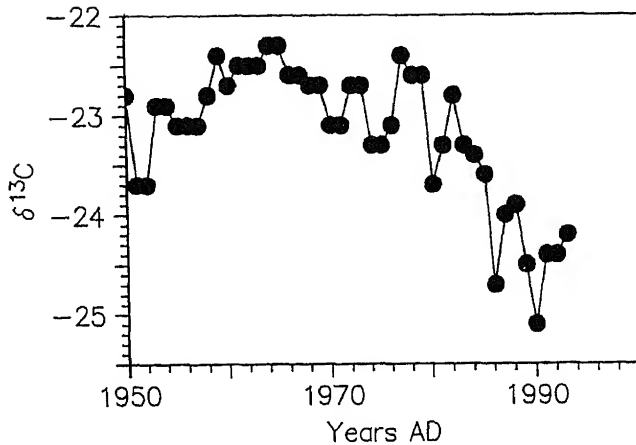**Keywords.** Carbon isotopes; intercellular carbon dioxide; fertilization effect; hydrogen isotopes.

Figure 1.   Carbon isotope ratio of cellulose from an oak tree from Kalamazoo, SW Michigan as a function of time.

The fractionation model is given by:

$$\delta^{13}C_p = \delta^{13}C_{air} - a - (b-a)\frac{C_i}{C_a} \qquad (1)$$

where,

$\delta^{13}C_p$ = the isotope ratio of the fixed carbon (photosynthate)

$\delta^{13}C_{air}$ = the isotope ratio of the source i.e. atmospheric CO_2

a = the fractionation due to diffusion of CO_2 into the leaf (4.4)

b = fractionation due to fixation of CO_2 via enzyme action (~ 27 for C_3 plants)

C_i & C_a = Concentration of CO_2 in the leaf intercellular space and in the atmosphere.

The above model applies to fractionation at the leaf and ignores possible isotope effects, apparently a systematic one, between leaf and tissue matter (Leavitt and Long 1982). This would not affect the applicability of the model in the present context as long as this effect is systematic. The C_i/C_a ratio is a very useful index of stomatal control on photosynthesis and is also tightly connected to WUE, Water Use Efficiency (Farquhar and Richards 1984, Farquhar *et al* 1988; Ehleringer 1988). If A is the instantaneous rate of carbon assimilation and E the transpiration rate, A/E defines the water-use efficiency (WUE) A with:

$$W = \frac{A}{E} = \frac{C_a - C_i}{1.6\nu} \qquad (2)$$

where C_a and C_i are concentrations of CO_2 in the atmosphere and intercellular space respectively; $\nu =$ the difference in vapor pressures in the intercellular space and the atmosphere, 1.6 being the ratio of diffusivities of water vapor and CO_2 in air. WUE being a function of the gross assimilation rate, C_a-C_i should have a direct bearing on the assimilation rate. In

were determined. The $\delta^{13}C$ was obtained by combustion of cellulose extracted from the raw wood while the δD values were determined on the cellulose using an equilibration technique that involved heating the samples at 180°C for 15 hrs (Krishnamurthy and Machavaram 1998). The $\delta^{13}C$ record for the period 1950–1993 is shown in figure 1. The isotope values ($\delta^{13}C$ and δD) did not correlate with any of the climatic variables such as annual temperature or precipitation or growing season temperature or precipitation recorded in Kalamazoo (table 1). This is particularly striking in the case of δD which might be expected to record climate information (Yapp and Epstein 1982; Krishnamurthy and Epstein 1985; Ramesh *et al* 1986; Epstein and Krishnamurthy 1990).

The interpretation of $\delta^{13}C$ of plant carbon has been made somewhat simpler by a widely accepted carbon isotope fractionation model (Farquhar *et al* 1989).

Table 1.   *Isotopic and climatic values from Kalamazoo, SW Michigan, for the period 1980–1993. Isotope values are based on the analysis of an oak tree. Also given are the estimated C_i/C_a and C_a-C_i values obtained using the carbon isotope fractionation model.*

Year	Mean (Apr-Oct) CO_2 (ppm)	Mean (Apr-Oct) $\delta^{13}C$ atm	$\delta^{13}C$ of cellulose	δD of cell	Mean temp. (Apr-Oct) in °C	Mean precip. (Apr-Oct) in cm	Mean annual precipitation in cm	Ring width mm	C_i/C_a	C_i-C_a ppm based on C_i/C_a 0.524
1980	338.75	−7.58	−23.7	−66	19.84	69.28	114.25	10.3	0.52	161.3
1981	339.85	−7.64	−23.3	−65	19.53	48.35	93.1	5.8	0.50	161.8
1982	341.08	−7.58	−22.8	−77	19.39	57.85	123	8.4	0.48	162.5
1983	343	−7.68	−23.3	−66	20.19	50.5	110.1	11	0.50	163.7
1984	344.45	−7.75	−23.4	−70	19.21	38	93.4	9.4	0.50	164
1985	345.92	−7.66	−23.6	−71	19.31	45.25	124.48	9.6	0.51	164.7
1986	347.28	−7.63	−24.7	−73	19.64	81.4	130.4	11.7	0.56	165.3
1987	349.04	−7.71	−24	−65	21.14	51.63	98.33	10.4	0.53	166.4
1988	351.53	−7.80	−23.9	−60	21.21	43.35	112.13	8.5	0.52	167.3
1989	352.88	−7.81	−24.5	−54	19.02	71.75	117.2	10.2	0.54	168
1990	354.01	−7.80	−25.1	−55	18.64	56.76	137.63	7	0.54	168.5
1991	355.68	−7.80	−24.4	−55	20.49	46.1	127.75	6.9	0.54	169.3
1992	356.54	−7.83	−24.4	−65	17.72	48.18	108.08	7.1	0.54	169.7
1993	357.11	−7.77	−24.2	−58	19.04	67.33	122.88	9.5	0.53	170

general, photosynthesis is an optimization between stomatal opening and transpiration. Efficient WUE requires minimal stomatal opening which in turn results in lower C_i and lower transpiration. This might be expected where moisture availability is a limiting factor. Since during the past century there has been a significant increase in atmospheric CO_2 concentration, it would be interesting to investigate how C_i/C_a, WUE and photosynthesis have been influenced in trees. This can provide insight into the response of terrestrial vegetation to elevated levels of CO_2 and address the fertilizer effect (LaMarche *et al* 1984).

In the next step involving the exploitation of the isotope fractionation model, the $\delta^{13}C$ of atmospheric CO_2 as measured in air ($\delta^{13}C_{air}$) is input into the photosynthesis model. Such direct measurements are available since 1978 for the Northern Hemisphere. The time period 1980–1993 was chosen in view of the fact that monthly measurements of $\delta^{13}C_{air}$ are available on a continuous basis for this time interval (Keeling *et al* 1989). In the application of the fractionation model, it is further assumed that the photosynthesis in this as well as in vegetation in general in these latitudes is significant only during the growing season (typically April–October for higher plants). Therefore, the $\delta^{13}C_{air}$ for these months only need be considered. The available values, kindly provided by Dr Keeling's group, are shown in table 1. Since the sampled tree is not from any forested area it is safe to assume that the tree processed free atmospheric CO_2. This can also be verified by considering the significant correlation between the tree isotope record and the Northern Hemisphere growing season record of atmospheric CO_2 (figure 2). Such a good correlation would not be expected if the tree growth was controlled by local microenvironment. Also, since the isotope data of only the past 13 years are being used, interference from possible juvenile effects are absent. In these calculations the values of a, the diffusive fractionation factor and b, the enzyme related fractionation factors are taken as 4.4 and 27 respectively. In the final C_3 fixation, a value of 27 is preferred for b rather than 29 (Roeske and O'Leary 1984). This latter value was determined for Rubisco carboxylation with dissolved carbon dioxide as the source of carbon.

Using the $\delta^{13}C_{air}$ and the carbon isotope fractionation model a continuous C_i/C_a record for the time period 1980–1993 can be generated, as shown in table 1. It should be noted that C_i and C_a here represent the values for the growing season i.e. April–October. The interesting observation that emerges from this C_i/C_a record is that this parameter has remained fairly constant at 0.524 ± 0.025 over the past 13 years. This is not surprising since the strategy by plants would be to maintain a constant C_i/C_a ratio and thus C_a-C_i to maintain optimum photosynthetic efficiency. Evidence for the tendency by plants to maintain a constant C_i/C_a over an even longer time scale has been shown
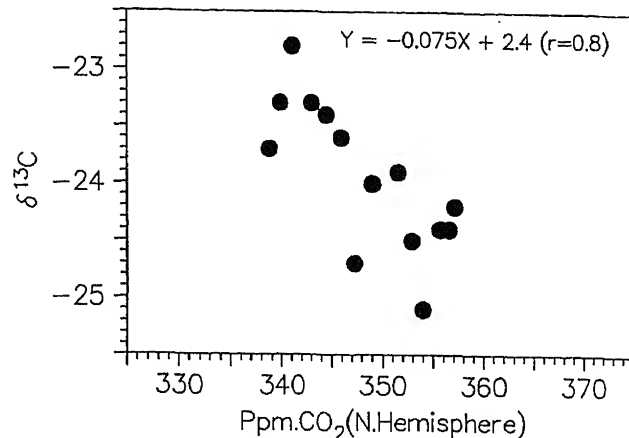

Figure 2. Relationship between the carbon isotope ratio of cellulose in oak and mean growing season (April–October) concentration of atmospheric carbon dioxide in the Northern Hemisphere.

(Krishnamurthy 1996). Since C_a, the concentration of external CO_2 has increased between the period 1980–1993, the constant C_i/C_a ratio would require that C_i and correspondingly C_a-C_i also increased during this period. Table 1 shows the estimated change in C_a-C_i during the past 13 years, calculated using the constant C_i/C_a of 0.524 and Keeling *et al* data of C_a. This data, also shown in figure 3, shows that C_a-C_i has changed by about 5.4% during the past 13 years. Van de Water *et al* (1994) reported that C_a-C_i increased by 13.6% between Glacial and Holocene periods, based on their study of limber pine needles (Van de Water *et al* 1994). It must be pointed out that the stomatal response to changes in external CO_2 and hence the effect on C_i/C_a and WUE is variable.

The increase in C_a-C_i, resulting from the tree's tendency to maintain a constant C_i/C_a, can be interpreted to be due to greater stomatal opening in response to the availability of higher amounts of CO_2. Recent studies indicate that plants growing over a carbon dioxide range of ~200–350 ppm tend to conserve C_i/C_a ratios (Polley *et al* 1993; Feng and
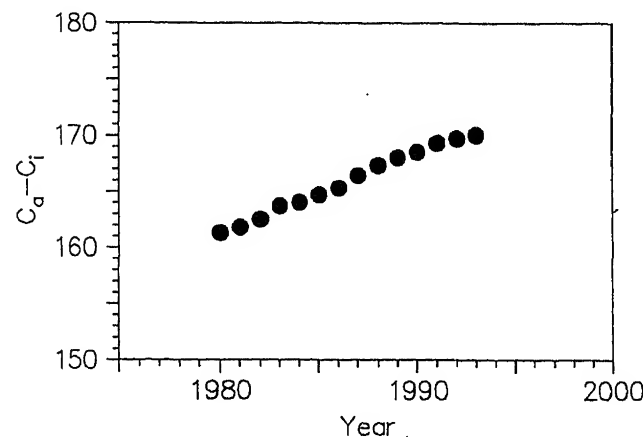

Figure 3. Estimated rate of increase in C_a-C_i in the oak tree during the past fourteen (1980–1993) years.
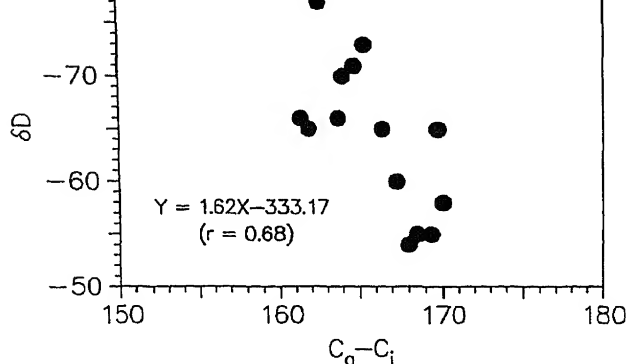
Figure 4. Relationship between δD and C_a-C_i.

Epstein 1995). If so, greater stomatal opening should result in greater water loss via evaporation at the leaf. This should result in the δD of the corresponding samples becoming higher as transpiration causes the water molecule with the lighter isotope i.e. hydrogen to escape preferentially. That this indeed is the case is deduced from figure 4 which shows the δD record for the same samples plotted against C_a-C_i for the time period 1980–1993. In turn this should have an impact on the WUE since the latter is related to this parameter. The important observation is WUE and thus the assimilation rate appears to have increased despite a contradiction. The contradiction is that a greater stomatal opening should inhibit WUE since it means greater water loss. The justification for this may lie in the fact that the sample site is not a moisture stressed area where the plants would tend to preserve water by reducing stomatal opening, especially when greater amounts of CO_2 are available. Therefore it can be argued that in the present case, the sample site is not restricted in moisture availability which might favor an increase in intercellular CO_2 concentration at the rate of increased transpiration. This interpretation would suggest that a response by terrestrial ecosystems to increasing atmospheric CO_2 via increased assimilation rates i.e. CO_2 fertilization effect might best operate in regions where moisture stress is not an important factor.

Another interesting observation that resulted from this study is that the ringwidth did not show any significant correlation ($r = 0.34$) with C_a-C_i. It is not clear if a greater assimilation rate *per se* should be reflected in ringwidth increase or that the increased biomass production can be in terms of plant fractions (e.g. leaf, foilage) that need not necessarily be converted into storable carbon (Condon *et al* 1987).

Acknowledgements

Condon A G, Richards R A and Farquhar G D 1987 Carbon isotope discrimination is positively correlated with grain yield and dry matter production in field-grown wheat; *Crop. Sci.* **27** 996–1001

Dixon R K, Brown S, Houghton R A, Solomon A M, Trexler M C and Wisniewski J 1994 Carbon pools and flux of global forest ecosystems; *Science* **263** 186–190

Ehleringer J R 1988 Carbon isotope ratios and physiological processes in arid land plants; In: *Stable isotopes in Ecological Research* (eds) P W Rundel, J R Ehleringer and K A Nagy Ecological Studies 68, (Amsterdam: Springer-Verlag) pp 40–52

Epstein S and Krishnamurthy R V 1990 Environmental information from the isotopic record in trees; *Phil. Trans. Roy. Soc. London* **A330** 427–439

Farquhar G D and Richards R A 1984 Isotopic composition of plant carbon correlates with water-use efficiency of wheat genotypes; *Aust. J. Plant Physiol.* **11** 539–552

Farquhar G D, Ehleringer J R and Hubick K T 1989 Carbon isotope discrimination and photosynthesis; *Ann. Rev. Plant. Physiol. Plant Mol. Biol.* **40** 503–537

Farquhar G D, Hubick K T, Condon A G and Richards R A 1988 Carbon isotope fractionation and plant water-use efficiency; In: *Stable isotopes in ecological research* (eds) P W Rundel, J R Ehleringer and K A Nagy, Ecological Studies 68, (Amsterdam: Springer-Verlag) pp 21–40

Feng X and Epstein S 1995 Carbon isotopes of trees from arid environments and implications for reconstructing atmospheric CO_2 concentration; *Geochim. Cosmochim. Acta* **59** 2599–2608

Keeling C D *et al* 1989 A three dimensional model of atmospheric CO_2 transport based on observed winds: 1. Analysis of observational data; *Am. Geophys. Monogr.*, No. 55 (ed) D H Peterson 165–235 (*Am. Geophys. Union*, Washington, DC)

Krishnamurthy R V and Epstein S 1985 Tree Ring D/H Ratio From Kenya, East Africa and its paleoclimatic significance; *Nature* **317** 160–162

Krishnamurthy R V 1996 Implications of a 400 year $^{13}C/^{12}C$ tree ring chronology; *Geophys. Res. Lett.* **23** 371–374

Krishnamurthy R V and Machavaram M 1998 Hydrogen isotope exchange in thermally stressed cellulose; *Chem. Geol.* **152** 85–96

LaMarche C V Jr, Graybill D A, Fritts C H and Rose M R 1984 Increasing atmospheric carbon dioxide: Tree ring evidence for growth enhancement in natural vegetation; *Science* **225** 1019–1021

Leavitt S W and Long A 1982 Evidence for $^{13}C/^{12}C$ fractionation between tree leaves and wood; *Nature* **298** 742–744

Polley H W, Johnson H B, Marino B D and Mayeux H S 1993 Increase in C_3 plant water-use efficiency and biomass over Glacial to present CO_2 concentrations; *Nature* **361** 61–63

Ramesh R, Bhattacharya S K and Gopalan K 1986 Climatic correlations in the stable isotope records of silver fir (Abies pindrow) trees from Kashmir, India; *Earth Planet. Sci. Lett.* **79** 66–74

Roeske C A and O'Leary M H 1984 Carbon isotope effects on the enzyme-catalyzed carboxylation of ribulosebiphosphate; *Biochemistry* **23** 6275–6284

Van de Water P K, Leavitt S W and Betancourt J L 1994 Trends in stomatal density and $^{13}C/^{12}C$ ratios of pinus flexills needles during last glacial-interglacial cycle; *Science* **264** 239–243

Yapp C J and Epstein S 1982 Climatic significance of hydrogen isotope ratios in tree cellulose; *Nature* **297** 636–639

Effect of intraband variability on stable isotope and density time series obtained from banded corals

S CHAKRABORTY[1], R RAMESH[1,*] and J M LOUGH[2]

[1]*Physical Research Laboratory, Ahmedabad 380 009, India.*
[2]*Australian Institute of Marine Science, Townsville, Queensland, Australia.*
email: ramesh@prl.ernet.in

Density, $\delta^{18}O$ and $\delta^{13}C$ were measured along two tracks, one close to the central growth axis and the other, $\sim 20°$ off the axis, in a coral (*Porites lutea*) collected from the Stanley Reef, Central Great Barrier Reef, Australia. The $\delta^{18}O$ variations in the coral are well correlated with sea surface temperature changes. The common variances between the two tracks were about 60% in the $\delta^{18}O$, $\delta^{13}C$, and the skeletal density variations. Part of the noise (40%) could be due to the difficulty of sampling exactly time contemporaneous parts of each band along the two tracks and part of it could be due to genuine intraband variability. In spite of the intraband variability, the time series obtained from the two tracks are similar, indicating that the dominant causative factor for the isotopic variations is external, i.e., the environmental conditions that prevail during the growth of the coral; density band formation does not appear to be directly controlled by the sea surface temperature.

1. Introduction

One of the aims of the PAst Global ChangES (PAGES) project under the International Geosphere Biosphere Programme (IGBP) is the reconstruction of the climatic history of the earth during the last 2000 years with a high resolution of one year or less (Eddy 1992). Such high resolution proxy climatic records are provided by ring width, ring density and stable isotope ratios of carbon, hydrogen and oxygen of tree rings on land (Fritts 1976; Hughes *et al* 1982; Yapp and Epstein 1982; Ramesh *et al* 1985; 1986) and by band density and stable oxygen isotope ratios of massive corals in the sea (Fairbanks and Dodge 1979; Patzold 1984; Druffel 1985; McConnaughey 1989; Cole and Fairbanks 1990; Lough and Barnes 1990; Aharon 1991; Chakraborty and Ramesh 1993; 1997; 1999; Charles *et al* 1997). If the time series of these proxy climatic indicators is entirely governed by the ambient climate, then there should not be any significant variations of these parameters within a single annual ring (tree) or band (coral). However, both in trees and corals, there exist significant intra-ring and intra-band variability in isotope ratios and other climate indices. This shows that at least part of the variance in a time series obtained from trees and corals is due to internal, growth related effects. Therefore it is important to assess how much "noise" is introduced into the "signal" because of this intra-ring and intra-band variability. Such an exercise has already been carried out for tree rings (Ramesh *et al* 1985). Here we repeat this exercise for corals, because a systematic study of the effect of the intraband variability for corals does not exist except for the oxygen isotope measurements of McConnaughey (1989) in a single band of a coral showing significant intraband $\delta^{18}O$ variability of 1.2‰ (cf. experimental precision of ± 0.05‰). Our exercise would lead to an estimate of the signal/noise ratio which will enable evaluation of how much of the variance in the coral based time series is controlled by external (climatic) influence and how much is controlled by internal (growth-related) effects.

Keywords. Carbon isotope; oxygen isotope; SST; climate; coral; Great Barrier Reef.

of the density band formation in corals. Highsmith (1979) and Weber *et al* (1975) concluded that the sea surface temperature (SST) controls the density band formation in corals, while Buddemeier (1974) and Wellington and Glynn (1983) have attributed the seasonally varying growth rate to be the cause of the annual banding. One might probably argue that the variation in SST controls the growth rate and thereby affects the band formation. However, it has been seen that the same species of corals form high or low density bands in summer/winter in different geographical locations (Chivas *et al* 1983; Barnes and Lough 1989). Therefore it appears that the availability of sunlight and nutrients rather than SST controls the growth rate. It is possible to distinguish between the High-smith-Weber hypothesis and Buddemier-Wellington-Glynn hypothesis by measuring the stable carbon and oxygen isotope ratios in the same points of the coral band where density has been measured; if the density variation correlates with $\delta^{18}O$, which depends mostly on SST (and to a small extent on the salinity or $\delta^{18}O$ of sea water), then the former hypothesis is valid. On the other hand, if density variation correlates with $\delta^{13}C$, which depends on growth rate (McConnaughey 1989) the latter hypothesis is valid.

Thus in this paper, we address the following two questions:

- effect of intra-band variability on the coral time series and
- the causal mechanism for density band formation in corals.

We have chosen the genus *Porites* for this study because:

- they produce fairly well defined annual density bands clearly identifiable in an X-ray picture;
- their growth rate is relatively higher (1 to 2 cm/yr), and their polyp size is smaller ($\sim$1 mm) than most massive corals;
- they have a wide geographical distribution and thus offer a good spatial coverage and
- their oxygen isotope ratios have been shown to be related to SST (Weber and Woodhead 1972; Druffel 1985 and McConnaughey 1989).

We have made density, $\delta^{18}O$ and $\delta^{13}C$ measurements along two tracks of a *Porites lutea* collected from shallow water (few metres at low tide) depth in the Stanley Reef (19°15′S, 148°07′E), Australia in December, 1986. To our knowledge there is no earlier study in which stable isotopes have been measured in the same coral subsamples where density measurements were made.

In general the $\delta^{18}O$ of coralline $CaCO_3$ depends on the SST and the $\delta^{18}O$ of sea water. As the latter is not a routinely measured oceanographic parameter, one uses the linear relationship between $\delta^{18}O$ of the sea
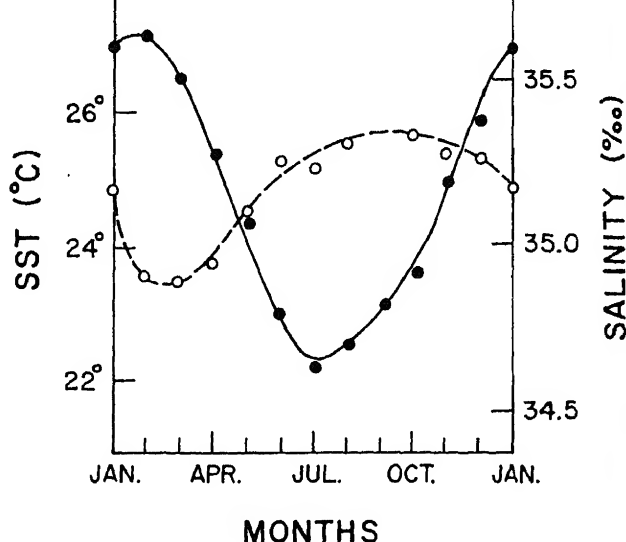

Figure 1. Annual cycle of sea surface temperature (filled circle) and salinity (open circle) in the Stanley Reef, Australia. (Data from Pickard *et al* 1977).

water and its salinity to calculate its effect on the $\delta^{18}O$ of the coralline $CaCO_3$. For south Pacific, where our coral comes from the coefficient for $\delta^{18}O$-salinity variation is 0.65‰ per ‰ (Craig and Gordon 1965). Figure 1 shows the annual cycle in the SST and salinity of the coral site (data from Pickard *et al* 1977). SST ranges from a minimum of $22.5 \pm 0.5°$ in winter (July) to a maximum of $27.0 \pm 1.2°C$ in summer (January). Salinity varies from 34.9 to 35.3‰, with a range that corresponds to 0.26‰ in $\delta^{18}O$ of the sea water, using the above slope. Thus the salinity induced $\delta^{18}O$ variation in the coral (0.26‰) is smaller than that induced by SST change (1.1 ± 0.27‰, assuming a temperature coefficient of -0.2‰ °C^{-1}). Therefore, for the purpose of this paper, we neglect the salinity influence on the coralline $\delta^{18}O$, even though it is quite significant.

2. Experimental methods

A 1 cm thick slice of the coral was prepared and an X-ray picture was taken (figure 2). Dates were assigned to the bands by counting from the top, which was assigned the year of collection. Density was measured along three tracks shown in figure 2 using gamma densitometry. The procedure is described in detail by Barnes and Lough (1989) and Lough and Barnes (1990). For stable isotope analysis we choose two tracks one close to the central growth axis (track-1) and the other $\sim$20° off the axis (track-2). We chose not to analyze stable isotope ratios in the third track as it caused sampling problems due to reduced band width. The mean growth rates for track-1 and track-2 are 0.97 and 0.91 mm/month respectively. The word "growth rate" in coral literature has been replaced
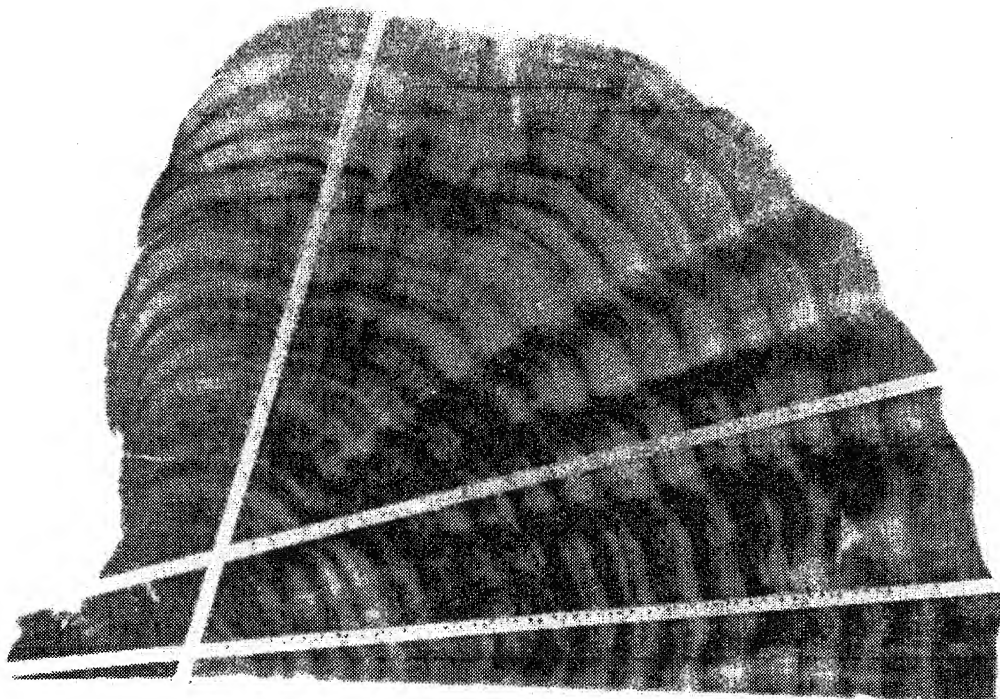
Figure 2. X ray positive of the *Porites* coral used for this study. Tracks 1 and 2 along which measurements have been carried out are marked (bottom strip: track 1; middle strip: track 2).

by appropriate terms like "extension rate" or "calcification rate" since they show a strong positive correlation (correlation coefficients of 0.98 and 0.93 for track-1 and 2 respectively, figure 3). Such a positive correlation between the calcification and extension rates was also shown by Scoffin *et al* (1992) in a *P. lutea* coral at Kotti, South Thailand. Stable isotope measurements were made on 3 to 5

Figure 3. Linear correlation between calcification rate and skeletal extension rate along the two tracks, (a) track 1; (b) track 2.

samples in a year, including the highest and lowest density points along the two tracks following standard techniques (for details see Chakraborty and Ramesh 1992; 1997). The X-ray positive was used as a guide to select these subsamples for isotopic measurements.

3. Results and discussion

3.1 *Oxygen isotopes and SST*

Before proceeding to answer the two questions addressed earlier, we first show that the $\delta^{18}O$ of this coral is indeed correlated with SST. The monthly averaged SST data were available from the Comprehensive Ocean Atmospheric Data Set (COADS). The maxima and minima in the $\delta^{18}O$ time series correspond to July and January respectively. Assuming a linear growth rate for summer and a different (linear) growth rate for winter, the $\delta^{18}O$ values other than the maxima and minima were approximately assigned a month. A linear regression was then carried out between $\delta^{18}O$ and SST.

For track-1

$$\delta^{18}O = (-0.116 \pm 0.024)\text{SST} - (1.96 \pm 0.06)$$
$$(n = 46, \ r = -0.885) \tag{1}$$

For track-2

$$\delta^{18}O = (-0.154 \pm 0.013)\text{SST} - (1.14 \pm 0.03)$$
$$(n = 46, \ r = -0.64) \tag{2}$$

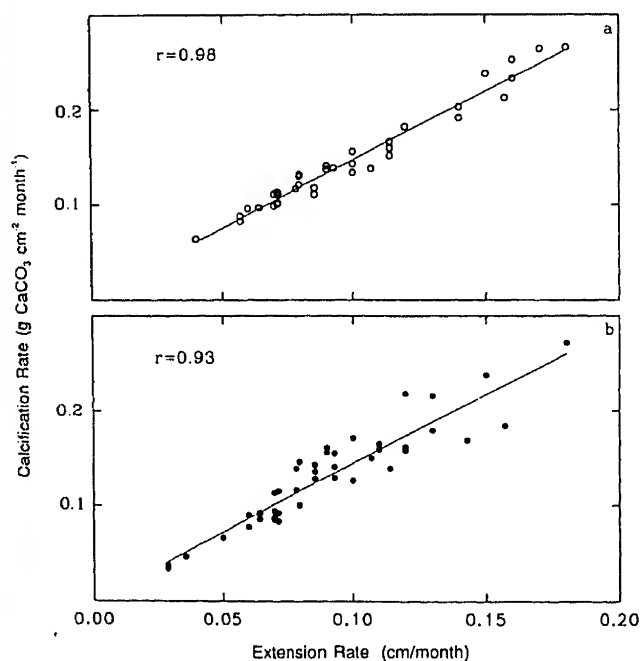both correlation coefficients (r) are significant at 0.01 level (Student's t test). These equations are similar to

the one reported for the same species from a nearby reef (Matsumoto 1993), using data from a single track.

$$\delta^{18}O = (-0.131)SST - 1.35 (r = -0.907). \qquad (3)$$

The coral *Porites lobata* from Galapagos (1°S, 90°20'W) showed a temperature coefficient of -0.21‰ °C^{-1} (McConnaughey 1989). Therefore it appears that there may be significant differences in the temperature coefficients of different species of the same genus, growing in different geographical regions. Nevertheless, our result shows that $\delta^{18}O$ of the coral analyzed by us is indeed related to SST (and may be to a smaller extent to salinity, as discussed earlier) and as we move away from the central axis, the correlation coefficient decreases significantly, probably indicating the effect of intra-band $\delta^{18}O$ variability. As the sampling clearly captures the maxima and minima in $\delta^{18}O$, we get a reasonably good correlation for track-1. This also ensures that we have not grossly missed the maxima/minima by sampling 3 to 5 points in a band. Had we not used the density curve for sub-sampling the bands, we could have missed the seasonal cycles by sampling only 3 to 5 points in a band.

3.2 Oxygen, carbon isotopes and density

The density, $\delta^{18}O$ and $\delta^{13}C$ variations along track-1 are shown in figure 4 and those for track-2 are shown
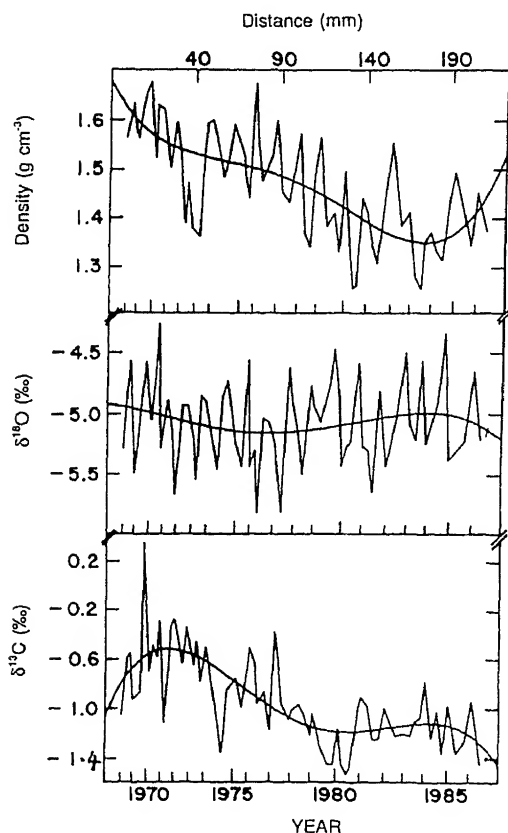

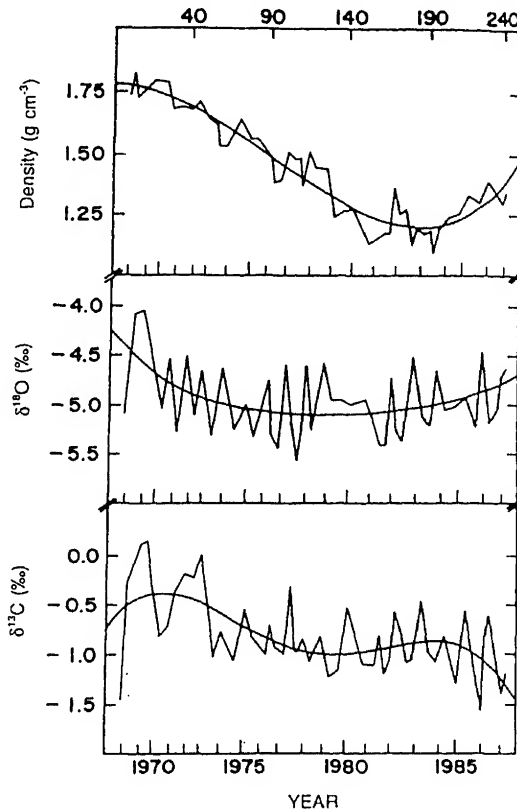
Figure 5. $\delta^{18}O$, $\delta^{13}C$ and density variations along track 2. Smooth lines indicate trends (4th order polynomial fit).

Figure 4. $\delta^{18}O$, $\delta^{13}C$ and density variations along track 1. Smooth lines indicate trends (4th order polynomial fit).

in figure 5. Smooth curves in these figures indicate trends (obtained by fitting a fourth order polynomial). Though the density was measured at much closer intervals (0.0254 cm) those values corresponding to the points sampled for isotopic analysis alone are shown in these figures. In neither of the tracks the $\delta^{18}O$ shows any significant trend, whereas the $\delta^{13}C$ shows a decreasing trend in both the tracks. The most likely reason for this decreasing trend is the growth-rate-related carbon isotopic fractionation. This coral shows a progressive increase in growth rate ($\sim$7 to 15 mm/yr in track-1 and $\sim$8 to 15 mm/yr in track-2) during its life span, which results in a decreasing trend in $\delta^{13}C$ (McConnaughey 1989). The other possible reason, viz., the changes in surface water $\delta^{13}C$ due to the uptake of fossil fuel CO_2, which is about -0.4‰ in the Pacific (Quay et al 1992) cannot completely account such a large change (-1‰).

The mean $\delta^{18}O$ of track-1 is -5.07 ± 0.35‰, and that of track-2 is -4.97 ± 0.36‰. These values are not significantly different at the 5% significance level (Student's t-test for the difference between two means). Similarly, the mean $\delta^{13}C$ values are -0.95 ± 0.38‰ for track-1 and -0.83 ± 0.39‰, again in good agreement. The mean densities for the two tracks are respectively 1.47 ± 0.11 and 1.42 ± 0.21, not significantly different. The variances in both the
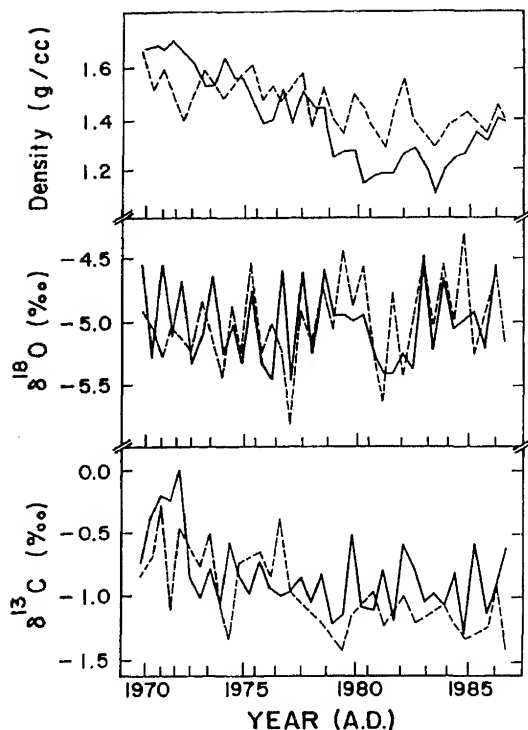
Figure 6. $\delta^{18}O$, $\delta^{13}C$ and density of the two tracks plotted by choosing the data from both tracks that formed approximately at the same time (solid line, track 1 and dashed line, track 2).

isotope ratios in both the tracks are remarkably similar. It is clear that the effect of intra band isotopic variability on the proxy-SST time series is small when the sampling is done within $\pm 20°$ of the central growth axis.

Figure 6 shows that the long term trends in $\delta^{18}O$, $\delta^{13}C$ and the density are similar along the two tracks, even though the absolute values do not always coincide. The annual range of temperature in this region is $4.5 \pm 1.3°C$ (Pickard et al 1977). This corresponds to a range of $\delta^{18}O$ about $0.9 \pm 0.27‰$ (neglecting the effect of salinity). This is in agreement with the observed amplitude of $\sim 0.7 \pm 0.2‰$, within uncertainties. While this confirms that we have not missed the seasonal maxima and minima during sampling, some effect of reduced sampling size per band could result in a lesser range than expected (for details see Chakraborty and Ramesh 1998). As high density points in general show minima in $\delta^{18}O$ (and low density, maxima in $\delta^{18}O$) we infer that in this region Porites lutea generally accretes high density bands in summer and low density bands in winter. This is in agreement with Lough and Barnes (1992), who made a detailed investigation on this aspect using fluorescent bands produced in Porites due to flood discharge and concluded that in this region, high density bands form during summer.

To find the common variance between the time series of density, $\delta^{18}O$ and $\delta^{13}C$ between the two tracks we performed the analysis of variance as outlined by

Fritts (1976) for tree rings. In this procedure the total variance in the data set (including data from both the tracks) is expressed as a sum of variances in tracks and among tracks. The variance which is common to both the tracks is then calculated (for details see Fritts 1976). This is approximately similar to calculating the correlation coefficients between the data of the two tracks, but is statistically a more robust measure of the common signal. These common variances between the two tracks are 67%, 54% and 68% respectively for $\delta^{18}O$, $\delta^{13}C$ and density. This suggests that the intra-band variability introduces about 33%, 46% and 32% noise in the $\delta^{18}O$, $\delta^{13}C$ and density signals. Understandably, $\delta^{13}C$ is controlled by varying growth rates (to be discussed later) and more prone to intra-band variability due to minor variations in the growth rates along different tracks.

Part of the noise could be an experimental artifact. That is, we have assumed that the pair of samples in the same annual bands, along the two tracks, were precipitated during the same time. In practice, it is difficult to confirm this assumption, and errors could be introduced if the samples precipitated a few weeks apart. Each sample taken for analysis will average about 3–4 weeks of growth. This problem will be accentuated when samples are taken from narrow bands (0.5 cm) and when the samples represent seasonal transition zones like winter to summer. Secondly, there could be genuine differences in the isotopic ratios as demonstrated by McConnaughey (1989), who showed a progressive enrichment in $\delta^{13}C$ of the portion of a Porites coral growing at a lower rate due to the deficiency of sunlight. Our results indicate that the coral isotope ratio time series is not significantly affected by the intra-band isotope variability, as long as the sampling track is not more than 20° off the central growth axis.

Table 1 shows the linear correlation coefficients between $\delta^{18}O$ and density, $\delta^{13}C$ and density, $\delta^{18}O$ and $\delta^{13}C$ for the two tracks, calculated from the measured time series without any detrending. There are long

Table 1. Linear correlation coefficients between $\delta^{18}O$, $\delta^{13}C$ and density.

	Linear correlation coefficient	
	Actual data	Detrended data
$\delta^{18}O$ and Density		
Track 1	0.23	0.29
Track 2	0.36	0.18
$\delta^{3}C$ and Density		
Track 1	0.56	0.20
Track 2	0.54	0.17
$\delta^{18}O$ and $\delta^{13}C$		
Track 1	0.02	0.04
Track 2	0.28	0.31

To be significant at 0.5% level the correlation coefficient should be greater than 0.36

term trends in the records as shown by smooth lines in figures 4 and 5. As correlations between any two time series could be either due to seasonal variations or due to long term trend, or both, it is necessary to check the correlations after detrending the data. Therefore, the linear correlation coefficients are shown for the detrended data as well (the detrending was done by subtracting calculated values from the fourth order polynomial fit, from the observed data). There is no significant correlation between $\delta^{18}O$ and density in either track, before or after detrending (table 1), suggesting that the density band variations are probably not directly controlled by SST variations. However, there is a significant correlation between $\delta^{13}C$ and density in each track before the data are detrended. This implies that the density band formation takes place due to the changes in the growth rate rather than SST. This correlation becomes insignificant when the data are detrended, probably implying that long term density variations are influenced by endogenic rather than exogenic factors (e.g. long term changes in light and hence growth rates).

The coral density decreases with time in both the tracks (figures 4 and 5). The magnitude of decrease is about 0.25 g/cm^3 for track-1 and 0.5 g/cm^3 for track-2 between 1968 and 1984 A.D. The reduction in density is more pronounced in the track which is farther away from the central growth axis. The $\delta^{13}C$ also decreases by 0.5‰ in both the tracks during this period. The positive correlation between $\delta^{13}C$ and density in each of these tracks, therefore, arises due to the long term trend in the data. Slower growth rate corresponds to higher density during 1968–74, the early part of the record, as seen in figures 4 and 5. The later part of the record shows higher growth rates and lower densities in general. As shown by McConnaughey (1989), the $\delta^{13}C$ values in years of slow growth are isotopically enriched compared to those of years of higher growth rate. Therefore we infer that the density banding is more likely to be determined by variation in growth rate rather than by variation in SST. This is to some extent corroborated by the fact that $\delta^{18}O$ and $\delta^{13}C$ are not correlated. If the kinetic effects were dominant during the incorporation of the isotopes from the sea water to the coral skeleton, one would observe a strong positive correlation between the $\delta^{18}O$ and $\delta^{13}C$ (McConnaughey 1989). The absence of such a correlation also indicates that metabolic (growth related) fractionation is dominant in the case of $\delta^{13}C$.

4. Conclusions

Density, $\delta^{18}O$ and $\delta^{13}C$ time series obtained from two tracks of a *Porites* coral, one close to the central growth axis and another 20° off the axis indicate that there is a small but systematic intraband variability across the central growth axis. Oxygen isotope ratio

shows significant correlation with SST in both the tracks. The carbon isotopic composition seems to be largely controlled by intrinsic factors like metabolism and the variable growth rate. The correlation between density and $\delta^{13}C$ implies that the density band formation is controlled possibly by variable growth rate rather than SST.

References

Aharon P 1991 Recorders of reef environment histories: stable isotopes in corals giant clams and calcareous algae; *Coral Reefs* **10** 71–90

Barnes D J and Lough J M 1989 The nature of skeletal density banding in scleractinian corals: fine banding and seasonal patterns; *J. Exp. Mar. Biol. Ecol.* **126** 119–134

Buddemeier R W 1974 Environmental controls over annual and lunar monthly cycles in hermatypic coral calcification; *Proc. Second Int. Coral Reef Symp.* Great Barrier Reef Committee, Brisbane 259–267

Chakraborty S and Ramesh R 1992 Monsoon induced sea surface temperature changes recorded in Indian corals; In; *Oceanography of the Indian Ocean* (ed) B N Desai (New Delhi, Oxford & IBH) pp. 473–478

Chakraborty S and Ramesh R 1993 Monsoon induced sea surface temperature changes recorded in Indian coral; *Terra Nova* **5** 546–551

Chakraborty S and Ramesh R 1997 Environmental significance of carbon and oxygen isotope ratios of banded corals from Lakshadweep India; *Quaternary International* **37** 55–65

Chakraborty S and Ramesh R 1998 Stable isotope variations in a coral from the Gulf of Kutch: environmental implications; *Proc. Indian. Acad. Sci. (Earth Planet. Sci.)* (Special volume on Isotopes in the Solar System) **107** 331–341

Charles C D, Hunter D E and Fairbanks R G 1997 Interaction between the ENSO and the Asian monsoon in a coral record of tropical climate; *Science* **277** 925–928

Chivas A R, Aharon P, Chappell J, Vlaustuin C and Kiss E 1983 Trace elements and stable isotope ratios of annual growth bands as environmental indicators; *Proc. Inaugural Great Barrier Reef Conference* (Townsville JCU Press) 77–81

Craig H and Gordon L I 1965 Deuterium and oxygen 18 variations in the ocean and the marine atmosphere; In; *Stable Isotopes in Oceanographic Studies and Paleotemperatures.* Third SPOLETO Conference on Nuclear Geology Pisa Italy 161–181

Cole J E and Fairbanks R G 1990 The southern oscillation recorded in the $\delta^{18}O$ of corals from Tarawa atoll; *Paleoceanography* **5** 669–683

Druffel E R M 1985 Detection of El Nino and decade time scale variations of sea surface temperature from banded coral records: implications for the carbon dioxide cycles; In: *The Carbon Cycle and the Atmospheric CO$_2$: Natural Variations Archean to Present* (eds) E T Sundquist and W S Broecker Geophys Monograph **32** (Washington DC: American Geophysical Union) pp. 111–122

Eddy J A 1992 The PAGES project: Proposed implementation plans for research activities; *IGBP Report* 19

Fairbanks R G and Dodge R E 1979 Annual periodicity of the $^{18}O/^{16}O$ and $^{13}C/^{12}C$ ratios in the coral *Montastrea annularis*; *Geochim. Cosmochim. Acta* **43** 1009–1020

Fritts H C 1976 *Tree rings and climate* (London: Academic Press)

Highsmith R C 1979 Coral growth rates and environmental control of the density banding; *J. Exp. Mar. Biol. Ecol.* **37** 105–125

Hughes M K, Kelly P M, Pilcher J R and LaMarche V C Jr 1982 *Climate from tree rings;* Cambridge University Press

Lough J M and Barnes D J 1990 Possible relationships between environmental variables and skeletal density in a coral colony from the Central Great Barrier Reef; *J. Exp. Mar. Biol. Ecol.* **134** 221–241

Lough J M and Barnes D J 1992 Comparisons of skeletal density variations *in situ* from the central G.B.R.; *J. Exp. Mar. Biol. Ecol.* **155** 1–25

Matsumoto E 1993 Sclerochronological study on climatic and oceanographic changes; *Proc. PAGES Workshop on High Resolution Records of Past Climate from Monsoon Asia: The Last 2000 Years and Beyond* (Taipei, Taiwan April 21–23) pp. 24–26

McConnaughey T 1989 C and O isotopic disequilibrium in biological carbonates: I Patterns and II *In vitro* simulation of kinetic isotope effects; *Geochim. Cosmochim. Acta* **53** 151–171

Patzold J 1984 Growth rhythms recorded in stable isotopes and density bands in the reef coral *Porites lobata* (Cebu Philippines); *Coral Reefs* **3** 87–90

Pickard G L Donguy J Y Henin C and Rougerie F 1977 *A review of the Physical Oceanography of the Great Barrier Reef and Western Coral Sea* Monograph **2** (Australian Institute of Marine Science Townsville) p. 135

Quay P D, Tilbrook B and Wong C S 1992 Oceanic uptake of fossil fuel CO_2: carbon-13 evidence; *Science* **254** 74–79

Ramesh R, Bhattacharya S K and Gopalan K 1985 Dendroclimatological implications of isotope coherence in trees from Kashmir Valley India; *Nature* **317** 802–804

Ramesh R, Bhattacharya S K and Gopalan K 1986 Climatic correlations in the stable isotopic records of silver fir (*Abies pindrow*) trees from Kashmir India; *Earth. Planet. Sci. Lett.* **79** 66–74

Scoffin T P, Tudhope A W, Brown B E, Chansang H and Cheeny R F 1992 Patterns and possible environmental controls of skeletogenesis of *Porites lutea*, South Thailand; *Coral Reefs* **11** 1–11

Weber J N and Woodhead P M J 1972 Temperature dependence of oxygen-18 concentration in reef coral carbonates; *J. Geophys. Res.* **77** 463–473

Weber J N, White E W and Patricia H W 1975 Correlation of density banding in reef coral skeletons with environmental parameters: the basis for interpretation of chronological records preserved in the corolla of corals; *Paleobiology* **1** 137–149

Wellington G M and Glynn P W 1983 Environmental influences on skeletal banding in eastern Pacific (Panama) corals; *Coral Reefs* **1** 215–222

Yapp C J and Epstein S 1982 Climatic significance of hydrogen isotope ratios in the cellulose; *Nature* **297** 636–639

Glacial-interglacial changes in the surface water characteristics of the Andaman Sea: Evidence from stable isotopic ratios of planktonic foraminifera

S M Ahmad[1], D J Patil[1], P S Rao[2], B N Nath[2], B R Rao[2] and G Rajagopalan[3]

[1] National Geophysical Research Institute, Uppal Road, Hyderabad 500 007, India;
email: postmast@csngri.ren.nic.in
[2] National Institute of Oceanography, Dona Paula, Goa 403 004, India.
[3] Birbal Sahni Institute of Palaeobotany, Lucknow 226 007, India.

Stable carbon and oxygen isotopic analyses of the planktonic foraminifera (*Globigerinoides ruber*) from a deep sea sediment core (GC-1) in the Andaman Sea show high glacial-to-Holocene $\delta^{18}O$ amplitude of 2.1‰ which is consistent with previously published records from this marginal basin and suggest increased salinity and/or decreased temperature in the glacial surface waters of this region.

A pulse of ^{18}O enrichment during the last deglaciation can be attributed to a Younger Dryas cooling event and/or to a sudden decrease of fresh water influx from the Irrawady and Salween rivers into the Andaman Sea. High $\delta^{13}C$ values observed during the isotopic stages 2 and 4 are probably due to the enhanced productivity during glacial times in the Andaman Sea.

1. Introduction

Extensive studies in the north Atlantic showed that the deglacial warming proceeded in two steps (Termination 1a and Termination 1b), separated by a near glacial cooling event that occurred between 11,000 and 10,000 years B.P. (Broecker *et al* 1988; Overpeck *et al* 1989). This strong cooling is also observed on the European continent and is referred to as Younger Dryas. Subsequent high resolution oxygen isotopic investigations in the foraminiferal shells from radiocarbon dated cores from Sulu Sea and northwest Pacific suggested the global nature of the Younger Dryas cooling (Kallel *et al* 1988a; Kudrass *et al* 1991). Recent high precision ^{10}Be measurements in the Lake Moraine from western North America provided additional evidence that the Younger Dryas was at least hemispheric, if not a global phenomenon (Gosse *et al* 1995).

The initial studies on the Younger Dryas in north Atlantic and surrounding regions led researchers to conclude that its origin was due to a perturbation of physical conditions in the north Atlantic Ocean, such as the sudden diversion of melt water from Mississippi to St. Lawrence drainage, a rapid variation in temperature of north Atlantic atmosphere or a rapid change in sea ice cover. However stable isotopic records from deep sea sediment cores, ice cores and numerous radiocarbon dated glacial deposits have led several authors to suggest a change in the global atmospheric-oceanic mixing as the cause for the Younger Dryas cooling event (Kudrass *et al* 1991; Alley *et al* 1993; Gosse *et al* 1995).

The Andaman Sea is a marginal oceanic basin with a maximum water depth of ~4.4 km. Excessive runoff from major rivers like Irrawady and Salween results in low surface salinity which is reflected in the $\delta^{18}O$ distribution pattern of Holocene planktonic foraminifers (Duplessy 1982). Thus any change in the freshwater riverine input into this basin can significantly alter the $\delta^{18}O$ values of the surface dwelling planktonic foraminifera. Irrawady and Salween rivers are also characterised by modest dissolved nutrient levels resulting in the low primary productivity (Naqvi *et al* 1994).

Carbon and oxygen isotopic ratios in the planktonic and benthic foraminifera from several deep sea cores of the northeast Indian Ocean have indicated significant changes in the chemical characteristics of the surface and deep waters of this region since the last glaciation (Duplessy 1982; Kallel *et al* 1988b; Sarkar *et al* 1990; Ahmad and Labeyrie 1994; Naqvi *et al* 1994). However, not much information is available on the surface and deep-water characteristics of the Andaman Sea because of the scarcity of high sedimentation rate cores from this region. In this paper we present high-resolution stable isotopic records from a new deep-sea core of the Andaman Sea.

2. Methodology and stratigraphy

Gravity core (GC-1) was collected from the Andaman Sea (9°N and 94° 17'E; water-depth 2909 m; core length 4.2 m; figure 1). The core was sub-sampled at 1 cm interval in the top 20 cm and alternatively 1–2 cm interval for the rest of the core. Sub-samples separated at 10–20 cm intervals were selected for this study. Samples were washed through a 150 μm sieve and subsequently dried at 60°C. About 40–80 speci-

Table 1. *Carbon and oxygen isotopic data represented in per mil vs. PDB in the planktonic foraminifera (Globigerinoides ruber).*

Sub-bottom depth (cm)	$\delta^{18}O$	$\delta^{13}C$
0	-3.2	1.11
20	-3.02	1.37
30	-3.09	1.23
40	-2.89	1.53
50	-3.44	1.21
60	-3.08	1.26
70	-2.83	1.21
80	-2.94	1.06
90	-2.56	1.09
100	-1.59	1.25
110	-1.78	1.17
120	-1.9	1.29
130	-1.82	1.19
140	-2.21	0.96
150	-1.19	1.63
160	-0.97	1.59
180	-1.16	1.53
200	-1.72	1.08
220	-1.63	1.27
240	-1.7	1.26
260	-1.72	1.49
280	-1.86	1.4
300	-1.82	1.59
330	-1.71	1.6
340	-1.85	1.61
350	-1.49	1.66
380	-1.56	1.61
400	-1.94	1.6
410	-1.89	1.32
420	-1.94	1.38

mens of *Globigerinoides ruber* (white) in the size range of 250–315 μm were picked for the stable isotopic measurements. The CO_2 was extracted by reaction with 100% phosphoric acid and isotopic ratios were measured using a VG Micromass 903 mass spectrometer at NGRI, Hyderabad. The precision based on replicate measurements of the international standard (NBS-19) and inhouse standard (CRS) was better than $\pm 0.10‰$ and $\pm 0.15‰$ for carbon and oxygen respectively. The results are summarized in table 1.

Age determination and correlation of cores are based on the planktonic oxygen isotopic stratigraphy by tuning the data of GC-1 core with the SPECMAP $\delta^{18}O$ stack record of Imbrie *et al* (1984). We have also determined ^{14}C date in one sediment sample from GC-1 core corresponding to the timing of $\delta^{18}O$ shift during the deglaciation. This sample showed an age of $10,900 \pm 1000$ years B.P. (figure 2). The sedimentation rate during the last glacial period is considerably high (8.3 cm/kyr) compared to the average rate (5.3 cm/kyr) of this core.

3. Discussion

The $\delta^{18}O$ variations measured in the foraminiferal shells reflect both the global variations of the ocean
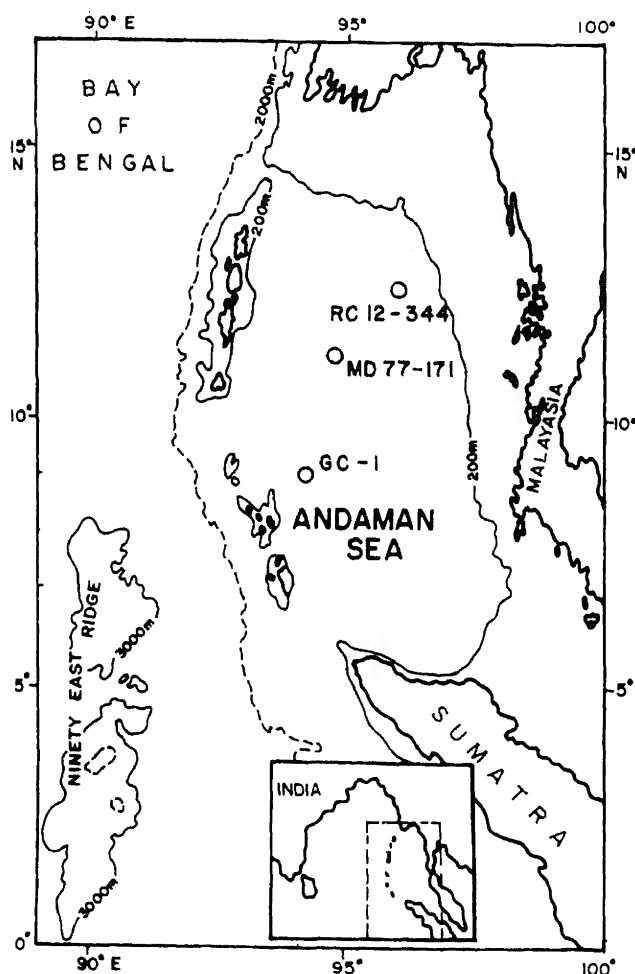

Figure 1. Location map of sediment cores.

water $\delta^{18}O$ due to ice volume change and isotopic fractionation between calcium carbonate and water (Emiliani 1955). Oxygen isotopic fractionation between $CaCO_3$ and water increases by ~0.2‰ for each degree water is cooled (Shackleton 1974), whereas a 1‰ increase in salinity causes a ~0.3‰ enrichment in $\delta^{18}O$ (Craig and Gordon 1965).

Glacial-to-Holocene $\delta^{18}O$ amplitude in GC-1 is considerably higher (2.1‰) compared to the ice-volume change of 1.2‰ reported for this transition (Labeyrie *et al* 1987). Subtracting this value from the total G/H amplitude of GC-1, a difference of 0.9‰ was obtained which could arise either due to the cooling of surface water by ~ 4°C, or, alternatively, by an increase in salinity (~3‰) or a combination of both.

Based on the CLIMAP (1981) results, the high G/H $\delta^{18}O$ amplitude of the previously published data from the northeast Indian Ocean cores was explained in terms of salinity variations only, as the temperature change from the LGM and to the Holocene was considered very small (Duplessy 1982; Sarkar *et al* 1990; Ahmad 1995). However, this assumption may not be valid today in the light of recent oxygen isotopic and alkenones data which clearly demonstrate a significant decrease (2–4°C) in the sea surface temperature (SST) of the Indian Ocean and other low-latitude regions of the world during the LGM (Rostek *et al* 1993; Norton *et al* 1997). Therefore a net 0.9‰ change in $\delta^{18}O$ between the LGM and Holocene in the surface waters of the Andaman Sea may be due to the combination of both decreased temperature and increased salinity during the LGM.

The $\delta^{18}O$ values in this core decreases from a maximum glacial value of −0.97‰ to minimum Holocene value of −3.44‰ (table 1). This shift from glacial to interglacial conditions is clearly interrupted by a return to near glacial value. Though the timing of this $\delta^{18}O$ shift approximately corresponds to the Younger Dryas cooling event it could also be due to the decreased discharge of fresh water from the Irrawady and Salween rivers into the Andaman Sea.

Examination of the $\delta^{18}O$ record of the planktonic foraminifera (*G. ruber*) from two other cores of the Andaman Sea (RC 12–344 and MD 77–171) also indicates the presence of similar $\delta^{18}O$ oscillation during the last deglaciation (Fontugne and Duplessy 1986). The magnitude of the $\delta^{18}O$ shift in all these three cores varies from 0.4‰ to 0.7‰, which is very close to the global Younger Dryas shift of 0.6‰.

The $\delta^{13}C$ values in GC-1 core varies considerably from 1.0 to 1.7‰ with higher values generally coinciding to glacial stages 2 and 4 (mean $\delta^{13}C = 1.58$‰) compared to the Holocene (mean $\delta^{13}C = 1.23$‰). Because planktonic $\delta^{13}C$ depends on the $\delta^{13}C$ of total dissolved carbon in the upper water column which is controlled by biological productivity, the relatively high glacial $\delta^{13}C$ values could be due to the increased productivity. The intensification of the northeast
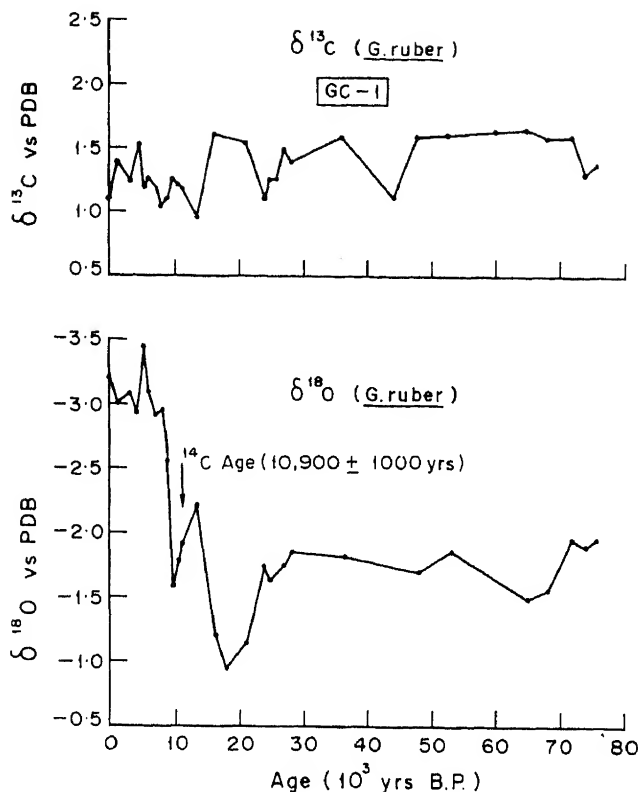

Figure 2. Carbon and oxygen isotopic composition of the planktonic foraminifera (*Globigerinoides ruber*) from GC-1 core plotted against age.

monsoon during the last glacial period might have increased biological production resulting in the preferential incorporation of lighter isotope ^{12}C relative to the ^{13}C from the water column (Duplessy 1982; Sarkar *et al* 1990). Similar enriched $\delta^{13}C$ values have also been reported earlier from the glacial foraminifera of MD 77–169 core of the Andaman Sea (Fontugne and Duplessy 1986).

References

Ahmad S M and Labeyrie L D 1994 Glacial to Holocene ^{13}C variations in the intermediate depth water masses of north Indian Ocean; *Geo-Mar. Lett.* 14 36–40

Ahmad S M 1995 Carbon and oxygen isotopic records of planktonic and benthic foraminifera from a new deep sea core of the northeast Indian Ocean; *Curr. Sci.* 69 691–695

Alley R B and 10 others 1993 Abrupt increase in Greenland snow accumulation at the end of Younger Dryas event; *Nature* 362 527–529

Broecker W S, Andree M, Wolfli W, Oeschger H, Bonani G, Kennett J, Peteet D 1988 The chronology of the last deglaciation: Implications to the cause of Younger Dryas event; *Paleoceanography* **3** 1–19

CLIMAP Project Members 1981 Seasonal reconstruction of the earth's surface at the last glacial maximum; *Geol. Soc. Am. Map Chart Ser.* MC-36 Boulder CO

Craig H and Gordon L 1965 Isotopic oceanography, deuterium and oxygen variation in the ocean and marine atmosphere; In: *Stable isotopes in oceanographic studies and paleotemperatures* (ed) E Tongiorgo, *Cons. Naz. Rich. Lab. Geol. Nucl. Pisa* 9–103

Duplessy J C 1982 Glacial to interglacial contrasts in the northern Indian Ocean; *Nature* **295** 494–498

Emiliani C 1955 Pleistocene temperatures; *J. Geol.* **63** 538–578

Fontugne M R and Duplessy J C 1986 Variations of the monsoon regimes during the upper Quaternary: Evidence from carbon isotopic records in the north Indian Ocean; *Palaeo-3* **56** 69–88

Gosse J C, Everson E B, Klein J, Lawn B and Middleton R 1995 Precise cosmogenic [10]Be measurements in western North America: Support for a global Younger Dryas cooling event; *Geology* **23** 877–880

Imbrie J, Hays J D, Martinson D G, McIntyre A, Mix A C, Morley J J, Pisias N G, Prell W and Shackleton N J 1984 The orbital theory of Pleistocene climate, support from a revised chronology of the marine δ^{18}O record. In: *Milankovich and Climate* (eds) A Berger *et al* (Dordrecht) 269–305

Kallel N, Labeyrie L D, Arnold M, Okada H, Dudley W C and Duplessy J C 1988a Evidence of cooling during the Younger Dryas in the western North Pacific; *Oceanol. Acta* **11** 369–375

Kallel N, Labeyrie L D, Julliet-Leclerc A and Duplessy J C 1988b A deep hydrological front between intermediate and deep water masses in the glacial Indian Ocean; *Nature* **333** 651–655

Kudrass H R, Erienkeuser H, Vollbrecht R and Weiss W 1991 Global nature of the Younger Dryas cooling event inferred from oxygen isotope data from Sulu Sea cores; *Nature* **439** 406–408

Labeyrie L D, Duplessy J C and Blank P L 1987 Variations in the mode of formation and temperatures of oceanic deep waters over the past 125,000 yrs; *Nature* **327** 477–482

Naqvi W A, Charles C D and Fairbanks R G 1994 Carbon and oxygen isotopic records of benthic foraminifera from the north Indian Ocean: implications on glacial-interglacial atmospheric CO_2 changes; *Earth Planet. Sci. Lett.* **121** 99–110

Norton F L, Ezra III, Hansman D and McElroy M B 1997 Hydrospheric transports, the oxygen isotopic record, and tropical sea surface temperatures during the last glacial maximum; *Paleoceanography* **12** 15–22

Overpeck J T, Peterson L C, Kipp N, Imbrie J and Rind D 1989 Climate change in the circum-north Atlantic region during the last glaciation; *Nature* **338** 553–557

Rostek F, Ruhland G, Bassinot F C, Muller P J, Labeyrie L D, Lancelot Y and Bard E 1993 Reconstructing sea surface temperature and salinity using δ^{18}O and alkenone records; *Nature* **364** 319–321

Sarkar A, Ramesh R, Bhattacharya S K and Rajagopalan G 1990 Oxygen isotope evidence for a stronger winter monsoon during the last glaciation; *Nature* **343** 549–551

Shackleton N J 1974 Attainment of isotopic equilibrium between ocean water and benthonic foraminifera genus Uvigerina: Isotopic changes in the ocean during the last glacial; In: *Les Methodes quantitatives d'etude des variation du climat au cours du pleistocene. Coll. Int. CNRS Paris* **119** 203–210

Palaeomonsoon and palaeoproductivity records of δ^{18}O, δ^{13}C and CaCO$_3$ variations in the northern Indian Ocean sediments

A SARKAR[1,*], R RAMESH[1,†], S K BHATTACHARYA[1] and N B PRICE[2]

[1]*Physical Research Laboratory, Ahmedabad 380009, India.*
[2]*Grant Institute of Geology, University of Edinburgh, Edinburgh, EH9 3JW, UK*
Current address: Indian School of Mines, Dhanbad.
[†]*email: ramesh@prl.ernet.in*

δ^{18}O and δ^{13}C of *G. sacculifer* have been measured in five cores from the northern Indian Ocean. In addition, high resolution analysis (1 to 2 cm) was performed on one core (SK-20-185) for both δ^{18}O and δ^{13}C in five species of planktonic foraminifera. CaCO$_3$ variation was measured in two cores. The results, presented here, show that

- the summer monsoon was weaker during 18 ka and was stronger during 9 ka, relative to modern conditions;
- δ^{13}C variations are consistent with independent evidence that shows that during the last glacial maximum (LGM; 18 ka) the upwelling was reduced while during 9 ka it was vigorous;
- calculation of CaCO$_3$ flux shows that the LGM was characterized by low biogenic productivity in the Arabian Sea while during the Holocene productivity increased by $\sim$65%, as a direct consequence of the changes in upwelling. Similar changes (of lesser magnitude) are also seen in the equatorial Indian Ocean. The amount of terrigenous input into the Arabian Sea doubled during LGM possibly due to the higher erosion rate along the west coast.
- δ^{18}O values indicate that the Arabian Sea was saltier by 1 to 2‰ during LGM. The northern part was dominated by evaporation while in the equatorial part there was an increased precipitation.

Keywords. Oxygen isotopes; carbon isotopes; sediments; foraminifera; productivity; monsoon.

1. Introduction

Stable isotope ratios of oxygen (δ^{18}O) and carbon (δ^{13}C) in foraminiferal calcitic tests from ocean sediments have been widely used for palaeoclimatic reconstruction during the Quaternary (Shackleton and Opdyke 1973; Duplessy *et al* 1981; Berger *et al* 1985; Mix 1987; Clemens and Prell 1991; Clemens *et al* 1991; Naidu *et al* 1992; Sirocko *et al* 1993, 1996; Naqvi and Fairbanks 1996; Beufort *et al* 1997; Rostek *et al* 1997). The δ^{18}O value of the foraminiferal calcite depends on the temperature and δ^{18}O of the water in which it is formed (Shackleton 1974). Both these parameters exhibit global and regional variations with time. The global components include changes in the sea-surface temperature (SST) and in the distribution of the total water between the world oceans and the continental ice sheets. The regional components depend on variations in SST and δ^{18}O induced by local upwelling, mixing of water masses and the amount of fresh water discharge near coastal regions. Similarly δ^{13}C variations in foraminifera have global components like changes in the δ^{13}C of ΣCO$_2$ induced by fluctuations in the deep water formation and circulation and in the global productivity due, for instance, to changing wind strengths. The local variations in the input of terrestrial carbon and upwelling also produce a significant effect on the δ^{13}C of foraminifera. By appropriately assessing and subtract-

ing the global component from the total signal, one can derive information about regional palaeoclimatic changes like the vagaries of the South Asian summer monsoon (Prell 1978; Duplessy 1982; Sarkar *et al* 1990a). Here we report one such study carried out in the Indian Ocean and Arabian Sea based on $\delta^{13}C$ and $\delta^{18}O$ variations in foraminifera from five sediment cores.

2. Core collection

Core locations and bottom topography are shown in figure 1 and the details are presented in table 1. The cores were collected during two cruises, one each in ORV Sagar Kanya (Cruise # 20) and RRV Charles Darwin (Cruise # 17). An attempt was made to collect the cores from regions with a reasonably flat bottom topography to ensure obtaining continuous and undisturbed climatic records. The two gravity cores SK-20-185 and 186 were sub-sampled at 1 to 2 cm intervals for the top 50 cm and at 5–10 cm intervals for the remaining parts of the cores. The other piston and box cores were sub-sampled at 5 cm intervals.

Table 1. *Description of the sediment cores.*

| Core no.	Location Lat./Long.	Water depth (m)	Core length (cm)	Type
SK-20-185*	10°N,71°50′E	2523	300	Gravity core
SK-20-186*	0°N,68°30′E	3564	500	Gravity core
CD-17-30+	19°56′N,61°39′E	3850	800#	Piston core
CD-17-15+	16°38′N,60°39′E	4012	600#	Piston core
CD-17-32+	21°45′N,60°49′E	3150	50	Box core

*SK: Sagar Kanya, an Indian Ship, Department of Ocean Development.
+ CD: Charles Darwin, a British Ship, NERC, UK
# Analysed only up to 300 cm

3. Methods

Sediment samples were soaked in 10% Calgon solution overnight in glass beakers and subsequently washed through a 150 μm sieve with a jet of distilled water. The fraction >150 μm, consisting of adult planktonic foraminiferal tests was oven dried at 60°C. About 30–40 individuals of a given species were picked up under a stereoscopic binocular microscope for isotopic analysis. For the present analyses, foraminiferal tests were chosen from a narrow size range of 250 to 400 mm
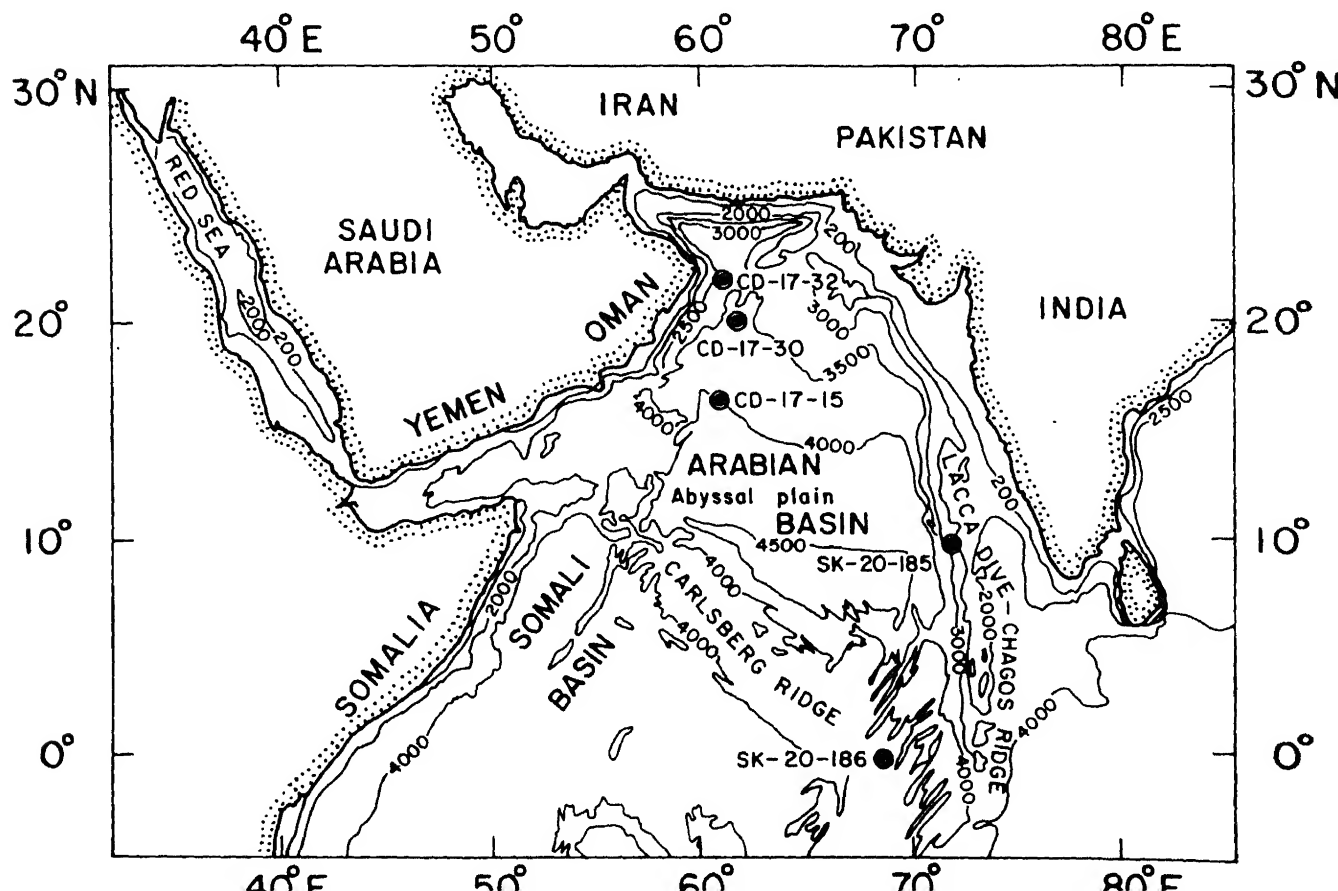
cles, the samples were given an ultrasonic treatment under distilled water for a few seconds and the water was subsequently absorbed by tissue paper. The samples were dried under vacuum at 150°C for an hour. The details are described elsewhere (Sarkar *et al* 1990b).

The samples were then reacted with 100% H_3PO_4 at 50°C under vacuum in an on-line extraction system (Sarkar and Bhattacharya 1988). Water vapour was removed from the evolved CO_2 gas by passing it through three traps (-100°C). $\delta^{18}O$ and $\delta^{13}C$ were measured in a VG Micromass 602 D mass spectrometer with a precision of ± 0.1‰; this is based on replicate measurements of internal laboratory standards ($CaCO_3$), Z-Carrara and Marble V, kindly provided by N. J. Shackleton of the Cambridge University. All the samples were run at least in duplicate. The mean intra-sample variability for 300 such duplicate analyses is ± 0.15‰ and the data presented in this paper are mean values of duplicates relative to V-PDB standard.

In addition to stable isotope ratios, the $CaCO_3$ content was measured in two cores as a function of depth. About 100 mg of the bulk sediment was subjected to a 2% acetic acid leaching in batches, centrifuged and the clear solution was made to 100 ml and titrated against 0.01 M standardized EDTA. The reproducibility of $CaCO_3$ measurement, estimated from replicate analyses of both standard carbonate and samples is ± 1%. Three sediment cores were also dated by ^{14}C, U-Th methods (Sarkar *et al* 1992). Details of the procedures are reported elsewhere (Sarkar 1989). The dates refer to uncorrected radiocarbon ages and are *not calendar ages*.

4. Results and discussion

4.1 *Sedimentation rates*

The sedimentation rates of three cores SK-20-185, SK-20-186 and CD-17-30 based on ^{14}C and U-Th methods are presented in table 2. SK-20-185 has a uniform sedimentation rate during the last 25 ka while in SK-20-186, there is a break at 22–23 cm depth. The

Table 2. *Sedimentation rates by various methods*

Core	Method	Sedimentation rate (cm/kyr)
SK-20-185	[14]C	2.2±0.1 (up to 70 cm)
	[230]Th (excess)	2.5±0.5 (up to 145 cm)
SK-20-186	[14]C	2.4±0.1 (0 to 23 cm)
		0.6±0.1 (below 23 cm)
	[230]Th (excess)	0.6±0.1 (up to 147 cm)
CD-17-30	[14]C	7.7±0.6 (up to 185 cm)

latter core is 0.6 cm/ka, a factor of 4 less than the Holocene rate. CD-17-30 has a higher sedimentation rate due to higher biological productivity in the upwelling zone of the western Arabian Sea and a much higher terrigenous accumulation. [230]Th-based sedimentation rates, where available, agree well with those based on the ^{14}C methods within experimental uncertainties. The details are published elsewhere (Sarkar *et al* 1992).

After the retrieval of gravity cores SK-20-185 and SK-20-186, the top parts in both were found to be disturbed by the coring operation and a small portion of the surface was slumped. Considering the cross sectional area of the corer and the weight of the material slumped, the length of the sediment disturbed was found to be 1 to 2 cm, taking the density to be about 0.7 gm/ml (for top parts) in both the above cores. [This material, with the overlying water in the core spread to a distance of 15 cm and Naidu *et al* (1989), who shared these cores with us for studying foraminiferal assemblages, assumed this length (15 cm) of the core top to be disturbed]. The depth assignments have been made after making due correction for this slumping. These disturbed sediments in SK-20-185 and SK-20-186 have a ^{14}C age of 4.0 ± 0.1 ka and 5.2 ± 0.1 ka respectively. Such core top ages are typical of cores with bioturbation, but these datings show the surface sediments to be of Holocene age.

4.2 *Modern oceanographic conditions*

The present day oceanographic condition over the Arabian Sea is dominantly controlled by seasonally varying insolation and wind system, which cause both monsoonal rain over the Indian region and intense upwelling in the western Arabian Sea. Freshwater discharge through the peninsular rain-fed rivers into the southeast Arabian Sea, coupled with a strong evaporation in the northern sector controls the salinity pattern which increases from 35‰ to 36.5‰ (Wyrtki 1971). During the summer a pronounced temperature drop of about 4°C takes place along the Somali and Arabian coasts, due to upwelling induced by the monsoon circulation. This has been discussed in detail by Wyrtki (1973) and Duplessy (1982).

4.3 *Isotopic composition of core-top foraminifera*

Using GEOSECS (Gote-Ostlund *et al* 1987) surface water $\delta^{18}O$ values and mean annual SST data (Wyrtki 1971), equilibrium calcite $\delta^{18}O$ values have been calculated for the five core locations, CD-17-15, CD-17-30, CD-17-32, SK-20-185 and SK-20-186. These values are in good agreement with the measured core top *G. sacculifer* $\delta^{18}O$ values (table 3), except for SK-20-186. There are no $\delta^{18}O$ data for this station and the

Table 3. $\delta^{18}O$, $\delta^{13}C$ values of calcite* and the observed values of core top *G. sacculifer* (250–400 μm).

Core No	Mean Annual SST(°C)	$\delta^{18}O^1$ Calc. (‰) PDB	$\delta^{18}O^2$ Gs (‰) PDB	$\delta^{13}C^3$ Calc. (‰) PDB	$\delta^{13}C^4$Gs (‰) PDB	$\Delta^{18}O^5$ (‰)	$\Delta^{13}C^6$ (‰)
CD-17-32	24.5	−1.1	−1.22	3.78	1.11	0.12	2.67
CD-17-30	25.5	−1.32	−1.28	3.81	1.35	−0.04	2.46
CD-17-15	26.0	−1.43	−1.43	3.83	1.27	0.0	2.56
SK-20-185	27.5	−1.73	−1.72	3.77	1.76	−0.01	2.01
SK-20-186	28.5	−1.94	−1.39	3.91	1.79	−0.55	2.12

* Calculated using equations (Shackleton 1974 and Emrich *et al* 1970).
[1] $\delta^{18}O$ values, for all the 5 core locations are calculated, taking surface $\delta^{18}O$ of water as 0.56‰ (PDB), station 416, GEOSECS 1987.
[2,4] $\delta^{18}O$ and $\delta^{13}C$ values of core top *G. sacculifer* (250–400 μm) respectively.
[3] $\delta^{13}C$ values are calculated based on bicarbonate-$\delta^{13}C$ data of GEOSECS (Gote-Ostlund *et al* 1987). For first 3 core locations, data from closest location i.e. station 416 are used. For the other two (185 and 186) cores, values of stations 417 and 418 are used respectively.
[5,6] Difference in $\delta^{18}O$ and $\delta^{13}C$ between calculated and observed core top δ values respectively.

assumed $\delta^{18}O$ value of 0.56 (relative to CO_2-PDB) for surface water may be incorrect. Even so, we believe that our data in general, indicate that *G. sacculifer* grows in oxygen isotopic equilibrium at least for the 250 to 400 mm size range, confirming earlier results (Erez and Luz 1983). This species has thus been preferred for analysis in the other cores.

Contrary to this, the $\delta^{13}C$ values of core-top *G. sacculifer* show a depletion of about 2‰ or more (table 3) relative to calculated equilibrium values. Carbon isotopic ratios are known to deviate from the equilibrium values (Duplessy *et al* 1981) but the offset is assumed to be constant with time and does not affect the glacial-interglacial differences in $\delta^{13}C$ (Kallel *et al* 1988).

4.4 *Oxygen isotopes as a function of time*

$\delta^{18}O$ values for five species of foraminifera in SK-20-185 are shown in table 4(a) (high resolution) and for *G. sacculifer* alone (lower resolution, same core) are presented in table 4(b). Data for the other four cores are presented in tables 5 and 6 and in figure 2. Data from CD-17-32 are not plotted as this core does not reach the last glacial maximum (LGM). In SK-20-185 there is a negative spike of about 1‰ at LGM (i.e. 28–34 cm), which possibly represents the enhancement of the winter monsoon current (Sarkar *et al* 1990a, see discussion at the end of this section), and is not shown in figure 2. Core CD-17-30 has a sedimentation rate of 7.7 cm/ka (^{14}C based) and has been analysed up to

Table 4(a). *Oxygen and carbon isotope data on core SK-20-185. High resolution analysis on 5 species*.

Depth (cm)	$\delta^{18}O$ (‰) 1	2	3	4	5	$\delta^{13}C$ (‰) 1	2	3	4	5	CaCO₃ (‰)
2.50	−1.34	−1.87	−1.49	−	−0.81	1.74	1.43	1.94	−	1.37	67.5
4.50	−1.72	−2.24	−1.61	−0.94	−0.82	1.76	1.32	1.80	0.60	1.37	65.8
6.50	−1.70	−2.23	−1.44	−0.96	−1.02	1.53	1.27	1.50	0.58	1.34	−
8.50	−1.41	−1.90	−1.38	−1.04	−0.74	1.53	1.01	1.61	0.59	1.16	−
10.50	−1.17	−1.89	−0.69	−0.58	−0.21	1.42	1.25	1.62	0.57	1.21	60.3
12.50	−0.60	−1.17	−0.63	−0.11	−0.15	1.50	1.17	1.21	0.50	1.47	−
14.50	−0.94	−1.45	−0.52	−0.04	−0.52	1.31	0.90	1.34	0.59	1.13	52.6
16.00	−0.46	−1.37	−0.01	0.12	−0.04	1.05	0.84	1.45	0.65	1.36	51.6
18.00	−0.16	−0.61	−0.08	0.55	0.64	1.50	1.17	1.44	0.65	1.39	48.1
20.00	−0.16	−1.21	−0.12	0.82	0.15	1.36	0.96	1.51	0.67	1.48	−
22.00	−0.09	−0.72	0.38	1.03	0.51	1.48	1.11	1.43	0.92	1.53	−
24.00	0.08	−0.48	0.38	0.85	0.78	1.49	1.21	1.47	0.62	1.61	42.6
26.00	0.23	−0.21	0.43	1.13	0.87	1.40	1.19	1.35	0.76	1.63	−
28.00	−0.14	−0.42	0.23	1.13	0.59	1.54	1.30	1.47	0.76	1.57	−
30.00	−0.30	−0.53	0.31	0.95	0.87	1.36	1.24	1.71	0.70	1.70	41.0
32.00	−0.97	−0.75	0.05	0.95	0.40	1.66	1.21	1.72	0.70	1.42	−
34.00	−0.88	−0.67	−0.69	−	0.65	1.62	1.23	1.66	−	1.65	−
37.50	0.34	−0.28	0.65	−	0.80	1.54	1.04	1.58	−	1.71	40.2
42.50	0.26	−0.42	0.20	−	0.57	1.73	1.26	2.01	−	1.62	−
47.50	0.26	−0.63	0.22	−	0.79	1.65	0.85	1.94	−	1.54	38.5

(1) *G. sacculifer* (250–400 μm); (2) *G. ruber* (250–355 μm); (3) *O. universa* (400–500 μm); (4) *P. obliquiloculata* (250–400 μm); (5) *G. menardii* (250–400 μm); * (30–40) individuals per aliquot.

Table 4(b). *Oxygen and carbon isotope data on core SK-20-185. Analysis on G. sacculifer at larger intervals.*

Depth (cm)	$\delta^{18}O$ (‰)	$\delta^{13}C$ (‰)	CaCO$_3$ (%)	Depth (cm)	$\delta^{18}O$ (‰)	$\delta^{13}C$ (‰)	CaCO$_3$ (%)
52.50	0.40	1.92	–	147.50	−0.30	1.65	37.4
57.50	0.22	1.88	40.2	152.50	−0.24	1.32	32.6
62.50	0.11	1.83	40.2	157.50	−0.12	1.46	31.4
67.50	−0.02	1.84	42.8	162.50	−0.44	1.52	32.6
72.50	−0.25	1.79	45.2	167.50	−0.68	1.50	28.6
77.50	−0.17	1.69	44.4	172.50	−0.34	1.41	32.5
82.50	−0.48	1.65	46.7	177.50	−0.90	1.36	35.2
87.50	−0.06	1.74	45.6	182.50	−0.90	1.36	33.0
92.50	−0.23	1.53	–	190.00	−0.51	1.53	44.0
97.50	−0.21	1.71	45.7	200.00	−0.80	1.63	48.6
102.50	−0.44	1.62	46.1	210.00	−1.09	1.87	53.5
107.50	−0.21	1.75	–	220.00	−0.60	1.82	42.7
112.50	−0.67	1.50	42.9	230.00	−0.87	1.42	56.0
117.50	−0.53	1.42	45.4	240.00	−0.89	1.47	59.4
122.50	−0.49	1.48	–	250.00	−1.05	1.48	55.1
132.50	−0.32	1.47	43.4	260.00	−1.18	1.76	52.1
137.50	−0.14	1.54	45.8	270.00	−1.10	1.71	49.7
142.50	−0.07	1.49	41.4	280.00	−1.13	1.45	49.2
–	–	–	–	290.00	−0.84	1.55	51.0

Table 5. *Oxygen and carbon isotope data* on cores from Charles Darwin cruise.*

	CD 17-30			CD 17-15			CD 17-32	
Depth (cm)	$\delta^{18}O_{PDB}$ (‰)	$\delta^{13}C_{PDB}$ (‰)	Depth (cm)	$\delta^{18}O_{PDB}$ (‰)	$\delta^{13}C_{PDB}$ (‰)	Depth (cm)	$\delta^{18}O_{PDB}$ (‰)	$\delta^{13}C_{PDB}$ (‰)
5.0	−1.28	1.35	47.5$^{\#}$	−1.43	1.27	5.0	−1.22	1.11
15.0	−1.21	1.13	–	–	–	15.0	−1.05	1.12
25.0	−0.61	1.21	–	–	–	25.0	−0.65	1.22
42.5	−0.36	1.14	0.0^{+}	−0.08	0.81	32.0	−1.11	1.29
50.0	0.21	1.36	1.0	0.73	1.18	41.0	−0.89	1.13
55.0	0.14	1.06	11.0	0.76	1.11	49.0	−0.95	1.31
65.0	0.87	1.13	20.5	0.52	1.00			
75.0	0.69	1.07	26.5	−0.35	0.83			
85.0	0.87	1.34	37.5	0.34	0.95			
92.5	0.28	0.82	47.5	0.65	1.07			
100.0	0.61	1.27	57.5	0.89	0.88			
112.5	0.35	0.95	67.5	0.47	0.91			
130.0	1.01	1.13	77.5	0.90	0.64			
150.0	0.90	0.90	112.5	0.32	1.03			
165.0	1.03	1.17	127.5	0.61	1.20			
195.0	0.74	1.22	142.5	0.17	0.77			
212.5	0.42	1.02	157.5	0.19	0.93			
235.0	0.58	1.02	175.0	−0.51	0.98			
250.0	0.52	1.13	182.5	0.19	0.73			
262.5	0.26	0.86	205.0	0.23	0.93			
277.5	0.18	0.64	227.5	0.50	0.91			
307.5	0.15	0.78	262.5	−0.49	0.20			
–	–	–	297.5	0.41	1.15			

* Measured on *G. sacculifer* (250–400 μm) with 30–40 individuals per aliquot.
$^{\#}$ Box core (foraminifera absent above this depth). $^{+}$Piston core, disturbed top.

isotope-stage-3. SK-20-185 has a mean sedimentation rate of 2.2 cm/ka and extends up to stage-5e. SK-20-186 has a long climatic record ending at stage-11. Bold arrows in these three cores indicate the 18 ka LGM level (based on ^{14}C dates). The different stage allotments have been done in comparison with SPECMAP data (Imbrie *et al* 1984). The timing of various isotope stages, calculated using ^{14}C data for the top part of

SPECMAP data. This indicates that the sedimentation rate (estimated from the top part of this core) was relatively constant throughout. This is not true in the case of SK-20-186; the extrapolated ^{14}C ages disagree with SPECMAP data. The variation in sedimentation rate here is indicated by the ^{14}C data during the last 40 ka (table 2).

CD-17-15 (piston core) does not yield a good $\delta^{18}O$

Table 6. *CaCO₃, oxygen and carbon isotope data (G. sacculifer, 250–400μm, 30–40 tests)on core SK-20-186.*

Depth (cm)	$\delta^{18}O$ (‰)	$\delta^{13}C$ (‰)	CaCO₃ (%)	Depth (cm)	$\delta^{18}O$ ‰	$\delta^{13}C$ ‰	CaCO₃ (%)	Depth (cm)	$\delta^{18}O$ (‰)	$\delta^{13}C$ (‰)	CaCO₃ (%)
1.00	−1.37	1.67	–	94.5	−0.07	1.48	81.6	257.0	−0.66	1.33	88.3
2.50	−1.39	1.79	87.8	104.5	0.01	1.43	80.4	267.00	−0.78	1.33	85.8
11.50	−1.10	1.68	87.9	114.5	0.00	1.39	79.9	277.00	0.06	1.21	85.8
13.50	−0.85	1.71	82.0	124.5	−0.21	1.49	86.2	287.00	0.12	1.49	83.3
15.50	−0.51	1.74	83.3	129.5	−0.35	1.32	83.2	297.00	−0.48	1.37	84.0
17.50	−0.49	1.76	84.3	134.5	−0.61	1.45	82.3	307.00	−0.47	1.38	83.5
19.50	−0.57	1.82	82.5	139.5	−0.42	1.46	84.1	317.00	0.31	1.44	83.3
21.50	−0.47	1.78	81.8	144.5	−0.5	1.54	84.9	327.00	0.21	1.60	83.4
24.50	−0.32	1.65	82.5	149.5	−0.52	1.71	87.0	337.00	0.13	1.72	83.7
26.50	0.00	1.99	82.2	154.5	−0.75	1.55	86.2	347.00	0.05	1.64	82.8
28.50	0.13	1.84	82.0	159.5	−0.60	1.48	86.9	357.00	−0.38	1.65	83.5
30.50	−0.30	1.73	81.3	164.5	−0.54	1.53	83.8	367.00	−0.59	1.45	85.6
32.50	−0.31	1.76	83.7	169.5	−0.35	1.51	83.1	377.00	−0.40	1.62	88.9
43.00	−0.37	1.78	79.5	174.5	−0.40	1.64	86.7	387.00	−0.03	1.42	81.5
47.00	−0.46	1.79	80.9	179.5	−0.60	1.51	86.2	397.00	−0.22	1.56	85.5
53.00	−0.83	1.68	82.3	184.5	−0.90	1.46	85.1	407.00	−0.73	1.41	87.1
57.00	−0.70	1.91	85.1	189.5	−0.62	1.46	86.1	417.00	−0.46	1.53	86.4
64.50	−0.68	1.70	85.6	197.5	−0.43	1.44	84.1	427.00	−0.28	1.37	87.5
69.50	−0.84	1.57	83.6	207.00	−0.18	1.31	83.4	437.00	−0.47	1.46	86.5
74.50	−0.92	1.62	84.2	217.00	−0.13	1.38	82.8	447.00	−0.27	1.45	86.7
79.50	−0.71	1.42	83.2	227.00	−0.39	1.67	83.4	457.00	−0.45	1.27	87.1
84.50	−1.00	1.29	85.1	237.00	−0.41	1.54	87.5	467.00	−0.69	1.43	87.9
89.50	−0.70	1.24	79.6	247.00	−0.56	1.52	88.6	477.00	0.01	1.26	88.7
								487.00	0.43	1.15	84.1

(compare with other core-top $\delta^{18}O$ values in the nearby cores) and an erratic excursion of $\delta^{18}O$ is seen (figure 2) all through the 300 cm analysed. This reflects the slumped nature of the sediments, consistent with the litholog showing distinct turbidite layers.

The Holocene-LGM amplitudes in SK-20-185 and CD-17-30 are 2.12 and 2.28‰ respectively. For SK-20-185 Holocene (most depleted $\delta^{18}O$) depth is taken to be 4.5 cm and LGM (based on ^{14}C age) depth to be 31.0 cm; for CD-17-30 Holocene depth is taken to be 5.0 cm and LGM depth to be 100 cm. Considering the glacial ice volume effect to be 1.6‰ (Imbrie et al 1984), these large amplitudes in the Arabian Sea core show an extra 0.5 to 0.7‰ effect, which is local in nature. Such an enrichment in both the northern and southern cores during LGM indicates that most of the Arabian Sea is likely to have been more saline than today by about 1 to 2‰ [we use the data of Duplessy et al (1981) to calculate that for a 1‰ change in salinity, $\delta^{18}O$ changes by about 0.33‰]. We ascribe this to a lesser fresh water run off into the Arabian Sea, because of a weakened summer monsoon during LGM. The Holocene difference in $\delta^{18}O$ between these two locations (∼0.4‰) is slightly smaller than the LGM difference (∼0.6‰), thus making the respective total amplitudes (2.12 and 2.28‰) slightly different. This could be due to a stronger evaporation in the northern Arabian Sea compared to the southern Arabian Sea. This differential rate of evaporation was probably strong enough to compensate the effect

of warming in the north due to reduced upwelling because of the weaker summer monsoon.

In the equatorial Indian Ocean, the Holocene-LGM $\delta^{18}O$ amplitude (SK-20-186) is only 1.5‰ An increased precipitation over the equatorial Indian Ocean during LGM could have been responsible for such a reduced amplitude. The above findings confirm the earlier work of Duplessy (1982). Alternatively, a smaller ice volume effect (1.1‰ contrary to 1.6‰, Labeyrie et al 1987) coupled with a 2°C reduction in SST could have produced such an amplitude.

In the beginning of this section we referred to a negative excursion of about 1‰ in the oxygen isotopic composition of three planktonic foraminifera in core SK-20-185 from the Arabian Sea during LGM. We interpreted this as the combined effect of sea surface warming due to a weaker southwest monsoon and an enhanced northeast monsoon (Sarkar et al 1990a). Krishnamurthy (1990) and Gupta et al (1992) have questioned this since the river discharge from peninsular India, according to them, is only 13% during winter, from modern river discharge data. They have ignored two major rivers, Cauvery and Pennar and also fail to note that during winter there are frequent cyclones in the Bay of Bengal which bring enormous amounts of rain to the east coast of India causing loss of life and property. We had proposed that as the northeast monsoon became stronger during LGM (Duplessy 1982; Van Campo et al 1982), the frequency of such flooding events must have increased (Sarkar et al 1990a). Krishnamurthy (1990) and Gupta et al
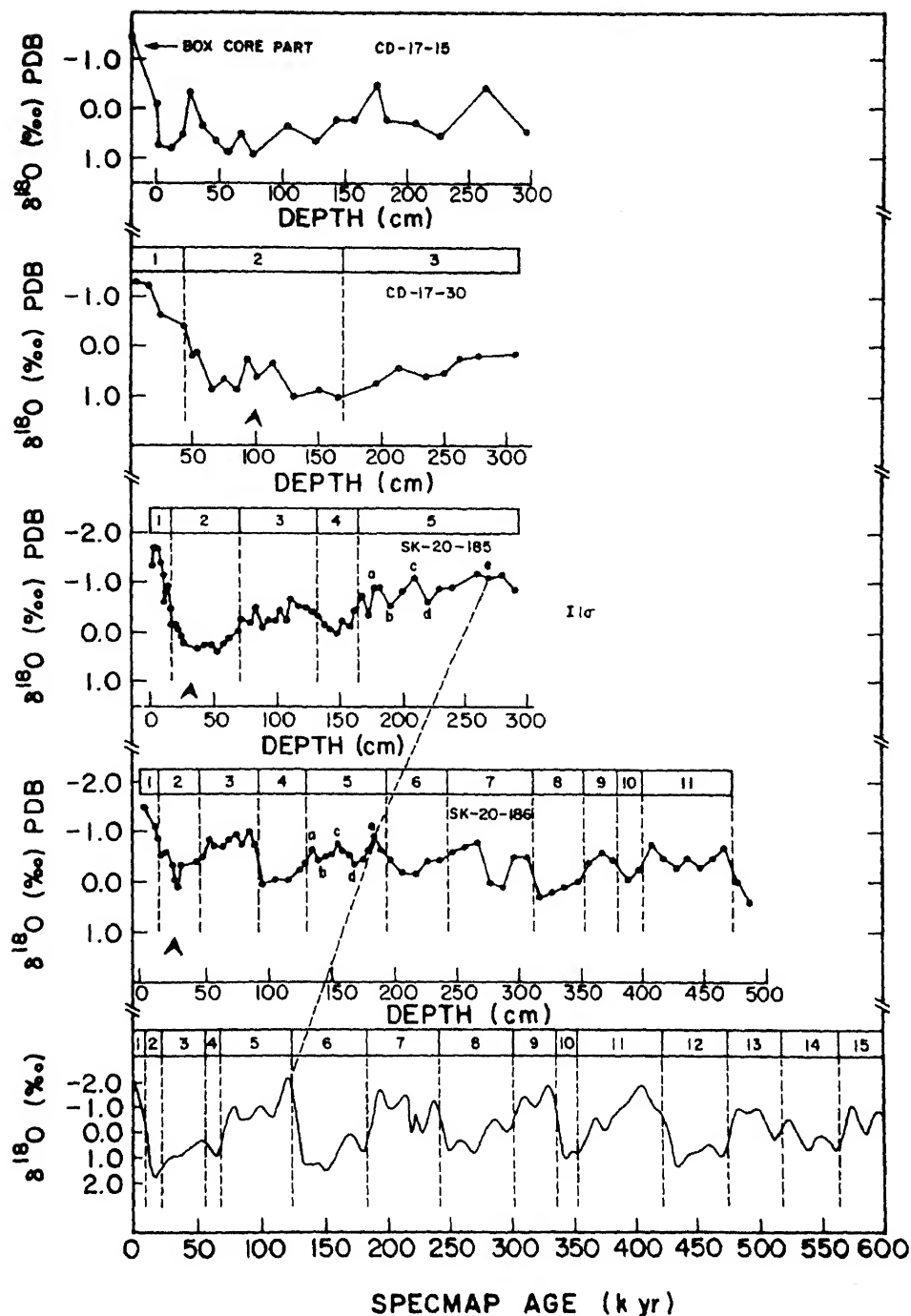
Figure 2. Oxygen isotope data of *G. sacculifer* from cores CD 17-15, CD 17-30, SK 20-185, SK 20-186 and SPECMAP for comparison.

(1992) have overlooked this aspect. Further, modern river discharge is regulated by many dams giving a low flux value not applicable during LGM. Duplessy's (1982) data also support our contention; salinity contours which run east-west today due to fresh water discharge from the Ganges and Brahmaputra in the north, ran north-south due to a reduction in such discharge due to the weakening of the southwest monsoon and probable enhancement in the discharge from he peninsular rivers, which drained vast amounts of

The alternative mechanisms proposed by Krishnamurthy (1990) and Gupta *et al* (1992) do not stand scrutiny. Krishnamurthy conjectured that the seasonal abundances of *G. ruber* and *G. sacculifer* peak respectively during summer and late summer early autumn, whereas the available plankton tow data (Guptha *et al* 1990) do not support this. Gupta *et al* (1992) propose that the negative excursion was caused by warming and consequent melting of the Tibetan ice sheet [based on *incorrect* plotting of data lifted from

Gupta and Sharma (1993) in reply to a note by Naqvi (1993)]. This is contrary to Broecker and Denton's (1989) observation that during LGM, the equilibrium line altitude of glaciers (including tropical high altitude ones) was considerably lower in both the hemispheres. Further, there is no evidence for an ice sheet in the Himalaya during LGM (Benn and Owen 1998). Gupta et al (1992) quote two observations to support their view: (i) Increased abundance of *Juniperus* pollen during LGM in Tsokar Lake, Ladakh (Bhattacharyya 1989) and (ii) Oxygen isotope data from the Dunde ice cap (Thompson et al 1989). The former could be due either to changes in the wind pattern and consequent change in the source of pollen to the lake or due to enhanced precipitation from the western disturbance, which brings rain to the dry Ladakh region during winters. The latter has a number of problems. Cole et al (1991) have measured the stable isotope ratios in the Dunde ice cap and show that the oxygen isotopic record is complex and does not depend on temperature in the usual sense. They also suggest that changes in the source and direction of air masses are mainly responsible for the observed isotopic variations. Similar conclusions were reached by Pande et al (in press) for the isotopic composition of precipitation in Ladakh Himalaya. Finally Gupta et al's crude model which aims to calculate the required increase in the northeast monsoon to explain the negative spike has major flaws. They assume the top 100 m of the Bay of Bengal to be laterally well mixed. This is incorrect as even today we can see a salinity gradient, 30 per mil in the north to 35 per mil in the south. Furthermore the transport of low salinity water from the Bay of Bengal to the Arabian Sea takes place through an ocean current, limited in dimensions. Gupta et al ignore this fact and by mixing up everything, they "show" that a factor of 10 increase in the northeast monsoon precipitation is required. In view of the above such a large increase is not needed to explain 1 per mil negative excursion.

4.5 *Carbon isotopes*

Phytoplanktons preferentially fix more ^{12}C than ^{13}C of the available carbon within the euphotic zone of the ocean. As a result, phytoplankton $\delta^{13}C$ is depleted (-20 to $-26‰$) and CO_2 of the surface ocean becomes enriched ($+2‰$) (Kroopnick 1985). Oxidation of this organic matter in the deeper water produces a depleted $\delta^{13}C$ of the ΣCO_2. Local effects like up-welling alter the $\delta^{13}C$ profiles of the water column. Changes in productivity and upwelling are therefore likely to be recorded in the $\delta^{13}C$ planktonic foraminifera.

$\delta^{13}C$ values of *G. sacculifer* in the five cores are presented in tables 4(a), 4(b), 5 and 6. In SK-20-185, four other species of planktic foraminifera have been analysed in addition to *G. sacculifer*. These species have different depth habitats and part of this core was
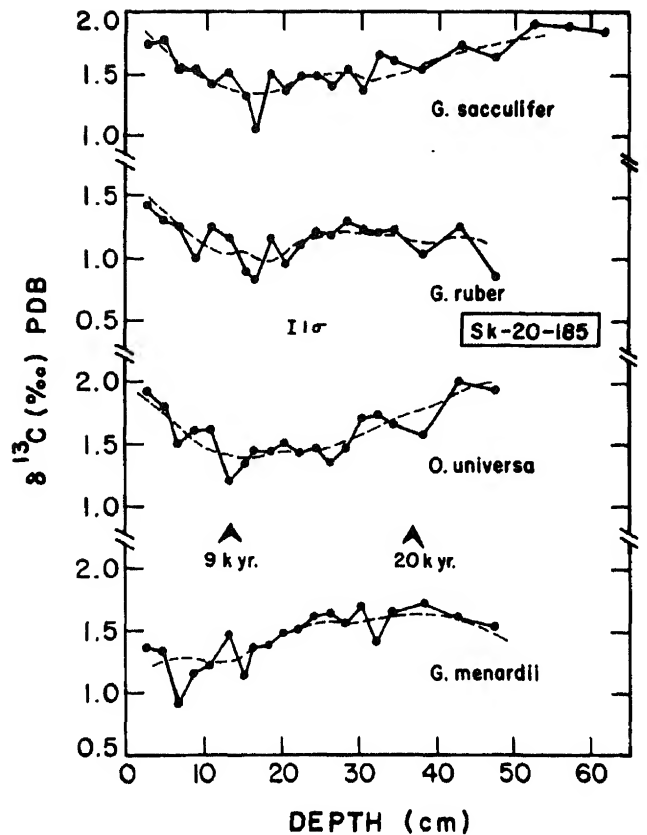

Figure 3. Carbon isotope data for four species in SK 20 -185.

analysed with a high resolution of 1 to 2 cm from surface to the glacial level. A plot of $\delta^{13}C$ with depth is shown in figure 3 for the four species. Early Holocene (~9 ka) and glacial (~20 ka) periods are indicated by bold arrows. The three species *G. sacculifer*, *G. ruber* and *O. universa* show more or less similar variations. A 5-point moving average (dashed line) has been calculated to smooth out the data, which reveals the following features:

- Around 9 ka, there are $\delta^{13}C$ minima in *G. sacculifer*, *G. ruber* and *O. universa*. The magnitudes of these minima, relative to the surface values, is about $0.5 \pm 0.1‰$.
- Relative to 9 ka, glacial $\delta^{13}C$ values in these species show an enrichment by 0.2‰ (*G. ruber*) to 0.6‰ (*O. universa*).
- *G. menardii* does not show a significant difference between surface and 9 ka levels. However, the glacial value is enriched relative to surface by about 0.4‰.
- *P. obliquiloculata* (not shown in figure 3) has near constant $\delta^{13}C$ ($\sim 0.66 \pm 0.1‰$) values throughout this length (2 to 48 cm).
- Down-core variations in $\delta^{13}C$ of *G. sacculifer* are positively correlated with those of *G. ruber* and *O. universa* (figure 3), both with a correlation coefficient of 0.6, significant at 2.5% level.

The present day value of $\delta^{13}C$ of dissolved CO_2 in the Arabian Sea surface water is 1.6 to 1.8‰, while deeper (100 to 200 m) waters have a value of 0 to 0.3‰ (Gote-Ostlund *et al* 1987). Mixing of the upwelled water with the surface could produce a depletion in the surface water $\delta^{13}C$ by a maximum of 1.5‰. On the other hand, the surface productivity is linked to the upwelling, that brings nutrients from the deeper layers. An increased upwelling will enhance productivity which in turn will enrich the $\delta^{13}C$ of surface water CO_2 and hence that of the planktonic foraminifera. Therefore, the resultant change in the surface water $\delta^{13}C$ is dependent on which of these two effects (mixing with $\delta^{13}C$ depleted deeper water due to upwelling on the one hand and enhanced productivity on the other) is stronger.

Independent evidence shows that during LGM, the summer monsoon was weaker than today (Nair and Hashimi 1980; Prell 1984; Sarkar *et al* 1990a); upwelling was weaker and consequently the productivity reduced. The surface dwelling planktonic foraminifera analysed by us show a ^{13}C enrichment of 0.2 to 0.6‰ during LGM, consistent with the effect of weaker upwelling. They also show a depletion of about 0.5‰ during 9 ka, consistent with an enhanced summer monsoon activity and a stronger upwelling.

G. menardii shows only a 0.4‰ enrichment in ^{13}C during LGM; it shows no significant change between 9 ka and the present. This is probably because of the deeper habitat of this species (Duplessy 1982). With lower productivity during LGM, the deeper waters would have been relatively enriched in $\delta^{13}C$ because of the reduced supply of organic matter from the top. *P. obliquiloculata* (with the most depleted $\delta^{13}C$) has the deepest habitat ($\sim$100 m) and is not affected by the change in the $\delta^{13}C$ gradient in the upper water column; therefore it does not exhibit any significant variation during the last 25 ka.

$\delta^{13}C$ values for *G. sacculifer* are shown in figures 4 and 5 for cores SK-20-186, CD-17-30 and CO-17-15. The $\delta^{13}C$ minimum around 9 ka (as found in SK-20-185) is not present in these cores. Whereas SK-20-186 is far away from any coastal upwelling regime and is not expected to show a temporal change in $\delta^{13}C$, CD-17-30 is clearly within the upwelling centre off Arabia. This core does not show the $\delta^{13}C$ change probably

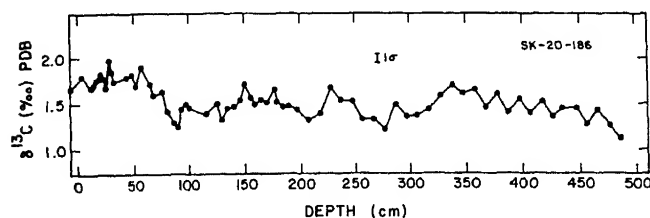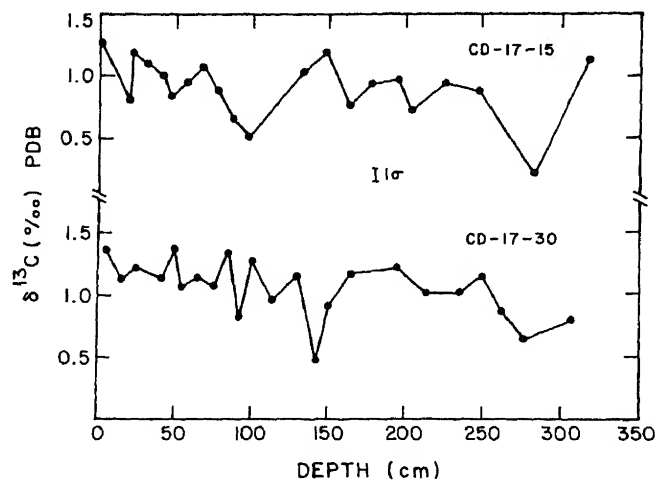Figure 5.   Carbon isotope data *G. sacculifer* from CD 17-15 and CD 17-30.

because the productivity is so high that the corresponding enrichment in $\delta^{13}C$ balances the effect of vertical mixing. Prell and Curry (1981) have observed that core top foraminifera across this upwelling zone do not record any $\delta^{13}C$ change.

4.6 *CaCO₃ variations and palaeoproductivity*

$CaCO_3$ as percentage of the bulk sediment has been measured in 2 cores SK-20-185 and SK-20-186 (tables 4(a), 4(b) and 6). Along with $CaCO_3$, the coarse fraction (>150 mm), mainly foraminifera, was also measured.

Depth profiles of $CaCO_3$ and the coarse fraction abundances in SK-20-185 are shown in figure 6. $\delta^{18}O$ stages are also shown for the chronological framework. Bold arrows indicate 18 ka level. $CaCO_3$ decreases from Holocene ($\sim$68%) to LGM ($\sim$40%). It increases again to 60% during the interglacial stage 5e. $CaCO_3$ and $\delta^{18}O$ show a negative correlation ($\sim$-0.6), significant at 2.5% level. Major $\delta^{18}O$ stages are also reflected in the $CaCO_3$ profile. In stage 5, however, only two sub-stages are found as against five in $\delta^{18}O$. This is possibly because of the coarser resolution with which $CaCO_3$ was measured below 150 cm depth. The coarse fraction also varies sympathetically with $CaCO_3$ in this core; from 27% in Holocene, it decreases to 5% during LGM. Such a similarity indicates that most of the $CaCO_3$ is mainly biogenic calcite. Considering the depth of the core, dissolution seems to be unlikely to produce these variations in $CaCO_3$ and coarse fraction (Peterson and Prell 1985). The variation, we believe, is due to change in biological productivity through time (Naidu and Malmgren 1995a, 1995b, 1996).

Based on the sedimentation rates derived from ^{14}C and $\delta^{18}O$ stratigraphy and using $CaCO_3$ abundance, the time variation of terrigenous and carbonate fluxes
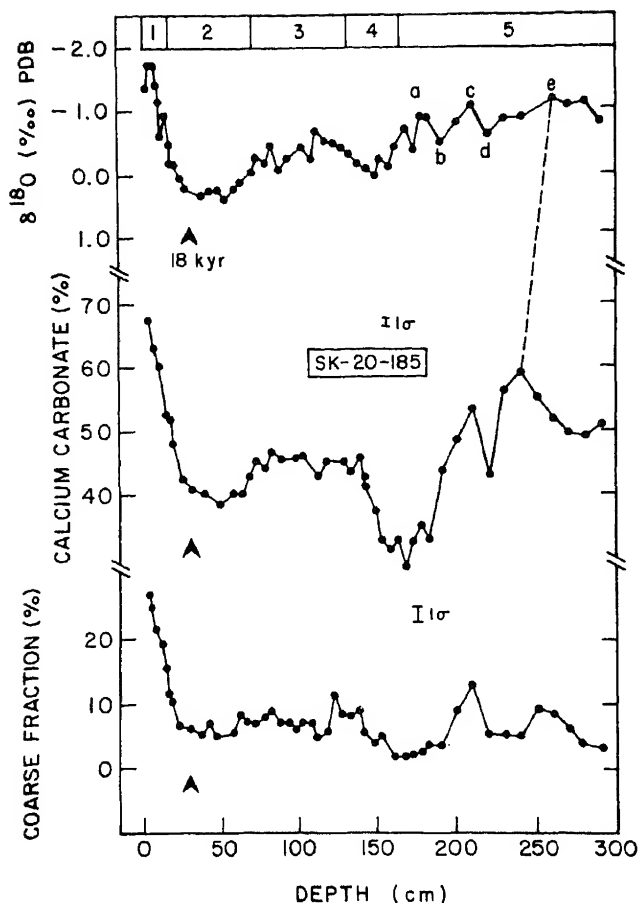

Figure 4.   Carbon isotope data of *G. sacculifer* from SK 20-186.

Figure 6. A comparison between oxygen isotope data (*G. sacculifer*), $CaCO_3$ % and coarse fraction % in SK 20-185.

$0.88 - 0.22\,C - 0.03\,C^2$, where ρ is the density and C is the weight fraction of $CaCO_3$ in the dry sediment. Terrigenous and carbonate fluxes are anticorrelated in this core. Carbonate flux (in $gm\,cm^{-2}\,ka^{-1}$) decreases from Holocene value of 1.02 to 0.62 during LGM, while terrigenous flux increases from 0.49 to 1.05. The lower carbonate flux probably indicates lowering of productivity due to weaker upwelling and summer monsoon conditions during LGM. On the other hand higher terrigenous flux during LGM was probably due to increased rate of erosion when the rivers were cutting across the newly exposed shelf after the lowering of sea level. However, the maximum decrease in productivity and simultaneous increase in terrigenous input took place in stage 4. During the last interglacial (stage 5) productivity was again high, though not as much as during Holocene.

Depth profiles of $CaCO_3$, the coarse fraction and $\delta^{18}O$ in core SK-20-186 are shown in figure 8. In general, the $CaCO_3$ in this core is very high compared with SK-20-185 (~80%). ^{14}C based sedimentation rate and $CaCO_3$ content gives a Holocene carbonate flux of 1.57 $gm\,cm^{-2}\,ka^{-1}$ at this equatorial region, comparable to sediment trap measurements (Nair *et al* 1989). The terrigenous flux in this core is almost constant (0.1 to 0.3 $gm\,cm^{-2}\,ka^{-1}$) throughout and since the $CaCO_3$ abundance is very high, its variation is taken as an index of productivity. Holocene $CaCO_3$ abundance of ~90% in this core reduces to ~80% during LGM indicating lower productivity. There also exists an apparent negative correlation between $\delta^{18}O$ and $CaCO_3$ in this core, too (shown by dashed lines, figure 8). So by and large, it appears that the LGM was characterized in both Arabian Sea and equatorial Indian Ocean by low biogenic production compared to Holocene. This trend was persistent in the preceding glacial-interglacial cycles as well.
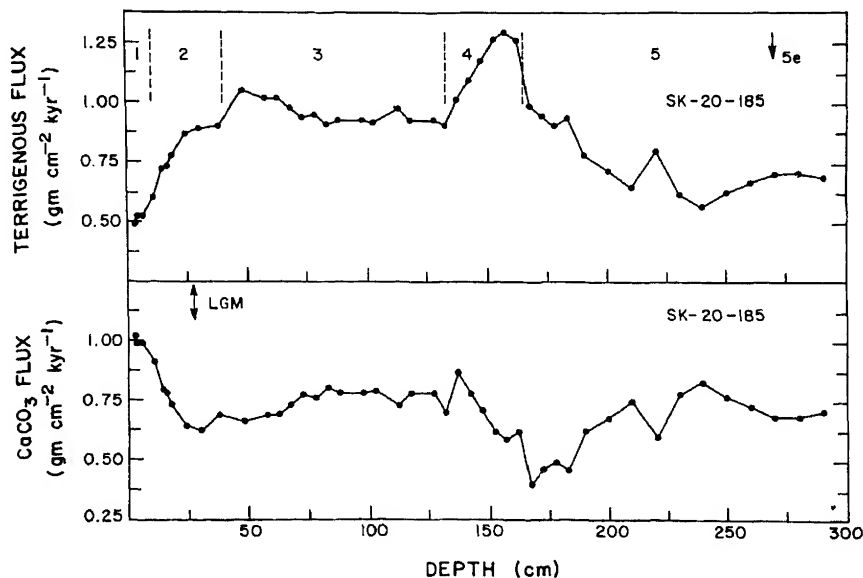
have been calculated for SK-20-185 and are shown in figure 7. For this calculation we have assumed that the density of the sediments varies with the $CaCO_3$ content as shown by Lyle and Dymond (1976); $\rho^{-1} =$

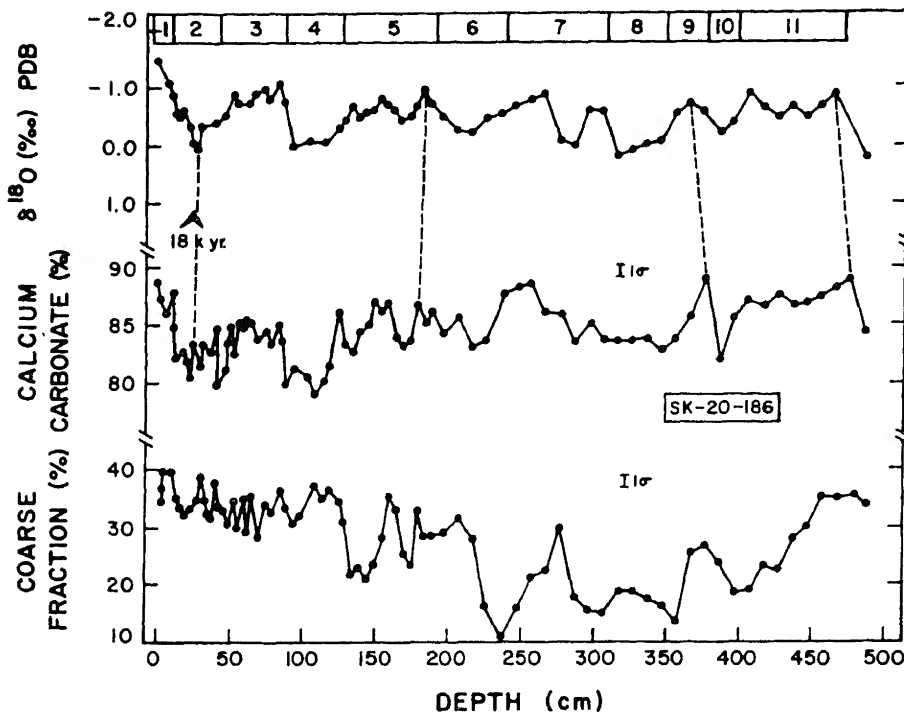Figure 7. Terrigenous and carbonate fluxes inferred from SK 20-185.

Figure 8. A comparison between oxygen isotope data (*G. sacculifer*), CaCO₃ % and coarse fraction % in SK 20-186.

5. Conclusions

$\delta^{18}O$ data from five deep sea cores from the Arabian Sea and the equatorial Indian Ocean provide stratigraphic records ranging from 30 ka to more than 400 ka. During the last glacial-interglacial transition, the Arabian Sea cores in general show a higher $\delta^{18}O$ amplitude than that expected from global ice-volume considerations. This indicates that the Arabian Sea was in general 1 to 2% more saline during the last glacial maximum than at present. The northern Arabian Sea cores show a higher amplitude than the southern ones, whereas the equatorial core shows a lower amplitude. An excess evaporation over the northern Arabian Sea and increased oceanic precipitation in the equatorial Indian Ocean could be responsible for this effect. This was due to the weakening of the summer monsoon during the last glacial period. These results are in agreement with earlier studies (Duplessy 1982; Van Campo *et al* 1982). The weakening of the monsoon led to a reduced upwelling and productivity recorded by $\delta^{13}C$ and CaCO₃ abundances. Calculation of the CaCO₃ flux shows that the biogenic productivity in the Arabian Sea decreased by ~65% during LGM relative to Holocene. A similar reduction has also been observed in the equatorial Indian Ocean, though to a lesser extent (~ 10%). Terrigenous input into the Arabian Sea doubled at the same time possibly due to higher erosion rate along the west coast of India. Around 9 ka the summer monsoon intensified and the effect of enhanced upwelling is seen in the $\delta^{13}C$ of three species of planktonic foraminifera.

References

Benn D I and Owen L A 1998 The role of Indian summer monsoon and the mid-latitude westerlies in Himalayan Glaciation: review and speculative discussion; *J. Geol. Soc. London* **155** 353–363.

Bhattacharyya A 1989 Vegetation and climate during the last 30,000 years in Ladakh; *Palaeogeog. Palaeoclim. Palaeoecol.* **73** 25–38

Berger W H, Killingley J S, Metzler C V and Vincent E 1985 Two step deglaciation: ¹⁴C dated high resolution $\delta^{18}O$ records from the tropical Atlantic; *Quat. Res.* **23** 258–271

Beufort L, Lancelot Y, Camberlin P, Cayre O, Vincent E, Bassinot F and Labeyrie L D 1997 Insolation cycles as a major control of Equatorial Indian Ocean primary production; *Science* **278** 1451–1454

Broecker W S and Denton G H 1989 The role of ocean-atmosphere reorganizations in glacial cycles; *Geochim. Cosmochim. Acta* **53** 2465–2501

Clemens S, Prell W, Murray D, Shimmield G and Weedon G 1991 Forcing mechanisms of the Indian Ocean Monsoon; *Nature* **353** 720–725

Clemens S and Prell W 1991 Late Quaternary forcing of Indian Ocean summer-monsoon winds: A comparison of Fourier model and General Circulation Model results; *J. Geophys. Res.* **96D12** 22683–22700

Cole J, Fairbanks R, Rind D, Koster R, Thompson L and Mosley-Thompson E 1991 Comparison of a high resolution deuterium record from the Dunde ice cap (Tibetan Plateau) and GCM isotope tracer simulations; *XIII INQUA Congress Abstracts* Beijing China (2–9 August 1991) 63

Duplessy J C, Be A W H and Blanc P L 1981 Oxygen and carbon isotopic composition and biogeographic distribution of planktonic foraminifera in the Indian Ocean; *Palaeogeog. Palaeoclim. Palaeoecol.* **33** 9–46

Duplessy J C 1982 Glacial to interglacial contrasts in the northern Indian Ocean; *Nature* **295** 494–498

Emrich K, Ehhalt D H and Vogel J C 1970 Carbon isotope fractionation during precipitation of calcium carbonate; *Earth Planet. Sci. Lett.* **8** 363–371

Erez J and Luz B 1983 Experimental palaeotemperature equation for planktonic foraminifera; *Geochim. Cosmochim. Acta* **4** 1025–1031

Gote-Ostland H, Craig H, Broecker W S and Spenser D (ed) 1987 *Geosecs Atlantic Pacific and Indian Ocean expeditions* **7** Washington DC: National Science Foundation

Gupta S K, Sharma P and Shah S K 1992 Source of fresh water spike at LGM in the Indian Ocean: An alternative interpretation; *J. Quat. Sci.* **7(3)** 247–255

Gupta S K and Sharma P 1993 Enigma of the negative δ^{18}O pulse at LGM -a reply; *Curr. Sci.* **65(7)** 514–515

Guptha M V S, Naidu P D and Muralinath A S 1990 Premonsoon living planktonic foraminifera from the south-eastern Arabian Sea; *J. Geol. Soc. India* **36** 654–660

Imbrie J, Hays J D, Martinson D G, Mix A C, Morley J J, Pisias N G, Prell W L, and Shackleton N J 1984 The orbital theory of pleistocene climate: support from a revised chronology of the marine δ^{18}O record; *Milankovitch and Climate Part-I* (eds) A Berger, J Imkbrie, J D Hays and B Saltzman (Dordrecht: Reidel) 269–305

Kallel N, Labeyrie L D, Juille-Leclere A and Duplessy J C 1988 A deep hydrological front between intermediate and deep water masses in the glacial Indian Ocean; *Nature* **333** 651–655

Krishnamurthy R V 1990 Oxygen in the Arabian Sea; *Nature* **348** 118

Kroopnick P M 1985 The distribution of δ^{13}C of ΣCO_2 in the world oceans; *Deep Sea Res.* **32** 57–84

Labeyrie L D, Duplessy J C and Blanc P L 1987 Variations in mode of formation and temperature of oceanic deep waters over the past 125,000 yrs; *Nature* **327** 477–482

Lyle M W and Dymond J 1976 Metal accumulation rates in the south east Pacific-errors introduced from assumed bulk densities; *Earth. Planet. Sci. Lett.* **30** 164–168

Mix A C 1987 The oxygen-isotope record of glaciation *The Geology of North America and adjacent oceans during the last deglaciation* **K-3** (Geological Society of America) 111–135

Naidu P D, Rao P S and Pattan J N 1989 Planktonic foraminifera from a Quaternary deep sea core from the southern Arabian Sea; *J. Geol. Soc. India* **34** 393–397

Naidu P D, Babu P C and Rao Ch M 1992 The upwelling record in the sediments of the western continental margin of India; *Deep Sea Res.* **39**³/₄ 715–723

Naidu P D and Malmgren B A 1995a Monsoon upwelling effects on test size of some planktonic foraminiferal species from the Oman Margin, Arabian Sea; *Paleoceanography* **10(1)** 117–122

Naidu P D and Malmgren B A 1995b Do benthic foraminifer records represent a productivity index in oxygen minimum zone areas? An evaluation from the Oman Margin, Arabian Sea; *Marine Micropaleontology* **26** 49–55

Naidu P D and Malmgren B A 1996 A high resolution record of Late Quaternary upwelling along the Oman Margin, Arabian Sea based on planktonic foraminifera; *Paleoceanography* **11(1)** 129–140

Nair R R and Hashimi N H 1980 Holocene climatic inferences from the sediments of the Western Indian continental shelf; *Proc. Indian Acad. Sci.* **89-A** 299–315

Nair R R, Ittekkot V, Manganini S J, Ramaswamy V, Haake B Degens E T, Desai B N and Honjo S 1989 Increased particle flux to the deep ocean related to monsoons; *Nature* **338** 749–751

Naqvi S W A 1993 Enigma of the negative δ^{18}O pulse at LGM; *Curr. Sci.* **65(7)** 512–514

Naqvi S W A and Fairbanks R G 1996 A 27,000 year record of Red Sea outflow: Implication for the timing of post-glacial monsoon intensification; *Geophys. Res. Lett.* **23(12)** 1501–1504

Pande K, Padia J T, Ramesh R and Sharma K K Stable isotope systematics of surface water bodies in the Himalayan and trans-Himalayan (Kashmir) region; *Proc. Indian Acad. Sci. (Earth Planet. Sci.)* **109**, 109–115

Peterson L C and Prell W L 1985 Carbonate preservation and rates of climatic changes: An 800 kyr record from the Indian Ocean; *The carbon cycle and atmospheric CO_2; Natural Variations Archean to Present* (eds) E T Sandquist and W S Broecker 251–269

Prell W L 1978 Glacial-Interglacial variability of monsoonal upwelling: western Arabian Sea; *International Conference on Evolution of Planetary Atmospheres and Climatology of the Earth* Centre Nice: National d'Etude Spatiales 129–136

Prell W L and Curry W B 1981 Faunal and isotopic indices of monsoonal upwelling: western Arabian Sea; *Oceanologica Acta* **4** 91–98

Prell W L 1984 Monsoonal climate of the Arabian Sea during the late Quaternary: A response to changing solar radiation; *Milankovitch and Climate Pt 1* (eds) A L Berger *et al* (Dordrecht: Riedel) 349–366

Rostek F, Bard E, Beufort L, Sonzogni C and Ganssen G 1997 Sea surface temperature and productivity records for the past 240 kyr in the Arabian Sea; *Deep Sea Res.* **44(6–7)** 1461–1480

Sarkar A and Bhattacharya S K 1988 An on-line CO_2 extraction system for stable isotope analysis of carbonates; *Preprints Volume Fourth National Symposium of Mass Spectrometry* (eds) T R Kasturi *et al* 1–7 Bangalore: Indian Society of Mass Spectrometry 1–3

Sarkar A 1989 Oxygen and carbon isotopes in Indian Ocean sediments and their palaeoclimatic implications; Unpublished PhD thesis, Gujarat University, India

Sarkar A, Ramesh R, Bhattacharya S K and Rajagopalan G 1990a Oxygen isotope evidence for a stronger winter monsoon current during the last glaciation; *Nature* **343** 549–551

Sarkar A, Ramesh R and Bhattacharya S K 1990b Effect of sample pre-treatment and size fraction on the δ^{18}O and δ^{13}C of foraminifera in Arabian Sea sediments; *Terra Nova* **2** 489–493

Sarkar A, Bhattacharya S K and Sarin M M 1992 Geochemical evidence for anoxic deep water in the Arabian Sea during the last glaciation; *Geochim. Comochim. Acta* **57** 1009–1016

Shackleton N J and Opdyke N D 1973 Oxygen isotope and palaeomagnetic stratigraphy of equatorial Pacific core V28–238: Oxygen isotope temperatures and ice volumes on a 10^5 year and 10^6 year scale; *Quat. Res.* **3** 35–55

Shackleton N J 1974 Attainment of isotopic equilibrium between ocean water and the benthonic foraminifera genus *Uvigerina*: Isotopic changes in the ocean during the last glacial; *Variation du Climat au Cours du Pleistocene* CNRS Paris 203–209

Sirocko F, Sarnthein M, Erlenkeuser H, Lange H, Arnold M and Duplessy J C 1993 Century scale events in monsoonal climate over the past 24,000 years; *Nature* **364** 322–324

Sirocko F, Schoenberg D G, McIntyre A and Molfino B 1996 Teleconnections between the subtropical monsoons and high

latitude climates during the last glaciation; *Science* **272** 526-
-529

Thompson L G, Mosley-Thompson E, Davis M E, Bolzan J F, Dai J, Yao T, Gundestrup N, Wu X, Klain L and Xie Z, 1989 Holocene-late Pleistocene climatic ice core records from Qunghai-Tibetan Plateau; *Science* **246** 474–477

Van Campo E, Duplessy J C and Rossignol-Strick M 1982 Climatic conditions deduced from a 150 kyr oxygen isotope-pollen record from the Arabian Sea; *Nature* **296** 56–59

Wyrtki K 1971 *Oceanographic Atlas of the International Indian Ocean Expedition* (Washington DC: National Science Foundation)

Wyrtki K 1973 *The Biology of the Indian Ocean* (ed) Zeitschel (New York: Springer) 18–36

Long-term records of erosional change from marine ferromanganese crusts

R KEITH O'NIONS* and MARTIN FRANK

Department of Earth Sciences, University of Oxford, Parks Rd., Oxford OX1 3PR, UK
email: keith.onions@earth.ox.ac.uk

Ferromanganese crusts from the Atlantic, Indian and Pacific Oceans record the Nd and Pb isotope compositions of the water masses from which they form as hydrogenous precipitates. The $^{10}Be/^9Be$-calibrated time series for crusts are compared to estimates based on Co-contents, from which the equatorial Pacific crusts studied are inferred to have recorded ca. 60 Ma of Pacific deep water history.

Time series of ε_{Nd} show that the oceans have maintained a strong provinciality in Nd isotopic composition, determined by terrigenous inputs, over periods of up to 60 Ma. Superimposed on the distinct basin-specific signatures are variations in Nd and Pb isotope time series which have been particularly marked over the last 5 Ma.

It is shown that changes in erosional inputs, particularly associated with Himalayan uplift and the northern hemisphere glaciation have influenced Indian and Atlantic Ocean deep water isotopic compositions respectively. There is no evidence so far for an imprint of the final closure of the Panama Isthmus on the Pb and Nd isotopic composition in either Atlantic or Pacific deep water masses.

1. Introduction

Tectonics and climate combine to influence the rates and mechanisms of rock weathering and erosion. However, details of their interrelationships are not well understood. Part of the problem is to identify records of the relevant changes that have taken place. Because a significant portion of the terrigeneous products of continental weathering and erosion enter the oceans and leave an imprint on the chemical and isotopic composition of seawater much effort has been devoted to the recovery of marine records of seawater composition.

Of particular interest have been records of the abundance and isotopic composition of metals in seawater. These are controlled primarily by the nature of their terrigeneous and hydrothermal sources on the one hand and their oceanic residence times on the other. As a consequence, different elements display quite different isotopic distribution patterns in the oceans. For example, despite the large variation in isotopic composition of the various Sr inputs into the ocean the $^{87}Sr/^{86}Sr$ ratio of seawater is uniform globally. This is because the oceanic residence time of Sr is ca. 2 Ma (1 Ma = 1 million years) and thus much longer than the ca. 1.5 ka ocean circulation time (1 ka = 1,000 years). In contrast, Nd has a residence time very similar to the circulation time of the ocean and consequently shows significant differences in isotopic composition between the main ocean basins and even different water masses (e.g. Piepgras *et al* 1979). Thus at any one time the isotopic distribution pattern of metals in the oceans is a result of the interplay between the advection of the dissolved metal input by the circulation and their removal into the marine sediments. In principle it should be possible to reconstruct details of any time-dependent changes in the isotopic distribution patterns arising from either changes in the inputs (erosion and hydrothermal) and the ocean circulation from the marine sedimentary record.

Considerable progress has been made in reconstructing the distribution of Nd and Pb isotopes in Atlantic, Indian and Pacific Ocean water masses from hydrogenous ferromanganese crusts (hereafter called

crusts), in some cases as far back as 60 Ma ago (Goldstein and O'Nions 1981; Albarède and Goldstein 1992; Abouchami and Goldstein 1995; von Blancken-burg et al 1996a; b; Burton et al 1997; Christensen et al 1997; Albarède et al 1997; Ling et al 1997; Abouchami et al 1997; 1998). These metals have short oceanic residence times, similar to or shorter than the global circulation time, and therefore display a strong provin-ciality in their isotopic distribution. From these records it has been possible to assess the impact of changes in the balance of erosion products from different input sources to the oceans as well as changes in ocean circulation.

Crusts are widely distributed in the oceans and provide intact and often long-term records of Nd, Pb and Hf isotopes from which water mass characteristics have been derived. This reconstruction has been facilitated by successful dating of the crusts using cosmogenic ^{10}Be (Segl et al 1984; Ling et al 1997; O'Nions et al 1998), which is introduced into the ocean after production in the upper atmosphere and scavenged from seawater by the Mn-Fe oxyhydroxides of which the crusts mainly consist. ^{10}Be chronologies have a practical limit of around 10 Ma imposed by the 1.5 Ma half-life of ^{10}Be. Linear extrapolation of the growth rates beyond 10 Ma has resulted in maximum ages up to 60 Ma (Ling et al 1997; O'Nions et al 1998) which has recently been supported by using a chrono-meter based on Co-contents (Frank et al 1999).

In this contribution the progress made in the use of well-dated crusts to reconstruct the Nd and Pb isotopic composition of ocean water masses over the last 10 to 60 Ma will be reviewed. The importance of the changing balance of terrigeneous inputs into the ocean, particularly over the last 3 Ma is summarised together with evidence for the apparently very limited response of the Nd- and Pb-isotopic composition of deep water to the paleoceanographic changes related to the closure of the Panama Gateway over the last 10 Ma.

2. Chronology of ferromanganese crusts

The attempts to derive chronologies and growth rates for ferromanganese crusts have broadly been of three types based respectively upon *in situ* radioactive decay, Co-contents and ^{87}Sr/^{86}Sr ratios. The periods datable with the decay-based methods range from 300 ka for ^{230}Th to approximately 10 Ma for ^{10}Be. The approach based on Co-content assumes a constant and known flux of Co to the crust growth surface and has theoretically no age limitations whereas the third method is based upon matching ^{87}Sr/^{86}Sr variations in the Mn-Fe-oxyhydroxide material of the crusts to the known global ocean ^{87}Sr/^{86}Sr evolution. Of these the Sr isotope approach although the subject of much careful work has been the least successful due to

apparent isotope exchange (Burton et al 1997; Ling et al 1997; O'Nions et al 1998).

Hydrogenous ferromanganese crusts have growth rates typically in the range from 2 to 5 mm/Ma but occasionally up to 15 mm/Ma (cf. Segl et al 1984; Manheim 1986; Puteanus and Halbach 1988). There-fore the U-series based methods are useful only for the outer 1–2 mm of crusts but have been used widely (Segl et al 1984; Banakar and Borole 1991; Eisenhauer et al 1992; Chabaux et al 1995; 1997; Bollhöfer et al 1996; Abouchami et al. 1997). Recent evidence for mobility of ^{234}U suggests that ^{230}Th-based approaches are more reliable than U-based ones (Neff et al 1998). Methods for determining growth rates based on the decay of ^{10}Be have overall been the most successful for the period of the last 10 Ma (Segl et al 1984; McMurtry et al 1994). In the Oxford laboratory we have used profiles of direct and high precision measurements of the ^{10}Be/^{9}Be ratio in crusts (Belshaw et al 1995) to determine their growth rates (Ling et al 1997; O'Nions et al 1998; Frank and O'Nions 1998). This method has the advantage of being independent of the amount of Be incorporated into the crust and succeeds because ^{10}Be/^{9}Be ratios in the oceans appear to have varied little over the last 5 to 10 Ma.

The Co-method in many cases provides a check on the uniformity of crust growth over the ^{10}Be dated intervals and the viability of extrapolated growth rates to deeper levels in the crust. The Co-method assumes a constant "rain rate" of Co to the growth surface of the crust and its concentration in the crust then depends upon the rate of addition of the other more abundant elements such as Fe and Mn. Thus as long as the "rain rate" has been constant the Co content will provide a reliable estimate of growth rate varia-tions. The original calibration of the Co content as a chronometer was based on U-series dating of Co-rich crusts with Co contents >1% from the central equatorial Pacific (Halbach et al 1983; Puteanus and Halbach 1988). An alternative relationship between Co-content and growth rate which is supposed to be applicable over a wider range of genetically different ferromanganese crusts and nodules and even pelagic sediments was developed by Manheim (1986).

Some of these aspects of crust chronology are illustrated here. In figure 1 the age-depth relationships obtained for crust D11-1 from the central equatorial Pacific based on ^{10}Be/^{9}Be ratios (Ling et al 1997) and Co contents (Frank et al 1999) are compared. The ages derived from the ^{10}Be/^{9}Be ratios suggest an average growth rate of 1.4 mm/Ma between 7 Ma ago and present and 2.7 mm/Ma between 11 and 7 Ma ago. Extrapolation of the latter suggests an age of about 58 Ma at the base of the crust. The Co content measured by electron probe confirms that the growth rate has indeed deviated very little from the average growth rate of the uppermost 20 mm over the entire depth interval. The great value of the Co method is
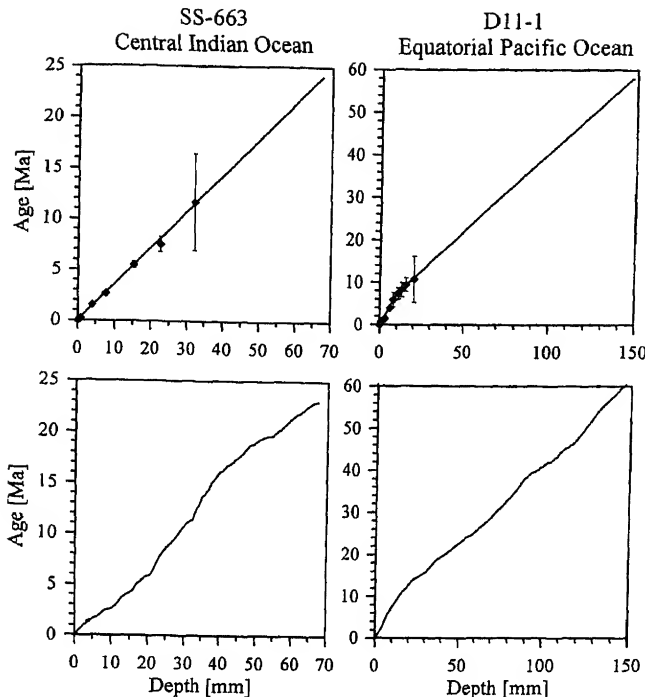
Figure 1. Comparison of age-depth relationships based on ^{10}Be/^{9}Be and Co-content chronometers for crusts SS-663 and D11-1 from the Central Indian and Pacific Ocean respectively. The upper diagrams show ages calculated from ^{10}Be/^{9}Be ratios assuming that the growth surfaces of the crusts have had the present day surface value during their growth and that the decrease in ^{10}Be/^{9}Be ratio with depth is due to decay of ^{10}Be (Ling et al 1997; O'Nions et al 1998). The lower diagrams show the age-depth relationships obtained from the Co-content chronometer (Frank et al 1999) using the relationships proposed by Manheim (1986) for SS-663 and by Puteanus and Halbach (1988) for D11-1. Note the excellent overall agreement between the two approaches and particularly the agreement between the Co-content age estimate and the extrapolated ^{10}Be/^{9}Be age estimates for D11-1.

the support it provides for the ^{10}Be/^{9}Be method and the justification for assuming that 60 Ma of equatorial Pacific deep water history is recorded by this crust.

It should be recalled that there is an element of circularity in these age estimates. In the case of ^{10}Be/^{9}Be ratios the age estimates assume that the ^{10}Be/^{9}Be ratio at the present-day growth surface is the same as that over the last 10 Ma. The self-consistent nature of the data supports this view but does not prove it. Similarly the claim of a uniform growth rate over the whole 150 mm of the crust assumes that the Co rain rate has been constant throughout and that there have been no hiati which is apparently supported by the good correspondence between the two approaches.

Self-consistent results from the ^{10}Be/^{9}Be ratio and Co-content chronometers as obtained for equatorial Pacific samples such as D11-1 (figure 1) are not found at all locations tested so far. The Co rain rate is not uniform everywhere in the ocean and appears to depend on the proximity to and intensity of the oxygen minimum layer; age models using the relationship of Puteanus and Halbach (1988) which were

developed for Co-rich central Pacific seamount crusts are not directly applicable to other parts of the oceans. For Co-poor crusts anywhere else in the ocean the relationship of Manheim (1986) appears to be more suitable to estimate changes in growth rate (Frank et al 1999). The results for crust SS-663 from the central Indian Ocean (figure 1) provide an example of the application of the Co chronometer as adapted for crusts with low Co contents (Manheim 1986). The ^{10}Be/^{9}Be ratios obtained for SS-663 suggest a uniform growth rate for the crust over the outer 35-mm and an age at the base of the crust close to 25 Ma (Frank and O'Nions 1998). The Co-derived ages for this crust are in good agreement and also indicate an age between 20 and 25 Ma at the base (Frank et al 1999). At present these are the only methods which have any general applicability and there is considerable merit in applying them in a complementary manner.

3. Global pattern of Nd and Pb distribution

The isotopic composition of seawater Nd varies as a function of water depth and water mass in the modern oceans as illustrated by published profiles of seawater ε_{Nd} from the Atlantic Ocean (figure 2). It also varies between ocean basins in a way that primarily reflects the age distribution pattern of the surrounding continental crust. At present seawater contains a large component of anthropogenic Pb but the pre-anthropogenic distribution also appears to reflect local provenance and residence time (von Blanckenburg et al 1996b). The surfaces of ferromanganese crusts and nodules from the Atlantic, Indian and Pacific Oceans have Nd isotope compositions, which obviously match those of the water masses in which they have grown (Albarède and Goldstein 1992; Abouchami and Goldstein 1995; Albarède et al 1997). They offer therefore the possibility that variations in the Nd and Pb isotope compositions of ocean water masses or changes in the pathways of water masses may be reconstructed from time series of ferromanganese crusts. In the case of the equatorial Pacific this may be back as far as 60 Ma (Ling et al 1997; Frank et al 1999).

In order to reconstruct the Nd and Pb isotope composition of deep water at a particular location back through time it is necessary to acquire Nd and Pb isotope profiles on accurately dated crusts which are unaffected by diagenesis on the scale sampled for analysis. These conditions are apparently met for seven crusts from the Atlantic, Indian and Pacific Oceans and the results of Nd and Pb isotope analyses are displayed in figures 3 and 4. These Nd and Pb isotope time series differ from those originally published (Ling et al 1997; Burton et al 1997; O'Nions et al 1998; Frank and O'Nions 1998) in that they use the modified age-depth relationships for three crusts (109D-C, BM1969.05, VA13-2) from Frank et al (1999).
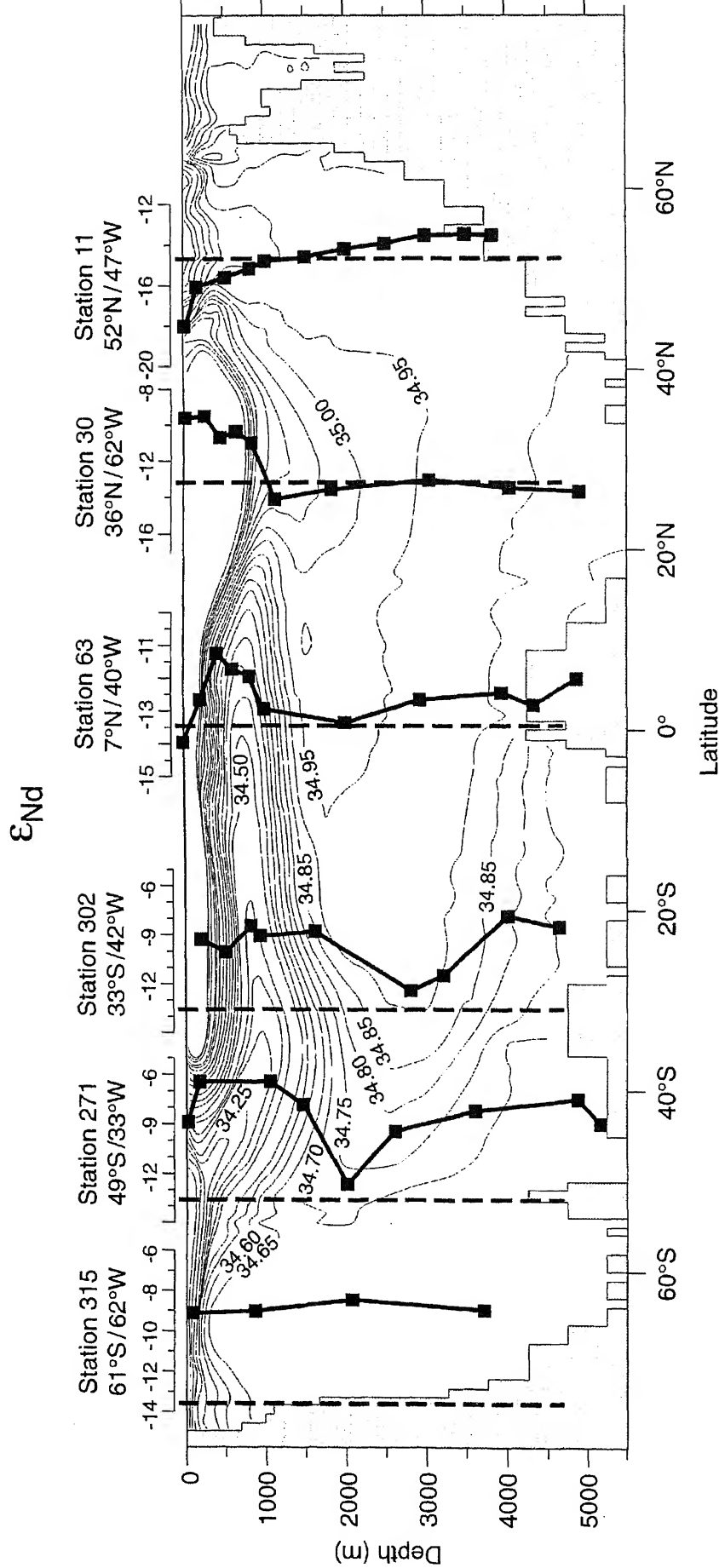
Figure 2. Depth profiles of Nd isotopes, expressed as ε_{Nd} values, at 6 stations in the present day Atlantic (Piepgras and Wasserburg 1982, 1987; Jeandel 1993). These profiles are superimposed on contours of the present-day salinity in the Atlantic as observed along a north-south transect (Levitus 1982). The sea floor topography along the profile is shown in grey. North Atlantic deep water generated by sinking of saline water at a number of sites in the N. Atlantic is identified at mid-ocean depths by its high salinity core and is advected into the S. Atlantic where it is recognisable until about 50°S. The ε_{Nd} value of NADW close to its formation in the N. Atlantic is close to −13.5, and thus several ε_{Nd} units lower than Atlantic surface, intermediate or bottom waters such as Antarctic Intermediate Water or Antarctic Bottom Water which are derived in the S. Atlantic. NADW retains a characteristic ε_{Nd} vale of −13 as far south as 49°S in the southern Atlantic and corresponds well with the water mass distribution defined by salinity.
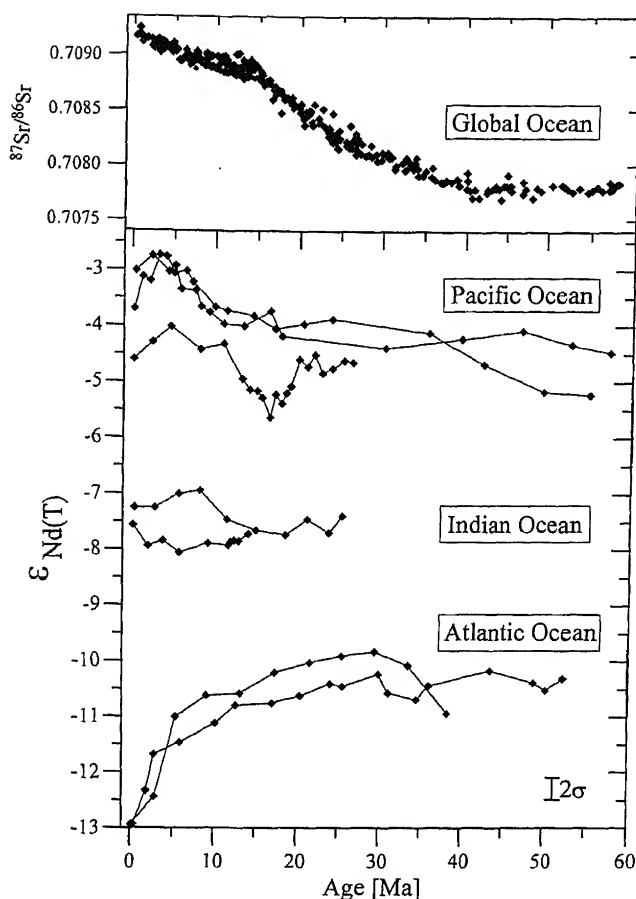
Figure 3. Comparison of ε_{Nd} time series of ferromanganese crusts from the Atlantic, Indian and Pacific Oceans (Ling *et al* 1997; Burton *et al* 1997; O'Nions *et al* 1998) using the revised chronologies for SS-663, BM1969.05 and VA13/2 (Frank *et al* 1999). Note the strong inter-ocean provinciality of ε_{Nd}, which is caused by the different overall ε_{Nd} value of the terrigeneous inputs into the ocean basins and the residence time of Nd which is similar to the ca. 1.5 ka global ocean circulation time. This is too short for efficient mixing of Nd between the major ocean basins. These ε_{Nd} results are compared with the global ocean Sr isotope evolution derived from analyses of foraminifera (Koepnick *et al* 1985; DePaolo 1986; Hess *et al* 1986; Hodell *et al* 1991).

These authors have used Co-content profiles for each crust to identify changes in growth rate in those parts of the profiles which are beyond the range of ^{10}Be/^{9}Be dating. The most significant change compared to the originally published age-depth relationships was found for VA13-2 from the central Pacific (Segl *et al* 1984; Ling *et al* 1997), for which the Co content profile reveals a change from high growth rates around 13 mm/ Ma prior to 14 Ma ago to the lower rates of 3.75 and 2.3 mm/Ma determined by ^{10}Be/^{9}Be afterwards.

The Nd isotope time series in figure 3 reveal some remarkable features as follows:

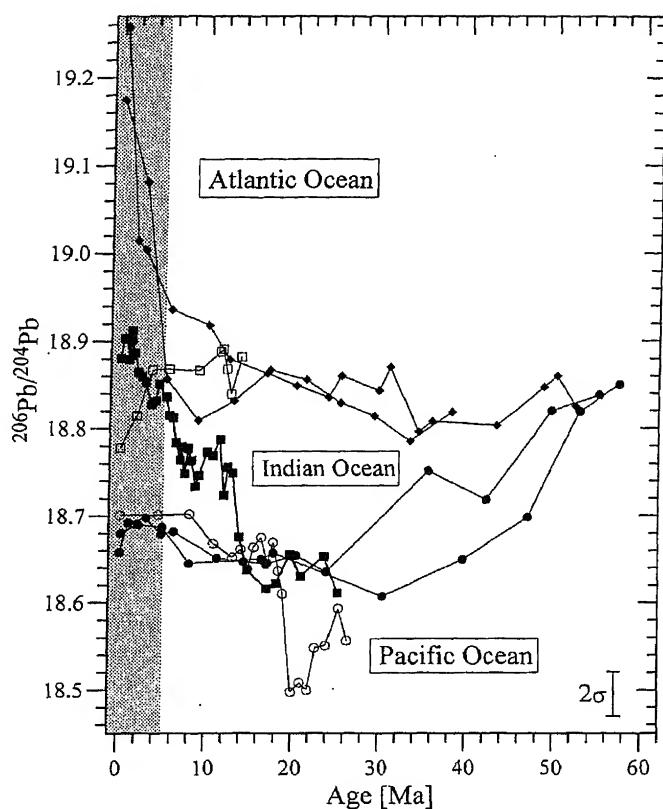- Although the mechanically sampled growth surfaces of the crusts represent 100 ka or more of growth and integrate any variations in ε_{Nd} over this

Figure 4. Comparison of ^{206}Pb/^{204}Pb time series of the same crusts as in figure 3. The North Atlantic crusts are marked by diamond symbols (Burton *et al* 1997; O'Nions *et al* 1998), the southern Indian Ocean crust by open squares (O'Nions *et al* 1998), the central Indian Ocean one by closed squares (Frank and O'Nions 1998), the Pacific deep water crust by open circles (Ling *et al* 1997) and the two Pacific seamount crusts by closed circles (Ling *et al* 1997). The shaded area highlights the last 5 Ma over which separate Atlantic, Indian and Pacific Ocean signatures of the Pb isotopes in the deep water have apparently existed.

- For the last 20 Ma, and probably also the last 60 Ma, deep water masses in the Atlantic, Indian and Pacific Oceans have maintained separate identities in terms of ε_{Nd} values. These different identities reflect the ε_{Nd} values of the terrigeneous inputs into the three ocean basins which in turn reflect the age patterns of the surrounding continental crust. Thus, the more negative ε_{Nd} values in the Atlantic reflect the inputs from the old Precambrian cratons surrounding the N. Atlantic, whereas the much higher values in the Pacific have originated from the young volcanic arcs in the Pacific Ocean and its young continental margins.
- The equatorial Pacific deep water crust VA 13-2 was dredged from a depth of 4830 m compared with depths between 2400 and 1700 m for the other two Pacific seamount crusts. The ε_{Nd} values of VA 13-2 are lower than the other two crusts for the entire 26 Ma record and suggest the long term presence of

In addition to the long-term provinciality of Nd in the oceans there are superimposed shorter-term variations of ε_{Nd} in each of the records. These are most evident for the samples from the NW Atlantic where ε_{Nd} has decreased by about two units to reach the present day NADW value over the last few Ma. The records from the equatorial Pacific display smaller (less than 1 ε_{Nd} unit) but significant decreases over the same time period. In the two Indian Ocean crusts only small and barely significant variations in ε_{Nd} occurred; slight increases of 0.5–0.7 ε_{Nd} units are recorded in the southern Indian Ocean during the last 1 Ma and in the central Indian Ocean at about 8 Ma ago.

In addition to ε_{Nd} time series, Pb isotopes are also presented for Atlantic, Pacific and Indian Ocean samples again using the revised chronology of Frank et al (1999). These are displayed as $^{206}Pb/^{204}Pb$ ratios in figure 4. Because Pb has a residence time of 80–100 years in deep waters (Schaule and Patterson 1981) it is expected a priori to show a similar behaviour to that of Nd, at least if processes occur on the basin scale. A comparison of the time series in figures 3 and 4 indeed shows similarities but also reveals major differences between Pb and Nd. $^{206}Pb/^{204}Pb$ ratios, like ε_{Nd} values, show an inter-ocean provinciality for the last few Ma, with well-resolved differences between the Atlantic, Indian and Pacific samples. Such differences have also existed for the other Pb-isotope ratios (Frank and O'Nions 1998). Unlike the ε_{Nd} time series, however, $^{206}Pb/^{204}Pb$ ratios show much less provinciality further back in the past. This is particularly the case if the Atlantic and Pacific records are compared, which had a similar Pb isotope composition until about 50 Ma ago and then started to diverge. The highlighted area in figure 4 emphasises the pronounced divergence in Pb isotopes over the last 5 Ma, much of which, as in ε_{Nd}, is accounted for by variations in the N. Atlantic crusts.

4. Records of continent erosion

Weathering and erosion of continental crust is the dominant source of Nd in the oceans: the contribution from submarine hydrothermal sources was shown to be negligibly small in terms of mass balance (Michard et al 1983; Piepgras and Wasserburg 1985). Thus ferromanganese crusts bear a record of dissolved Nd of terrigeneous origin at their deep water growth sites over the last up to 60 Ma. The variations in ε_{Nd} at any particular site must reflect either changes in the ε_{Nd} of a particular input or its distribution by the ocean circulation. The effects of ocean circulation are at present substantial as evidenced by the advection of NADW with $\varepsilon_{Nd} = -13.5$ from the sites of NADW generation in the North Atlantic into the southern Atlantic Ocean (figure 2).

The major part of pre-anthropogenic Pb in the oceans has also been terrigeneous in origin. Although Pb has a shorter residence time than Nd it can obviously also be advected on the basin scale depending on the residence times of the respective water masses (Abouchami and Goldstein 1995; Abouchami et al 1998). This implies that Pb isotope time series in a particular crust, similar to Nd isotopes, reflect potential changes in input as well as in circulation. In this section those parts of the records which most clearly reflect changes in erosional inputs to the oceans and their significance will be reviewed.

4.1 Neodymium

- Erosion of the continents and the input of the erosion products into the oceans, either as particulates (including atmospheric dust) or as part of the dissolved river load are the ultimate source of Nd present in the crusts.
- The most spectacular shifts in ε_{Nd} in any of the time series occurs in the two western N. Atlantic crusts (Burton et al 1997; O'Nions et al 1998). Over the last few Ma they have shifted from the long-term (50 Ma) characteristic ε_{Nd} value of the N. Atlantic of ~ -10 by approximately 3 ε_{Nd} units to $\varepsilon_{Nd} = -13.5$, which is the characteristic value for NADW in the present day Atlantic (e.g. Piepgras and Wasserburg 1987). The contribution which is responsible for this unradiogenic Nd isotope composition of NADW is known to be located in the Labrador Sea (Stordal and Wasserburg 1986; Piepgras and Wasserburg 1987). This is the only known source where water masses with ε_{Nd} values < -20 are found.

There are two possibilities for the cause of the dramatic shift of ε_{Nd} in the western N. Atlantic. The first is that there was no change at all in the amount and composition of Nd delivered to the oceans by erosion over the last 5 to 10 Ma. In this case the shift in ε_{Nd} would be due to an intensification of deep water generation in the Labrador Sea and as a consequence an increased amount of Nd with a low ε_{Nd} value contributing to NADW (Burton et al 1997). The second possibility is that amount and composition of the Nd input did change in a way expected to have accompanied the onset of the Northern Hemisphere Glaciation. It is has been shown that prior to ca. 3 Ma ago the amount of erosional input in the Labrador Sea region was small (Shackleton et al 1984; Raymo 1994) and it has also been suggested that deep water formation in the Labrador Sea region may have been much less important before about 3 Ma than afterwards (Burton et al 1997). Von Blanckenburg and O'Nions (1999) have argued that the constant $^{10}Be/^9Be$ ratio in the N. Atlantic seawater over this time period requires that the balance between terrigeneous ^9Be
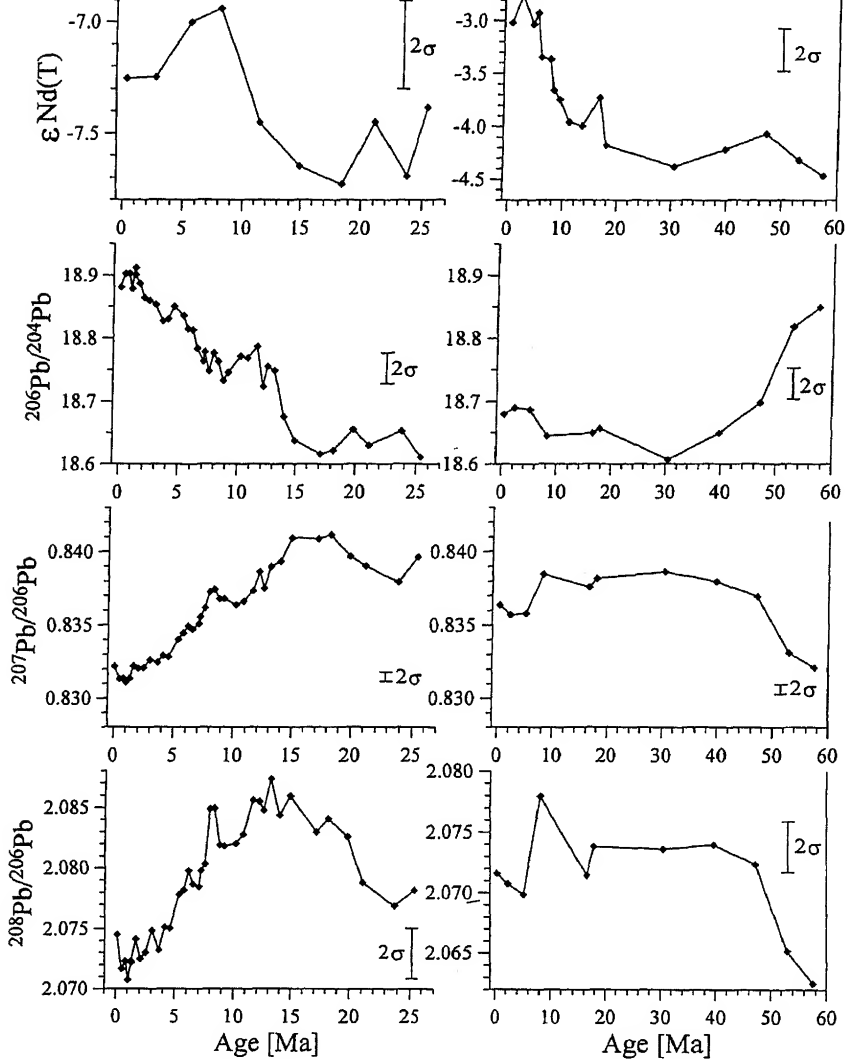
Figure 5. Comparison of ε_{Nd} (age corrected) and Pb isotope time series for crusts SS-663 (O'Nions *et al* 1998; Frank and O'Nions, 1998) and D11-1 (Ling *et al* 1997) based on the ^{10}Be/^{9}Be chronologies given in figure 1. Note the ^{208}Pb/^{206}Pb structure in SS-663 which has been related to the uplift and erosion of the Himalyas (Frank and O'Nions 1998).

input and cosmogenic ^{10}Be input into the N. Atlantic remained fixed in which case a change in the integrated ε_{Nd} value of the terrigeneous input into the N. Atlantic is more likely as a cause for the observed isotopic shifts than a change in circulation. Thus, there appears to be a close link between the Quaternary glaciation and the input of Nd with highly unradiogenic isotope composition in the area of the Labrador Sea. This is supported by results of Winter *et al* (1997) on ferromanganese micronodules from marine sediments in the Arctic Ocean which also show a major shift in ε_{Nd} towards more negative values around 2 Ma ago.

A second point concerns the approximately contemporaneous shift in ε_{Nd} towards more unradiogenic values evident in the time series of crusts from the Pacific. Although these effects are more subtle with ε_{Nd} varying by only 1 unit or less they are nevertheless

significant (Ling *et al* 1997). It was initially suggested that the overall increase in ε_{Nd} from 20 to around to 5 Ma ago in the Pacific crusts may have been arrested by an increased influx of water from the Antarctic Circumpolar Current (ACC) in combination with an intensification of NADW production which enhanced the transfer of unradiogenic Nd from the North Atlantic into the Pacific Ocean via the ACC (Ling *et al* 1997; Burton *et al* 1997). Later missing evidence for a trend towards more unradiogenic Nd in a crust that has grown from ACC water (O'Nions *et al* 1998) has suggested that this was not the case and that the unradiogenic trend in the Pacific crusts since about 3–5 Ma ago may have been caused by regional changes of Nd sources in the Pacific. This is also suggested by the approximately contemporaneous changes in Pb isotopes in the Pacific crusts which trend towards more Pacific-type values (Ling *et al*

1997; Christensen *et al* 1997) and can not be explained by any kind of contribution from the N. Atlantic.

4.2 *Lead*

Pb is advected over shorter lengthscales than Nd in the oceans because it is more particle reactive. Nevertheless there is a very close correspondence between the Pb and Nd isotope time series in some crusts such as those from the western N. Atlantic. It is thus likely that there is a straightforward connection between these isotopic changes and a change in the source of terrigeneous erosion products or a change in circulation. In the specific case of the western N. Atlantic crusts the isotope time series of both Nd and Pb apparently recorded changes in the erosional input into NADW.

Crust SS-663 from the central Indian Ocean provides another good illustration of the way in which the crusts record changes of erosion inputs into the ocean (O'Nions *et al* 1998; Frank and O'Nions 1998). The ε_{Nd} and Pb isotope time series for SS-663 are compared in figure 5. The first point to note is that ε_{Nd}, the variation of which is barely outside the assigned experimental error, shows a minimum between 19 and 15 Ma ago and a shift towards more positive values 8 Ma ago. The structure in the Pb isotope time series is much better resolved, particularly for $^{207}Pb/^{206}Pb$ and $^{208}Pb/^{206}Pb$ ratios. In the latter case the $^{208}Pb/^{206}Pb$ ratios are the highest observed in the ocean so far and show a pronounced maximum between 20 and 15 Ma ago. Frank and O'Nions (1998) have suggested that the Pb with this unusual isotopic composition has been derived from the products of Himalayan erosion and that the maximum values correspond to the period of maximum uplift rate. If this interpretation is correct then it is perhaps surprising that the ε_{Nd} signal is so damped in the record of SS-663, particularly given that the Himalayan erosion products as preserved in the Bengal Fan have a low and relatively uniform ε_{Nd} of around -16 ± 2 (Derry and France-Lanord 1996). There may be three contributing factors responsible for this observation. The first is that no deep water has been generated in the northern Indian Ocean and, unlike the Labrador Sea area, there has not been a direct route for the transfer of an isotopic signal from surface waters to deep water in the northern Indian Ocean. The second factor is the low Pb/Nd ratio of seawater compared with the anticipated much higher ratio in particulates produced by erosion of the Himalayas: interaction between seawater and such particulates may have had a more profound effect on dissolved Pb than Nd (Frank and O'Nions 1998). The third factor may be that a Pb isotope signal from the Himalayas is scavenged more efficiently than Nd due to the higher particle reactivity of Pb and was thus recorded close to the source of input whereas an Nd signal may have been mixed and diluted.

5. Influence of gateway and circulation changes

The establishment of the Antarctic Circumpolar Current (ACC) following the opening of the Drake passage between Antarctica and South America about 23 Ma ago (Barker and Burrell 1977) was a key prerequisite on the way to the contemporary pattern of the global thermohaline circulation. The more recent closure of the Panama Gateway has been considered an important factor in further moderating this global circulation pattern. Modelling has suggested that unrestricted exchange of low salinity Pacific water masses with the Atlantic and the contemporaneous wind-forced flow of high salinity Atlantic surface waters into the Pacific prevented the formation of NADW deep water (Meier-Reimer *et al* 1990). Since 12 Ma ago the throughflow became increasingly restricted (Keller and Barron 1983; Duque-Caro 1990) with some indication for a transient landbridge as early as 9.3–8 Ma ago (Marshall 1985). The consequent redirection of the saline Carribean Current to the north contributed to an increase of the strength of the Gulf Stream (Kaneps 1979) thus increasing the salinity and heat transfer to the North Atlantic. Cooling of this highly saline surface water enabled the production of deep water in the N. Atlantic to start, probably as early as 10 Ma ago (Woodruff and Savin 1989; Delaney 1990). Support for a further enhancement of NADW flow at 3–4 Ma was deduced from sediment accumulation patterns on drifts in the North Atlantic (Wold 1994) and Atlantic versus Pacific benthic foraminiferal carbon isotope gradients (Raymo *et al* 1990; Billups *et al* 1998). Final establishment of the modern circulation mode was suggested to have been in principle completed by 4.6 Ma (Haug and Tiedemann 1998; Driscoll and Haug 1998). The ε_{Nd} and Pb-isotope records of ferromanganese crusts summarised above may provide some further insights into these effects.

The opening of the Drake Passage is not reflected by any shifts in the Nd or Pb isotope time series in the Atlantic and Pacific crusts analysed so far. Although none of the Atlantic and Pacific crusts available which cover the period of this event is located close to the Passage the observation is surprising given the large changes in ocean circulation that presumably occurred.

A similar conclusion arises for the effects of the closure of the Panama Gateway. Whereas final closure at about 3 Ma ago must have affected the exchange of surface and shallow waters between the Atlantic and Pacific Oceans, the complex archipelagic character of the Gateway and missing precise bathymetric data make it difficult to estimate how and when water mass exchange between the Atlantic and Pacific was affected. The marked change of the Pb and Nd isotope time series in the western N. Atlantic at about 3–4 Ma ago was suggested to be linked to the final closure

of northern hemisphere glaciation at about 3.2–2.6 Ma ago (Shackleton *et al* 1984; Raymo 1994) was responsible for a large increase in supply of unradiogenic Nd and radiogenic Pb at about the same time (O'Nions *et al* 1998; Frank and O'Nions 1998; von Blanckenburg and O'Nions 1999). In addition, it was shown that similar patterns in Nd and Pb isotope time series have occurred in the Arctic Ocean (Winter *et al* 1997) which suggests that the increased input of detrital material was the dominant process.

A trend towards more radiogenic Nd-isotopic composition starting around 12 Ma in the equatorial Pacific isotope records may have been caused by a decreasing supply of unradiogenic Nd from the Atlantic to the Pacific due to the shallowing of the Panama Gateway and the subsequent change of the trend towards more unradiogenic Nd may be related to the intensification of the global thermohaline circulation (Burton *et al* 1997). However, this change of the trend must have been caused by the transfer of a signal via the thermohaline circulation for which there is no evidence in crusts from the ACC and the central Indian Ocean (O'Nions *et al* 1998). It appears therefore that the closure of the Panama isthmus and the associated circulation changes have together left a surprisingly small imprint on the Nd and Pb isotopic composition of the deep water and that the change of provenance and supply of detrital material has been the dominating process controlling dissolved Nd and Pb in the deep ocean.

6. Concluding remarks

The Nd and Pb isotope time series of well-dated crusts from the Atlantic, Indian and Pacific Oceans have retained a remarkable record of deep water mass compositions in some cases back to 60 Ma. It is suggested that the Nd and Pb isotope record through time has been mainly controlled by variations of composition and amount of terrigeneous inputs into the oceans and their dispersal by the ocean circulation. Major events suggested to be recorded in the isotope time series are Himalayan uplift and erosion and the Northern Hemisphere Glaciation. The records in the Atlantic and Pacific crusts show little unambiguous evidence for circulation changes which accompanied the opening of the Drake Passage and the start of the circum-Antarctic circulation as well as the closure of major oceanic gateways such as Panama.

The isotope records in the ferromanganese crusts are expected to provide further information on more subtle shifts in water mass distribution. Of particular interest will be crusts located over a range of depths at a particular locality, which will be sensitive to vertical shifts in the positions of different water masses.

References

Abouchami W and Goldstein S L 1995 A lead isotopic study of Circum-Antarctic manganese nodules; *Geochim. Cosmochim. Acta* **59** 1809–1820

Abouchami W, Goldstein S L, Galer S J G, Eisenhauer A and Mangini, A 1997 Secular changes of lead and neodymium in central Pacific seawater recorded by a Fe-Mn crust; *Geochim. Cosmochim. Acta* **61** 3957–3974.

Abouchami W, Galer S J G and Koschinsky A. 1998 Pb and Nd isotopes in NE Atlantic Fe-Mn crusts: proxies for trace metal paleosources and paleocean circulation; *Geochim. Cosmochim. Acta* (in press)

Albarède F and Goldstein S L 1992 World map of Nd isotopes in sea-floor ferromanganese deposits; *Geology* **20** 761–763

Albarède F, Goldstein S L and Dautel D 1997 The neodymium isotopic composition of manganese nodules from the Southern and Indian Oceans, the global oceanic neodymium budget, and their bearing on deep ocean circulation; *Geochim. Cosmochim. Acta* **61** 1277–1291

Banakar V K and Borole D V 1991 Depth profiles of $^{230}Th_{excess}$, transition metals and mineralogy of ferromanganese crusts of the Central Indian basin and implications for paleoceanographic influence on crust genesis; *Chem. Geol.* **94** 33–44

Barker P F and Burrell J 1977 The opening of Drake Passage; *Mar. Geol.* **25** 15–34

Belshaw N S, O'Nions R K and von Blanckenburg F 1995 A SIMS technique for $^{10}Be/^{9}Be$ measurement in environmental materials; *Int. J. Mass Spectrom. Ion Proc.* **142** 55–67

Billups K, Ravelo A C and Zachos J C 1998 Early Pliocene deep water circulation in the western equatorial Atlantic: implications for high-latitude climate change; *Paleoceanography* **13** 84–95

Bollhöfer A, Eisenhauer A, Frank N, Pech D and Mangini A 1996 Thorium and uranium isotopes in a manganese nodule from the Peru basin determined by alpha sectrometry and thermal ionization mass spectrometry (TIMS): Are manganese supply and growth related to climate?; *Geol. Rundsch.* **85** 577–585

Burton K W, Ling H-F and O'Nions R K 1997 Closure of the Central American Isthmus and its effect on deep-water formation in the North-Atlantic; *Nature* **386** 382–385

Chabaux F, Cohen A S, O'Nions R K and Hein J R 1995 ^{238}U-^{234}U-^{230}Th chronometry of Fe-Mn crusts: Growth processes and recovery of thorium isotope ratios of seawater. *Geochim. Cosmochim. Acta*; **59** 633–638

Chabaux F, O'Nions R K, Cohen A S and Hein J R 1997 ^{238}U-^{234}U-^{230}Th disequilibrium in hydrogenous oceanic Fe-Mn crusts: Paleoceanographic record or diagenetic alteration?; *Geochim. Cosmochim. Acta* **61** 3619–3632

Christensen J N, Halliday A N, Godfrey L V, Hein J R and Rea D K 1997 Climate and ocean dynamics and the lead isotopic records in Pacific ferromanganese crusts; *Science* **277** 913–918

Delaney M L 1990 Miocene benthic foraminiferal Cd/Ca records: South Atlantic and Western Equatorial Pacific; *Paleoceanography* **5** 743–760

DePaolo D J 1986 Detailed record of Neogene Sr isotopic evolution of seawater from DSDP site 590B; *Geology*; **14** 103–106

Derry L A and France-Lanord C 1996 Neogene Himalayan weathering history and river $^{87}Sr/^{86}Sr$: impact on the marine Sr record; *Earth Planet. Sci. Lett.* **142** 59–74

Driscoll N W and Haug G H 1998 A short circuit in the thermohaline circulation: A cause for northern hemisphere glaciation; *Science* **282** 436–438

Duque-Caro H 1990 Neogene stratigraphy, paleoceanography and paleobiogeograpy in northwest South America and the evolution of the Panama Seaway; *Palaeogeog. Palaeoclimatol. Palaeoecol.* **77** 203–234

Eisenhauer A, Gögen K, Pernicka E, and Mangini A 1992 Climatic influences on the growth rates of Mn crusts during the late Quaternary; *Earth Planet. Sci. Lett.* **109** 25–36

Frank M. and O'Nions R K 1998 Sources of Pb for Indian Ocean ferromanganese crusts: A record of Himalayan erosion?; *Earth Planet. Sci. Lett.* **158** 121–130

Frank M, O'Nions R K, Hein J R and Banakar V K 1999 60 Ma records of major elements and Pb-Nd isotopes from hydrogenous ferromanganese crusts: Reconstruction of seawater paleochemistry. *Geochim. Cosmochim. Acta,* (accepted.)

Goldstein S L and O'Nions R K 1981 Nd and Sr isotopic relationships in pelagic clays and ferromanganese deposits; *Nature* **292** 324–327

Halbach P, Segl M, Puteanus D and Mangini A 1983 Co-fluxes and growth rates in ferromanganese deposits from central Pacific seamount areas; *Nature* **304**, 719–722.

Haug G H and Tiedemann R 1998 Influence of Panamanian Isthmus formation on Atlantic Ocean thermohaline circulation; *Nature* **393** 673–676

Hess J, Bender M L and Schilling J G 1986 Seawater $^{87}Sr/^{86}Sr$ evolution from Cretaceous to present; *Science* **231** 979–984

Hodell D A, Mueller P A and Garrido J R 1991 Variations in strontium isotopic compositions of seawater during the Neogene; *Geology* **19** 24–27

Jeandel C 1993 Concentration and isotopic composition of Nd in the South Atlantic Ocean; *Earth Planet. Sci. Lett.* **117** 581–591

Kaneps A G 1979 Gulf Stream: Velocity fluctuations during the late Cenozoic; *Science* **204**, 297–301

Keller G and Barron J A 1983 Paleoceanographic implications of Miocene deep-sea hiatuses; *Geol. Soc. Am. Bull.* **94** 590–613

Koepnick R B, Burke W H, Denison R E, Hetherington E A, Nelson H F, Otto J B and Waite L E 1985 Construction of the seawater $^{87}Sr/^{86}Sr$ curve for the Cenozoic and Cretaceous; *Chem. Geol.* **58** 55–81

Levitus S 1982 Climatological Atlas of the world ocean; *NOAA Prof. Pap.* **13** 1–173

Ling H-F, Burton K W, O'Nions R K, Kamber B S, von Blanckenburg F, Gibb A J and Hein J R 1997 Evolution of Nd and Pb isotopes in Central Pacific seawater from ferromanganese crusts; *Earth Planet. Sci. Lett.* **146** 1–12

Manheim F T 1986 Marine cobalt resources; *Science* **232** 600–608

McMurtry G M, VonderHaar D L, Eisenhauer A, Mahoney J J and Yeh H-W 1994 Cenozoic accumulation history of a Pacific ferromanganese crust; *Earth Planet. Sci. Lett.* **125** 105–118

Marshall L G 1985 Geochronology and land-mammal biochronology of the transamerican faunal interchange; in F G Stehli and S D Webb (eds), *The Great American Biotic Interchange,* (New York: Plenum Press) 49–85.

Meier-Reimer E, Mikolajewicz U and Crowley T 1990 Ocean general circulation model sensitivity experiment with an open central American isthmus; *Paleoceanography* **5** 349–366

Michard A, Albarède F, Michard G, Minster J F and Charlou J L 1983 Rare-earth elements and uranium in high-temperature solutions from East Pacific Rise hydrothermal vent field (13°N); *Nature* **303** 795–797

Neff U, Bollhöfer A and Mangini A 1998 Explaining discrepant depth profiles of $^{234}U/^{238}U$ and $^{230}Th_{ex}$ in Mn-crusts; *Mineral. Mag.* **62A** 1064–1065 (abstr.).

O'Nions R K, Frank M, von Blanckenburg F and Ling H.-F 1998 Secular variation of Nd and Pb isotopes in ferromanganese crusts from the Atlantic, Indian and Pacific Oceans *Earth Planet. Sci. Lett.* **155** 15–28

Piepgras D J, Wasserburg G J and Dasch E J 1979 The isotopic composition of Nd in different ocean masses; *Earth Planet. Sci. Lett.* **45** 223–236

Piepgras D J and Wasserburg G J 1982 Isotopic composition of neodymium in waters from the Drake Passage; *Science* **217** 207–214

Piepgras D J and Wasserburg G J 1985 Strontium and neodymium isotopes in hot springs on the East Pacific Rise and Guyamas Basin; *Earth Planet. Sci. Lett.* **72** 341–356

Piepgras D J and Wasserburg G J 1987 Rare earth transport in the western North Atlantic inferred from isotopic observations; *Geochim. Cosmochim. Acta* **51** 1257–1271

Puteanus D and Halbach P 1988 Correlation of Co concentration and growth rate – A method for age determination of ferromanganese crusts; *Chem. Geol.* **69** 73–85

Raymo M E, Ruddiman W F, Shackleton N J and Oppo D W 1990 Evolution of Atlantic-Pacific $\delta^{13}C$ gradients over the last 2.5 m.y; *Earth Planet. Sci. Lett.* **97** 353–368

Raymo M E 1994 The initiation of northern hemisphere glaciation; *Annu. Rev. Earth Planet. Sci.* **22** 353–383

Schaule B K and Patterson C C 1981 Lead concentrations in the north Pacific: evidence for global anthropogenic perturbations; *Earth Planet. Sci. Lett.* **54** 97–116

Segl M, Mangini A, Bonani G, Hofmann H J, Nessi M, Suter M, Wölfli W, Friedrich G, Pluger W L, Wiechowski A and Beer J 1984 ^{10}Be dating of a manganese crust from Central North Pacific and implications for oceanic paleocirculation; *Nature* **309** 540–543

Shackleton, N J, Backman J, Zimmermann H, Kent V D, Hall M A, Roberts D G, Schnitker D, Baldauf J G, Desprairies A, Homrighausen R, Huddleston P, Keene J B, Kaltenbach A J, Krumsiek K A O, Morton A C, Murray J W and Westberg-Smith W J 1984 Oxygen calibration and the onset of ice-rafting and history of glaciation in the North Atlantic region; *Nature* **307** 620–623

Stordal M C and Wasserburg G J 1986 Neodymium isotopic study of Baffin Bay water: sources of REE from very old terranes; *Earth Planet. Sci. Lett.* **77** 259–272

von Blanckenburg F, O'Nions R K, Belshaw N S, Gibb A and Hein J R 1996a Global distribution of beryllium isotopes in deep ocean water as derived from Fe-Mn crusts; *Earth Planet. Sci. Lett.* **141** 213–226

von Blanckenburg F, O'Nions R K and Hein J R 1996b Distribution and sources of pre-anthropogenic lead isotopes in deep ocean water from Fe-Mn crusts; *Geochim. Cosmochim. Acta* **60** 4936–4957

von Blanckenburg F and O'Nions R K 1999 Response of beryllium and radiogenic isotope ratios in northern Atlantic deep water to the onset of Northern Hemisphere Glaciation; *Earth Planet. Sci. Lett.* (accepted)

Winter B, Johnson C M and Clark D L 1997 Strontium, neodymium and lead isotope variations of authigenic silicate sediment components from the Late Cenozoic Arctic Ocean: Implications for sediment provenance and the source of trace metals in sea water; *Geochim. Cosmochim. Acta* **61** 4181–4200

Wold C N 1994 Cenozoic sediment accumulation on drifts in the North Atlantic; *Paleoceanography* **9** 917–941

Woodruff F and Savin S M 1989 Miocene deepwater oceanography; *Paleoceanography* **4** 87–140

Cosmogenic ^{10}Be: A critical view on its widespread dominion in geosciences

D. LAL

Scripps Institution of Oceanography, Geosciences Research Division, La Jolla CA 92093-0220.
email: dlal@ucsd.edu

The radionuclide ^{10}Be (half-life $= 1.5$ my), produced naturally in the Earth's atmosphere by nuclear interactions of cosmic rays, was sought in ocean sediments in the late fifties, considering its potential usefulness as a radiotracer for dating sediments. ^{10}Be was discovered independently by two groups, one in India and the other in the USA, and used only for dating marine sediments and manganese nodules until the seventies. Subsequently, as a result of a technical advance resulting in the improvement in the sensitivity of measurement of ^{10}Be by about a factor of 10^6, there was a global rush to measure this nuclide in most materials participating in the physical, chemical and biological processes in the dynamic geosphere. This paper outlines the reasons for this "isotope rush", and the lessons learned from these studies. I also present my personal views of the special attractive features of this nuclide on the one hand, and on the other, the pitfalls or the wrong message this nuclide could convey!

1. Introduction

The search for the radionuclide ^{10}Be (half-life $= 1.5$ my), expected to be produced by nuclear interactions of cosmic rays in the atmosphere, began in India at the Tata Institute of Fundamental Research (TIFR), Bombay, following a theoretical paper by Peters (1955), in which he stated that conditions for observing the resulting activity of this nuclide in various regions of the Earth are favorable, and that it might be useful for measuring sedimentation rates and other geophysical surface changes during the tertiary. The potential of ^{10}Be as a dating tool also led J. R. Arnold, who, with W.F. Libby, had successfully developed the cosmogenic radiocarbon method for applications in archaeology (Anderson *et al* 1947; Libby *et al* 1949), to look for it in his laboratory at the University of Chicago. The two groups, at the TIFR and the Univ. of Chicago, unaware of each other's researches on ^{10}Be, looked for the radionuclide in marine sediments from the eastern Pacific Ocean and found a measurable, unambiguous signature of its activity, also at about the same time (Arnold 1956; Goel *et al* 1957). Interestingly, both groups also looked for another

cosmic ray produced isotope, ^{7}Be (half-life $= 53$ days), this time Arnold's work preceding that of the TIFR group by about a year (Arnold and Al-Salih 1955). The remarkable stories of the independent searches for the cosmogenic ^{10}Be by the two groups in distant continents have been written by Arnold (1991) and Lal (1991a).

The driving force for the two groups was quite correctly the urge to find a tool for dating continental and marine sediments in the time window extending to the past 5–10 my. Naturally synthesized radionuclides of half-lives $< 10^8$ y are extinct today. No other natural radionuclides of half-life in the million-year range, except for those continually produced in nuclear interactions of cosmic rays, are available for this purpose. The longest-lived daughter nuclide in the U and Th series is ^{230}Th, which has a half-life of $75,200$ y. The cosmogenic ^{10}Be did serve as a dating tool in the million-year range, but its measurements were difficult, requiring samples containing $> 2 \times 10^{12}$ atoms, to result in activity of > 1 disintegration per minute (^{10}Be is a beta emitter, with $E_{max} = 0.555$ MeV). Extraction of ^{10}Be from large amounts of sediments (~ 100 g) involved highly selective and

time-consuming radiochemical methods. Its studies were therefore limited to a few tough experimenters such as Somayajulu (1977), who studied it in marine sediments with a view to determine sediment accumulation rates. The work of Somayajulu also led to a very important realization, namely that ^{10}Be could be used to determine the growth rates of marine manganese nodules, for which he determined growth rates of the order of mm/My, a thousand times slower than the slowest accumulating red clay sediments in the Pacific Ocean (Somayajulu 1967). Only in these marine accretions and in other authigenic phases, were the ^{10}Be activity levels high enough to permit its measurement by beta-counting, as was done until the early eighties (Amin *et al* 1966, 1975; Somayajulu 1977; Sharma and Somayajulu 1982; Somayajulu *et al* 1984a).

2. The great isotope rush of the '80s

In the late seventies, two groups, one in Canada (Nelson *et al* 1977) and one in the USA (Bennett *et al* 1977), independently showed that ^{14}C could be detected at natural levels by using electrostatic tandem accelerators. In this technique, sample carbon atoms are sputtered using caesium ions and accelerated in the tandem as negative ions to MeV energies, and the ^{14}C atoms are directly identified in the mass spectrometer. Thus it becomes possible to identify ^{14}C ions in the beam, and measure their abundance relative to stable carbon isotopes, without having to wait for the ^{14}C atoms to decay. The AMS technique works efficiently for several nuclides (^{14}C, ^{41}Ca, ^{36}Cl, ^{26}Al, ^{10}Be and ^{129}I), permitting detection of $\sim 10^6$ atoms in each case (cf. Elmore and Phillips 1987), provided the isotope/element ratio is $< 10^{-14}$, yielding a gain factor over isotope detection by the decay-counting method, of $1/10^6 \lambda$; the disintegration constant, λ, is expressed in (min^{-1}) to correspond to the detection limit of 1 dpm by the counting method. The 4–6 orders of magnitude higher isotope measurement sensitivity meant a large reduction in sample sizes, from 10–100 g to (1–10) mg, and in turn reopening a host of investigations carried out earlier using the decay-counting method, for a deeper introspection. The decrease in sample size meant:

- economy on precious samples, e.g. the extraterrestrial and air-filter samples;
- making measurements not possible earlier with the sample sizes available, e.g. nuclide time series in ice cores;
- making adequate number of measurements to characterise geochemical entities, e.g. marine sediments and weathered soil profiles;
- measuring concentrations of cosmogenic nuclides produced *in situ* in terrestrial solids.

The principal considerations in choosing a radio-tracer are:

1. its half-life,
2. its chemical behavior,
3. knowledge of its source function(s), and
4. ease of its detection.

The interpretation of the tracer data would have to explicitly take into account the first three parameters, of course, and importantly whether supplementary data on other elements/isotopes could be brought to bear in constructing robust geophysical/geochemical models of transport/mixing. These are important but generally complex issues needing careful attention. Historically, geochemists have always rushed in at the availability of techniques to follow a tracer through different reservoirs, and only later on, they have examined the critical issues 1 thru 3 in the light of the experimental data. This strategy rests on two premises: (i) opportunities must be seized and (ii) all tracer data are useful. In studies of global scale phenomena it is generally difficult to forecast the tracer behavior, and it may seem prudent to carry out an experiment first and to think later, with the data in hand. This approach gets justified often, with occasional big surprises.

With this background it is easy to see why there was a great isotope rush in the eighties, when the AMS technique became available in the USA, Canada and Europe to the scientific community. The first wave of AMS studies dealt with measurements of ^{10}Be in extraterrestrial samples, in marine sediments and in manganese nodules. There are far too many published papers for one to cite here; only a few references are given here as examples. These studies confirmed earlier data acquired the old fashioned way, but generated a new extensive data base. The next wave concerned acquisition of new data on ^{10}Be not obtainable using the decay counting method:

1. In wet precipitations (Somayajulu *et al* 1984b; Monaghan *et al* 1985/86),
2. in polar ice cores (Raisbeck *et al* 1981; Beer *et al* 1984),
3. in oceanic water columns (Kusakabe *et al* 1982; Measures and Edmond 1982),
4. in marine sediments and manganese nodules (Sharma and Somayajulu, 1982; Ku *et al* 1982; Eisenhauer *et al* 1994; Sharma *et al* 1987; von Blanckenburg *et al* 1996),
5. in weathered soil profiles (Pavich *et al* 1986; Barg *et al* 1997),
6. in aeolian dust deposits (Heller *et al* 1993; Gu *et al* 1996, 1997),
7. in terrestrial rocks (Yiou *et al* 1984; Nishiizumi *et al* 1993), and
8. in diverse terrestrial samples where ^{10}Be could be measured (Raisbeck and Yiou 1984; Bourles *et al* 1984; Valette-Silver *et al* 1987).

Several of these studies also combined measurements of other cosmogenic radionuclides, ^{36}Cl and ^{26}Al, but ^{10}Be was the principal nuclide studied. Note here the important achievement of AMS in obtaining time series of ^{10}Be in polar ice cores. In 1955, the author processed about 200,000 gallons of ice in Kashmir to measure its concentration. This measurement was imprecise because of a weak ^{10}Be signal (Lal 1991a).

Armed with the new data, we can now look at our gains in geosciences, focussing our attention on ^{10}Be, the most widely studied cosmogenic tracer today, next to cosmogenic ^{14}C. Natural radiocarbon is present in all living organic matter at a ratio $^{14}C/^{12}C = 1.17 \times 10^{-12}$, with the result that 50 mg of living carbon has 2.5×10^6 atoms, easily detectable with the AMS. The dynamic carbon in the carbon cycle has specific activities within about 20% of this value, and is easily measurable in samples of < 1 mg C. Samples of "age" up to ~ 30 ky, "age" defined as the time of isolation from the carbon cycle, can be studied with the AMS.

In the case of ^{10}Be, the $^{10}Be/^9Be$ ratios in the principal dynamic reservoirs in which it is diluted with its stable isotope ^9Be, namely soils, groundwaters, oceans, biogenic and authigenic matter in the hydrosphere, are several orders of magnitude higher than 10^{-14}, the lower range for ^{10}Be measurement using the AMS. Furthermore, since beryllium is particle-active (You et al 1989; Anderson et al 1990), i.e. it is associated with particles in aqueous systems by virtue of its preferential attachment to inorganic and organic surfaces, it attaches first to surficial solids, and is subsequently widely distributed among the dynamic constituents of the geosphere. (For a review of the mixing histories of ^{10}Be, reference is made to McHargue and Damon 1991; and Morris 1991). The resulting concentrations of ^{10}Be in surficial soils and in marine sediments ($CaCO_3$-free basis) are about 10^7–10^9 ^{10}Be atoms/g with $^{10}Be/^9Be$ ratios in the range of 10^{-8}–10^{-7}. Tens of mg, or a gram at most, suffice to measure ^{10}Be in all recent authigenic materials, a great convenience in its study. Note that although its production rate is about two orders of magnitude lower than that of ^{14}C, the comparable ease of measurement in the case of ^{10}Be arises because (i) the dilution factor (with its stable isotope) is much smaller for ^{10}Be, and (ii) its longer half-life results in its accumulation in the geosphere over longer periods of time.

Thus, it is seen that ^{10}Be can be measured in tens of mg samples of continental materials from the dynamic exchange reservoirs, and in authigenic materials on the ocean floor. In the case of ^{14}C it can be measured in milligram size carbon samples from the carbon cycle reservoirs. In the earlier days of applications of radiotracers, major attention was directed toward development of techniques for their sensitive measurements. Today, the primary focus is on identification of principal tracer pathways, on their measurement in different reservoirs of importance, and on building robust models. From studies of tracers, we hope to learn of their pathways through the geophysical and geochemical discontinuities. They teach us about the behaviors of natural systems. With this realization, geoscientists rushed to measure their distribution in space and time. Therein lies the justification for the great isotope rush of the eighties, which continues at a fairly high level of activity in the nineties, for both ^{14}C and ^{10}Be.

For some of us, ^{10}Be has become our *raison d'être*, inasmuch as some of us develop their researches around one or more stable isotopes, e.g. ^{18}O, ^{13}C, or radionuclides, e.g. the radioactive decay schemes, e.g. ^{147}Sm–^{144}Nd, ^{40}K–^{40}Ar, or the daughter nuclides in the U,Th series. *Studies of ^{10}Be have assumed the stature of an industry operated by geoscientists, for characterizing physical, chemical and biological systems.*

3. ^{10}Be: Its comparison with ^{14}C as a radiotracer

Isotopes, like everything else, are not created equal. The cosmogenic ^{14}C finds very diverse applications, because it is mixed within the dynamic carbon cycles, and serves as a tracer for (i) mixing time scales of carbon within the carbon cycle reservoirs, and (ii) for dating the time since a sample containing carbon was separated from any of the carbon cycle reservoirs, with the $^{14}C/^{12}C$ ratios providing robust constrains on mass transfer/mixing processes. This is so because the exchange of ^{14}C between, and the flux of ^{14}C out of, carbon cycle reservoirs occurs along with the stable carbon isotopes ^{12}C and ^{13}C, with which it is well mixed in organic/inorganic compounds in the carbon cycle reservoirs. It is therefore expected that the pathways of stable C and ^{14}C are the same in all carbon cycle reservoirs except for any chemical isotopic fractionation, which can be properly taken into account.

The greatest handicap of ^{10}Be as a tracer is that its pathway through the atmosphere, hydrosphere and lithosphere neither "relate" to, nor are "parallel" to, those of beryllium's stable isotope, ^9Be. In the atmosphere and in wet precipitations, ^{10}Be and ^9Be pathways are mostly not "related". In the oceans, ^{10}Be is primarily introduced via wet precipitations, whereas ^9Be sources are "run-off" and "aeolian" transport of dust/soils. On the other hand, the single-most unique attribute of ^{10}Be over ^{14}C is its half-life. ^{14}C covers only the recent period in the Quaternary, while the half-life of ^{10}Be equals the duration of the Quaternary and should permit addressing questions within the recent Tertiary, back to about 7–8 my, taking five tracer half-lives as the range of its applicability.

By virtue of its longer half-life, ^{10}Be considerably extends the range of time in "dating" continental and marine sediments, and in the study of geomorphic

processes. These should in fact be considered principal applications of the cosmogenic radiotracer ^{10}Be. Note here, however, that since the ^{10}Be dates must be based on some initial concentrations which cannot be estimated accurately (compare the case of ^{14}C, where dates are based on the known initial ^{14}C/^{12}C ratios), the uncertainties in ^{10}Be age estimates are large, $> (10-20)\%$.

Limitations in the use of cosmogenic ^{10}Be produced in the Earth's atmosphere as a tracer often arise due to our inability to model a geophysical/geochemical reservoir. In the simplest case, robust tracer models can be constructed if the radiotracer is "conservative", meaning that it strictly follows the pathways of the reservoir matrix. Such situations are rare indeed, for example, the rather unique case of ^{3}H, which would be expected to faithfully track water molecules within and between watery reservoirs; the handicap of ^{3}H is its short half-life, 12.3 y. The non-availability of conservative radiotracers is not an obstacle, however, because often it becomes possible to use non-conservative tracers very effectively. The cosmogenic ^{14}C and ^{32}Si are two examples of non-conservative tracers, which are very useful for studying large-scale vertical mixing and biological processes in the oceans.

In view of its chemical behavior, the principal handicap in the case of ^{10}Be is often the lack of knowledge of its source functions—because it is fractionated from the atmosphere soon after its formation in the atmosphere, due to attachment on aerosols. Thereafter it is eventually removed from the lower atmosphere principally by wet precipitations. However, based on our knowledge of the large-scale circulation of air, and aerosol scavenging processes, we have a fair idea of the geographic and seasonal pattern of its fallout (Lal and Peters 1967). These considerations help determine the oceanic injection pattern of ^{10}Be.

Interestingly, ^{10}Be studies provide information even when timescales involved in its transport/mixing are very short, say, less than a few thousand years. In these applications, ^{10}Be is being treated as a "stable" tracer; i.e., its concentrations in a reservoir are related to one or more processes of interest which control its movement to, within and out of the reservoir(s). The application of ^{10}Be in studies of atmospheric circulation, aerosol scavenging by wet precipitations, climatic variations in precipitation, changes in its atmospheric production rates (due to temporal changes in cosmic ray intensity) and biological/gravitational processes occurring in the oceans, are all examples where the half-life of ^{10}Be does not enter in the models. Thus, ^{10}Be serves as a "label" for air, aerosols, water and soils. In studies of soils, marine sediments and manganese nodules, its half-life is of principal consequence in models which, in their simplest form, assume that ^{10}Be is quickly removed to the sediment/nodule in short time periods (< 1000 y) after production in the atmosphere. Some interesting applications

of ^{10}Be have been discussed by Brown (1987). Special mention is made here to studies of soil erosion and island-arc volcanism (see also Morris, 1991).

The applications of cosmogenic *in situ* produced ^{10}Be in surficial rocks are relatively straightforward. The cosmic ray intensity at sea level and at mountain altitudes are well known, and intensity changes associated with changes in solar activity and geomagnetic field intensity can be modeled fairly well (Lal 1988). Its production rate in quartz, which is widespread in terrestrial rocks, is also well known (Lal 1991b). In rocks exposed at sea level and at high latitudes, and undergoing steady-state erosion at the rate of 1 cm/1000 y, one expects a concentration of $\sim 3 \times 10^5$ ^{10}Be/g quartz. Ten grams quartz are needed to get a good ^{10}Be signal with the AMS. Again, it must be noted here that in short term geophysical processes, $< 10^4$ y, ^{10}Be serves as a stable cosmogenic tracer, and complements other radiotracers of shorter half-lives (Lal 1991b). For a sample of geomorphic problems which can be addressed using cosmogenic *in situ* ^{10}Be and other nuclides, reference is made to Lal (1991b) and Nishiizumi *et al* (1993).

We discussed earlier that although the source function of atmospheric ^{10}Be is known, it does not track air masses faithfully because of its attachment onto aerosols. This should not be considered as a serious problem invalidating its use as a tracer. In fact, an important facet of tracers is their chemical behavior, which only enhances their value provided meaningful models can be constructed. With the acquisition of a large data base of concentrations of ^{10}Be in polar ice cores, it becomes clear that the crude scavenging models which do not explicitly consider air circulation patterns, vapor fluxes and tracer chemical behaviors, are not useful. Since several cosmogenic nuclides are available, well constrained models can be constructed. Similarly, one realizes that oversimplified models of incorporation of atmospheric ^{10}Be in soils are not useful. One has to explicitly consider ^{10}Be losses due to surficial run-off and erosion. Furthermore, it is necessary to include other tracers to constrain the models (cf. Barg *et al* 1997).

Before concluding our discussion on ^{10}Be applications, we would like to point out that although the pathways of ^{10}Be and ^{9}Be are generally quite different, the ^{10}Be/^{9}Be ratios in terrestrial reservoirs (excluding the atmosphere and polar ice) lie within a narrow range (Barg 1992; Barg *et al* 1997). The extensive ^{10}Be data in ocean waters, in continental and marine sediments, and authigenic minerals including the manganese nodules, shows that whereas their ^{10}Be concentrations are spread over several orders of magnitude, the ratios remain within an order of magnitude (Barg 1992; von Blanckenburg *et al* 1996; Barg *et al* 1997). As should become evident, this makes it possible to consider viable models for mass fluxes and chemical/biological processes in which beryllium isotopes participate.

Cosmogenic ^{10}Be is continually produced on the Earth: in the atmosphere and in surficial matter, principally in nuclear interactions of cosmic rays with oxygen, with a production rate that makes it easy to measure its concentration in diverse materials participating in biogeochemical cycles. Its half-life and its chemical behavior make it an ideal tracer to study large-scale circulation of aerosols in the atmosphere and a wide range of particles in the oceans (aeolian and biogenic). The chronology of accumulation of matter in the hydrosphere can be determined from its measured concentrations in these deposits, back to 7–8 my. The rate of ^{10}Be production in the atmosphere and in surficial materials can be determined for the cosmic ray fluxes as measured during the past five decades. The radiotracer ^{10}Be is thus unique in several respects, but it should be realized that interpretation of data on its concentrations in the geosphere requires suitable models to appropriately consider the various processes which control its transport through the Earth's dynamic reservoirs. Studies of ^{10}Be have often made us realize that we know so little about how the atmosphere, oceans and the lithosphere evolve through an ever-changing Earth. Occasionally, ^{10}Be time-series data have revealed large temporal oscillations, which must be interpreted as either due to changes in its atmospheric production rate (due to modulation of cosmic ray flux by Sun, changes in the geomagnetic dipole moment, or short term increases due to a nearby supernova, etc.), or due to climatic fluctuations leading to an appreciable change in its concentrations from the "normal". These data have been interpreted differently by researchers (cf. Raisbeck *et al* 1987). From the foregoing, it should be obvious that it is necessary to first understand the transport pathways of ^{10}Be, and its sensitivity to climatic forcing, before drawing any firm conclusions about past changes in cosmic ray intensity.

Studies of cosmogenic nuclides began in India at TIFR, Bombay, with its first success of discovering ^{10}Be in 1956, which was followed by the discovery of nine more cosmogenic nuclides within a few years (Lal and Peters 1967). Those were exciting days of new searches and rewards, for members of a group which was christened the "geocosmophysics" group. It stood out as a dynamic entity by demonstrating its capacity to discover new facts about nature. The group derived its energy from synergistic processes within the group, composed of scientists working in diverse fields, freelance. It was composed of personnel who had made their mark in studies of cosmic rays and elementary particle physics. Prof. K. Gopalan joined the group in 1970, and infused everyone with new possibilities which could be addressed using the mass spectrometer. Our resources were limited, although TIFR scientists were better endowed than other groups in India. For

confidence to make them with their own hands, literally, which K. Gopalan did: he made a mass spectrometer tube by carving out a mould in a graphite black, freehand. This mass spectrometer is still functional, at the Physical Research Laboratory (PRL), Ahmedabad. As mentioned earlier, members of this group used to bounce ideas off each other; Dr. Gopalan played his role actively, both as a catcher and a bouncer. To this day we are occasionally showered with his new ideas, many of which we have not yet been able to put to practice to date. To this modest idea-man, a creative and hard working colleague, I dedicate this article. Prof. Gopalan helped build state-of-the-art programs in climatology and geochronology at the Physical Research Laboratory (PRL) during his stay there from 1973–1984. Even after having moved to the National Geophysical Research Institute (NGRI), he continues to help PRL and NGRI develop good programs and instruments at the cutting edge of earth science research.

References

Amin B S, Kharkar D P and Lal D 1966 Cosmogenic ^{10}Be and ^{26}Al in marine sediments; *Deep Sea Research* **13** 805–824

Amin B S, Lal D and Somayajulu B L K 1975 Chronology of marine sediments using the ^{10}Be method; intercomparison with other methods; *Geochim. Cosmochim. Acta* **398** 1187–1192

Anderson E C, Libby W F, Weinhouse S, Reid A F, Kirschenbaum A D and Grosse A V 1947 Natural radiocarbon from cosmic radiation; *Phys. Rev.* **72** 931–936

Anderson R F, Rowe G T, Kemo P, Trumbore Hofmann H J and Wolfli W 1990 Boundary scavenging in the Pacific Ocean: A comparison of ^{10}Be and ^{231}Pa; *Earth Planet. Sci. Lett.* **90** 287–304

Arnold J R and Al-Salih H A 1955 Beryllium-7 produced by cosmic rays; *Science* **121** 451–453

Arnold J R 1956 Beryllium-10 produced by cosmic rays; *Science* **124** 584–585

Arnold J R 1991 The discovery of cosmogenic ^{7}Be and ^{10}Be; *Curr. Sci.* **61** 727–729

Barg E 1992 Studies of beryllium geochemistry in soils: feasibility of using ^{10}Be/^{9}Be ratios for age determination. Ph D dissertation, Univ. of California, San Diego, 181 pp.

Barg E, Lal D, Southon J R, Caffee M W, Finkel R C and Pavich M J 1997 Beryllium geochemistry in soils: evaluation of ^{10}Be/^{9}Be ratios in authigenic minerals as a basis for age models; *Chemical Geology* **140** 237–258

Beer J, Oeschger H, Siegenthaler U, Bonani G, Hofmann H, Morenzoni E, Nessi M, Suter M, Woelfli W, Finkel R C and Langway C 1984 The Camp Century ^{10}Be record: implications for long term variations of the geomagnetic dipole moment; *Nucl. Instr. Methods Phys. Res.* **B5** 380–384

Bennett C L, Beukens R P, Clover M R, Gove H E, Liebert R B *et al* 1977 Radiocarbon dating using electrostatic accelerators: negative ions provide the key; *Science* **198** 508–510

Bourles D, Raisbeck G M, Yiou F, Loiseaux J M, Lieuvin M, Klein J and Middleton R 1984 Investigation of the possible association of ^{10}Be and ^{26}Al with biogenic matter in the marine environment; *Nucl. Instr. Methods Phys. Res.* **B5** 365–370

Brown L 1987 ^{10}Be: recent applications in the earth sciences; *Phil. Trans. R. Soc. London* A323 75–86

Eisenhauer A, Spielhagen R F, Frank M, Hentzschel G, Mangini A, Kubik P W, Dittrich-Hannen B and Billen T 1994 ^{10}Be records of sediment cores from the high northern latitudes: implications for environmental and climatic changes; *Earth Planet. Sci. Lett.* 124 171–184

Elmore D and Phillips F M 1987 Accelerator mass spectrometry for measurement of long lived radioisotopes; *Science* 236 543–550

Goel P S, Kharkar D P, Lal D, Narsappaya N, Peters B and Yatirajam V 1957 The beryllium-10 concentration in deep sea sediments; *Deep Sea Res.* 4 202–210

Gu Z Y, Lal D, Liu T S, Southon J, Caffee M W, Guo Z T and Chen M Y 1996 Five million year ^{10}Be record in Chinese loess and red-clay: climate and weathering relationships; *Earth Planet. Sci. Lett.* 144 273–287

Gu Z Y, Lal D, Liu T S, Guo Z T, Southon J, and·Caffee M W 1997 Weathering histories of Chinese loess deposits based on uranium and thorium series nuclides and cosmogenic ^{10}Be; *Geochimica et Cosmochimica Acta* 61(24), 5221–5231

Heller F, Shen C D, Beer J, Liu X M, Liu T S, Bronger A, Suter M and Bonani G 1993 Quantitative estimates of pedogenic ferromagnetic mineral formation in Chinese loess and paleomagnetic implications; *Earth Planet. Sci. Lett.* 114 385–390

Ku T L, Kusakabe M, Nelson D E, Southon J R, Korteling R G, Vogel J and Nowikow I 1982 Constancy of oceanic deposition of ^{10}Be as recorded in manganese crusts; *Nature* 299 240–242

Kusakabe M, Ku T L, Vogel J, Southon J R, Nelson D E and Richards J 1982 ^{10}Be profiles in sea water; *Nature* 299 712–714

Lal D and Peters B 1967 Cosmic ray produced activity on the earth; *Handb. der Phys.* 46 551–612

Lal D 1988 In-situ produced cosmogenic isotopes in terrestrial rocks; *Ann. Rev. Earth Planet. Sci.* 16 355–388

Lal D 1991a The discovery of cosmogenic ^{10}Be in India; *Curr. Sci.* 61 722–727

Lal D 1991b Cosmic ray tagging of erosion surfaces: *in situ* production rates and erosion models; *Earth Planet. Sci. Letts.* 104 424–439

Libby W F, Anderson E C and Arnold J R 1949 Age determination by radiocarbon content: world-wide assay of natural radiocarbon; *Science* 109 227–228

McHargue L R and Damon P E 1991 The global beryllium-10 cycle; *Rev. Geophys.* 29 141–158

Measures C I and Edmond J M 1982 Beryllium in the water column of the Central Pacific; *Nature* 297 51–53

Monaghan M C, Krishnaswami S, and Turekian K K 1985/86 The global average production rate of ^{10}Be; *Earth and Planet. Sci. Lett.* 76 179–187

Morris J D 1991 Applications of cosmogenic ^{10}Be to problems in the earth sciences; *Annu. Rev. Earth and Planet. Sci.* 19 313–350

Nelson D E, Koertling R G and Stott W R 1977 Carbon-14: direct detection at natural concentrations; *Science* 198 507–508

Nishiizumi K, Kohl C P, Arnold J R, Dorn R, Klein J, Fink D, Middleton R and Lal D 1993 Role of *in situ* cosmogenic nuclides ^{10}Be and ^{26}Al in the study of diverse geomorphic processes; *Earth Surface Proc. and Landforms* 18 407–425

Pavich M J, Brown L, Harden J, Klein J and Middleton R 1986 ^{10}Be distribution in soils from Merced river terraces, California; *Geochim. Cosmochim. Acta* 50 1727–1735

Peters B 1955 Radioactive beryllium in the atmosphere and on the earth; *Proc. Indian Acad. Sci.* 41 67–71

Raisbeck G M, Yiou F, Fruneau M, Loiseaux J M, Lieuvin M, Ravel J C, and Lorius C 1981 Cosmogenic ^{10}Be concentrations in Antarctic ice during the past 30,000 years; *Nature* (London) 292(5826) 825–826

Raisbeck G M and Yiou F 1984 Production of long lived cosmogenic nuclei and their applications; *Nucl. Instr. Methods Phys. Res.* 233 91–99

Raisbeck G M, Yiou F, Bourles D, Lorius C, Jouzel J and Barkov N I 1987 Evidence for two intervals of enhanced ^{10}Be deposition in Antarctic ice during the last glacial period; *Nature* 326 273–276

Sharma P and Somayajulu B L K 1982 Beryllium-10 dating of large manganese nodules from world oceans; *Earth Planet. Sci. Lett.* 59 235–244

Sharma P, Klein J, Middleton R and Church T 1987 ^{26}Al and ^{10}Be in authigenic materials; *Nucl. Instr. and Methods in Physics Res.* B29 335–340

Somayajulu B L K 1967 Beryllium-10 in a manganese nodule; *Science* 156 1219–1220

Somayajulu B L K 1977 Analysis of causes of the beryllium-10 variations in deep sea sediments; *Geochim. Cosmochim. Acta* 41 909–913

Somayajulu B L K, Sharma P and Berger·W H 1984a Be-10, C-14, U-Th decay series nuclides and delta O-18 in a box core from the Central North Atlantic; *Marine Geol.* 54 169–180

Somayajulu B L K, Sharma P, Beer J, Bonani G, Hoffman H J, Morenzoni E, Suter M and Wolfli W 1984b ^{10}Be annual fallout in rains in India; *Nucl. Instr. Methods Phys. Res.* B5 398–403

Valette-Silver J W, Tera F, Klein J and Middleton R 1987 Beryllium-10 in hydrothermal vent deposits from the East Pacific Ridges: role of sediments in the hydrothermal processes; *J. Geophys. Res.* 92 11304–11372

von Blanckenburg F, O'Nions R K, Belshaw N S, Gibb A and Hein J R 1996 Global distribution of beryllium isotopes in deep ocean water as derived from Fe-Mn crusts; *Earth Planet. Sci. Lett.* 141 213–226

Yiou F, Raisbeck G M, Klein J and Middleton R 1984 ^{26}Al and ^{10}Be in terrestrial impact glasses; *J. Non-crystalline Solids* 67 503–509

You C F, Lee T P and Li Y H 1989 The partition of Be between soil and water; *Chem. Geol.* 77 105–118

Sr isotopes in the Orgueil CI meteorite: Chronology of early solar system hydrothermal activity

J D MACDOUGALL

Scripps Institution of Oceanography, La Jolla, CA 92093-0220, USA.
email: jdmacdougall@ucsd.edu

New Sr isotopic analyses and calculated formation ages of carbonates from the Orgueil CI meteorite are reported. Among the samples analyzed in this work, dolomites give the youngest formation ages and may have been deposited intermittently starting near the time of parent body formation and continuing for at least 30 Ma. The Sr isotope data also suggest that breunnerites (Fe-Mn-Mg carbonates) crystallized after dolomite formation. Leaching experiments on bulk meteorite samples provide evidence for a very mobile, water soluble Sr reservoir in Orgueil that is characterized by extremely radiogenic Sr ($^{87}Sr/^{86}Sr \approx 0.81$–0.82). This unsupported Sr reflects recent element redistribution, possibly at the time of parent body breakup recorded by the ~ 10 Ma exposure age of Orgueil. The carbonate data in particular corroborate earlier indications that hydrothermal processes were among the earliest events to affect the CI parent body.

1. Introduction

The CI meteorites appear to be extensively altered mineralogically compared to their precursor material. However, because their relative bulk elemental abundances closely match those of the sun, they are also (somewhat paradoxically) believed to be little changed chemically. The original mineralogy of the CIs is not known with certainty, but it is generally accepted that the inferred mineralogical transformations occurred through the action of water, probably liquid water, within the CI parent body (e.g. DuFresne and Anders 1962; Richardson 1978; Kerridge and Bunch 1979). The mineral assemblage now observed in these meteorites includes a variety of phyllosilicates, sulfides and sulphates, magnetite, and carbonates—an assemblage that on the earth is typical of low temperature hydrothermal alteration of mafic material. Although these meteorites are brecciated to clast sizes that are frequently < 1 mm, there is petrographic as well as mineralogical evidence for aqueous alteration, in the form of remnants of mineralized fractures filled with sulphates, or, more rarely, carbonates (Richardson 1978). Based on petrographic criteria, Richardson (1978) concluded that the carbonate vein fragments comprise the oldest generation of aqueous deposits now observable in the CI meteorites.

In addition to the phases noted above, the CI meteorites also contain small amounts of olivine and pyroxene that show no sign of interaction with hydrous fluids (Kerridge 1968; Reid *et al* 1970; Kerridge and Macdougall 1976). It is likely that these grains were added to the meteorite parent body after the main phase(s) of aqueous activity but before final lithification. A study by Goswami *et al* (1976) showed that in Orgueil, $\sim 15\%$ of a group of 40 olivines examined for particle tracks exhibit evidence for irradiation with little or no shielding; considering both track and noble gas data, these authors concluded that the irradiated grains probably had a completely different pre-lithification history than the bulk meteorite. Whether the irradiation of these grains occurred in the regolith of the CI parent body, or in space before they were added to the parent body, is unknown. In any event, their addition must represent one of the last processes that occurred before consolidation of the CI parent body.

Carbonate minerals in Orgueil are the focus of the present paper. Although relatively rare, they have

chemical compositions provide clues to their formation environment, and they occur at grain sizes large enough to be amenable to hand picking and electron and ion microprobe analysis (Fredriksson and Kerridge 1988; Johnson and Prinz 1993; Riciputi *et al* 1994; Endress and Bischoff 1996). Dolomite dominates among the CI carbonates; in the most comprehensive study to date (Endress and Bischoff 1996), 85% of all carbonates analyzed in 18 thin sections of four CI meteorites were dolomites. Breunnerite (ferroan magnesite) was found by these authors to be the next most abundant, followed by calcite at only about 1%. These results are broadly similar to those of other workers, although the fraction of calcite observed by Endress and Bischoff (1996) is lower than found in some other studies. Numbers of grains, however, may not provide an especially accurate accounting of the importance of these phases. In Orgueil, dolomite and calcite occur as much smaller grains than breunnerite, typically $< 100\,\mu m$ compared with breunnerite grains up to 1 mm and larger (Fredriksson and Kerridge 1988). Breunnerites also frequently exhibit well-formed crystal faces and they usually occur as isolated grains, whereas dolomite is typically anhedral and sometimes occurs as elongated clusters or fragments that have been interpreted as vein fragments (Richardson 1978). However, although Richardson (1978) also reported the presence of entire veins or veinlets in the sections he examined, later workers have not corroborated this observation, reporting instead only isolated carbonate grains and multi-grain clusters or fragments.

Ion probe data for carbonates in the CM carbonaceous chondrites suggest that calcite and dolomite in these meteorites formed from different fluids (Riciputi *et al* 1994), and, by inference, the same may be true for the CI meteorites. Some carbonate fragments in Orgueil contain at least two separate carbonate generations, which may be physically separated by a band of another phase, such as magnetite. This is a further indication that different fluids, possibly representing different hydrothermal episodes, were responsible for the formation of the different carbonates. Multiple stages of alteration are also suggested by the matrix mineralogy of Orgueil (Tomeoka and Buseck 1988).

The temperatures of carbonate deposition are not well known, although all estimates, both isotopic and those based on chemical composition, suggest that they were relatively low, probably well below 250°C (Clayton and Mayeda 1984; Johnson and Prinz 1993; Endress and Bischoff 1996). The heat energy necessary to drive hydrothermal processes in the CI parent body is believed to have come mainly from decay of short-lived radionuclides such as [26]Al (DuFresne and Anders 1962; Grimm and McSween 1989), and secondarily from impact processes (Grimm and McSween 1989). Oxygen isotope data also suggest a

of the aqueous alteration of Orgueil (Clayton and Mayeda 1984). This in turn implies that significant amounts of water flowed through the Orgueil parent material during alteration, presumably accompanied by a large mass flux of readily soluble species. Such a scenario is consistent with the generally accepted pervasive nature of CI meteorite alteration, but at odds with the observation that there is considerable chemical and mineralogical heterogeneity at the millimeter or smaller scale that suggests "local" variation in hydrothermal activity (McSween and Richardson 1977; Tomeoka and Buseck 1988; Endress and Bischoff 1996). This small-scale variability may have been produced during the waning stages of hydrothermal activity, after the main, pervasive, episode of fluid flow. One important caveat should be emphasized in this discussion: although Orgueil is by far the largest CI recovered (total mass $\sim 10\,kg$), most of the petrographic, mineralogic, and chemical observations cited here were made on very small amounts of material, typically thin sections of a few cm^2 or bulk samples weighing no more than a few grams, and often much less. Discussions of processes at the parent body scale therefore require very large extrapolation.

Proper understanding of the evolution of CI meteorites requires knowledge of the chronology of processes inferred to have affected these bodies. Petrographic observations provide a relative timescale for some events; for example, the observation that most carbonate veins have been completely disaggregated implies that brecciation either occurred entirely after their formation, or was partly coeval but continued after carbonate vein deposition. Chemical considerations and analogy with terrestrial processes suggest that there was a calcite-dolomite-sulphate depositional sequence. However, only radioactive decay processes offer the possibility of deducing the actual timescale for these events. Two approaches have been employed to date, both focused on carbonates: Mn-Cr (Endress *et al* 1996; Hutcheon and Phinney 1996) and Rb-Sr (Macdougall *et al* 1984) dating. Both of these methods require an accurate knowledge of the initial isotope ratio (radiogenic daughter/stable) at the time of formation of the CI parent body. Results from both types of study imply that the carbonates are ancient, formed within tens to at most a hundred million years or so after the parent body. In this paper, new Sr isotope data are presented for Orgueil. These data help to clarify some of the conclusions reached earlier about the carbonate formation processes.

2. Methods

As in our previous work (Macdougall *et al* 1984), the samples of Orgueil used in the experiments described here were generously provided by the late P. Pellas.

Sample	Type	Weight	Treatment
ORG-A-L1	Water leach of bulk Orgueil fragment	101.3 mg	Bulk sample leached in distilled water, ~44 hrs
ORG-A-L2	0.5 N HCl leach of solid residue from ORG-A-L1	–	Solid residue from ORG-A-L1 leached in 0.5 N HCl, ~40 min
ORG-A-L3	2 N HCl leach of solid residue from ORG-A-L2	–	Solid residue from ORG-A-L2 leached in 2 N HCl, ~6 hr
ORG-B-L1	Water leach of bulk Orgueil fragment	102.5 mg	Bulk sample leached in distilled water, ~44 hrs
ORG-B-L2	0.5 N HCl leach of solid residue from ORG-B-L1	–	Solid residue from ORG-B-L1 leached in 0.5 N HCl, ~60 min
ORG-B-L3	2 N HCl leach of solid residue from ORG-A-L2	–	Solid residue from ORG-B-L2 leached in 2 N HCl, ~6 hr
ORG-CA-1	Single dolomite fragment from clast	94 μg	Multiple distilled water washes, then dissolved in 1 N HCl
ORG-CA-2	Single dolomite fragment from clast	48 μg	Multiple distilled water washes, then dissolved in 4.5 N HCl
ORG-CA-3	Breunnerite grains picked from clast	795 μg	Multiple distilled water washes, then dissolved in warm 4.5 N HCl
ORG-CA-4	Dolomite grains from same clast as ORG-CA-2	56 μg	Multiple distilled water washes, then dissolved in 4.5 N HCl
ORG-CA-5	Breunnerite grains from same clast as ORG-CA-3	2.51 mg	Multiple distilled water washes, 0.5 N HCl wash, then dissolved in warm 4.5 N HCl

All were coherent fragments with no visible traces of the contaminating terrestrial material sometimes found mixed with Orgueil samples. Two types of analysis were carried out. First, a series of leaching experiments was conducted on small Orgueil fragments without fusion crusts (see table 1). Two fragments, each weighing approximately 100 mg, were separately and sequentially leached first in distilled water, then 0.5 N HCl, and finally 2 N HCl. The leach solutions from each step were removed, spiked and analyzed for Rb and Sr concentrations and Sr isotopic composition. Slight effervescence occurred when H_2O was initially added to these fragments, and the fragments disintegrated into smaller pieces. The water leach solution remained very clear and uncoloured, while the 0.5 N HCl leach was slightly cloudy and brownish-yellow, and the 2 N HCl leach clear and bright yellow. After the supernatant leach solution was removed at each step, the residual solid was rinsed several times in distilled water, and the rinse added to the leach solution.

Other fragments of Orgueil were examined microscopically for carbonate grains and clasts. Three multicrystal clasts, two identified as being predominantly dolomite and one breunnerite, were chosen for analysis. Mineral identification was based on energy dispersive X-ray spectra obtained from a few small grains from each clast, examined with the scanning electron microscope; it was assumed that these grains were representative of the whole clast. Crystals from these clasts that appeared to be inclusion-free and without significant amounts of adhering or intergrown matrix were picked for analyses. All were sonified and rinsed repeatedly in distilled water prior to dissolution for Sr isotope analysis. In addition, breunnerite sample

CA-5 (see table 1) was also sonified for 5 minutes in 0.5 N HCl prior to dissolution.

Sr isotopic data are reported relative to a value of 0.710260 ± 0.000024 for NBS 987, where the uncertainty is the total range of standard values over the course of these analyses. Procedural blanks averaged 3 pg for Rb and 15 pg for Sr during this work; all reported concentration and isotope data are blank-corrected where necessary.

3. Results

3.1 *Bulk Orgueil leaching experiments*

Data from the leaching experiments (tables 1 and 2) turned out to be especially interesting. In earlier work, Fredriksson and Kerridge (1988) showed that most of the Na, K and $SO_3^=$, as well as about $\frac{1}{2}$ of the Ca and more than 10% of the Mg in Orgueil are water soluble. Their data were based on extraction of a 1 gm bulk sample with boiling water. The data reported here, based on room-temperature extraction using distilled water, indicate that large fractions of the Sr and Rb are also water-soluble, as might be expected from the major element data. Although a bulk rock analysis was not carried out in this work, data in the literature can be used to estimate the fraction of Sr and Rb removed by the leaching treatments. Anders and Ebihara (1982) indicate that the CI meteorites contain about 7.91 ppm Sr and 2.30 ppm Rb; similar results were obtained by Mittlefehldt and Wetherill (1979) for three separate samples of Orgueil. The elemental data for the leach solutions are given in table 2, as concentrations calculated using the original sample weight. It should be noted that these are approximate

Table 2. *Isotope and concentration data.*

Sample	$^{87}Sr/^{86}Sr_m$	$^{87}Sr/^{86}Sr_c$	Sr (ppm)	Rb (ppm)
ORG-A-L1	0.818913±24	0.818913±24	2.70	1.1
ORG-A-L2	0.735634±24	0.735634±24	3.90	0.71
ORG-A-L3	0.743264±30	0.743264±30	0.30	0.3
ORG-B-L1	0.812281±24	0.812281±24	2.70	1.03
ORG-B-L2	0.732276±24	0.732276±24	4.07	0.74
ORG-B-L3	0.749362±24	0.749362±24	0.20	0.34
ORG-CA-1	0.699366±58	0.699315±62	39	0.002
ORG-CA-2	0.699075±56	0.699034±60	98	0.10
ORG-CA-3	0.70121±13	0.70101±17	0.99	0.019
ORG-CA-4	0.699157±56	0.69911±6	73	0.39
ORG-CA-5	0.70084±12	0.70075±14	0.80	0.005

Concentrations are corrected for procedural blanks of 15 pg (Sr) and 3 pg (Rb). Subscripts "m" and "c" for Sr isotope ratios refer to measured and blank-corrected, respectively. $^{87}Sr/^{86}Sr = 0.712$ was used for the blank composition. Uncertainties in the isotope ratios refer to the final digits and are the larger of the total range for standards during this work (± 0.000024), or the single-run uncertainty.

concentrations, because samples were not dried before weighing; the CI meteorites are known to change weight with variations in ambient humidity. Note also that the mobile nature of Rb and/or Sr is implied by the "young" model ages obtained by Mettlefehlt and Wetherill (1979) in their study of Orgueil. These authors found that $^{87}Sr/^{86}Sr$ in the small fragments they analyzed was always "too low" for the measured Rb/Sr, assuming an age for Orgueil near 4.55 Ga. It is clear that at some scale – and probably at a variety of scales – Orgueil has been an open system.

The leaching data show that the combined water and HCl leaches together extract about 90% of the Sr and Rb contained in the meteorite. The remaining 10% must be retained in the undissolved residue, composed primarily of phyllosilicates and magnetite. The amounts of Sr and Rb extracted in comparable leach steps are very similar for the two Orgueil samples (fragments ORG-A and ORG-B), except for Sr in the final leach of ORG-B, which is significantly lower than for the same step in ORG-A. Especially interesting are the data for the water leaches. Roughly a third of the Sr in Orgueil, and almost 50% of the Rb, are extracted in a simple water leach at room temperature. The only readily identifiable phase in this meteorite that is water soluble is Mg sulphate, which may contain variable amounts of Na, Ni, Ca, Fe and Mn (Fredriksson and Kerridge 1988). It is likely that there are also very fine-grained soluble species on grain surfaces distributed throughout the meteorite, as suggested by earlier work (Macdougall et al 1984) in which it was observed that water rinses of hand-picked carbonate grains contained large amounts of Sr with isotopic ratios very different from the grains themselves.

The Sr isotopic compositions of the two water leaches are similar and very radiogenic (table 2). They are significantly higher than that of the bulk meteorite, which has $^{87}Sr/^{86}Sr$ 0.753 (Mittlefehldt and Wetherill 1979). The high values in the leach solutions are consistent with our earlier data on Sr from the water rinses of picked carbonate grains; these had values of 0.85337 and 0.80592 for $^{87}Sr/^{86}Sr$ (Macdougall et al 1984). In spite of the fact that a large amount of Rb was also extracted in the bulk sample water leaches, the radiogenic Sr is unsupported by the Rb contained in the leaches. About 1.6 to 1.7 times the observed Rb amounts would be required to produce the measured Sr isotopic ratios over 4.56 Ga. This indicates either that there has been a relatively recent redistribution of Rb and Sr in the meteorite, so that some Rb now resides in a different phase than its daughter Sr, or that some of the soluble Rb was transferred to the phyllosilicate matrix minerals during the leaching process. The fact that one of the two carbonate grain rinses measured in our earlier investigation (Macdougall et al 1984) – which had no contact with matrix phyllosilicates – had $^{87}Rb/^{86}Sr$ essentially equivalent to those of the two water leaches discussed in the present work suggests that the unsupported radiogenic Sr is not an artifact of sample processing, but is indeed unsupported *in situ* in Orgueil.

The first HCl leaches (0.5 N) of the residues from the water leaching experiment contained even more Sr than the water leach, about 50% of the total meteorite Sr, but less Rb (table 2). These acidic leaches presumably dissolve Ca carbonate, Ca sulphate, and at least partly dissolve dolomite and breunnerite. Consistent with this scenario, $^{87}Sr/^{86}Sr$ in these solutions is lower than in the bulk meteorite, and also is the lowest of the three leach treatments. The final (2 N) HCl leach must continue to dissolve remaining carbonates, and also must extract some Sr (and Rb) from phyllosilicates and other matrix minerals. Its $^{87}Sr/^{86}Sr$ is higher than the 0.5 N HCl leach, but is lower than that of the bulk meteorite. The HCl leaches also reflect the redistribution of Rb and Sr evident in the water leach results.

3.2 *Dolomites and breunnerites*

Elemental and isotopic data for the dolomites and breunnerites are given in table 2. As already mentioned, all data are blank corrected, where necessary, for 3 pg Rb and 15 pg Sr blanks. While the Sr data in table 2 are probably robust, the Rb concentrations may not be accurate because in most cases the total amounts analyzed are no larger than a few times the blank levels. Thus precise knowledge of the actual blank amount in each sample would be required for accurate data. During this work, procedural blanks for Rb averaged near 3 pg, but occasionally significantly higher blanks occurred, probably due to scratched beakers, which are difficult to clean, or similar problems. There is also the possibility that the washing procedure did

not always entirely remove matrix Rb from the surfaces of these low-Rb grains. Thus the Rb concentrations in table 2 should be treated as upper limits. This is emphasized by the fact that initial $^{87}Sr/^{86}Sr$ ratios (at 4.56 Ga), calculated using the measured $^{87}Rb/^{86}Sr$ values, are lower than the presumed initial solar system value of 0.69897 (Lugmair and Galer 1992) for the three carbonates with highest Rb contents (CA-2, CA-3 and CA-4).

Sr concentrations in the breunnerites are clearly much lower than in the dolomites (table 2), as already noted by Macdougall *et al* (1984). In the dolomite, Sr is quite variable and ranges from 39 to 98 ppm, while both breunnerite samples have Sr < 1 ppm. Note that the Sr isotopic ratios are higher for breunnerite than for dolomite. It is conceivable that this is in part due to incomplete removal of the surface-correlated, easily leachable radiogenic Sr discussed above, although sample ORG-CA-5 was the largest of all carbonate samples measured, and therefore, in spite of its low Sr concentration, contained a significant total amount of Sr. Furthermore, this sample was rinsed with 0.5 N HCl in addition to water. Thus the effect of non-indigenous radiogenic Sr should be minimized in this sample, yet its $^{87}Sr/^{86}Sr$ is still higher than those measured in any of the dolomites.

Time scales for formation of the carbonates are given in table 3 and shown in figure 1 calculated assuming an initial ratio for Orgueil of 0.69897 and using the average $^{87}Rb/^{86}Sr$ for bulk Orgueil (0.87282) reported by Mittlefehldt and Wetherill (1979). They are also calculated using the measured Sr isotopic ratios rather than age-corrected values, because, as explained above, the measured Rb concentrations are upper limits and in some cases appear to be too high. Thus the ages themselves are upper limits. The data indicate that some carbonates were precipitated within a few million years of Orgueil's formation, and that there may be a significant gap (tens of millions of years) between dolomite and breunnerite formation. Note that for the two carbonates with lowest measured $^{87}Rb/^{86}Sr$, formation times are also given using age-
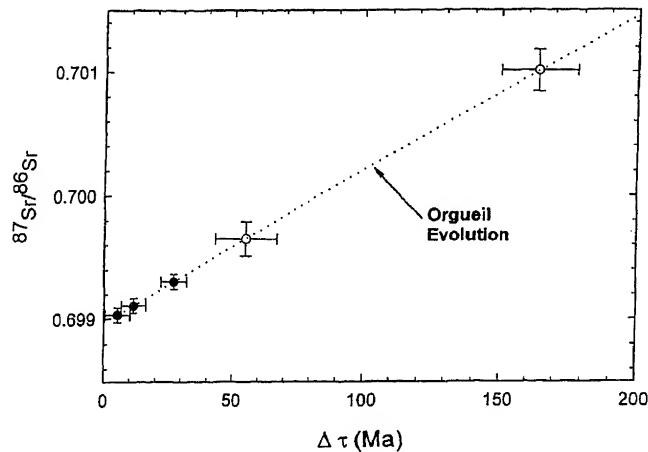
Figure 1. Isotope data from table 3 plotted along the Orgueil evolution line. Filled circles are dolomite data; open circles are breunnerite. See text for discussion of the formation ages ($\Delta\tau$).

corrected (4.56 Ga) Sr isotope ratios. Although these ages are slightly smaller than the uncorrected ones, they do not change the basic conclusion that there is a time difference between dolomite and breunnerite formation.

4. Discussion

The very high Rb/Sr ratio in the CI meteorites provides high time resolution for events early in their history, provided that initial ratios for these events can be determined accurately. The carbonates, with very low Rb/Sr and thus minimal ingrowth of radiogenic Sr since their formation, are ideal phases for such chronology. The concept is very simple for such phases: formation ages are simply the times required to acquire the measured (or initial) $^{87}Sr/^{86}Sr$ ratio in the carbonate given the bulk Orgueil $^{87}Rb/^{86}Sr$ and initial $^{87}Sr/^{86}Sr$. The possibility of determining the formation times for carbonates in the CI meteorites using Sr isotopes was first explored by Macdougall *et al* (1984); the main conclusion reached by these authors was that the carbonates in Orgueil formed very early in the meteorite's history. Formation times calculated for the samples they analyzed ranged from essentially contemporaneous with meteorite assembly to several hundred million years after formation. Very early formation of carbonates was corroborated by Endress *et al* (1996) and Hutcheon and Phinney (1996), who used ion probe techniques to measure Cr isotopes in dolomites and breunnerites from Orgueil. Both groups found ^{53}Cr excesses in Mn-rich carbonates, produced *et al* by short-lived ^{53}Mn, which has a half life of only 3.7 Ma. The new results presented here also corroborate the earlier data, and they give additional information about both the soluble phases in Orgueil, and the relationship between the two major carbonate types, dolomite and breunnerite.

Table 3. *Formation times for Orgueil carbonates.*

Sample	Mineral	$^{87}Sr/^{86}Sr_c$	Δt (Ma)
CA-1	Dolomite	0.699315±62	28±5
		0.699304±62	27±5
CA-2	Dolomite	0.699034±60	5.2±4.8
CA-4	Dolomite	0.699110±60	11.3±4.8
CA-3	Breunnerite	0.70101±17	164±14
CA-5	Breunnerite	0.70075±14	143±12
		0.69965±14	55±12

As in table 2, the subscript "c" refers to blank-corrected Sr isotope data. For CA-1 and CA-5, the second line for each entry gives the age-corrected (4.56 Ga) isotope ratio, calculated using the measured $^{87}Rb/^{86}Sr$. The formation time, Δt, is calculated for an initial ratio of 0.69897 (Lugmair and Galer 1992).

As already discussed, the carbonate formation times given in table 3 and illustrated in figure 1 must be treated as upper limits because of the possibility that small amounts of non-carbonate radiogenic Sr were included in the analyses, and the fact that age corrections are only possible for two of the carbonates.

Dolomites CA-2 and CA-3 are both from the same carbonate clast, and their calculated formation times overlap within the experimental uncertainties. Since virtually all experimental factors affecting the calculated ages tend to *increase* them, it is reasonable to consider the smaller age as being the more accurate. Alternatively there could be more than one generation of carbonate within the same clast, as described by Endress and Bischoff (1996). Regardless, the data for CA-2 indicate that hydrothermal activity and carbonate precipitation began within a few million years of formation of the Orgueil parent body; in fact, at the lower end of the experimental uncertainty range, Δt is only 0.4 Ma. The formation time for CA-2 is consistent with those calculated by Endress *et al* (1996), who measured five dolomite fragments, all with ^{53}Cr excesses, and concluded that they formed within 20 Ma of the earliest solar system objects known (Allende calcium-aluminum rich inclusions). Sample CA-1 has a significantly larger calculated formation time, and the Sr isotope data presented here therefore suggest that dolomite formation could have extended over a time span of nearly 30 Ma. An important test of this conclusion will be further Cr isotope analyses of a range of petrographically documented dolomites. Grains formed 30 Ma or longer after parent body formation should have very small or no ^{53}Cr excess, even for those with high Mn/Cr.

The breunnerite samples, both from the same clast, have much higher measured ^{87}Sr/^{86}Sr than the dolomites. Like the dolomites CA-2 and CA-4, their measured isotopic compositions and calculated formation times overlap (barely) within the experimental uncertainty (table 3). The rubidium content of sample CA-3 is clearly "too high", and results in an unacceptably low initial ratio if the isotope ratio for this sample is age-corrected. However, the data for CA-5 – which was acid rinsed before dissolution – indicate a much lower indigenous Rb content. Even so, the age-corrected initial ratio for this sample is higher than those of the dolomites, and the calculated formation time (55 Ma) is also. This does suggest that the breunnerites are significantly older than the dolomites. On the other hand, Hutcheon and Phinney (1996) measured Cr isotopes in several breunnerites with high Mn/Cr, and estimated that they formed within 12–16 Ma of Orgueil parent body formation. This is clearly earlier than the Sr isotope data for CA-5 would suggest, but it is also considerably older than the youngest formation age determined for dolomite in this work. Again, further ion probe Cr isotope studies, with the potential for higher time resolution than is possible with Sr isotopes, may help to determine the variability of breunnerite ages more accurately.

The results of the bulk-meteorite leaching experiments are particularly intriguing, especially the data from the water leaches (table 2). They indicate that there is a large, very radiogenic Sr component in Orgueil that is readily soluble, and that has ^{87}Sr/^{86}Sr significantly greater than the bulk meteorite. What is the origin of this component? It is possible, but unlikely, that it is a contaminant. ^{87}Sr/^{86}Sr is so high in this component that most terrestrial reservoirs – with the exception of old, high Rb/Sr crustal rocks – are ruled out as a source. The radiogenic Sr is apparently pervasively present in Orgueil, as is shown by the fact that in our earlier investigations (Macdougall *et al* 1984) the same component was encountered on the surfaces of picked carbonate grains. It therefore does not appear to be associated with a specific phase. It is well known that Mg sulphate crystals grow on freshly exposed surfaces of Orgueil, especially in humid environments, and presumably the soluble Sr is part of this mobile material. Its Sr isotopic composition, however, places some constraints on its history. It dictates that until recently, this Sr reservoir had Rb/Sr much higher than the bulk meteorite. It is likely that it represents the final, interstitial residue of the hydrothermal fluids that ultimately produced the mineral assemblage now present in Orgueil. The "orphan" nature of the radiogenic Sr, however, indicates that there has been recent redistribution of at least some of this residue. In particular, some of the Rb in the water soluble component became fixed in less-soluble phases. The timing of this redistribution cannot be determined accurately from the Sr isotope data, but it must be recent to explain the very high ^{87}Sr/^{86}Sr. The cosmic ray exposure age of Orgueil is ~10 Ma (Jeffery and Anders 1970; Kerridge *et al* 1979), so it is conceivable that parent body breakup is the event reflected by these data.

5. Conclusions

The new Sr isotope data reported here for Orgueil carbonates and bulk meteorite leaches corroborate earlier indications that the carbonates were deposited by very early hydrothermal activity within the CI parent body, and that some very recent (probably within the past 10 Ma or so) chemical processing has also affected element distribution within Orgueil. The earliest deposition time recorded in the samples analyzed in this work is for dolomite CA-2, which has very low ^{87}Sr/^{86}Sr indicating crystallization ≤ 5.2 Ma after parent body formation, assuming an initial ratio of 0.69897. The data also suggest that carbonate deposition continued over a time span of as much as several tens of millions of years, and that the Fe-Mn-Mg carbonates were mostly formed after

dolomite deposition. Thus hydrothermal activity was an early and long-lasting feature of the CI parent body.

Postscript

This paper is dedicated to Professor K Gopalan on the occasion of his retirement from the National Geophysical Research Institute. Early in his career, K Gopalan, together with G Wetherill, wrote a series of papers on the Rb-Sr ages of various chondritic meteorite groups (Gopalan and Wetherill 1968, 1969, 1970, 1971). They were, in their time, groundbreaking contributions, and the papers are much cited in the literature. Some thirty years later our analytical capabilities are greatly improved, but the general approach is not radically different. The present manuscript adds to those earlier papers of Gopalan and Wetherill (and the papers of many others who have published on this topic in the interim) by presenting a Rb-Sr study of the CI meteorite Orgueil.

It has been my privilege to work with K Gopalan periodically over a substantial portion of his career—not, as it turns out, on meteorites, but rather on the isotopic geochemistry and geochronology of Indian rocks. This collaboration has been fruitful, and, for me at least, enlightening. It has been a scientific adventure, but it has been made even more enjoyable by countless adventures of other sorts on Indian highways, in Indian airports, cities and guesthouses, and in the Indian countryside.

The sciences, especially the Earth Sciences, are international endeavours, but it is only through the efforts of perceptive scientists such as K. Gopalan that the potential of international collaborations can be fully realized. So it is to be hoped that his retirement will be so in name only.

Acknowledgments

References

Anders E and Ebihara M 1982 Solar-system abundances of the elements; *Geochim. Cosmochim. Acta* **46** 2363–2380.

Clayton R N and Mayeda T K 1984 The oxygen isotope record in Murchison and other carbonaceous chondrites; *Earth Planet. Sci. Lett.* **67** 151–161.

DuFresne E R and Anders E 1962 On the chemical evolution of the carbonaceous chondrites; *Geochim. Cosmochim. Acta* **26** 1085–1114.

Endress M and Bischoff A 1996 Carbonates in CI chondrites: Clues to parent body evolution; *Geochim. Cosmochim. Acta* **60**, 489–507.

Endress M, Zinner E and Bischoff A 1996 Early aqueous activity on primitive meteorite parent bodies; *Nature* **379** 701–703.

Fredriksson K and Kerridge J F 1988 Carbonates and sulfates in the CI chondrites: Formation by aqueous activity on the parent body; *Meteoritics* **23** 35–44.

Gopalan K and Wetherill G W 1968 Rubidium-strontium age of hypersthene (L) chondrites; *J. Geophys. Res.* **73** 7133–7136.

Gopalan K and Wetherill G W 1969 Rubidium-strontium age of amphoterite (LL) chondrites; *J. Geophys. Res.* **74** 4349–4358.

Gopalan K and Wetherill G W 1970 Rubidium-strontium studies on enstatite chondrites: Whole meteorite and mineral isochrons; *J. Geophys. Res.* **75** 3457–3467.

Gopalan K and Wetherill G W 1971 Rubidium-strontium studies on enstatite chondrites: Whole meteorite and mineral isochrons; *J. Geophys. Res.* **76** 8484–8492.

Goswami J N, Hutcheon I D and Macdougall J D 1976 Microcraters and solar flare tracks in crystals from carbonaceous chondrites and lunar breccias; *Proc. Lunar Sci. Conf.* **7** 543–562.

Grimm R E and McSween H Y 1989 Water and the thermal evolution of carbonaceous chondrite parent bodies; *Icarus* **82** 244–280.

Hutcheon, I D and Phinney D L 1996 Radiogenic $^{53}Cr^*$ in Orgueil carbonates: Chronology of aqueous activity on the CI parent body; *Lunar. Planet. Sci. XXVII*, 577–578. LPI, Houston.

Jeffery P M and Anders E 1970 Primordial noble gases in separated meteoritic minerals–I; *Geochim. Cosmochim. Acta* **34** 1175–1198.

Johnson C A and Prinz M 1993 Carbonate compositions in C M and CI chondrites, and implications for aqueous alteration; *Geochim. Cosmochim. Acta* **57** 2843–2852.

Kerridge J F 1968 Occurrence of olivine in a Type I carbonaceous meteorite; *Nature* **217** 729–730.

Kerridge J F and Bunch T E 1979 Aqueous alteration on asteroids: Evidence from carbonaceous meteorites. In *Asteroids* (ed.) T. Gehrels, (Tucson, Univ. Arizona Press) 745–764.

Kerridge J F and Macdougall J D 1976 Mafic silicates in the Orgueil carbonaceous meteorite; *Earth Planet. Sci. Lett.* **29** 341–348.

Kerridge J F, Macdougall J D and Marti K 1979 Clues to the origin of sulfide minerals in CI chondrites; *Earth Planet. Sci. Lett.* **43** 359–367.

Lugmair G and Galer S J G 1992 Age and isotopic relationships among the angrites Lewis Cliff 86010 and Angra dos Reis; *Geochimica Cosmochimica Acta* **56**, 1673–1694.

Macdougall J D, Lugmair G W and Kerridge J F 1984 Early solar system aqueous activity: Sr isotope evidence from the Orgueil CI meteorite; *Nature* **307** 249–251.

McSween H Y and Richardson S M 1977 The composition of carbonaceous chondrite matrix; *Geochim. Cosmochim. Acta* **41** 1145–1161.

Mittlefehldt D and Wetherill G W 1979 Rb-Sr studies of CI and CM chondrites; *Geochim. Cosmochim. Acta* **43** 201–206.

Reid A M, Bass M N, Fujita H, Kerridge J F and Fredriksson K 1970 Olivine and pyroxene in the Orgueil meteorite; *Geochim. Cosmochim. Acta* **34** 1253–1255.

Richardson S M 1978 Vein formation in the C1 carbonaceous chondrites; *Meteoritics* **13** 141–159.

Riciputi L R, McSween H Y, Johnson C A and Prinz M 1994 Minor and trace element concentrations in carbonates of carbonaceous chondrites, and implications for the compositions of coexisting fluids; *Geochim. Cosmochim. Acta* **58** 1343–1351.

Tomeoka K and Buseck P R 1988 Matrix mineralogy of the Orgueil CI carbonaceous chondrite; *Geochim. Cosmochim. Acta* **52** 1627–1640.

Conceptual problems with remote element synthesis

O K Manuel

Department of Chemistry, University of Missouri, Rolla, MO 65401, USA
email: om@umr.edu

The notion of remote element synthesis has recently been modified to explain the presence of nucleogenetic isotopic anomalies and decay products of short-lived nuclides by injection of a small amount of *exotic* nucleogenetic material. Even with this modification, remote element synthesis seems inconsistent with the following observations:

- Evidence of coupled variations in the chemical and isotopic compositions of the source material for meteorites.
- Residual coupling of chemical and isotopic heterogeneities across planetary distances in the solar system today.
- The mass-fractionation relationship seen across isotopes of elements in the planetary system, in the solar wind, and in solar flares.
- Linkage of short-lived radioactivities with isotopic anomalies and with physical properties of their host grains, as expected for early condensate of fresh stellar debris.
- Temporal and spatial distributions of short-lived nuclides and their decay products.
- Mirror-image (+ and −) isotopic anomalies in meteorite grains that sum to "normal" isotopic ratios, as expected of unmixed products of the same nuclear reactions that produced our bulk elements.
- The lack of supporting evidence for "presolar" grains or nearby stars that injected *exotic* material into the early solar nebula.

1. Introduction

It has long been assumed that our elements were made elsewhere and collected from vast regions of space into a homogeneous cloud of material that somehow formed the solar system. The discovery of decay products of short-lived radioactivities and nucleogenetic isotopic anomalies in meteorites has forced modifications to this assumption. Begemann thus introduced his survey on isotopic anomalies, "The classical picture of the pre-solar nebula is that of a hot, well-mixed cloud of chemically and isotopically uniform composition. Recent measurements have shown this conception to be erroneous, however" (Begemann 1980, p. 1309).

The idea of homogeneous starting material for the solar system has been largely abandoned, while the idea of remote element synthesis has been retained. Late addition of a small amount of alien nucleogenetic matter to an otherwise homogeneous mix of elements from many stellar sources is now the popular explanation for meteorite grains that condensed before short-lived radioactivities decayed away, even before the isotopes of individual elements were mixed. However, this explanation neglects the possibility that these observations may indicate local element synthesis (Manuel and Sabu 1975, 1977; Lavrukhina 1980; Sabu and Manuel 1980).

For example, Fowler (1984) and Wasserburg (1987) endorsed the late addition of 0.0001 parts *exotic* nucleogenetic material to 0.9999 parts *normal* solar system material to explain decay products of short-lived nuclides and nucleogenetic isotopic anomalies

in meteorites. Their opinions, expressed in lectures given on receipt of the Nobel Prize in Physics and the Crafoord Prize in Geosciences, respectively, are especially inuential.

Earlier, Clayton championed the idea that isotopic anomalies and short-lived nuclides were brought into the solar system in interstellar grains that became embedded in meteorites (e.g., R N Clayton *et al* 1973; D D Clayton 1975, 1982; D D Clayton and Hoyle 1976). Cameron and coworkers proposed, then refuted, and recently revived the idea of a nearby supernova that injected alien nucleogenetic material into an interstellar cloud of material and simultaneously triggered its collapse to form the Solar System (e.g., Cameron and Truran 1977; Cameron 1984; Cameron *et al* 1995).

The idea of interstellar grains embedded in meteorites has caught the fancy of many leading scientists. In an invited review, Anders and Zinner (1993) conclude that interstellar grains from outside the Solar System are the source of isotopically anomalous elements and decay products of short-lived nuclides found in diamonds, silicon carbide and graphite of primitive meteorites. On receiving the Leonard Medal from the Meteoritical Society, Professor Begemann (1996, p. 171) states that carbonaceous chondrites contain "stardust" with "undiluted nucleosynthesis products of individual stars".

Scientists from nuclear astrophysics, observational astronomy and cosmochemistry recently gathered in Saint Louis, Mo and endorsed the concept of presolar grains as carriers of exotic nucleogenetic material. The uniformity of this consensus is reflected in the 750-page Conference Proceedings (Bernatowicz and Zinner 1997) and in the opening statement of an ensuing news report on the conference, "Amazingly, individual grains of dust from stars that existed before the Sun was born have made their way to Earth in meteorites." (Bernatowicz and Walker 1997, p. 26).

The St. Louis conference was devoted to a discussion of short-lived nuclides and nucleogenetic isotopic anomalies, but the continued allure of remote element synthesis and an initially homogeneous nebula is obvious in papers selected for publication in the conference proceedings.

For example, on the first page of the conference overview Zinner (1997, p. 3) states that: "It was realized early on that the solar system not only is a very homogeneous mixture of material from many different stellar sources but that these stars themselves incorporated the debris of previous generations of stars ('galactic chemical evolution')." In the introduction to the second paper in the proceedings, Hoppe and Ott (1997, p. 27) note "While most of the material that went into the making of the solar system was thoroughly processed and mixed, thus losing isotopic heterogeneity and all memory of its origin,

formation of the solar system in the parent bodies of primitive meteorites" (Anders and Zinner 1993; Ott 1993).

Some problems with the concept of remote element synthesis and injection of alien nucleogenetic material into the early solar system are presented below. First, it seems appropriate to acknowledge that the author was among the first to champion an injection, noting trends in the experimental data which might suggest that anomalous Xe-X "represents material that has been added to our solar system from a nearby supernova, although no evidence for the addition of products from a separate nucleosynthesis event has been found in other elements." (Manuel *et al* 1972, p. 100). Xe-X, with excess ^{124,126}Xe and ^{134,136}Xe from the p- and r-processes of nucleosynthesis, is also called Xe-HL (Huss and Lewis 1995).

2. Primordial coupling of chemical and isotopic heterogeneities

Coupling of chemical and isotopic heterogeneities in meteorites was the first observation that could not be explained by remote element synthesis plus the addition of exotic nucleogenetic material.

2.1 *Primordial coupling of He and Ne with Xe-X*

A few years after suggesting an injection of alien nucleogenetic material from a nearby supernova (Manuel *et al* 1972), it was noticed that primordial (not produced *in situ*) He and Ne in meteorites are always trapped with isotopically anomalous Xe-X. Further, meteorite phases containing isotopically normal Xe were found to be almost totally devoid of primordial He and Ne (Manuel and Sabu 1975, 1977). Figure 1 shows the first recognized example of this linkage of elemental abundances of He with isotopically strange Xe. Later work showed that the coupling of He and Ne with Xe-X (and with isotopically strange Kr and Ar) is a common feature of noble gases in meteorites (Sabu and Manuel 1980).

The primordial linkage of light elements with specific isotopes of heavy elements, as shown in figure 1 for noble gases, may indicate that the solar system formed directly from debris of a single supernova (SN) (Manuel and Sabu 1975, 1977; Sabu and Manuel 1980).

According to that interpretation, nuclear fusion reactions in the stellar interior depleted He from the source region of isotopically normal Xe, Kr and Ar, shown on the left in figure 1. The supernova explosion produced Xe-X, shown on the right in figure 1, in outer stellar layers that remained rich in light elements like H, He, C, etc.

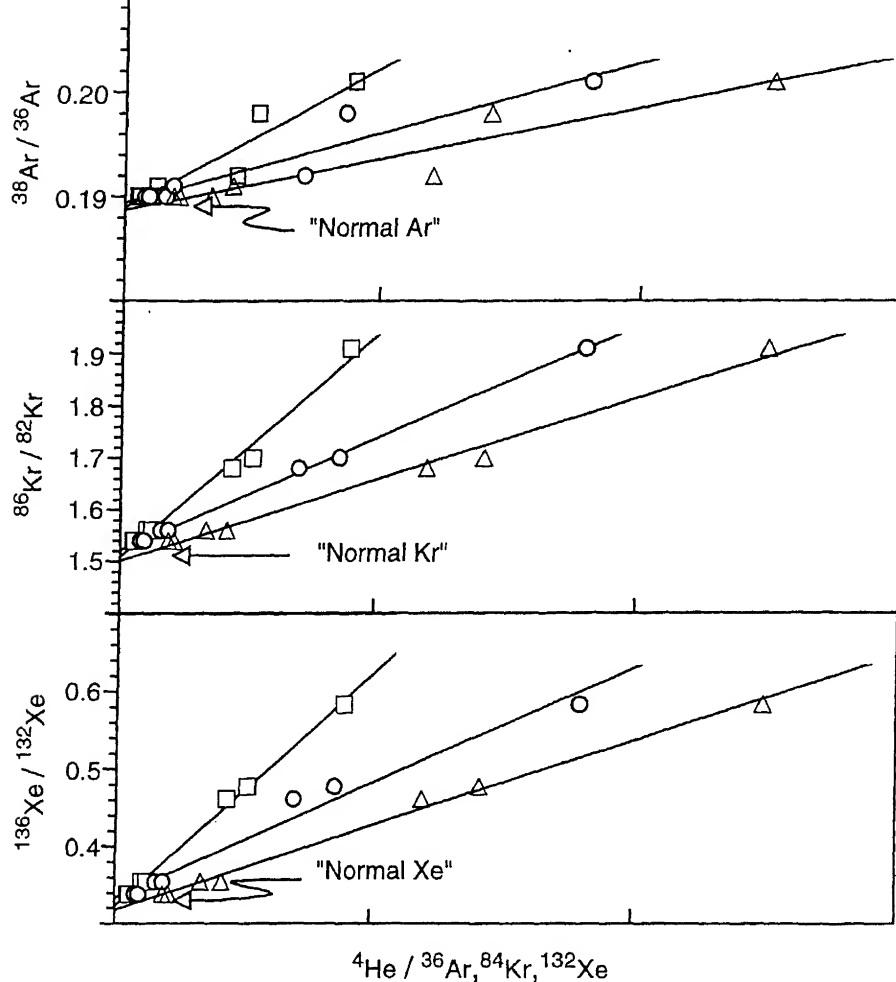Since He is widely regarded as the second most

Figure 1. Elemental abundances of primordial He correlate with isotopic ratios of Ar, Kr and Xe in mineral separates of the Allende meteorite and extrapolate to zero at isotopic ratios of "normal" Ar, Kr and Xe. This primordial linkage of He with specific isotopes of the heavier noble gases is a common feature of noble gases in meteorites (Sabu and Manuel 1980). ^{132}Xe, ^{84}Kr and ^{36}Ar are represented by □, and ○, respectively.

synthesis plus the addition of a small quantity of exotic nucleogenetic material – in the form of interstellar grains or a nearby star – offers no explanation for the example of many experimental observations illustrated in figure 1: The ubiquitous linkage of primordial He with *exotic* Ar, Kr and Xe in meteorites (Sabu and Manuel 1980).

2.2 *Primordial coupling of He, Ne and Xe-X with C*

When the carrier of Xe-X was first partially isolated from the Allende meteorite, Anders *et al* (1975) suggested that the host mineral was probably chromite, enriched in "noble metals (congeners of elements 107–111) and volatiles (congeners of elements 113–118)." Such a composition was unexpected for condensate from the outer layers of a supernova, where the dominant elements are expected to be H, He, C, etc.

Subsequent work has shown, however, that the host phase is actually C in the form of nanometer-sized diamonds (Lewis and Anders 1988). It has also been shown that diamonds may form directly by chemical vapor deposition from a methane-hydrogen mixture (e.g., Shindo *et al* 1985). Thus, the diamond host phase of noble gases on the right of figure 1 is a plausible vapor condensation product from a region of the presolar nebula with high abundances of H, He and C.

This coupling of primordial He, Ne, and Xe-X with diamond has been confirmed in seven different classes of chondritic meteorites (e.g., Huss and Lewis 1995). The isotopic compositions of He, C, and Ne in these diamonds appear "normal" for solar system materials, unlike that expected if these were exotic imports from beyond the solar system.

2.3 *Primordial coupling of Silicon Carbide with Xe-S*

Xe-S is enriched in the intermediate mass isotopes, $^{128-132}$Xe, that are made by the s-process of nucleo-synthesis. It is thus a complementary component to

Xe-X. Xe-S is found in SiC inclusions of meteorites, accompanied by Ne-E(H), a neon component that is enriched in ^{22}Ne. This primordial coupling of isotopically anomalous Xe-S and Ne-E(H) with SiC has been confirmed in seven classes of chondritic meteorites (Huss and Lewis 1995). Indeed, the primordial coupling of noble gas isotopic ratios with the chemical compositions of their host minerals in chondrites was *apparently* pervasive throughout the presolar nebula. Thus, Huss and Lewis (1995) were able to estimate the abundances of diamond, as well as silicon carbide and graphite grains by isotopic analyses of the noble gases.

2.4 *Primordial coupling of Xe-T with Fe and S*

The occurrence of terrestrial-type xenon (Xe-T) in troilite (FeS) inclusions of iron meteorites was noted several years ago (Hwaung and Manuel 1982). More recently, Xe-T was identified as the trapped xenon component in FeS-rich mineral separates of the Allende carbonaceous chondrite (Lee *et al* 1996). It was also noted that Xe-T is the dominant xenon component in the atmospheres of Earth and Mars, two inner planets rich in Fe and S. It was concluded that Xe-T was the primary xenon ingredient in the central, Fe, S-rich region of the solar nebula, just as the main xenon component in the outer, He, C-rich region was Xe-X (Lee *et al* 1996).

Murty and Marti (1987) found isotope ratios of xenon in metal and in troilite inclusions of the Cape York iron meteorite that are closer to those in air than to those in stone meteorites .(Marti 1967). Mathew and Begemann (1995) also report isotopic ratios of xenon in schreibersite, (Fe, Ni)$_3$P, and graphite inclusions from the El Taco iron meteorite that are close to Xe-T, whereas xenon in olivine, feldspar and pyroxene of the El Taco meteorite is closer to that found in stone meteorites (Marti 1967).

The above four examples of inter-linked isotopic and chemical abundances show the effects of nuclear fusion and evolution of a massive first generation star into chemical layers of successively higher atomic number, from an outer layer that remains rich in light elements to an inner layer that is rich in iron. Xe-X is associated with low-Z elements (He, C, etc.) expected in the outer layers of an evolved star. Xe-T is coupled with the high-Z elements (Fe, P, S, etc.) identified with the central region of an evolved star. Xe-S is linked with low-to-intermediate Z elements (C, Si) that might be abundant below the outer layers of an evolved star.

Remote element synthesis and the injection of exotic nucleogenetic material offers no explanation for the observed linkage of isotopic ratios of noble gases with the chemical compositions of their carrier phases, including both refractory and low-temperature minerals.

3. Residual coupling of chemical and isotopic heterogeneities

Large chemical heterogeneities exist in the planetary system today. Planets near the Sun are rich in high-Z elements like Fe and S, especially in the cores of these inner planets. Giant, low-density planets beyond the asteroid belt are rich in low-Z elements like H, He and C. If this diversity is the remnant of a heterogeneous solar nebula, then this coupling of chemical and isotopic abundances may still be observed as variations in the isotopic compositions of elements across the planetary system.

There are at least three indications of residual coupling of isotopically distinct xenon with chemical gradients in the planetary system, plus some intriguing isotopic compositions of elements that comprise the Sun.

Isotopically distinct primordial xenon was first found in carbonaceous chondrites many years ago (Reynolds 1960b). The term AVCC Xe was widely used to designate the isotopically distinct xenon in average carbonaceous chondrites. Later, it was shown that AVCC Xe is a mixture of Xe-X plus a mass fractionated form of Xe-T, the dominant xenon component in Mars, the Earth and the Sun (Manuel *et al* 1972). However, this early work by Reynolds clearly established that the average isotopic composition of primordial xenon on Earth is different than that in material which formed carbonaceous chondrites further away from the Sun.

The latest advancement in our understanding of isotopic diversity in the solar system resulted directly from Dr. Daniel S. Goldin's decision on January 7, 1998 to release isotopic data from the Galileo probe entry into Jupiter (Goldin 1998). The isotopic composition of xenon there is much closer to Xe-X than to that of xenon in the solar wind (Manuel *et al* 1998). Since Jupiter is rich in He and C – elements that were initially linked with Xe-X in the solar nebula (Sabu and Manuel 1980) – the presence of Xe-X in Jupiter today probably represents residual coupling of these elemental and isotopic components from the heterogeneous solar nebula.

Xe-T is dominant in the atmospheres of both Earth and Mars, which are also rich in Fe and S. This same type of primordial xenon is trapped in troilite (FeS) of diverse meteorites, including the very isotopically heterogeneous material incorporated into the Allende carbonaceous chondrite (Lee *et al* 1996). Today's presence of Xe-T in Earth and Mars is probably a remnant of the primordial coupling of Xe-T with Fe and S.

Residual coupling of elemental and isotopic abundances across the planetary system today is again unexplained by remote element synthesis.

If the various chemical and isotopic components in the solar nebula collectively formed the Sun, then the isotopic composition of its elements may indicate the relative abundances of these ingredients. Several

groups (Boulos and Manuel 1971; Kaiser 1972; Bernatowicz and Podosek 1978) concluded that SW xenon is predominantly Xe-T, with the lighter mass isotopes selectively enriched by about 4% per mass unit. Manuel and Hwaung (1983) attempted to decipher the presence of mass fractionated Xe-T at the solar surface, where light elements (He, C) initially linked with Xe-X are much more abundant than the heavy elements (Fe, S) initially linked with Xe-T. This dilemma will be discussed below.

4. Fractionated isotopes in the solar wind and in solar flares

Isotopic anomalies are not only limited to elements found in meteorites or in other planets. Solar wind (SW) elements display one set of isotopic anomalies, for example, and those in solar flares display another.

Isotopic ratios of certain SW noble gases are selectively enriched in lighter mass isotopes, as expected from mass-dependent fractionation (Kuroda and Manuel 1970; Kaiser 1972; Manuel and Hwaung 1983). Manuel and Hwaung (1983) found that a systematic mass fractionation pattern could be discerned across the isotopes of all five SW noble gases if He, Ne and Ar in the Sun are predominantly type-X gases, if its xenon is Xe-T, and if its Kr is a mixture of these primordial noble gas components.

When resolved this way, lighter mass isotopes in the solar wind are enriched by $\approx$ 4%, 6%, 9%, 27% and 200% per amu for Xe, Kr, Ar, Ne and He, respectively. Manuel and Hwaung (1983) suggested that internal diffusion in the Sun enriches lighter nuclei at its surface. If so, the composition of the solar surface may conceal that of its interior. Noble gas atoms are volatile, but diffusive fractionation in an ionizing plasma would be independent of the chemical nature of atoms. They therefore suggested isotopic analyses of a refractory element like SW Mg to test this hypothesis.

Even before the results of isotopic analyses of Mg in the solar wind were reported, confirmation of diffusive fractionation in the Sun came from isotopic analyses of noble gases in solar flares (Rao et al 1991). Isotopic ratios of flare gases are systematically less enriched in lighter isotopes, as expected if internal diffusion in the Sun is disrupted by energetic events at the solar surface (Manuel and Ragland 1997).

Selesnick et al (1993) reported isotopic ratios for Mg in solar flare particles. Later, Boschler et al (1996) reported that isotopic ratios of SW Mg are consistent with terrestrial values. However, isotopic ratios of SW Mg vary systematically with velocity, and like SW He, Ne and Ar, heavier isotopes become increasingly abundant at higher velocities (Manuel and Ragland, 1997). It was also noted (Manuel and Ragland 1997) that hydride formation is an interference that apparently increases with SW velocity. The natural abundances of ^{25}Mg and ^{26}Mg are nearly equal, but lower than that of ^{24}Mg by a factor of 8. Therefore, hydride formation of ^{24}MgH$^+$ contributes a much larger fraction of the signal from ^{25}Mg$^+$ than ^{25}MgH$^+$ contributes to the signal from ^{26}Mg$^+$.

To demonstrate that shifts in isotopic ratios of He, Ne, Mg and Ar are caused by internal solar diffusion, Manuel and Ragland (1997) tabulated the results of Geiss et al (1972), Rao et al (1991), Selesnick et al (1993) and Boschler et al (1996) in the manner shown in table 1. The top section compares values of ^{3}He/^{4}He, ^{20}Ne/^{22}Ne, ^{24}Mg/^{26}Mg and ^{36}Ar/^{38}Ar ratios in the solar wind with those in the solar flares. Note that these ratios are always higher in the solar wind than in solar flares. Shifts in these ratios, tabulated in the bottom section of table 1, follow values of $\Delta m/m_{avg.}$, as expected if diffusion in the Sun is disrupted by the energetic events that produce solar flares (Manuel and Ragland 1997).

The results shown in table 1 are consistent with internal diffusion in the Sun that enriches lighter elements and the lighter isotopes of individual elements at the solar surface (Manuel and Hwaung 1983; MacElroy and Manuel 1986; Manuel and Ragland 1997). Thus, the presence of Xe-T in the solar wind is consistent with other measurements indicating that Fe may be the most abundant element in the Sun's interior (Hoyle 1975; Manuel and Hwaung 1983; Rouse 1983, 1985).

Isotopic anomalies in the solar wind and in solar flares, as shown in table 1, are unexplained by synthesis of elements in multiple stellar sources to produce an initially homogeneous solar nebula. Furthermore, this discrepancy between remote element synthesis and observation cannot be resolved by injecting a small amount of exotic nucleogenetic material.

5. Short-lived radioactivities, isotopic anomalies and host grains

If elements were made locally and the solar system condensed directly from chemically and isotopically

Table 1. *Fractionation relationship between isotopic ratios of He, Ne, Mg and Ar in the solar wind and in solar flares (Manuel and Ragland 1997)*

A. Isotope Ratios	Solar Wind (SW)	Solar Flare (SEP)
^{3}He/^{4}He	4.1×10^{-4}	2.6×10^{-4}
^{20}Ne/^{22}Ne	13.6	11.6
^{24}Mg/^{26}Mg	7	6
^{36}Ar/^{38}Ar	5.3	4.8

B. Isotope Ratios	SW/SEP	$\Delta m/m_{avg.}$
^{3}He/^{4}He	1.58	0.29
^{20}Ne/^{22}Ne	1.17	0.09
^{24}Mg/^{26}Mg	1.17	0.08
^{36}Ar/^{38}Ar	1.1	0.05

heterogeneous SN debris (Manuel and Sabu 1975, 1977), natural mixing would decrease the diversity with time. Short-lived nuclide abundances would also decrease naturally with time. The magnitude of isotopic anomalies may be linked with the level of extinct radioactivity contained in condensate from a local supernova.

If the solar system condensed directly from SN debris, the earliest nucleation seeds would likely form grains with physical properties like those exhibited by other high-temperature condensation products.

All of these expectations are borne out by the five X-type grains of SiC recovered from the Murchison carbonaceous chondrite (Amari et al 1992). They apparently represent the earliest known condensate. These grains formed soon after the explosion of a supernova (Kuroda and Meyers 1997), over a period of time as the $^{26}Al/^{27}Al$ ratio decayed from a value of 0.60 to a value of 0.10 (Amari et al 1992). As expected of early condensate from isotopically heterogeneous material, they contain very large isotopic anomalies in several elements, including C, N, Si, Ti and Ca.

Levels of extinct radioactivity in these SiC grains decrease with particle size, similar to fallout particles from nuclear weapons (Kuroda and Meyers 1997). Higher values of the $^{26}Al/^{27}Al$ ratio are seen in SiC grains that started to nucleate early and grew larger; lower values of the $^{26}Al/^{27}Al$ ratio are seen in smaller grains that started their growth later.

This linkage of isotopic anomalies with extinct radioactivity was first seen when Reynolds (1960a) discovered the decay product of extinct ^{129}I embedded in xenon with a general isotopic anomaly pattern across all nine xenon isotopes (Reynolds 1960b). Remote element synthesis, even with a late injection of exotic material, does not explain the observed linkage of extinct radioactivity with isotopic anomalies and with the size of their host grains.

6. Short-lived nuclides and their decay products

The shorter-lived nuclides and their decay products are also an enigma for remote element synthesis. Lugmair et al (1996) found that excess ^{53}Cr from the decay of ^{53}Mn ($t_{1/2} = 3.7\,My$) correlates with distance from the Sun. As noted above, abundances of elements like Fe and He also correlate with heliocentric distance, as do abundances of isotopically distinct forms of elements that were initially linked with those elements, e.g., Xe-T and Xe-X. Remote element synthesis does not explain radial heterogeneities in the primitive solar nebula.

Some of the earliest critics of local element synthesis (Lewis et al 1977) have recently discovered that "a single stellar source is responsible for generating" ^{53}Mn and other short-lived nuclides with half-lives

of 0.1–10 My, such as ^{41}Ca, ^{26}Al, ^{60}Fe and ^{107}Pd (Sahijpal et al 1998, p. 559). The presence of extant, even more short-lived nuclides requires shorter interstellar distances from the parent source, if these radioactivities are injected into the early solar nebula, as implied.

Although there is no convincing evidence that even shorter-lived radioactivities existed in the solar nebula, the presence of Ne-E requires an even shorter time scale if the decay of ^{22}Na ($t_{1/2} = 2.6\,y$) is the source of excess ^{22}Ne in this neon component (see Black 1978 and references therein). Recent measurements at Mainz suggest that r-products in the isotopes of Kr, Te and Xe must have been separated from precursor nuclei like ^{83}Br, ^{125}Sb and ^{131}I within 10^4 seconds of the supernova event to explain the isotopically anomalous Kr, Te and Xe seen in diamonds of the Allende meteorite (Ott 1996; Richter et al 1998).

7. Complementary isotopic anomalies

If elements were made elsewhere and collected into a mostly homogeneous cloud that formed the solar system, then isotopic compositions of elements in the exotic component injected into that cloud are not expected to have any special relationship to the "normal" isotopic compositions of bulk elements in the well-mixed cloud. On the other hand, if elements were made locally and the solar system formed out of material that was isotopically heterogeneous, then material not thoroughly mixed to form isotopically "normal" elements may show "excesses" and "depletions" of any given isotope (Oliver et al 1981). Observations match the latter case.

This was first seen in xenon. For example, Xe-X is enriched in light and heavy isotopes, $^{124,126}Xe$ and $^{134,136}Xe$, respectively, from the p- and r- processes of nucleosynthesis (Manuel et al 1972). A complimentary component, Xe-S, is enriched in the intermediate mass isotopes, $^{128-132}Xe$ (Srinivasan and Anders 1978).

Recently, Begemann (1993) noted that the seven isotopes of Ba, Nd and Sm in grains separated from two different carbonaceous chondrites reveal the "mirror-image" anomaly patterns expected in unmixed products of the same nuclear reactions that made bulk Ba, Nd and Sm in the solar system. Inclusion EK-1-4-1 of the Allende carbonaceous chondrite is enriched in isotopes of Ba, Nd and Sm from the r- and p-processes of nucleosynthesis. SiC grains from the Murchison carbonaceous chondrite are depleted in these same isotopes. The relative depletions in SiC grains are in the same proportions as the enrichments in inclusion EK-1-4-1, i.e., the isotopic anomaly patterns are "mirror-images." This is illustrated in figure 2 for any element with seven stable isotopes.
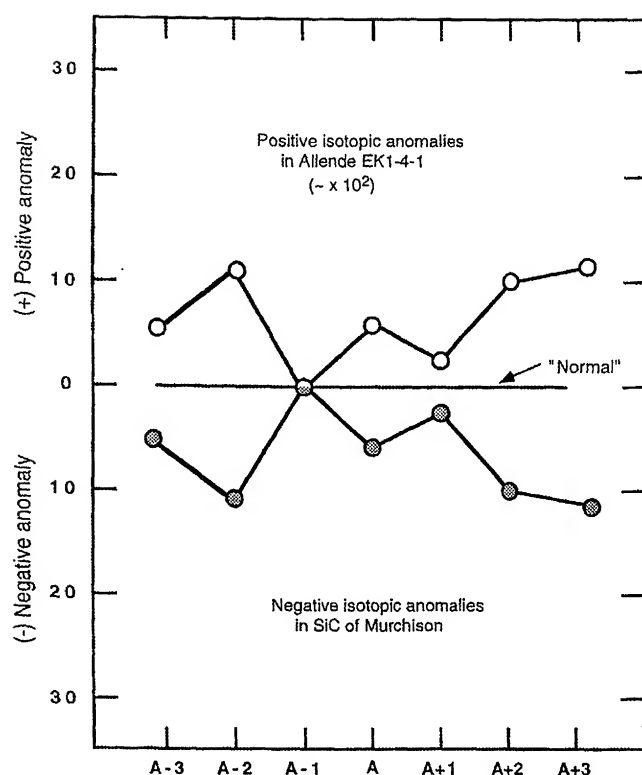
Figure 2. The enrichment pattern of isotopes of elements in the E-K-141 inclusion of Allende is the "mirror-image" of the depletion pattern of these same isotopes in SiC grains from the Murchison meteorite. Individual plots for the stable isotopes of Ba, Nd and Sm are shown in figure 2 of Begemann (1993) and in figure 3 of Zinner (1997).

The "mirror-image" isotopic anomaly patterns observed in Ba, Nd and Sm are expected in poorly mixed products of the same nuclear reactions that made bulk Ba, Nd and Sm in the solar system. These "mirror-image" anomaly patterns are unexpected if elements in the bulk solar system were well mixed and the isotopic anomalies came from an injection of *exotic* nucleogenetic material.

8. Mystical interstellar grains and nearby stars

Interstellar carrier grains from distant stars and/or direct injections of material from nearby stars were proposed in an effort to explain how the findings of heterogeneities from fresh nucleosynthesis products might be compatible with the concept of remote element synthesis and an initially homogeneous nebula (see articles in Bernatowicz and Zinner 1997). However, both of these mechanisms are *ad hoc* and lacking in corroborative evidence.

These solutions leave several questions unanswered. There is no convincing evidence, for example, that any "presolar" grains are older than the solar system. Neither is there any convincing evidence for their bombardment by cosmic rays during a journey across interstellar distances before becoming embedded in meteorites. Likewise, it is reasonable to ask what happened to the nearby star(s) that was so conveniently present at the birth of the solar system to inject exotic nucleogenetic material.

Thus, supporting evidence of presolar grains and/or nearby stars that might have injected material into the solar system is lacking. Decay products of short-lived nuclides and nucleogenetic isotopic anomalies are more easily understood as products of local element synthesis.

For these reasons, local element synthesis and an initially heterogeneous solar nebula seem a more plausible explanation for the chemical and isotopic heterogeneities that we observe in the solar system today.

Acknowledgements

References

Amari S, Hoppe P, Zinner E and Lewis R S 1992 Interstellar SiC with unusual isotopic compositions: Grains from a supernova? *Ap. J.* **394** L43–L46

Anders E, Higuchi H, Gros J, Takahashi H and Morgan J W 1975 Extinct superheavy element in the Allende meteorite; *Science* **190** 1262–1271

Anders E and Zinner E 1993 Interstellar grains in primitive meteorites: Diamonds, silicon carbide and graphite; *Meteoritics* **28** 490–514

Begemann F 1980 Isotopic anomalies in meteorites; *Rep. Prog. Phys.* **43** 1309–1356

Begemann F 1993 Isotope abundance anomalies and the early solar system: MuSiC vs. FUN; In *Origins and Evolution of the Elements* (eds.) E N Prantzos, E Vangioni-Flam and M Casse pp. 518–527, (Cambridge: Cambridge Press)

Begemann F 1996 Noble gases and meteorites. (The Leonard Award Address); *Meteoritics* **31** 171–176

Bernatowicz T J and Podosek F A 1978 Nuclear components in the atmosphere; In: *Terrestrial Rare Gases* (eds.) E C Alexander and M Ozima 99–135, (Tokyo: Center for Academic Publications Press)

Bernatowicz T J and Walker R M 1997 Ancient stardust in the laboratory; *Physics Today* **50** no. 12 26–32

Bernatowicz T J and Zinner E (editors) 1997 *Astrophysical Implications of the Laboratory Study of Presolar Materials*, AIP Conference Proceedings 402, American Institute of Physics, Woodbury, N.Y., 750 pp.

Black D C 1978 Isotopic anomalies in solar system material – What do they tell us?; In: *The Origin of the Solar System* (ed.) S F Dermott 583–596, (New York: John Wiley and Sons)

Boschler P, Gonin M, Sheldon R B, Zurbuchen Th, Gloeckler G, Hamilton D C, Collier M. R. and Hovestadt D 1996 Abundance of solar wind magnesium isotopes determined with WIND/MASS; In: *Solar Wind 8 Proceedings* pp. 1–4

Boulos M S and Manuel O K 1971 The xenon record of extinct radioactivities in the Earth; *Science* 174 1334–1336

Cameron A G W and Truran J W 1977 The supernova trigger for formation of the Solar System; *Icarus* 30 447–461

Cameron A G W 1984 Star formation and extinct radioctivity; *Icarus* 60 416–427

Cameron A G W, Höflich P, Myers P C and Clayton D D 1995 Massive supernovae, Orion gamma rays, and the formation of the Solar system; *Ap. J.* 447 L53–L57

Clayton D D 1975 Extinct radioactivities: Trapped residuals of presolar grains; *Ap. J.* 199 765–769

Clayton D D 1982 Cosmic chemical memory: a new astronomy; *Q. Jl R. Astr. Soc.* 23 174 212

Clayton D D and Hoyle F 1976 Grains of anomalous isotopic composition from novae; *Ap. J.* 203 490–496

Clayton R N, Grossman L and Mayeda T K 1973 A component of primitive nuclear composition in carbonaceous chondrites; *Science* 182 485–488

Fowler W A 1984 Experimental and theoretical nuclear astrophysics: the quest for origin of the elements; *Rev. Mod. Phys.* 56 149–179

Geiss J, Bühler F, Cerutti H, Eberhardt P. and Filleaux C H 1972 Solar-wind composition experiment; In: *Apollo 15 Preliminary Science Report, Section 15* NASA SP-289

Goldin D S 1998 *Future of Space Science.* Talk presented to the 191st Meeting of the American Astronomical Society, January 7, 1998, Washington, D.C. C-SPAN tape: 98-01-07-22-1, available from Purdue University Public Affairs Video Archives, Lafayette, IN, USA.

Hoppe P and Ott U 1997 Mainstream silicon carbide grains from meteorites; In: *Astrophysical Implications of the Laboratory Study of Presolar Materials* (eds.) T J Bernatowicz and E Zinner pp. 27–58. AIP Conference Proceedings 402, (Woodbury, N.Y.: American Institute of Physics)

Hoyle F 1975 A solar model with low neutrino emission; *Ap. J.* 197 L127–L131

Huss G R and Lewis R S 1995 Presolar diamond, SiC and graphite in chondrites: Abundances as a function of meteorite class and petrologic type; *Geochem. Cosmochim. Acta* 59 115–160

Hwaung G and Manuel O K 1982 Terrestrial-type xenon in meteoritic troilite; *Nature* 299, 807–810

Kaiser W A 1972 Rare gas studies in Luna-16-G-7 fines by stepwise heating technique. A low fission solar wind Xe; *Earth Planet. Sci. Lett.* 13 387–399

Kuroda P K and Manuel O K 1970 Mass fractionation and isotope anomalies in neon and xenon; *Nature* 227 1113–1116

Kuroda P K and Myers W A 1997 Aluminum-26 in the early solar system; *J. Radioanal. Nucl. Chem.* 211 539–555

Lavrukhina A K 1980 On the nature of isotopic anomalies in meteorites; *Nukleonika* 25 1495–1515

Lee J T, Li B and Manuel O K 1996 Terrestrial-type xenon in sulfides of the Allende meteorite. *Geochemical Journal* 30 17–30

Lewis R S, Srinivasan B and Anders E 1977 Reply to Manuel and Sabu; *Science* 195 209–210

Lewis R S and Anders E 1988 Xe-HL in diamonds from the Allende meteorite-composite nature; *Proc. Lunar Planet. Sci. Conf.* 19 679–680

Lugmair G W, Shukolyukov A and MacIsaac Ch 1996 Radial heterogeneity of ^{53}Mn in the early solar system and the place of origin of ordinary chondrites; *Lunar Planet. Sci.* 27 785–786

MacElroy J M D and Manuel O K 1986 Can intrasolar diffusion contribute to isotopic anomalies in the solar wind?; *J. Geophys. Res.* 9 D473–D482

Manuel O K, Hennecke E W and Sabu D D 1972 Xenon in carbonaceous chondrites; *Nature* 240 99–101

Manuel O K and Hwaung G 1983 Solar abundances of the elements; *Meteoritics* 18 209–222

Manuel O K and Ragland D E 1997 Diffusive mass fractionation effects across the isotopes of noble gases and magnesium in the solar wind and in solar flares. Abstract 281, 1997 *Midwest Regional Meeting of the American Chemical Society*, Osage Beach, Missouri, USA.

Manuel O, Ragland D, Windler K, Zirbel J, Johannes L, Nolte A 1998 Strange isotope ratios in Jupiter. Paper to be presented at 192nd Meeting of the American Astronomical Society, June 7–11, 1998, San Diego, CA, USA.

Manuel O K and Sabu D D 1975 Elemental and isotopic inhomogeneities in noble gases: the case for local synthesis of the chemical elements; *Trans. of the Missouri Acad. of Sci.* 9 104–122

Manuel O K and Sabu D D 1977 Strange xenon, extinct superheavy elements, and the solar neutrino puzzle; *Science* 195 208–209

Mathew K J and Begemann F 1995 Isotopic composition of xenon and krypton in silicate-graphite inclusions of the El Taco, Campo del Cielo, IAB iron meteorite; *Geochim. Cosmochim. Acta* 59 4729–4746

Marti K 1967 Isotopic composition of trapped krypton and xenon in chondrites; *Earth Planet Sci. Lett.* 3 243–248

Murty S V S and Marti K 1987 Nucleogenetic noble gas components in the Cape York iron meteorite; *Geochim. Cosmochim. Acta* 51 163–172

Oliver L L, Ballad R V, Richardson J F and Manuel O K 1981 Isotopically anomalous tellurium in Allende: Another relic of local element synthesis; *J. Inorg. Nucl. Chem.* 43 2207–2216

Ott U 1993 Interstellar grains in meteorites; *Nature* 364 25–33

Ott U 1996 Interstellar diamond xenon and timescales of supernova ejecta; *Ap. J.* 463 344–348

Rao M N, Garrison D H, Bogard D D, Badhwar G and Murali A V 1991 Composition of solar flare noble gases preserved in meteorite parent body regolith; *J. Geophys. Res.* 96 19321–19330

Reynolds J H 1960a Determination of the age of the elements; *Phys. Rev. Lett.* 4 8–10

Reynolds J H 1960b Isotopic composition of primordial xenon; *Phys. Rev. Lett.* 4 351–354

Richter S, Ott U and Begemann F 1998 Tellurium in pre-solar diamonds as an indicator for rapid separation of supernova ejecta; *Nature* 391 261–263

Rouse C A 1983 Calculation of stellar structure III. Solar models that satisfy the necessary conditions for a unique solution to the stellar structure equations; *Astron. Astrophys.* 126 102–110

Rouse C A 1985 Evidence for a small, high-Z, iron-like solar core; *Astron. Astrophys.* 149 65–72

Sabu D D and Manuel O K 1980 Noble gas anomalies and synthesis of the chemical elements; *Trans. Mo. Acad. Sci.* 9 104–122

Sahijpal S, Goswami J N, Davis A M, Grossman L and Lewis R S 1998 A stellar origin for the short-lived nuclides in the early solar system; *Nature* 391 559–561

Selesnick R S, Cummings A C, Cummings J R, Leske R A, Mewalt R A, Stone E C and von Rosenbinge T T 1993 Coronal abundances of neon and magnesium isotopes from solar energetic particles; *Ap. J.* 418 L45–L48

Shindo H, Miyamoto M, Matsuda J and Ito K 1985 Vapor deposition of diamond from methane-hydrogen mixture and its bearing on the origin of diamond in urelite: A preliminary report (abstract); *Meteoritics* **20** 754

Srinivasan B and Anders E (1978) Noble gases in the Murchison meteorite: Possible relics of s-process nucleosynthesis; *Science* **201** 51–56

Wasserburg G J 1987 Isotopic abundances: inferences on solar system and planetary evolution. *Earth Planet. Sci. Lett.* **86** 129–173

Zinner E 1997 Presolar material in meteorites: an overview. In *Astrophysical Implications of the Laboratory Study of Presolar Materials* (eds.) T J Bernatowicz, and E Zinner pp. 3–26. AIP Conference Proceedings 402, (Woodbury, N.Y.: American Institute of Physics)

The author wishes to apologise for the anger expressed in some of his comments here. Any perceived misbehaviour by others does not excuse misbehaviour in me.

Proceedings of the Indian Academy of Sciences

Earth and Planetary Sciences

CONTENTS

Special issue on: Isotopic Windows on Earth and Planetary Processes

Indexed in CURRENT CONTENTS